

**Identification of novel therapeutic targets in
Osteosarcoma for the development of Nanoparticle
based drug delivery systems**



A thesis submitted for the degree of Doctor of Philosophy by

Kusal Shasheen Payoe

College of Health, Medicine and Life Sciences

Brunel University London

February 2023

Declaration of Authorship

I, Kusal Shasheen Payoe, hereby declare that this report titled, "Identification of novel therapeutic targets in Osteosarcoma for the development of Nanoparticle based drug delivery systems" and all work undertaken in this thesis is of my own unless otherwise specified.

I confirm that:

- This work was done while in candidature for the degree of Doctor of Philosophy at Brunel University.
- Where the published work of others has been consulted, it is always clearly attributed.
- Where I have quoted from the work of others, the source is always given. With the exception of such quotations, this thesis is entirely my work.
- I have acknowledged all main sources of help.
- Where the thesis is based on work jointly with others, I have acknowledged those responsible and noted their contributions.

Shasheen Payoe

Date: 05/06/2023

Abstract

Osteosarcoma (OS) is the most common primary malignant tumour of the bone, with a high incidence rate in children and adolescents. Importantly, OS therapeutics has remained unimproved for the last 30 years and therefore, clinically unsatisfactory. It is understood that determining the mechanisms underlying OS tumorigenesis and progression, along with the identification of novel therapeutic targets can greatly aid in the clinical management of the disease. Thus, one important area in need of further exploration is the tumour microenvironment (TME), which consists of a plethora of extracellular matrix components, tumour associated fibroblasts and immune cells.

To determine the underlying mechanism(s) and identify novel therapeutic targets, we searched an OS gene microarray dataset deposited within the Gene Expression Omnibus, which included 84 primary OS biopsies and 12 primary Mesenchymal stem cell control samples. An alternative to R coding (GEO2R) was utilised to identify differentially expressed genes (DEGs) in OS, with further R analysis conducted to quantify levels of genetic association to OS. 1161 DEGs in OS were identified, consisting of 535 upregulated and 626 downregulated genes at cut-offs of $|\log_2FC| > 1$ and an adjusted $P\text{-value} < 0.01$. Through functional annotations, we show that the DEGs are involved in immune system processes, including defence and general immune responses. This suggests that the immune system is strongly linked to the OS microenvironment with DEGs potentially contributing to OS development and metastasis.

For the identification of immune based therapeutic targets in the OS TME, upregulated genes were additionally refined based on the gene ontology (GO) term “immune receptor activity”. Through GO based refinement, the immune receptor Formyl-Peptide

Receptor 3 (FPR3) was found to be significantly upregulated in OS and to have a close genetic association.

Through both in vitro and in vivo staining, we first show that FPR3 is specifically expressed on malignant bone cells of mesenchymal origin, with a lack of expression on normal bone cells. Thereafter, through functional in vitro cell migration assays, we determined its potential in becoming a therapeutic target in OS. Results showed that when targeted with a FPR3 specific peptide antagonist (WRW4), cell migration in two OS cell lines were significantly reduced. Observable differences in responsiveness to the peptide antagonist, between the two assayed OS cell lines, could be explained by differences in receptor expression levels as shown by flow cytometric analysis. An alternate role could relate to its use as a prognostic biomarker in OS.

For the therapeutic targeting of FPR3 in OS, we propose the use of Nanoparticle based drug delivery systems (NP-DDS). Nanoparticles (NPs) are highly promising tools for both clinical and therapeutic purposes. The surfaces of NPs can be modified for targeted therapy and the NPs themselves are able to controllably release drugs when used as drug carriers in NP-DDS. However, NPs are known to exhibit varying levels of toxicity, therefore, their biosafety still remains a concern. Here, we put forward the *Galleria Mellonella* (GM) model organism as an efficient, low-cost, high-throughput tool for determining NP toxicity in vivo. We utilise, for the first time, techniques such as flow cytometry, immunohistochemistry and a 4HNE ELISA, on GM larvae for the determination of NP-induced toxicity, in vivo. Based on the various assays, NP toxicity was found to be heavily dependent on physicochemical properties such as surface composition and size.

In addition, we investigate cellular ROS production, both in vitro and in vivo, to determine the mechanism's likelihood in playing a major role in NP induced toxicity, observed in vivo. Results show that intracellular ROS production is the likely mechanism underlying NP toxicity in vivo, however, tissue aggregation is an important feature of CNTs that induces strong toxicity.

Lastly, SPION induced immunotoxicity was observed in vivo with the use of GM larvae. Therefore, we aimed to determine if NP intracellular trafficking, intracellular fate and in particular, SPION related endosomal escape played a role in SPION induced immunotoxicity. Preliminary data is presented for this aspect in this study.

Overall, certain NP variants that were identified to be biologically safe, can be put forward as potential drug delivery agents for the treatment of diseases such as OS. These NPs can be designed for tumour specific delivery of therapeutic compounds such as receptor peptide ligands, whereby, the tumour target can be a receptor of interest with therapeutic potential such as FPR3.

Table of Contents

Abstract	ii
Acknowledgements	ix
List of abbreviations	xi
1. Introduction	1
1.1 Osteosarcoma	2
1.1.1 Osteosarcoma bone malignancy	2
1.1.2 Incidence and regions of primary OS malignancy.....	3
1.1.3 Types of OS.....	6
1.1.4 Histological characteristics of OS	7
1.1.5 Causation of OS.....	9
1.1.6 Current OS therapeutics	10
1.1.7 Components of the human immune system	14
1.1.8 The tumour microenvironment of OS and the immune niche.....	18
1.2 Nanotechnology and Nanotherapeutics	33
1.2.1 Overview of Nanotechnology	33
1.2.2 Nanomedicine: overview.....	34
1.2.3 Nanoparticle-based drug delivery systems	38
1.2.4 Therapeutic applications of NP-based DDS.....	44
1.2.5 Examples of Nanoparticle drug delivery vehicles.....	48
1.2.6 Nanotherapeutics in cancer.....	51

1.2.7	NP interactions with the immune system.....	52
1.2.8	Nanoparticle cellular uptake.....	54
1.2.9	Mechanisms of NP cellular uptake	56
1.2.10	Intracellular trafficking and cellular fate of NPs	61
1.2.11	Nanotoxicology.....	67
1.2.12	Differing mechanisms underlying NP toxicity	68
1.3	<i>Animal models to assess NP toxicity in vivo</i>	73
1.3.1	Use of animal models in NP toxicity assays	73
1.3.2	GM: a novel in vivo model organism to determine NP toxicity.....	75
1.3.3	GM larval innate immune system	78
1.3.4	Utility of GM in determining environmental NP toxicity.....	80
1.3.5	Utility of GM in determining NP potential as drug delivery agents	82
	<i>Aims and hypotheses.....</i>	85
	<i>2. Materials and Methods</i>	87
2.1	<i>Materials.....</i>	88
2.2	<i>Cell culture.....</i>	92
2.3	<i>Treatment of cells with SPIONs.....</i>	95
2.4	<i>Fluorescent imaging</i>	96
2.5	<i>Flowcytometric analysis</i>	102
2.6	<i>Antibodies and dilutions</i>	107
2.7	<i>Statistical analysis.....</i>	109

3. Novel Upregulated Immune Receptors in Osteosarcoma as Potential Therapeutic Targets	110
3.1 Introduction.....	112
3.2 Methodology.....	121
3.3 Results	156
3.4 Discussion.....	209
4. Formyl-Peptide Receptor 3 (FPR3) as A Novel Immune-Based Therapeutic Target in Osteosarcoma.....	231
4.1 Introduction.....	233
4.2 Methods	240
4.3 Results	248
4.4 Discussion.....	267
5. Galleria Mellonella Larvae: An Invertebrate Model System to Study Nanoparticle Toxicity	276
5.1 Introduction.....	278
5.2 Material and Methods	281
5.3 Results	296
5.4 Discussion.....	326
6. Reactive Oxygen Species (ROS) Production: A Major Mechanism Underlying Nanoparticle Toxicity.....	350
6.1 Introduction.....	352
6.2 Methods	354
6.3 Results	357

6.4 Discussion.....	373
7. Intracellular Trafficking and Cellular Fate of Superparamagnetic Iron Oxide Nanoparticles in Mouse Macrophages.....	378
7.1 Introduction.....	380
7.2 Methods	386
7.3 Results	394
7.4 Discussion.....	401
8. General Discussion.....	407
9. References	420
Appendices	i

Acknowledgements

Brunel, during my PhD journey, you have become a second home, a place of growth, a place of vast unforgettable memories, a place where lifelong relationships and friendships were created and a place, I will forever hold close to my heart. My progress through this roller-coaster of a PhD and eventual completion of a thesis I am hugely proud of, would not have been possible without the help, guidance, care, support and love of some people.

Firstly, I would like to share my utmost gratitude and appreciation to my amazing supervisor Dr Gudrun Stenbeck for her support, guidance, time and dedication towards my progress at Brunel. You have always been a wonderful mentor, a wealth of knowledge and a constant positive figure to help me overcome failures and move forward. As you always say, onwards and upwards! Thank you for always having your door open, for the amazing opportunities and for always having my best interest in mind. I look forward to keeping in touch and catching up to share all of our amazing endeavours to come. To those of you in the Stenbeck lab, past and present, you have taught me a lot over the years and during tough times, you have always been supportive and helpful. I will forever be grateful for the amazing friendships I have made during my time in the group. To the academics, I am grateful to have met and learnt from, thank you for your constant support, advice and constructive feedback over the years. A huge thank you in particular to Dr Terry Roberts, Dr Ronan McCarthy, Dr Christian Rudolph, Professor Felicity Gavins and Dr Annette Payne. To the technical staff of Heinz Wolff, thank you for your understanding and support during my time as a researcher. You have all played significant roles during my time at Brunel and I will never forget the memories I have made with each of you.

To my parents, you have always provided me with love, care, guidance, and advice to help me excel in all things I have put my mind to. During my time as a researcher, you have provided me with the strength, courage, and motivation to keep pushing forward every day. At times when most would give up, you showed me the importance of perseverance and always reminded me that great things happen to those who don't give up. To my brother, thank you for making me laugh after a tough day and for always keeping me on my toes. To my grandparents, from the very beginning, you filled me with knowledge and provided me with love, guidance and undying support. To my grandfather, you showed me the importance of knowledge, academia, hard work and dedication. But you also showed me the importance of balance, family and happiness, I live by your teachings of the more you do the more you learn and I will cherish these teachings forever.

To my colleagues in Heinz Wolff and particularly, to my work family in HNZW 102c. During my time at Brunel, I made this office a home away from home. To those close friends I have made in this office, I am truly thankful to have met you, for the lifelong friendships we have made, for the constant support you have provided me and for the unforgettable memories. And last, but certainly not least, to my most amazing, loving, caring, and understanding girlfriend Stefany. During this challenging time, you have been a constant pillar of support and love. You've helped me up when things weren't great and at moments of frustration, you made me see the brighter side of things. Over this past year, you made my time at Brunel and my experience as a researcher an enjoyable one, you played a huge part in motivating me and I am truly grateful to Brunel for bringing you into my life. I can't wait to see what amazing things you are destined to accomplish and never forget; you are a fantastic researcher and an even greater partner.

List of abbreviations

- 4-HNE: **4-Hydroxynonenal**
- AGE: **All of Gene Expression**
- AgNPs: **Silver Nanoparticles**
- AMPs: **Antimicrobial Peptides**
- APC: **Antigen-Presenting Cells**
- ARV: **Antiretroviral**
- ATP: **Adenosine Triphosphate**
- AuNPs: **Gold Nanoparticles**
- BBB: **Blood-Brain-Barrier**
- BM-MSCs: **Bone-Marrow Mesenchymal Stem Cells**
- BSA: **Bovine Serum Albumin**
- CFU: **Colony Forming Unit**
- CIE: **Clathrin/caveolae-independent endocytosis**
- CMC: **Carboxymethyl Cellulose**
- CME: **Clathrin-mediated endocytosis**
- CNTs: **Carbon Nanotubes**
- CTL: **Cytotoxic T Lymphocytes**
- CuO: **Copper Oxide**
- Cyclo: **Cyclophosphamide**
- DC: **Dendritic Cells**
- DDS: **Drug Delivery System**
- DCFDA: **2',7' -dichlorofluorescein diacetate**
- DEGs: **Differentially Expressed Genes**

- DMEM: **D**ulbecco's **M**odified **E**agle's **m**edium (DMEM)
- DO: **D**isease **O**ntology
- DAB: **D**iaminobenzidine
- DOSE: **D**isease **O**ntology **S**emantic and **E**nrichment
- ECL: **E**nhanced **C**hemiluminescent
- ECM: **E**xtracellular **M**atrix
- EDTA: **E**thylenediaminetetraacetic acid
- ELISA: **E**nzyme-linked **I**mmunosorbent **A**ssay
- FACS: **F**luorescence **A**ctivated **C**ell **S**orting
- FBS: **F**etal **B**ovine **S**erum
- FDA: **F**ood and **D**rug **A**dministration
- FPR3: **F**ormyl-peptide **R**eceptor **3**
- GC: Human **G**erminal **C**entre
- GEO: **G**ene **E**xpression **O**mnibus
- GEPIA: **G**ene **E**xpression **P**rofilng **I**nteractive **A**nalysis
- GM: **G**alleria **M**ellonella
- GO: **G**ene **O**ntology
- GO-ORA: **GO** overrepresentation enrichment analysis
- HIV: **H**uman **I**mmunodeficiency **V**irus
- HOB: **H**uman **O**steoblasts
- HRP: **H**orseradish **P**eroxidase
- ICI: **I**mmune **C**heckpoint **I**nhibitors
- IFN: **I**nterferon
- Ig: **I**mmunoglobulin
- IHC: **I**mmunohistochemistry/**I**mmunohistochemical

- IIS: **I**nate **I**mmune **S**ystem
- IL: **I**nterleukin
- IMS: **I**ndustrial **M**ethylated **S**pirit
- IONPs: **I**ron **O**xide **N**anoparticles
- KEGG: **K**yoto **E**nCyclopedia of **G**enes and **G**enomes
- LB: **L**ysogeny **B**roth
- L-MTP-PE: **L**iposome-**E**ncapsulated **M**uramyl **T**ripeptide
Phosphatidylethanolamine
- MDA: **M**alondialdehyde
- MM: **M**odule **M**embership
- MRI: **M**agnetic **R**esonance **I**maging
- MSC: **M**esenchymal **S**tem **C**ell
- MTP: **M**uramyl **T**ripeptide
- NAT: **N**ormal **A**djacent **T**issue
- NK: **N**atural **K**iller
- NP/s: **N**anoparticle/**N**anoparticles
- OS: **O**steosarcoma
- OD: **O**ptical **D**ensity
- OA: **O**verrepresentation **A**nalysis
- PA14: **P**seudomonas **A**eruginosa
- PAOS: **P**arosteal **O**steosarcoma (PAOS)
- PBS: **P**hosphate **B**uffered **S**aline
- PCA: **P**rincipal **C**omponent **A**nalysis
- PFA: **P**hosphate-buffered paraformaldehyde
- PI: **P**ropidium **I**odide

- PLGA: **P**oly (**L**actide-co-**G**lycolide)
- PM: **P**lasma **M**embrane
- PNS: **P**ost-**N**uclei **S**upernatant
- PNPs: **P**olymeric **N**anoparticles
- PO: **P**henol**o**xidase
- PPO: **P**rophenol**o**xidase
- ROS: **R**eactive **O**xygen **S**pecies
- SDS: **S**odium **D**odecyl **S**ulphate
- SPIONs: **S**uperparamagnetic **I**ron **O**xide **N**anoparticles
- TAM: **T**umour-**A**ssociated **M**acrophages
- TBHP: **t**ert-**b**utyl **h**ydroperoxide
- TCR: **T**-**C**ell **R**eceptor
- TEM: **T**ransmission **E**lectron **M**icroscopy
- THC: **T**otal **H**emocyte **C**ount
- TIL: **T**umour **I**nfiltrating **L**ymphocytes
- TiO₂: **T**itanium **d**ioxide
- TME: **T**umour **M**icro**e**nvironment
- TNP: **T**heranostic **N**anoparticle
- TOS: **T**elangiectatic **O**steosarcoma
- WGA: **W**heat **g**erm **a**gglutinin
- WGCNA: **W**eighted **g**ene **c**o-expression **n**etwork **a**nalysis (WGCNA)
- ZnONPs: **Z**inc **O**xide **N**anoparticles

1. Introduction

1.1 Osteosarcoma

1.1.1 Osteosarcoma bone malignancy

The cancerous disease Osteosarcoma (OS) (An et al., 2021; Nagarajan et al., 2011; Armakolas et al., 2016) is known to be the most common non-haematological primary malignant tumour of the bone (Bielack et al., 2009; Luetke et al., 2014; Picci, 2007; Nagarajan et al., 2011; Mirabello et al., 2009b), as shown in figure 1.1, accounting for 20-40% of all identified bone cancers (Ho et al., 2017; Whelan et al., 2012). The disease has been identified to occur most commonly in bone tissue of children and adolescents (Grimer, 2005; Akiyama et al., 2008; Bielack et al., 2009; Brown et al., 2017; Mirabello et al., 2009b; Armakolas et al., 2016; Nagarajan et al., 2011; Wang et al., 2020) and is said to be the 8th most common form of malignancy among all childhood malignancies (Ottaviani and Jaffe, 2009), however, it has also been identified in patients over the age of 40 (Bielack et al., 2009). Despite the rarity of the malignancy, overall, OS is still the most common malignant tumour found in the bone tissues of children (Nagarajan et al., 2011), typically requiring neoadjuvant chemotherapy and/or surgical resection as forms of treatment (Sun et al., 2019).

Like in all malignancies, OS tumour cells are hallmarked by six biological capabilities that are acquired during tumour development. These include sustaining proliferation, evading growth suppressors, resisting cell death/apoptosis, evading cellular senescence, inducing angiogenesis, and becoming invasive and metastatic. Genomic instability is known to be a major mechanism underlying OS tumorigenesis and thus, the described hallmarks of cancer. Due to progresses in tumour developmental research, two further cancer hallmarks which also apply to OS were identified to be energy metabolism and immune evasion (Hanahan and Weinberg, 2011).

1.1.2 Incidence and regions of primary OS malignancy

The incidence rate of OS in children and adolescents, which is defined as 0-24 years age range, averages at 4.2 per million new cases in males and 3.1 per million new cases in females (Ho et al., 2017). Furthermore, a decrease in OS incidence rate is observed for persons aged 25-59, which has been reported to be 1.7 and 1.4 per million new cases in males and females, respectively. The decrease in incidence rate is followed by a steep increase among persons older than 60 years, with the rate being 4.6 and 3.3 per million in males and females, respectively (Mirabello et al., 2009a; Simpson and Brown, 2018). Therefore, OS portrays two separate peaks in incidence presented in figure 1.1, which are observed between the ages of 10 and 19 years and in the elderly age group after the age of 60 years. The peak in children and young adults is associated with the pubertal growth spurt and in the older age group, with Paget's disease (Simpson and Brown, 2018; Picci, 2007; Mirabello et al., 2009b; Whelan et al., 2012). The overall ratio of male-to-female cases of OS within the respective age groups (0–24 years, 25–59 and over 60 years) has been reported to be 1.43:1; 1.28:1; 1.01: 1, respectively (Mirabello et al., 2009a). Overall, OS is said to be more common in men than in women in the majority of countries, with worldwide incidence of OS being approximately 3–4 per million new cases (Mirabello et al., 2009b). In the clinical setting, OS patients commonly describe pain and body swellings as lifestyle related adverse effects of the malignancy. In addition, systemic symptoms of OS have been reported to include weight loss, pallor, fever and anorexia (Picci, 2007).

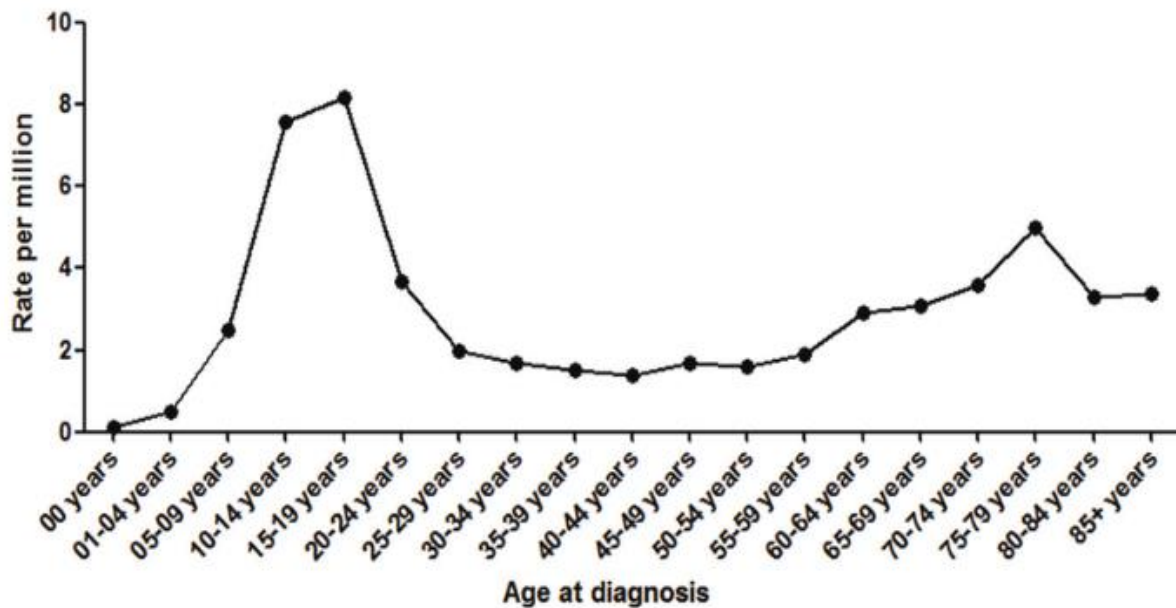


Figure 1.1: **Incidence rate of OS in children, adolescents, and adults.** The incidence rate per million dot plots for OS, presents the described two separate peaks in OS incidence observed between the ages of 10 and 19 years and in the elderly age group, after the age of 60 years. Image from: (Nie and Peng, 2018).

It has been reported that the majority of all OS malignancies arise within the metaphyseal area of long tubular bones of the lower limb (60%) (Bielack et al., 2002; Alfranca et al., 2015), which can be split into the distal femur (40%) and proximal tibia (20%) (Xi et al., 2019; Moore and Luu, 2014; Alfranca et al., 2015) (Figure 1.2). Therefore, OS frequency is greatest in the distal femur, with approximately 75% of all patients suffering from OS located around the knee (Huang et al., 2018). Thereafter, the remaining OS malignancies have been reported to arise within the metaphyseal area of long skeletal bones of the upper limb (9%), such as the humerus, and the pelvis (8%) (Moore and Luu, 2014; Whelan et al., 2012). Therefore, it can be inferred that OS occurs less commonly in the axial skeleton and within other non-long tubular bones. Furthermore, in relation to its primary localisation within the host skeleton, OS is said to rarely arise in soft tissue (Picci, 2007).

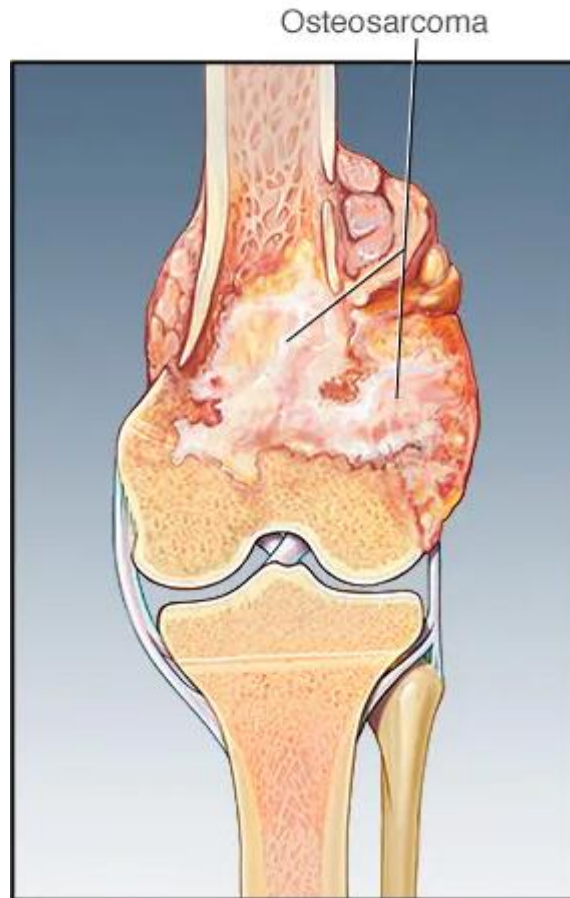


Figure 1.2: Schematic representation of a primary Osteosarcoma tumour on the distal head of a human femur. The image presents an example of a primary Osteosarcoma tumour, that are known to commonly occur within the metaphyseal area of long tubular bones of the lower limb, such as the femur. Image from: Mayo Clinic.

Since OS typically occurs in the metaphyses of long bones, disease presentation is regularly associated with the onset of pain and swelling in the tumour associated bone. The onset of pain is often hallmarked by a level of intensity sufficient enough to wake the patient from sleep (Isakoff et al., 2015).

Metaphyses of long bones have rich anatomical blood supplies, hence, OS tumour cells portray a strong tendency to metastasise early on, commonly through hematogenous spread and at times through lymphatic spread to regional lymph nodes (Hattori and Yamamoto, 2012; C. J. Li et al., 2016; Martin et al., 2012). Therefore, in

general, malignant OS is known to progress rapidly (C. J. Li et al., 2016; Martin et al., 2012), with approximately 15-20% of OS patients presenting clinically detectable metastases at the time of diagnosis (Isakoff et al., 2015). When OS metastasis takes place, the lung is said to be the most common site of tumour metastasis, with a 98% chance of potential development of a secondary metastasised tumour. The lung tissue is followed by alternate bone sites having a 37% chance, the thoracic pleura (33%), the heart (20%), kidney and liver (17%), diaphragm (15%) and finally, the mediastinum of the thorax (11%) (Westra et al., 1998; SALAH et al., 2014).

1.1.3 Types of OS

OS is thought to originate from transformed bone mesenchymal stem cells and is characterised by the production of osteoid tissue and osteoid or spindle shaped stromal cells that deposit immature bone within the tumour. (Wadhwa, 2014; Abarrategi et al., 2016). The osteoid tissue and immature bone characteristics of OS, are known to be produced by the malignant osteoblast tumour cells located adjacent to the growth plates (Luetke et al., 2014; Mirabello et al., 2009b; Bielack et al., 2002; Zhang et al., 2019; Jo and Fletcher, 2014; Picci, 2007; Abarrategi et al., 2016). Tumours are generally classified as primary and secondary. Primary OS is then divided into intramedullary/central and surface osteosarcomas (Kundu, 2014), which further divide to make up a broad spectrum of subclassifications based on tissue histological appearance (Abarrategi et al., 2016).

Central

Conventional Osteosarcoma

Conventional OS is described as the most common type of OS, due to its representation in 80% of all OS cases that primarily affects individuals during their first

and second decades of life. The OS type has a broad spectrum of histological appearances, therefore, giving rise to four distinct tumour subclassifications based on the predominant type of malignant stromal cell composing the tumour tissue (osteoblastic, chondroblastic, fibroblastic, giant cell rich). However, there is no significant prognostic relevance between the groups (Franceschini et al., 2019).

Telangiectatic osteosarcoma

Telangiectatic osteosarcoma (TOS) represents 4% of all OS cases. A histological examination has shown that TOS is characterised by dilated blood-filled cavities and high-grade sarcomatous cells, which are located on the septae and the peripheral rim (Liu et al., 2013).

Surface

Parosteal osteosarcoma

Parosteal osteosarcoma (PAOS) originates from the periosteum and is determined to be a low-grade OS. PAOS represents 4-6% of all OS cases and most cases of PAOS affect the posterior-distal femur, however, other sites that have also been affected include the proximal humerus and proximal tibia (Samardziski et al., 2009).

Periosteal osteosarcoma

Periosteal osteosarcoma is less common than PAOS and has a mostly cartilaginous matrix component. It commonly arises within the periosteum, specifically between the cortex and the cambium layer of the periosteum (Misaghi et al., 2018).

1.1.4 Histological characteristics of OS

OS is thought to originate from mesenchymal tissue and specifically, mesenchymal stem cells (An et al., 2021). Therefore, a histological examination of conventional OS will show that it is characterised by malignant spindle or polyhedral shaped

mesenchymal cells with pleomorphic nuclei, scattered mitotic figures, varying levels of anaplasia and an ability to generate immature neoplastic bone (osteoid) (C. J. Li et al., 2016; Durfee et al., 2016a) (Figure 1.3). Therefore, disorganised and immature osteoid production is a hallmark of OS and must be present for a positive diagnosis. Conventional osteosarcomas have a cellular matrix consisting of osseous, cartilaginous and fibrous elements; however, one cellular matrix type will always dominate. Therefore, the OS tumours can be further subtyped based on the dominant cellular matrix type portrayed. Similarly, other OS types will also show high-grade morphology in addition to areas of ample giant cells, small cells, or epithelioid morphology. Finally, low grade central and surface OS will display woven micro trabeculae of bone, contained within a cellular fibrous stroma (Durfee et al., 2016a).

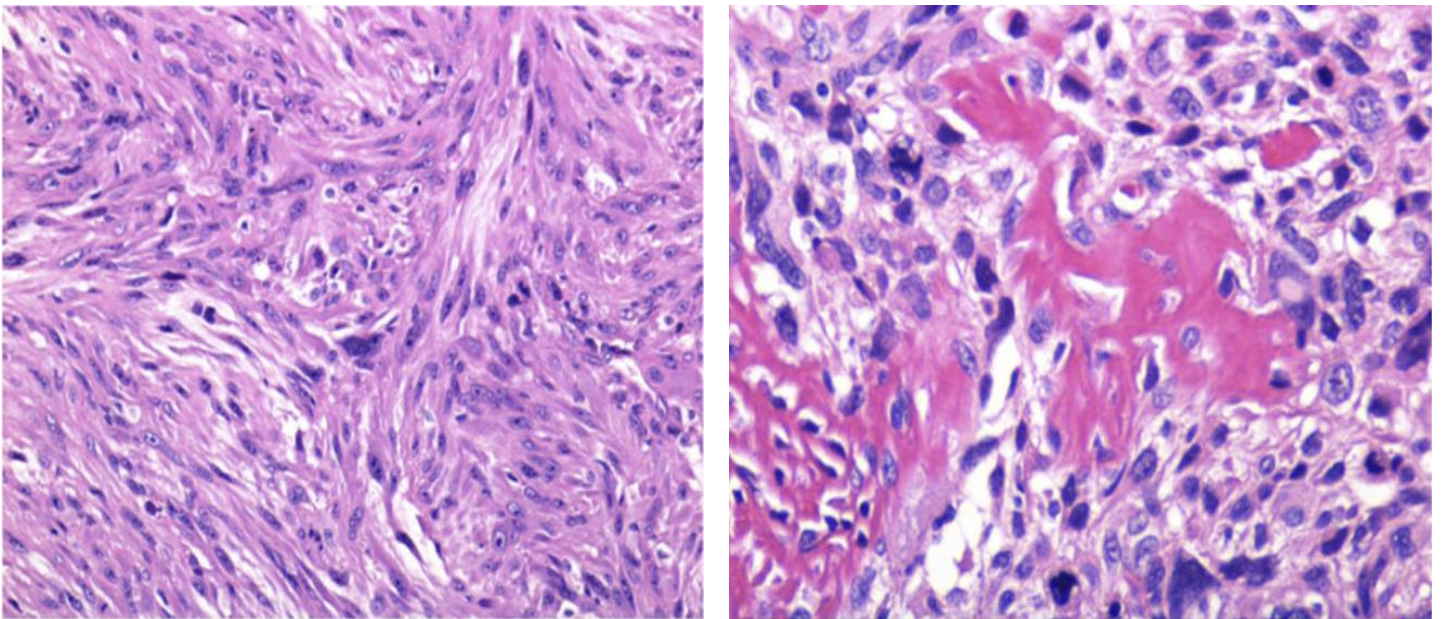


Figure 1.3: Histopathological analysis of primary Osteosarcoma tumour tissue. The above images show histological analysis conducted on tissue sections obtained from a primary Osteosarcoma tumour, whereby, the tissue sections were stained using a standard Haematoxylin and Eosin stain for the visualisation for cellular nuclei and surrounding tissue. The coloured bright field image (A) presents the malignant spindle and polyhedral shaped mesenchymal cells that are said to characterise conventional Osteosarcoma tumours. Image (B), presents the malignant Osteosarcoma tumour cells (stained blue with Haematoxylin) forming immature neoplastic bone, termed Osteoid. Image from: (Camacho-Vanegas et al., 2013).

1.1.5 Causation of OS

OS portrays common hallmarks of human cancer, which include genomic instability/disorganisation, chromosomal aberrations, dysregulation of tumour suppressor genes and absence of DNA repair (de Azevedo et al., 2020). Thus, a definitive causation behind OS tumorigenesis has yet to be determined. However, a specified list of risk factors has been collated, that are known to predispose individuals to OS (Ho et al., 2017). These risk factors include rapid bone growth, radiation and some genetic predispositions to OS. The specific syndromes that have been identified to genetically predispose individuals to OS include Li-Fraumeni syndrome. It is the most common genetically predisposing syndrome to OS and is caused by a mutation in the TP53 gene. Li-Fraumeni syndrome is then closely followed by hereditary retinoblastoma. Less common genetic predispositions to OS include Rothmund-Thomson syndrome type 2, Werner syndrome, Bloom syndrome and Diamond Blackfan anaemia (Kansara et al., 2014; Calvert et al., 2012). In addition, new and current research indicates that the risk factors associated with OS development, may be related to genetic variations at the germline level and physiological factors such as height, high birth weight (Mirabello et al., 2011) and high levels of pubertal hormones (Musselman et al., 2012).

Overall, reports have shown that in most cases, OS pathogenesis is an after-effect of chromosomal aberrations and genomic instability (Kruzelock et al., 1997; Morrow and Khanna, 2015). With relevance to genetic predispositions, 70% of all patients suffering from OS have loss-of-function gene mutations, often associated with the TP53 and Retinoblastoma (RB) genes (Rickel et al., 2017; Martin et al., 2012; de Azevedo et al., 2020; Corre et al., 2020), which are found to play critical roles in most OS tumour developments. In addition to chromosomal abnormalities, studies have shown that

somatic mutations that induce the malfunction of tumour suppressor functionalities are a defining mechanism behind OS tumorigenesis and progression. Therefore, it can be said that there are a diverse range of genetic changes that may lead to the development of OS (Durfee et al., 2016b). However, there isn't one specific genetic causative event that has been identified as the true cause for OS development (Durfee et al., 2016a).

1.1.6 Current OS therapeutics

OS is reported to have a tendency to frequently metastasise (Bouvier et al., 2016), with 80-90% of OS patients being assumed to have developed micro-metastatic disease at time of disease diagnosis (Luetke et al., 2014). Therefore, due to characteristics of a high degree of malignancy, strong invasiveness, rapid disease progression, and a unignorable high mortality rate, many scientific studies have looked into the treatment of OS (Zhao et al., 2021).

The overall improvement of OS patient survival has long proved to be a challenge for researchers and clinicians alike, with advancements in OS disease treatment being a significant requirement (Gill and Gorlick, 2021). Based on current knowledge in the field of OS therapeutics, the gold standard for clinical OS treatment remains as systemic chemotherapy and the surgical resection of the malignancy, in cases that portray sufficient surgical margins allowing for tumour removal (An et al., 2021). Prior to 1970, OS treatment primarily involved surgical resection which had an undesirably low impact on patient survival. However, when Rosen et al. introduced pre-operative chemotherapy as a therapeutic strategy in the early 1980s (An et al., 2021; Chou et al., 2008; Tarone et al., 2022), there was a dramatic improvement in the long-term survival of OS patients with localised disease (Isakoff et al., 2015; Tarone et al., 2022).

Henceforth, neoadjuvant chemotherapy using methotrexate, doxorubicin, cisplatin and ifosfamide, has increased in popularity over the years (Longhi et al., 2006; Tarone et al., 2022). Studies have shown that through the utilisation of neoadjuvant OS chemotherapy strategies, the size of OS tumours can be significantly reduced. Furthermore, micro-metastases that potentially follow as a consequence of OS tumour surgical resection, are eradicated. Thus, the combination of neoadjuvant chemotherapy and further systemic chemotherapy is now standard for OS treatment (Lamplot et al., 2013; Tarone et al., 2022).

Due to the clinical advancements of standard OS therapeutic strategies, the clinical management of OS cases and the long-term survival rate of OS patients have shown noticeable improvements overtime (Xi et al., 2019). The patient survival rate which began at a reported dismal 20-30% prior to the 1970s, has gradually increased to the current survival rate of 60-70%. (Isakoff et al., 2015; Ferrari et al., 2012; Marina et al., 2016). However, since this significant improvement in patient survival, patient overall outcomes have not shown further significant improvements (Longhi et al., 2006; Lamplot et al., 2013), with the overall prognosis of OS patients remaining poor and not significantly improved in over 30 years (Kawai et al., 2017). This provided evidence towards a lack of general scientific progress in the field of OS therapeutics and the need for novel and more efficacious therapeutic strategies.

This lack of prognostic improvement is especially the case for patients with metastasis at diagnosis, with the five-year survival rate remaining as (19-30%) and therefore, clinically unsatisfactory (Huang et al., 2012; Mialou et al., 2005; Thayanithy et al., 2012; Sheng et al., 2021). Importantly, patients who present metastatic disease, along with patients presenting tumour reoccurrence after treatment, continue to suffer from unsatisfactory outcomes due to failures presented by current therapeutic strategies

(Sheng et al., 2021). This is also the case for patients presenting localised OS tumours, with some groups of patients remaining at high risk of eventual relapse, post-surgical resection and chemotherapy. Moreover, patients with tumours presenting a low degree of necrosis in response to chemotherapy, are said to have poorer survival than patients with more chemotherapy-responsive tumours (Ferguson and Goorin, 2001). In relation, development of metastatic tumour resistance to current neoadjuvant chemotherapeutic drugs has been observed, in addition to depleted long-term survival in patients (Kawai et al., 2017). Therefore, overall, it can be said that tumour size, stage at presentation and tumour response to chemotherapy can prove to be reliable indicators of overall patient prognosis (Masood, 2016).

In order to improve patient prognosis, it is evident that an earlier diagnosis of OS is of great importance (Z. Liu et al., 2022). If an OS patient is diagnosed at an early stage, it is likely that the patient will have a localised primary tumour lesion and a markedly greater five-year survival rate (70%) (Huang et al., 2012; Mialou et al., 2005) when compared to patients with metastatically active OS (19-30%) (Huang et al., 2012; Mialou et al., 2005; Thayanithy et al., 2012). However, OS is still often diagnosed at a late stage (Sakamoto and Iwamoto, 2008; Brown et al., 2017; Kager et al., 2003). Hence, these high-risk patients, in particular, may potentially benefit from investigations into novel therapeutic targets and novel agents (Ferguson and Goorin, 2001).

Novel OS therapeutics targeting tumour cells or the tumour microenvironment (TME), may help to overcome the limitations portrayed by current therapeutics and thus, improve patient survival. An example includes immunotherapy, whereby, immunotherapeutic strategies have shown improved prognoses with reduced side effects when compared to conventional therapies, particularly in melanoma and

hematologic malignancies (Luke et al., 2022; Mei et al., 2022). Frequently used immunotherapeutic strategies for OS include immune checkpoint inhibitors (ICIs), cytokines, adoptive T-cell therapy and cancer vaccines. ICIs, which are known to be the representative immunotherapy for OS, work by activating and enhancing the antitumour effects of immune cells in OS patients (Lu et al., 2022). Examples of ICIs, include cytotoxic T-lymphocyte antigen 4 (CTLA-4) inhibitors, programmed cell death protein-1 (PD-1) and programmed death-ligand 1 (PD-L1) (Luke et al., 2022; Mei et al., 2022). However, despite their advantageous therapeutic effects on various kinds of malignant tumours, particularly hematopoietic tumours, the prognostic improvement of OS patients through ICI intervention remains clinically unsatisfactory (Zhang et al., 2022).

From the aforementioned, it is clear that there is an urgent need for further scientific advancements in the field of OS treatment (Grimer, 2005; Akiyama et al., 2008). It can be said that the identification of novel and effective biological therapeutic targets, therapeutic strategies, disease biomarkers and/or novel molecular mechanisms underlying OS, is of utmost importance to avoid chemotherapy resistance, reduce lung metastasis, improve the therapeutic efficacy of OS treatment and thus, improve the clinical prognosis of OS patients (Xi et al., 2019; Z. Liu et al., 2022). Of interest, is the significant need for the identification of novel biological therapeutic targets highly associated with the OS trait, and the development of novel targeted OS therapeutic strategies for the treatment of OS (Otokesh et al., 2018). Thereby, potentially overcoming the inefficacies of current therapeutic strategies. However, despite the scientific research conducted on OS over the years, only a few diagnostic biomarkers and therapeutic biological targets have been identified in OS patients (Xi et al., 2019). Therefore, several studies have been conducted to investigate the molecular

characteristics of the malignancy and thus, determine novel therapeutic targets. However, many have struggled in identifying these novel targets due to high levels of disease heterogeneity (Kansara et al., 2014).

In relation, improvements in OS molecular profiling, along with the generation of validated cellular model systems and large OS tissue banks have led to an increase in the understanding of OS biology and the identification of therapeutic biomarkers. OS tumour cells have been previously investigated, for the identification of cell surface proteins that may be of relevance as potential therapeutic targets. These surface proteins, including B7-H3, GD2 and HER2, have been targeted using techniques such as antibody–drug conjugates and/or adoptive cell therapies for the treatment of OS (Gill and Gorlick, 2021).

However, the identification of novel therapeutic targets and disease biomarkers for OS is still of great importance. Therefore, novel studies investigating the surrounding OS TME to identify novel druggable OS therapeutic targets can be of significant importance.

1.1.7 Components of the human immune system

The immune system is described as an interactive and intricate network consisting of lymphoid organs, cells, humoral factors, and cytokines. Being the host's first line of systemic defence, the immune system carries out a major function of detecting exogenous agents such as microbes or chemicals, thereby, protecting and preserving the integrity of the host (Mogensen, 2009; Schultz and Grieder, 1987). Abnormal function of the immune system, such as underactivity, results in issues such as severe infections, immunodeficiency disorders and in some cases, the formation of tumours. On the other hand, overactivity can result in allergic and autoimmune diseases

(Mogensen, 2009). The immune system is divided into two subsystems, the innate and adaptive immune systems, which are differentiated based on the speed and specificity of the required immune response. The innate immune system is the first point of interaction between foreign substances and the immune system. Thus, the term innate immunity encompasses elements of the immune system which provide immediate host defence: neutrophils, monocytes, macrophages, complement proteins, cytokines, and acute phase proteins (Parkin and Cohen, 2001). The innate immune system, therefore, is the first to mount an immune response against exogenous agents. This is mediated by phagocytic macrophage recognition of surface receptors on foreign substances, which in turn, induce inflammatory cytokine production (Mogensen, 2009). Figure 1.4 presents an overview of the described elements that make up the innate immune system and the role they play in providing immediate host defence.

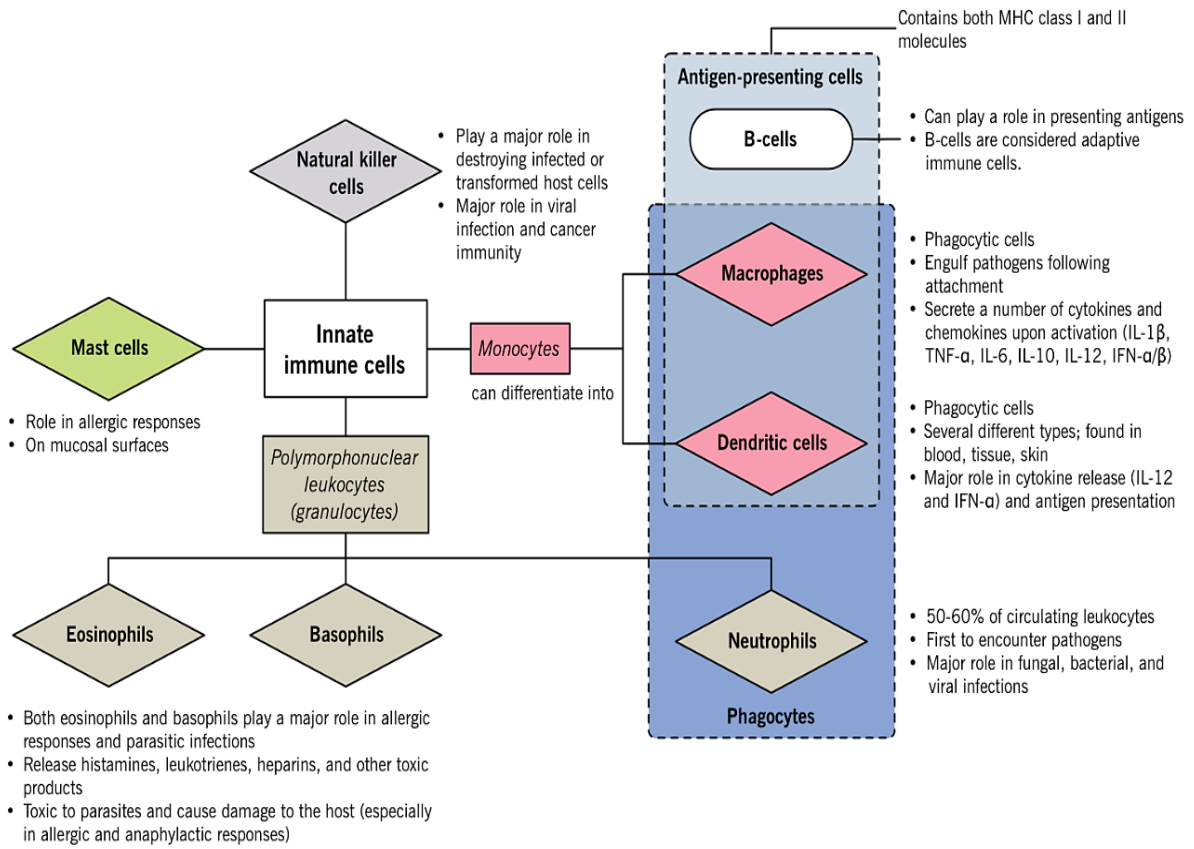


Figure 1.4: Flow-diagrammatic overview of the human innate immune system. The figure shows a flow-diagrammatic representation of the cellular component of the human innate immune system, and their role in being the host's first line of defence. The major immune cell population in the innate immune system are phagocytic cells, such as macrophages, dendritic cells and neutrophils, with macrophages and dendritic cells differentiating from monocyte precursor cells. The innate and adaptive immune systems are linked through the interplay between phagocytic cells of the innate immune system and B and T lymphocytes of the adaptive immune system. The phagocytic cells are known to activate B and T cells through antigen recognition and presentation. Image from: Chaudhry, 2016.

As shown in figure 1.4, innate immune progenitor cells are capable of activating and differentiating into specialised phagocytic innate immune cells, such as macrophages and dendritic cells. The differentiated phagocytic cells play a major role in cytokine release, which in turn, attracts other phagocytic cells in circulation that express chemokine receptors on their surface, such as neutrophils and monocytes (Janeway CA Jr Walport M, et al., 2001).

The innate immune system, as described, provides immediate defence against foreign artefacts. On the other hand, the adaptive immune system, despite the lack of immediate immune response, provides long-lasting immunity against exposed foreign substances. In brief, the adaptive immune system provides long-lasting immunity against infections, diseases and other foreign matter by developing an immunological memory that is mediated by the differentiation of B-lymphocytes into memory lymphocytes. During host development, immature B and T lymphocytes undergo antigen receptor gene expression, whereby, they acquire an enormously diverse set of antigen-specific receptors that allow the cells to recognise a vast amount of potential host challenges (Bonilla and Oettgen, 2010). Once the foreign substance is eliminated following exposure, the foreign artefact specific long-lived memory lymphocytes are generated, which strongly and rapidly respond to the foreign substance during the subsequent period of exposure. In the case where the innate immune system was unable to destroy the foreign substance(s), the adaptive immune system is usually activated a few days after (Chaplin, 2010). The two main types of an adaptive immune response, include humoral immunity, which is antibody mediated and relies on B lymphocyte mediated antibody production, and cell mediated immunity, which relies on T lymphocytes and other cells (Snyder, 2017) (Figure 1.5). The figure presented below provides an overview of the adaptive/acquired immune system, the cells involved and how immature immune cells differentiate into specialised adaptive immune cells to carry out antigen specific immune functionalities.

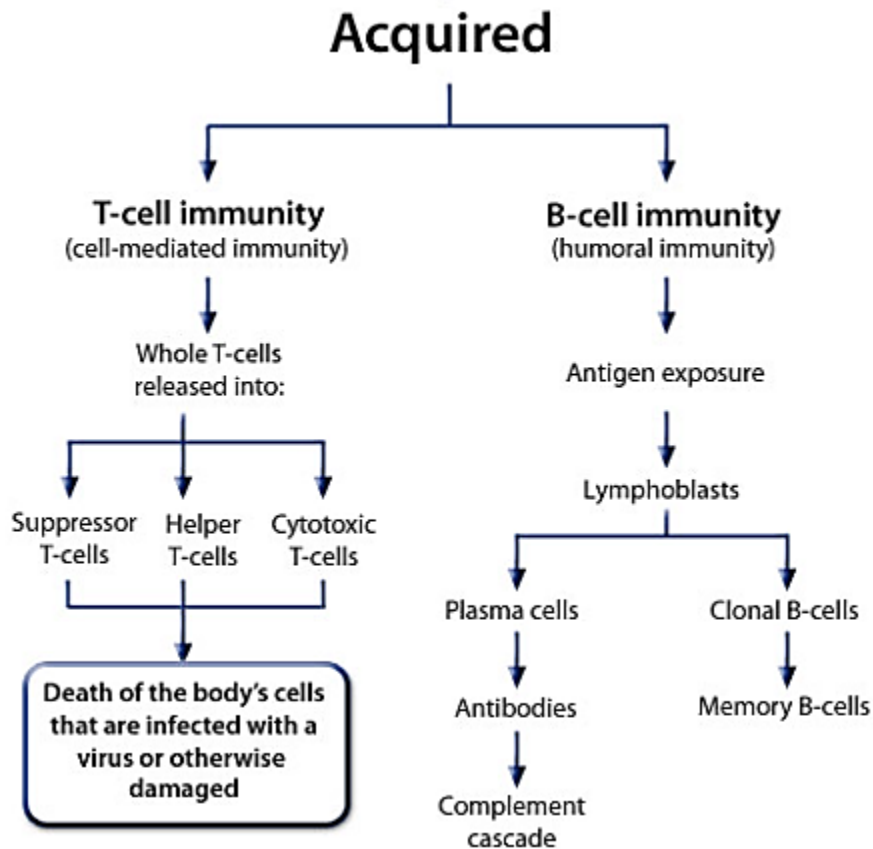


Figure 1.5: Flow-diagrammatic overview of the human adaptive immune system. The figure shows a flow-diagrammatic representation of the cellular and humoral components of the human adaptive immune system, and their role in antigen specific immune responses. Humoral immunity is mediated by circulating antibodies, produced by B lymphocytes that recognise antigens presented to them by phagocytic cells of the innate immune system. Cell mediated immunity of the adaptive immune system relies on T lymphocytes and other T lymphocyte derived cell populations. Image from: Paul et al.

1.1.8 The tumour microenvironment of OS and the immune niche

The OS-TME is a highly specialised and complex heterogenous milieu consisting of different local cell types, mineralised extracellular matrix components, tumour associated stromal cells, vascular cells and infiltrating immune cells, in a growth factor rich matrix containing an abundance of calcium (Jahanban-Esfahlan et al., 2018; Jahanban-Esfahlan, Seidi, and Zarghami, 2017; Baghban et al., 2020; Corre et al., 2020; Labani-Motlagh et al., 2020). Therefore, the TME is made up of a complex interconnected network of protagonists and portrays significant cellular diversity.

These cells interact via direct cellular contact or in an autocrine/paracrine/endocrine manner with the use of cytokines and growth factors (Heymann and Heymann, 2017).

It is understood that the phenomena of tumorigenesis and tumour progression are influenced by two independent factors, namely the rearrangement of components of the TME through dynamic and mutual crosstalk and the genetic/epigenetic changes within tumour cells (Jahanban-Esfahlan, Seidi, Monhemi, et al., 2017). Thus, it is well understood that the TME, embedded in a modified extracellular matrix, has a strong influential role in the initiation of cancerous tumours (tumorigenesis) and tumour development (Brassart-Pasco et al., 2020). The TME promotes tumorigenesis and tumour progression, by promoting the emergence of cancer-initiating cells and providing all the non-cellular factors required for their quiescence, proliferation and migration (Neophytou et al., 2021). Furthermore, in the context of tumour progression, the TME has an important influential role in tumour growth, tissue invasion and metastasis (Whiteside, 2008), which is reported to be carried out through the metabolic based communications between the TME and malignant tumour cells. These metabolic communications are vital for tumour progression, especially in oxygen or nutrient-deprived microenvironments (Gourand et al., 2018). However, in addition to communications between tumour cells and non-malignant cells of the TME, the tumour cells are also frequently communicating with the extracellular matrix (ECM) that makes up the tertiary component of the TME (Winkler et al., 2020). Bidirectional communication between cells in the TME and the ECM, is said to be carried out through cell-cell contact mechanisms and ECM macromolecules. These communications have been proposed to determine tumour progression and cancer metastasis (Winkler et al., 2020; Neophytou et al., 2021).

The cells of the TME can be separated into three well-defined niches based on their functionality: an immune niche that takes part in local immune tolerance, a vascular niche that plays a role in tumour cell migration and a metastatic niche that is made up of metastatic tumour cells (Plaks et al., 2015; Ordóñez-Morán and Huelsken, 2014; Murgai et al., 2015). With respect to OS, over recent years, more importance has been given to the theory that the TME has a role in determining the “bone niche”. The consolidated bone niche then participates in the progression of bone tumours and in establishing resistance against current neoadjuvant chemotherapies (Heymann and Heymann, 2017). However, it has been understood that in order to develop accurate, efficacious and tumour targeted novel therapeutic strategies for OS, a more in-depth understanding of the complex OS TME and its niches are required. Therefore, further leading to the potential identification of therapeutic biomarkers in the TME for targeted OS therapy (Wessel and Kaplan, 2022). Figure 1.6 presents a schematic representation of the complex OS TME. The schematic diagram shows the known interactions between the three well-defined niches of the OS TME and provides information on how the niches may promote or prevent tumour progression.

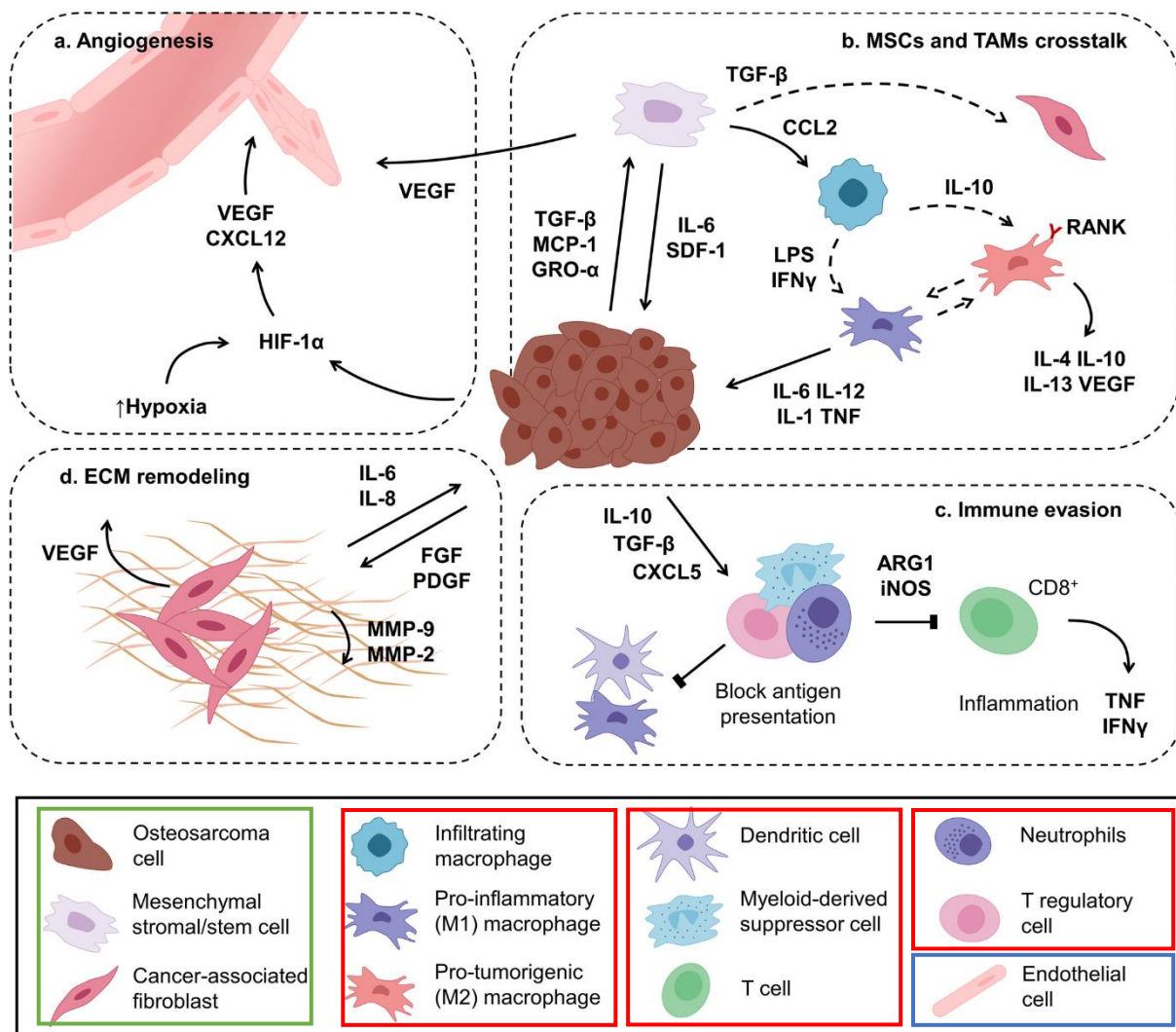


Figure 1.6: The complex OS tumour microenvironment. The figure presents a schematic representation of the OS TME and its three well-defined niches, described in the text above. Within the schematic diagram, known interactions between the immune (highlighted red), vascular (highlighted blue) and metastatic niches (highlighted green) are clearly shown. (a) Tumour cells interact with endothelial cells and MSCs to promote the release of HIF-1 α VEGF, which induces angiogenesis. (b) Bone marrow-MSCs are attracted to the tumour site by CXCL12 and MCP-1, secreted by OS cells. Within the TME, MSCs are normally reprogrammed by tumour cells, which promote their differentiation into cancer-associated fibroblasts. Circulating macrophages can infiltrate the TME and differentiate into pro-inflammatory M1-like macrophages that have anti-cancer activity, or anti-inflammatory M2-like macrophages that promote tumour proliferation and angiogenesis. (c) OS cells promote immunosuppression through the activation of T regulatory cells, myeloid-derived suppressor cells, and neutrophils. (d) Cancer-associated fibroblasts are activated by FGF and PDGF released by tumour cells, which subsequently promote ECM remodelling. ARG1, arginase 1, iNOS, inducible nitric oxide synthase, LPS, lipopolysaccharide, SDF-1, stromal cell-derived factor-1. Image from: (Rodrigues et al., 2022).

Scientific evidence supporting the fact that tumours are generally infiltrated by immune cells has been thoroughly documented over the years (Mihm et al., 1996; Balkwill and Mantovani, 2001), with some theories providing evidence towards tumour-immune

infiltrating cells promoting tumour invasion and metastasis (Man et al., 2013). OS is considered less immunogenic than cancers such as melanoma or renal cell carcinoma, thus, potentially making immunotherapy for OS less effective (Yahiro and Matsumoto, 2021). However, due to the proximity of OS tumours to the hematologic niche, immune cells are often found closely associated to the tumour and when these cells infiltrate the tumour, they generate the tumour immune niche (Heymann et al., 2019). The well characterised human immune system, consisting of both innate and adaptive immunity components, along with defined immunocytes, are known to play critical roles within the poorly understood and complex OS TME (Farc and Cristea, 2020; Gajewski et al., 2013). Within the TME, the immune system interacts with the malignant tumour, thus, immunological changes within the TME and immune niche heterogeneity have been reported to impact patient prognosis (Qi et al., 2021; B. Li et al., 2016).

Previous studies have reported high levels of immune cell tumour infiltration being associated with favourable patient prognosis (Tas and Erturk, 2017), in disease cases such as prostate cancer (Donovan et al., 2018), cutaneous melanoma (Yang et al., 2020), and breast cancer (Papatestas et al., 1976; Manuel et al., 2012). In addition, increases in tumour immune cell infiltration are associated with an enhanced response to adjuvant chemotherapy (Pruneri et al., 2018). Overall, due to the strong immune cell influence within the OS-TME, it is evident that there is a significant functional role of the immune system in OS malignancies. Therefore, assessing tumour immune microenvironment heterogeneity and potential changes in response to differential tumour gene expression may unveil promising targets for cancer treatment (Qi et al., 2021).

The OS cells of the tumour dictate immune infiltrate recruitment and differentiation to establish a favourable immune niche, which then supports tumour growth, drug

resistance and the occurrence of metastases (Heymann et al., 2019). With this understanding of the OS tumour immune microenvironment, immune escape is considered to be an important feature of OS development. This phenomenon is thought to be due to the downregulation of infiltrated immune cell anti-tumour functionalities, largely as a consequence of tumour-derived cellular signalling (Whiteside, 2008). The tumour cells that make up the heart of the TME, are known to control the functionality of both the cellular and non-cellular components of the microenvironment. The cells utilise complex cellular signalling networks in order to control the functionality of non-malignant cells of the TME, such as immune infiltrates, and promote adverse pro-tumorigenesis functions. As a result of the described tumour-cell induced crosstalk within the microenvironment, there is an observable increase in tumour formation and maintenance, along with a reduced response to disease therapeutic strategies and multi-drug resistance (Hanahan and Coussens, 2012; Frisch et al., 2019; Baghban et al., 2020).

Despite the downregulation of anti-tumour functionalities in the TME, inflammatory cells continue to infiltrate the TME and are known to vary in size and diversity from one tumour to another (Pagès et al., 2010). Hence, their presence within the TME provides evidence supporting the fact that the host's defences recognise the developing tumour and mount an attempt to hinder tumour progression. This phenomenon of tumour detection and immune response is referred to as immune surveillance (Zitvogel et al., 2006; Whiteside, 2008). Cancer immunosurveillance involves tumour-specific antigen recognition, recognition of mutated gene products and recognition of overexpressed genes or genes that encode viral proteins (Swann and Smyth, 2007). Under normal circumstances, immune cells of the innate and adaptive immune system will detect tumour cells and eliminate them by natural killer (NK) cell activation, interferon (IFN)

secretion and the eventual activation of dendritic cells (DCs) (Miwa et al., 2019). However, tumour cells are capable of evading immune recognition and attack via various mechanisms. These mechanisms include the downregulation of tumour antigen expression, downregulation of surface major histocompatibility complexes, altering the TME, upregulating inhibitory receptors on T cells and upregulating inhibitory ligands on tumour cells (Diaz-Montero et al., 2014; Laoui et al., 2014; Nishikawa and Sakaguchi, 2014).

The immune niche in OS consists mainly of tumour infiltrating lymphocytes (TILs) and tumour-associated macrophages (TAMs) (Endo-Munoz et al., 2012; Théoleyre et al., 2005). In the case of TILs, selected T lymphocytes located within secondary lymphoid organs migrate towards the tumour site and invade the tumour tissue. The lymphocytes are made up of various T lymphocyte subpopulations and portray greater specificity in immunological reactivity when compared to circulating and non-infiltrating lymphocytes (Rosenberg, 2001). An immune response induced by T lymphocyte activation is complex and dependent on T cell type (e.g. Treg) and the presence of other immune protagonists such as macrophages (Heymann and Heymann, 2017). TAMs are the predominant solid tumour infiltrating leukocytes; thus, they make up approximately 50% of a tumour's mass. TAMs are known to have a major influence on tumour behaviour, which is portrayed by the relationship between TAM density and prognosis (Lewis and Pollard, 2006; Bingle et al., 2002; Zhang et al., 2012). Furthermore, they have been reported to exert anti-tumour activities; however, ambiguity in their role is based on TAMs being found to have an active role in each stage of cancer development and progression (Laoui et al., 2014).

Due to the therapeutic potential of targeting the immune niche within the OS TME, immunotherapy as a therapeutic strategy for OS treatment can be said to be a highly

attractive option. Within the TME, the diverse range of immunocytes portray various cellular features and functional characteristics. An example can be infiltrating neutrophils, which act as inhibitors of infiltrating NK innate immune cells, thus, resulting in the extravasation of tumour cells and subsequently tumour metastasis. Therefore, it is well understood that cancer immunotherapeutic strategies greatly rely on the antitumour immunocompetence of the human immune system, which as described, plays a critical role in the TME (Koury et al., 2018). In relation, a deeper understanding of the immune related profiles of cancer patients, such as immune-related gene expression changes and immune cell tumour infiltration, can be useful when successfully implementing immunotherapeutic strategies (Miwa et al., 2019; Baghban et al., 2020).

The human immune system, as previously described, has a significant influential role within the OS TME which is based on its functionalities that include tumour detection and tumour growth suppression. It has been shown that both the innate and adaptive immune components work in combination to carry out these roles. Therefore, it is evident that an active patient's immune response to a malignant tumour, such as OS, can play a major role in determining overall patient prognosis (Elder et al., 1983; Baxevanis et al., 1994). A study conducted by McMaster et al, involving an in-vitro micro cytotoxicity test utilising cultured tritiated thymidine labelled osteosarcoma cells and autologous fibroblasts, showed that OS patients possess a normal cellular immune response which exhibits non-specific cytotoxicity when assessed in-vitro (McMaster et al., 1975). Due to the study providing evidence of a normal cellular immune response in OS patients, the implementation of various immune based and immunotherapeutic strategies as a form of OS treatment can be said to be a good strategy. Figure 1.7 presents a schematic representation of the immune microenvironment within the OS

TME. The figure shows how both arms of host immunity (adaptive and innate) are involved in pro-tumorigenic and anti-tumorigenic activities, thus, having a significant impact on OS progression and metastasis. Specifically, within the immune microenvironment, there are key adaptive and innate immune cell populations that play crucial roles in determining overall OS tumour progression.

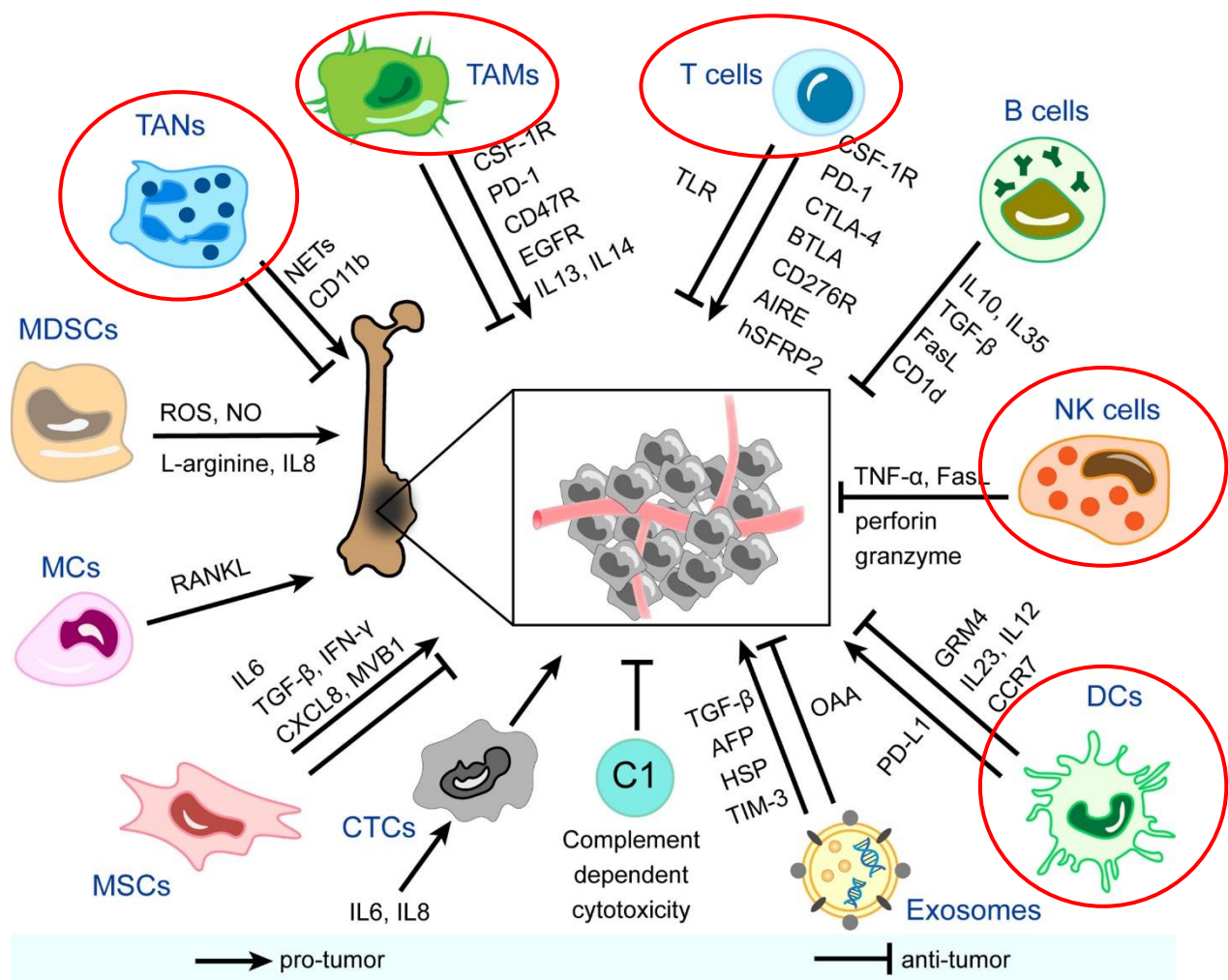


Figure 1.7: The OS tumour immune microenvironment. The figure presents a schematic representation of the OS tumour immune microenvironment and its components. In the schematic representation, the interplay between both arms of host immunity (adaptive and innate) within the immune microenvironment is shown, with respect to pro and anti-tumorigenic activities. However, especially, certain adaptive and innate immune cells populations are known to play vital roles in determining the overall rate of OS tumour progression and therefore, metastasis. These key immune cells populations are further discussed below, with respect to their impact on tumour progression and in the diagram above, they are circled red. Image from: (Zhu et al., 2022).

With regards to the adaptive immunity component of the host immune response, the major immune effector cell population that targets the OS tumour cells are the cytotoxic T lymphocytes (CTLs) (Wang et al., 2019). Previous studies have demonstrated that the host CTLs played an important functional role in immune surveillance within OS patients (Tsukahara et al., 2006). Furthermore, studies have reported that the adoptive transfer of T cells has successfully resulted in significant inhibition of tumour progression in mouse models of OS (Ahmed et al., 2009, 2015; B. Li et al., 2014). In addition to the adoptive transfer of conventional circulating CTLs, several studies have assessed the immunotherapeutic potential of genetically modified T cells in OS malignancies. As a consequence of the development of gene transduction technologies, conventional T cells have been successfully genetically transduced with T cell receptors (TCRs) or chimeric antigen receptors (Miwa et al., 2019). Specific TCRs, such as HLA-A2-restricted TCRs have the ability to recognise several malignancy related antigens, including MART-1, gp100, MAGE-A3, and NY-ESO-1 (Hughes et al., 2005; Morgan et al., 2003). Henceforth, TCR presenting cell therapies have demonstrated noticeably favourable outcomes in patients with melanoma and synovial sarcoma malignancies (Robbins et al., 2015, 2011).

In recent years, studies have investigated the functional role of innate immune cell populations, to determine their potential as inhibitory mediators of tumour progression (Wang et al., 2019). It has been reported that the innate immune system suppresses malignant tumours through direct recognition of tumour cells and killing, through self-regulated activation and induction of a stronger adaptive immune response, or a combination of both modalities (Woo et al., 2015). Due to the antitumor immunoactivity of innate immune cells, this protective cell population provides a basis for the potential use of immune cell-based therapies in malignancies. In relation, earlier research has

shown promise for the use of the therapeutic modality in the treatment of hematopoietic malignancies and solid tumours, such as OS (Bonneville and Scotet, 2006). In cases of OS malignancies, the successful treatment of the malignancy has been reported in preclinical studies with the use of innate immune cells (Tarek and Lee, 2014; Li, 2013). Thus far, major classes of innate immune cells such as DCs, macrophages, NK cells, natural killer T cells, and $\gamma\delta$ T cells have shown definitive anti-osteosarcoma tumour functional roles, thus, they show promise to be utilised in novel innate immune cell-based therapy for the effective treatment of OS (Wang et al., 2019).

A major innate immune cell population that has portrayed anti-OS characteristics are DCs. Conventionally, DCs are defined as highly functional antigen-presenting cells (APCs), that uptake and present antigens to circulating naïve T cells, and thus, subsequently induce the differentiation of naive T cells into tumour killer cells (Den Haan et al., 2000). In relation to their functional role as major APCs, a list of differing recent studies have reported that conventional DCs also portray the capability to enhance the activation of related innate immune cell populations that portray distinguished and robust tumour-specific immune activity in vivo, such as $\gamma\delta$ T cells and cytokine-induced killer cells (Fiore et al., 2007; Van Acker et al., 2018; Wongkajornsilp et al., 2005). However, established tumours have been reported to induce a reduction in the antigen presentation availability of APCs, thus, resulting in malignancy mediated immunosuppression and the disruption of an antitumour immune response generation (Suryawanshi and Manicassamy, 2015; Cornwall et al., 2016).

Henceforth, various kinds of DC cellular immunotherapy for advanced sarcoma malignancies have been developed (Miwa et al., 2017). Reports of pre-clinical studies have shown that treatment of sarcomas with DC vaccines, such as DCs co-cultured/pulsed with tumour lysates (Garg et al., 2017), significantly increased the

induction and hence, levels of cytotoxic T lymphocytes activity (Y. T. He et al., 2016). Consequently, an increase in serum levels of IFN- γ was observed, along with reduced pulmonary metastases, and increased numbers of CD8-positive T lymphocytes in areas of tumour metastasis (Kawano et al., 2010; Y. T. He et al., 2016). Therefore, Kawano et al, investigated the therapeutic efficacy of a combination treatment which consisted of DCs pulsed with tumour lysate and an anti-cytotoxic T lymphocyte antigen-4 (CTLA-4) antibody in a mouse model of osteosarcoma. The study reported that the treatment with either the anti-cytotoxic T-lymphocyte antibody or the DCs pulsed with the tumour lysate, resulted in an increase in the number of CD8+ cytotoxic T lymphocytes, a reduced number of regulatory T lymphocytes, an increase in serum levels of IFN- γ , prolonged mouse survival and inhibition of primary and metastatic malignancy growth. The combination of both these treatment modalities then resulted in an enhanced systemic host immune response (Kawano et al., 2013).

TAMs can be classified based on two general subpopulations, which are either the anti-tumour (pro-inflammatory) M1-polarized macrophages or the pro-tumour (anti-inflammatory) M2-polarized macrophages (Noy and Pollard, 2014; Mantovani et al., 2004; Quatromoni and Eruslanov, 2012). Due to the cellular abundance of TAMs within the OS-TME, three differing immunotherapeutic strategies that specifically target the TAM immune cell population have been clinically assessed and have shown potential for the treatment of OS. The first strategy involves the prevention of cellular polarisation of M1 anti-tumour macrophages to M2 pro-tumour macrophages, or alternatively, the direct inhibition of the M2 macrophage phenotype (Wang et al., 2019). The second therapeutic strategy involves the enhancement of circulating macrophage recruitment into the TME. The recruitment of circulating macrophages has been reported to exert anti-tumour effects and consequently, inhibit OS metastasis (Wang et al., 2019; Zhao

et al., 2018). Lastly, a therapeutic strategy involving TAMs for the treatment of OS, involves the pharmacological activation of circulating macrophages and the TAMs themselves. Pharmacological activation of macrophages, through the use of immunoadjuvant therapeutic drugs, is currently approved for OS therapy in the European Union and portrays the ability to activate the inert tumoricidal properties of macrophages, thus, inhibiting human OS cell growth (Schroit and Fidler, 1982; Pahl et al., 2014). Despite these TAM related therapeutic strategies, infiltrating TAMs have been shown to contribute towards OS tumour progression through multiple signalling pathways (Heymann and Heymann, 2017). Reports from pre-clinical studies, show that macrophages recruited by interleukin (IL)-34 cytokines released by OS cells have the ability to promote tumour progression and metastatic processes (Ségaligny et al., 2015).

Lastly, human NK cells have been characterised to express a diverse range of activating and inhibitory cell surface receptors. These cell surface receptors are known to recognise alterations in gene expression patterns on target cells, thus, controlling NK cell functionalities (Wang et al., 2019). In cases of gene expression alterations that are typically portrayed by cells undergoing malignant transformation, the activating receptors on NK cells are stimulated, therefore, resulting in spontaneous cytolytic activity against the malignantly transforming cells (Spits et al., 2013). More recent reports have shown that NK cells enhance DC infiltration into the TME, therefore, resulting in the inhibition of tumour growth (Böttcher et al., 2018). OS patients portrayed lower numbers of NK cells at the time of diagnosis when compared to normal controls (Markiewicz et al., 2012). Therefore, providing evidence of OS induced immunosuppression and the potential significance of NK cells in OS. However, after the combined therapeutic application of IL-2 and polychemotherapy, OS patients showed increased numbers of NK cells in circulation with increased activity.

Furthermore, it was also reported that the magnitude of increase was strongly correlated with a favourable patient clinical outcome (Luksch et al., 2003). From the data, it can be said that the NK cells, similar to DC, portray anti-tumour immune activity and play a vital role in immune surveillance within OS patients (Wang et al., 2019).

In contrast to immune cell-based immunotherapeutic strategies for the potential treatment of OS, several known host circulating cytokines have also been investigated as immunotherapeutic strategies for the treatment of OS (Miwa et al., 2019). Circulating IFN- α cytokine has the ability to not only induce cell differentiation and apoptosis, but also to inhibit cell proliferation and angiogenesis. Due to the anti-proliferative and anti-angiogenic capabilities of IFN- α in OS, several studies have investigated the clinical efficacy of the cytokine in several malignancies and reported positive results (Whelan et al., 2010; Bukowski et al., 2002; Tarhini and Kirkwood, 2012). A study conducted in 1977, reported IFN- α induced growth inhibitory effects in a cultured human osteosarcoma cell line (Strander and Einhorn, 1977). In addition, the observed human IFN- α induced growth inhibition in vitro was reproduced in vivo within a mouse model of human OS (Brosjö et al., 1985). Similarly, circulating cytokine IL-2 has demonstrated promising immunotherapeutic potential in OS patients, however, adverse side effects were observed. In a study assessing the immunotherapeutic potential of IL-2 in OS patients, a high-dose of IL-2 treatment in relapsed paediatric OS patients portrayed an efficacious response in 50% of the patients. However, the severe adverse side effects that were observed included an increase in white blood cells, creatinine, γ -glutamyltransferase, C-reactive protein, glucose, and body weight, along with a decrease in red blood cells, platelets, protein, albumin, and cholinesterase (Schwinger et al., 2005). Henceforth, based on the described studies, host circulating cytokines such as IFN- α and IL-2 have the potential to induce antitumor immune

responses, however, with no significant improvement in overall OS treatment outcomes (Miwa et al., 2019).

Overall, it is evident that the immune system has a significant influential role within the TME, whereby, it contributes to both anti-tumour and pro-tumour biological processes. Specifically, in the case of OS, multiple studies have shown the importance and prevalence of the immune system and tumour immune niche, in both tumour progression and metastasis. The above studies describe a strong influence of both the adaptive and innate immune components in OS, thereby, making immunological targets within the tumour immune microenvironment of high therapeutic interest. However, as mentioned, current immunotherapies for OS, which include the use of ICIs, have shown limited therapeutic effects in patients with bone sarcoma (OS and chondrosarcoma) (Chen et al., 2021). For example, a bone sarcoma clinical trial evaluated the safety and efficacy of pembrolizumab, a single-agent PD-1/PD-L1 ICI. The results of the clinical trial showed that only 5% of patients with bone sarcoma showed a therapeutic response, therefore, significantly away from achieving the intended effect (Tawbi et al., 2017). This was further validated in a novel phase two study, where the ICI pembrolizumab portrayed good systemic tolerance but insignificant anti-tumour activity in adult patients with advanced OS (Boye et al., 2021). To overcome this limitation, certain clinical studies suggest combining immunotherapy with conventional chemotherapies, radiation therapies, tyrosine kinase inhibitors and oncolytic viruses to aid in turning these "cold" Sarcoma tumours "hot". Thereby, improving the effectiveness of immunotherapies such as ICIs in Sarcomas (Rytlewski et al., 2021).

Therefore, a better understanding of the immune profiles of OS patients, such as significantly differentially expressed immune related genes may bring about a deeper

understanding of OS pathophysiology (Cascini and Chiodoni, 2021; Miwa et al., 2019) and define successful immune based strategies for the treatment of OS. Furthermore, due to the particular bone microenvironment in OS, it is thought that the immune niche of the OS TME might host immune-related therapeutic targets of interest (Heymann and Heymann, 2017), that can be put forward as novel therapeutic targets in immunotherapeutic strategies. These novel therapeutic approaches for advanced Sarcomas, such as OS, have been sought after over the years for the improvement of OS treatment (Miwa et al., 2019).

1.2 Nanotechnology and Nanotherapeutics

1.2.1 Overview of Nanotechnology

Nanotechnology is known to be a multi-disciplinary scientific field, which applies engineering and manufacturing principles at the molecular level (Emerich and Thanos, 2006). It can be defined as the science and engineering involved in the design, synthesis, characterisation and application of materials and devices whose functional organisation, is on the nanometre scale (Saini et al., 2010). The scientific field has understandably built the reputation of being the first major worldwide research initiative of the 21st century (Mangematin and Walsh, 2012). This achievement can be dedicated to the fact that it is understood to be a general-purpose technology, which can act as a solution for various industrial problems, but also be a bridge, connecting technologies like biotechnologies, computational sciences, physical sciences, communication technologies, cognitive sciences, social psychology, and others (Freitas, 2013).

In society today, nanotechnology plays a vital role in revolutionising various multi-billion-dollar industrial sectors. These sectors which include tissue engineering, imaging, surface texturing and bio-interfaces, are all utilising nanomaterials to

transform their products. Therefore, it can be said that nanotechnology is a multi-trillion dollar sector that covers vast areas such as medicine, electronics and chemistry (Chakraborty et al., 2016). Importantly, in the context of medicine, nanotechnology portrays an exciting new scientific path that can be applied in medical/biomedical areas such as disease diagnosis, drug delivery and imaging. The nanometre scaled materials/particles, when specifically designed, are capable of interacting with cells and tissues at a molecular level. Therefore, nanotechnology has been able to bridge the gap between technology and biological sciences (Saini et al., 2010).

1.2.2 Nanomedicine: overview

Nanoparticles (NPs) can be defined as materials with an overall dimension in the range of (1-100nm). The knowledge and techniques of nanotechnology, when used for medical/biomedical purposes, have been termed nanomedicine. Thus, nanomedicine can be defined as the use of nanomaterials, such as NPs, for disease diagnosis, monitoring, prevention, and treatment (Tinkle et al., 2014). Specific applications of these nanomaterials include fluorescent biological labelling, drug and gene delivery, pathogen detection, tumour detection and magnetic resonance imaging (MRI) contrast enhancement (Saini et al., 2010; Boisselier and Astruc, 2009). Nanomedicines have gained significant interest over the years with NPs being extensively studied by scientists across the globe. This is due to the realisation that NPs, in addition to their use in disease diagnosis, prevention and treatment, can be utilised in therapeutic interventions including drug delivery in nano-based drug delivery systems (DDS) (Patra et al., 2018; Rizzo et al., 2013).

NPs, in addition to the applications described above, are further used in nanomedicines to carry out roles such as biosensing and tissue engineering. In recent

years, they have become targets for many scientific studies as they show potential for use in a wide range of human/clinical applications (Bouwmeester et al., 2014). In addition to their standalone therapeutic biomedical applications, NPs have also been investigated for the potential of merging their therapeutic and diagnostic properties, thus, utilising one NP formulation for disease diagnosis and treatment. These unique nanomedicine formulations are known as nanotheranostics, and they have become an attractive therapeutic modality for personalised medicine, due to their ability to both diagnose and treat in a patient specific manner (T. H. Kim et al., 2013). The clinical use of nanotheranostics can potentially result in the generation of personalised NP formulations, through the acquisition of useful data on pharmacokinetics and NP drug delivery vector efficiency (Rizzo et al., 2013).

NPs can be separated into two general categories based on their composition: organic and non-organic NPs. NPs can then be further classified into different classes based on their properties, shape or size. These different classes include lipid NPs, fullerenes, metal/magnetic NPs, ceramic and polymeric NPs (Khan et al., 2019). NPs commonly used in biomedical applications include carbon nanotubes (CNTs), quantum dots, ferroferric oxide NPs, liposomes, polymeric micelles and gold NPs (AuNPs) (Kong et al., 2017). Magnetic NPs are a sub-category of NPs that falls under non-organic NPs. Figure 1.8 shows transmission electron microscopy (TEM) images of six different examples of magnetic NPs which vary in shape, size and composition.

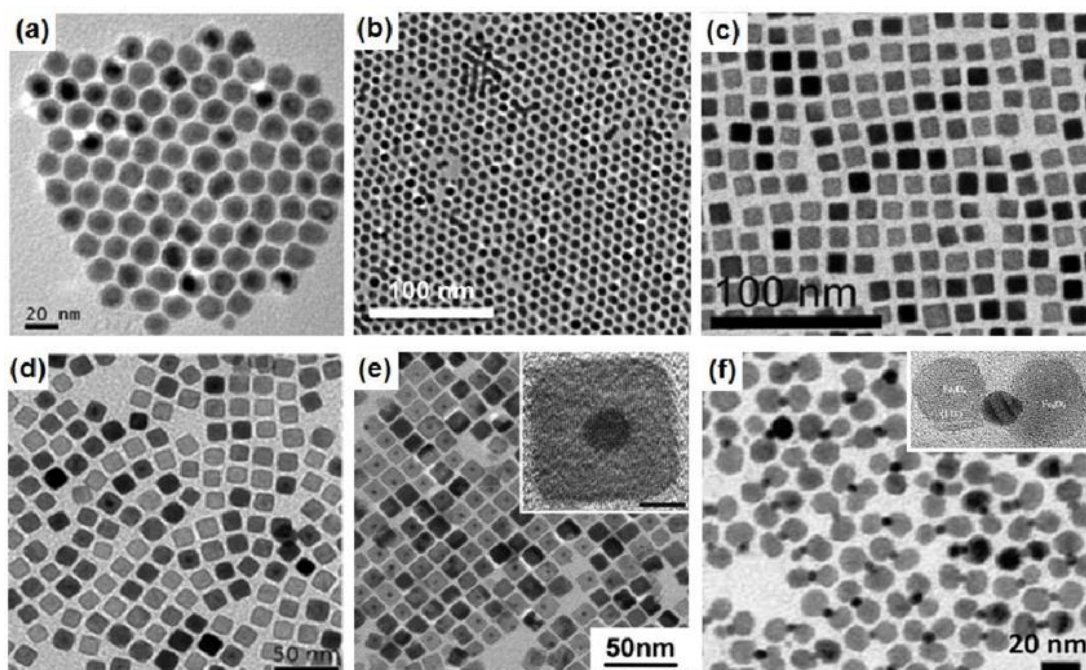


Figure 1.8: Images of differing magnetic NPs obtained using TEM. (a) Iron (Fe) NPs; (b) Cobalt NPs; (c) cubic Nickel NPs; (d) cubic Fe_3O_4 NPs; (e) core-shell FePt/PbS NPs; (f) dumbbell Fe_3O_4 -Au- Fe_3O_4 NPs. Image from: (Wu et al., 2016).

These engineered NPs are currently being used in an ever-expanding range of applications and their wide utility has been solely due to their versatility, with regard to modifications to their shape, size, surface, and chemical properties. In connection with modifications, the surface of these nanomaterials can be altered to accommodate their specific application. An example of this can be seen in the application of drug delivery, where specific targeting ligands can be attached to the surface, to improve biocompatibility and enhance target specificity (Thanh and Green, 2010).

Due to their unique physicochemical properties, acquired as a consequence of their small size and large surface area, NPs can move more freely in the human body in comparison to larger materials (Patra et al., 2018). Thus, NPs are now widely employed in industrial as well as biomedical applications (Bouwmeester et al., 2014;

Khan et al., 2019). The NPs portray greater solubility and thus enhanced bioavailability, the ability to cross the blood-brain barrier (BBB), enter the pulmonary system and be absorbed through the tight junctions in-between the endothelial cells of the skin (Kohane, 2007).

NPs are currently being used in various consumer items, such as silver NPs in sheets and clothing, titanium dioxide NPs in various cosmetics and creams, carbon NPs in automotive items and clay NPs in drink bottles (Tsuzuki, 2009). Furthermore, popular elements like iron, carbon and gold are being used extensively due to their known clinically beneficial properties. Superparamagnetic iron oxide NPs (SPIONs) are commonly used in biomedical applications, such as imaging contrast agents, iron replacement therapies, drug delivery and tissue repair (Ghaffari et al., 2020), due to the possible incorporation of a biocompatible coating (Arias et al., 2018). CNTs have long been used in structural materials for optics, plastics, and electronics. However, since the beginning of this century, CNTs have been introduced as a vehicle in DDS (He et al., 2013). AuNPs have repeatedly been used as a form of treatment for rheumatoid arthritis, as well as in cancer therapy and drug delivery (Alkilany and Murphy, 2010). Finally, Zinc Oxide NPs (ZnONPs) are being widely used in common household items such as electronic devices and sunscreens (Nurullahoğlu, Eskin and Kaya, 2015).

The physicochemical properties portrayed by NPs are largely size-related and offer a range of opportunities for novel discoveries. Moreover, the often-unpredictable behaviour of NPs bears great potential for innovative technological applications (Heiligtag and Niederberger, 2013). However, their real potential within biomedicine lies within drug delivery, where the unique NP physicochemical properties such as superior drug bioavailability as well as target-specific delivery are envisaged (Patra et

al., 2018; Lee Ventola, 2012). Therefore, there is a strong belief that nanomedicines will bring about advances in the diagnosis and treatment of diseases and engineered NPs are essential to realising these specific NP applications (De Jong and Borm, 2008).

Unique NP intrinsic and extrinsic physicochemical properties, including magnetism, large surface area, surface charge, shape, aggregation state and surface composition, are said to aid in NPs overcoming the limitations of conventional DDS (Gatoo et al., 2014). These limitations include drug degradation and poor drug retention, hence, requiring an increase in the frequency and dosage of the drug. Moreover, conventional drug delivery also displays poor drug bioavailability, drug absorption into the body and drug solubility, alongside issues related to target-specific delivery (Patra et al., 2018).

1.2.3 Nanoparticle-based drug delivery systems

Drug delivery can be defined as the method or process of administering a pharmaceutical compound(s) to achieve a therapeutic effect in humans or animals (Tiwari et al., 2012). However, the efficient delivery of therapeutic compounds to a target site is often considered a major drawback in the effective treatment of many diseases. This, in addition to the limitations described above, can be explained by the limitations portrayed by conventional DDS, which include poor drug biodistribution, limited efficacy and lack of tissue specificity (Adepu and Ramakrishna, 2021; Patra et al., 2018).

Conventional DDS are the classical methods of drug delivery into the body, including oral, buccal/sublingual, rectal, intravenous (IV), subcutaneous, and intramuscular delivery (Tiwari et al., 2012). On the other hand, NPs exhibit unique biological and physicochemical properties as previously described, which makes them desirable

materials for use in various biomedical applications. Thus, NPs are rapidly gaining investigative interest as potential drug and gene delivery vectors, for the treatment of multiple diseases such as cardiovascular diseases (Deng et al., 2020) and cancer (Yao et al., 2020). In NP-based therapeutic delivery systems, where the nanostructures either encapsulate the therapeutic cargo, covalently conjugate to them or adsorb the biomolecules to their surface, the therapeutic agent is transported via NPs to the target site (Wilczewska et al., 2012). NP-based delivery systems utilise targeting agents on the surface of NPs, for tissue specific delivery of the therapeutic cargo. An example of an NP-based therapeutic delivery system, in the form of a complete functionalised SPION-based drug/gene delivery system, is shown in figure 1.9.

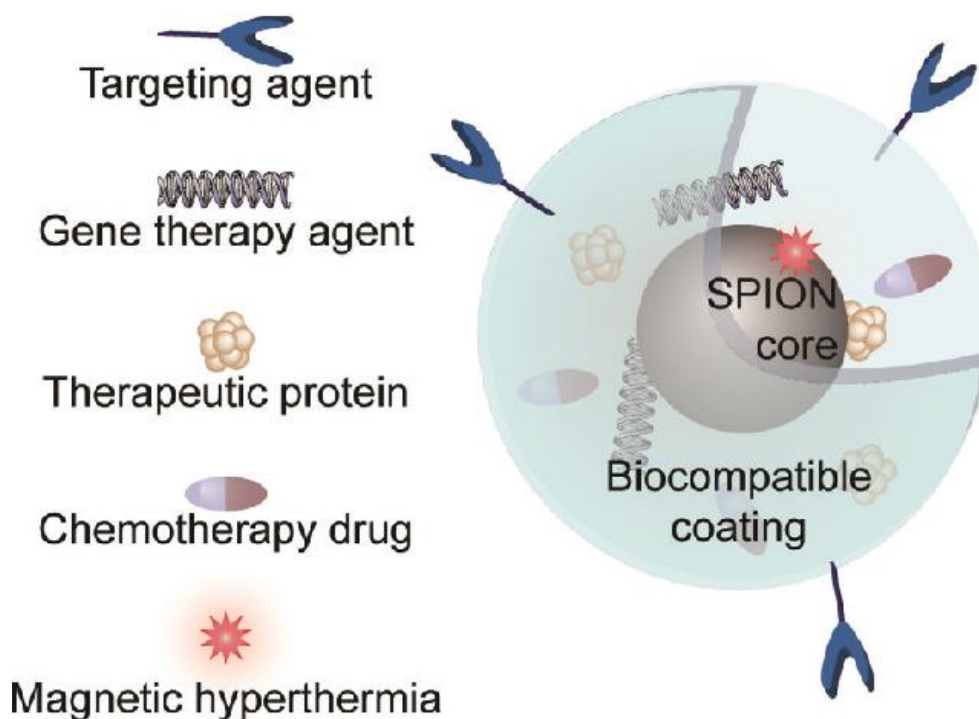


Figure 1.9: Fully functionalised SPION for use in NP-based therapeutic delivery systems. This image provides a visual representation of a fully functionalised SPION, for subsequent use in a NP-based therapeutic delivery system. The inclusion of a biocompatible coating is shown, to improve NP-host interactions and thus, NP biosafety. Furthermore, the image presents an overview of the therapeutic potential of functionalised SPIONs, when used in NP therapeutic formulations. These include the ability to carry therapeutic compounds, the potential of binding therapeutic agents to the NP surface, thus, allowing tissue specific therapeutic compound delivery and the ability to induce magnetic hyperthermia when used in cancer therapeutics. Image from: (Kievit and Zhang, 2011b).

Targeting of NP formulations can be achieved by utilising two different methods, passive and active targeting. Under certain conditions, such as inflammation/hypoxia, which is typical of a cancerous setting, the endothelium of blood vessels becomes more permeable. To overcome the hypoxic condition, rapidly growing tumour cells recruit new vessels (tumour angiogenesis) or utilise existing blood vessels. The newly formed but “leaky” blood vessels portray enhanced but selective permeation to nanosystems and macromolecules larger than 40 kDa to the tumour stroma. Moreover, tumours do not present normal lymphatic drainage, hence, aiding in NP retention. This feature does not apply to small molecule drugs which have a short circulation time and rapidly wash away from the tumour. Therefore, NP-based DDS enhance drug pharmacokinetics (due to increased retention), provide tumour selectivity and decreases adverse side effects. This method of targeting is termed “passive” targeting, as it relies only on carrier characteristics such as size as well as tumour biology (Attia et al., 2019).

On the other hand, active targeting of NP formulations relies on a biological interaction between ligands present on the NP surface and receptors expressed on the surface of the target cells. Numerous biological ligands have been identified and studied for their ability to facilitate active targeting of NPs. These ligands increase the cellular uptake of drug-containing NPs, thus, increasing their therapeutic efficacy due to a higher intracellular concentration of the drug (Yoo et al., 2019). Once taken up by the cells, a controlled release of the therapeutic agent from NPs is achieved due to the changes in the NPs physiological environment such as pH, osmolality and enzymatic activity (Assa et al., 2017).

The main purpose of utilising NPs as drug delivery vehicles in the treatment of diseases is, therefore, specific cell/tissue targeting and controlled release of the

therapeutic compound. Targeted delivery thus, decreases their action on non-target tissues and minimises undesirable adverse side effects from damage caused to normal and healthy tissues of the body (Yan et al., 2020). Moreover, NPs protect the drugs from rapid degradation in the gastrointestinal tract or being cleared rapidly by the kidney. This enhances drug concentration in target tissues, therefore, lower doses of the drug can be administered (Wilczewska et al., 2012). To summarise, the key advantages of nanoparticle DDS are (1) improved drug bioavailability due to greater solubility, (2) increased resistance time in circulation (increasing half-life for clearance) and most importantly (3) targeting the drug to a diseased site within the body (Mudshinge et al., 2011).

The physiochemical characteristics of the NPs can determine how they behave in vivo, if they are to be used as a carrier in nano-based DDS. The shape and size of NPs determine how cells recognise them and thus dictate their distribution, toxicity, and targeting ability. Reports show that 100 nm NPs exhibit a 2.5-fold greater uptake compared to 1 μm diameter particles and a 6-fold greater uptake compared to 10 μm particles (Rizvi and Saleh, 2018). Smaller NPs are filtered from the bloodstream and cleared by the kidneys, whilst larger NPs are rapidly removed from circulation by the macrophages of the reticuloendothelial system (figure 1.10) (Cole et al., 2011). Even though complete clearance of NPs will eventually be desired, once treatment is complete, the NPs must avoid rapid clearance to achieve the desired targeting efficiency. Overall, NP half-life in circulation should be prolonged so that they circulate passed the target site multiple times, allowing them to accumulate there (Yoo et al., 2010).

The composition of NPs, for possible use as carriers in drug delivery, varies. Source materials for the NPs may be of biological origins, such as phospholipids, liposomes,

gelatine, dextran and chitosan (Fang et al., 2020). Furthermore, the source material could also be of a more “chemical” origin, such as polymers, carbon, silica, and metals. The interaction between the biological components of NPs, such as phospholipids and cells will be significantly different to the interaction between non-biological “chemical” components of NPs such as metals like iron or cadmium, and cells. With relation to engineered NPs that have polymers as source materials, there is a vast area of possibility for their chemical composition. NPs used in nano-based DDS are required to release the drug they are carrying once they reach the intended diseased site within the body. Therefore, for drug delivery, biodegradable nanoparticle formulations are required as the intention is to transport and release the drug in order to be effective (De Jong and Borm, 2008).

As mentioned, the size of the NPs can influence the performance of the nanoparticle-based drug formulation (Rizvi and Saleh, 2018). However, NP surface modification is another important method in creating the ideal DDS (Bantz et al., 2014). For an optimum nanoparticle DDS to be created, the incorporation of appropriate targeting ligands, surface curvature and reactivity are required. This is required to prevent aggregation and to promote stability, receptor binding and the subsequent pharmacological effects of the drug (Khanbabaie and Jahanshahi, 2012). NPs that are composed of biodegradable polymers will undergo hydrolysis in circulation to produce biodegradable metabolite monomers, such as lactic acid and glycolic acid. Kumari et al, reported minimal systemic toxicity with the use of Poly Lactic-co-Glycolic Acid (PLGA) NPs for drug delivery or biomedical applications (A. Kumari et al., 2010). Drug-biodegradable polymeric NP conjugates for use in drug delivery have shown to be stable in blood, non-toxic and non-thrombogenic. Moreover, they have also shown to be non-immunogenic and non-pro-inflammatory as they neither activate neutrophils

nor affect the reticuloendothelial system. As a result, such biodegradable NPs are biocompatible as they do not elicit an immune response (des Rieux et al., 2006).

Despite the significant contributions of physiochemically different NPs in the treatment of diseases and thus, the field of nanomedicine, only a small number of drug-conjugated NP formulations have been approved for clinical use in cancer and disease therapeutics (Mitchell et al., 2021). This is said to be a consequence of limiting factors which need to be considered when synthesising NPs for potential use as drug delivery agents (Cole et al., 2011). Ultimately, for NPs to be used in medical applications, they must be biocompatible. This means that they should be able to integrate with the host's biological system, without eliciting an immune response. Furthermore, the NPs themselves should not be toxic to the host (Kus-lińkiewicz et al., 2021). Many factors may determine the biological safety of NPs, including hydrodynamic size, shape, amount, surface chemistry, route of administration, interaction with the immune system (specifics include the route of uptake by macrophages and granulocytes) and circulation time in the bloodstream (Cole et al., 2011; Alkilany and Murphy, 2010; Wahajuddin and Arora, 2012). Furthermore, engineered NPs must overcome various physiological barriers, *in vivo*, that may be encountered when NP drug delivery formulations are administered. Therefore, further making the task of engineering and tailoring NPs for tissue specific targeted drug delivery a major challenge (Thomas and Weber, 2019). The potential barriers that need overcoming and their respective scientifically proven solutions are briefly detailed in figure 1.10.

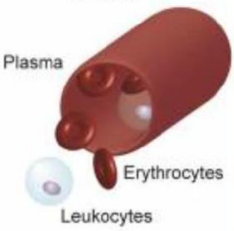

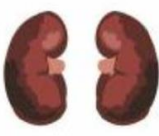
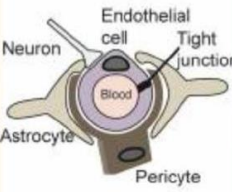
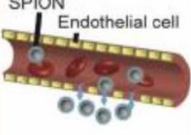
	Blood	Liver and Spleen	Kidneys	Blood-brain Barrier	Extravasation
Barrier					
Restrictions	<ul style="list-style-type: none"> Highly complex fluid Enzyme degradation Immune recognition 	<ul style="list-style-type: none"> Objects larger than 100 nm recognized and removed from circulation 	<ul style="list-style-type: none"> Objects smaller than the 10 nm pores of the glomerulus are filtered out of the blood 	<ul style="list-style-type: none"> Tight junctions between endothelial cells in the brain prevent passive access 	<ul style="list-style-type: none"> Gaps between endothelial cells restrict material escape from the blood
Strategies	<ul style="list-style-type: none"> PEGylation Zwitterionic polymers Encapsulation of drug or biotherapeutic 	<ul style="list-style-type: none"> Hydrodynamic size less than 100 nm 	<ul style="list-style-type: none"> Hydrodynamic size greater than 10 nm 	<ul style="list-style-type: none"> Osmotically shrink endothelial cells to open junctions Active transport across vasculature 	<ul style="list-style-type: none"> Enhanced permeability and retention effect Hydrodynamic size 30 - 100 nm

Figure 1.10: Host presented physiological barriers and restrictions faced by NPs during administration. The table provides an overview of some of the barriers and restrictions faced by NPs, *in vivo*, during nanoparticle therapeutic administration. The image also presents some cellular and NP physicochemical alterations that can be investigated to help overcome host barriers, when engineering NPs for subsequent use in NP-based drug delivery systems. Image from: (Kievit and Zhang, 2011a).

Overall, nanomedicines and in particular, NP-based DDS portray numerous advantages over conventional therapeutic drug treatment as described (Lee Ventola, 2012). In the case of NP-based DDS, the NP drug carriers are likely to portray greater therapeutic bio-circulation due to reduced levels of hepatic biodegradation and systemic excretion, despite known rapid removal of NPs by the reticuloendothelial system. Furthermore, diseased tissue specific targeting and therapeutic compound delivery using NP-based DDS will improve the bioavailability of the drug at the diseased site, thus, improving the therapeutic index of the delivered drug compound (Bala Tannan et al., 2021).

1.2.4 Therapeutic applications of NP-based DDS

The therapeutic applications of NP-based delivery systems range from cancer therapy, vaccine and gene delivery, diagnostic testing, antimicrobial actions and site-specific targeting to prevent adverse side effects of the therapeutic agent (Cheng et al., 2010). Although conventional chemotherapeutics have saved countless lives, the side effects of chemotherapy are harsh, affecting the entire body due to the non-specificity of the

chemotherapeutic agents. Current chemotherapy aim to destroy all rapidly dividing cells. A disadvantage of this therapy involves the death of the body's other rapidly proliferating cells, such as hair follicles and intestinal epithelium, causing life-changing side effects (Baudino, 2015). With the use of engineered NPs, targeted chemotherapeutic drug delivery at the tumour site or a certain group of cells becomes possible, so to largely avoid the toxic effects on other normal tissues and organs. Many chemotherapeutic drugs such as carboplatin, paclitaxel, doxorubicin and etoposide have successfully been loaded onto NPs in the past (Din et al., 2017). These NP-drug formulations have shown to be very potent against various cancers. For example, PLGA NPs loaded with the chemotherapeutic agent paclitaxel were shown to be an effective formulation against various cancer cells in vitro and in vivo in an animal model (Cheng et al., 2010).

Gene therapy involves the modification of the genetic makeup of a cell through the introduction of exogenous genes (transgenes) using delivering integrative, non-integrative or nonviral vectors (Mali, 2013). Gene therapy allows for the permanent correction of the defective gene and thus provides a definitive cure. This therapeutic process involves the therapeutic transgene substituting its defective endogenous counterpart. The success of gene therapy depends on the transgenes to be expressed and the delivery vectors used. In the last few years, multiple research groups have reported using NPs to complex with and deliver other vectors and nucleic acids, causing the emergence of a new approach known as Magnetofection. Magnetofection (magnetic nanoparticle transfection) is a non-viral approach that utilises superparamagnetic NPs to improve gene delivery with the use of a magnetic field. Mixing the genetic material (transgenes) with NPs and applying a magnetic field allows for an increase in the sedimentation of the complex and kinetics of transfection, as well

as increasing the concentration of vectors at the cell surface (Herranz et al., 2011). NPs are regarded as non-viral vectors when they are complexed with DNA or RNA in gene therapy. Examples of NPs used as non-viral vectors include inorganic NPs, carbon nanotubes, liposomes, protein and peptide-based NPs, as well as nanoscale polymeric materials. Non-viral vectors have significant advantages over viral vectors, such as decreased immune response, flexibility in design and targeting of specific sites with low cytotoxicity (Riley and Vermerris, 2017).

Moreover, viral infections with human immunodeficiency virus (HIV) for example, are currently treated with combination therapy which requires the patient to take a couple of pills every day down from 20-40 pills a few years ago (Bartlett and Moore, 1998). However, recent research has shown a method to make therapy even more effective, which involves the creation of polymeric NPs that will deliver antiretroviral (ARV) drugs intracellularly and across the blood-brain barrier (Mamo et al., 2010). This technology and method can also be put together with vaccinations and will involve the delivery of the appropriate vaccine to prevent HIV infections (Khalil et al., 2011). Due to a large diversity between HIV-1 strains, many experimental vaccines aim to utilise broadly neutralizing antibodies (bNAbs) which can neutralise the majority of circulating HIV-1 strains, by targeting the envelope glycoprotein (Env) trimer located on viral membranes. Hence, a study by Brinkkemper and Sliepen introduced the aspect of NPs in Env vaccinations, which involved the multimeric presentation of Env on NPs (Brinkkemper and Sliepen, 2019).

Furthermore, the use of NPs for diagnostic purposes is an area that is being explored heavily in academia but is not currently available for clinical use (Kolluru et al., 2013). Current technology for diagnostic testing is limited by the insufficiencies of fluorescent markers including fading of fluorescence after a single-use, colour matching, and

restricted use of dyes due to a bleeding effect. However, fluorescent NPs can overcome these limitations, thus allowing researchers to utilise NPs as a tool for diagnostic purposes (Wolfbeis, 2015).

With growing fears regarding antimicrobial resistance as well as the uncontrollable nature associated with biofilm-associated infections, came an important need for the development of alternative methods for the treatment of bacterial diseases (Karaman et al., 2017). Therefore, NPs are increasingly being used as an alternative to antibiotics to target bacteria (L. Wang et al., 2017). Their unique physical and chemical properties may lead to fine-tuned interactions between NPs and bacteria (Karaman et al., 2017). The actual antibacterial mechanisms of the NPs are poorly understood, but currently accepted mechanisms include oxidative stress induction, metal ion release and non-oxidative mechanisms. Due to the multiple simultaneous mechanisms of actions of the NPs against the microbes, the microbes would require multiple simultaneous gene mutations to develop any antibacterial resistance against NPs. Therefore, it is very difficult for bacteria to build resistance against NPs (L. Wang et al., 2017).

1.2.4.1 *Theranostics*

In 1960, biological NPs (liposomes), were the first to be reported and studied as a nanoparticle DDS to efficiently diagnose and treat diseases. As described before in lesser detail, therapy and diagnosis once integrated are defined as theranostic. A “theranostic” nanoparticle (TNP) can be defined as a nanoparticle, containing both therapeutic and diagnostic agents on a single platform (Zavaleta et al., 2018). Specific TNPs can aid in disease diagnosis, locating the disease, determining the disease stage and providing a possible treatment option. TNPs can carry out these functions, as they can be attached to certain dyes/fluorescent molecules or have intrinsic imaging properties, allowing them to be imaged via various imaging modalities such as

magnetic resonance imaging (MRI), ultrasound and computed tomography (CT) (Patra et al., 2018). Furthermore, these theranostic NPs can also provide a therapeutic platform by 1) being combined with imaging modalities that convert light-sensitive compounds into toxic agents, once exposed to a specific wavelength, 2) using their intrinsic properties to induce therapeutic effects or 3) being loaded with or attached to a therapeutic agent (Chen et al., 2014; Janib et al., 2010). Therefore, it is a strong belief that these multifunctional NPs can be utilised to provide both a therapeutic and diagnostic platform in novel “theranostic” NP delivery systems. However, this type of novel delivery system relies completely on the abilities of the NPs. The NPs must be able to specifically target the diseased site, allow for that site to be diagnostically imaged and be able to deliver the therapeutic agent.

The ideal TNPs may have molecular conjugates that can be imaged while in circulation. Once arriving at their destination, they may have other molecular targeting conjugates to interact with the cell membrane, become internalised into the cytosol and release the therapeutic agent they are carrying (Janib et al., 2010).

1.2.5 Examples of Nanoparticle drug delivery vehicles

1.2.5.1 *Superparamagnetic iron oxide NPs (SPIONs)*

Figure 1.11 shows TEM images of SPIONs, which are magnetic NPs/spheres that are engineered in varying sizes (Lundquist et al., 2014). Over the years, SPIONs have been the most studied inorganic NPs for use in DDS (Chee et al., 2018). Magnetic NPs were initially developed to overcome two major issues that organic NPs presented. These included reticuloendothelial system clearance and poor diseased tissue site-specificity (Price et al., 2018). Iron is an element, which due to its magnetic properties, is an excellent material source from which therapeutic NPs can be fabricated. Its

magnetic behaviour becomes very useful in systemic drug delivery. The magnetic behaviour of the NPs allows for the movement of the SPIONs to be controlled with the use of a magnetic field applied externally, and it allows for SPIONs to act as contrast agents in MRI (Neuberger et al., 2005). Furthermore, SPIONs can also be used to induce localised heating in areas such as tumour regions. The localised high temperatures (hyperthermia) can trigger the release of a loaded drug and possibly cause cell death by temperature-induced apoptosis (Chee et al., 2018).

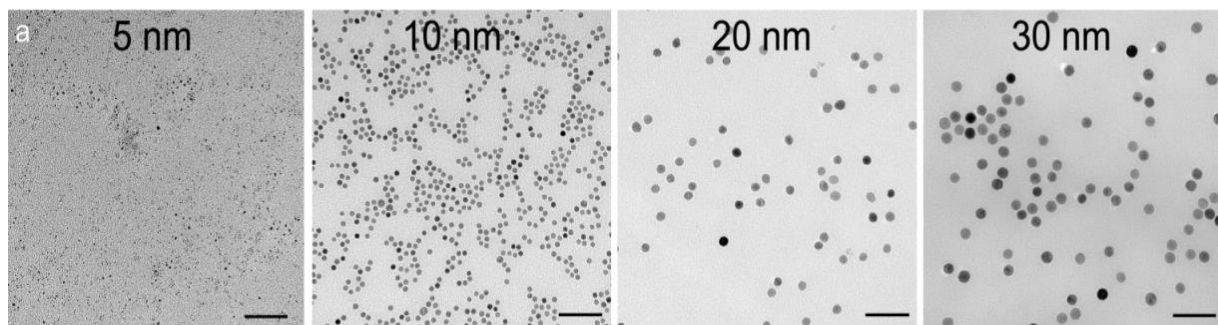


Figure 1.11: Images of different sized superparamagnetic iron oxide NPs (SPIONs) obtained using TEM. The images represent TEM images taken of SPIONs of varying core sizes. Images were taken of 5, 10, 20, and 30 nm SPIONs on 400 mesh formvar carbon grids, imaged at 200,000x direct magnification (bars = 100 nm). Image from: (Lundquist et al., 2014).

Once loaded with drugs SPIONs allow for magnetic drug targeting to a specific region. Widder et al introduced this idea of magnetic drug delivery in the '80s, but in the past decade, interest in magnetic targeting has markedly increased mainly due to the development of stronger magnets and sophisticated magnetic probes, such as SPIONs with multiple functions i.e. theranostic (Price et al., 2018).

Henceforth, among all NP drug delivery carriers, SPION-based delivery systems have gained considerable attention because of desirable clinical features such as biocompatibility and superparamagnetism. Their superparamagnetic properties allow for detection by MRI, thus, aiding in the monitoring of treatment responses and the

enablement of magnet-driven drug delivery and release (Kievit et al., 2012; Rudge et al., 2001; Kievit and Zhang, 2011a, 2011b; Veiseh et al., 2011; Fang and Zhang, 2010). An example of SPION-based tissue specific drug delivery and improvement of drug bioavailability is portrayed in the treatment of glioma. Chlorotoxin is a potential therapeutic peptide in clinical trials for the treatment of glioma (Mamelak and Jacoby, 2007). Chlorotoxin was conjugated to the surface of SPIONs for tissue specific peptide delivery, which in turn, showed multivalent interactions with glioma cells and a significant increase in cellular uptake of peptide when compared to free chlorotoxin (Veiseh et al., 2009).

Moreover, SPIONs can easily be functionalised, they are non-toxic, biodegradable and are cleared from the body efficiently, via the iron metabolism pathways (Chee et al., 2018). However, with these advantages come concerns regarding the possible unexpected onset of adverse side effects post-exposure. Furthermore, despite the numerous potential uses of SPIONs, current information on their potential toxicity is lacking and debatable data have been reported (Valdiglesias et al., 2016).

1.2.5.2 *Gold NPs (AuNPs) and Carbon nanotubes (CNTs)*

Similar to the described SPIONs, AuNPs are one of the alternate metallic NPs that have peaked scientific interest as they portray multiple advantages in relation to their biomedical use. AuNP advantages include ease of synthesis in various shapes and NP sizes, presence of a negative charge which allows for functionalisation with various efficacious biomolecules and lastly, AuNPs have been proven to be biocompatible and non-toxic. Henceforth, an example of AuNP use as drug delivery agents, was the conjugation of the commonly used chemotherapeutic agent Methotrexate to the surface of 13 nm colloidal AuNPs. The results from the study showed that the NP-drug conjugates portrayed tumour growth inhibition in a syngeneic lung tumour model (Kong

et al., 2017). In addition to metallic NPs, CNTs have also been investigated for their potential use in DDS to improve the pharmacological efficacies of delivered drugs, while reducing toxicological effects on off-target tissues (W. Zhang et al., 2011). Similar to the AuNPs, a study was conducted to investigate the efficacy of doxorubicin loaded functionalised multiwalled-CNTs on an MCF-7 tumour-induced mouse model. The results from the study showed that the chemotherapeutic loaded CNT based DDS treated mice had a longer survival span, when compared to mice treated with free doxorubicin or PBS as appropriate controls (Zeglis et al., 2015).

1.2.6 Nanotherapeutics in cancer

Despite significant technological and pharmaceutical advancements, cancer remains one of the leading causes of death worldwide (Siegel et al., 2021). Consequently, there is a dire need for the discovery and development of novel cancer therapeutic modalities that can aid in the improvement of cancer treatment and possibly, be of use for the prevention of cancer. Currently, cancer treatment involves a variety of modalities, including surgery, radiotherapy, and anticancer drugs (chemotherapy) (Ali et al., 2021).

Major obstacles in cancer treatment arise from factors such as tumour heterogeneity, drug resistance, and systemic toxicities (Jamal-Hanjani et al., 2015). Therefore, NP-based DDS are rapidly gaining popularity as systems for tumour specific delivery of antineoplastic therapeutic agents, while portraying minimal side effects, and efficiency against drug-resistant cancer when compared to free drugs (Tynga and Abrahamse, 2018). In addition to the investigation of NPs as vehicles for chemotherapeutic drug delivery in NP-based DDS, recent studies have investigated the use of theranostic multifunctional NPs, for cancer diagnosis and therapy. Due to strong NP interactions with enzymes, receptors, and antibodies, NPs can be functionalised through various

coatings and integrations with the described biomolecules, thus, converting them to appropriate nanomedicines that can detect and treat various carcinomas. Henceforth, in relation to cancer, theranostic NPs portray the ability to selectively accumulate in cancer tissues, deliver the therapeutic load in a selective way, have long circulating half-life and undergo eventual biodegradation (Ali et al., 2021).

An example of a NP formulation investigated for its use in cancer therapeutics includes the use of polymeric NPs (PNPs). PNPs are a type of inorganic NP that are defined as “colloidal macromolecules” based on their structural architecture that is formed of different monomers (Samadian et al., 2016). For the purpose of drug delivery and efficient drug release at the target site, the drug is either entrapped within or attached to the NP’s exterior, creating a nanosphere or a nanocapsule (Gavas et al., 2021). A study that investigated the efficacy of PNP capsules loaded with indomethacin, reported a significant decrease in tumour size and improved survival in a glioma xenograft rat model (Andronescu et al., 2016). However, with specificity going towards OS, several nanosystems have been developed in order to aid in OS disease management and improve therapeutic outcomes. An example of a NP formulation investigated for its therapeutic efficacy against OS, includes ZnONPs with no chemotherapeutic encapsulation or load. The results from the study reported a significant increase in ZnONP mediated OS cell death, in vitro, which was said to be a consequence of NP-induced excessive cellular reactive oxygen species (ROS) production (Pereira-Silva et al., 2020).

1.2.7 NP interactions with the immune system

As mentioned before, the innate immune system provides the first line of defence against foreign substances, which as expected, included exogenous particulate

materials. It has been reported that engineered NPs, once in systemic circulation within the host, can interact with the immune system in many different ways. Henceforth, NPs may induce inflammatory responses against themselves through interactions with innate immune cells such as neutrophils, macrophages and other effector cells. In relation, NP physicochemical properties such as size, shape and deformability influence nanoparticle uptake by a plethora of immune cells, thus, determining between acute and chronic inflammation in response to NP exposure. It is important to determine NP interactions with the immune system, in order to determine potential levels of NP-induced inflammation or immunotoxicity and thus, NP biosafety (Boraschi et al., 2017).

Inflammasomes are known to be a critical component of the innate immune system, which mediate majority of the inflammatory responses against exogenous engineered NPs. Studies have previously shown that SPIONs induce inflammasome activations, thus, providing evidence towards innate immune system recognition of SPIONs and induction of a protective inflammatory response. A further study investigated the impact of NP morphology on the inflammasome-activating property of SPIONs, with results showing that NP morphology plays a critical role in determining the level of inflammasome activation and therefore, induction of an innate immune response (Liu et al., 2018). Similarly, for other metal-based NPs, reports have shown that these NPs readily activate innate immune responses when they enter into the host's system. This is presented by NPs being readily internalised by phagocytic immune cells, such as macrophages and dendritic cells, in addition to the activation of mast cells and induction of inflammatory cytokine release (Luo et al., 2015).

Overall, when engineered NPs are administered, it is very likely that they will interact with the immune system and subsequently, induce both an innate and adaptive immune response (Kononenko et al., 2015). Over the years, significant advancements have been made in regard to the understanding of interactions between NPs and the immune system. However, a number of questions remain to be answered on the biological safety of engineered NPs, based on their immunomodulatory/immunotoxic interactions with both the innate and adaptive immune systems. Furthermore, it is important to determine the impact changes to NP physicochemical properties and further NP surface modifications may have in determining their effects on the immune system (J. Liu et al., 2022). Therefore, investigations into NP interactions with the immune system, both in vivo and in vitro, may provide useful indications towards their biosafety prior to potential use in biomedical applications. Since the innate immune system is the immediate line of defence against foreign particulates, NP interactions with the innate immune system may provide useful indications towards the initial biosafety of NPs when administered.

1.2.8 Nanoparticle cellular uptake

The major function of the cell plasma membrane (PM) is to protect the cell and its intracellular components from the surrounding environment (Mosquera et al., 2018). Furthermore, the PM is important in maintaining cellular homeostasis, providing structural support, maintaining ion concentration gradients (Behzadi et al., 2017) and strictly regulating the exchange of substances between the cell and its environment (Mosquera et al., 2018). Exchange across the PM can generally be divided into two main categories: passive and active transport. Gases, hydrophobic molecules and uncharged molecules can cross the PM by diffusion, from a region of high

concentration to a region of low concentration. This type of transport requires no energy; hence, it is called passive transport. On the other hand, active transport occurs when substances move against a concentration gradient; hence, energy is required and is provided by the hydrolysis of adenosine triphosphate (ATP) (Foroozandeh and Aziz, 2018).

A major factor that needs to be considered, when determining the potential biological applications of an active substance such as NPs, is its ability to be internalised by cells. Molecules that can readily cross the PM, are required in both biological research and medicine as most therapeutic agents function intracellularly (Mosquera et al., 2018). Hence, for most NPs safe uptake by cells is an important first step that is needed to achieve a high level of prognostic and therapeutic efficacy. Thereafter, the fate of these NPs post-uptake is important when playing the role of a carrier, to deliver therapeutic molecules to specific intracellular sites (Behzadi et al., 2017).

Despite their microscopic size and seemingly easy entry into host cells, NPs are characterised as polar molecules, thus, they do not have the capability to passively diffuse across the cellular PM. Since the PM is known to be permeable only to small and non-polar biological molecules, such as glucose, water and gases, NPs have to undertake ATP dependent active transport in order to enter cells through endocytosis (Chou et al., 2011). The endocytic pathway taken by the NPs has an important role in determining their biodistribution, biomedical applications and cytotoxicity. Therefore, understanding the cellular uptake and intracellular trafficking of NPs is crucial when trying to design safe and efficient nanomedicines (Foroozandeh and Aziz, 2018).

1.2.9 Mechanisms of NP cellular uptake

The cellular PM is said, to a certain level, mainly function in the regulation of cellular uptake processes including endocytosis (S. Kumari et al., 2010). Figure 1.12, shows the different modes of NP entry into the human body, including inhalation and injection. Furthermore, the figure portrays the creation of the NP protein-corona, which as described before, is caused by the adherence of biological fluid proteins to the surface of NPs. Lastly, the figure presents the different mechanisms of NP cellular uptake, including endocytosis as the ATP driven process of active uptake and in some cases, passive cellular uptake of NPs.

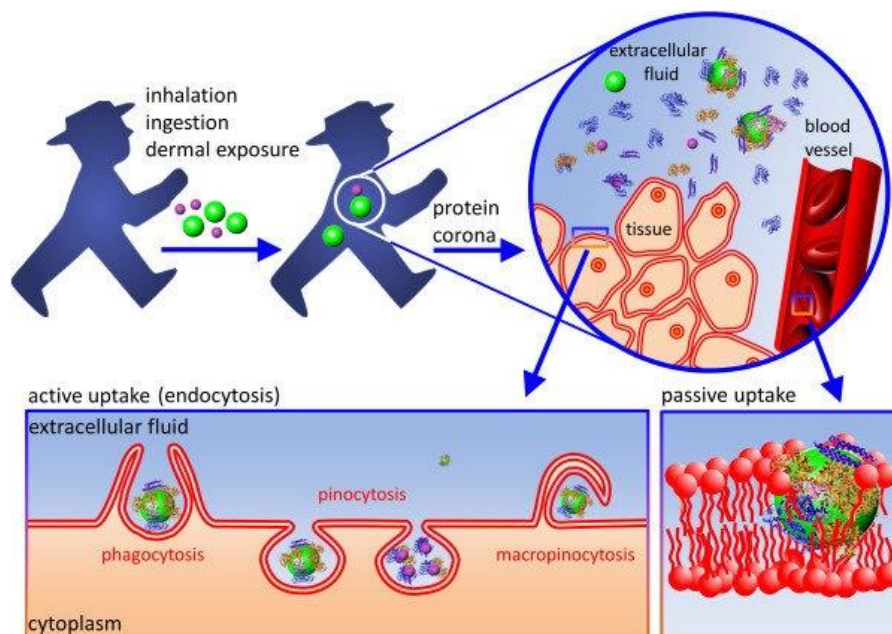


Figure 1.12: Modes of NP entry into the host and major mechanisms of NP uptake. The figure shows the different modes of NP entry into the host body and the mechanisms of NP cellular uptake, which include active and passive uptake mechanisms. Also shown, is the creation of the NP protein-corona, which is caused by the adherence of proteins to the NP surface. Image from: (Shang et al., 2014).

During the process of endocytosis, there is invagination of the PM, which subsequently takes up the biomolecules contained within the extracellular fluid. Next, there is budding off of the membrane inside the cell, thus, forming a membrane bound vesicle

termed an endosome (Makaraci and Kim, 2018; Doherty and McMahon, 2009) that translocate the biomolecules, such as proteins, extracellular fluids and lipids, across the plasma membrane and into the cell (Saheki and De Camilli, 2012). Depending on the type of biomolecule to be internalised into the cell, there are different mechanisms of cellular uptake, presented in figure 1.13.

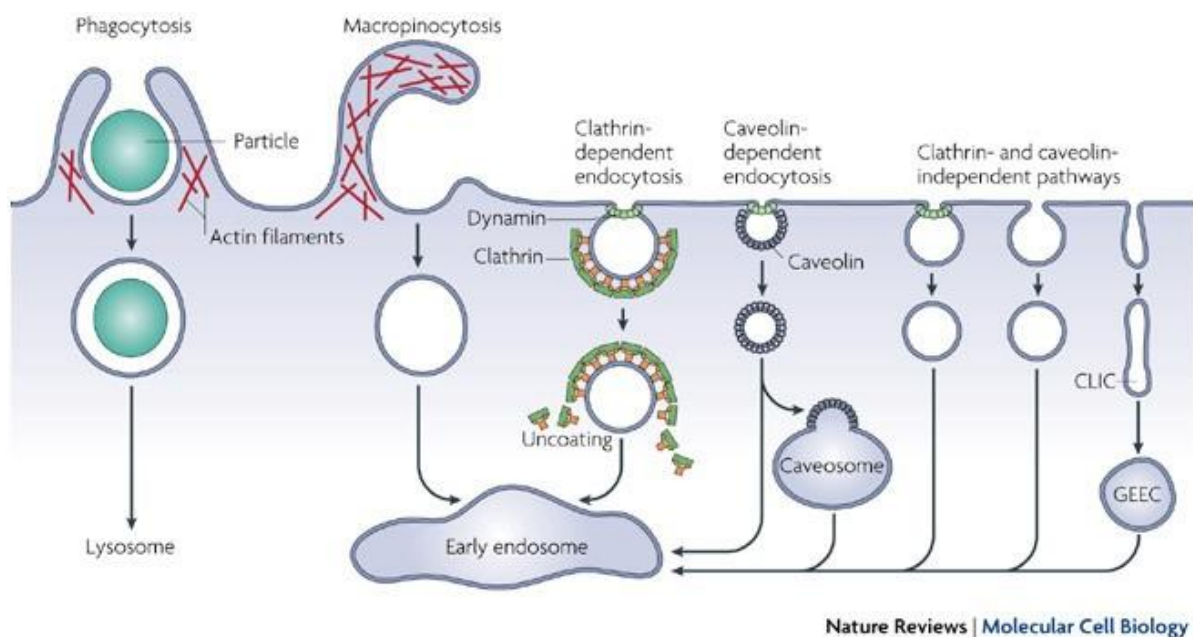


Figure 1.13: Mechanisms of endocytosis at the plasma membrane. The figure presents the different endocytic pathways commonly followed by various substances, including NPs, to gain entry into cells. It is said that the physicochemical properties of NPs and other biomolecules, determine the mechanism of endocytosis. Image from: (Mayor and Pagano, 2007).

The process of endocytosis can be generally classified into two large divisions, termed phagocytosis and pinocytosis (Foroozandeh and Aziz, 2018). Due to the microscale size of NPs, cellular uptake is generally carried out by pinocytosis (Zhao et al., 2011). Pinocytosis can be further subcategorised into four subtypes: macropinocytosis, clathrin-mediated endocytosis, caveolae-mediated endocytosis and clathrin/caveolae-independent endocytosis (Hirota and Ter, 2012; Yu, 2018). The described cellular

uptake pathways are known to be present in all cell types, however, the endocytic pathway undertaken will have an important role in determining the intracellular trafficking and cellular fate of internalised NPs (Jovic et al., 2010). Moreover, the specific endocytic pathway employed by NPs is determined by their physicochemical properties, with lipid NPs being known to specifically utilise clathrin-mediated endocytosis pathways during cellular uptake (Rivolta et al., 2011). Hence, physicochemical properties of NPs, such as size, shape and surface properties have been shown to significantly impact cellular uptake and consequently, impact intracellular trafficking and targeting of NPs (Qiu et al., 2010; Wu et al., 2011; Hillaireau and Couvreur, 2009).

Clathrin-mediated endocytosis (CME) is a major endocytic pathway that is one of the most studied in eukaryotic cells, due to its importance in the uptake of nutrients, membrane recycling, and intracellular signalling (Kirchhausen, 2000). More than fifty different cell surface proteins mediate the formation of clathrin coated vesicles at the PM (Popova et al., 2013), which in turn, work together to form a slight invagination of the PM followed by the formation of a spherical clathrin-coated vesicle (Macro et al., 2012). Once clathrin-coated vesicles are formed, dynamins assemble around the neck of the vesicle to create a bottleneck/ring like structure (presented in figure 1.13). Hence, the constriction of the dynamin proteins causes the release of the clathrin-coated vesicles from the PM and into the intracellular environment (Traub and Bonifacino, 2013; Popova et al., 2013). Intracellularly, the clathrin coat is removed by auxilins and chaperons such as Hsc70. The uncoated vesicle then fuses with early endosomes, thereby, undertaking the typical endocytic pathway which results in lysosomal degradation of its content or recycling back to the PM. CME is the main endocytic pathway for receptor mediated cellular uptake of NPs (Yameen et al., 2014).

In particular, PLGA NPs with sizes of approximately 100nm were reported to be taken up by cells mainly through CME. However, there have been no studies yet that show a direct link between NPs of 100nm in overall dimension and CME (Harush-Frenkel et al., 2007).

Caveolae-mediated endocytosis involves membrane bound structures called caveolae. These structures are known to play roles in multiple processes including protein endocytosis, signal transduction and cholesterol homeostasis (Parton and Simons, 2007). Specifically, caveolae are defined as small invaginations of the PM, typically between 50-100nm in size, and are known to be present in cells and tissues including fibroblasts, endothelial cells, smooth muscle cells and adipocytes (Cohen et al., 2004). Similar to the clathrin coated vesicles, caveolae are coated mainly by caveolins; particularly Cav1, Cav2 and Cav3 (Parton and Simons, 2007). Other proteins that coat caveolae and contribute to their formation include proteins known as cavins (Parton and Del Pozo, 2013). The protein coating caveolae are known to have the ability to oligomerise, a process that is important in the generation of the endocytic vesicle (Cohen et al., 2004). Similar to CME, the constriction of dynamin proteins causes the release of caveolae from the PM and into the intracellular environment (presented in figure 1.13). The caveolae fuse with cellular caveosomes or immediately with early endosomes, depending on the endocytosed material (Kiss and Botos, 2009).

Clathrin/caveolae-independent endocytosis (CIE) is known to play a role in processes such as cell polarisation, plasma membrane repair, intracellular signalling, and cellular division (Sandvig et al., 2008). Unlike clathrin and caveolae mediated endocytosis, CIE does not require intracellular vesicular coatings, however, it does involve vesicle formation on the surface of the plasma membrane. The formation of coating independent vesicles is dependent on the presence of actin and actin-associated

proteins (Mayor and Pagano, 2007). As shown in figure 1.13, the coating independent vesicles carry the internalised cargo to early endosomes, which then sort the cargo for lysosomal degradation or PM recycling (Hansen and Nichols, 2009).

Macropinocytosis is also a subcategory of pinocytosis. Macropinocytosis is an actin-dependent endocytic pathway and involves the formation of large membrane bound vesicles called macropinosomes (Lim and Gleeson, 2011). The pathway of macropinocytosis is the preferred route of uptake for larger biomolecules, including bacteria, viruses, apoptotic cell fragments and large amounts of extracellular fluids (Zeineddine and Yerbury, 2015). Since larger substances are generally taken up by macropinocytosis, larger vesicles of $>1\mu\text{m}$ in diameter are generated, as opposed to phagocytosis, whereby particles of $>0.5\mu\text{m}$ in diameter are taken up (Cardelli, 2001). As shown in figure 1.13, the formation of macropinosome membrane bound vesicles is promoted by actin polymerisation and actin-mediated ruffling (Kerr and Teasdale, 2009). Once macropinosomes are formed, containing the trapped biomolecules, the vesicles undergo a maturation process. The macropinosomes mature through extensive tubulation, which allows for a more spherical shape to be attained as they migrate centripetally towards the early endosomes (Lim and Gleeson, 2011).

Most literature, thus, suggest that NPs are internalised into cells through many different endocytic pathways. Therefore, understanding NP uptake mechanisms, intracellular trafficking pathways and eventual NP cellular fate, is important in determining the biological response(s) triggered against NP exposure and hence, the overall biosafety of certain NPs.

1.2.10 Intracellular trafficking and cellular fate of NPs

As described above, due to their overall microscale size, NPs are able to easily enter host cells. Furthermore, the small size of NPs allows for NP translocations across whole tissues and organs. NP cellular uptake at the NP-cellular interface and the related endocytic mechanism by which NPs are taken up, are crucial factors in determining their biomedical functionalities, host biodistribution and systemic and cellular toxicities (Foroozandeh and Aziz, 2018).

Although NPs interact with the host system in numerous ways, their consequent beneficial and/or deleterious properties are known to originate from their interactions at the cellular and subcellular levels. At this described NP-cellular interface, where cellular NP uptake takes place and NP cellular fate is determined, the NPs are capable of modulating cell fate, inducing or preventing mutations, initiating communications between cells, and modulating cellular structures (Behzadi et al., 2017). In nanomedicines and specifically NP therapeutic formulations, the safe internalisation by host cells is the first crucial step in obtaining high NP therapeutic efficacy (Foroozandeh and Aziz, 2018). Henceforth, NPs are used widely in biomedical applications as they have the ability to pass through strict biological barriers and enter host cells to exert their therapeutic functions. However, there is potential for adverse effects that may arise from the NP's capability to cross certain protective biological barriers, which include the BBB (Lai et al., 2007; Nishikawa and Sakaguchi, 2014).

In addition to cellular uptake, the cellular fate of NPs also has an impact in determining cellular and systemic nanoparticle toxicities post-cellular uptake (Wang et al., 2012; Meng et al., 2013). The cellular fate of NPs is defined as their intracellular translocation, post-cellular uptake, and their final destiny within the cell cytoplasm (Chu

et al., 2014). Once cellular NP internalisation has taken place, the NPs then undergo cellular transport down a range of cellular trafficking pathways to reach various intracellular destinations, which then becomes their ultimate intracellular destiny. In most cases, NP cellular internalisation occurs via endocytic pathways. Therefore, post endocytosis, NPs are confined within a membrane bound vesicle or are delivered to endosomes. The membrane bound vesicles then transport the encapsulated NPs through complex intracellular trafficking patterns, to ultimately reach the end of the cellular trafficking pathway. Similar to NP cellular uptake, NP intracellular trafficking and cellular fate are also dependent on host cell type and the physicochemical properties portrayed by the NPs at the biological interface (Donahue et al., 2019).

Intracellular trafficking and NP fate, post-cellular uptake, are vital processes with regards to the therapeutic success of the NPs (Chou et al., 2011; Petros and Desimone, 2010; Pridgen et al., 2015; Yameen et al., 2014). However, of greater importance with respect to NP biosafety, is the induction of NP mediated cellular toxicity which, in some cases, is mediated by intracellular fate/localisation in addition to the specific endocytic pathway utilised. Therefore, it is important to better understand the diverse range of intracellular trafficking pathways that can be taken by the internalised NPs and their ultimate intracellular fate (Albanese et al., 2012). The known intracellular trafficking pathways for NPs, once internalised, are shown in the schematic representation below (Figure 1.14).

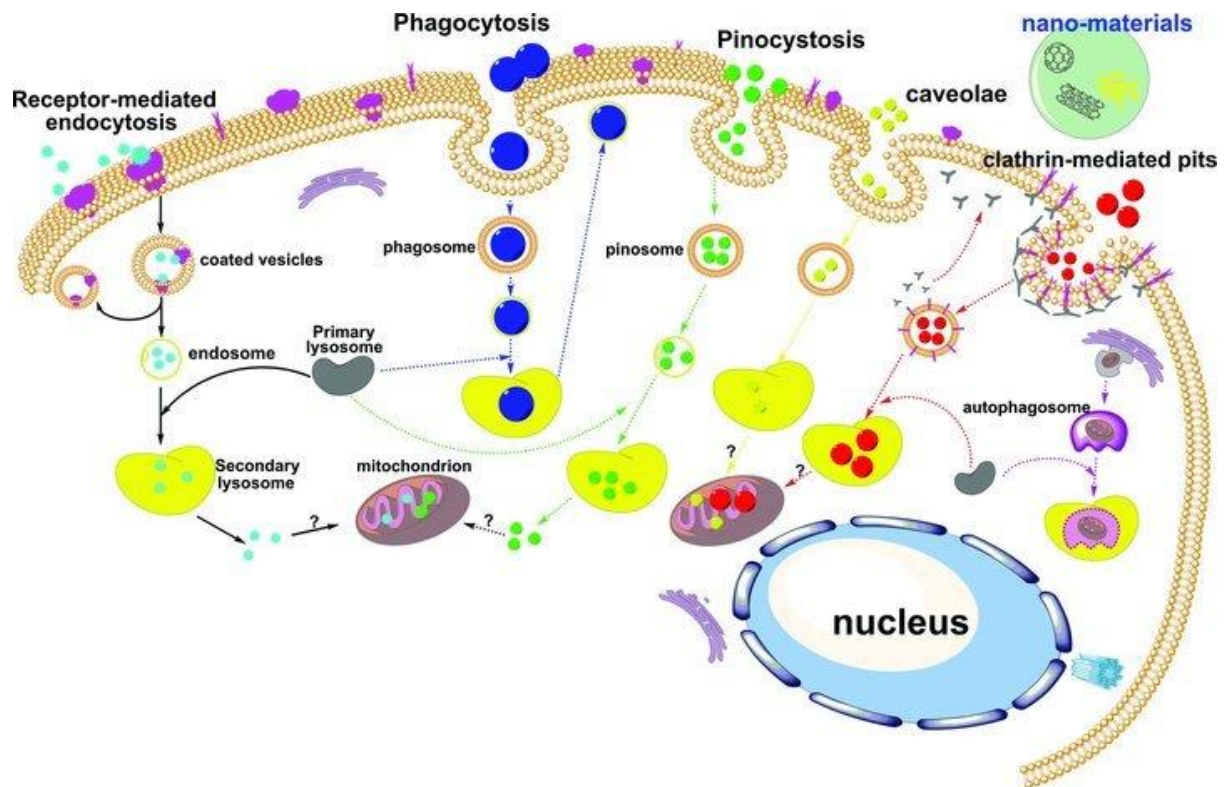


Figure 1.14: **Cellular uptake and intracellular trafficking of NPs.** The figure presents a schematic representation of the known cellular pathways involved in NP cellular uptake and intracellular trafficking. The schematic diagram shows the NP physicochemical property dependent modes of cellular uptake, along with their respective intracellular trafficking pathways. Therefore, the diagram further provides information on the various possible cellular fates for the internalised NPs, based on their mechanism of uptake and intracellular trafficking pathway. Image from: (Zhao et al., 2011).

Due to endocytosis being the major mechanism behind NP internalisation, the intracellular translocation and ultimate NP fate are largely dependent on the NP's ability to undergo endosomal escape (Chu et al., 2014). Therefore, cellular endosomal entrapment of NPs portrays a major biological barrier with regard to nanotherapeutic efforts in disease and in particular, drug delivery (Pei and Buyanova, 2019). Lack of endosomal escape would result in the maturation of the intracellular NP endosomal carriers and fusion between endosomes and lysosomes to form endolysosomes. Endolysosomal formation results in the enzymatic breakdown of encapsulated NPs (Paillard et al., 2010). On the other hand, endosomal escape would result in the cytoplasmic release of the encapsulated NPs.

In the event of lysosomal degradation, the NP intended biological and therapeutic functions can be inhibited. Consequently, NPs must overcome the described cellular endosomal barrier prior to gaining access to the cellular cytoplasm, cellular organelles and intracellular compartments, where they can conduct their intended biomedical functionality, such as drug delivery (Andrian et al., 2021). Hence, mechanisms through which NP carriers escape intracellular degradative vesicles have become a centre point of intense research (Degors et al., 2019). Through knowledge acquired from the innate ability of bacteria and viruses to escape endosomal vesicles, post-uptake, various NP endosomal escape mechanisms have been proposed. These NP endosomal escape strategies include cell membrane fusion, pore formation, “proton sponge” effect, vesicle budding and collapse and lastly, membrane disruption (Smith et al., 2019). Hence, various strategies to enhance NP endosomal escape have also been implemented. These include the alteration of NP surface chemistries, through the modification/coating of NP surfaces with cell penetrating peptides and other membrane disrupting surface modifications. Consequently, the endosomal membrane is disrupted and degenerated, leading to subsequent NP endosomal escape into the cytoplasm (Andrian et al., 2021). Therefore, the described NP endosomal escape strategies portray the importance of engineered NP physicochemical properties and surface alterations, in the determination of NP intracellular fate and in the generation of varying cellular fates.

On the other hand, NPs post cellular internalisation may not remain localised within the intracellular compartment to potentially become degraded by lysosomal enzymes. Or in the alternate scenario, if NP endosomal escape takes place, NPs are released into the cellular cytoplasm. Instead, the NPs may follow a differing intracellular trafficking pathway that may lead to the cellular excretion of the endocytosed NPs back

into the extracellular environment. Therefore, defining an alternate extracellular NP cellular fate (Chu et al., 2011). Cellular exocytosis is characterised by the expelling of intracellular contents into the extracellular space in membrane wrapped vesicles. In general, exocytosis occurs in an attempt to maintain cellular homeostasis and can occur through endosome mediated exocytosis during cellular component recycling or lysosomal mediated exocytosis (Gleichman, 2020; Sakhtianchi et al., 2013). Furthermore, the importance of cell type with regards to NP cellular fate is further emphasised, due to the fact that as in cellular internalisation of NPs, NP exit from cells also seems to be cell dependent. This conclusion was derived from the fact that different cell types that share similar NP endocytic pathways, portrayed markedly different exocytic processes and rates of cellular NP excretion (Oh and Park, 2014; Sakhtianchi et al., 2013; Behzadi et al., 2017). Therefore, studies have attempted to determine methods and mechanisms for reducing NP exocytosis, thus, increasing NP cellular retention and potentially enhancing their biomedical or therapeutic efficacy (Sakhtianchi et al., 2013).

In addition, physicochemical properties of NPs are determined in the unaltered, pristine state, therefore, interactions with biological fluids such as host blood and cell-culture medium are not accounted for as property altering factors. When NPs are in contact with biological fluids, such as blood, a protein corona is deposited, thus, altering the surface chemistry of NPs (Qin et al., 2020; Yan et al., 2013). In addition to the generation of the NP “protein corona”, which can have an impact on NP cellular recognition, interaction with the cell membrane and subsequently, intracellular NP fate, the NPs must also interact with the cellular microenvironment (Francia et al., 2019). Prior to reaching the plasma membrane of target cells, NPs must interact with the microenvironment surrounding target cells, which includes the extracellular matrix and

various microenvironmental factors. The cellular microenvironment is known to also alter the physicochemical properties of NPs, thus, impacting their interaction with target cell membranes and consequently, impacting their cellular fate (Engin et al., 2017).

In addition to NP related physicochemical properties and differing biological interactive factors at the NP-bio interface, cellular changes at the interface, such as differing host cell types, can play a dependent factor in NP cellular interactions. Therefore, a change in internalising cell type can impact NP cellular uptake, intracellular trafficking pathways and consequently, NP intracellular fate (Sohaebuddin et al., 2010). When cellular uptake and intracellular fate of carboxylated polystyrene particles were investigated in primary human hepatocytes, it was found that the NPs were not localised within early endosomes or lysosomes. However, here the NPs were only observed within the mitochondria of hepatocytes (Johnston et al., 2010). Unlike the carboxylated polystyrene particles, when cellular uptake and intracellular fate of silver NPs were investigated in human mesenchymal stem cells, the NPs were observed to be agglomerated in the perinuclear region of the cells. Thus, the NPs were found within endo-lysosomal vesicular structures of the cells, but not in the cell nucleus, endoplasmic reticulum or Golgi complex (W. He et al., 2016). Overall, apparent contradictory observations presented by various scientific studies looking into NP intracellular fate, in addition to the poorly understood significant interplay between various chemical, biological, electrostatic and NP morphological factors at the NP-bio interface, makes the overall understanding of the mechanisms behind and the ultimate determination of NP intracellular fate difficult (Chu et al., 2014).

1.2.11 Nanotoxicology

Despite the potential for positive applications of NPs in various fields, an increasing number of studies have shown that these NPs portray systemic (Song et al., 2012; Patlolla et al., 2015; Yu et al., 2020) and cellular adverse effects following exposure (AshaRani et al., 2009; Lee et al., 2014; Yu et al., 2020). Therefore, NP mediated toxicity is still a clinical concern and depends on their size and shape (Yu et al., 2020), which in turn, determines their propensity to induce ROS generation (Akter et al., 2018; Rajoria et al., 2019; Yu et al., 2020), to disrupt cellular compartments and induce undesirable immune responses (Wolfram et al., 2015). In addition, the physicochemical properties of the NP formulations can lead to a change in drug pharmacokinetics, such as drug absorption, distribution, elimination and metabolism. Moreover, NP toxicity and their persistence within the human body and in the environment, are also concerns (Soares et al., 2018). These concerns emphasise the need for rigorous methods for the determination of NP biosafety (Moya-Andérico et al., 2021). Henceforth, a screening tool that is high throughput and can rapidly and reliably determine in vivo NP toxicity is of great importance.

SPIONs as well as AuNPs produce toxic effects, most likely via the induction of oxidative stress. The production of the ROS, nitric oxide, leads to the oxidation of DNA and various other cellular proteins, hence, potentiating cellular necrosis or apoptosis. The toxic effects of AuNPs are known to be size-dependent, with smaller NPs having greater biodistribution mainly accumulating in the liver and spleen (Shrivastava et al., 2016; De Jong et al., 2008). The toxicity of CNTs on the other hand is largely dependent on their properties, such as length, aspect ratio, surface area and level of aggregation. Furthermore, CNTs, like SPIONs and AuNPs, are known to induce oxidative stress, inflammation, and apoptosis. However, unlike the other two NPs,

CNTs are also known for pulmonary inflammation, fibrosis and granuloma in the lungs (Francis and Devasena, 2018). Moreover, long CNTs are known to induce so-called frustrated phagocytosis in macrophages, which triggers persistent inflammatory responses and increases the production of ROS and cytokines (Yuan et al., 2019).

Various in vitro cellular toxicity assays and multi-cellular model organisms, such as mice, daphnia and sea urchins (Gambardella et al., 2014), have been used to determine NP toxicity. Toxicological effects of NPs, in vitro, are dependent on factors such as nanoparticle concentration, the number of NPs internalised, incubation time and importantly, the cell line used (Mukherjee et al., 2012). For example, identical concentrations of SPIONs induced significant cytotoxicity in brain-derived neuronal-glial and lung cells, but minimal toxicity in all other tested cell types (L. Li et al., 2013).

Therefore, in vivo experiments are essential when investigating the biological effects of NPs to observe regulations of pH, ionic strength and chemical composition in circulating blood (Moore et al., 2000). Moreover, in vivo experiments replicate the true physiological responses living organisms may have to nanomaterials (Barile, 2013). Hence, along with the exponential rise of engineered NPs and their products, there is a critical need for a model organism that can assess nanotoxicity accurately and at a high-throughput level (Chakraborty et al., 2016).

1.2.12 Differing mechanisms underlying NP toxicity

The cellular and molecular mechanisms underlying NP toxicity, both in vivo and in vitro, are known to vary from simple cellular interactions with NPs to adverse cellular responses against NP exposure. In relation, for a better understanding of NP toxicity and thus, biological safety, the mechanisms by which NPs exhibit toxicity have been extensively studied (Gupta and Xie, 2018; Cypriana P J et al., 2021). The major

cellular and molecular mechanisms underlying NP toxicity are said to include, (1) NP-induced cellular ROS production and subsequent oxidative stress, thus, resulting in cellular enzymatic and DNA damage, (2) dissolution of NPs post-cellular uptake, resulting in the release of free ions that subsequently induce toxic effects within the host organism, generally through enzyme impairment and/or DNA damage, and (3) direct NP interaction with the cell membrane, causing cell membrane damage and/or the initiation of downstream signalling pathways that result in cell death or destruction, such as apoptosis (Buchman et al., 2019). Some of the major mechanisms underlying NP toxicity are represented in figure 1.15.

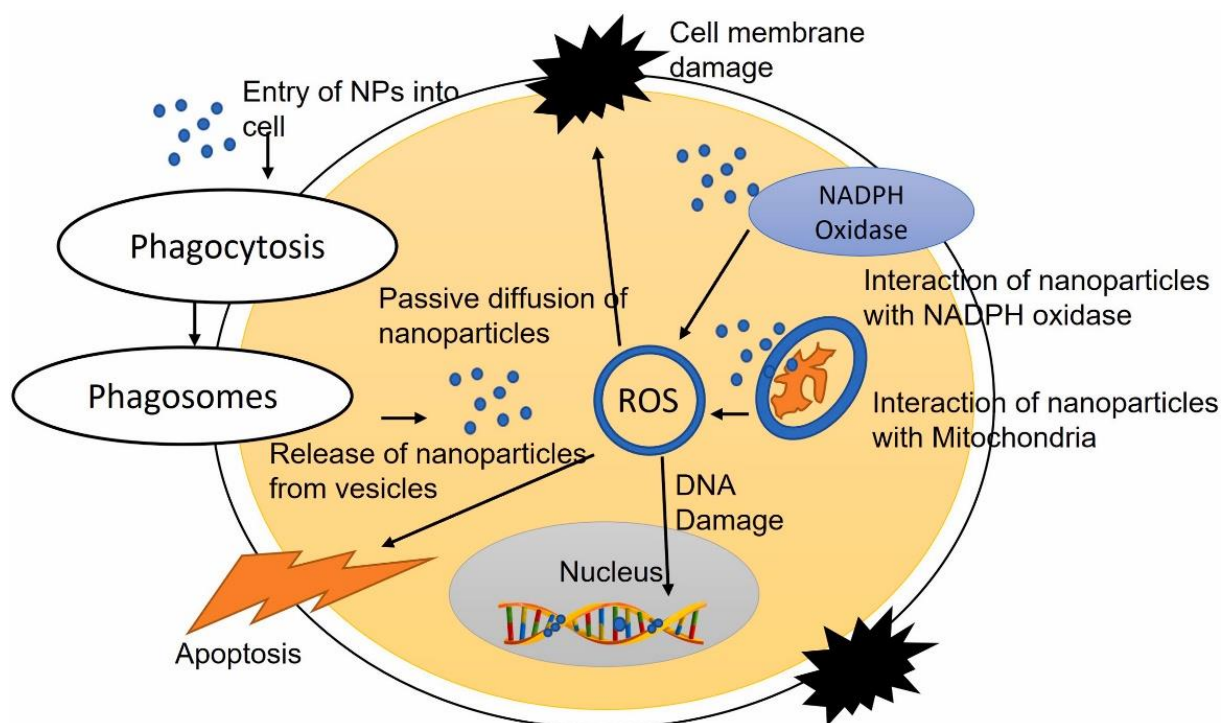


Figure 1.15: Major mechanisms underlying nanotoxicity. The figure above presents the major investigated mechanisms behind nanoparticle toxicity, which are dependent on NP-cellular interactions and cellular internalisation. Mechanisms including cell membrane damage and bursts of cellular reactive oxygen species are shown. In addition, the resulting damage of NP-induced cellular ROS species increases and cellular oxidative stress are shown, which include damage of cellular proteins, DNA damage and activation of signalling pathways that result in cell autophagy or apoptosis. Image from: (Cypriana P J et al., 2021).

1.2.12.1 *NP-induced excessive cellular ROS production*

NP-induced excessive cellular ROS production and therefore, cellular oxidative stress, has been described as the foremost mechanism underlying NP toxicity. The propensity of differing NPs to induce excessive cellular ROS production is highly correlated with particle size, shape, surface area, and chemistry. Furthermore, NP-induced cellular ROS production is particularly associated with metal and carbon-based NPs. (Dayem et al., 2017). However, under normal conditions, cellular ROS production possesses multiple functions in common cellular biology processes, including the modulation of cellular signalling pathways involved in cell death, proliferation, and differentiation (Sena and Chandel, 2012; Shadel and Horvath, 2015; Dayem et al., 2017). Therefore, in general, most cell types tolerate small and transient increases in ROS, through cellular antioxidant networks that scavenge excessively produced ROS. In general, a long-term balance between the production and scavenging of excessively produced ROS results in cellular homeostasis. However, at times, the balance is sifted in favour of free radical formation, like in the case of NP-induced cellular ROS production (Poljsak et al., 2013).

Following exposure to exogenous NPs and cellular NP uptake, normal levels of intracellular ROS production may sharply increase due to NP-induced ROS bursts within the cells (Yu et al., 2020). It is said that the main mechanism behind NP-induced cellular ROS bursts, involves free ions released by internalised NPs, which promote the overproduction of ROS through the impairment of mitochondrial respiration (Lee et al., 2018; Gaetke and Chow, 2003). The NP released free ions themselves, induce adverse effects within the cell through involvement in Fenton reactions (Nel et al., 2006). In addition, the disassociated free ions have been shown to cause cellular

enzyme deactivations, membrane structure disruptions and further enhances in the accumulation of intracellular ROS (Carlson et al., 2008).

Therefore, due to the disruption of normal cell physiological functionalities, excessive cellular ROS production and oxidative stress have been shown to result in a range of physiopathological outcomes. These include genotoxicity/DNA damage, apoptosis, necrosis, inflammation, fibrosis, metaplasia, hypertrophy, and carcinogenesis (AshaRani et al., 2009, 2012; Nel et al., 2006). In addition, NP toxicity has also been associated with increases in pro-inflammatory cytokine expression levels, therefore, resulting in the activation of inflammatory cells and further increases in the production of intracellular ROS (Nel et al., 2006; Gojova et al., 2007). Figure 1.16 presents a summary of the adverse cytotoxic effects caused by NP-induced excessive cellular ROS production.

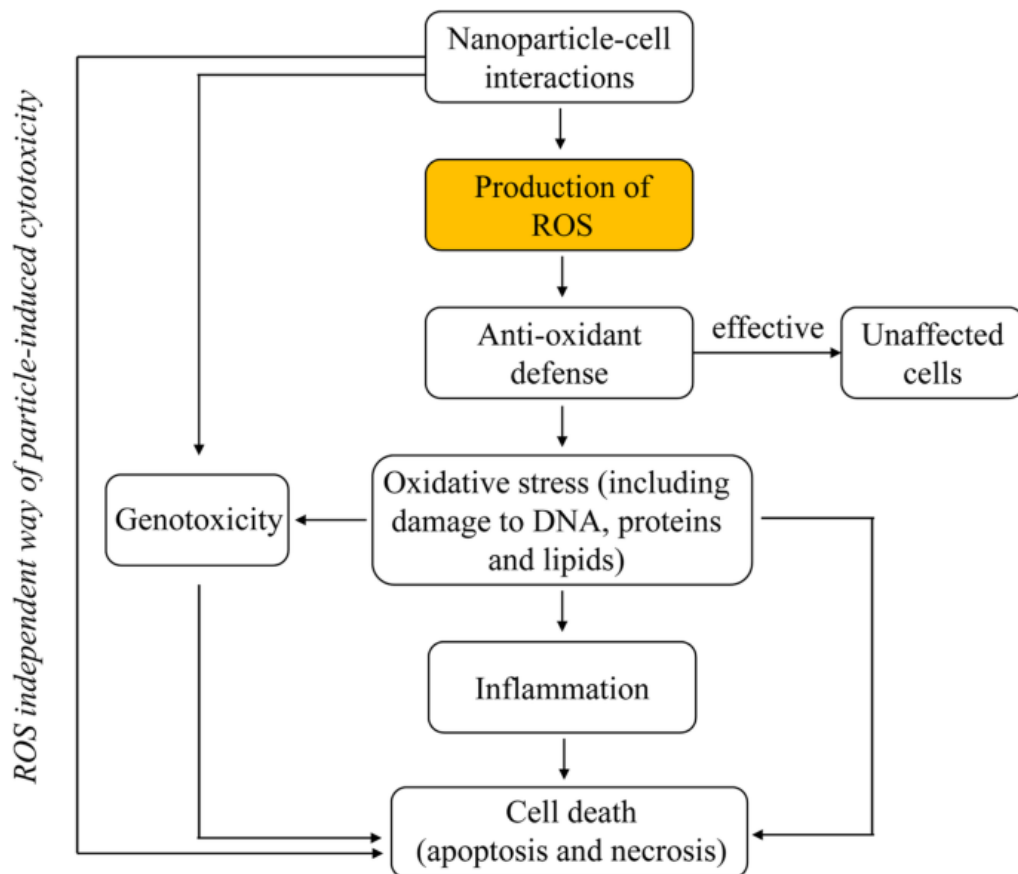


Figure 1.16: Nanotoxicity through ROS production and cellular oxidative stress. The above figure presents a flow-diagrammatic representation of the cell damaging consequences behind NP-induced cellular ROS production and oxidative stress (Tomankova et al., 2015). The diagram shows that NP-cellular interactions known to induce increases in cellular ROS production. Normally, these free radicals are scavenged by cellular antioxidants which allow the cells to be unaffected. However, ROS mediated cellular oxidative stress can cause unrepairable cell damage, which include protein and DNA damage, inflammation and activation of cell death pathways (apoptosis and necrosis). Image from: (Yu et al., 2020).

1.3 Animal models to assess NP toxicity in vivo

1.3.1 Use of animal models in NP toxicity assays

Animal models have been used for scientific purposes since the time of ancient Greece. However, only since the beginning of the 1900s did vertebrate models represent the gold standard for in vivo testing, as in certain aspects, they portray a human-like phenotype. Therefore, these vertebrate models have provided essential mechanistic, efficacious and toxicological information (Cutuli et al., 2019). A significant number of major scientific and medical research breakthroughs can be dedicated to observations and testing carried out on animal models. Their use has not only been based on the fact that they share vast biological commonalities with most mammals, but also due to the fact that other animal species are often affected by human diseases, such as Type I diabetes (Barré-Sinoussi and Montagutelli, 2015).

However, testing using traditional mammalian species raises many ethical concerns. Henceforth, national and international government agencies put forward a need to replace, reduce or refine (“Three R’s” principle) toxicological testing with mammalian species, by utilising alternative testing methods and non-mammalian in vivo models (Peterson et al., 2008). The proposition of alternative in vivo models aims to lower the cost of drug development experiments and increase the speed of data output (Cools et al., 2019).

Over the years, several model organisms have been exploited to improve our understanding of human disease mechanisms, genetic disorders, development and more. Most commonly used in vivo model organisms include monkeys (Riccio et al., 2015), Zebrafish (*Danio rerio*) (Montazerolghaem et al., 2015), mice (*Mus musculus*) (Iguchi et al., 2015), *Drosophila melanogaster* (Foriel et al., 2015) and yeast

(*Saccharomyces*) (Delorme-Axford et al., 2015). Table 1.1 provides an overview of the model organisms commonly being used in biomedical research and the most common research applications for the respective organism.

Table 1.1: Differing model organisms and their biomedical research applications. The table below present the various model organisms commonly being utilised in biomedical research. Furthermore, the table also presents the common name for each organism and the biomedical research applications the respective organisms are commonly used for. Table from: (Rosenthal and Brown, 2007).

Model Organism	Common Name	Research Applications
<i>Saccharomyces cerevisiae</i>	Yeast	Used for biological studies of cell processes (e.g., mitosis) and diseases (e.g., cancer)
<i>Pisum sativum</i>	Pea plant	Used by Gregor Mendel to describe patterns of inheritance
<i>Drosophila melanogaster</i>	Fruit fly	Employed in a wide variety of studies ranging from early gene mapping, via linkage and recombination studies, to large scale mutant screens to identify genes related to specific biological functions
<i>Caenorhabditis elegans</i>	Roundworm (nematode)	Valuable for studying the development of simple nervous systems and the aging process
<i>Danio rerio</i>	Zebra fish	Used for mapping and identifying genes involved in organ development
<i>Gallus gallus domesticus</i>	Chicken	Used for embryology and developmental research
<i>Mus musculus</i>	House mouse	Commonly used to study genetic principles and human disease
<i>Rattus norvegicus</i>	Brown rat	Commonly used to study genetic principles and human disease

Invertebrates such as *Drosophila melanogaster* and *Caenorhabditis elegans*, are seen as excellent models for the study of human genetics. These models have acted as tools in molecular biology, to help us understand the role of complex interacting proteins in various signalling pathways (Wilson-Sanders, 2011). On the other hand, vertebrate model organisms such as mice, zebrafish and monkeys are preferred over invertebrate models, when trying to understand human disease mechanisms. This is because vertebrates conserve major developmental and physiological processes and key organ systems, such as the digestive, nervous and cardiovascular systems (Hsu

et al., 2007). However, vertebrate model organisms are complex and difficult to fully understand (Chakraborty et al., 2016).

Therefore, non-mammalian model organisms are commonly used to study and assess nanotoxicity, they include *Drosophila melanogaster* (Ong et al., 2015), Zebrafish (*Danio rerio*) (Haque and Ward, 2018) and *Caenorhabditis elegans* (*C. elegans*) (Gonzalez-Moragas et al., 2015).

1.3.2 GM: a novel in vivo model organism to determine NP toxicity

A model organism that is rapidly gaining popularity as an alternative to vertebrate models, is the larvae of the greater wax moth, *Galleria Mellonella* (GM). GM, also known as the honeycomb moth is an insect of the Galleriinae subfamily within the Pyralidae family of the Lepidopteran order (Cutuli et al., 2019). GM are found throughout the world in beehives or often in stored waxes, where the larvae feed on honey, pollen and wax (Vertyporokh and Wojda, 2020). Like their relative the lesser wax moth, they have four distinct life stages: egg, larva, pupa and adult (Cutuli et al., 2019) (figure 1.14). GM have a high fertility rate, their larvae have a rapid growth rate, are relatively large and have a short life cycle, thus, they portray features that are expected from a good model organism (Mikulak et al., 2018). Concerning their relatively large size, it makes manipulation more convenient and therefore, facilitates injection and hemolymph collection (Vertyporokh and Wojda, 2020). For their use in the lab, the larvae offer several advantages that include ease of handling, low cost, good tolerance to a wide range of temperatures, space efficiency and a low biohazard risk (Trevijano-Contador and Zaragoza, 2019) (Figure 1.17). Their short lifespan also means they are suitable for high throughput studies (Conery et al., 2014). Finally,

unlike other alternative insect models, the larvae can survive at 37°C, allowing for the study of biological agents at a human body temperature (Junqueira, 2012).

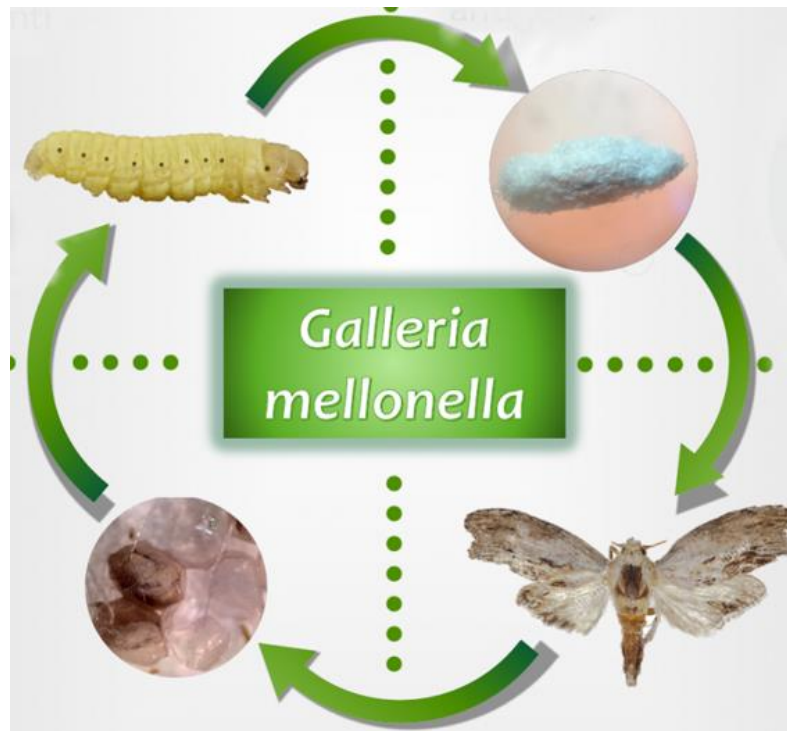


Figure 1.17: The life cycle of the model organism (*Galleria Mellonella*). The image above shows the life cycle of the model organism *Galleria Mellonella*, also referred to as the Greater wax moth. The four distinct life stages of the organism (egg, larva, pupa and adult) are shown. Image from: (Maker Faire Rome, 2019).

Over the years, GM larvae have been used as powerful *in vivo* infection models in studies of pathogenesis, virulence mechanisms, immune response and host resistance, as they are well-established models of the mammalian innate immune system (IIS) (Hernandez et al., 2019). GM larvae are thus commonly used to study host-pathogen interactions, including the highly virulent strain *Pseudomonas aeruginosa* (PA14) (Jander et al., 2000), to aid in the identification of bacterial virulence factors. Hence, allowing the discovery of novel components that play vital roles in host driven innate immune responses (Miyata et al., 2003). Furthermore, the larvae are used to provide a rapid, inexpensive, and reliable evaluation of the toxicity and efficacy of new antimicrobial and fungicidal agents *in vivo*, at an early stage during drug

development (Desbois and Coote, 2012). The results obtained from these studies have been useful in predicting the human body's response to antibiotics (Thomas et al., 2013). Figure 1.18 presents an overview of the advantages offered by GM larvae, for their use in research applications. Furthermore, the figure presents an overview of the research applications the larvae are currently being used for. Henceforth, the use of GM can decrease the use of the more expensive yet needed mammalian models by screening out agents that show a low likelihood of success and thus will reduce the overall cost of drug development (Desbois and Coote, 2012).

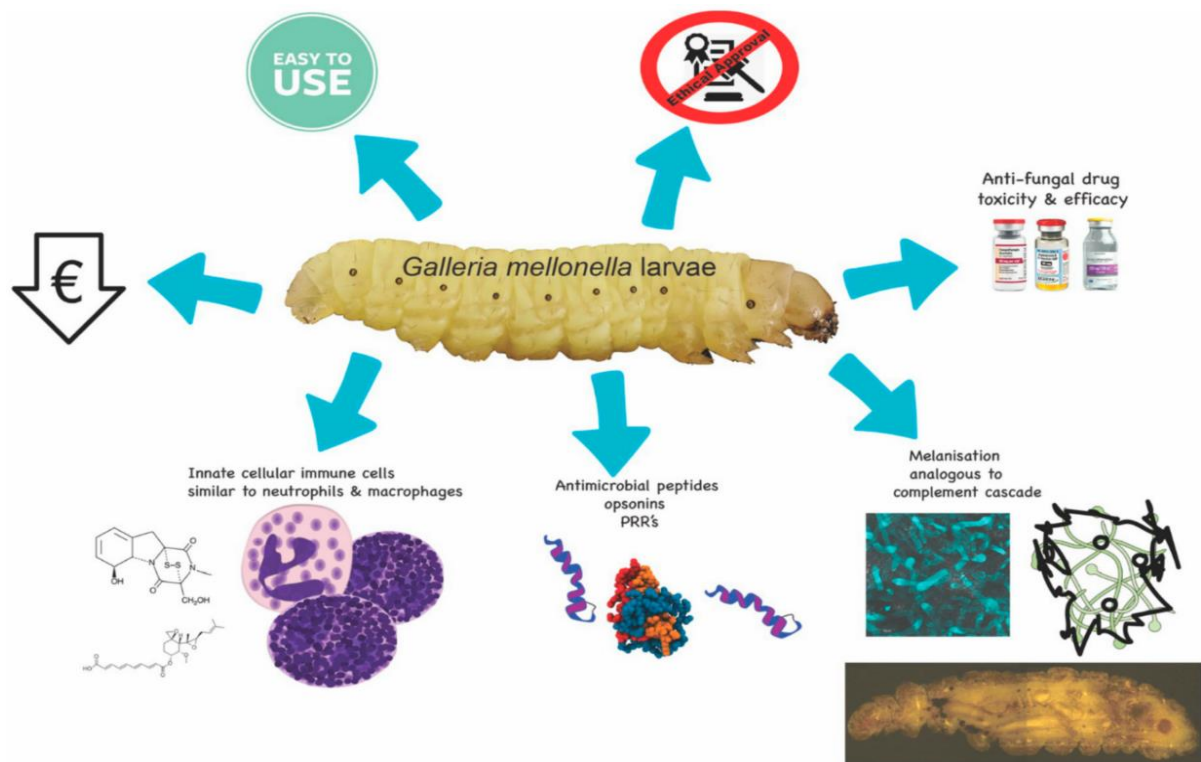


Figure 1.18: The advantages and research applications of *Galleria Mellonella* larvae. The figure above shows the various advantages portrayed by GM larvae, thus, making them an attractive model organism for use in biomedical research. These advantages include low cost, ease of use, lack of needing ethical approval and a cellular innate immune system that is homologous to the mammalian innate immune system. Furthermore, the figure also shows the different research applications the GM larvae are currently being used for, which include determining the toxicity of novel anti-bacterial and antifungal therapeutic agents. Image from: (Kavanagh and Sheehan, 2018).

1.3.3 GM larval innate immune system

Comparative genome studies between invertebrates and humans have shown that invertebrates including GM larvae express numerous homologous of human genes that code for proteins involved in pathogen recognition and signal transduction (Mikulak et al., 2018). Invertebrates like the GM larvae possess a very complex innate immune system, closely resembling that of mammals. Therefore, GM larvae are known to be a well-established model of the mammalian IIS (Hernandez et al., 2019). The GM IIS can be divided into two components, the cellular component and the humoral component. The GM larvae have an open circulatory system that is known as hemolymph, which is contained within the general body cavity (hemocoel) (Trevijano-Contador and Zaragoza, 2019). In addition, cells of the larval hemolymph, which are generally referred to as hemocytes, make up the cellular immune response and are able to phagocytose or encapsulate invading microbes. Furthermore, the humoral immune response consists of lysozyme production, the production of small antimicrobial peptides and melanisation (Ramarao et al., 2012). Overall, studies have shown that the GM immune response is highly selective and has the ability to distinguish between various classes of microorganisms (Trevijano-Contador and Zaragoza, 2019).

1.3.3.1 *Cellular immune response*

As mentioned, the cellular immune response is mediated by the larval hemocytes (blood cells of GM). Unlike mammalian blood cells, hemocytes play no role in the transportation of gases, since the larvae have a complex network of tubes to carry out this requirement. Therefore, hemocytes play a multifunctional role, with functions including storage of various active substances, while providing a defensive barrier via

coagulation mechanisms, phagocytosis, nodulation and melanisation. There are up to eight identified classes of hemocytes within the GM, which include, prohemocytes, plasmatocytes, granular cells, coagulocytes, spherulocytes and oenocytoids (Cools et al., 2019; Trevijano-Contador and Zaragoza, 2019)

Prohemocytes are small in size, have large nuclei and can differentiate into any cell type found within the hemolymph. Plasmatocytes, are larger than prohemocytes and are the most abundant cell type in the hemolymph. Coagulocytes are hemocytes that are responsible for carrying out hemolymph clotting, which is an important process as it is the first line of defence against invading microorganisms. Many studies mention that only plasmatocytes are involved in phagocytosis; however, further studies have shown that both plasmatocytes and granular cells carry out this immune function along with encapsulation (Trevijano-Contador and Zaragoza, 2019).

1.3.3.2 *Humoral immune response*

Antimicrobial peptides (AMPs)

AMP synthesis makes up the majority of the humoral immune response, as the initial contact with microorganisms induces the transcription of AMP-encoding genes. These molecules play a crucial role in GM's defence and are produced mainly in the fat body with subsequent release into the hemolymph. In addition, AMPs are divided into two groups, cationic and anionic AMPs. The anionic AMPs are only activated against pathogens that are resistant to the cationic peptides (Trevijano-Contador and Zaragoza, 2019).

Lytic enzymes (Lysozymes)

Lysozymes found in the GM hemolymph are antibacterial enzymes, which carry out their antibacterial function through the hydrolysis of β -1,4 linkages between N-

acetylmuramic acid and N-acetyl-D-glucosamine residues in peptidoglycan, a major component of the bacterial cell wall. There have also been reports of their antifungal activity via growth inhibition, through their enzymatic activity against fungal cell walls (Trevijano-Contador and Zaragoza, 2019).

Melanisation

Melanin is synthesised in response to foreign bodies and plays a crucial role in multiple defence reactions. Production of melanin causes the accumulation of nodules that contain the replication of microorganisms. The enzyme responsible for catalysing the synthesis of melanin is phenoloxidase (PO). PO is found in the hemolymph and hemocytes of GM in its inactive form prophenoloxidase (PPO). PPO is activated to PO by cell wall components of fungi and bacteria, such as lipopolysaccharides and peptidoglycan (Trevijano-Contador and Zaragoza, 2019).

1.3.4 Utility of GM in determining environmental NP toxicity

NPs, including metal and metal-oxide NPs, have particularly presented many challenges to terrestrial ecotoxicology due to their ever-increasing use in industrial and commercial platforms (Ray et al., 2009). Therefore, many studies that have previously utilised GM larvae for the evaluation of NP toxicity in vivo, specifically aimed to determine NP toxicological effects on the surrounding environment and living organisms. These studies were conducted as opposed to studies that utilised GM larvae to determine NP biosafety, prior to their potential use as drug delivery agents. The table below presents a summary of specific studies that utilised GM larvae, in order to investigate the toxicological impact of NPs on the surrounding environment (Table 1.2).

Table 1.2: Utility of GM larvae in NP ecotoxicological studies. A table presenting specific studies that utilised GM larvae to investigate the potential toxicological impacts of NPs, on the surrounding environment and organisms. The table presents the types of NPs investigated for their environmental toxicity, the NP concentrations assayed in each study and a summary of in vivo toxicity results gathered. Majority of the NP ecotoxicological studies were conducted by groups including (Nurullahoğlu, Eskin and Kaya, 2015), (Eskin et al., 2019), (Zorlu et al., 2018) and (Tuncsoy and Ozalp, 2017).

Type of Nanoparticle (NP)	Concentration(s) of NP introduced and method	Summary of in vivo toxicity
Zinc Oxide NPs (Nurullahoğlu, Eskin and Kaya, 2015).	(100, 500, 1000, 3000 and 5000 ppm) were added to the diet of second instar larvae	Total hemocyte counts (THC) in larval groups exposed to 1000, 3000 and 5000 ppm ZnO NPs decreased significantly.
Zinc Oxide NPs (Eskin et al., 2019).	(0.5, 1, 2.5, 5 µg/10 µl) of NPs were introduced using the force-feeding method	24h post-feeding, THC showed statistically insignificant changes in all treatments compared with the control.
Titanium dioxide (TiO ₂) (Zorlu et al., 2018).	(100, 500, 1000, 3000 and 5000 ppm) were added to the diet of larvae	Dietary exposure to low concentrations, resulted in larval developmental times increasing and shortening of lifespan.
Titanium dioxide (TiO ₂) (Zorlu et al., 2018).	(100, 500, 1000, 3000 and 5000 ppm) were added to the diet of first instar larvae	Weights of pupae and adults increased, along with the ratio of morphological abnormalities in adults.
Copper oxide (CuO) (Tuncsoy and Ozalp, 2017).	(10, 100 and 1000 mg/L) of NPs were added to the diet of larvae	72h post-feeding, all larvae exhibited normal behaviour and no mortality was observed. Low concentrations induced higher THC with high concentration (1000 mg/L) inducing a decrease in THC.

Silver NPs (AgNPs) (Eskin et al., 2014).	(100, 500, 1000, 3000 and 5000 ppm) were added to the diet of last instar larvae	Groups of larvae exposed to 500, 1000, 3000 and 5000 ppm AgNP concentrations respectively, had a significantly lower THC.
--	--	---

1.3.5 Utility of GM in determining NP potential as drug delivery agents

In the described studies involving the utility of GM larvae to study NP toxicity and biological safety, the studies specifically utilised the GM larvae model organisms to study the potential toxicological effects of NPs released into the environment. However, within biomedical and clinical platforms, NPs have also been studied as potential drug delivery agents for the treatment of various diseases. In studies involving both NPs as drug delivery agents and GM larvae as model organisms, the larvae are usually used as infection models to determine the antibacterial or antifungal efficacy of specific NP formulations. Henceforth, Passos et al, evaluated the antifungal efficacy of topical lipid NPs loaded with the drug Itraconazole. Due to the limitations and adverse side effects of oral Itraconazole therapy, nanostructured lipid carriers were studied as topical drug delivery agents to potentially increase drug localisation in skin lesions and decrease systemic side effects. In the study, the GM larvae were first used as a model for toxicity and the results showed a lack of toxicity, therefore, deeming the unloaded and Itraconazole-loaded NPs to be safe (based on survival and health index of GM). Thereafter, the antifungal efficacy of Itraconazole-loaded NPs was evaluated by utilising GM larvae infected with *S. brasiliensis* yeasts and *Candida albicans*. Treatment with loaded NPs, improved the survival rate and health index of infected GM larvae, hence, demonstrating antifungal efficacy (Passos et al., 2020).

Similarly, Vera-González et al, evaluated the antifungal efficacy of liposomal NPs loaded with the drug Anidulafungin, a potent antifungal. The goal of developing this NP formulation was to increase drug solubility and drug localisation to fungi. In the study, liposomal NPs were fabricated with three different concentrations of Anidulafungin. With regards to the GM larvae, they were utilised as infection models, where they were infected with *Candida albicans*. The developed liposomal NP formulations were then tested in vivo, with the use of the infected GM larvae. Treatment with the drug-loaded NPs, resulted in increased larval survival when compared to the free drug treated group. Results showed a larval survival rate of 33-67% over 7 days, depending on the liposomal formulation, compared to 25% larval survival in the free drug treated group (Vera-González et al., 2020).

In addition to the described potential use of NPs as antifungal drug delivery agents, the NPs can also be used as tools to increase the antibacterial activity of antimicrobial compounds/agents. *Helicobacter pylori*, for example, inhabit the gastric epithelium and plays a role in the development of gastric disorders, such as peptic ulcers and gastric adenocarcinomas. *Helicobacter pylori* infections are known to be difficult to control, hence, Almeida Furquim De Camargo et al, suggest a new strategy for battling *H. pylori* infections. The strategy described by the group consists of an antibacterial silver compound, loaded into polymeric NPs. The compound alone had a minimum inhibitory concentration for *Helicobacter pylori* of 3.90 µg/mL, which was optimised to 0.781 µg/mL once loaded into the NPs. Similarly, the minimum bactericidal concentration was optimised 5-fold from 7.81 µg/mL to 1.56 µg/mL, once loaded. With regards to the GM larvae, the NP formulation allowed for GM larval survival at a concentration of 200 µg/mL, thus, demonstrating the antibacterial activity of the formulation against *Helicobacter pylori* (Almeida Furquim De Camargo et al., 2020).

As mentioned previously, there are many advantages that come with the potential use of NPs as drug delivery agents. One advantage is the decrease in systemic adverse effects due to the targeted drug delivery. Hence, NPs can be utilised to reduce the toxicity of already defined therapeutic agents. Miltefosine is a therapeutic agent that has been defined as an alternative antifungal agent, however, it presents many adverse effects. Henceforth, Spadari et al, aimed to produce a NP formulation consisting of Miltefosine-loaded alginate NPs, to reduce drug toxicity and for potential use as an alternative mode of treatment for cryptococcosis and candidiasis infections. The GM larvae were infected with *Candida albicans*, *Cryptococcus neoformans* and *Cryptococcus gattii*. Thereafter, treatment efficacy was evaluated by survival curve, colony forming unit (CFU) counting and histopathological analysis. The results first determined the NP formulation to be safe, due to the lack of hemolytic activity and toxicity in GM larvae. Thereafter, treatment with the NP formulation improved the survival rate of larvae infected with *Candida albicans* and *Cryptococcus gattii*. The results support the use of alginate NPs as drug delivery agents, for drug toxicity reduction and for the treatment of fungal infections, in vivo (Spadari et al., 2019).

Aims and hypotheses

The aims of this thesis can be separated into two interrelated parts, whereby we aim to identify novel therapeutic targets for Osteosarcoma and in relation, investigate Nanotherapeutics as a novel therapeutic modality. The first part was to study the mechanisms underlying Osteosarcoma (OS) pathogenesis and the identification of potential novel therapeutic targets in the treatment of OS. In silico differential gene expression analysis was used to identify differentially expressed immune receptor genes in OS. Immunohistochemistry on primary OS tissues as well as functional assays was used to validate identified targets.

The second part of the study explored the use of nanoparticle (NP)-based drug delivery systems. Here, the main aim was to study the biological safety and toxicity of a range of inorganic NPs, using the invertebrate model system *Galleria mellonella* which we established as a useful tool in determining NP systemic and immune toxicities. We hypothesise that NP intracellular trafficking pathways and cellular fate can play roles in determining immune toxicity and thus, aimed to measure endosomal escape of NPs as a potential mechanism underlying NP-induced immunotoxicity.

2. Materials and Methods

2.1 Materials

All NP suspensions, buffers and solutions in this section were prepared as stated below unless otherwise specified.

Nanoparticle suspensions:

- **Anionic charged (uncoated) SPIONs:** product code: nano-screenMAG-UC/A, purchased from the manufacturer Chemicell. SPION stock concentration: 25 mg/ml (in aqueous dispersion). Particle size: 100nm.
- **Starch-coated (uncharged) SPIONs:** product code: nano-screenMAG-D/R/G, purchased from the manufacturer Chemicell. SPION stock concentration: 25 mg/ml (in aqueous dispersion). Particle size: 100nm.
- **Iron oxide nanoparticles (IONPs):** product code: 637106, purchased from the manufacturer Sigma-Aldrich. Prepared IONP stock concentration: 20 mg/ml (dispersed in 1x PBS solution). Particle size range: 50-100nm, confirmed by scanning electron microscopy (SEM).
- **Carbon nanotubes (CNTs):** Prepared CNT stock concentration (for all variants): 20 mg/ml (dispersed in 1x PBS solution). Particle size: ~600nm (for all variants), confirmed by SEM (Figure 2.1).
- **Gold nanoparticles (AuNPs):** product code: GCIKITDIAG, purchased from the manufacturer BBI solution. AuNP stock concentration: OD1 (0.0565 mg/ml) in aqueous dispersion. Gold colloidal NPs of varying sizes were purchased from this manufacturer (20,40,60 and 80nm).
- **Gold nanoparticles (AuNPs):** product code: 753688, purchased from the manufacturer Sigma-Aldrich. AuNP stock concentration: OD1 (0.0565 mg/ml) in aqueous dispersion. Particle size: 100nm.

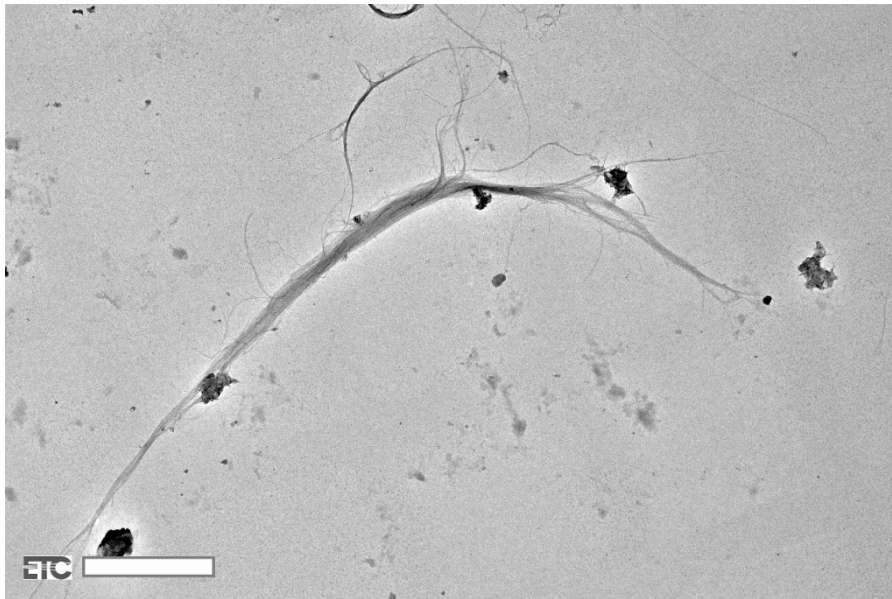


Figure 2.1: Visualisation of a CNT under SEM. An image acquired using SEM, presenting the physiological structure of a commercially purchased singular CNT. These CNTs were subsequently used in bulk, for the NP biosafety assays carried out and presented in this thesis. Scale bar: 100nm.

Phosphate Buffered Saline (PBS) (Thermo Fisher Scientific, Inc.)

PBS was prepared using Oxoid™ Phosphate Buffered Saline Tablets (Dulbecco A), which were dissolved in dH₂O and autoclaved at 121°C.

Phosphate Buffered Saline (PBS) - Tween (Thermo Fisher Scientific, Inc.)

0.001% Tween-20 in 1x PBS

Poly-D-lysine Hydrobromide solution (Sigma-Aldrich, Poole, UK)

MG63 OS cells were cultured on Poly-D-Lysine coated coverslips (5 µg/ml), according to the protocol provided by the supplier during immunofluorescent experiments. A pre-dissolved solution was purchased from the manufacturer at a stock concentration of 0.1 mg/ml.

Sodium citrate solution for immunohistochemistry

10 mM Sodium citrate dissolved in dH₂O and 0.05% Tween-20 (pH 6.0).

Blocking buffer for immunohistochemistry

5% bovine serum albumin (BSA) in 1x PBS

Blocking buffer for immunofluorescence

2% BSA in 1x PBS

Fluorescence activated cell sorting (FACS) buffer

0.5% BSA in 1x PBS

Acid citrate-dextrose (ACD) solution (Sigma-Aldrich, Poole, UK)

ACD solution was used in this study as a larval hemolymph anticoagulant, during *Galleria Mellonella* larval experiments. The solution was purchased from the supplier and is composed of 22.0 g/L Citric Acid, trisodium salt, dihydrate; 7.3 g/L Citric Acid, anhydrous; and 24.5 g/L D-(+)-Glucose.

Homogenisation medium (density gradient based subcellular fractionation)

0.25M sucrose, 1mM of Ethylenediaminetetraacetic acid (EDTA) and 20mM HEPES-NaOH (pH 7.4). In addition, a universal protease inhibitor (complete Mini EDTA free protease cocktail) (Roche, UK) was added fresh prior to use for the prevention of

proteolytic degradation of exposed cellular contents. The buffer was stored at 4 °C.

Optiprep density gradient medium

The non-ionic density gradient medium Optiprep was purchased from the supplier (Sigma-Aldrich, Poole, UK). It is composed of 60% (w/v) Iodixanol dissolved in water. The stock was diluted using a HES buffer to make a 50% working solution of Optiprep.

Optiprep diluent HES buffer

0.25M sucrose, 2mM EDTA and 40mM HEPES-NaOH (pH 7.4). The buffer was stored at 4 °C.

MES buffer for cell homogenisation

150mM NaCl and 25mM 2-(N-morpholino) ethanesulfonic acid sodium salt (Sigma-Aldrich, Poole, UK) dissolved in ddH₂O (pH to 6.5). A universal protease inhibitor (complete Mini EDTA free protease cocktail) (Roche, UK) was added fresh prior to use. The buffer was stored at 4 °C.

SDS acrylamide gel (stacking gel)

12% acrylamide mix (37:1), 0.375M Tris (pH = 8.8), 0.1% SDS, 0.1% ammonium persulfate, 0.001% TEMED and dH₂O.

SDS acrylamide gel (resolving gel)

3.75% acrylamide mix (37:1), 0.125M Tris (pH=8.8), 0.1% SDS, 0.1% ammonium persulfate, 0.1% TEMED and dH₂O.

SDS sample buffer

50mM Tris (pH=6.8), 100mM dithiothreitol, 2% SDS, 0.1% bromophenol blue and 10% glycerol.

SDS-PAGE Running buffer

25mM Tris (pH=8.3), 192mM Glycine and 0.1% SDS.

SDS-PAGE Transfer buffer

25mM Tris (pH=8.3), 192mM Glycine and 20% w/v methanol.

Enhanced Chemiluminescence (ECL) substrate solution

- Solution A: 0.1M Tris (pH 8.8), 90mM Coumaric acid and 250mM Luminol.
- Solution B: 0.1M Tris (pH 8.8) and 30% hydrogen peroxide.

2.2 Cell culture

FPR3 study

To investigate and quantify FPR3 expression on the surface of OS and normal primary bone cells, in addition to determining therapeutic efficacies presented by targeting FPR3, Saos-2 (ECACC 89050205) and MG63 (ECACC 86051601) human OS cells were cultured, along with primary human osteoblasts (HOBs). The primary HOBs, isolated from femoral trabecular bone tissue of the knee or hip joint region, were obtained from Promocell (PromoCell GmbH, Germany). Primary HOBs were purchased at passage 2 and were thus, classified as normal human osteoblasts. Saos-2 are human OS cells derived from the primary OS tumour of an 11-year-old Caucasian

female. Similarly, M6-63 are human OS cells that have fibroblast morphology and are derived from the primary OS tumour of a 14-year-old White male. All cells were cultured using aseptic techniques and incubated at 37°C in humidified conditions at 5% CO₂. Cells were regularly sub-cultured when reached 80% confluency, in T25 and T75 filter head flasks (Thermo Fisher Scientific, Inc.). Saos-2 and MG63 were cultured in low glucose Dulbecco's modified Eagle's medium (DMEM) (Thermo Fisher Scientific, Inc.) supplemented with 10% foetal bovine serum (FBS) and 1% penicillin-streptomycin (Thermo Fisher Scientific, Inc.). The primary human HOBs were cultured in an Osteoblast growth medium (PromoCell GmbH, Germany) supplemented with Promocell SupplementMix (PromoCell GmbH, Germany). MG63 cells do not adhere to glass surfaces, therefore, for the immunofluorescence experiments conducted with MG63 OS cells, cells were cultured on poly-D-lysine coated coverslips. Therefore, the 13mm diameter glass coverslips were coated according to the protocol provided by the supplier (Sigma-Aldrich, Poole, UK). Coverslips were allowed to dry for 15 minutes within wells of a 24 well tissue culture microplate. Thereafter, 200 µl of 0.01% poly-D-lysine (5 mg/ml stock solution) was added to each well for 10 minutes. After 10 minutes, the poly-D-lysine was aspirated and the coverslips were washed three times with deionised water. The coverslips were then allowed to dry overnight before cells were seeded. For all adherent cell dissociations, 1x Trypsin-EDTA at concentrations of 0.5 g/L trypsin and 0.2 g/L of EDTA was used (Thermo Fisher Scientific, Inc.).

Cellular ROS assay (in vitro)

For the measurement of NP-induced cellular ROS production, the mouse macrophage cell line RAW264.7 was used. This mouse macrophage cell line is known to be both phenotypically and functionally stable, thus, portraying macrophage mediated immune,

metabolic and phagocytic functionalities, similar to that of human macrophages (Taciak et al., 2018). Therefore, the cell line was seen as an appropriate model to mimic NP interactions with human innate immune cells, such as macrophages. Furthermore, due to its immune functionalities, the cell line is able to mimic subsequent cellular responses to NPs, including increases in cellular ROS production after uptake.

The cells were maintained in (Roswell Park Memorial Institute (RPMI)) 1640 medium (Biosera), fortified with 1% stable glutamine (2 mM) and supplemented with 10% FCS (Foetal Calf Serum) and 1% Pen Strep (Penicillin 100 U/ml and Streptomycin 100 µg/ml; Thermo Fisher Scientific, Inc.), in the presence of phenol red. The adherent cells were resuspended in the culture medium using a cell scraper and seeded in a 48-well microplate, at a cell concentration of 2×10^4 cells per 150 µl, per well. The cells were cultured in the microplate using aseptic techniques and incubated overnight at 37°C in humidified conditions at 5% CO₂.

Intracellular fate of NPs

RAW264.7 cells were also used to investigate intracellular trafficking pathways and cellular fate of NPs. RAW264.7 murine macrophage cells, were seeded with RPMI into T75 filter headed flasks (Thermo Fisher Scientific, Inc.) and cultured to approximately 80-90% confluence on the day of the experiments. Thus, respective T75 flasks were seeded with approximately 7×10^6 cells and the cells were then cultured overnight, to achieve the desired 80-90% confluence. Cells were cultured using aseptic techniques and incubated at 37°C in humidified conditions at 5% CO₂.

2.3 Treatment of cells with SPIONs

The starch-coated (SC) SPIONs used in this thesis are commercially available, consisting of a magnetite core that is first encased inside a lipophilic fluorescence dye, followed by a secondary encapsulation within a hydrophilic polysaccharide matrix (starch) coating, thus, having two coatings overall (Manufacturer: Chemicell) (Figure 2.2). Similarly, the anionic-charged SPIONs lack a starch matrix coating, therefore, presenting only a lipophilic fluorescence dye coating around the magnetic core and an overall negative charge.

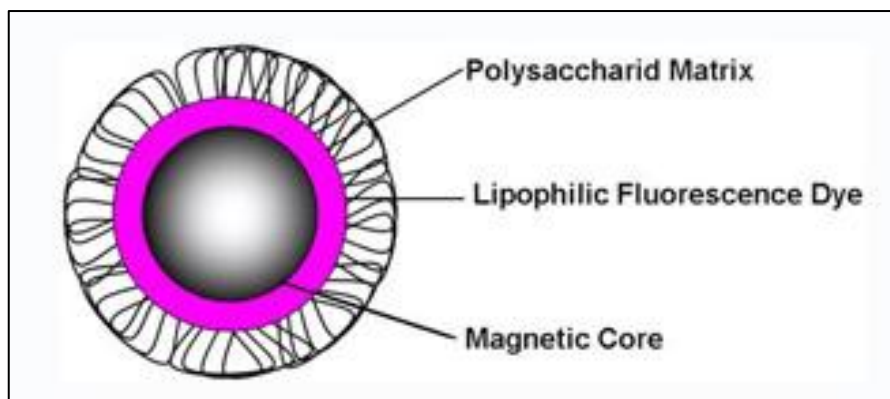


Figure 2.2: Physicochemical structure of a SC-SPION. An image presenting the physicochemical structure of a commercially purchased SC-SPION. The NP consists of a magnetite core, a primary lipophilic fluorescence dye coating and a secondary hydrophilic polysaccharide matrix (starch) coating. Image taken from the manufacturer's website (Chemicell).

The SPIONs were purchased at a stock concentration of 25 mg/ml, which was diluted with 1x PBS in all experiments involving SPIONs to a final concentration of 10 µg/ml. This working concentration was determined in previous experiments conducted within our group. The concentration has previously been shown to induce appropriate and detectable levels of NP mediated host responses, while preventing excessive NP-induced cellular and systemic toxicities. Furthermore, additional studies have shown that IONPs used at concentrations of (25-200 µg/ml), maintained greater cell viability,

therefore, allowing for prolonged NP exposure times and greater amounts of measurable data from viable cells and organisms, when compared to higher NP concentrations (300-500 $\mu\text{g/ml}$) (Naqvi et al., 2010). Moreover, due to current supply shortages presented by the manufacturer, the amount of SPIONs used in experiments had to be carefully managed.

In addition to NP-induced toxicities, spherical shaped magnetic NPs provide a greater surface area for therapeutic compound adsorption and surface medications using various biomolecules, for their subsequent use in targeted drug delivery systems (Natarajan et al., 2019). Therefore, it is of importance to investigate the biological safety of spherical magnetic NPs, due to their physiochemical advantages over NPs of different shapes and compositions. In this thesis, magnetic SPIONs and AuNPs with overall diameters of 100nm were used in the metallic NP biosafety experiments.

2.4 Fluorescent imaging

FPR3 study

Saos-2 and HOBs were seeded onto 13mm diameter glass coverslips, within wells of a 24 well tissue culture microplate, at a concentration of 3.5×10^4 cells per well. Similarly, MG63 cells were seeded onto glass coverslips which had been pre-coated with poly-D-lysine. Cells were cultured overnight in 500 μl of DMEM supplemented with 10% FBS and 1% penicillin-streptomycin (Thermo Fisher Scientific, Inc.). Thus, cells were incubated at 37°C in humidified conditions at 5% CO_2 . After 24h, cells were washed three times with 1x PBS solution (Thermo Fisher Scientific, Inc.), fixed with 4% paraformaldehyde pH7 (PFA) in PBS (warmed to room temperature) (Thermo Fisher Scientific, Inc.) for 10 mins at 37°C and thereafter, washed three times with PBS. Fixed cells were then blocked with 2% BSA in PBS (Thermo Fisher Scientific,

Inc.) for 30 mins at room temperature. Once blocked, cells were immunostained for FPR3 using a mouse monoclonal anti-FPR3 (R&D Systems, Inc, Abingdon, UK) primary antibody (1:80 in 2% BSA in PBS) for 1h at room temperature, in a humidity chamber. Cells of the negative control condition were incubated with only the blocking buffer (2% BSA in PBS), in a humidity chamber. After immunostaining, cells were washed through repeated immersions in 2% BSA in PBS to remove excess and unbound primary antibody. Cells were then incubated once again with 2% BSA in PBS for 30 minutes at room temperature, to block any remaining unbound antibodies. Once washed and incubated in blocking buffer, cells from both the receptor stained and negative control conditions were exposed to a secondary goat anti-mouse Alexa Fluor 488 conjugated antibody (1:100) (Thermo Fisher Scientific, Inc.) for the detection of bound primary antibody. Furthermore, cells from both conditions were counterstained for cellular nuclei with Hoechst 33342 (1:10,000) (Invitrogen; Thermo Fisher Scientific, Inc.) and the plasma membrane with Rhodamine labelled Concanavalin A (1:300) (Vector Laboratories). Cells were incubated in a humidity chamber containing moist pieces of tissue paper to prevent the coverslips from drying out (Figure 2.2), in the dark, for 30 minutes at room temperature. Once stained, cells were washed three times with PBS and coverslips were mounted onto slides using a drop of Fluoromount G mounting medium (Fisher Scientific, Loughborough, UK). Coverslips were then observed with a Leica DM4000 Fluorescence microscope (LAS software) (Leica, Wetzlar, Germany) and a Nikon Eclipse TE2000-S Confocal microscope (EZ-C1 software).

Immunocytochemical analysis of isolated GM hemocytes

To qualitatively analyse NP-induced hemocyte proliferation/immunotoxicity and for the visualisation of larval hemocyte-mediated NP internalisation, hemocytes from

respective larval test groups were isolated. In a 24 well microplate, 13mm circular coverglasses were added and onto each coverslip, 250µl of PBS was placed. Thereafter, each coverslip received the hemolymph of three larvae, extracted from the respective experimental conditions - 24h post-NP inoculations. The hemolymph was immediately fixed with 350 µl of 4% PFA to prevent rapid hemolymph oxidation and cellular coagulation. Adding the fixative immediately after extraction is of importance, as the larval hemolymph when exposed to air, undergoes rapid oxidation represented by black discolouration and an increase in hemolymph viscosity, due to the formation of clots (Kenny et al., 2018). This procedure was repeated for each well and hemocytes were fixed for approximately 20-30 minutes. Once the hemocytes were fixed onto the coverglasses, the fixative solution was aspirated and the coverglasses were washed thrice with PBS.

Cells on coverslips were then stained with 40µl of a staining master-mix in a humidity chamber (Figure 2.3), in the dark at room temperature for 30 minutes. The staining master mix contained 1x PBS, HOECHST 33342 at 10nM for the visualisation of cellular nuclei and Alexa Fluor 546 labelled wheat germ agglutinin (WGA), for the visualisation of the plasma membrane at 1:100 dilution (Thermo Fisher Scientific, Inc.). Thereafter, to remove the excess staining solution, the individual coverglasses were removed from the chamber and washed thrice with 1x PBS within the microplate wells. Coverslips were mounted onto slides using a drop of Fluoromount G mounting medium (Fisher Scientific, Loughborough, UK) and observed with a DM400 fluorescent microscope (Leica, Wetzlar, Germany) using LAS software.

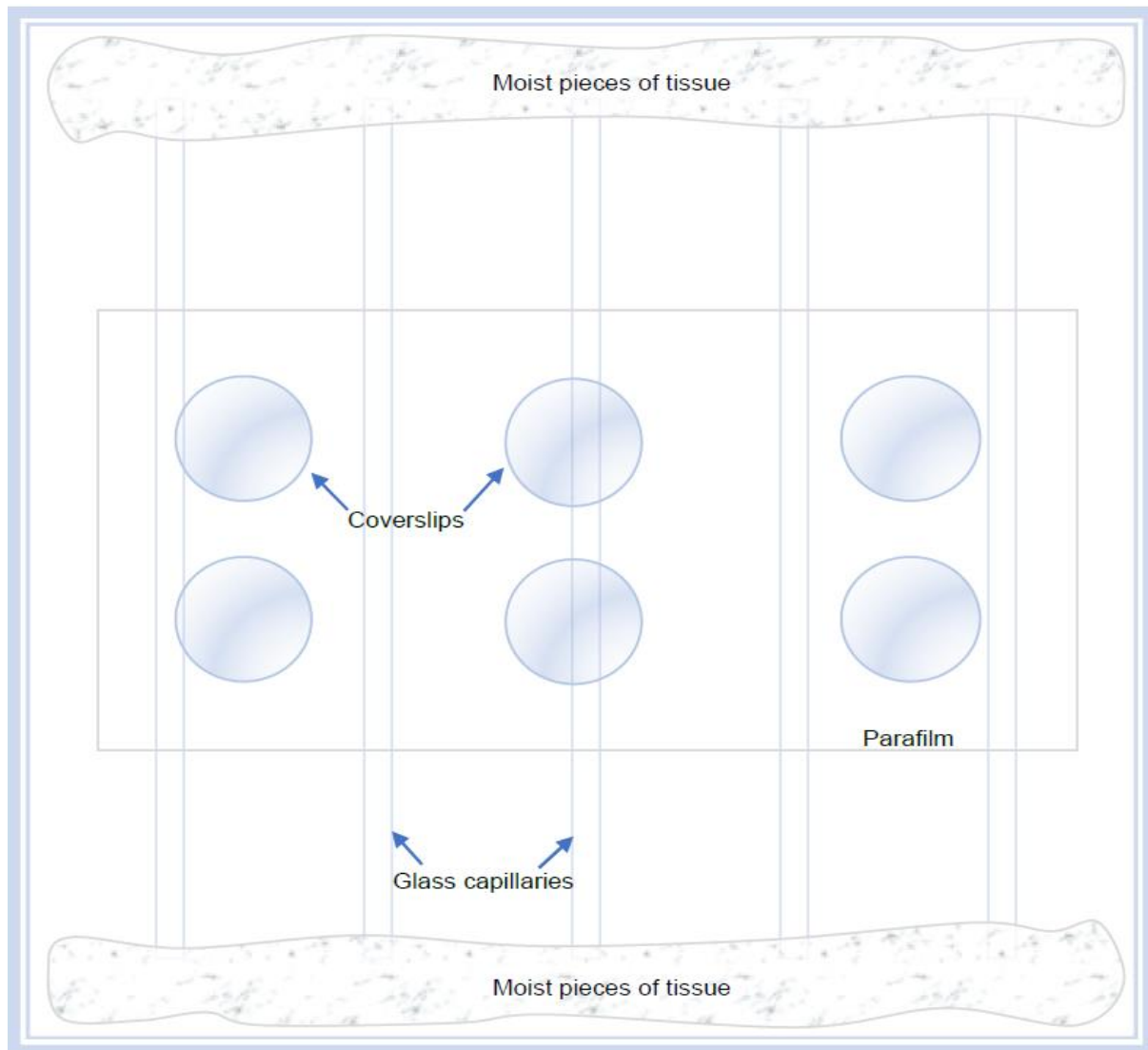


Figure 2.3: Set up of the humidity chamber for immunofluorescent staining. The above illustration shows the setup of the humidity chamber used for staining cells seeded onto coverglasses. Coverslips were placed on a sheet of parafilm prior to adding the staining master mix, to allow for the hydrophobic properties of the material to aid in the retention of the stain on top of the coverslips. Moist pieces of tissue paper were placed on either side of the chamber and a lid was placed on top, to create a humid environment within the chamber, thus, preventing the master mix from evaporating and the coverslips from drying out. Image from: (Mann 2021).

Cellular ROS assay (in vitro)

NP-induced intracellular ROS production, in live RAW264.7 cells, was qualitatively assessed using the 2',7' –dichlorofluorescein diacetate (DCFDA/H₂DCFDA) assay (Abcam, UK) according to the manufacturer's guidelines. DCFDA is a stable non-fluorescent, lipophilic, cell permeable compound. DCFDA, upon cell penetration, gets deacetylated in the cytoplasm by non-specific cellular esterases to a non-fluorescent

compound (DCFH), which remains stable and trapped within the cell for up to 6 h post-conversion. The deacetylated product is later oxidised by intracellular ROS when present, to yield the highly fluorescent compound, 2,7-dichlorofluorescein (DCF, $\lambda_{EX}/\lambda_{EM} = 485\text{ nm}/535\text{ nm}$). DCF upon excitation at 488nm, emits a green fluorescence and the fluorescence intensity is directly proportional to the intracellular levels of ROS. Therefore, an increase in DCF fluorescence, which can be visualised with live cell fluorescence microscopy, will signify the intracellular accumulation and increase of ROS (Sarkar et al., 2006).

On the day of the experiment, the ROS reagents included in the assay kit were equilibrated to room temperature. Thereafter, the NP samples were prepared for the subsequent treatment of cells. The 100nm SPIONs (anionic (charged) and starch coated NPs) were prepared at a final concentration of 10 $\mu\text{g}/\text{ml}$, along with the non-coated (powdered) IONPs. The 100nm AuNPs were prepared at a concentration of 1.6 $\mu\text{g}/\text{ml}$, all diluted in the RPMI culture medium. Next, the control reagent tert-butyl hydroperoxide (TBHP) (Abcam, UK) was prepared at a concentration of 55 μM by diluting it in RPMI culture medium. The control reagent induces intracellular ROS production and therefore, was used as the positive control condition.

RAW264.7 cells were seeded in a 48-well microplate at a cell concentration of 2×10^4 cells per 150 μl , per well, and incubated overnight at 37°C in humidified conditions at 5% CO_2 . The following day, before treating the cells, relevant NPs were ultrasonicated in a water bath sonicator (Transonic T460, Camlab) for 15-20 minutes to disperse them in the RPMI medium. After the treatment samples had been prepared, the culture medium the cells had been growing in overnight was aspirated from all relevant wells. The sonicated NPs were then added to the relevant wells of the 48-well culture plate containing the RAW cells. For the untreated control, the media was aspirated, and the

cells were re-supplemented with medium. For the treatment wells, the RPMI culture medium was aspirated, and the cells were subsequently treated with either NPs or TBHP diluted in culture medium. Thereafter, a magnet (Neodymium magnets) was slowly moved across the underside of the plate, in order to pull the magnetic (metallic) NPs to the bottom of the wells. The magnet was used to reduce the time usually taken by the NPs to settle at the bottom of the well, thus, coming into direct contact with the cells in the wells. The time taken by the NPs to settle at the bottom of the well, plays an impactful role on the intended length of cellular treatment with NPs, as NPs are known to take approximately 11-16h to naturally reach the bottom of the well and interact with the cultured cells (Mann 2021).

The cells were treated with NPs for 3h and 24h, respectively. However, for the positive control, the cells were treated with TBHP for 3h only due to the instability of the reagent. During the treatment, the cells were placed in an incubator at 37°C and 5% CO₂.

Just prior to the end of the desired length of treatment, the DCFDA stain was prepared at a concentration of 20µM by diluting in culture medium. At the end of the treatment, the medium was aspirated from all wells including the untreated wells. Thereafter, all wells including the untreated ones were stained with the diluted 20µM DCFDA stain. The cells were then incubated for 45 minutes at 37°C, in the dark. Thereafter, the media was aspirated, and the cells were washed once with 1x wash buffer (Abcam, UK). The cells were then immediately transferred for live-cell imaging with a Cytation automated imaging microscope (Agilent technologies, Inc, Santa Clara, USA). x20 magnification fluorescent microscopy images were used to qualitatively assess intracellular ROS production, by observing the intensity of the green fluorescence emitted by DCF.

2.5 Flowcytometric analysis

FPR3 study

Flow cytometric analysis was conducted on OS cell lines (Saos-2 and MG63), in order to quantify the percentage of cells positively stained for FPR3. Cultured OS cells were collected in DMEM growth medium, once trypsinised using 1x Trypsin-EDTA at concentrations of 0.5 g/L trypsin and 0.2 g/L of EDTA. Cells were centrifuged at 1000g for 5 mins to pellet the cells and then, resuspended in 250µl of 1x PBS (Thermo Fisher Scientific, Inc.). Subsequently, cells were fixed by adding equal volumes of 4% PFA (Thermo Fisher Scientific, Inc.), resuspending and incubating for 15 mins at room temperature. Once fixed, cells were washed twice with 1x PBS and resuspended in fluorescence activated cell sorting (FACS) buffer (0.5% BSA in 1x PBS). Thereafter, the resuspended cells were divided amongst the experimental conditions (FPR3 stained and unstained control). Cells intended to be surface stained for FPR3 were then incubated for 1h at room temperature, in the dark, with the mouse monoclonal anti-FPR3 (R&D Systems, Inc, Abingdon, UK) primary antibody (diluted 1:80). The untreated control, however, was not incubated with the primary antibody. Once stained, cells were washed twice with FACS buffer and bound antibodies were revealed by incubating with secondary goat-anti mouse Alexa Fluor 488 (Thermo Fisher Scientific, Inc.), for 1h at room temperature, in the dark. Once labelled, cells were washed twice with FACS buffer and resuspended in 150µl of FACS buffer. Cells were then analysed using a NovoCyte flow cytometer (Agilent technologies, Santa Clara, United States) and the percentage of cells stained positive for FPR3 was calculated, once debris was eliminated (Figure 2.4a-b). A minimum total of 10^4 events for each sample were acquired in all analyses.

Quantification of NP treated GM larval hemocytes

To quantify the concentration of circulating larval hemocytes, a cluster of extracted hemocytes from each condition was passed through a NovoCyte flow cytometer (Agilent technologies, Santa Clara, United States). Thus, we assessed the effects of NPs, Cyclophosphamide and the combination of Cyclophosphamide plus NPs on larval total hemocyte count (THC), by comparing circulating hemocyte counts to that of an appropriate control. The effect induced by inoculating GM larvae with the bacterial strain PA14, on larval hemocytes, was measured in the same way.

For flow cytometry, the hemolymph of three larvae from each condition was extracted and placed in labelled Eppendorf tubes. Immediately after, 350µl of 4% PFA was added to each tube, thus, preventing oxidative discolouration and coagulation. The hemocytes were then left to be fixed for 20-30 minutes. Once the hemocytes were fixed, samples were centrifuged at 4 °C for 5 minutes at 3000×g (Sigma-Aldrich, Poole, UK) to isolate the hemocytes. The Eppendorf tubes were checked to see if the hemocytes had pelleted effectively, if not, the samples were diluted 1:1 with PBS and centrifuged again with the same parameters. Once the hemocytes were pelleted, the supernatant was removed from each sample, leaving behind the pelleted hemocytes which were washed once with 1x PBS (Sigma-Aldrich, Poole, UK).

Washed cells were stained with the red fluorescent nucleic acid stain Propidium Iodide (PI), in preparation for flow cytometry. To do so, the cells were resuspended in 500µl of PBS containing a 1:500 dilution of PI (at a final concentration of 2ng/µl) (Sigma-Aldrich, Poole, UK). The stain was used as a secondary confirmation of debris removal during flow cytometry analysis, as PI is also known to stain groups of fragmented DNA and RNA which can account for cellular debris. Thereafter, samples were analysed on a NovoCyte flow cytometer (Agilent technologies, Santa Clara, United States).

Round-base flow cytometry test tubes were used, one for each condition, which were labelled according to the sample set. The samples were passed through the flow cytometer and the number of events/cells for each condition was acquired via polygon gating of the subsequent density plot charts. The density plot chart used for live cell gating displayed the axes of forward scatter height and side scatter height, which is a measure of cell size and complexity, respectively (Figure 2.4a). The polygon gate (P1) allows for the elimination of debris and any double or triple conjugated cells found in the sample (diploids and triploids), resulting in only individual cells being accounted for during the analysis (Figure 2.4b). The most used method of eliminating sample debris, involves gating out the population of events typically found at the bottom left corner of the density plot, hence, having low forward scatter and side scatter (Figure 2.4a-b). Events found at the bottom left corner of the density plot, therefore, have too low of size and cellular complexity to be accounted for as uniform cells. Furthermore, conjugated cells (diploids and triploids) were typically eliminated by gating out events that portray high side scatter (Figure 2.4b). The elimination of cellular debris was then confirmed by applying the live cell gate to another density plot chart, displaying the axes of PE Texas red height and side scatter height. The density plot, therefore, presented events fluorescing red and stained positive for PI (Figure 2.4c). Once the gate had been applied, it was evident that a population of events that were positively stained for PI had now been eliminated. Therefore, it can be confirmed that total cellular debris that was also stained positive with PI, had been successfully eliminated from the analysis (Figure 2.4d). Finally, THC per μl of the sample was calculated for each condition to determine hemocyte/cell concentration. Cellular concentration was calculated by dividing the number of live cells by the volume of sample analysed.

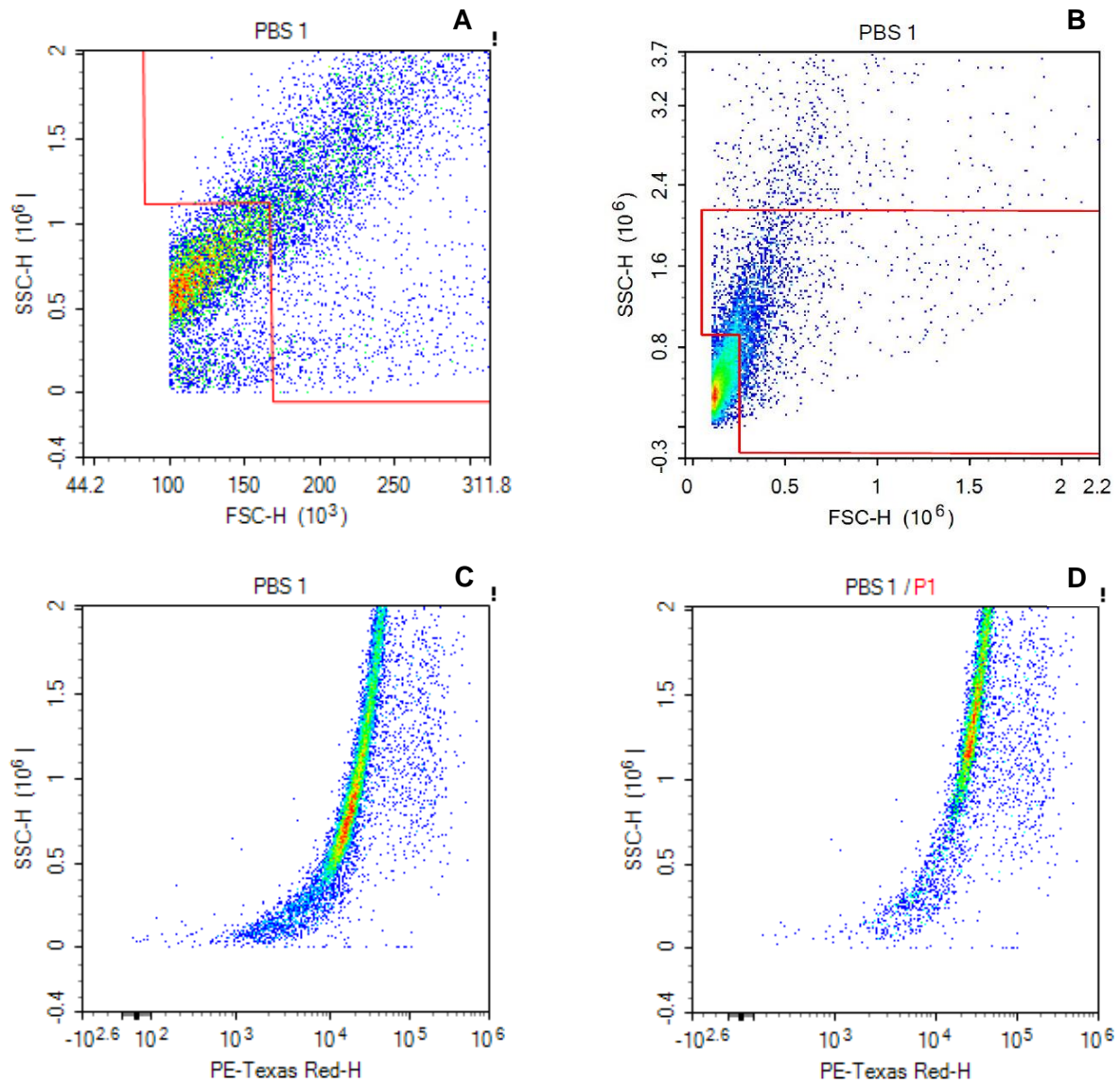


Figure 2.4: Gating techniques for flow cytometric analysis of GM larval hemocytes. The graphs in the figure above, portray flow cytometry density plot charts representing the events/larval hemocytes that were flow cytometrically analysed from the example larval condition (PBS control). (A) Cellular debris is initially eliminated using a live cell gate, based on the forward scatter/side scatter gating method. (B) Aggregated cells are identified based on their high side scatter values, which are eliminated using the live cell gate to only obtain individual cells. (C) All the events/cells that are positively stained for the nuclear acid stain (PI) are visualised. (D) Lastly, the created live cell (polygon gate) is applied to the PI positive events to confirm cellular debris elimination.

Cellular ROS assay (in vitro)

For the quantitative assessment of NP-induced intracellular ROS production, flowcytometry analysis was conducted. This is opposed to the qualitative assessment of intracellular ROS production, which was carried out through live cell imaging of RAW264 cells stained with 2',7' -dichlorofluorescein diacetate (DCFDA). For flow cytometric quantification of cellular ROS production, cells were seeded, cultured and

treated in the same way as described for the assessment of ROS production through live cell imaging.

At the end of the desired length of treatment, the RPMI medium was aspirated from all relevant wells, including untreated wells. Thereafter, the cells from each well were washed once with 1x PBS, by adding 150 μ l of PBS to each well and then aspirating to remove any remaining FBS containing culture medium. The medium contains protease inhibitors, in particular α 1-antitrypsin, which inhibits trypsin activity and prevents the lifting of adherent cells. Cells were harvested with 1x Trypsin-EDTA, at concentrations of 0.5 g/L trypsin and 0.2 g/L of EDTA (Thermo Fisher Scientific, Inc.). For trypsinisation, 150 μ l of trypsin was added to each well and the microplate was placed back in the incubator for 5-7 minutes. Thereafter, 150 μ l of fresh RPMI media was added to each well to quench trypsin activity. The microplate was agitated a few times to completely detach the cells.

Cells now in suspension were transferred to appropriately labelled Eppendorf tubes and stained in the presence of culture medium with 20 μ M DCFDA, with exception of the untreated unstained condition and the anionic-charged SPION treated unstained condition. These cells acted as appropriate controls during flow cytometry analysis. The cells were incubated for 30 minutes at 37°C in the dark. Thereafter, the cells were centrifuged at 3000 rpm for 5 minutes in order to pellet the cells and the culture media supernatant was extracted from all samples. Subsequently, the cells were gently resuspended in 300 μ l PBS, ensuring a single cell suspension and transferred to appropriately labelled flow tubes. The cells were immediately analysed by flow cytometry on an ACEA NovoCyte flow cytometer (Agilent technologies, Santa Clara, United States) under the settings used for detecting FITC. Using flow cytometric analysis, the number of cells within the live cell population that were positive for DCF

were analysed. For this ROS assay, a minimum of 10 thousand cells were quantitatively analysed for each condition using the Novoexpress software. During the analysis, a dot and density plot were used to establish an event forward and side scatter based (live cell) gate (Figure 2.4a-b), for the exclusion of cellular debris and aggregates from the analysis. Thereby, only analysing the level of fluorescence within singular cells. Furthermore, a density plot displaying events fluorescent in the FITC channel, the untreated (unstained) control and a range gate were used in combination to quantify the percentage of cells stained positive for DCF within the live cell populations.

2.6 Antibodies and dilutions

The table below presents a list of all cellular stains and antibodies (primary and secondary) used in this thesis, for the purpose of immunofluorescence staining, flow cytometric analysis and western blot analysis.

Table 2.1: Table of stains and antibodies used in immunofluorescence, flow cytometry and western blot analyses. A table showing all stains and antibodies used in this thesis, along with their respective dilution factors and manufacturers. Ex=excitation, Em=emission.

Antibody	Dilution	Stains	Primary/ Secondary	Host	Manufacturer
Hoechst 33342	1:10000	Nucleic acids	-	-	Invitrogen
Propidium iodide	1:500	Nucleic acids	-	-	Sigma-Aldrich
488nm					
Rhodamine labelled Concanavalin A (Ex: 555nm, Em: 580nm)	1:300	Plasma membrane	Lectin	-	Vector Laboratories

Alexa Fluor 546- conjugated Wheat Germ Agglutinin (WGA)	1:250	Plasma membrane	Lectin	-	Invitrogen
Anti-human FPR3	1:80	Human FPR3	Primary	Mouse	R&D Systems
Anti-Lamp1	1:1000	Lysosomes	Primary	Rabbit	Cell Signalling Technology
Anti-Rab9A	1:1000	Endosomes	Primary	Rabbit	Cell Signalling Technology
Anti-Rab27	1:1000	Secretory exosomes	Primary	Rabbit	Synaptic Systems
Anti-GM130	1:1000	Golgi apparatus	Primary	Mouse	BD Transduction Labs
Anti-ERp72	1:1000	Endoplasmic reticulum	Primary	Rabbit	Cell Signalling Technology
Alexa Fluor 488 anti-mouse	1:100	-	Secondary	Goat	Invitrogen
HRP conjugated anti-mouse/rabbit	1:3000	-	Secondary	Goat	Bio-Rad

2.7 Statistical analysis

All statistical graphs presented in this thesis were designed and generated using GraphPad prism9® software (GraphPad Software, Inc.). With respect to the bioinformatical analysis of an Osteosarcoma centred gene microarray, the volcano plot was generated using the statistical R-package provided automatically by GEO2R. Furthermore, the heatmap displaying results of the principal component analysis of top differentially expressed genes in Osteosarcoma was designed using the ClustVis online tool (<https://biit.cs.ut.ee/clustvis/>) (Metsalu and Vilo, 2015). For the different gene expression and Sarcoma patient overall survival (Kaplan-Meier) statistical graphs, presented for each of the genes of interest in Osteosarcoma, graphs were generated within the appropriate analytical tools utilised (GEPIA and Kaplan-Meier plotter), respectively. Statistical graphs and figures presented for WGCNA were designed within the described R-package itself.

All dataset averages and variability within data were determined by calculating the mean and standard deviation (SD), respectively, using GraphPad prism9® software. Variability within data is denoted by appropriate error bars on graphs. All statistical tests were performed using GraphPad Prism. Standard unpaired T-tests with Welch's correction were carried out to determine statistical significance, when comparing independent datasets from differing conditions. Furthermore, multiple-unpaired T-tests and one-way ANOVA were carried out to determine the significance when comparing an independent dataset to more than one other independent dataset (as recommended by Prism based on the datasets being analysed). Differences between independent datasets were deemed to be of significance when $P\text{-value} < 0.05$.

3. *Novel Upregulated Immune Receptors in Osteosarcoma as Potential Therapeutic Targets*

Aims and hypotheses

We hypothesise that immune based mechanisms play a role in OS development and metastasis and thus, immune receptors located in the tumour immune niche, may portray significant potential as therapeutic targets for the treatment of OS. The primary aim of this chapter was to use in silico analyses to identify significantly differentially expressed immune receptor genes in OS and quantify their link to the OS disease trait.

3.1 Introduction

Gene-based analytical techniques in OS

Due to the limitations and lack of prognostic improvement portrayed by current therapeutic strategies for the treatment of OS, there is a significant need to better understand the mechanisms underlying OS pathogenesis and identify novel therapeutic targets for the treatment of OS (Sun et al., 2019). Furthermore, as described previously, the majority of OS cases display chromosomal abnormalities and gene mutations, with the identified gene mutations being related to loss-of-function mutations (Kruzelock et al., 1997; Morrow and Khanna, 2015). It has been reported that the molecular causations behind gene dysregulations, include genomic aberrations, DNA copy number changes and DNA methylation (Yen et al., 2009). Therefore, due to the significant influence of genetic aberrations in the development of OS, systematic research conducted from a gene-based perspective and with the utility of gene expression data may improve our current understanding of the molecular mechanisms underlying OS (Sun et al., 2019). Furthermore, the gene expression data gathered can aid in the identification of oncogenes and tumour suppressor genes in OS (Kresse et al., 2009) and may lead to the identification of novel tumour specific therapeutic targets for the treatment of OS.

It has been noted that the detection of gene expression levels across complete genomes is a highly useful technique, which has therefore, been utilised in previous studies for the detection of significant and unusual genetic alterations (Garnis et al., 2004). Henceforth, high-throughput gene-based technologies such as gene microarrays have been utilised in OS to identify unusual genomic alterations or differentially expressed genes (DEGs) in OS patients, when compared to a relevant

control subset (Yang et al., 2014; Sun et al., 2019). Identification of unusual genomic alterations or DEGs in OS has greatly expanded the current knowledge around the cellular and molecular mechanisms underlying OS (Paoloni et al., 2009; Sadikovic et al., 2009). Furthermore, through the identification of significantly DEGs in OS, researchers can assess an individual gene's potential in becoming a novel therapeutic target for OS therapeutic strategies (Pilarsky et al., 2004). However, despite recent OS studies identifying lists of DEGs in OS, inconsistencies between the identified DEG lists have been brought forward (Yang et al., 2014). These inconsistencies have been said to be due to the limitations of small sample sizes, variations amongst study groups (test and control), data acquisition through differing laboratory protocols, use of differing microarray platforms and differing data analytical techniques (Siddiqui et al., 2006). Therefore, it can be said that the use of one set of data, with a large OS sample size, from one study group that utilised a specific microarray platform and therefore, used defined analytical techniques, would help overcome the challenge of DEG inconsistencies and provide more significant results with further analysis. Overall, this type of gene-based technique has potential for the generation of novel OS therapies, through the identification of new therapeutic targets.

Gene microarrays

Systematic research into the gene expression profiles of cells and tissues has become a highly useful analytical tool for the discovery of novel medicines (Tarca et al., 2006). Microarrays are a group of technologies in which a large collection of DNA sequences (probes) are either deposited or synthesised in a 2D or 3D array on a solid support surface via covalent or non-covalent bonds. Typically, DNA arrays are used in combination with a solution of a mixture of fluorescently labelled nucleic acids, to assess the presence and relative concentration of complementary DNA or mRNA

present in the solution (Bumgarner, 2013; Gresham et al., 2008). Thus, gene microarrays can be used as powerful, robust, high-throughput tools, to obtain gene expression profiles via efficient and accurate simultaneous measurement of gene expression levels from thousands of genes within a DNA or mRNA sample (Korkor et al., 2011; Heller et al., 1997; Lockhart et al., 1996).

Gene expression profiling via the use of gene microarrays has been increasing in popularity, particularly in areas such as genetics and cancer research (Korkor et al., 2011). The utility of this molecular tool provides an in-depth description of genome-wide changes in gene expression in both healthy and diseased conditions. In the case of diseased conditions, gene microarrays can describe disease inducing changes in gene expression when compared to a healthy control (Yoo et al., 2009). Overall, by comparing expression profiles of clinical conditions to healthy controls, it is possible to identify diagnostic and prognostic biomarkers, classify diseases and understand the mechanisms involved in disease initiation and progression. Therefore, gene microarrays are useful tools in research areas such as clinical medicine (Tarca et al., 2006). Furthermore, microarray-based approaches provide a useful alternative to whole genome sequencing, for the rapid detection of normal genomic variations in healthy conditions (Bumgarner, 2013; Gresham et al., 2008). In addition, undergoing unbiased and systemic studies into gene expression profiles of diseased conditions may bring about new disease taxonomies for different syndromes. Henceforth, disease processes and various clinical disorders can be characterised using such molecular tools (Tarca et al., 2006).

High-throughput gene expression microarrays in OS

Gene microarrays, as described, are powerful tools commonly utilised to gather gene expression profiles from various DNA or mRNA samples. The high-throughput tool allows for comparisons to be made between normal (healthy) and cancerous tumour samples for the potential identification of significantly dysregulated or DEGs. The majority of genotypically analysed diseases, including OS, are expected to portray disease specific gene expression profiles and abnormalities in gene regulation patterns, which may have led to disease pathogenesis (Sun et al., 2019; Lage et al., 2008). Despite the disadvantages portrayed by gene microarrays when compared to RNAseq, such as decreased specificity, sensitivity and the inability to analyse whole transcriptomes, gene microarrays can be used as high-throughput tools to analyse multiple samples at one time. In regards to OS, this means that multiple patient samples can be genetically characterised during a single analysis.

Commonly, in gene microarray array-based gene expression profiling analyses, the identification of significantly DEGs in the diseased condition is carried out through the filtration of the output list of DEGs, based on gene fold change (\log_2FC), P-values and false discovery rates (Zhang and Cao, 2009; Reiner et al., 2003).

Use of weighted gene co-expression network analytical techniques

Gene co-expression networks, also known as gene correlation networks, are rapidly gaining popularity within the biosciences field, thus, they are being utilised increasingly in various bioinformatical applications. Weighted gene co-expression network analysis (WGCNA) is characterised as being a systems biology method that is used for calculating and describing correlation patterns among genes analysed for gene expression across differing microarray samples (Langfelder and Horvath, 2008).

The bioinformatical gene expression analytical tool, WGCNA, is a comprehensive collection of R functions that can be acquired from the Bioconductor R-packages repository and is commonly used to identify clusters of genes that share similar gene functionalities and thus, are highly correlated. These strongly linked genes are subsequently known as gene modules. Furthermore, the WGCNA method can be used for summarising the identified gene modules based on module eigengene or an intramodular hub gene, for calculating the relationship between identified gene modules, for recalculating the relationship between gene modules and external clinical traits (using the eigengene network methodology) and lastly, for calculating the membership or significance of genes within the identified gene modules. These bioinformatical methods have been successfully implemented in various biological studies, such as oncology studies, mouse genetics and yeast genetics (Langfelder and Horvath, 2008).

In relation to the utility of the generated weighted gene co-expression network, for the calculation of relationships between gene modules and external sample traits, it can be utilised to calculate gene module relationships to an external clinical trait of interest, such as OS trait. Thereafter, the constructed gene co-expression network enables network-based gene screening methodologies. Therefore, genes that are significantly closely associated with the OS clinical trait and thus, strongly involved in OS pathogenesis can be identified. These identified genes can then be proposed as candidate biomarkers for the disease and/or as potential therapeutic targets in therapeutic strategies for the treatment of OS.

Disease ontology based functional annotations

It is known that public health plays an important motivational role when it comes to biological and medical research. However, a major gap exists between laboratory based biological research and its clinical applications, which requires bridging together (Clermont et al., 2009). In relation, high-throughput gene-based data provide a unique method of bridging this gap, with the bioinformatical characterisation of human disease-disease relationships, mining of specified gene-disease associations and the identification of candidate gene-gene similarities providing significant insights when analysing gene-based datasets (Mathur and Dinakarpanian, 2012). These diseases and gene-based associations can be utilised to gather better understandings of the underlying molecular mechanisms behind complex diseases.

Recent studies have consistently shown that characteristically dissimilar diseases share common cellular and molecular mechanisms. Henceforth, understanding semantic similarities that are inferred and molecularly characterised between diseases can aid in advancements in early disease diagnosis, approved drug repurposing and novel drug developments. In addition to identifying similarities between diseases, it is also of importance to determine candidate genes that have been experimentally determined or inferred to be associated with particular clinical diseases. Identification of specific genes annotated under diseases or the determination of disease annotations for individual genes or gene sets, can be carried out through gene enrichment analysis (Zhang et al., 2020).

Enrichment analysis can then uncover potential novel therapeutic targets for the treatment of complex diseases and can aid in the identification of novel disease biomarkers. Moreover, the identification of a candidate gene within one or few disease

annotations, can aid in the development of specific novel-targeted drug therapeutic strategies for the treatment of diseases with greater efficacy than other dissimilar diseases. Furthermore, by conducting gene-disease association functional enrichment on a list of differentially expressed candidate genes that were obtained through the conduction of high-throughput experimental techniques such as gene expression microarray (Li et al., 2011), the biological question can be further explored in a disease context and may lead to the discovery of unpredicted gene functionalities (G. Yu et al., 2015).

Through the identification of candidate genes that are molecularly shared between a cluster of similar or seemingly dissimilar diseases, there is potential for the development of novel-drug therapeutic targets that are effective across a variety of diseases. Moreover, there is significance in identifying candidate genes that are clinically annotated to a particular disease of interest and has been shown to portray clinical potential to being therapeutic targets for disease treatment. However, through the determination of gene similarities, further functionally and clinically similar candidate genes can be identified as alternate therapeutic targets for particular disease treatments (Li et al., 2011).

Disease ontology (DO) is known to be a gene functional annotation tool that consistently describes candidate genes from a disease perspective. Through various webpages and bioinformatical techniques, genes can be mapped to annotated diseases through gene functional enrichment. Since DO is organised as a directed acyclic graph, it provides the foundation for the calculation of similarities among diseases and among genes, through the utility of semantic similarity algorithms (G. Yu et al., 2015). In order to determine semantic similarities between disease and disease annotations for candidate genes, a significant knowledge of gene-disease

associations is required. In addition, a significant knowledgebase of experimentally determined or inferred gene-gene interactions is required. Gene ontology (GO), in many studies, has been utilised to consistently describe gene products and represent the biological significance of queried candidate genes or gene lists (Harris et al., 2004). On the other hand, DO is utilised to consistently describe gene products from a human disease perspective, thus, essential for determining the significance of candidate genes in a disease context (Li et al., 2011). As briefly mentioned, accurate gene-disease annotations can uncover novel gene-disease relationships, provide novel functions for previously uncharacterised genes, and potentially bring upon novel disease therapeutic targets.

Present study

In this study, the gene expression microarray derived gene expression data, which was gathered from an individual microarray platform (GPL10295; Illumina, Inc.) was identified and extracted from the Gene Expression Omnibus (GEO) to subsequently identify DEGs in OS. The resulting list of DEGs in OS, which were a mixture of up and downregulated genes, were filtered based on log₂FC and adjusted P-values for each gene to identify the list of significantly DEGs in OS ($|\log_2FC| > 1$ and $\text{adjP-value} < 0.01$). The log₂FC values, which are positive or negative, were said to identify specifically, the respective up or downregulated genes in OS. Thereafter, the total identified significantly DEGs were functionally annotated based on GO and Kyoto EnCyclopaedia of Genes and Genomes (KEGG) functional enrichment analyses, to determine the biological significance of the outputted DEGs. The isolated significantly upregulated DEGs in OS were further filtered based on the GO term of interest being “immune receptor activity”, in order to identify the upregulated immune related receptors in OS. As described thoroughly in chapter 1.1.7, the reasoning behind the

investigation of upregulated immune receptors in OS was due to the described significant involvement of the immune system in OS. In addition to the understanding that the immune niche of the OS TME might host immune related therapeutic targets of interest.

As a consequence of the immune system and immune infiltrate involvement in OS, we hypothesised that significantly dysregulated immune-related receptors could potentially behave as novel therapeutic targets for the treatment of OS. WGCNA conducted through the WGCNA R-package, was utilised to identify clusters of genes (gene modules) that were significantly closely associated with the OS clinical trait. Furthermore, WGCNA analysis and the subsequently generated gene co-expression network were also utilised to identify individual genes closely associated to OS, through their classification within gene modules closely associated to the clinical trait. Disease Ontology Semantic and Enrichment (DOSE) analysis conducted through the DOSE R-package, was utilised to functionally enrich the inputted candidate genes based on DO and to conduct semantic similarity computations. Therefore, determining similarities among clinical diseases and among candidate genes. Significantly dysregulated immune related receptors, that were also determined to be within a gene module closely associated with the OS condition, were further analysed to determine gene functionality, dysregulation patterns across malignancies, biological relationships and therapeutic targeting potential. The immune receptors of interest were screened through clinical databases, including PharmGKB, oncoKB, Clinical Interpretations of Variants in Cancer (CIViC) and general pharmacological databases, to determine if they can potentially behave as druggable therapeutic targets for the treatment of OS.

It is understood that the search for novel therapeutic targets and/or obtaining a better understanding of the underlying molecular mechanisms behind OS disease prognosis, is of great importance for the much-needed significant improvement of OS treatment and patient prognosis (Peng et al., 2016; Donegan, 1997; An et al., 2021). A greater understanding of the underlying mechanism behind OS and the pathobiology of OS, may improve its clinical management and lead to the development of rational OS treatment options through potential identifications of novel biomarkers for targeted OS therapy (Yang et al., 2014). The results gathered here may improve our current understanding of the molecular mechanisms behind OS tumorigenesis, improve our understanding of the immune influence in OS, provide novel therapeutic targets within the tumour immune microenvironment for the treatment of OS and overall, contribute towards the improvement of OS clinical management and treatment.

3.2 Methodology

Dataset search strategy

For the task of searching and retrieving relevant OS centred differential gene expression studies and their respective gene expression microarray datasets, three different databases storing gene microarray datasets were browsed. These databases included Gene Expression Omnibus (GEO) (www.ncbi.nlm.nih.gov/geo/) (Barrett et al., 2013), All of gene Expression (AOE) (<https://aoe.dbcls.jp>) (Bono, 2020) and ArrayExpress (www.ebi.ac.uk/arrayexpress/) (Sarkans et al., 2021). The databases were used to retrieve relevant differential gene expression studies that used the Illumina human-6 v2.0 expression beadchip (using nuIDs as identifier) microarray platform (GPL10295; Illumina, Inc.), to analyse mRNA expression profiles within

primary pre-chemotherapy tumour tissues obtained from OS patients or primary bone-marrow mesenchymal stem cells (BM-MSCs) from healthy disease-free controls.

To search for relevant OS centred differential gene expression studies and their respective gene expression microarray datasets within the GEO database, the GEO datasets search tool was utilised. Within the GEO homepage, the link (Search for studies at GEO datasets) was followed. Thereafter, under GEO tools, the link (Dataset browser) was selected to then open the dataset browser in which relevant gene expression microarray datasets can be identified and retrieved.

Similarly, in AOE (Japanese based gene expression database), the search term OS was entered into the search bar. Thereafter, to retrieve the list of OS related studies and gene microarray datasets, the data list tab was subsequently selected. In cases where OS based study and gene microarray dataset can also be found within the GEO database, the GSE reference series was provided by AOE for subsequent redirection onto the GEO database.

ArrayExpress was used similarly to GEO and AOE, to identify and acquire relevant gene microarray datasets. Within ArrayExpress, the “browse” tab was selected and the search term OS was entered into the search bar. Like AOE, the relevant studies and datasets which are also included within the GEO database were presented along with their corresponding GSE reference series for subsequent redirection.

In both of the databases, when the GSE reference series was selected, an accession display containing all the relevant information regarding the gene expression dataset and differential biology study was made available. Important information such as experiment type, summary, and overall experiment design was derived from this overview page, for the subsequent step of study selection. Thus, all datasets were

published within the GEO database and enabled subsequent differential gene expression analysis. The search terms utilised to retrieve the studies from within the databases included “OS” or “GPL10294”. The species for the studies was limited to *Homo sapiens*.

OS study selection

The inclusion criteria for the relevant OS centred differential gene expression studies consisted of studies that investigated a mixture of tissue types, derived from patients with OS or healthy control patients. Within these studies, only the gene expression data from primary OS tumour tissues/pre-chemotherapy biopsies and healthy human BM-MSCs were used. Studies that used cell lines derived from OS tissue or healthy human mesenchymal cells, or bone derived cells retrieved from patients with alternate bone diseases to OS including osteoporosis and osteoarthritis, were excluded.

Differential gene expression analysis

To acquire a preliminary list of DEGs (DEGs), between the diseased pre-chemotherapeutic OS and control tissues, we utilised the interactive differential gene expression analysis web tool provided by NCBI, named GEO2R. At the end of the studies accession display, the tab “Analyse with GEO2R” when selected, opened the interactive gene expression datasets analysis tool (GEO2R) (Figure 3.1). GEO2R was used to carry out gene expression comparisons between two sets of samples in a GEO Series, in order to identify genes that are differentially expressed across the experimental conditions.

Platforms (1) [GPL10295](#) Illumina human-6 v2.0 expression beadchip (using nuIDs as identifier)

Samples (118) [GSM717846](#) 220-Msc
[GSM717847](#) 240-Msc
[GSM717848](#) Kaat-Msc

This SuperSeries is composed of the following SubSeries:
[GSE28974](#) Genome-wide gene expression profiling of mesenchymal stem cells
[GSE33382](#) Genome-wide gene expression analysis of high-grade osteosarcoma
[GSE42351](#) Genome-wide gene expression profiling of high-grade osteosarcoma cell lines

Relations
 BioProject [PRJNA181139](#)

[Analyze with GEO2R](#)

Download family	Format
SOFT formatted family file(s)	SOFT ?
MINiML formatted family file(s)	MINiML ?
Series Matrix File(s)	TXT ?

Figure 3.1: **GEO2R based differential gene expression analysis.** A list of DEGs between diseased OS tumour and control tissues, was acquired with the use of GEO2R based differential gene expression analysis. To carry out differential gene expression analysis, the tab “Analyze with GEO2R” at the end of the studies accession display (circled in red) was navigated to and selected.

GEO2R was used for the normalisation of RAW gene expression data and for the subsequent analysis of differential gene expression, between OS and control tissues, to acquire a list of DEGs. GEO2R conducts these steps without the need for specialist methodologies such as R-studio and it’s respective Bioconductor packages (“affy” and “limma”). In the R-studio methodology, which requires semi-competent knowledge of coding, the Bioconductor “affy” package (<http://bioconductor.org/packages/affy>) is utilised to normalise the RAW gene expression data, while the “limma” package (<http://bioconductor.org/packages/limma>) is used to compare DEGs between OS tumour tissues and relevant control tissues. Comparatively, GEO2R conducts an automated normalisation of RAW gene expression data and through the utility of an in-built R-studio script derived from the Bioconductor “limma” package, the tool identifies DEGs in OS. Therefore, GEO2R nullifies the need for competent knowledge

of R-code, the utility of R-studio and the subsequent utility of the Bioconductor “limma” package, to conduct differential gene expression analysis.

Within the GEO2R tool, the groups of experimental samples to be compared (OS and control tissues) were defined and a table of top 250 dysregulated genes in OS was generated by selecting the tab “Top 250”. These were then presented as a table of genes ordered by statistical significance of their dysregulation (P-value), ordered from smallest to largest. Thereafter, genes with positive log₂FC values were checked to see if they were upregulated in OS. Gene upregulation was confirmed by selecting an individual gene with a positive log₂FC value and visualising the subsequently generated graph, presenting the gene’s expression values for each tissue sample involved in the comparison. If gene upregulation did not match a positive log₂FC value, the order in which the sample groups were defined was altered, to match the upregulated genes with positive log₂FC values and downregulated genes with negative values. If this had no effect, the upregulated genes in OS were noted to have negative log₂FC values and the downregulated genes to have positive values. The log₂FC values were of importance during the subsequent refinement of the full list of dysregulated genes, thereby, acquiring significantly DEGs in OS.

Once the table of dysregulated genes in OS was generated, the table settings were reconfigured to display the gene symbols for the respective probe IDs in the microarray and the link (save all results) was selected. This resulted in a follow-up page presenting the full list of dysregulated genes (with gene symbols), sorted based on the P-value of their dysregulation. This list was then saved as a Text file, for subsequent data importation into Microsoft Excel. Within Microsoft Excel, a new spreadsheet was opened, and the saved text file was imported through the “from Text/CSV” option found under the “Data” tab.

Refinement of dysregulated genes

Once the list of dysregulated genes in OS was loaded onto an excel spreadsheet, the list of genes was refined based on the adjusted P-value and Log₂FC values for each gene. This refinement was conducted to subsequently acquire only the significantly DEGs in OS, with genes being considered DEGs if they portray a Log₂FC>1 and an adjusted P<0.01. To acquire the list of DEGs in OS, a number filter (less than 0.01) was first applied to the adjusted P-value column of the dysregulated gene list. However, the list still consisted of genes with various Log₂FC in gene expression and with the respective Log₂FC for each gene being positive or negative. A negative Log₂FC should reflect a negative regulation of the gene in OS, therefore, genes with a negative Log₂FC value were classified as downregulated genes in OS. Similarly, a positive Log₂FC represents a positive regulation of the gene in OS, thus, genes with positive Log₂FC values were classified as upregulated genes in OS. The gene list, thus, consisted of genes that are significantly differentially expressed, either up or downregulated in OS and portray various Log₂FC in expression. Hereafter, with the cut-off for significantly DEGs being a gene fold-change of (Log₂FC>1), the gene list was refined by applying a number filter (greater than 1) to the Log₂FC column of the list. Based on this refinement, the output list of DEGs were specifically, significantly upregulated genes in OS. Similarly, to acquire the significantly downregulated genes in OS, the number filter (less than -1) was applied to the Log₂FC column of the list. The total number of DEGs in OS, thus, consisted of the total number of upregulated and downregulated genes at the specified cut-off values (adjusted P<0.01 and Log₂FC>1). In cases where single genes were measured by multiple microarray detection probes, mean gene expression values were calculated.

Principal component analysis

Principal component analysis (PCA) was conducted in this study using the ClustVis online tool (<https://biit.cs.ut.ee/clustvis/>) (Metsalu and Vilo, 2015). The analysis was conducted on the principal components (significantly upregulated and downregulated genes in OS), to determine if the identified list of DEGs can distinguish between OS condition and the respective normal (healthy) controls. To do so, an excel spreadsheet was created to enter all the relevant information required for the analysis and was formatted per the data template provided by the online tool. Within the spreadsheet, the first row was used to enter the sample description/ID for each sample utilised in the analysis. For this study, 12 Mesenchymal stem cell (MSC) controls and 84 primary pre-biopsy OS tumour samples were analysed. Next, the second row was used to describe the disease status for each sample in the analysis (healthy vs OS). Regarding the columns, column A consisted of all the DEGs in OS (up and downregulated), column B consisted of a description of the dysregulation of each DEG (up or downregulation), and each subsequent column consisted of the respective gene expression value for each DEG, under the respective experimental sample. The entire data matrix was then copied for the subsequent PCA analysis. Within the ClustVis tool, the tab “data import” was first selected and the enter data column was navigated to. Thereafter, within the column, the option paste data was selected. Thereafter, the copied data matrix was pasted into the dataset box and with all the default settings being maintained, the tab “data-processing” was selected. The data processing tab gave an in-depth description of the inputted data and allowed for the visualisation of correct data input/formatting. Finally, the PCA and heat-map tabs were utilised to generate and export the respective results figures from the analysis.

Characterisation of DEG functionality and significance

Once the list of dysregulated genes was refined, based on statistical significance (adjusted P-value<0.01) and Log₂FC>1, to acquire a list of significantly DEGs in OS, various online overrepresentation analysis and gene list enrichment analysis tools were utilised to annotate the DEGs based on gene functionality and thus, determine their biological significance. These tools included WebGestalt (Web-based gene set analysis toolkit) (<http://www.webgestalt.org/>) (Liao et al., 2019), FunRich (Functional enrichment analysis tool) (<http://www.funrich.org/>) (Atkin-Smith et al., 2015) and the bioinformatics microarray analysis web-tool DAVID (<https://david.ncifcrf.gov/>) (Sherman et al., 2022). Gene list enrichment analysis was conducted based on GO and KEGG biological pathways, independently. This relates to GO annotations being able to reflect complex gene functional relationships, whereas KEGG pathway enrichment, only portrays the significantly enriched biological processes.

GO overrepresentation enrichment analysis (GO-ORA) of biological process, cellular component and molecular function, was conducted using the gene list enrichment analysis web tool WebGestalt. This analysis was utilised to identify the GO terms the DEGs were most overrepresented in. To carry out GO-ORA, the WebGestalt webpage was first navigated to and the appropriate settings were selected for the respective analyses. In the case of GO-ORA, the organism of interest was selected as *Homo sapiens* and the analysis method of interest was selected as overrepresentation analysis (ORA). Thereafter, the functional database was selected as geneontology and the independent GO category in which the listed DEG products will be enriched under was specified. Once the basic parameters had been specified, within the gene list section of the tool, the gene identification (ID) type for the DEGs yet to be uploaded was selected as gene symbol. Thereafter, the list of DEGs to be analysed was

uploaded into the gene list area by copying the refined list from the spreadsheet. Lastly, prior to submission, the reference gene list was selected as the respective platform used in the original study's gene expression microarray analysis (Illumina human-6 v2.0). Once the analysis was submitted, the resulting page of the analysis portrayed the list of GO terms that the DEGs were most overrepresented in. These terms were presented as a table, displaying the adjusted significances for the respective enriched GO terms, amongst other statistical values for each term.

Furthermore, GO based gene list enrichment analysis was carried out with the use of FunRich, to further functionally annotate the list of DEGs in OS through the identification of enriched GO terms. For GO gene enrichment analysis, the FunRich gene functional enrichment software was first opened, and the homepage navigated to. Thereafter, under manage databases, the tab manage was selected to change the enrichment database to Gene Ontology. Subsequently, the Gene Ontology database was selected, or the Gene Ontology databases (specifically human) were first imported and then selected. Thereafter, under upload datasets, the tab add dataset was selected to upload a gene list of interest that will be subsequently enriched based on GO. Within add dataset, the dataset was named and the corresponding gene list was pasted into the box. The separate gene lists of interest to be functionally enriched based on GO, included all the significantly DEGs in OS ($\text{Log}_2\text{FC} > 1$, $\text{adjP} < 0.01$), the significantly upregulated genes in OS alone and finally, the significantly downregulated genes in OS. Thereafter, for each gene list, the Gene enrichment tab was selected for gene enrichment analysis and the subsequent analysis tab was selected to conduct the said gene enrichment analysis. Henceforth, for each gene list described, GO based functional enrichment analysis of gene biological process, cellular component and molecular function was conducted.

In addition to the GO-ORA carried out with the use of WebGestalt, further KEGG pathway overrepresentation analysis was also conducted using this tool. Similarly, to GO-ORA analysis, the organism of interest (*Homo sapiens*) and the analysis method of interest (ORA) was selected. Unlike GO-ORA, the functional database was selected as pathway, with the database of interest specified as KEGG. The list of DEGs was uploaded into the gene list portion of the web tool, with the gene ID type maintained as gene symbol. The reference gene list was maintained as the respective platform used in the array (Illumina human-6 v2.0) and the gene list was submitted for analysis. Unlike the GO-ORA, the output of the analysis was a list of KEGG biological pathways that the DEGs were most overrepresented in.

In addition, further KEGG pathway enrichment analysis was conducted to functionally annotate the DEGs based on the enriched biological pathways, using the bioinformatics analytical web-tool DAVID. To conduct the gene list enrichment analysis, the database webpage was visited. Within the homepage, the tab “start analysis” was selected to start the enrichment analysis. Once selected, the output page allowed for entering a list of genes to be subsequently analysed. Therefore, the list of DEGs in OS was pasted into the gene list upload box located under step 1. Thereafter, under step 2, the identifier format was selected as official gene symbol, and under step 3, the option “gene list” was selected. Lastly, under step 4, the gene list was submitted by selecting the tab, submit list. The subsequent output page opened under the tab “list” and allowed for the management of inputted gene lists. On this page, *Homo sapiens* was specified as the organism of interest and within the analysis wizard area of the page, step 2 was navigated to. Under step 2, a list of DAVID provided gene list analytical tools were provided, which allowed for the subsequent analysis of the uploaded gene list. The tool to be utilised in this part of the study, was

the functional annotation tool, thereby, functionally annotating the DEGs through KEGG biological pathway enrichment. Once the functional annotation tool was selected, the resulting page presented a gene annotation summary. Of interest was the KEGG pathways analysis tool, therefore, the drop-down “pathways” was selected. Once selected, the various biological pathway functional annotation databases were presented and since KEGG was the database of interest, KEGG pathway was chosen. To view the results of the KEGG pathway enrichment analysis, the tab “chart” was selected to visualise the various KEGG biological pathways the genes were enriched in. The chart displayed the various KEGG biological pathways, along with the number of genes enriched under the respective pathways.

Refinement of DEGs – based on Gene Ontology (GO)

GO describes gene products with three independent categories: biological process, cellular component, and molecular function. Therefore, multiple GO terms can be assigned to one gene sequence (Han et al., 2016).

The identified DEGs in OS were further enriched and refined based on a pre-determined GO term of interest, using the gene list enrichment tool Uniprot (<https://www.uniprot.org/>) (Bateman et al., 2021). In this study, we wanted to understand the molecular role of the human immune system in OS and specifically identify any potential immune system related targetable proteins, such as immune receptors, that are upregulated in OS. Thus, Uniprot was used to specifically refine the list of significantly upregulated genes in OS, based on the GO term “immune receptor activity”.

To conduct the GO term-based refinement of the identified significantly upregulated genes in OS, the gene enrichment analysis tool Uniprot was visited. Within the enrichment tool, the retrieval/ID mapping function was selected to map the inputted genes of interest to their respective GO terms and pathways (Figure 3.2). Once the ID mapping tool was opened, the list of upregulated genes in OS was pasted into the gene identifiers input box, located under the first step. Thereafter, step two was subsequently referred to, where the input option was specified as gene name and with the output result specified as UniprotKB. Thus, the genes will be described through the utility of Uniprot's protein knowledgebase.

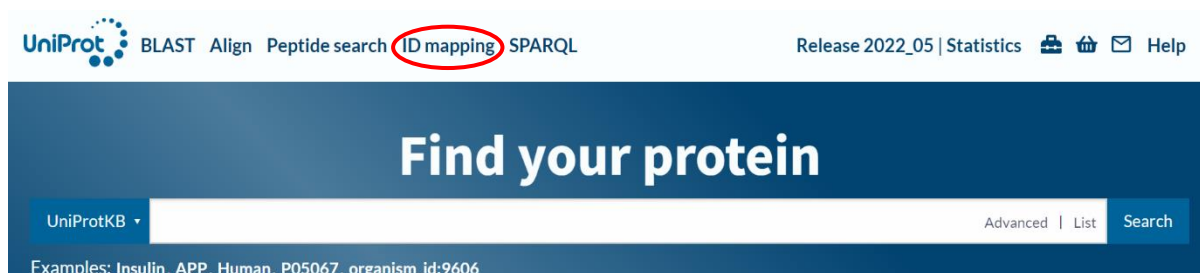


Figure 3.2: **Gene ontology-based gene list enrichment and refinement.** Significantly upregulated genes in OS were first functionally enriched using the ID mapping tool from Uniprot (circled red). Thereafter, significantly upregulated genes that are functionally enriched under the GO term “immune receptor activity” were subsequently identified.

Lastly, the organism reference was set to *Homo sapiens*, and the gene list was submitted for enrichment analysis. Once gene list enrichment analysis had been carried out, the tab Gene Ontology was selected and the GO term of interest that the enriched list of DEGs will be refined by was queried for in the search tab. After the GO term query, the output result was the mapped genes that were narrowed down by the GO term “immune receptor activity”. Once the result tab was selected, the list of genes that were classified under the queried GO term was displayed and then downloaded as an excel file (uncompressed), for ease of manipulation.

The list of genes classified under the GO term was then overlaid with the list of significantly upregulated genes in OS, using the online gene list comparison tool, GeneVenn (<http://genevenn.sourceforge.net/>) (Pirooznia et al., 2007). The web tool was used to compare the list of upregulated genes and the list of genes acquired from the GO term query. The tool, thus, created a Venn diagram which displayed the number of genes found in both lists. The genes found in both lists were of interest, as the genes were both significantly upregulated in OS and classified under the immune system related GO term of interest.

The list of GO term refined genes was copied onto a new excel spreadsheet, into column A. Subsequently, on the same spreadsheet, the original list of significantly upregulated genes in OS, that had been filtered based on adjusted P and Log2FC values, was placed in column C. Thereafter, in column B, the excel formulae (MATCH, A:A,C:C, FALSE), was used to match the list of genes in column A to the list in column C. Therefore, each gene in column A acquired a position value relating to its position amongst the list of genes in column C. Next, a new sheet was created within the same spreadsheet and the list of genes in Column A, along with their respective position values, were transferred into Column A and B respectively. Finally, using windows Excel's sort function, the genes in Column A were sorted based on their respective gene position values in Column B, from smallest to largest. Briefly, the genes in Column A were highlighted, along with their position values in Column B. Thereafter, the sort function was selected and the relating sort by option was set to Column B. Subsequently, the sort options were set to cell values from smallest to largest. Since the position values related to the gene's position in the initial list of significantly upregulated genes in OS, previously sorted based on adjusted P-value, the genes in

Column A were now also sorted based on adjusted P-value, ranging from smallest to largest.

Therefore, the result is a list of genes that are both upregulated in OS and classified under the specific GO term of interest (immune receptor activity). The genes are also placed in order, based on the statistical significance of their differential expression in OS.

Refined genes of interest - characterisation and further analysis

Human protein atlas

The online web atlas entitled the Human protein atlas (<https://www.proteinatlas.org/>) (Thul et al., 2017), characterises and provides an in-detail summary of the currently known and variably understood human expressed proteins. This web protein atlas was subsequently used to perform an in-depth characterisation and generate a detailed summary of the identified genes of interest. The atlas was used to gain descriptive information on the respective gene's tissue specificity within the human body, along with human single cell type and immune cell specificity. Furthermore, the atlas provided a general summary on the clinical significance of the protein, along with its potential to be used as a prognostic marker in various cancer types. In relation, the atlas provided information on the cancer specificity of the gene and if the protein can be used as a potential identifying biomarker for specific cancer types. In addition, the protein atlas provided further information on the cellular and sub-cellular localisation of the protein, if known. The protein atlas also conducted and provided some functional annotations for the queried protein of interest, by utilising the gene enrichment tool Uniprot as the default tool for gene enrichment. With regards to gene enrichment and protein functional annotations, the atlas provided a detailed summary of the protein's

functions and a brief summary of the protein's molecular functions and involved biological processes. Finally, the atlas provided information on the queried gene's involvement in diseases such as cancer and a final descriptive summary on the protein of interest, being described through the utility of the NCBI gene database.

To conduct the said protein characterisation and further functional annotations of the identified proteins of interest, the human protein atlas webpage was visited. Within the webpage, the gene name of interest was searched for by entering into the search bar. Subsequently, the atlas suggested a list of similar genes, inclusive of the gene of interest, however, the specified gene of interest was selected. The initial output page generated, provided a human protein atlas summary of the protein and allowed for the characterisation of the protein of interest. As mentioned, the protein atlas summarised tissue, single cell type and immune cell specificity. Furthermore, protein localisation and further functional annotations were also described.

GEPIA (gene expression profiling interactive analysis)

The gene expression profiling analytical web tool (GEPIA) (<http://gepia.cancer-pku.cn/>) (Tang et al., 2017), is commonly used as a powerful tool to generate gene expression profiles for various queried genes of interest. These gene expression profiles are generated through the quantification of candidate gene expression levels within various cancerous tissue types and their respective normal tissues.

In this study, level of gene expression for the queried genes of interest in various cancer types, was validated through the use of GEPIA. Firstly, the gene of interest was queried within the web tool, to generate statistical graphs/figures, portraying the levels of expression for the queried gene in various cancer types and their respective normal tissues. Thus, the graph portrays the various cancer types where the queried

gene of interest was quantified to be dysregulated in its expression. Next, survival analysis was conducted with the queried gene of interest, to determine the clinical significance of the gene on the overall survival of patients with a specific cancer type. In this study, the specified cancer type was Sarcoma (Sarcoma), due to the cancer subtype's clinical relevance to OS.

To generate the described visual gene expression profile for the queried gene of interest and to conduct the subsequent cancer survival analysis with the gene, the webpage for the GEPIA web tool was visited. Within the web tool, the tab "single gene analysis" was selected for the analysis of the queried gene of interest. Thereafter, the gene name was entered into the search box. The subsequent output page, under the general tab, consisted of the interactive human body map portraying median gene expression in various tumours and normal organs/tissues. Furthermore, the page also presented statistical graphs, such as a dot plot and a bar graph, portraying the gene expression patterns for the gene across various cancer and their respective normal tissues. Prior to saving the statistical graphs, the tab $\text{Log}_2(\text{TPM}+1)$ scale was selected to convert all the gene expression values represented in the graphs to the Log_2 scale.

Effects of gene expression on patient survival

In order to determine the prognostic value of candidate gene expression in relevant cancer types of interest, Kaplan-Meier plots for patient overall survival were used. Thus, we used the web-tool Kaplan-Meier Plotter (www.kmplot.com) (Nagy et al., 2021) to conduct overall survival analysis for various cancer types with respect to candidate gene expression and generate Kaplan-Meier plots for patient overall. The tool allows for specific genes to be queried within survival analysis to determine its prognostic significance to overall survival of patients.

For the generation of Kaplan-Meier plots, the Kaplan-Meier Plotter webtool was first navigated to. Thereafter, on the top right corner of the webpage, the database containing mRNA data gathered for various human cancers using RNA-sequencing was navigated to. Under this database, the pan-cancer dataset was selected to acquire mRNA levels for various genes that were measured across differing human cancer types. Within the pan-cancer mRNA dataset, the Affymetrix gene symbol for the gene of interest was entered and survival analyses conducted. Thereafter, with the remaining parameters for survival analysis and generation of Kaplan-Meier plots being kept the same, the cancer type Sarcoma was selected due to its clinical relevance and similarity to OS. The sarcoma dataset contained clinical data obtained from 259 different patients. Lastly, the Kaplan-Meier plot for patient overall survival was generated using the draw Kaplan-Meier plot tab. The resulting Kaplan-Meier survival plot presents Sarcoma patient overall survival, with respect to level of candidate gene expression.

STRING analysis

The interactive gene analytical web-tool STRING (<https://string-db.org/>) (Szklarczyk et al., 2021), was used as a tool to generate and visualise functional protein association networks, which are thus, gene-gene interaction networks. The analysis tool was utilised to generate gene-gene interaction networks, with a singular protein of interest, queried by the gene name or protein sequence. In this study, the top genes of interest (CXCR4 and CD74) were entered into STRING to determine the functional proteins associated or predicted to be associated with the genes of interest. In addition, by entering the queried genes into STRING, the gene-gene interaction networks interconnecting the gene of interest to the functional proteins in questions, was visualised and generated.

Within the STRING web tool, the option protein by name was selected, to analyse the protein of interest based on gene name. Thereafter, the gene name was entered into the search bar and the organism was selected as *Homo sapiens*. The subsequent output page presented a list of genes that were similar to the gene of interest, a summary of each protein and their respective related organism. On this page, the specific protein of interest was selected, with the respective organism being *Homo sapiens*. Once continued, the results page generated presented gene-gene interaction network for the queried gene. On this page, various viewing platforms can be selected to visualise the protein association network in differing arrangements and the interaction network can be increased or reduced in size, to visualise more or less interacting proteins. Furthermore, the legend can be visualised to determine the nature of the protein interaction (predicted or known). The generated gene-gene interaction network was exported and used to determine the proteins closely associated with the protein of interest. Lastly, under the analysis tab, the GO-based functional annotations for the generated gene-gene interaction network were visualised and noted (adjusted $P < 0.01$). These annotations included the various biological processes, molecular functions and cellular components involved in the generated network.

Weighted gene co-expression network analysis (WGCNA)

In order to identify key gene modules and individual genes that are closely associated with the OS clinical trait, WGCNA was conducted. This was conducted through the utility of the R 'WGCNA' package (version 1.46) (Langfelder and Horvath, 2008), which was acquired from the R-packages database Bioconductor and processed through the use of R-studio. The first step was to input the data, which was followed by cleaning, and pre-processing of the normalised gene expression data, which was inputted and used in subsequent WGCNA. Henceforth, normalised gene expression data from the

probed genes and relevant samples (both diseased and control), to be included in the WGCNA, was loaded into the R-studio working directory as a tab delaminated csv file.

Thereafter, in line with the first step of any gene network analysis, the subsequent steps involved pre-processing the loaded normalised gene expression data into a format that is suitable for further network analysis, along with checking and cleaning the loaded dataset. Cleaning of the dataset involved removing samples and genes with excessive missing values and removing microarray samples that are obvious outliers.

However, prior to checking for excessive missing values generated by certain genes and microarray samples and prior to identifying potential sample outliers, the loaded gene microarray dataset was correctly formatted for network analysis. In relation, the loaded dataset could contain extra auxiliary information about the surveyed gene probes, that aren't required in the network analysis and need to be removed. However, our loaded gene microarray datasets didn't contain any auxiliary information surrounding the surveyed probes. Despite this, within the dataset, the column containing probe IDs for the surveyed probes in the microarray was removed to enable the subsequent step of transposing the expression dataset for further analysis. Thereafter, the dataset was transposed by assigning the probe IDs as its new column names and the microarray sample names as the dataset's new row names.

Thereafter, the newly generated and correctly formatted expression dataset was first checked for excessive missing values, that may have been generated by surveyed gene probes or microarray samples. The dataset was analysed through the use of the 'goodsamplesgenes' function, a function found within the WGCNA investigative package. If the result proved to be false/negative, meaning there are certain gene(s)

and/or sample(s) with excessive missing values, the offending genes and/or samples can be removed. Once the expression dataset was checked for these and any offending genes and/or samples were removed, the dataset was then checked for any potentially obvious outlying microarray sample(s). In order to identify these, the inputted microarray samples were clustered and a respective clustering dendrogram of the samples was generated. Through the use of the clustering dendrogram, we visualised any potentially obvious outliers and if any were found, they were removed through an automatic approach. The said automatic approach, involves setting a pre-determined clustered dendrogram height cut-off value, based on the height value of the outlying microarray sample(s). Once the height value cut-off is chosen, a branch cut at the specified height can be used to remove the outliers. Overall, once the loaded gene microarray datasets had been loaded, properly formatted, checked for excessive missing values and potential outliers and finally, cleaned to remove offending genes and/or samples, the resulting processed expression dataset is saved as a new independent variable (ExpressDATA1) for subsequent network analysis.

In addition to loading and pre-processing the gene microarray datasets, prior to network analysis, we also loaded the clinical traits data for the respective microarray samples. This step and data are of importance, in order to ultimately identify gene modules and genes closely associated with a trait of interest, in this case, being OS. As a result, clinical trait data for all the relevant samples (both diseased and control), to be included in the WGCNA, was loaded into the R-studio working directory as a tab delimited csv file. Thereafter, the loaded clinical trait data is formatted, similarly to the expression data, by the removal of columns that hold information not required for the subsequent analysis, while only keeping necessary information, such as the respective sample and clinical traits. However, this step was omitted from the

methods, due to the contents of the loaded clinical traits dataset in this study. The loaded dataset only contained information on one external clinical trait of interest for this study, OS or healthy, and the respective samples for which the trait of interest was measured. Therefore, the step of auxiliary information removal from the dataset was omitted. Once formatted, the samples in the clinical traits' dataset, for which the trait of OS or healthy was measured, was to be matched to the respective samples in the expression dataset. This step is vital, if the order in which the samples are inputted within the two independent datasets do not match. However, in this study, the loaded datasets had a list of samples that matched in terms of the order they were inputted. Therefore, the function of matching the respective samples in the two independent datasets was omitted. The loaded and processed clinical traits data was then saved as an independent variable (`allClintraits`), similar to that of the gene expression data, for subsequent network analysis. Once the two datasets had been saved as variables within the R-studio working directory, it was important to visualise how the external clinical trait (OS) related to the generated clustering dendrogram of microarray samples. Thereafter, we continued with the gene co-expression network construction and identification of gene modules closely associated with OS.

For the subsequent steps of automated gene co-expression network construction and gene module detection, we first loaded the generated independent R variables containing the pre-processed datasets of gene expression and clinical trait data, respectively. The subsequent step, involved the step of choosing the method of gene co-expression network construction and gene module identification, which is said to be the most vital step of all network analyses within the WGCNA analysis. Hence, for the construction of weighted gene/topology networks and for the subsequent

generation of gene modules closely associated to OS, the one-step network construction method was used.

In order to construct a weighted gene topology network and subsequently detect gene modules, we first needed to choose the soft-thresholding power that is required for the process of network construction. The chosen soft-thresholding power will thus, become the power to which gene co-expression similarity is raised, so gene adjacency can be calculated. In relation, the soft-thresholding power was calculated using the one-step network construction provided default parameters. The authors of the tutorial proposed that the soft-thresholding power should be chosen based on the criterion of approximate scale-free topology. Consequently, the 'pickSoftThreshold' function that is provided by the WGCNA package, was used to perform the analysis of network topology and thus, aided in choosing the appropriate soft-thresholding power to be subsequently used in network construction and module detection. Henceforth, default parameters described were observed. In addition, when choosing a set of candidate soft-thresholding powers, suitable default values provided by the 'pickSoftThreshold' function were utilised, thus, making defining a set of suitable candidate powers an important step in the analysis. Subsequently, the network topology analysis function described was used to carry out the analysis which returned a set of network indices that needed to be inspected. Therefore, the resulting indices were then plotted with the utility of two varying graphical plots. The first plot that was utilised portrays scale-free topology fit index as a function of the soft-thresholding power. Thereafter, the indices were also plotted to show mean connectivity as a function of the soft-thresholding power. Thereafter, the indices that were plotted on the graph displaying scale-free topology fit index, were used to choose the appropriate soft-thresholding power required for the subsequent one-step weighted gene network construction. The

power was chosen based on the default rule provided by the authors in the WGCNA tutorial. Henceforth, the appropriate soft-thresholding power chosen, was the lowest power for which the scale-free topology fit index curve flattens out upon reaching a high value.

Once the appropriate soft-thresholding power had been determined, we carried out the one-step network construction and module detection methodology, with the utility of the calculated and chosen power. To conduct this methodology and thus, generate a gene network and identify gene modules, the function 'blockwisemodules' provided by the WGCNA package was used. In addition to the utility of the calculated soft-thresholding power as an argument for this function, we specified further parameters for the network construction and module detection process, with the parameters being default parameters gathered from the WGCNA analysis tutorial. Thus, the first specified parameter consisted of the maximum number of gene modules to be subsequently generated and this parameter was set as a default pre-determined value of 30. In addition, another analytical parameter that was gathered from the tutorial and used, was the module cluster splitting sensitivity which was set to a medium sensitivity. Lastly, the default pre-determined threshold height value for merging of gene modules was set to a module height of <0.25 .

Once we had carried out the network analysis and thus, constructed the weighted gene network and identified the respective gene modules, we then visualised the identified gene modules along with the hierarchical gene clustering dendrogram used for module identification. Henceforth, the mentioned gene clustering dendrogram was plotted for subsequent visualisation, together with the identified gene modules that had been assigned a specific colour through the utility of the 'labels2colours' function, provided by the package. Lastly, the respective colour assignments for the identified modules

and the gene module eigengene information was saved for subsequent analysis, which involved the inclusion of the external trait of interest, OS.

The subsequent steps, following gene network construction and gene module identification, involves relating the identified gene modules to external trait information. Henceforth, we can identify important gene modules and genes that are either positively or negatively associated with OS. To carry out this relationship and identify the said important gene modules, we first loaded the previously saved network file obtained from the one-step network construction and module detection method. The network file consisted of the gene module colour assignments and the module eigengene information, which is necessary for subsequent analysis. Thereafter, we related the identified gene modules to our external clinical trait of interest (OS) and subsequently quantified gene module-trait associations. Once respective module-trait associations were quantified, we used the resulting association values to identify gene modules that are significantly associated with the measured clinical trait OS.

To quantify module-trait associations, we utilised the gathered eigengene information for each module and correlated that information with the external clinical trait OS. Lastly, we identified the gene modules with the most significant associations to the trait. Consequently, we correlated the eigengene data for each module to the OS trait and colour coded each association, based on the module-trait correlation value. Thereafter, we visualise the module-trait correlations through a heatmap graphical representation and identified the gene module(s) significantly associated with the OS trait. The gene modules that had a high module-trait correlation value, had their association to the OS trait highlighted red and thus, were said to be positively associated with the trait.

Through the quantification of gene module-trait associations and visualisation of module-trait relationships through a heatmap graphical representation, we thereby identified gene modules significantly associated with the OS external clinical trait. Thereafter, we further quantified gene associations between individual assayed genes and the trait of interest (OS). To conduct the further quantification, we first defined a gene significance (GS) value for each gene, as the absolute value of the correlation between the respective gene and the OS trait. Thereafter, for each gene module, a quantitative value of module membership (MM) was defined as the level of correlation between the module summary data/eigengene and the analysed gene expression profile. The MM value, thus, allows for the quantification of the similarity between all genes on the array and the respective gene module. The trait of interest was specified as OS and the described quantitative values were generated by using the functions of 'geneModuleMembership' and 'geneTraitSignificance', provided by the WGCNA package. The functions were therefore, used to generate the GS and MM values respectively. Once the quantitative measures of GS and MM had been defined, they were used to identify genes that have a high significance for the OS trait, as well as a significantly high module membership within interesting modules. Consequently, we plotted a scatter plot of Gene significance vs Module membership for a specified gene module, in order to determine if the two measured values are highly correlated. If a highly significant positive correlation was identified between the two measures, within the specified gene module, it illustrated that genes within the module with a significant association with the OS trait are often also the most functionally important genes.

From the conducted quantification and analyses described, we found gene modules(s) with a significant level of association with our external trait of interest (OS). Furthermore, we identified the functionally important genes within the highly

associated modules, through the use of the Module Membership measure. Lastly, we collated all the measured statistical information and wrote out a file, within R-studio, which summarised the most important values and results. The file was written in an easy-to-read format, which allowed it to be later inspected and referred to during subsequent analyses, by using a standard spreadsheet software platform such as MS excel. An R data frame was created that held information of interest for all of the gene probes in the assay. The information of interest included the already inputted probe IDs, the module colours assigned to the respective gene modules, GS values for each gene in relation to OS, module membership values and P-values for its membership in all gene modules. Furthermore, the gene modules were ordered based on their significance to the OS trait.

From our previous gene network construction and module detection analysis, the results presented the identified gene module(s) that were significantly associated with the OS trait. However, to aid in making biological interpretations and for the determination of biological significance, the genes within the closely associated gene modules were functionally annotated. In relation, we conducted GO and KEGG pathway gene list enrichment analyses, to identify the topmost GO terms and KEGG pathways that were significantly overrepresented once the respective gene lists were enriched. In addition to the functional enrichment of genes closely related to the OS trait, we conducted STRING analysis on genes categorised under the gene module most closely associated to the OS trait, to visualise protein-protein interactions within the module. Furthermore, STRING analysis and the generation of a protein interaction network would aid in the visualisation of gene interactions and further allow for the identification of potential immune receptors within the highly associated gene module.

Once the weighted gene network was constructed, the gene modules that were significantly highly associated with OS were identified, and further statistical analysis was conducted. Subsequent to the further statistical analysis, relating to the measures of gene significance and module membership, we then determined the relationships among the identified modules. Henceforth, we plotted and visualised the network of eigengenes to visualise and study the inter-modular relationships. For the construction of the eigengene network, the summary profiles for each gene module (eigengenes), were used as representative profiles. Thereafter, the eigengenes were used to quantify gene module similarity based on eigengene correlation. The WGCNA package provided a R-function, titled 'plotEigengeneNetworks', that was subsequently used to construct the eigengene network and generate a summary plot that portrayed the constructed network. Moreover, to studying the inter-modular relationship between identified gene modules, we deemed it informative to add the OS clinical trait to the list of eigengenes, to visualise how the external clinical trait relates to the gene modules within the eigengene network. Therefore, the OS clinical trait was isolated and the mentioned R-function was used to plot the relationships among the eigengenes and the OS trait. The respective function, thus, outputted a clustered dendrogram of the eigengenes with the addition of the OS trait, and a heatmap representing the level of relationship among the eigengenes and the trait.

Disease Ontology Semantic and Enrichment analysis (DOSE)

Generic quality web tools and libraries have been previously employed for the functional enrichment of genes based on DO and for the computation of semantic measures, such as DO semantic similarity and gene-gene semantic similarity measurements, respectively. However, a lack of a bioinformatically dominant R/Bioconductor package brought upon several shortcomings, with regards to semantic

similarity computation. Therefore, for DO based gene enrichment analysis and for the computation of semantic similarity among DO terms and genes, the DOSE R-package was used. Once gene lists had been enriched based on DO, the package allowed for the measurement of semantic similarity among the identified DO terms and inputted candidate genes, through the utilisation of several information-content and graph-structure based algorithms (G. Yu et al., 2015). The DOSE package was thus, used for the evaluation of disease based functional associations within inputted gene lists of interest. To conduct these evaluations, DOSE carries out gene set enrichment analysis (GSEA) and hypergeometric test, which incorporates experimentally determined gene expression measurements to subsequently determine the biological significance of genes within the disease context (G. Yu et al., 2015).

So, the Disease Ontology Semantic and Enrichment analysis (DOSE) R package (version 3.10.0; <http://bioconductor.org/packages/DOSE>) (G. Yu et al., 2015) was used to enrich candidate DEGs or lists of DEGs in OS, respectively, through the use of DO enrichment analysis. Furthermore, the DOSE R package was used to calculate semantic similarity scores between DO enrichment analysis generated DO terms, gene clusters annotated by respectively generated DO terms of interest and individual gene products annotated under DO terms of interest. In this study, we utilised the method proposed by Wang and included in the DOSE package, to quantify semantic similarity based on the graph structure between DO terms and gene products (individual genes and gene clusters).

The R-package DOSE was first used to enrich specified gene lists of interest based on DO, which was conducted through the DO enrichment analysis function provided by the package. Consequently, to conduct the gene list DO enrichment analysis within the DOSE package, the 'enrichDO' R-function that is provided by and contained within

the DOSE package was utilised. However, in order to conduct the described DO enrichment analysis, the gene identifiers utilised in the gene list of interest needed to be of an appropriate format. Once the individual genes in the gene list are identified with an appropriate identifier format, they can then be entered into the R-platform, saved as a vector and recognised as a gene list vector within 'enrichDO' R-function. For the 'enrichDO' R-function to carry out the DO gene list enrichment analysis, the individual genes in the gene list first need to be inputted into the R-platform as a vector, with the gene identifiers being in an EntrezID gene identifier format. However, the genes gathered from the conducted OS differential gene expression analysis, were provided as gene symbols and Illumina platform probe IDs. Henceforth, in this study, an alternate R package named org.Hs.eg.db was utilised to convert the individual gene symbols in the gene list to be enriched, into their respective Entrez ID gene identifiers. Consequently, the gene symbols for the gene list of interest were loaded as a csv file into the R-platform. Thereafter, the individual gene symbols of the gene list only was saved as an R-vector entitled symbols. Lastly, the vectorised gene symbols were converted to their respective EntrezIDs, using the org.Hs.eg.db R package (version 3.14; <https://bioconductor.org/packages/org.Hs.eg.db/>) (Carlson, 2022).

The generated list of mapped EntrezIDs were then saved as a new vector within the R-platform for subsequent DO gene list enrichment analysis. To conduct the described DO enrichment analysis on the inputted gene list and generate the relevant DO terms the genes are enriched in, the vector containing the mapped EntrezIDs was submitted into the 'enrichDO' R-function within DOSE. Lastly, the R data frame function was used to visualise the list of DO terms. All identified significantly DEGs in OS (both up and downregulated) and the list of significantly upregulated and significantly

downregulated genes, were enriched through DO enrichment analysis in separate enrichment analyses.

Determination of druggable targets in close relation to OS

The top two upregulated immune receptors in OS (CXCR4 and CD74), in addition to the novel immune receptor (FPR3), were further analysed to determine their potential as therapeutically druggable targets for the treatment of OS. Two different drug and protein clinical annotation databases were mainly utilised to carry out a detailed drug survey and thus, clinically annotate the identified immune receptors of interest for their potential as druggable targets. These databases include PharmGKB (<https://www.pharmgkb.org/>) (Whirl-Carrillo et al., 2021) and oncoKB (<https://www.oncokb.org/>) (Chakravarty et al., 2017). The PharmGKB database was used to first generate a clinical overview for each immune receptor of interest, by obtaining clinical, variant, and other relating annotations. Thereafter, the precision oncology knowledge base (oncoKB) was used to query the immune receptors of interest and determine their true potential as druggable targets, from an oncology perspective. Furthermore, the Clinical Interpretations of Variants in Cancer (CIViC) database (<https://civicdb.org/>) (Griffith et al., 2017) was used to consolidate any findings gathered from using the two main databases. Thus, we hoped to identify any Food and Drug Administration (FDA) approved drugs currently manufactured to induce pharmacological effects on the potential target protein.

For the PharmGKB clinical database, the database was used to query the gene of interest and uncover any experimentally identified relationships between the gene of interest and various diseases, disease progression or disease survival. To query and annotate the gene of interest within the database, the database homepage was visited.

On the homepage, the gene name of the gene of interest was entered into the search bar. Once queried, the database provided various options related to the gene, such as information on the gene itself or various published information with experimental results relating to the gene of interest. For this study, we were interested purely on the gene. Therefore, the name of the gene of interest was selected from the list of options and the subsequent output page provided a descriptive overview of the gene. From the subsequent overview page of the gene, the tab 'variant annotation' was selected. The subsequent page portrayed the various potential variants of the queried gene, and any FDA approved drugs currently manufactured to induce varied effects on the target protein. In addition, the variant annotation page also provided information on potential associations between the gene variant and various diseases, with particular interest in cancer subtypes. From the variant annotation page, the name of the approved drug(s) in close association to the target protein was noted, along with any determined associations between the gene and various diseases. Lastly, the tab "related to" was selected, in order to determine gene relationships to identified pharmacological molecules and various known diseases.

For the oncoKB database, the database acts similar to the clinical database described above, however, with a more specific interest in the Oncology field. Therefore, oncoKB is commonly used as a more precise oncology centred clinical database for various genes. Like PharmGKB, the database also acts as a drug database, which can be used to query a gene of interest and identify any FDA approved drugs currently being manufactured against the protein. In addition, the database also provides information on any known mutation(s) of the gene in question, level of association between the gene and certain cancer types and prognostic/diagnostic capabilities of the gene. To carry out the analysis on the queried gene, the database homepage was visited. On

the homepage, the gene to be queried was entered into the search gene box. Thereafter, the resulting output page portrayed an overview of the gene, providing information on gene functionality and any known mutation(s) for the gene of use were the tabs located at the bottom of the overview page. The tabs can be navigated to and further information on the gene's therapeutic, prognostic and diagnostic annotations can be gathered, if available.

Lastly, with regards to the CIViC database, the database is similar to the oncology centred database oncoKB, due to its role in providing clinical annotations for various genes and their potential mutations in cancer. Therefore, the CIViC database was used to consolidate any findings gathered from using the two main databases described above. To conduct the analysis on the gene of interest and determine the clinical annotations associated with the gene, the cancer related protein database was visited. On the homepage, the name of the gene to be queried was entered into gene/gene variant search bar. Thereafter, the resulting output page consisted of an overview page for the queried gene and portrayed all the relevant clinical annotations associated with the gene. From the overview page, the tab titled 'DGIdb' (Drug gene interaction database) was selected to obtain any approved drug-gene interaction information for the queried gene. From the redirected interaction database page, generated for the queried gene, the tab "interactions" was selected. The resulting page provided a list of approved drugs currently manufactured against the gene of interest and inducing varied pharmacological effects. The page also provided information on the type of interaction the drug will have with the protein, such as agonistic or antagonistic. From this page, the most significant drugs that induce an inhibitory effect on the queried protein is identified.

Tumour immune estimation resource (TIMER) analysis

Targeted immunotherapeutic methods for cancer, necessitates the interaction between malignant tumour cells and the immune system to be properly investigated. However, when trying to understand the complexities involved in the interaction between cancer cells and immune infiltrates, major experimental and computational challenges have been brought forward. These challenges mainly revolve around the complicity of tumour genomes and the plasticity of the immune system. Thus, a diverse range of computational methodologies have been developed to estimate tumour immune infiltrates in disease the condition and its changes with altering levels of tumour gene expression (T. Li et al., 2017). It is said that these estimated immune cell populations that infiltrate the tumour, have been associated with both transcriptomic and genomic change within the tumour. Henceforth, the estimated immune population provide an insight into how the tumour interacts with the immune system (T. Li et al., 2020). The determined infiltrates, can then also be used to investigate the immunological characteristic of tumours and develop novel immunotherapies (T. Li et al., 2017).

In this study, the web server Tumor Immune Estimation Resource (TIMER; cistrome.shinyapps.io/timer) (T. Li et al., 2017) was used as a comprehensive web server to systematically analyse the molecular characterisations of tumour-immune interactions and statistically visualise tumour infiltrating immune cell populations, across diverse cancer types. The server provided inferences for six different tumour infiltrating immune cell populations (B cells, CD4 T cells, CD8 T cells, macrophages, neutrophils, and dendritic cells) abundancies, based on immune deconvolution-based approaches. (T. Li et al., 2017). In essence, TIMER consists of two major components,

being immune association and cancer exploration, with the third component being user defined immune estimation.

Firstly, we chose to investigate tumour-infiltrating immune cells, based on the analytical characteristic of immune associations. The investigation of immune associations included the analysis of the associations between tumour immune infiltrating cell abundance and candidate gene expression. Furthermore, it included the analysis of the association between tumour immune infiltrating cell abundance or candidate gene expression and patient overall survival. Henceforth, we first utilised the gene analytical module, to investigate associations between candidate gene expression in tumours and tumour infiltrating immune cell abundance. Thus, within the gene analytical module, a gene symbol for a candidate gene, specific cancer types and tumour infiltrate populations of interest were defined. If the candidate gene is highly expressed in the cells that make up the tumour microenvironment (TME), the gene is expected to be negatively associated with tumour purity. On the other hand, if the gene is positively associated with tumour purity, it is expected to be highly expressed in the tumour cells. Henceforth, through the subsequently generated scatter plot panel, portraying the purity-corrected partial Spearman's correlations and statistical significance, we identified the cancer type and specific tumour infiltrating immune cell subsets, significantly correlated with the expression of the candidate gene of interest. Overall, to easily make comparisons across diverse cancer types, we chose multiple cancer types at one time within TIMER and simultaneously displayed all correlations. In the study, the gene symbol for a candidate gene was inputted into the gene module for at least one cancer type of interest and with the default immune infiltrates being maintained.

Thereafter, we then chose the survival analytical module, to investigate the association between tumour immune infiltrating cell abundance and patient overall survival. For each survival analysis, TIMER generated a pallet of Kaplan-Meier plots for the selected tumour infiltrating immune cell subsets, versus overall survival in selected cancer types. From the survival plots, the effects of high vs low immune cell subset infiltration on the overall survival of the chosen cancer types were visualised (T. Li et al., 2020). In addition, for each Kaplan-Meier plot, a log-rank P-value was calculated, to portray the significance of the differences in patient survival between upper and lower percentiles. Like the Gene module, the candidate gene symbol was inputted for at least one cancer type, and the default immune infiltrates were maintained, along with the default Kaplan-Meier curve parameters.

Once we had investigated immune associations, we then further explored various relevant cancer types in relation to candidate gene expression. Thus, we explored the level of correlation between two candidate genes based on their gene expression levels, within specified cancer types. The correlation analytical module, generated a scatterplot representing the gene expression levels for two candidate genes of interest within a specified cancer type, along with Spearman correlation and an estimated significance for their correlation (T. Li et al., 2017). Within the correlation module, a cancer type of interest was chosen, and the two candidate genes were inputted into the Y and X-axis respectively. With the correlation adjustments being none, the tool subsequently generated a scatter plot that displayed gene expression levels for the two genes within the cancer.

3.3 Results

Search strategy and included studies

Commonly, studies carrying out gene expression microarray-based investigation into OS, utilise OS cell lines as appropriate in vitro models. However, variations in gene expression profiles are known between OS cell lines (Sun et al., 2015), thus, they do not fully replicate the true physiological condition, observed in vivo, unlike pre-chemotherapeutic OS biopsies. Therefore, for the determination of gene dysregulations in OS, in vivo, differential gene expression analysis was carried out on pre-chemotherapeutic OS biopsies, versus an appropriate control. This strategy overcomes the limitations portrayed by in vitro models. In relation, OS is known to be of mesenchymal origin, therefore, an appropriate control for OS differential gene expression analysis would be normal primary human BM-MSCs. However, like OS cell lines, MSC derivatives do not fully replicate the true physiological condition of primary BM-MSCs in vivo. Therefore, for the accurate identification of differentially expressed genes in OS, the use of primary healthy BM-MSCs as an appropriate control was deemed to be important.

Once the described constrained search strategy and strict study inclusion criteria were implemented on OS related gene expression microarray studies found within the browsed databases, we identified a single eligible study that met the criteria. This study (GSE42352 - (Kuijjer et al., 2013)) was the only one found within GEO, which included both primary pre-chemotherapy tumour tissues from patients with OS and primary bone-marrow mesenchymal stem cells (BM-MSCs) from healthy disease-free controls. Therefore, this gene expression microarray dataset containing gene expression data derived from the individual patients was subsequently utilised.

Specifically, RNA expression data for the respectively probed genes in the microarray, were extracted from the relevant gene microarray dataset. From the GSE42352 gene microarray dataset, RNA expression data were extracted from a total of 84 OS patient primary tumour biopsies and 12 normal healthy BM-MSC samples (Table 3.1). The RAW gene expression data files for each patient in the study can be found and downloaded from the GEO webpage.

Table 3.1: OS centred gene expression microarray study used for bioinformatics analysis. Table describing in detail, the general characteristics of OS based gene expression microarray study, acquired via the GEO database and included in the present study. Information such as study authors, country of study origin, accession number within the GEO database, gene microarray platform used, number of relevant patients included and included sample types are shown. The respective patient samples analysed via gene expression microarray in the included study ($n=84$ for OS and $n=12$ for healthy controls).

Author, year	Region of origin	GEO accession	Platform	OS patients	Controls	OS sample type/control sample
Kuijjer ML et al, 2013	Europe	GSE42352	GPL10295	84	7 healthy donors 5 healthy biopsies from OS patients	High-grade OS biopsy/ BM derived MSCs

Differential gene expression analysis and identification of DEGs

GEO2R mediated differential gene expression analysis was conducted on the data set. Identification of DEGs in OS, in vivo, may lead to a greater understanding of the mechanisms underlying OS, unveil novel therapeutic targets and overall, improve the clinical management of the disease.

The web-based differential gene expression analysis tool, GEO2R, was used to initially pre-process the raw gene expression data acquired from the dataset, which involved background corrections and normalisation. Thereafter, GEO2R was used for

carrying out differential gene expression analysis and identifying DEGs. In total, from the GSE42352 gene microarray dataset, gene expression values from 48701 gene probes were acquired. The gene probes represented 30549 known genes with gene symbols, which were analysed through the use of GEO2R in the present study. Out of the 48701 gene probes used in the microarray, 8265 genes were found to be differentially expressed in OS (Figure 3). The dysregulated genes were identified at a cut-off of (adjusted $P < 0.01$), with all genes having valid gene IDs, however, with some genes not having known gene symbols. In addition, the identified DEGs can be further separated into statistically significantly upregulated and downregulated genes in OS (Figure 3.3).

However, the identified dysregulated genes were only said to be significantly differentially expressed when they met the cut-off values of $|\log_2FC| > 1$ (adjusted $P < 0.01$). Thus, the result was a total of 1161 genes with gene symbols that were found to be differentially expressed in OS, with the list of genes being further classified into 535 upregulated and 626 downregulated genes when compared to the healthy human BM-MSK controls (Figure 3.4). Similarly, if the cut-off values were set as $|\log_2FC| > 2$ (adjusted $P < 0.01$), a total of 267 genes were found to be differentially expressed, which consisted of 142 upregulated and 125 downregulated genes in OS when compared to controls. The top 10 most up and downregulated genes in OS, identified in this study, are shown in tables 3.2 and 3.3.

Volcano plot
GSE42352: Genome-wide gene expression
profiling of mesenchymal stem...
control vs OS, Padj<0.01

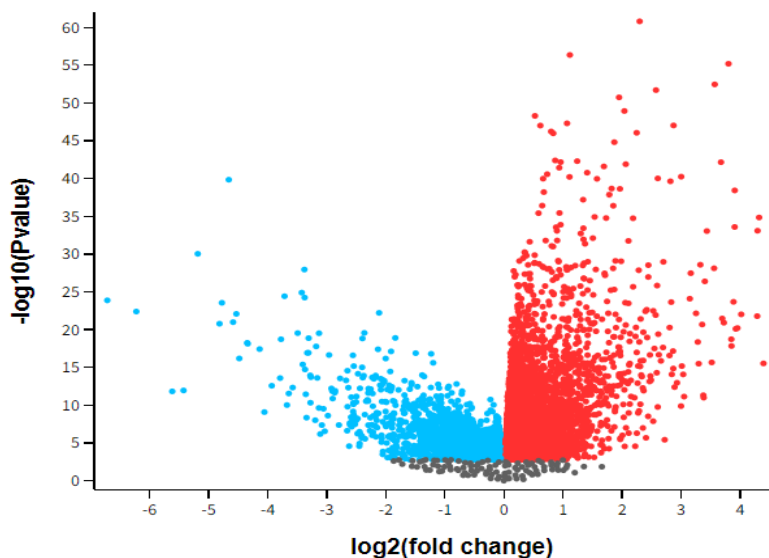


Figure 3.3: **Differentially expressed genes in OS.** Volcano plot representing \log_2FC of gene expression against statistical significance of gene dysregulation (P-value) in OS, for all probed genes in the gene microarray analysis. The figure represents the genes identified to be significantly upregulated (red) and downregulated (blue) in OS, based on the cut-off of ($P_{adj} < 0.01$), along with the genes with normal (unaltered) levels of expression. DEGs in OS were identified by comparing gene expression data gathered from human primary pre-chemotherapeutic OS tumours ($n = 84$) to healthy BM-MSCs ($n = 12$).

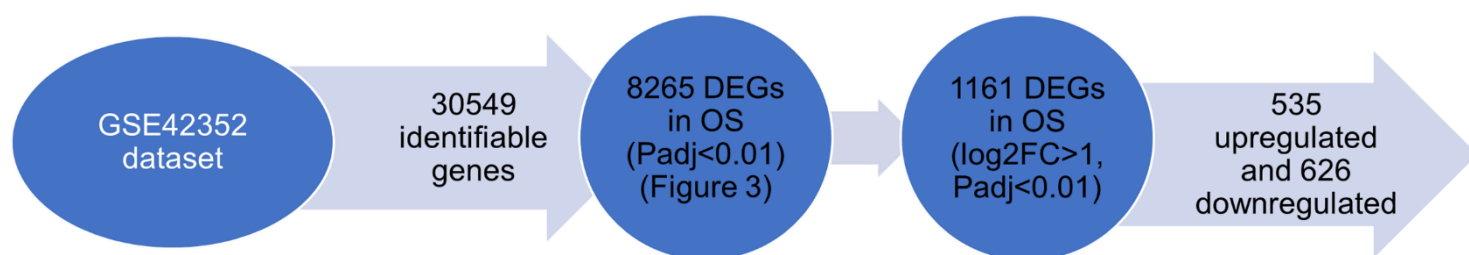


Figure 3.4: **Numerical based refinement of DEGs in OS.** Flow chart representing the GEO2R differential gene expression analysis and further numerical filtration steps conducted, to identify significantly DEGs in OS. Differential expression analysis was conducted on the 30549 identifiable genes, arrayed in the gene microarray, giving 8265 DEGs in OS at the cut-off of (adjusted $P < 0.01$). Further numerical refinement of DEGs, then gave 1161 significantly DEGs genes in OS (535 upregulated and 626 downregulated genes), at cutoff values of $|\log_2FC| > 1$ (adjusted $P < 0.01$). DEGs in OS were identified by comparing gene expression data gathered from human primary pre-chemotherapeutic OS tumours ($n = 84$) to healthy BM-MSCs ($n = 12$).

Table 3.2: Most significantly upregulated genes in OS. Table portraying the top 10 most upregulated genes in OS, identified in this study. Upregulated genes were identified using positive t-score values and at cutoff values of $|\log_2FC| > 1$ (adjusted $P < 0.01$). Genes have been sorted based on the \log_2FC value for each gene, from largest gene \log_2FC to smallest.

Gene Symbol	Log2FC	t-score	P-value	Adjusted P-value
MMP9	6.72	13.89	<0.0001	4.13E-22
SPP1	6.22	13.15	<0.0001	1.04E-20
HBB	5.61	8.14	<0.0001	7.28E-11
HBA1	5.42	8.20	<0.0001	5.67E-11
RNASE1	5.18	17.11	<0.0001	6.92E-28
C1QA	4.82	12.37	<0.0001	3.37E-19
TYROBP	4.78	13.73	<0.0001	8.2E-22
PLVAP	4.66	22.97	<0.0001	2.32E-37
APOE	4.59	12.47	<0.0001	2.14E-19
CSF1R	4.53	13.00	<0.0001	2.04E-20

Table 3.3: Most significantly downregulated genes in OS. Table portraying the top 10 most downregulated genes in OS, identified in this study. Downregulated genes were identified using negative t-score values and at cutoff values of $|\log_2FC| > 1$ (adjusted $P < 0.01$). Genes have been sorted based on the \log_2FC value for each gene, from largest gene \log_2FC to smallest.

Gene Symbol	Log2FC	t-score	P-value	Adjusted P-value
THBS1	4.39	9.88	<0.0001	2.76E-14
PTX3	4.32	19.85	<0.0001	1.63E-32
EFEMP1	4.30	18.82	<0.0001	7.93E-31
SERPINE1	4.29	12.85	<0.0001	3.83E-20
KIAA1199	4.02	12.97	<0.0001	2.28E-20
MFAP5	3.95	12.09	<0.0001	1.15E-18
CXCL12	3.93	12.04	<0.0001	1.46E-18
IL6	3.91	22.06	<0.0001	5.37E-36
HAK	3.91	19.11	<0.0001	2.69E-31
FHL2	3.89	13.79	<0.0001	6.21E-22

Principal component analysis of DEGs in OS

Once significantly DEGs in OS were identified, principal component analysis (PCA) was subsequently carried out on the top 10 most up and downregulated genes in OS when compared to the controls. Thereby, determining if the DEGs can differentiate the OS clinical trait from the normal (healthy) controls. The results of the conducted PCA analysis revealed that these top DEGs are capable of distinguishing the OS clinical trait from normal healthy controls (Figures 3.5 and 3.6). Therefore, the analysed DEGs may play a vital role in OS tumorigenesis and disease progression.

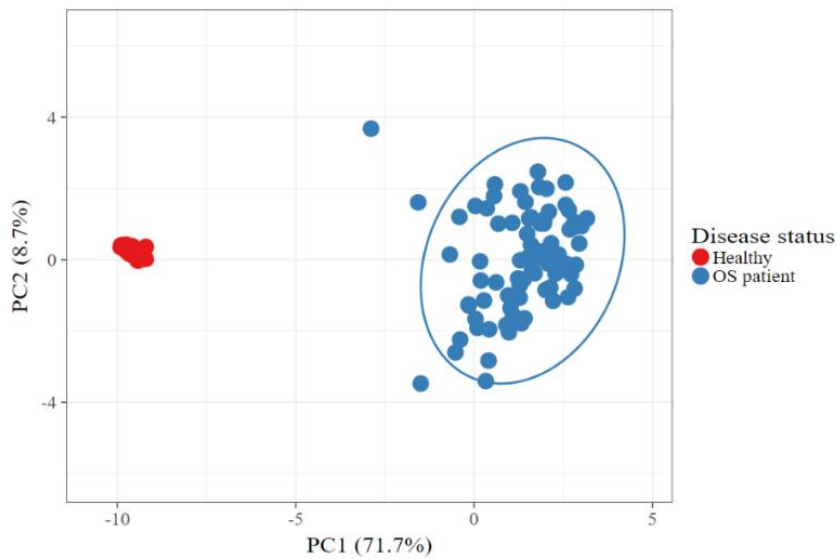


Figure 3.5: PCA: separation of external clinical traits based on expression of top DEGs. Scatterplot representing the principal component analysis conducted by utilising the top 10 most up and downregulated genes in OS, along with the respective gene expression values for each gene within OS biopsy tissues and the healthy control BM-MSCs. Unit variance scaling is applied to rows; SVD with imputation is used to calculate principal components. X and Y axis show principal component 1 and principal component 2 that explain 71.7% and 8.7% of the total variance, respectively. Therefore, the genes are able to separate the two clinical traits.

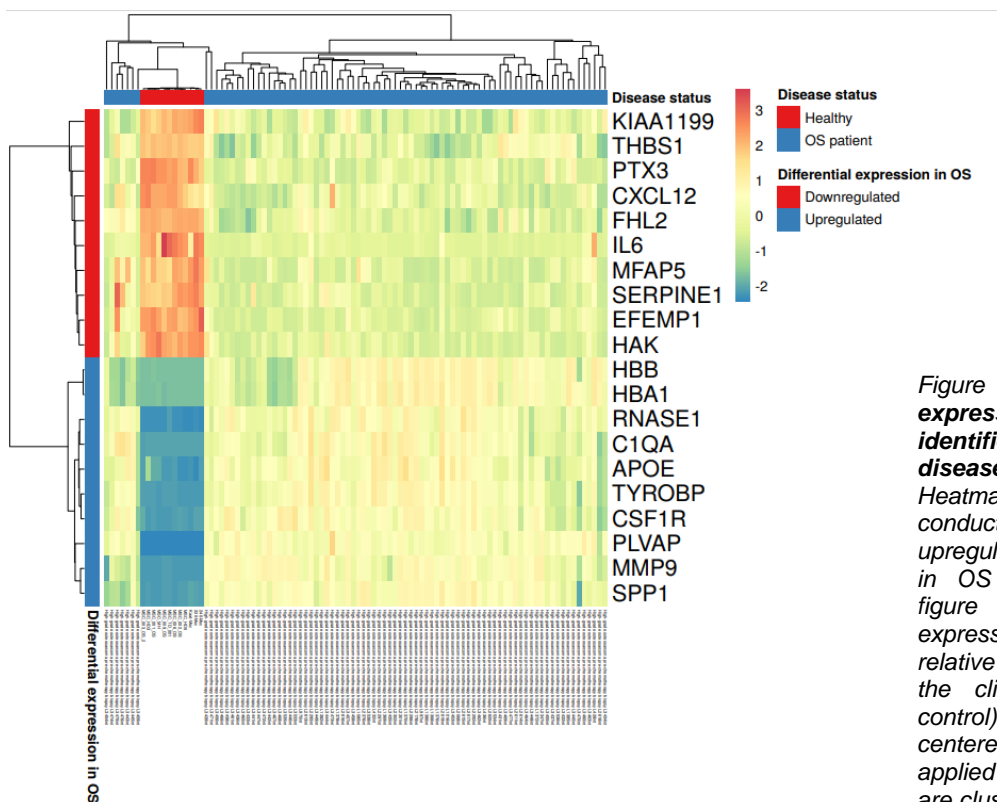


Figure 3.6: PCA: differences in expression levels shown by the identified DEGs, between the diseased and healthy clinical traits. Heatmap generated from PCA analysis conducted on the top ten significantly upregulated and downregulated genes in OS ($\log_2FC > 1$, $P_{adj} < 0.01$). The figure portrays the differential expression for each gene in OS and the relative level of gene expression across the clinical samples (disease and control). In the analysis, rows are centered; unit variance scaling is applied to rows. Both rows and columns are clustered using correlation distance and average linkage.

Functional enrichment of DEGs in OS

All identified DEGs

The identified DEGs in OS portray no biological significance and meaningfulness when represented as a raw list of genes. Therefore, for the determination of biological significance, the DEGs were annotated through gene enrichment analysis. Functional gene enrichment may provide a greater understanding of the role the DEGs play in the cellular and molecular mechanisms underlying OS. The total list of DEGs in OS was functionally enriched first, in order to determine the biological significance of genome wide dysregulation in the OS diseased trait. Thereafter, the lists of significantly upregulated and downregulated genes in OS were functionally enriched independently. Thus, determining the biological significances of the upregulated and downregulated genes, respectively, with respect to aiding OS tumorigenesis and progression.

The identified list of total DEGs in OS $|\log_2FC| > 1$ (adjusted $P < 0.01$), was first analysed with the use of GO-ORA, to determine the GO terms the DEGs were most overrepresented in. The results of the analysis showed overrepresentation in various GO terms relating to biological processes, cellular component, and molecular function. The identified DEGs were most overrepresented in processes including immune response, regulation of immune system process, cell activation, leukocyte activation, immune effector process, anatomical structure formation involved in morphogenesis, vasculature development, blood vessel development, extracellular structure organisation and extracellular matrix organisation (Figure 3.7). Similarly, the total DEGs were functionally enriched and overrepresented in cellular component GO terms including extracellular exosome, cytoplasmic vesicle part, cell junction,

secretory vesicle, secretory granule, cell surface, adherens junction, extracellular matrix, cell-substrate adherens junction and collagen-containing extracellular matrix (Figure 3.8). Lastly, the DEGs were most overrepresented in molecular functions including protein-containing complex binding, extracellular matrix structural constituent, cell adhesion molecule binding, structural molecule activity, collagen binding, integrin binding, fibronectin binding, identical protein binding, actin binding and cytoskeletal protein binding (Figure 3.9).

Likewise, further GO gene list enrichment analysis with FunRich, showed that the total DEGs participate in biological processes including cell adhesion, extracellular matrix organization, antigen processing and presentation of exogenous peptide antigen through MHC class II, peptide antigen assembly with MHC class II protein complex, immunoglobulin production involved in immunoglobulin mediated immune response and positive regulation of cell migration. The DEGs were enriched in cellular component GO terms including extracellular vesicular exosome, extracellular region, focal adhesion, extracellular space and endoplasmic reticulum lumen. Lastly, the DEGs were found to carry out molecular functions including extracellular matrix structural constituent, protein binding, integrin binding, and actin binding.

Sun et al reported strong associations between DEGs in OS, the extracellular matrix and extracellular matrix remodelling, as is expected with tumorigenesis (Sun et al., 2019). This was further supported by functional enrichment analysis of total DEGs in OS, whereby, the DEGs were enriched in biological process GO terms including Extracellular structure organisation and Extracellular matrix organisation. However, results from GO-ORA and further gene enrichment analysis, suggested a significant involvement of the host immune system and OS tumour immune niche in tumour development and metastasis.

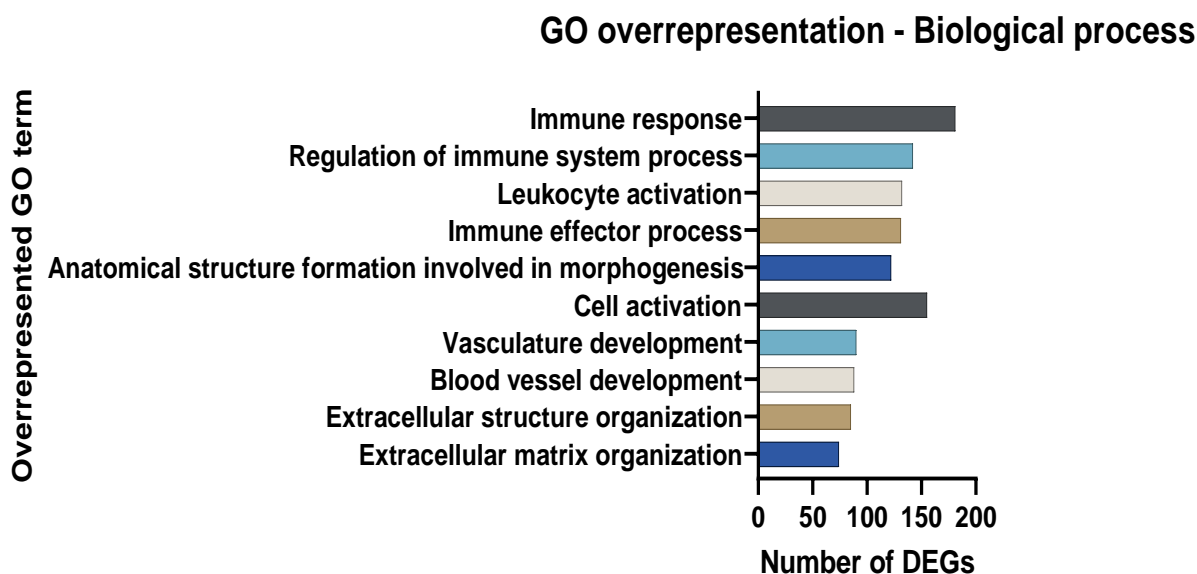


Figure 3.7: **GO overrepresentation analysis: biological process.** A bar graph depicting the top 10 GO terms, when GO overrepresentation analysis was conducted on the DEGs to identify overrepresented biological processes with a cutoff of (adjusted $P < 0.05$). The x-axis shows the number of DEGs that are categorised under an overrepresented GO term and the y-axis shows the different overrepresented GO terms. GO, Gene Ontology.

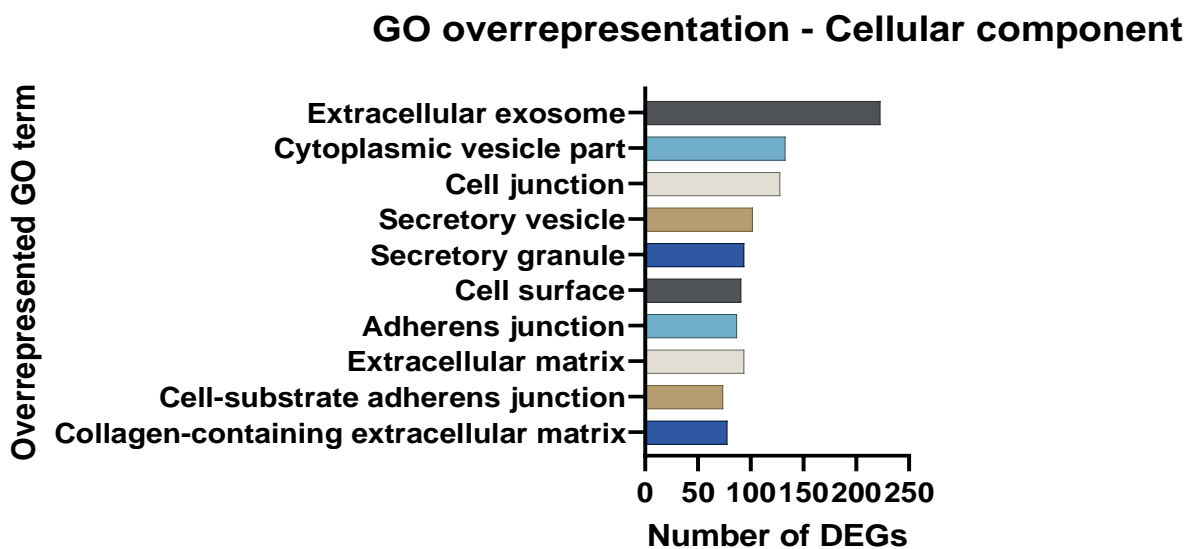


Figure 3.8: **GO overrepresentation analysis: cellular component.** A bar graph depicting the top 10 GO terms, when GO overrepresentation analysis was conducted on the DEGs to identify overrepresented cellular components with a cutoff of (adjusted $P < 0.05$). The x-axis shows the number of DEGs that are categorised under an overrepresented GO term and the y-axis shows the different overrepresented GO terms. GO, Gene Ontology.

GO overrepresentation - Molecular function

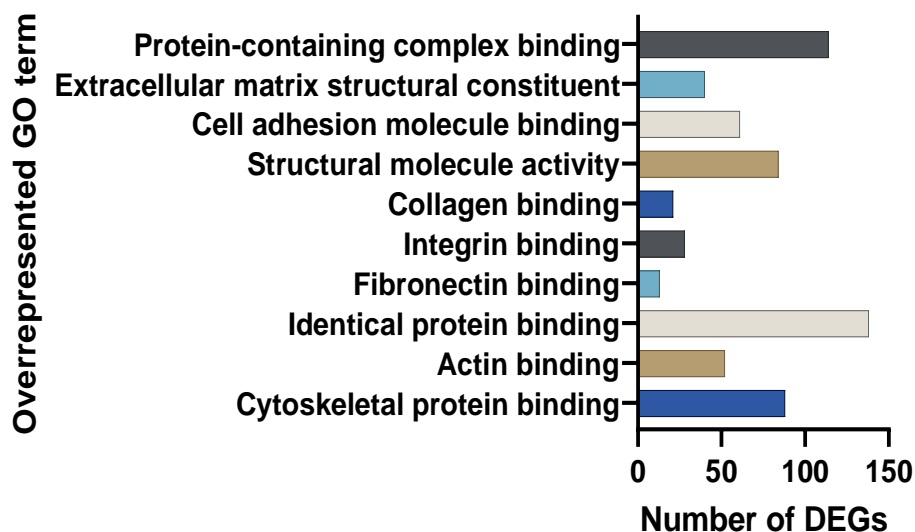


Figure 3.9: **GO overrepresentation analysis: molecular function.** A bar graph depicting the top 10 GO terms, when GO overrepresentation analysis was conducted on the DEGs to identify overrepresented molecular functions with a cutoff of (adjusted $P < 0.05$). The x-axis shows the number of DEGs that are categorised under an overrepresented GO term and the y-axis shows the different overrepresented GO terms. GO, Gene Ontology.

Like GO-ORA, KEGG overrepresentation analysis was also carried out on the list of DEGs in OS. Results from the analysis showed that the DEGs were significantly overrepresented in KEGG pathways including viral myocarditis, phagosome, hematopoietic cell lineage, ECM-receptor interaction, focal adhesion, Staphylococcus aureus infection, type I diabetes mellitus, Graft-versus-host disease, antigen processing and presentation and allograft rejection (Figure 3.10). In addition to the conducted KEGG overrepresentation analysis, further KEGG pathway gene list enrichment analysis demonstrated that the DEGs were enriched in KEGG pathways including phagosome, viral myocarditis, ECM-receptor interaction, focal adhesion, hematopoietic cell lineage, rheumatoid arthritis, type I diabetes mellitus, antigen processing and presentation, cell adhesion molecules and staphylococcus aureus infection.

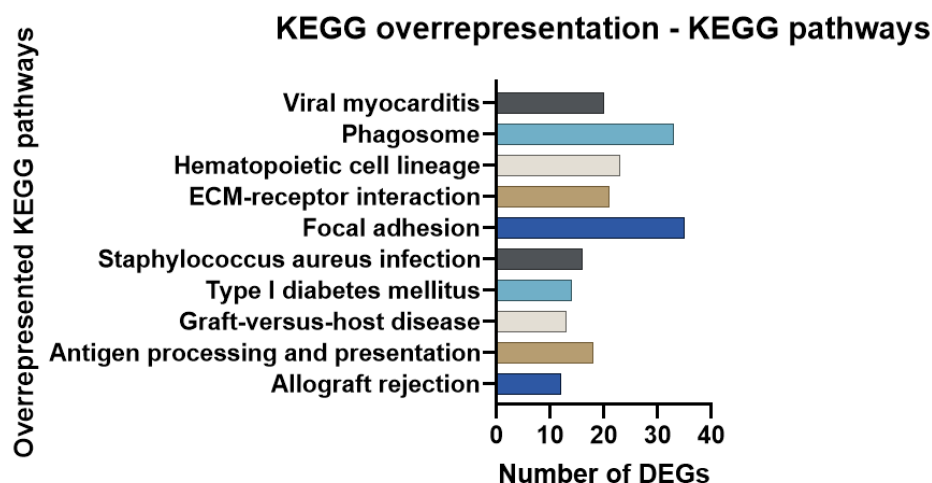


Figure 3.10: **KEGG overrepresentation analysis.** A bar graph depicting the top 10 KEGG pathways, when KEGG overrepresentation analysis was conducted on the DEGs in OS. The x-axis shows the number of DEGs that are categorised under an overrepresented KEGG pathway and the y-axis shows the different overrepresented KEGG pathways.

Upregulated genes

GO overrepresentation enrichment analysis, when conducted on the significantly upregulated genes ($\log_2FC > 1$, $P_{adj} < 0.01$) in OS, showed that the upregulated genes in OS were significantly overrepresented in biological processes including immune response, defence response, regulation of immune system process, cell activation, leukocyte activation, immune effector process, positive regulation of immune system process, innate immune response, response to cytokine and regulation of immune response. The genes were functionally enriched and overrepresented in cellular component GO terms including extracellular matrix, extracellular exosome, MHC protein complex, collagen-containing extracellular matrix, cytoplasmic vesicle part, MHC class II protein complex, endocytic vesicle membrane, lysosome, lytic vacuole, and side of membrane. Lastly, the genes were shown to carry out molecular functions including, MHC class II receptor activity, protein-containing complex binding, peptide antigen binding, identical protein binding, virus receptor activity, hijacked molecular

function, MHC class II protein complex binding, antigen binding and enzyme regulator activity.

In addition, further GO-based gene enrichment analysis with FunRich, showed that the DEGs (upregulated) participate in biological processes including antigen processing and presentation of exogeneous peptide antigen through MHC class II, peptide antigen assembly with MHC class II protein complex, immunoglobulin production involved in immunoglobulin mediated immune response, positive regulation of T cell activation, immune response and negative regulation of B cell proliferation. Furthermore, the genes were enriched in cellular component GO terms including extracellular region, MHC class II protein complex, extracellular vesicular exosome, extracellular space and integral to luminal side of endoplasmic reticulum membrane. Lastly, the DEGs were found to carry out molecular functions including MHC class II protein complex binding, MHC class II receptor activity, extracellular matrix structural constituent, peptide antigen binding, protein binding and viral receptor activity.

Similar to GO-ORA, KEGG overrepresentation analysis showed that the upregulated genes were overrepresented in KEGG pathways including antigen processing and presentation, type I diabetes mellitus, staphylococcus aureus infection, allograft rejection, viral myocarditis, phagosome, rheumatoid arthritis, Graft-versus-host disease, hematopoietic cell lineage and asthma.

Results from the conducted GO based gene enrichment analysis, show that the upregulated genes in particular portray a strong involvement in the extracellular matrix and extracellular matrix remodelling, similar to that of the enriched total DEGs in OS. Likewise, results from GO-ORA and further gene enrichment analysis, continue to

portray a significant involvement of the host immune system and OS tumour immune niche, which are shown to be upregulated in OS tumour development and metastasis.

Downregulated genes

GO overrepresentation enrichment analysis, when conducted on the significantly downregulated genes ($\log_2FC > 1$, $P_{adj} < 0.01$) in OS, showed that the downregulated genes in OS were significantly overrepresented in and thus, portrayed roles in biological processes including circulatory system development, enzyme linked receptor protein signalling pathway, extracellular structure organization, extracellular matrix organization, cell adhesion, biological adhesion, tissue development, anatomical structure formation involved in morphogenesis, locomotion and movement of cell or subcellular component. The genes were functionally enriched and overrepresented in cellular component GO terms including extracellular exosome, cell junction, anchoring junction, adherens junction, extracellular matrix, actin cytoskeleton, cell-substrate junction, cell-substrate adherens junction, focal adhesion, and collagen-containing extracellular matrix. Lastly, the genes were shown to carry out molecular functions including, cell adhesion molecule binding, actin binding, structural molecule activity, fibronectin binding, extracellular matrix structural constituent, protein-containing complex binding, growth factor binding, cytoskeletal protein binding, collagen binding and integrin binding.

In addition, further GO-based gene enrichment analysis undergone through FunRich, showed that the DEGs (downregulated) participate in biological processes including integrin-mediated signalling pathway, platelet aggregation, negative regulation of cell migration, cell adhesion, response to mechanical stimulus, positive regulation of

angiogenesis. Furthermore, the genes were enriched in cellular component GO terms including focal adhesion, extracellular vesicular exosome, stress fibre, actin cytoskeleton and extracellular region. Lastly, the DEGs were found to carry out molecular functions including fibronectin binding, actin binding, integrin binding, extracellular matrix structural constituent, protein binding, collagen binding.

Similar to GO-ORA, KEGG overrepresentation analysis showed that the downregulated genes were overrepresented in KEGG pathways including focal adhesion, Proteoglycans in cancer, ECM-receptor interaction, regulation of actin cytoskeleton, Hypertrophic cardiomyopathy (HCM), Dilated cardiomyopathy (DCM), Arrhythmogenic right ventricular cardiomyopathy (ARVC), Bacterial invasion of epithelial cells, Pathways in cancer and Biosynthesis of amino acids.

Results from the conducted GO based gene enrichment analysis, show that the downregulated genes in particular portray a strong involvement in the negative regulation of cell migration, mediation of cellular adhesion and regulation of angiogenesis. Thereby, downregulation of these genes can be said to be a consequence of OS tumour survival mechanisms, observed in vivo, which look to promote tumour cell survival, proliferation and tumour metastasis. Unlike the total DEGs in OS and the upregulated genes, results from GO-ORA and further gene enrichment analysis of downregulated genes, failed to portray a significant involvement of the host immune system and OS tumour immune niche. Therefore, emphasising the importance of the host immune system and tumour immune niche in OS tumour development and metastasis.

GO term refinement of (upregulated genes) in OS

Total identified DEGs in OS, along with upregulated and downregulated genes only were functionally enriched based on molecular function, cellular component and biological process, respectively. Thereby, functionally annotating the genes and determining their biological significance. However, due to the known significant interplay between the host immune system and OS, which was further emphasised during gene functional enrichment, this study concentrated on immune receptors that are differentially expressed, with specificity going towards significantly upregulated receptors in OS. Upregulated immune receptors were to be assessed for their novelty in OS and then, investigated for their potential as novel immune-based therapeutic targets in the treatment of OS. Thus, for the specific identification of upregulated immune receptors in OS, the total upregulated genes were refined based on the biological process GO term “immune receptor activity”.

The list of significantly upregulated genes in OS was refined using the gene enrichment analysis tool Uniprot. The subsequent gene-list enrichment, followed by the GO term-based refinement, provided a list of genes that were annotated under the specified GO term. Through gene list matching and excel spreadsheet data manipulations, a list of genes that were characterised to be upregulated immune receptor genes $|\log_2FC| > 1$ (adjusted $P < 0.01$) in OS was identified. The top 10 most upregulated immune receptor genes in OS, were identified to be CXCR4, CD74, HLA-DRA, FCER1G, HLA-DPA1, FPRL2, HLA-DQA1, CTSH, CSF2RA and HLA-DRB3, based on adjusted P-values for each gene, from most significant upregulation to least, as shown in table 3.4.

Table 3.4: GO based gene list refinement and upregulated immune receptors in OS. Table displaying the top 10 most upregulated immune-receptor genes in OS, that were functionally annotated by the GO term of interest “immune receptor activity”. Immune receptors have been sorted based on the statistical significance of gene dysregulation (adjusted P-value) for each gene, from smallest to largest. In addition, the table displays the log2FC values and adjusted P-values for each gene.

Immune receptors	log2FC	Adjusted P-value
<u>CXCR4</u>	3.38	5.74E-26
<u>CD74</u>	4.35	7.8E-17
HLA-DRA	4.48	6.62E-15
FCER1G	3.41	3.76E-14
HLA-DPA1	3.79	1.79E-12
<u>FPRL2/FPR3</u>	1.83	3.59E-09
HLA-DQA1	3.13	7.71E-09
CTSH	1.32	0.000000013
CSF2RA	1.97	0.000000753
HLA-DRB3	2.19	0.00000114

Weighted gene co-expression network analysis (WGCNA) analysis

To truly put forward candidate immune receptors as therapeutic targets within the immune niche of OS, their levels of genetic association to the OS clinical trait must first be measured. WGCNA utilises gene expression values to determine which DEGs in OS, specifically immune receptors, were most closely associated to the OS clinical trait. Thereby, immune receptors not closely associated to the disease trait can be separated from immune receptors showing close association to OS.

In the study, WGCNA was conducted to identify which groups of genes with functional similarities, known as gene modules, are closely associated with OS. Closely associated genes were determined based on each gene’s classification to a respective

gene module and through the generation of gene significance scores, which were calculated based on the significance of each gene's association to the disease trait.

For the identification of key gene modules and genes closely associated with OS, normalised gene expression data from all of the probed genes in the microarray and relevant samples (diseased and control) were included in the WGCNA. Furthermore, the gene microarray dataset was checked for excessive missing values and later checked for outlier gene expression microarray samples. The results of this dataset check, returned no excessive missing values, meaning that none of the probed genes or samples had any missing values above threshold. In addition, the microarray samples were checked to identify any potential sample outliers, with microarray samples being clustered based on their Euclidean distance in order to identify potential outliers. The results of the sample clustering indicated that none of the microarray samples were obvious outliers (Appendix A, figure A1).

Due to no excessive missing values and sample outliers being detected, all of the gene expression values from the inputted probed genes and relevant microarray samples were included in the continued WGNA. Once the gene microarray dataset was finalised and saved as a variable for further network analysis, the clinical trait data for the samples was loaded into the platform. The results of the data input, cleaning and pre-processing steps, provided us with two independent R variables, which included the gene expression data and the corresponding clinical trait data, respectively. Thereafter, prior to network construction and gene module detection, we visualised how the external clinical trait OS related to the respective microarray samples (Appendix A, figure A2). In the heatmap, shown, the clustered dendrogram of samples was paired with the inputted OS clinical trait data.

Once the gene microarray datasets and clinical trait data had been saved as independent variables, we conducted an automated method of gene network construction. This was then followed by the identification of key gene modules associated with OS. The `picksoftthreshold` function was used within the WGCNA package, to perform the analysis of network topology and aid in the selection of an appropriate soft-thresholding power. The results of the conducted network topology analysis are shown in (Appendix A, figure A3), whereby, network topology was analysed for various soft-thresholding powers. By utilising the generated panels, we choose the soft-thresholding power of 4. This was the lowest power for which the scale-free topology fit index curve flattens out upon reaching a high value (0.9).

Once the soft-thresholding power was determined, the weighted gene network construction and module detection was conducted through a simple one-step process. The output result was a total of 77 different gene modules that were then visualised through module colours being randomly assigned to each module. The gene modules are presented together with the hierarchical clustering dendrogram of genes, used during the module identification step (Appendix A, figure A4).

Post-identification of gene modules in which genes with similar functionality are grouped together, we quantified gene module-trait association levels, to identify modules that were significantly associated with OS clinical trait. Henceforth, a module-trait relationships heat map was generated, in order to identify which of the gene modules that were assigned module colours, were significantly associated with OS (Figure 3.11). A minimum module size of 30 and a medium sensitivity to gene cluster splitting was chosen. As shown in figure 3.11, the gene module colours pink and dark grey are positively associated with OS. On the other hand, the gene module colours of yellow and sienna 3 are negatively associated with OS.

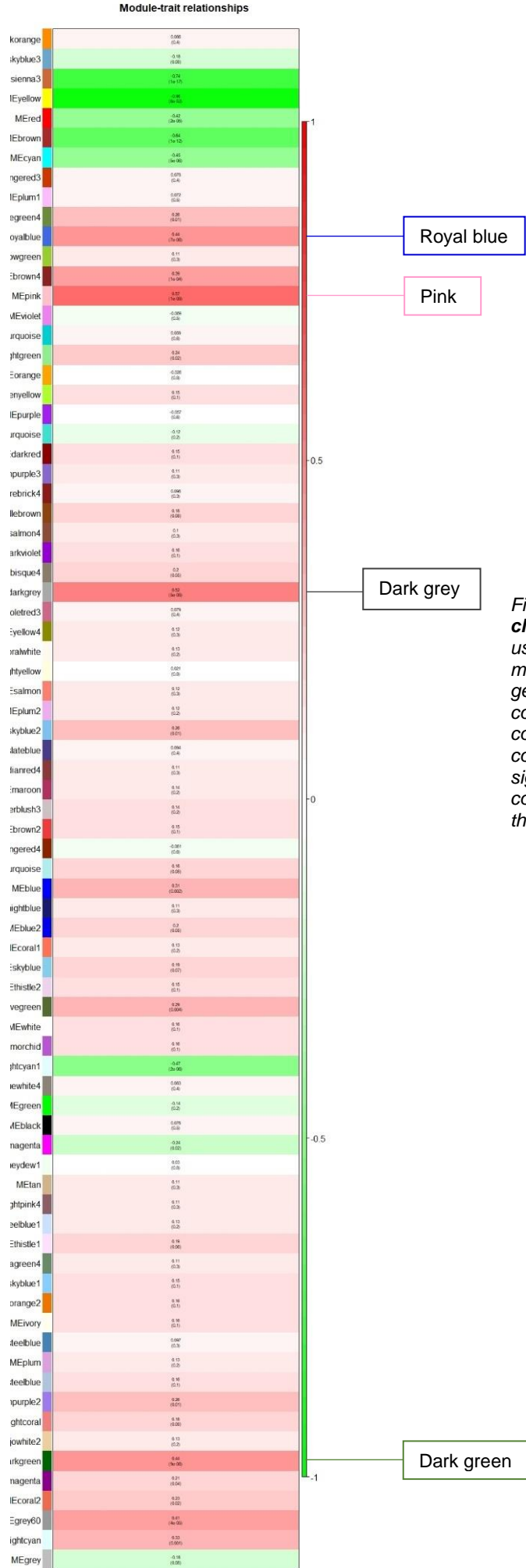


Figure 3.11: WGCNA: gene module to OS clinical trait associations. Heatmap generated using WGCNA, representing the level of gene module-OS clinical trait associations for each gene module constructed. Each row corresponds to a module eigengene and the column to OS clinical trait. Each cell contains the corresponding module-trait correlation and significance of correlation (p-value). The table is color-coded based on correlation according to the colour legend.

In addition to identifying gene modules closely associated with the OS external clinical trait, we carried out intra-gene module analysis, to further analyse individual genes within the closely associated modules. Through the utility of gene significance and module membership measures, we can identify genes that have both a high significance to OS and a high functional role within the module of interest. With the pink module being taken as an example, due to it having the greatest association to OS, we plotted a scatter plot of gene significance vs module membership (Appendix A, figure A5). The measures of gene significance and module membership were highly and significantly correlated. Therefore, we can say that the genes in the pink module that are highly significantly associated with OS, are also the genes that are the most important functionally.

From the generated module-trait relationships heatmap (Figure 3.11), it is evident that both the pink and dark grey gene modules are the modules most significantly associated with the external OS trait. Furthermore, with the pink module being the most significantly associated with the trait, further analysis was conducted with the genes found within the module. Results showed that 154 out of the 1072 genes in the module were found to be differentially expressed in OS. Out of the 154 dysregulated genes, 140 of the genes were found to be upregulated and 14 were found to be downregulated when the gene cut-off values were defined as $|\log_2FC| > 1$ and an adjusted $P < 0.01$. The top 30 genes from the pink module, that were sorted based on the significance of gene association to OS, from most significant to least, were isolated and their protein-protein interactions were visualised using STRING analysis (Figure 3.12). As shown in the interaction network, the genes C1QA, TYROBP, APOE and CSF1R were found to be among the top 10 genes that were previously identified to be significantly upregulated in OS. This result indicated that this set of genes may

potentially have important roles to play in OS. Likewise, the list of top 30 genes classified under the pink module, was then compared to the set of genes that were previously identified to be significantly upregulated in OS and classified under the GO term of interest “immune receptor activity”. The results from the comparison showed that four out of the top five most significantly upregulated immune receptors in OS, was also found within the top 30 genes of the pink module. These genes included CD74, HLA-DRA, FCER1G and HLA-DPA1. Henceforth, this result indicated that these specific immune receptors and thus, the immune system, may play important roles in OS due to the classification of the immune receptors within the gene module highly associated with the trait.

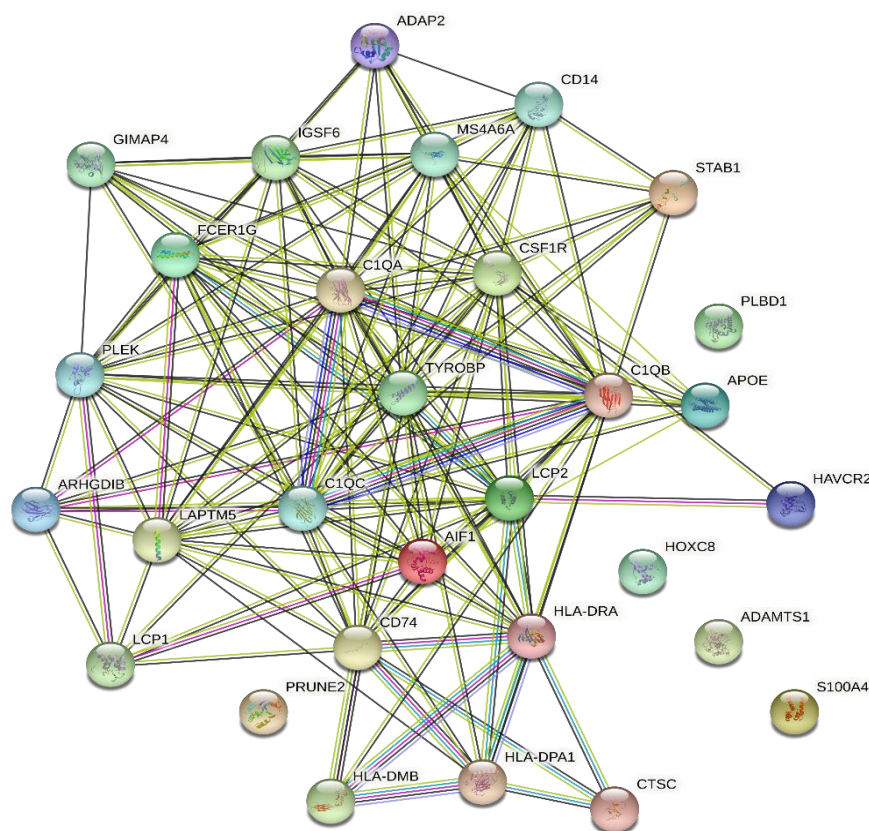


Figure 3.12: STRING analysis of top 30 genes in the pink module, highly associated to OS. Figure representing the protein-protein interaction network generated for the top 30 genes of the pink module, through the conduction of STRING analysis. The figure portrays the various known and predicted interactions between the genes in the module.

Functional enrichment of genes closely associated to OS

In addition to the intra-modular and STRING analyses conducted on the pink module, we functionally annotated several gene modules that were identified to be closely associated to OS. Thereby, determining the biological significance of specific genes/gene clusters that were calculated to have close genetic associations to the OS diseased trait. To conduct the functional annotations, we carried out both GO and KEGG pathways gene overrepresentation analyses on the lists of genes grouped under each respective module. Subsequently, we highlight the topmost overrepresented GO terms and KEGG pathways.

With regards to the pink gene module, which was identified to be the gene module with the highest level of module association to OS trait, results showed that the genes were significantly enriched in GO cellular component terms such as external side of plasma membrane, lytic vacuole, lysosome, cell surface and vacuole. Furthermore, the gene list was enriched in biological processes including myeloid leukocyte activation, cell activation involved in immune response, myeloid cell activation involved in immune response, immune effector process and cell activation. Lastly, the genes were enriched in molecular functions that included signalling receptor activity, cytokine receptor binding, molecular transducer activity, carbohydrate binding and antigen binding.

Moving onto the dark grey module, results showed that the genes were enriched in GO cellular component terms such as intrinsic component of plasma membrane, cell surface, integral component of plasma membrane, extracellular matrix and collagen-containing extracellular matrix. In addition, the genes participated in biological processes such as endothelium development, tube development, anatomical structure

formation involved in morphogenesis, circulatory system development and tube morphogenesis. Lastly, the genes portrayed molecular functions that included ion channel activity, substrate-specific channel activity, cation channel activity, channel activity and passive transmembrane transporter activity.

Next, with regards to the dark green module, results showed that the genes in the module were enriched in GO cellular component terms such as extracellular matrix, collagen-containing extracellular matrix, collagen trimer, endoplasmic reticulum lumen and endoplasmic reticulum part. Furthermore, the genes participated in biological processes such as ossification, animal organ morphogenesis, endochondral bone morphogenesis, skeletal system development and bone morphogenesis. Lastly, the genes portrayed molecular functions that included extracellular matrix structural constituent, extracellular matrix structural constituent conferring tensile strength, structural molecule activity, phosphatase activity and glycosaminoglycan binding.

Lastly, with regards to the royal blue module, results portrayed that the genes in the module were enriched in GO cellular component terms such as vacuole, vacuolar part, proton-transporting V-type ATPase complex, proton-transporting two-sector ATPase complex and lysosome. Moreover, the genes participated in biological processes such as ATP hydrolysis coupled proton transport, energy coupled proton transmembrane transport, against electrochemical gradient, ATP hydrolysis coupled ion transmembrane transport, ATP hydrolysis coupled transmembrane transport and transferrin transport. Finally, the genes portrayed molecular functions that included proton-transporting ATPase activity, rotational mechanism, proton-exporting ATPase activity, ATPase activity, coupled to transmembrane movement of ions, rotational mechanism, active transmembrane transporter activity and proton transmembrane transporter activity.

Once we conducted GO based overrepresentation analysis on the gene modules closely associated to OS, we further functionally annotated the gene modules by carrying out KEGG pathways gene overrepresentation analysis. Henceforth, with regards to the pink module, the results showed that the genes in the module were enriched in KEGG pathway terms including Intestinal immune network for IgA production, Inflammatory bowel disease (IBD), Autoimmune thyroid disease, Type I diabetes mellitus and Leishmaniasis. Similarly, with the dark grey module, results of the analysis showed that the genes in the module were enriched in KEGG pathway terms including Protein digestion and absorption, cGMP-PKG signalling pathway, PI3K-Akt signalling pathway, ECM-receptor interaction and Fluid shear stress and atherosclerosis. Likewise, with the dark green gene module, the results showed that the genes were enriched in terms including ECM-receptor interaction, Protein digestion and absorption, PI3K-Akt signalling pathway, Human papillomavirus infection and Focal adhesion. Lastly, with the royal blue module, the results showed that the genes were enriched in terms including Rheumatoid arthritis, Lysosome, Epithelial cell signalling in Helicobacter pylori infection, Vibrio cholerae infection and Collecting duct acid secretion.

In addition to identifying gene modules closely associated to OS and intra-modular analysis conducted to identify genes significantly associated with the disease, relationships between modules and the OS trait were also determined. Henceforth, we generated a summary plot of the eigengene network with the addition of the OS trait. This allowed the visualisation of inter-modular relationships and gene module relationships, with the diseased trait (Appendix A, figure A6). (A) portrays a clustering dendrogram of the identified eigengenes, that represents inter-modular relationships and gene module relationship with OS trait. In addition, the dendrogram allows for the

identification of groups of correlating eigengenes, that are thus, termed meta-modules. The generated dendrogram indicates that the pink, violet, brown, yellow green and royal blue modules are highly related, thus, generating a meta-module due to their localisation as a tight cluster of modules. The mutual correlations between the modules in the meta-module are stronger than their correlations with the OS trait. Similarly, (B) portrays a heatmap that represents the scores for eigengene adjacency, thus, the plot can also be used to identify meta-modules and visualise the relationships between the modules and OS trait. The heatmap indicates that the dark grey, green, pink and brown modules have the greatest number of significant adjacencies with other identified gene modules.

Disease ontology and semantic similarity analysis

Despite biological significances of DEGs in OS being determined through GO and KEGG pathways-based overrepresentation and gene enrichment analyses, significance of gene dysregulation from a disease specific perspective was required. Thus, in addition to the genes found closely associated to OS through WGCNA, gene list enrichment from a human disease perspective consolidated gene dysregulation and close association to the diseased trait in some cases. Furthermore, gene enrichment aided in identifying further DEGs closely associated to the OS diseased trait.

The complete list of DEGs in OS (up and downregulated), in addition to specific genes of interest CXCR4, CD74 and FPRL2 (FPR3), were functionally enriched based on DO and thus, the human disease perspective. Through the conduction of semantic similarity analysis between the DO terms acquired through DO enrichment analysis, results showed that the DO terms of OS and bone OS portray high levels semantic

similarity, when semantic similarity between the terms was quantified. However, when semantic similarity was calculated between OS and a broad group of bone and soft tissue related malignancies, being Sarcoma, a low level of semantic similarity was quantified. A similar result was observed when semantic similarity was calculated between bone OS and sarcoma. Like with semantic similarity calculated between the terms OS and Sarcoma, results of further analysis showed a low level of semantic similarity between OS and the bone marrow related malignancies being bone marrow cancer.

When the full list of DEGs in OS was functionally enriched based on DO, a total of 17 DEGs in OS were annotated under the DO term of interest OS. This list of DEGs in OS that are thus, inferred to be closely associated with OS trait can be further separated into 6 genes upregulated in OS and 11 genes downregulated in OS (Table 3.5). Likewise, DO based functional enrichment, resulted in a total of 6 DEGs in OS that were functionally annotated under the DO term bone OS. All 6 of the annotated DEGs were also found within the list of genes annotated under the DO term OS. The 6 genes can be separated into 1 upregulated in OS and 5 downregulated (Table 3.5). Like with OS and bone OS terms, when the DEGs in OS were enriched, a total of 17 DEGs were found to be annotated under the DO term bone marrow cancer. This list of DEGs in OS that is thus, inferred to also be closely associated with the various bone marrow associated malignancies, can be further separated into 8 genes that are upregulated in OS and 9 genes downregulated in OS (Table 3.5). Amongst the list of DEGs annotated under bone marrow cancer, are 7 genes that were also annotated under OS DO term (SPP1, MMP13, CXCR4, CXCL12, FN1, TNFRSF11B, ITGB1). Lastly, out of the functionally annotated DEGs in OS, a total of 15 DEGs were annotated under the DO term Sarcoma. This list of DEGs that are thus, inferred to be

associated with the broad group of bone and soft tissue related malignancies, can be further separated into 4 genes that are upregulated in OS and 11 genes downregulated in OS (Table 3.5).

Similar to the bone marrow cancer DO term, amongst the list of gene annotated under the DO term sarcoma, are 5 genes that were also annotated under OS DO term (MMP9, SPP1, CXCR4, IGFBP3, CAV1). Furthermore, results showed that specific upregulated genes in OS (SPP1 and CXCR4), were annotated under both the DO terms of bone marrow cancer and Sarcoma. Similarly, downregulated genes in OS (THBS1 and IL6) were also annotated under both the non-OS related DO terms. Overall, from the results gathered based on DO functional enrichment analysis and semantic similarity calculations conducted on the list of DEGs in OS, the upregulated genes in OS (S100A4 and EFNA1) are shown to be the most closely associated with OS trait, but not portraying specificity to primary OS malignancies in particular. Similarly, the results show that the downregulated genes in OS (ACTA2, ANXA2, FBN1 and DUSP1) are closely associated with OS trait, with the specific genes (CXCL12, ITGB1 and ACTA2), portraying increased specificity towards primary bone OS malignancies.

Table 3.5: DOSE analysis: enrichment of DEGs in OS based on disease ontology. Table showing the top significantly DEGs in OS, identified in this study at cutoff values of $|\log_2FC| > 1$ (adjusted $P < 0.01$), that are enriched by the bone cancer related DO terms of interest. DO, Disease Ontology.

OS DO term	Bone OS DO term	Bone marrow cancer DO term	Sarcoma DO term
MMP9	MMP9	SPP1	MMP9
SPP1	CXCL12	CD74	SPP1
MMP13	ITGB1	ACP5	CXCR4
CXCR4	CDKN1A	MMP13	EDNRA
S100A4	ACTA2	CXCR4	THBS1
EFNA1	CAV1	FGFR3	PTX3
CXCL12		MAFB	SERPINE1
FN1		APOC1	IL6
TNFRSF11B		THBS1	IGFBP3
IGFBP3		CXCL12	AXL
ITGB1		IL6	ADAMTS1
CDKN1A		FN1	VEGFC
ACTA2		TNFRSF11B	CDKN1A
ANXA2		NQO1	THBS2
FBN1		IER3	CAV1
DUSP1		ITGB1	
CAV1		CYP1B1	

Like with the calculation of semantic similarity between the functionally enriched DO terms, further semantic similarity analysis was conducted to calculate the semantic similarity levels between clusters of genes annotated by the respective DO terms of

interest. Results of the semantic similarity analysis showed that there is a high level of semantic similarity between the clusters of genes annotated under OS and bone OS DO terms, respectively. Similarly, semantic similarity was calculated between the cluster of genes annotated under the OS DO term and the gene clusters annotated under the DO terms bone marrow cancer and Sarcoma, respectively. The results showed, the gene clusters annotated by the terms bone marrow cancer and sarcoma, respectively, had high level of semantic similarity to the gene cluster annotated by the OS term. The calculated semantic similarity scores were similar to that of the score acquired when the analysis was conducted between the gene clusters of OS and bone OS.

Lastly, semantic similarity analysis was conducted to calculate the similarity levels between individual gene products annotated under the DO term of interest OS. Results from DOSE analysis showed that the upregulated genes in OS (S100A4 and EFNA1) are the most closely associated with the OS trait. Therefore, the CD74 gene, which has shown promise to be a therapeutic target for the treatment of OS, was compared to the closely associated upregulated genes through semantic similarity analysis and the level of similarity was calculated. Results from the analysis showed that the CD74 gene portrays a high level of semantic similarity to the genes closely associated to OS. Semantic similarity scores of 0.62 was calculated between CD74 and EFNA1 and 0.57 between CD74 and S100A4.

When candidate DEGs in OS were functionally enriched based on DO, the CXCR4 was identified to be functionally enriched by 30 different DO terms. These DO terms included the terms of interest, OS, bone marrow cancer and Sarcoma, along with additional DO terms including myeloma. On the other hand, the CD74 gene was identified to be enriched by 6 differing DO terms, including bone marrow cancer,

myeloma, carotid stenosis, carotid artery disease, cerebrovascular disease and pre-eclampsia. Lastly, the FPRL2 gene (FPR3) was not enriched by any of the DO terms in the DO database.

Further analysis of identified immune-receptor genes of interest

There are known significant involvements of the host immune system and the tumour immune niche in OS tumour development and progression (discussed in chapter 1.1.7). This was further emphasised by the enriched biological process GO terms, obtained through gene enrichment analysis of the total and upregulated only DEGs in OS. Through WGCNA and DOSE analysis, significantly upregulated immune receptors that are also closely associated to the OS diseased trait were identified, with some being further investigated as immune-related therapeutic targets of interest.

Of interest are the immune receptors CXCR4, CD74 and FPRL2 (FPR3). The receptors CXCR4 and CD74 were identified as the most upregulated immune receptors in OS, while FPR3 is the novel upregulated immune receptor. CXCR4 was identified to be negatively associated with the OS diseased trait and through DOSE analysis, the receptor expression was shown to be associated with a wide range of diseases. On the other hand, CD74 was found to have a close genetic association to OS through WGCNA and through DOSE analysis, the receptor showed greater specificity to bone malignancies than CXCR4. However, both immune receptors have been previously investigated and well annotated with respect to their roles in OS targeted therapy. Therefore, further investigations were carried out with both significantly upregulated receptors in OS, with one showing close disease association and one that is not. Further investigations were carried out to determine receptor therapeutic targeting potential, through the use of bioinformatical analyses.

Importantly, the novel immune receptor of interest (FPR3), like CD74, was found to have a close genetic association to OS through WGCNA, however, presented a lack of disease annotations. FPR3 was further investigated in conjunction, to compare receptor therapeutic targeting potential to that of well annotated receptors such as CXCR4 and CD74.

CXCR4

Summarised results acquired from the human protein atlas for CXCR4, showed that the gene displays tissue specificity towards bone marrow and lymphoid tissue. Furthermore, when assessing single cell type specificity, the gene was found to be expressed in various immune cells, both innate and adaptive, such as B-cells, T-cells, dendritic cells, macrophages, and monocytes. Henceforth, CXCR4 does not display immune cell specificity, due to detectable significant expression in other cell types. In relation to patient prognosis, CXCR4 is an unfavourable prognostic marker in renal (G. Li et al., 2013) and stomach cancer (Gu et al., 2021), however, it is identified to be a favourable marker in ovarian cancer (Liu et al., 2014). However, with regard to cancer specificity, the protein has low cancer specificity as it is expressed in all cancers. This excludes CXCR4 as a prognostic marker. CXCR4 is localised to the plasma membrane and the Uniprot database shows various functions such as C-X-C chemokine receptor, involvement in the AKT signalling cascade and a functional role in the regulation of cell migration.

CD74

Similarly, CD74 is expressed in human blood and lymphoid tissue. Furthermore, when single cell type specificity was investigated, the gene is specifically detectable in innate immune cells, such as Langerhans cells, monocytes, B-cells, including naïve B-cells,

memory B-cells; myeloid DCs, macrophages and Kupffer cells. Furthermore, the protein is a favourable prognostic marker for endometrial (Ma et al., 2020) and breast cancer (Z. Q. Wang et al., 2017). Like CXCR4, CD74 is localised to the cell membrane, however, unlike CXCR4, the subcellular localisation has been identified to be within the Golgi apparatus.

FPR3

For the immune receptor Formyl peptide receptor 3 (FPR3), the gene has been detected to be ubiquitous in various normal tissues, with high levels of gene expression seen in the respiratory system, bone marrow and lymphoid, kidney and urinary bladder normal tissues. Expression in the brain has low regional specificity. The results of expression clustering showed that FPR3 was clustered with genes significantly expressed in macrophages and with genes mainly linked to immune response.

The results of immune cell specificity analysis showed that the FPR3 gene is found to be expressed in a group of immune cells, including intermediate monocytes, myeloid dendritic cells and classical monocyte. At the cellular level, it is predicted to be localised at the cell membrane. Since the FPR3 gene functions as a low affinity G-protein coupled receptor for N-formyl-methionyl peptides, it can be inferred to be localised on the plasma membrane of cells.

Immune receptor gene expression profiles across cancer types

Further analysis for the determination of immune receptor therapeutic targeting potential in OS, also involved the use of a gene expression profiling interactive analysis web tool (GEPIA). The tool provides visual data on the gene expression profiles of queried genes, which was used to validate gene expression of candidate

immune receptor genes across various cancers. However, of interest was the screening of candidate immune receptor expression levels in Sarcoma malignancies, which may be of translatable relevance to OS.

CXCR4

When CXCR4 was queried within the search tool, the figure showed that CXCR4 is found to be upregulated in numerous cancers (represented by “T”), when compared to the normal tissue (represented by “N”). This includes Breast invasive carcinoma (BRCA), Glioblastoma multiforme (GBM), Kidney renal clear cell carcinoma (KIRC), Kidney renal papillary cell carcinoma (KIRP), Acute Myeloid Leukemia (LAML), Brain Lower Grade Glioma (LGG), Ovarian serous cystadenocarcinoma (OV), Pancreatic adenocarcinoma (PAAD), Skin Cutaneous Melanoma (SKCM), Sarcoma (Sarcoma), Stomach adenocarcinoma (STAD), Testicular Germ Cell Tumours (TGCT), Uterine Corpus Endometrial Carcinoma (UCEC) and Uterine Carcinosarcoma (USC) (Figure 3.13). However, the figure does not present CXCR4 expression levels for OS or its normal tissue, with the closest cancer subtype to OS where CXCR4 is found to be upregulated, being Sarcoma.

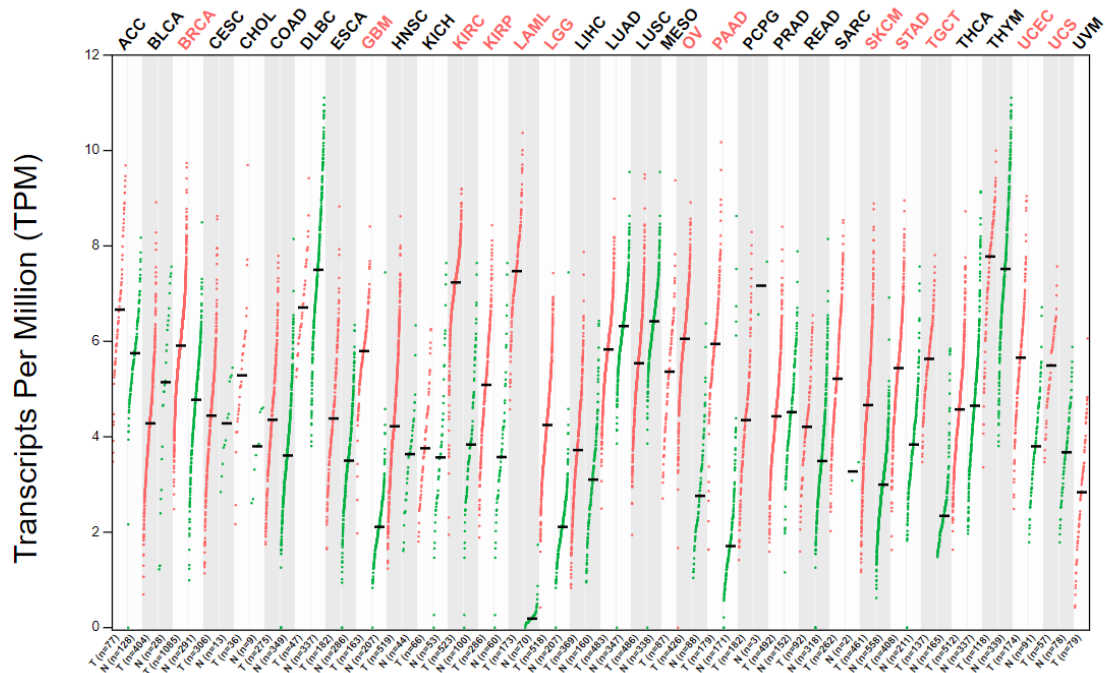


Figure 3.13: Candidate immune receptor expression profile across cancer types. A figure representing a dot plot generated by the gene expression functionality of the cancer and normal gene expression profiling web server (GEPIA). The figure portrays the gene expression patterns for the CXCR4 immune-receptor related gene, across various cancer types and their respective normal tissues. The cancer types in which gene expression has been identified to be significantly upregulated, when compared to respective normal tissues, are highlighted in red.

CD74

As can be seen in figure 3.14, CD74 is found to be upregulated in numerous cancer variants (represented by “T”), when compared to the normal tissue (represented by “N”). The cancer types where CD74 is upregulated include Lymphoid Neoplasm Diffuse Large B-cell Lymphoma (DLBC), Oesophageal carcinoma (OSCA), Glioblastoma multiforme (GBM), Kidney renal clear cell carcinoma (KIRC), Acute Myeloid Leukaemia (LAML), Brain Lower Grade Glioma (LGG), Liver hepatocellular carcinoma (LIHC), Ovarian serous cystadenocarcinoma (OV), Pancreatic adenocarcinoma (PAAD), Skin Cutaneous Melanoma (SKCM), Stomach adenocarcinoma (STAD), Testicular Germ Cell Tumours (TGCT), Thyroid carcinoma (THCA), Thymoma (THYM) and Uterine Corpus Endometrial Carcinoma (UCEC).

However, the figure does not present CD74 expression levels for OS or its normal tissue. The closest cancer subtype to OS is thus Sarcoma. Here, however, CD74 gene expression profiling in shows no significant changes in expression when compared to normal tissue.

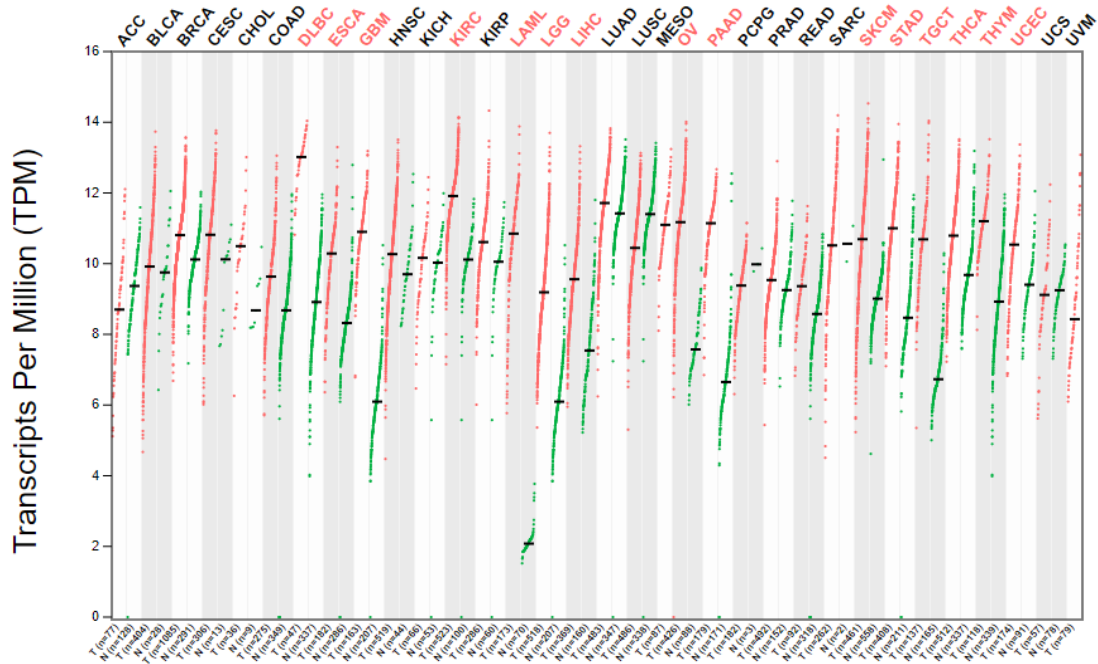


Figure 3.14: **Candidate immune receptor expression profile across cancer types.** A figure representing a dot plot generated by the gene expression functionality of the cancer and normal gene expression profiling web server (GEPIA). The figure portrays the gene expression patterns for the CD74 immune-receptor related gene, across various cancer types and their respective normal tissues. The cancer types in which gene expression has been identified to be significantly upregulated, when compared to respective normal tissues, are highlighted in red.

FPR3

As can be seen in figure 3.15, levels of FPR3 gene expression, are also found to be upregulated and in some cases downregulated in numerous malignant tumours (represented by “T”), when compared to the normal tissue (represented by “N”). The cancers where FPR3 is upregulated include Breast invasive carcinoma (BRCA), Cervical squamous cell carcinoma and endocervical adenocarcinoma (CESC), Lymphoid Neoplasm Diffuse Large B-cell Lymphoma (DLBC), Oesophageal carcinoma (OSCA), Glioblastoma multiforme (GBM), Kidney renal clear cell carcinoma

(KIRC), Brain Lower Grade Glioma (LGG), Ovarian serous cystadenocarcinoma (OV), Pancreatic adenocarcinoma (PAAD), Skin Cutaneous Melanoma (SKCM), Stomach adenocarcinoma (STAD), Testicular Germ Cell Tumours (TGCT), Thymoma (THYM) and Uterine Carcinosarcoma (UCS). Similarly, the cancer variants where FPR3 is downregulated include Adrenocortical carcinoma (ACC) and Acute Myeloid Leukaemia (LAML). However, the figure generated via GEPIA does not represent FPR3 expression levels in OS tumour tissue or in its respective normal tissue.

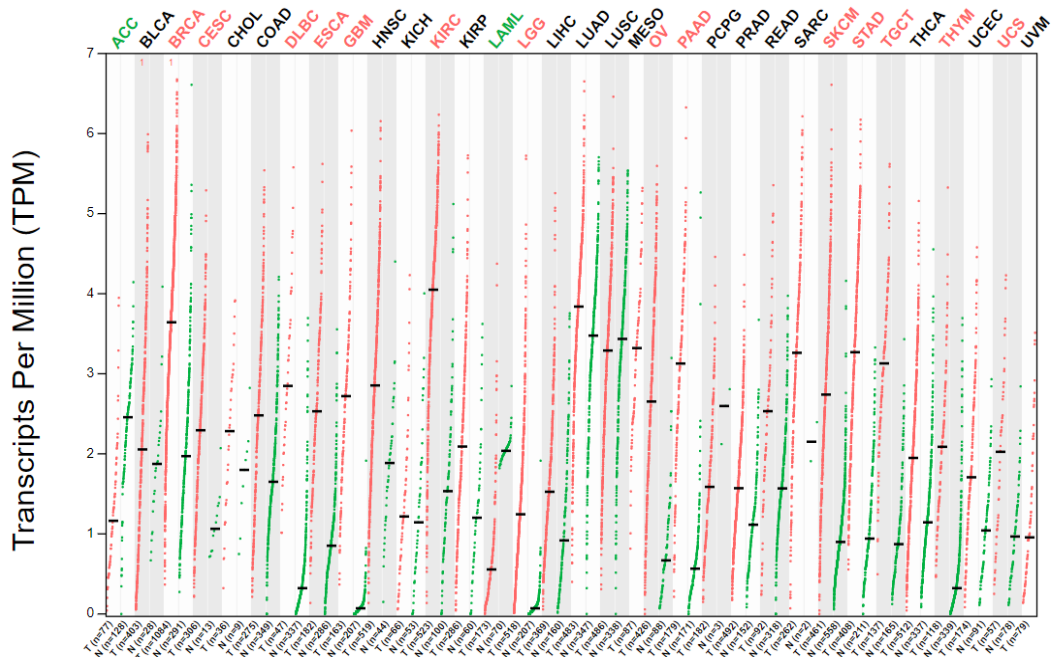


Figure 3.15: Candidate immune receptor expression profile across cancer types. A figure representing a dot plot generated by the gene expression functionality of the cancer and normal gene expression profiling web server (GEPIA). The figure portrays the gene expression patterns for the FPR3 immune-receptor related gene, across various cancer types and their respective normal tissues. The cancer types in which gene expression has been identified to be significantly upregulated, when compared to respective normal tissues, are highlighted in red. The cancer types in which gene expression is significantly downregulated, when compared to respective normal tissues, are highlighted in green.

STRING analysis

For further investigations into immune receptor therapeutic targeting potentials, the candidate receptor genes were entered into STRING analysis to determine their protein-protein interaction networks and thus, determine genes that are closely related to the receptor of interest. Closely related genes may provide alternate downstream/upstream therapeutically targetable proteins for the treatment of OS or provide an indication towards the signalling pathway impacted when the candidate receptor is targeted with therapeutic agents.

CXCR4

The webtool STRING was used to generate and visualise functional protein association networks for the candidate genes. Figure 3.16 displays the gene-gene interaction network generated by STRING for the gene of interest CXCR4. The figure shows CXCR4 at the epicentre of the interaction network, with genes that are either predicted or known to interact with CXCR4, surrounding the gene of interest and forming an interaction network. Amongst the various genes, CD74 (circled red) was identified. The network was shown to have proteins involved in biological processes such as cytokine-mediated signalling pathway, cell surface receptor signalling pathway, response to cytokine, regulation of response to stimulus and cellular response to chemical stimulus. In addition, the proteins in the network have molecular functions such as signalling receptor binding, G protein-coupled receptor binding, protein binding, enzyme binding and cytokine receptor activity.

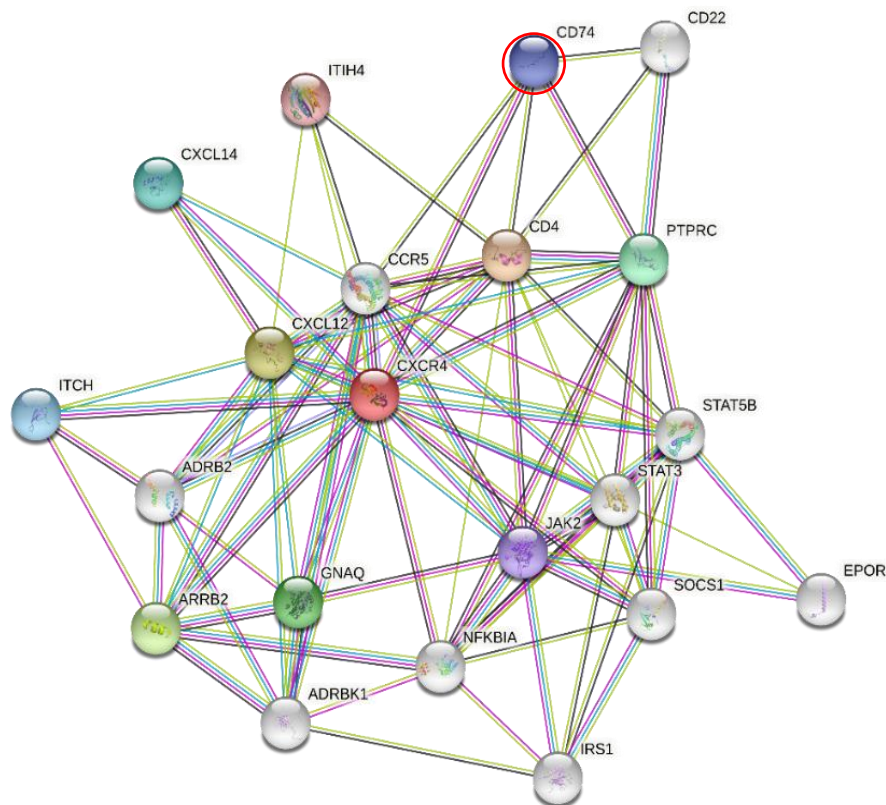


Figure 3.16: STRING analysis of CXCR4 and respective protein-protein interaction network. Figure representing the protein-protein interaction network generated for the gene of interest CXCR4, through the conduction of STRING analysis. The figure portrays the various other annotated genes that the gene of interest is known or predicted to interact with. The figure also shows the protein-protein interactions between both immune receptor genes of interest (CXCR4 and CD74).

CD74

Similarly, figure 3.17 displays the gene-gene interaction network generated by STRING for CD74. The figure shows CD74 at the epicentre of the interaction network. Amongst the various genes known or predicted to interact with CD74, are SPP1, CXCR4, HLA-DMB, HLA-DRA and HLA-DQA1 (circled red). Interestingly, HLA-DRA and HLA-DQA1 are also categorised under the GO term of interest and significantly upregulated in the OS. Lastly, regarding the genes SPP1 and HLA-DMB, the genes are also shown to be significantly upregulated in the OS, however, they are not

categorised under the GO term of interest. Thus, when comparing the two genes of interest (CXCR4 and CD74), CD74 interacts with more genes categorised under the GO term of interest that are upregulated in OS. Lastly, with regards to the GO-based functional annotations for the gene-gene interaction network, the network was shown to have proteins involved in biological processes such as cytokine-mediated signalling pathway, immune response, defence response, cellular response to organic substance, and antigen processing and presentation of exogenous peptide antigen through MHC class II. In addition, the proteins in the network have molecular functions such as immune receptor activity, MHC class II protein complex binding, CXCR chemokine receptor binding, MHC class II receptor activity and chemokine activity.

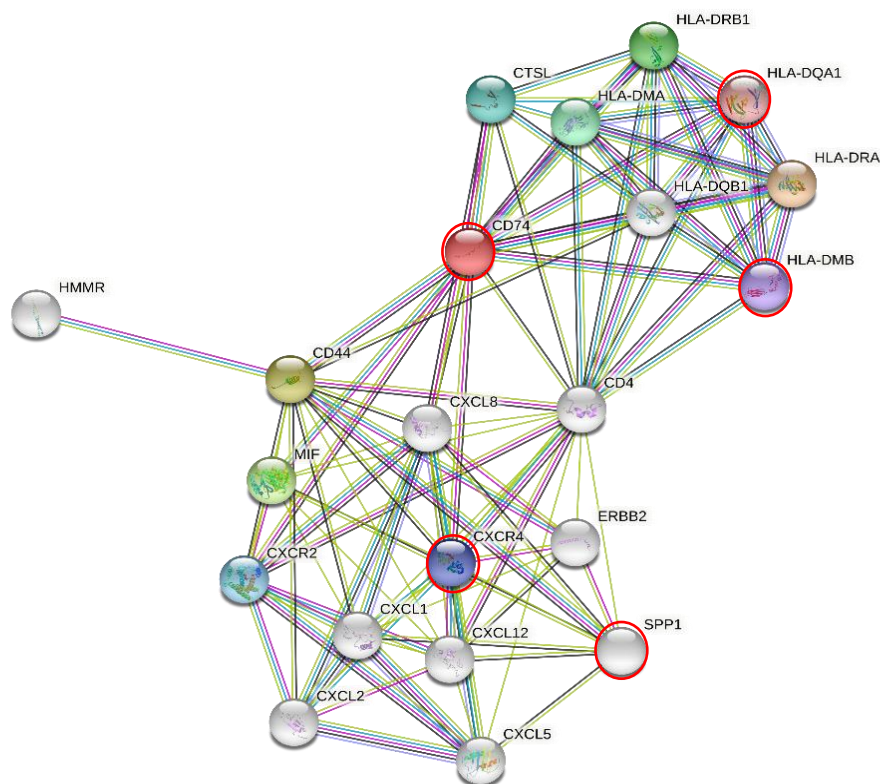


Figure 3.17: STRING analysis of CD74 and respective protein-protein interaction network. Figure representing the protein-protein interaction network generated for the gene of interest CD74, through the conduction of STRING analysis. The figure portrays the various other annotated genes that the gene of interest is known or predicted to interact with. The figure also shows the protein-protein interactions between both immune receptor genes of interest (CXCR4 and CD74).

FPR3

Figure 3.18 displays the protein interaction network generated by STRING for FPR3. Amongst the various genes said to be interacting with FPR3, is the gene VSIG4 (circled red). The gene VSIG4 is of relevance, as it is also a gene that is found to be significantly upregulated in OS ($P\text{-value} < 0.01$, $\text{Log}_2\text{FC} > 1$). Lastly, with regards to the GO-based functional annotations for the PPI network, the network was shown to have proteins involved in biological processes such as SRP-dependent co-translational protein targeting to membrane, Viral transcription, Nuclear-transcribed mRNA catabolic process, nonsense-mediated decay, Interspecies interaction between organisms and Translational initiation. In addition, the proteins in the network portray molecular functions such as structural constituent of ribosome, N-formyl peptide receptor activity, structural molecule activity, complement receptor activity and signalling receptor binding.

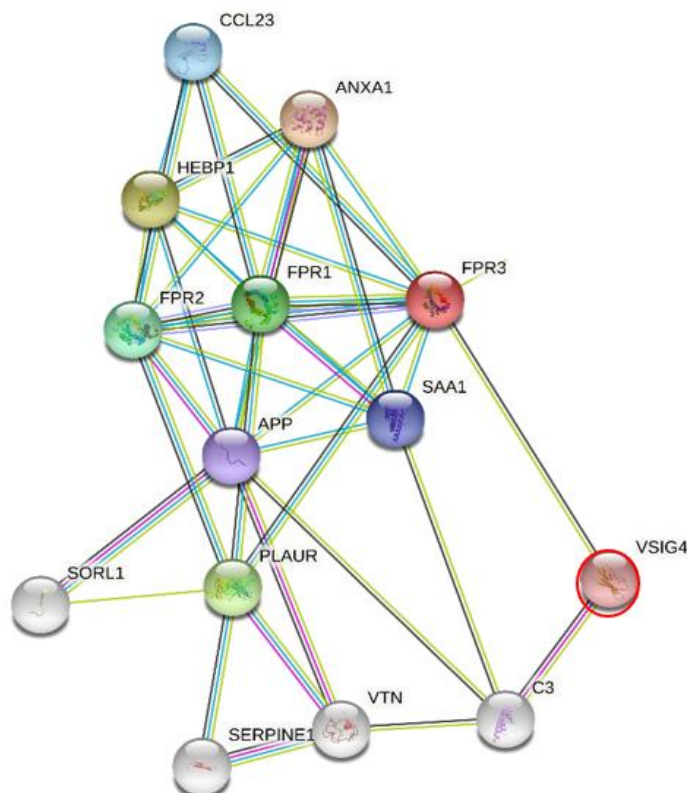


Figure 3.18: STRING analysis of FPR3 and respective protein-protein interaction network. Figure representing the protein-protein interaction network generated for the gene of interest FPR3, through the conduction of STRING analysis. The figure portrays the various other annotated genes that the gene of interest is known or predicted to interact with.

Tumour immune estimation resource (TIMER) analysis

In order to put forward the candidate receptors as immune-based therapeutic targets in OS, the receptors were investigated for their prognostic effects in cancer. As described in chapter 1.1.7, the host immune system and changes within the tumour immune niche have been reported to impact patient prognosis (Qi et al., 2021; B. Li et al., 2016). Furthermore, previous studies have reported high immune cell tumour infiltration being associated with favourable patient prognosis (Tas and Erturk, 2017). Therefore, in line with investigations of receptor therapeutic targeting potential, candidate immune receptors in OS were analysed using TIMER to determine their prognostic effects from a tumour immune infiltration perspective. The tool was used to investigate associations between tumour immune cell infiltrate abundance and candidate immune receptor gene expression. Furthermore, the analytical tool was used to assess the impact of tumour immune cell infiltrate abundance on cancer patient overall survival. The immune receptor CXCR4 was omitted from analysis due to a lack of close association to the OS clinical trait, unlike what was observed with CD74 and FPR3. Furthermore, since CXCR4 is dysregulated in a wide range of cancer types, inclusive of cold tumour portraying low immune infiltration, its significance in tumour immune infiltration was deemed inadequate.

TIMER analysis was first utilised, to investigate the level of association between CD74 receptor expression in specified tumour types and the abundance of a diverse set of tumour infiltrating immune cells. Unfortunately, gene expression and immune infiltrate data for OS was unavailable, hence, we chose Sarcoma (sarcoma), OV (ovarian serous cystadenocarcinoma), LUSC (lung squamous cell carcinoma), LIHC (liver hepatocellular carcinoma), and BRCA (breast invasive carcinoma) as the clinically similar multi-tumour types, based on Li et al (M. Li et al., 2020). As seen in figure 3.19,

expression level of the CD74 candidate gene was shown to be negatively associated with tumour purity, especially in Sarcoma. Therefore, it can be inferred from this result that CD74 is likely expressed in the TME and not on the surface of the tumour cells themselves. Similarly, as seen in figure 3.20, expression level of the FPR3 candidate gene was shown to be negatively associated with tumour purity, especially in Sarcoma. Therefore, like CD74, FPR3 is likely expressed in the TME and not on the surface of the tumour cells themselves. The additional scatterplots generated in the pallet, portrayed the level of immune infiltration for each immune cell infiltrate, against the level of candidate gene expression in the investigated cancer types. Henceforth, with particularity going towards Sarcoma, due to it being the most clinically relevant cancer type to OS, the results showed that CD74 expression is most significantly correlated with dendritic cell, B-cell and macrophage immune infiltration into the tumour. Furthermore, with particularity going towards Sarcoma, the results showed that FPR3 expression is most significantly correlated with dendritic cell, macrophage, and neutrophil immune infiltration into the tumour.

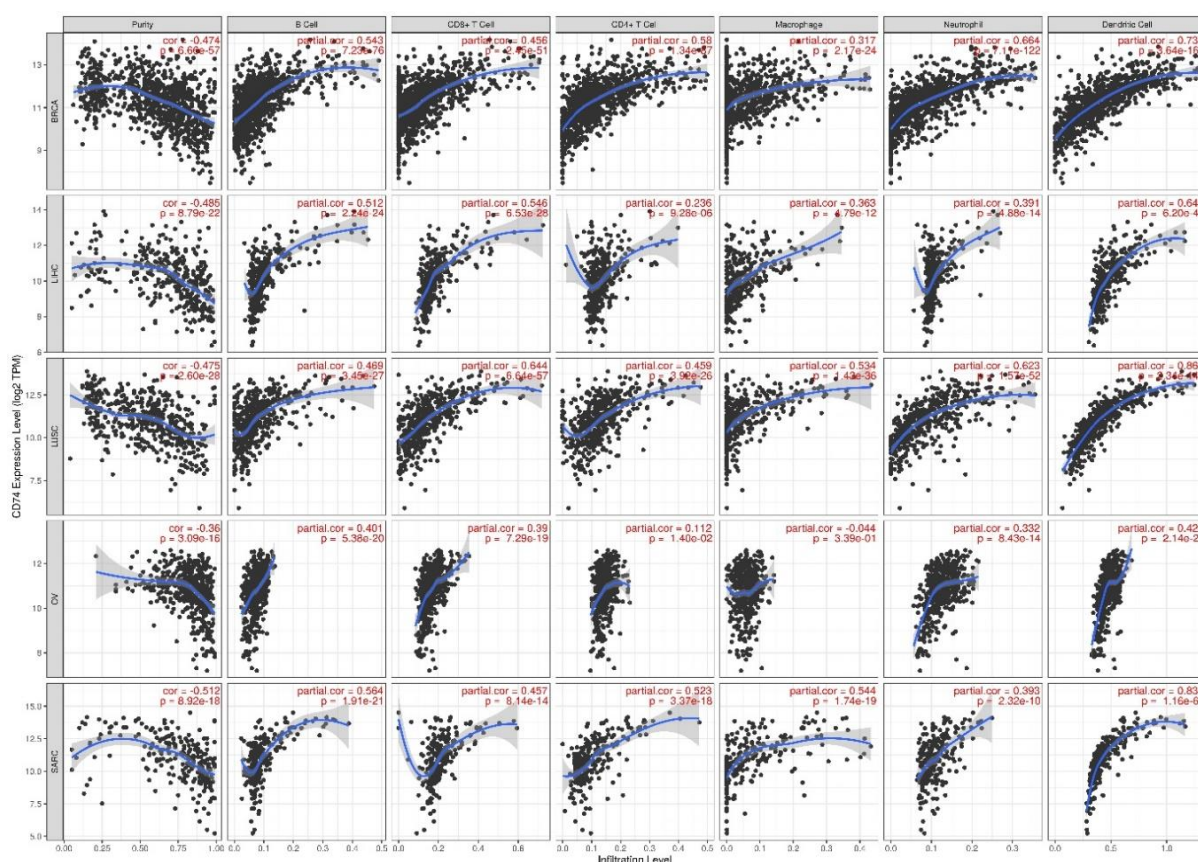


Figure 3.19: **TIMER analysis: tumour purity in relation to CD74 expression.** Figure displaying the pallet of scatterplots generated by the gene analytical TIMER module, with the inputted candidate gene of interest being CD74. The scatterplots first display tumour purity against CD74 gene expression. Furthermore, the remaining scatterplots depict the level of immune infiltration, for each immune cell infiltrate, against the level of CD74 gene expression within the investigated cancer types. (n=245 for Sarcoma, n=558 for OV, n= 482 for LUSC, n= 362 for LHC and n= 1017 for BRCA).

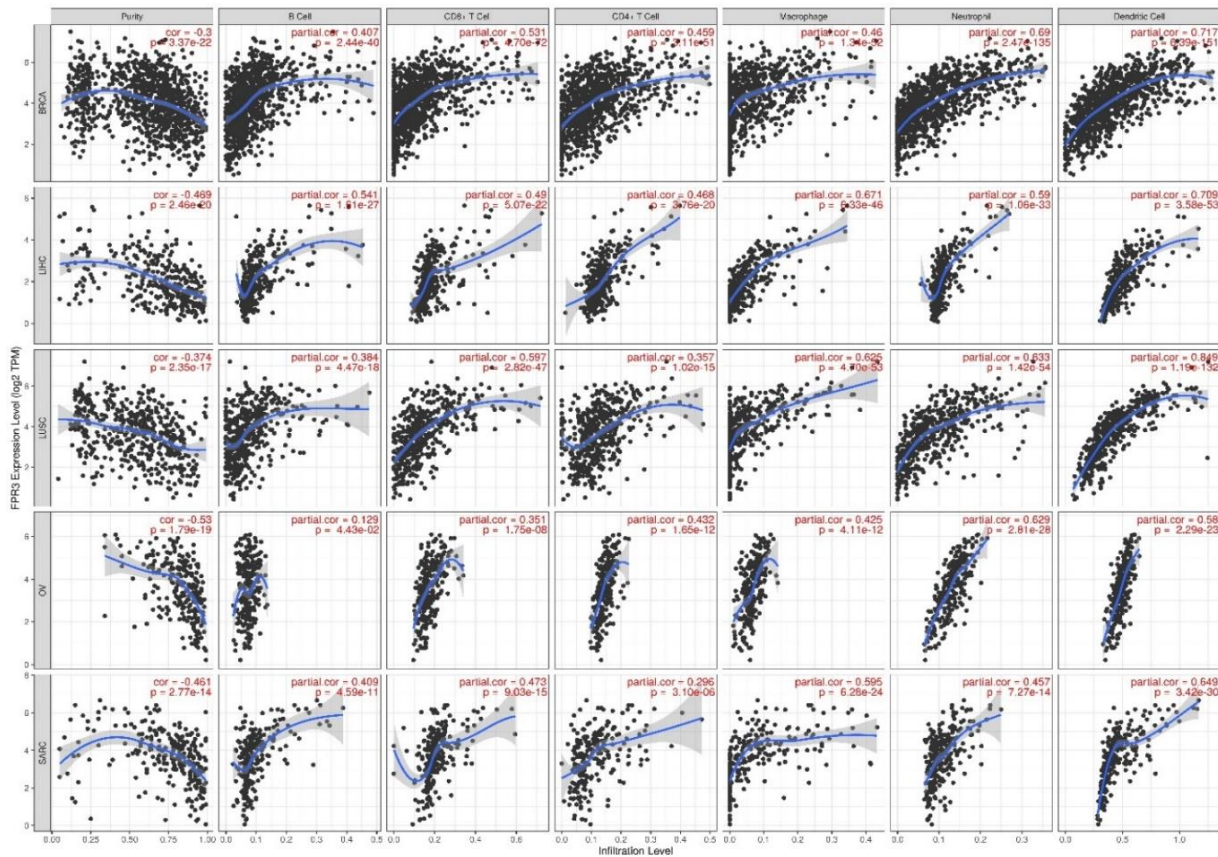


Figure 3.20: **TIMER analysis: tumour purity in relation to FPR3 expression.** Figure displaying the pallet of scatterplots generated by the gene analytical TIMER module, with the inputted candidate gene of interest being FPR3. The scatterplots display tumour purity against FPR3 gene expression, in addition to the level of immune infiltration for each immune cell infiltrate, against the level of FPR3 gene expression within the investigated cancer types. (n=245 for Sarcoma, n=558 for OV, n= 482 for LUSC, n= 362 for LIHC and n= 1017 for BRCA).

After investigating associations between candidate gene expression and tumour infiltrating immune cell abundance, we further investigated the association between tumour immune infiltrating cell abundance and patient overall survival. With interest going towards Sarcoma patients, the results of survival analysis show that high levels of neutrophil and CD4+ T-cell immune subset infiltrations are significantly associated with higher patient overall survival (Figure 3.21).

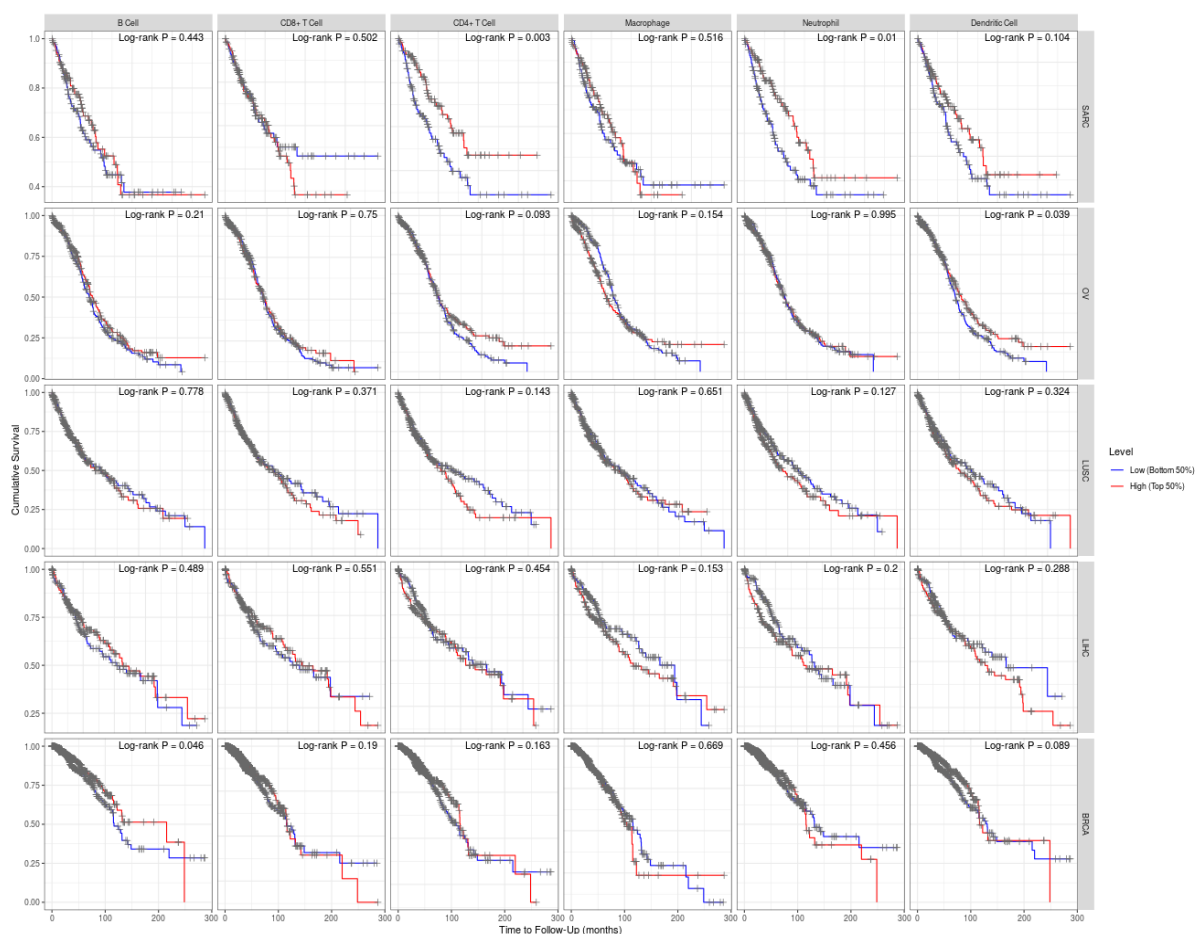


Figure 3.21: TIMER: Tumour immune infiltration and Sarcoma patient overall survival. Kaplan-Meier plots presented in a pallet, which was generated by the survival analytical TIMER module. The differing Kaplan-Meier plots reveal the effects of high or low immune cell infiltration, for the respective tumour immune infiltrating subsets, on patient overall survival for the investigated cancer types. Statistically significant differences in patient overall survival, between patient groups portraying high or low immune cell subset infiltration, was determined using a Log-Rank (Mantel-Cox) test with significance determined at ($P < 0.05$). ($n=245$ for Sarcoma, $n=558$ for OV, $n=482$ for LUSC, $n=362$ for LIHC and $n=1017$ for BRCA).

Effects of gene expression on patient survival

In addition to determining candidate immune receptor prognostic effects, from a tumour immune infiltration perspective, their prognostic effect in Sarcoma patient overall survival was also investigated. Due to clinical similarities between Sarcoma and OS, receptor prognostic effects in Sarcoma patients can be of relevance to OS, thereby, further validating their potential as immune-based therapeutic targets.

Prognostic value was assessed using Kaplan-Meier plots for overall Sarcoma patient survival.

The prognostic value of CXCR4 was assessed in Sarcoma clinical samples, using a Kaplan-Meier plot for overall survival (Figure 3.22). By conducting log-rank statistical analysis on the survival curves, the results show that lower CXCR4 expression is associated with poor overall survival in Sarcoma patients (n=259) ($P < 0.05$).

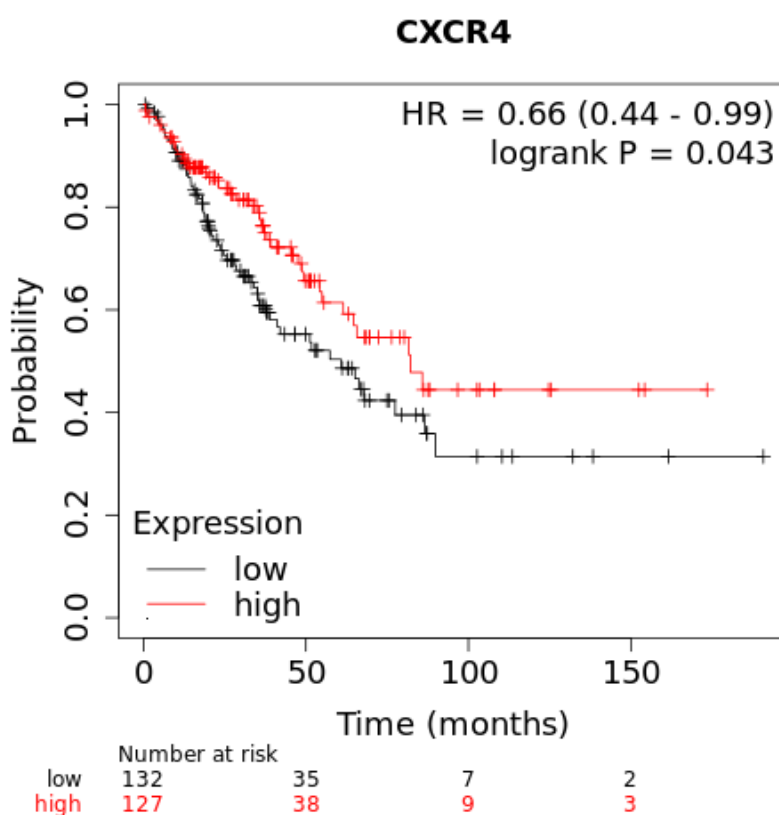


Figure 3.22: Prognostic effects of CXCR4 in Sarcoma. Kaplan-Meier plot presenting the prognostic effects of CXCR4 expression in overall survival of Sarcoma patients (n=259). The figure depicts the impact of CXCR4 gene dysregulation (high or low levels of gene expression), on the overall probability of Sarcoma patient survival. Furthermore, the figure shows the number of Sarcoma patients portraying high or low expression of CXCR4, respectively, along with the number of patients at risk during each timepoint of the survival plot. Statistically significant differences in Sarcoma patient overall survival, between patient groups portraying high or low levels of CXCR4 expression, was determined using a Log-Rank (Mantel-Cox) test with significance determined at ($P < 0.05$).

Similarly, the prognostic value of CD74 was assessed in Sarcoma clinical samples, using a Kaplan-Meier plot for overall survival (Figure 3.23). Like CXCR4, the results show that lower CD74 expression is associated with poor overall survival in Sarcoma patients. Thus, patients portraying higher levels of CD74 expression portray a significantly greater probability of survival, when compared to patients portraying lower expression (n=259) ($P < 0.05$).

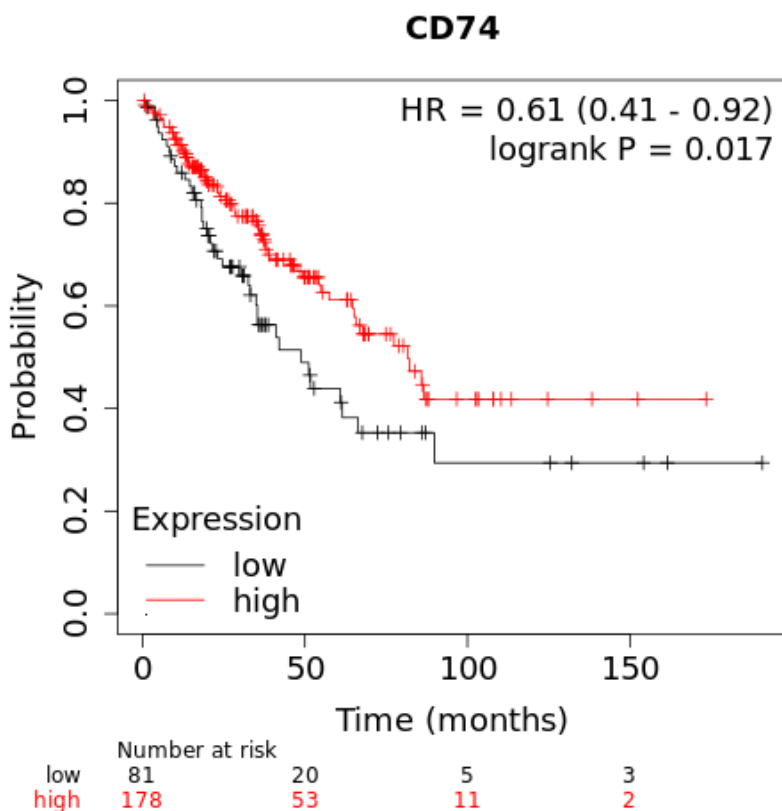


Figure 3.23: Prognostic effects of CD74 in Sarcoma. Kaplan-Meier plot presenting the prognostic effects of CD74 expression in overall survival of Sarcoma patients (n=259). The figure depicts the impact of CD74 gene dysregulation (high or low levels of gene expression), on the overall probability of Sarcoma patient survival. Furthermore, the figure shows the number of Sarcoma patients portraying high or low expression of CD74, respectively, along with the number of patients at risk during each timepoint of the survival plot. Statistically significant differences in Sarcoma patient overall survival, between patient groups portraying high or low levels of CD74 expression, was determined using a Log-Rank (Mantel-Cox) test with significance determined at ($P < 0.05$).

Lastly, the prognostic value of FPR3 was assessed in Sarcoma clinical samples, using a Kaplan-Meier plot for overall survival (Figure 3.24). Figure 3.24 portrays the generated Kaplan-Meier survival plot, which depicts the probability of overall Sarcoma patient survival, with respect to FPR3 expression (high levels or low). The results show that lower FPR3 expression is associated with poor overall survival in Sarcoma patients. Thus, patients portraying higher levels of FPR3 expression have a significantly greater probability of survival, when compared to patients portraying lower expression (n=259) (P<0.05).

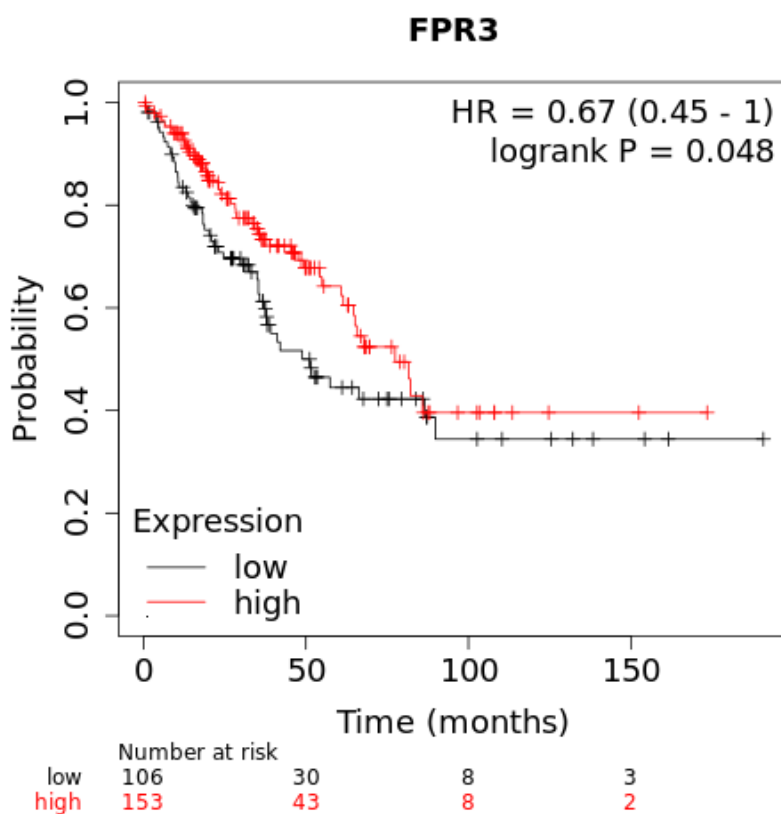


Figure 3.24: Prognostic effects of FPR3 in Sarcoma. Kaplan-Meier plot presenting the prognostic effects of FPR3 expression in overall survival of Sarcoma patients (n=259). The figure depicts the impact of FPR3 gene dysregulation (high or low levels of gene expression), on the overall probability of Sarcoma patient survival. Furthermore, the figure shows the number of Sarcoma patients portraying high or low expression of FPR3, respectively, along with the number of patients at risk during each timepoint of the survival plot. Statistically significant differences in Sarcoma patient overall survival, between patient groups portraying high or low levels of FPR3 expression, was determined using a Log-Rank (Mantel-Cox) test with significance determined at (P<0.05).

Potential druggable targets in close relation to OS

The genes of interest, CXCR4, CD74 and FPR3, portrayed functionalities as immune receptors and were identified to be significantly upregulated in OS. The candidate immune receptors were then screened for their therapeutic targeting potential in OS, through the use of various bioinformatical analytical tools. So far, the evidence positively indicates the use of the candidate immune receptors as therapeutic targets in OS. Therefore, we queried the receptors within known drug databases, thereby, determining their current clinical relevance and prior investigations validating their pharmaceutically druggable potential in cancer.

Unlike CXCR4, the receptors CD74 and FPR3 were found to be closely associated to OS through WGCNA. These receptors were further analysed through the use of various clinical and pharmacological protein databases, such as PharmGKB, oncoKB and Clinical Interpretations of Variants in Cancer (CIViC). Therefore, determining the potential held by the respective immune receptors in becoming druggable targets for the treatment of OS.

When CD74 was queried within the PharmGKB database, the gene was reported to be localised within the minus strand of chromosome 5 in humans, with only one alternate gene symbol. Thereafter, results of the gene variant annotations showed that there are two identified and characterised versions of the CD74 gene, with disease linked variant annotations. The first version of the gene is identified as allele A of the gene, while the second genetic variant is identified as allele C. Furthermore, the metallic molecule platinum is shown to have reoccurring relationships to disease associated versions of the gene of interest. The relationship between the gene variant and molecule is determined through experimentally identified gene-molecule

associations, hence, it can be inferred that the identified molecule has certain mechanistic relationships to both variants of the queried gene. Therefore, it can be said that the molecule has the ability to induce varied pharmacological effects, depending on the gene variant present in the diseased condition. In relation, the database further annotates the mechanistic relationship between the identified molecule and each disease linked variant of the gene. With regards to allele A of the gene, the gene variant is shown to be associated with an increased risk of drug induced toxicity, in non-small cell lung carcinoma patients who are treated with platinum, as compared to allele C. Henceforth, allele C is associated with a reduced risk of drug induced toxicity, in patients with non-small cell lung carcinoma, who are treated with platinum. Lastly, the gene's relationships to diseases and disease annotations were queried and the gene was shown to be clinically associated with non-small cell lung carcinoma and drug toxicity.

Similarly, the gene of interest CD74 was also further analysed by querying the gene within the cancer based clinical database oncoKB. The various options presented when CD74 was queried within the database, were mainly associated with the gene's relationship with other identified fusion proteins. The resulting list of CD74-fusion protein interactions included the interaction between CD74 and NTRK1, CD74 and ROS1 and CD74 and NRG1. When the fusion between CD74 and NTRK1 was further analysed, the results showed that the protein fusion was likely oncogenic and has a likelihood to be a gain of function protein fusion. The receptor tyrosine kinase NTRK1 is found to be altered by protein fusions in various cancer types and its fusion with CD74 is found in all solid tumour types. This particular protein fusion is labelled level 1 in the database, therefore, having FDA-approved drugs that are currently manufactured against the particular protein fusion. Henceforth, when the gene of interest is fused

with NTRK1, the protein becomes a druggable target for two currently FDA approved drugs, Entrectinib and Larotrectinib (Vaishnavi et al., 2013). Similarly, other protein fusions containing the gene of interest CD74 was shown to have FDA approved drugs targeted against it. In relation, the protein fusion between CD74 and ROS1 was identified as a protein fusion that is also a druggable target. Similar to the fusion between CD74 and NTRK1, the fusion between CD74 and ROS1 is identified as oncogenic, with the fusion said to be a gain of function protein fusion. ROS1, also characterised as a receptor tyrosine kinase, is altered by mutations or chromosome re-localisation in a wide range of cancer, with protein's fusion with CD74 found particularly in non-small cell lung cancers. The particular fusion is also labelled as level 1; therefore, the protein fusion has FDA-approved drugs currently manufactured against it. Henceforth, like with the additional protein fusions mentioned above, when CD74 is fused with ROS1, the protein becomes a druggable target for two currently FDA approved drugs, being Crizotinib and Entrectinib (Hashiguchi et al., 2021). Lastly, the protein CD74 is also known to fuse with the receptor ligand NRG1. Similar to the described protein fusions, the fusion is identified as oncogenic and said to be a gain of function fusion. However, unlike the previously described protein fusions, this fusion with CD74 is labelled level 3, therefore, having no FDA approved drugs currently being manufactured against it. Henceforth, the protein fusion, which is found in all solid tumours, has no clinically approved drugs manufactured against it, however, the drug Zenocutuzumab portrays clinically relevant effects on the protein fusion (Nagasaka and Ou, 2022). Thus, when CD74 is fused with the ligand NRG1, the protein of interest has the potential to become a druggable target for a potentially approvable drug.

When FPR3 was queried within the PharmGKB database, the gene was reported to be localised within the plus strand of chromosome 19 in humans, with no alternate

gene symbols. The immune receptor was shown to have no clinical, variant or drug labelled annotations. Therefore, emphasising a lack of knowledge surrounding FPR3 functionality, the novelty of the receptor from a disease perspective and a lack of clinical applicability. Similarly, FPR3 was queried within the precision oncology knowledgebase (oncoKB), to determine its potential as a druggable target with respect to cancer. However, no results were generated, thus, emphasising the novelty of the receptor with regards to targeted cancer therapeutics and a lack significant association between FPR3 and oncology.

The CIViC database was used to confirm the results gathered, when the immune receptors of interest were queried within the two main clinical databases, respectively. In the case of CD74, the results obtained when the gene was queried within the CIViC database, were the same as that gathered from querying the gene within the oncoKB database. The results obtained provide information on the same protein fusions described above, along with similar FDA approved drugs used against the said fusions. With regards to FPR3, a similar result was again observed, in the form of no relevant clinical annotations for the immune receptor.

3.4 Discussion

The aim of this study was to investigate and determine genes that are dysregulated/differentially expressed in pre-chemotherapeutic primary OS tumour tissue, when compared to healthy primary BM-MSCs. Thereby, improving current understandings surrounding the mechanisms underlying OS and potentially, unveiling novel therapeutic targets for the treatment of OS. This was done through GEO2R based differential gene expression analysis, whereby, we first identified significantly DEGs in OS. PCA analysis of the top upregulated and downregulated genes in OS suggested that these DEGs were able to differentiate the OS disease clinical trait from the healthy control. Further functional gene enrichment analysis of the DEGs emphasised the prevalence of the immune system and immune system functionalities within the OS trait. Thereafter, through WGCNA and DO gene enrichment analysis of identified DEGs in OS, gene modules along with individual genes closely associated with the OS clinical trait were identified. Overall, the identified closely associated DEGs provided an indication towards the biological mechanisms underlying OS. Furthermore, the DEGs themselves can be put forward as potential disease biomarkers and/or therapeutic targets for OS therapy. Functional gene enrichment of the DEGs closely associated to the OS trait strongly suggests that biological processes involved in the immune system, ECM reorganisation and immature bone formation are major mechanisms altered in OS tissues.

In comparison to previous studies, in which gene expression data was gathered from differing microarray platforms, and gene expressions of primary OS tissues and cell lines were profiled in combination, this study utilised a more refined inclusion criteria and a set of bioinformatical analytical methods proposed by Sun et al (Sun et al.,

2019). In the case of gene expression profiles being generated from OS cell lines, reports have shown that these cell lines from differing research laboratories portray various and significant levels of heterogeneity (Liu et al., 2019). Therefore, in this study, we decided to exclude OS cell line derived gene expression profiles. Furthermore, in cases where differing microarray platforms are used, each platform may potentially use a different microarray probe set to detect the same gene. Therefore, it can be said that results gathered with the use of different platforms are potentially lacking direct comparability (Sun et al., 2019). Thus, in order to reduce the described biases, in this study, we only included primary OS tissue samples and respective RNA gene expression profiles that were generated with the use of the GPL10295 microarray platform. Thus, only one study could be identified that had been previously conducted, deposited within the GEO database and matched the strict study inclusion criteria described in the methods. The included study, was a gene expression study based on OS and importantly, contained gene expression data from primary pre-chemotherapeutic OS tumour tissue samples, along with primary (BM-MSCs) from healthy controls. BM-MSC tissue samples gathered from healthy volunteers with no indications of malignant tissue, were used as suitable controls in differential gene expression analysis against OS tissue, as OS has been reported to be a bone malignancy arising from primitive transformed cells of a BM-MSCs origin (Luetke et al., 2014).

From DOSE analysis, the specific 6 DEGs that were enriched under the constrained DO term “bone OS”, and under the general DO term of “OS”, can be said to be genes closely associated with primary OS malignancies occurring in bone. On the other hand, it is well understood that OS malignancies commonly metastasise to anatomical areas such as the lung. Therefore, the remaining 11 DEGs in OS enriched under the

DO term OS, but not under the term bone OS, can be said to be less associated with primary OS malignancies and more associated with secondary (metastasised) OS tumours. Moreover, from the list of DEGs in OS, 17 of the DEGs were identified to be functionally enriched under the DO term bone marrow cancer. Amongst the list of 17 DEGs, were 7 genes that were also annotated under the DO term of "OS" (SPP1, MMP13, CXCR4, CXCL12, FN1, TNFRSF11B, ITGB1).

Due to the lack of significant semantic similarity between OS related DO terms and the bone marrow cancer term, it can be said that these 7 DEGs in OS are not closely associated with or related to OS disease in general. Similarly, amongst the list of 15 DEGs in OS enriched under the DO term Sarcoma, were 5 genes that were also annotated under OS DO term (MMP9, SPP1, CXCR4, IGFBP3, CAV1). Therefore, like with the bone marrow cancer DO term, due to the lack of significant semantic similarity between OS related DO terms and the Sarcoma term, it can be said that these 5 DEGs in OS are not specifically associated with OS. Lastly, results showed that specific upregulated genes in OS (SPP1 and CXCR4) and downregulated genes (THBS1 and IL6), were enriched under both the broad DO terms of bone marrow cancer and Sarcoma. Thus, due to the lack of semantic similarity between the broad DO terms and OS related terms, less specific association of these genes to OS is further emphasised.

Semantic similarity was further calculated between clusters of genes enriched by the respective DO terms of interest. A significant level of semantic similarity was calculated between the clusters of genes annotated under OS and bone OS DO terms, respectively. The high semantic similarity can be expected, as the full list of DEGs annotated by the bone OS DO term was also annotated under the OS DO term. Similarly, when semantic similarity was calculated between the cluster of genes

annotated under the OS DO term and the gene clusters annotated under the DO terms bone marrow cancer and Sarcoma, respectively, the results portrayed significant levels of semantic similarity in both calculations. The results of high semantic similarities are due to the enrichment of multiple DEGs under the two broad malignancy related DO terms, which are also annotated under the OS DO term. Furthermore, DEGs in OS annotated under the OS DO term, could portray similarities in gene functionality to the DEGs annotated under the broader DO terms but not annotated under the OS term. This can also be said vice versa.

The identified total list of DEGs in OS was then functionally annotated with the use of GO and KEGG pathway gene list enrichment analyses, to determine their biological and pathophysiological significance. The significant involvement of the identified DEGs in ECM remodelling and related biological processes, is expected due to the tumorigenic and malignant nature of OS, with the involvement of OS related DEGs in OS ECM having been found previously (Sun et al., 2019). In addition to the evident involvement of the identified DEGs in ECM remodelling, results gathered from gene enrichment analyses also showed an involvement of the DEGs in immune system related biological processes. The identified functional annotations for the DEGs provide an indication on how they may contribute to OS development. Thus, in addition to the current knowledge of significant immune involvement in OS development (Gomez-Brouchet et al., 2017), a strong relationship between immune system components and OS was established. Lastly, gene modules that were calculated to be closely associated to the OS clinical trait using WGCNA, were functionally enriched using GO and KEGG pathways gene overrepresentation analyses. Results from the functional enrichment of the pink module (most closely associated to OS), showed that

the genes partake in immunological processes, therefore, further presenting the strong relationship between the immune system and OS.

In contrast, when the filtered and identified downregulated genes in OS were functionally enriched through gene enrichment, the genes were shown to be enriched in biological processes including extracellular structure organization, extracellular matrix organization, cell adhesion, biological adhesion. This most likely reflects the downregulation of normal ECM modelling pathways, which enables OS tumours to generate a favourable TME that promotes tumorigenesis and metastasis. This is said to be conducted through bidirectional communications between resident tumour cells and ECM macromolecules, utilising cell-cell contact mechanisms but also ECM macromolecules (Winkler et al., 2020). Likewise, through the downregulation of cell-cell and/or cell-matrix adhesion pathways, metastasis is promoted. It is known that tumour cells often downregulate major groups of adhesion molecules, including cadherins and cell adhesion molecules (CAMs) (Cavallaro and Christofori, 2001). This causes a decrease in cellular adhesion, with mounting evidence supporting a correlation between the reduction in cell adhesion, tumour tissue invasion and metastasis.

It is well understood that the TME, embedded in a modified extracellular matrix, has a strong influential role in the initiation of tumorigenesis and tumour progression (Whiteside, 2008; Brassart-Pasco et al., 2020). The TME is defined to be a highly complex heterogenous milieu that consists of malignant tumour cells, non-malignant tumour stromal cells (such as fibroblasts and immune infiltrates) and an extracellular matrix that contains communicating growth factors, peptides and enzymes (Qi et al., 2021; Labani-Motlagh et al., 2020). Metabolic communications between the TME and tumour cells are vital for tumour progression, especially in oxygen or nutrient-deprived

microenvironments (Gouirand et al., 2018). In addition to the communications between the tumour cells and the non-malignant cells of the TME, the tumour cells are also frequently communicating with the extracellular matrix that makes up the tertiary component of the TME. Furthermore, the TME is also regarded as the environment in which the immune system interacts with tumour cells, thus, immunological changes and targeting of the immune niche within the TME may alter the fate of the malignancy (Wilczewska et al., 2012).

Over the years, a strong implication of the immune system and its components has been identified to be positively correlated with the OS disease trait. Specifically, immune dysregulation has been said to be strongly associated with OS tumour initiation and development (Liu et al., 2021). The significant role of the immune system in OS tumorigenesis and progression, was further emphasised in this study through functional gene list enrichment and the enrichment of genes identified to be closely associated to OS using WGCNA. Henceforth, identified significantly upregulated genes in OS, were filtered based on GO to identify upregulated immune receptors in OS for their proposal as novel biomarkers for targeted OS therapies in the immune niche of OS. The resulting gene list was further investigated for its therapeutic potential. Main consideration went towards the top two upregulated immune receptors (CXCR4 and CD74) and the immune receptor (FPRL2/FPR3), which had not been identified as upregulated in OS before.

To validate the role of FPRL2/FPR3 in OS, further investigations were carried out with both CXCR4 and CD74. These receptors were chosen as one of them (CD74), shows close disease association and the other (CXCR4) does not. Importantly, FPR3, like CD74, was found to have a close genetic association to OS through WGCNA.

Furthermore, we compared the receptor therapeutic targeting potential of FPR3 to that of the two well annotated receptors, CXCR4 and CD74.

Analysis using the human protein atlas database showed that CXCR4 expression is specific to bone marrow and lymphoid tissues. Due to the close proximity of primary OS tumours to the bone marrow niche (F. X. Yu et al., 2015), it can be inferred that CXCR4 receptor expression would be abundant and specifically localised within the tumour immune microenvironment. Therefore, CXCR4 can be proposed to be an effective biomarker for targeted OS therapy, located within the tumour immune microenvironment. This proposal is further supported by the expression of the receptor on various immune cells that are known to be tumour infiltrating, including T-cells, macrophages and dendritic cells. Thereby, further promoting the idea of CXCR4 abundant expression within the OS immune niche and its therapeutic targeting potential, which is supported by the receptor's predicted localisation at the cell membrane. Similarly, further analysis of CD74 showed receptor expression specificity to human blood. Like all cancerous tumours, OS is known to have a rich anatomical blood supply, which is especially great in primary OS malignancies due to their localisation in the metaphyses of long bones (Hattori and Yamamoto, 2012; C. J. Li et al., 2016; Martin et al., 2012). Therefore, it can be inferred that CD74 receptor expression would be abundant within the TME. In addition, similar to CXCR4, CD74 is said to be specifically detectable on innate immune cells that are known to be tumour infiltrating, including monocytes, B-cells and macrophages. Therefore, CD74 can be proposed to be an effective therapeutic target for OS therapeutic strategies, located within the tumour immune microenvironment. Similar to the top two upregulated immune receptors in OS (CXCR4 and CD74), high levels of FPR3 expression have been detected on bone marrow cells, thus, in close proximity to primary OS lesions

(Stempel et al., 2016). Furthermore, FPR3 is found to be expressed on typical tumour infiltrating immune cells, including monocytes and dendritic cells (Chen et al., 2017). Thus, like CXCR4 and CD74, FPR3 can too be proposed as an effective biomarker for tumour immune niche targeted OS therapy, which is further supported by its predicted localisation at the cell membrane.

The candidate upregulated immune receptors in OS, portray significant advantageous factors for their potential use as immunotherapeutic targets for the treatment of OS. This includes high expression levels in tissue with close proximity to primary OS lesions, high levels of expression on typical tumour infiltrating immune cells and predicted localisation to the cell membrane. Despite this, further investigations into receptor gene expression patterns across various malignancies showed that none of these receptors were specific to Sarcoma malignancies. All candidate immune receptors have been detected across various cancers, including breast, kidney and lymphoid tissue cancers-albeit at differential levels of expression- in addition to differential gene expression in Sarcoma (Su et al., 2005; Gil-Yarom et al., 2017; Qi et al., 2021; Berghuis et al., 2012).

However, from the conducted WGCNA in this study and subsequently generated gene modules, CXCR4 was identified to be categorised in the yellow gene module. The yellow gene module, as described, was negatively associated with the OS clinical trait. Therefore, due to the lack of close genetic association between CXCR4 and OS based on gene expression, it can be inferred that CXCR4 is unlikely to play a biologically meaningful role specific to the OS disease trait. CXCR4 belongs to the chemokine receptor family and has been shown to be overexpressed in several cancers, including prostate, ovarian, breast, melanoma, and OS. Therefore, CXCR4 is considered to be the most widely expressed chemokine receptor in most cancers (Zhao et al., 2015).

Cancer cell CXCR4 overexpression is said to contribute to tumour growth, invasion, angiogenesis, metastasis, relapse, and therapeutic resistance. Therefore, receptor antagonism has been shown to disrupt tumour-stromal cell interactions, increase cancer cell sensitivity to cytotoxic drugs and reduce tumour growth and metastasis (Chatterjee et al., 2014). With respect to OS, CXCR4 has been found to be expressed in 67% of OS tumours and its expression is said to be inversely correlated with patient survival (Kim et al., 2008; Laverdiere et al., 2005). However, the lack of CXCR4 expression specificity to OS was further emphasised by the DOSE analysis conducted in this study. When the CXCR4 gene was enriched based on DO, it was found to be annotated under 30 different disease ontological terms. Thus, it can be said that CXCR4 lacks disease specificity, due to the significant number of disease annotations. Hence, due to the lack of specificity and significant association to OS, CXCR4 cannot be suggested as an effective immunotherapeutic target for the treatment of OS.

On the other hand, the second most significantly upregulated immune receptor in OS (CD74) has been profiled to be associated with the class II major histocompatibility complex (MHC), thus, acting as an important chaperone that regulates antigen presentation for a subsequent immune response (Su et al., 2017). Specifically, the invariant chain (CD74) plays a significant role in antigen presentation by mediating assembly and subcellular trafficking of the class II MHC. Therefore, increased CD74 expression in the OS TME may be a result of an induced host immune response against the growing tumour.

In malignant tissue, it acts as a receptor for the immune cytokine macrophage migration inhibitory factor (MIF), which when bound, stimulates tumour cell survival pathways and cell proliferation (Farr et al., 2020). By querying the CD74 gene within the oncoKB database, the gene becomes a druggable target depending on the fusion

protein it generates with other associated receptors. As an example, it has been reported that when the gene is fused with NTRK1 in malignant tissue, the protein becomes a druggable target for two currently FDA approved drugs (Entrectinib and Larotrectinib) (Vaishnavi et al., 2013). Therefore, the results indicate that targeting CD74 may be effective in the treatment of OS, depending on the fusion protein it generates.

The WGCNA results showed that the pink gene module was the most positively associated gene module to OS clinical trait. Therefore, this gene module and the genes contained within it may play vital roles in OS development and metastasis. Unlike CXCR4, CD74 was identified to be categorised in the pink gene module. The CD74 gene had a calculated gene significance value of 0.753242 (strong correlation) to OS clinical trait and a P-value for the gene significance of 8.54E-19. Therefore, it can be said that CD74 is a biologically meaningful gene in OS and potentially plays a vital role in OS tumour progression. Furthermore, from the conducted DOSE analysis, CD74 was found to be annotated under only 6 different disease ontological terms, including bone marrow cancer. Therefore, due to a significant association between CD74 and OS trait and potential receptor specificity to pathologically similar bone malignancies, as seen by DOSE analysis, CD74 can be put forward as a potential immunotherapeutic target for the treatment of OS.

Past studies have reported significant evidence that promotes CD74 targeting in OS treatment. In the first study, it was reported that more than 55% of OS patients portrayed a high level of both the CD74 cell surface receptor and its receptor agonist MIF (Han et al., 2017). Hence, it can be inferred that CD74 expression and agonist relationship have a significant association with OS trait. In a second study, the CD74 gene was identified as one of 24 downregulated genes in OS patients that developed

metastasis, when compared to OS patients with no signs of metastasis. Therefore, it can be inferred that maintaining high levels of CD74 expression has the potential to prevent metastasis in OS patients, thus, improving overall patient survival. This inference was supported by survival analysis reports from the same study, whereby, Kaplan Meier plots showed that the CD74 high expression group had significantly better survival than the low expression group (M. Li et al., 2020). The inference of improved patient survival is further supported by the result obtained from sarcoma survival analysis with respect to CD74 expression (Figure 3.23). The Kaplan Meier survival plot showed that high levels of CD74 expression were significantly associated with improved Sarcoma patient survival, when compared to patients with low CD74 expression. Therefore, it can be inferred that maintaining high expression of CD74 with a synthetic receptor agonist may prevent metastasis in OS patients and significantly improve overall survival. In another study, DEGs were identified between two immunological subtypes of OS (immune high and immune low OS). In the study, it is reported that the immune high subtype of OS was associated with high levels of immune cell infiltration, a benefit to immunotherapy and therefore, a favourable prognosis. On the other hand, the immune low OS subtype was associated with low immune infiltration and poor patient prognosis. Differential gene expression analysis was conducted to reveal critical immune-linked genes that are associated with the immune high subtype of OS. Results showed that CD74 was significantly upregulated in the immune high subtype and is a key gene associated with the OS immunological subtype (Wang et al., 2021). Therefore, from the study, it can be inferred that the CD74 gene plays a pivotal role in modulating tumour immunity. Furthermore, upregulating CD74 gene expression with the use of synthetic agonists, could potentially promote immune high subtype characteristics, increase tumour immune cell infiltration and

thus, improve patient prognosis. This hypothesis was supported in a study, which reported that high expression of CD74 indicated a high infiltration of immune cells including macrophages, dendritic cells and neutrophils (Xu et al., 2021).

FPR3 is a newly associated immune receptor with OS malignancies, due to its lack of annotations and studies in relation to OS. The novelty of the immune receptor with regard to OS was further emphasised during DOSE analysis. Unlike CXCR4 or CD74, FPR3 was not annotated under any disease ontological term when DOSE analysis was conducted on the list of significantly upregulated genes in OS. This result provides evidence towards the novelty of the immune-related receptor with regard to disease relationships and specificity, along with its novelty in regard to OS.

When the receptor was queried within the drug and clinical databases, the results showed that the receptor lacked clinical annotations and there was a lack of scientific evidence for clinical drug associations. Henceforth, the clinical potential of targeting the FPR3 gene in OS cannot be derived from the utilised drug databases, thus, demonstrating the novelty of the receptor in disease therapeutics. Similar to CD74, the FPR3 receptor within WGCNA was identified to be categorised in the pink gene module. The FPR3 gene, was calculated to have a gene significance value of 0.597672 (strong correlation) to the OS clinical trait and a P-value for the gene significance of 1.29E-10. Therefore, it can be said that FPR3, like CD74, is a biologically meaningful gene in OS and potentially plays a vital role in OS tumour development and/or progression. Furthermore, the module membership value gathered from the WGNA, portrays the gene as having a vital role within the pink gene module and thus, potentially a vital role in OS progression (Appendix A, figure A5).

It is understood that tumour progression and cancer therapeutic efficacy, are highly dependent on both the diversity and abundance of immune infiltrate populations within the tumour immune niche (T. Li et al., 2020). Furthermore, immune infiltrate compositions within the immune niche are found to be heterogenous when comparing tumours from different patients. Interestingly, this is even if they present the same tumour type, thus, immune infiltrates may be patient specific and impact patient prognosis (T. Li et al., 2017). Previous studies have reported high levels of immune cell tumour infiltration resulting in favourable patient prognoses (Tas and Erturk, 2017), in diseases including prostate cancer (Donovan et al., 2018), cutaneous melanoma (Yang et al., 2020), and breast cancer (Papatestas et al., 1976; Manuel et al., 2012). In addition, increases in tumour immune cell infiltration is said to be associated with an enhanced response to adjuvant chemotherapy (Pruneri et al., 2018).

Therefore, TIMER analysis was utilised to first investigate the level of association between candidate immune receptor gene expression in specified tumour types and the abundance of a diverse set of tumour infiltrating immune populations. Firstly, when purity of the candidate immune receptor in the TME was assessed, the results showed that high levels of CD74 expression was negatively correlated with tumour purity across all the investigated cancer types. Therefore, it can be said that the receptor is highly expressed in the TME and not on the surface of assessed tumour cells, including Sarcoma tumour cells. The additional scatterplots generated in the pallet, portrayed the level of immune infiltration for each assayed immune infiltrate, against the level of candidate gene expression in the investigated cancer type. With Sarcoma being the most clinically relevant cancer type to OS, the results showed that CD74 expression is most significantly correlated with dendritic cell, B-cell and macrophage immune infiltration into the tumour. This result is in line with the candidate receptor's

immune cell surface expression. Henceforth, with increased expression of CD74 in the tumour immune microenvironment, there are greater levels of immune cell tumour infiltration, which may result in favourable patient prognoses through its effects on tumour progression and cancer therapeutic efficacy.

However, in order to further investigate associations between levels of particular immune subset tumour infiltrations and patient overall survival for the assayed cancer types, TIMER was used to generate patient overall survival plots (Kaplan Meier, KM plots). The Kaplan Meier graphs presented the prognostic effects of high or low immune cell tumour infiltration, for the investigated cancer types. The generated KM plots, show that low levels of neutrophil and CD4+ T-cell tumour immune infiltration were significantly associated with poor overall survival in Sarcoma clinical cases. From this result, it can be confirmed that higher levels of immune cell tumour infiltration by these two immune subtypes, may result in higher Sarcoma patient overall survival. High levels of CD4+ T-cell infiltration being associated with improved survival in Sarcoma patients, has been reported in a previous study. The study reported that CD4+ T-cell infiltration could predict Sarcoma prognosis, with higher infiltration being associated with improved survival (Bi et al., 2021). These results could be transferable to OS clinical cases due to the clinical similarities between OS and Sarcoma. Hence, increased neutrophil infiltration and abundance in OS tumours could be associated with improved patient survival. This theory is supported by previous observations in OS, whereby, increased levels of neutrophil infiltration has be associated with greater OS patient overall survival through the prevention of tumour metastasis (Yang et al., 2021). A previous study reported that increased numbers of neutrophils were observed in non-metastatic OS tissues when compared to metastatic tissues, where OS metastasis is known to significantly depreciate patient survival (Yang et al., 2021).

Like with CD74, the FPR3 receptor was shown to be negatively correlated with tumour purity across all the investigated cancer types. Therefore, it can be said that the receptor is likely expressed in the TME and not on the surface of tumour cells. Furthermore, the results showed that FPR3 expression is most significantly correlated with dendritic cell, macrophage and neutrophil immune infiltration into the tumour. This result is mostly in line with the receptor's profile to be expressed on intermediate monocytes, myeloid dendritic cells and classical monocytes. Henceforth, similar to CD74 expression, with increased expression of FPR3 in the tumour immune microenvironment, there are greater levels of immune cell tumour infiltration, which may result in favourable patient prognoses through its effects on tumour progression and cancer therapeutic efficacy.

Since neutrophil and CD4+ T-cell immune infiltration were of prognostic value in Sarcoma clinical cases, we further investigated the prognostic effects of CXCR4, CD74 and FPR3 expression, respectively, in Sarcoma patient overall survival. Using Kaplan-Meier plots for patient overall survival, generated with the use of Kaplan Meier plotter, the prognostic value of each immune receptor in Sarcoma prognosis was assessed. Results showed that for all three of the assessed immune receptors, lower receptor expression was significantly associated with poor patient overall survival. Therefore, revealing that the respective immune receptors portray a significant level of prognostic value in Sarcoma, which may be transferable to OS due to clinical similarities between the cancer subtypes. However, contradictory to the results, a previous study investigated the therapeutic efficacy of targeting CXCR4/CXCL12 complexes with a receptor peptide antagonist (CTCE-9908) and reported that receptor inhibition decreased OS tumour metastasis in murine tumour models (Kim et al., 2008). Therefore, based on the knowledge that OS metastasis significantly

depreciates patient survival, the results imply that receptor downregulation and lower expression may provide a more favourable prognosis in OS patients. Unlike CXCR4, reports from previous studies confirm the prognostic effects of CD74 determined in this study, whereby, lower receptor expression was associated with poor overall survival in Sarcoma cases. As previously mentioned, a study reported that an OS patient group portraying high levels of CD74 expression was associated with better overall survival, when compared to a group with lower receptor expression (M. Li et al., 2020). Lastly, with respect to FPR3, the immune receptor has only been previously discussed as a survival gene with prognostic value in breast cancer cases. In the study, FPR3 was identified as an immune-related prognostic biomarker that is associated with poor overall survival in breast cancer, in cases of higher expression. Thus, FPR3 was identified as an immunotherapeutic target in breast cancer (Qi et al., 2021). Based on this report, it can be hypothesised that higher expression of FPR3 is likely to be associated with poor overall survival in OS, therefore, receptor inhibition using a peptide antagonist may be a potential immunotherapeutic modality for OS treatment.

Interestingly, however, it has been reported that the TME of cancers has the ability to produce and provide receptor ligands, thus, subsequently activating cell surface receptors expressed on tumour and/or immune infiltrate cells of the microenvironment (Baghban et al., 2020). Henceforth, it can be inferred that ligand-receptor binding in the TME, may potentially activate downstream cancer associated pathways leading to tumour initiation and progression. Therefore, if the FPR3 receptor was localised on the surface of OS tumour cells, receptor activation could initiate G-protein coupled signalling pathways and potentially lead to modulation of pathways involved in tumour

progression. These may include sustained angiogenesis, cell proliferation and immune avoidance (Qi et al., 2021).

It can be hypothesised that targeting FPR3 in OS patients expressing upregulated levels of the receptor, with the synthetic receptor peptide ligand WKYMVm or WRW4, could bring upon improved OS patient prognosis through potential decreases in OS tumour growth and metastasis. The high-affinity FPR3 receptor peptide agonist WKYMVm has been reported by Choi et al as being useful in inducing neovascularisation, when encapsulated in injectable poly (lactide-co-glycolide) (PLGA) microspheres. In the study, the fabricated injectable PLGA microspheres controllably released WKYMVm in vivo (Choi et al., 2015). Thus, it can be hypothesised that these loaded PLGA microspheres could be used as a form of OS targeted immunotherapeutic modality. The PLGA microspheres could be used to specifically target the OS TME through the incorporation of surface ligands and subsequently, controllably release of the synthetic FPR3 ligand to allow for receptor activation. Thereafter, receptor activation could induce increases in immune cell infiltration and thereby, improve patient prognosis. Alternatively, in the case of FPR3 expression on OS tumour cells, receptor activation may result in the activation of anti-cancer mechanisms such as decreases in tumour cell migration and proliferation, or an increase in tumour cell death.

In contrast, the activation of FPRs have been found to be deleterious in cases of normal human cells and malignant tumours. For example, in human germinal centre (GC) cells that were identified to aberrantly express FPRs, upon activation, the receptors mediate epithelial–mesenchymal transition, proliferation, migration, and cell resistance to apoptosis (Kim et al., 2017). However, further mechanistic studies have shown that tumours made up of GC cells with silenced FPR1 cell-surface receptors,

portray increased vascular density. This suggests that FPR1, which belongs to the same receptor family as FPR3, may potentially promote the cellular production of antiangiogenic factors by GC cells, therefore, decreasing neovascular generation and consequently, reducing blood supply to the tumour (Chen et al., 2017). In cases of specific malignancies, however, the FPRs (1 and 2) have been identified to be also expressed on human breast cancer cells. In relation, receptor activation with the ligand AnxA1 was shown to enhance tumour cell proliferation (Khau et al., 2011). Furthermore, studies have shown that human liver cancer cells also express FPR1, with the receptor being shown to promote chemotaxis, cell invasion, proliferation and production of pro-angiogenic factors by the cancer cells (L. Li et al., 2016). Therefore, the silencing of FPR1 was shown to produce a marked reduction in the pro-tumorigenic capabilities of human liver cancer cells in immunocompromised mice (Ahmet et al., 2020).

Therefore, the opposing argument to FPR3 immune-related targeting and subsequent activation as a novel therapeutic strategy for OS treatment, is the suggestion that FPRs may actually induce OS tumour progression when stimulated. In the alternate context of FPR3 inactivation by inhibitory ligands such as WRW4, the receptor may be considered again as a possible immune-related target when designing novel therapeutics for the treatment of OS (L. Li et al., 2016).

Furthermore, from the survival analysis conducted using TIMER discussed earlier, results showed that high levels of neutrophil and CD4+ T-cell immune infiltration into the TME, significantly improved overall survival in Sarcoma patients. Due to the clinical similarity between Sarcoma and OS, it can be inferred that high levels of immune cell subset migration into the OS TME, may have a similar favourable effect on OS patient overall survival. In relation, a study conducted by Wang et al reported that the immune

high OS disease subset which portrayed high levels of immune cell infiltration, also portrayed a more favourable prognosis in OS patients (Wang et al., 2021). It has been shown that FPR3 is expressed on mature dendritic cells and T cells (Chen et al., 2018), therefore, it can be hypothesised that by specifically targeting the FPR3 receptors in the TME of OS patients expressing upregulated levels, with for example WKYMVm, CD4+ T-cell immune infiltration will be increased, and the T-cell population will become more abundant. Therefore, the overall prognosis of OS patients may become more favourable.

In conclusion, the present study identified significant DEGs in OS using meta-analytical techniques and bioinformatics analysis. Through WGCNA analysis, several genes that are significantly associated with OS were identified, which were further screened using gene annotative techniques. The identification of the DEGs and the subsequent functional annotations, aided in identifying significantly upregulated immune receptors in OS. This filtration was conducted due to the reported associations between the human immune system and OS. The results were confirmed and supported through functional enrichment analysis. The filtered immune receptor genes were further investigated through WGCNA analysis, to determine their level of association with OS.

This study puts forward the immune receptor FPR3 as a potential novel biomarker for targeted therapy in the immune microenvironment of OS tumours. Currently, there is a lack of annotations for FPR3 in OS malignancies and other human diseases analysed using DOSE analysis. Furthermore, through WGCNA, the receptor was found to be highly associated with OS. FPR3 shares similar functional and OS associative characteristics and thus, similar clinical potential with the annotated CD74 immune receptor that has been investigated as a therapeutic target for OS treatment

in previous studies. Due to the localisation of the receptor in the OS TME, a better understanding of the complex roles of the TME and in particular the immune microenvironment, is required to better determine the clinical potential of targeting FPR3 in OS treatment and progression. Lastly, it is understood that the detailed mechanisms of FPR3 activation and signalling in OS requires further investigation, to better determine its therapeutic potential (Qi et al., 2021). Furthermore, with the combined application of nanotechnology, such as the inclusion of microspheres encapsulating WKYMVm, there is potential for targeted ligand delivery to FPR3 receptors in the TME without interaction with systemically expressed receptors. Therefore, significantly decreasing adverse receptor activation and improving FPR3 targeted therapeutic efficacy during OS treatment.

Overall, the bioinformatics data presented in this chapter, provides an indication towards the therapeutic targeting potential of FPR3 in OS. Mostly due to the rarity of OS, the data gathered was in relation to the clinically similar cancer type Sarcoma. In order to properly investigate the potential held by FPR3 as a therapeutic target for the treatment of OS, further *in vivo* and *in vitro* investigations were conducted (chapter 4).

The presented study portrays several meta-analytical advantages. Firstly, the criteria utilised for the inclusion of relevant OS gene expression microarray studies has been improved from previous studies, with only RNA gene expression data from the same microarray platform and from primary OS and healthy BM-MSC control tissue being included. Furthermore, the identified DEGs were further analysed and categorised through WGCNA and DO gene enrichment analysis, to subsequently reduce the number of identified DEGs based on their association to OS. Immune receptor targets closely associated to OS were identified through the filtration of upregulated DEGs

based on the described GO term, and through the identification of the receptor within WGCNA analysis.

However, there were also some limitations in this *in silico* bioinformatics study, which need to be taken into consideration when deriving results such as biological mechanisms underlying OS and novel therapeutic targets. The major limitation was the inclusion of only one OS gene microarray study, thus, providing a limited overview of significantly DEGs in OS when compared to an appropriate control. Furthermore, the inclusion of further studies would increase the number of OS cases included in the analysis, therefore, generating results derived from a larger population of patients. The study does, however, include OS tumour biopsies and healthy control tissues acquired from patients originating from differing global populations/ethnicities. Thus, the study included samples that represent heterogenous OS tumour tissue and consequently, allows for the wider application of the gathered data. Lastly, due to the prevalence of the immune system in OS, only significantly upregulated immune receptors were investigated as potential novel therapeutic targets in OS. However, in further studies, the downregulated immune receptor genes in OS, along with other proteins within the differing compartments of the OS TME should be investigated for their therapeutic targeting potential. An example of which was shown in a study, which proposed the gene ADCK1 (AarF domain-containing kinase 1), a mitochondrial protein, as a potential novel therapeutic target in OS. Like the immune receptor FPR3, the non-immune related protein ADCK1 was identified to be upregulated in human OS tissue and OS cells (Zhuo et al., 2022).

**4. Formyl-Peptide Receptor 3 (FPR3)
as A Novel Immune-Based
Therapeutic Target in
Osteosarcoma**

Aims and hypotheses

The aim of this chapter was to investigate the therapeutic targeting potential of FPR3 in OS, by assessing its expression levels in OS, both in vitro and in vivo, and through the determination of receptor targeting efficacy on OS cell migration. We first hypothesise that FPR3 may be used as a novel therapeutic target for the treatment of OS and/or alternatively, as a potential prognostic biomarker in determining the overall survival of OS patients.

4.1 Introduction

Targeted therapy in OS

One way of overcoming deleterious side effects associated with chemotherapy and other current treatment limitations, involves the use of formulations that are designed to specifically target OS cancer cells or the tumour microenvironment (Zhou et al., 2014). This treatment modality is termed targeted therapy and aims to inhibit the proliferation of cancer cells, without affecting the surrounding healthy cells/tissue and various systemic processes. Studies have shown that nanotechnology holds great potential for use in targeted therapy for OS and specifically its utilisation in targeted drug delivery (Wang et al., 2020).

Effective cancer treatment requires the attainment of sufficient intracellular levels of a chemotherapeutic agent, which will subsequently lead to cancer cell death (Savvidou et al., 2016). Hence, chemotherapy is signified by an important balance between response and toxicity, with a low dosage having no efficacy and an overdose leading to excessive systemic toxicity (Saha et al., 2010). Moreover, drug distribution is affected by physiological barriers such as competitive uptake by the liver, excretion of small molecules by the kidneys, drug inactivation and low stability in biological fluids (Alavi and Hamidi, 2019). Therefore, NP based drug delivery systems have been studied extensively due to their potential to overcome these physiological barriers and enhance the efficacy of chemotherapeutics with fewer side effects, by improving drug protection, absorption, penetration and biodistribution (Saha et al., 2010).

Significant advances in nanotechnology and cancer biology have led to the development of tumour-targeted NP based drug delivery systems, with some having entered clinical application (Wang et al., 2020). The use of NPs in tumour-targeted

drug delivery provides several advantages that include: 1) protection of the therapeutic agent from degradation thereby increasing the retention time within the body; 2) possibly increasing the solubility of hydrophobic drugs; 3) targeted drug delivery and controlled release, thereby sustaining a high intracellular drug concentration and maximising efficacy; 4) possibility of multiple drug delivery to achieve a synergistic effect, or the ability to apply combination therapy such as chemo-photothermal therapy (Saha et al., 2010; Gu et al., 2013; Kumari et al., 2016). The various NPs commonly used in tumour-targeted drug delivery for OS targeted therapy, can be divided into two groups, organic and inorganic NPs (Gu et al., 2013). Organic NPs that have been used in NP-based targeted OS therapy include liposomes, certain polymeric NPs, micelles and dendrimers. On the other hand, inorganic NPs include metallic NPs, mesoporous silica NPs and carbon-based NPs (Wang et al., 2020).

Liposomes were the first nanosized drug delivery carriers to successfully reach clinical application, in regard to OS tumour specific targeted therapy (Bulbake et al., 2017; He and Tang, 2018; Skubitz, 2003). Liposomes are spherical vesicles, consisting of a hydrophilic cavity which is surrounded by one or multiple lipid bilayers, thereby allowing solubility independent drug encapsulation (Alavi and Hamidi, 2019; Menezes et al., 2019; Bulbake et al., 2017). Moreover, liposomes portray inherent advantages such as biocompatibility and biodegradability, with novel liposomes displaying better selectivity and increased retention (Lila and Ishida, 2017). Therefore, many liposomal formulations have been approved by the Food and Drug Administration (FDA) as drug delivery carriers for use in cancer therapy, including OS treatment (Bulbake et al., 2017; He and Tang, 2018; Skubitz, 2003)

A liposomal formulation that has been FDA approved for OS treatment is the liposome-encapsulated muramyl tripeptide phosphatidylethanolamine (L-MTP-PE) formulation,

which has shown significant clinical improvement in the long-term survival of OS patients (Meyers and Chou, 2014). This formulation combines the two modalities of targeted therapy and immunotherapy for OS treatment. Muramyl tripeptide (MTP) is a synthetic analogue of a bacterial cell wall component and works as a nonspecific immune modulator (Asano and Kleinerman, 1993), which targets and activates macrophages (Miwa et al., 2019). Kleinerman et al reported that treatment with L-MTP-PE caused an increase in TNF- α and IL-6 levels, which are inflammatory cytokines released by macrophages (Kleinerman et al., 1992). Hence, the liposomes encapsulating MTP-PE are capable of selectively delivering MTP to monocytes and macrophages, which then become activated and tumoricidal (Fidler et al., 1981; Macewen et al., 1989). It was further shown in pre-clinical studies, that chemotherapy did not interfere with L-MTP-PE induced macrophage cytotoxicity (Kleinerman et al., 1991). Furthermore, Meyers et al reported the combination of chemotherapy and L-MTP-PE, significantly improved the 6-year overall survival in patients with nonmetastatic OS from 70% to 78% (Meyers et al., 2008). This pro-survival effect, was further emphasised by the risk of death after 6 years being decreased by 28% for OS patients treated with the L-MTP-PE formulation (Miwa et al., 2019).

On the other hand, metallic NPs are separated into groups based on their composition. E.g. they can either be pure metallic NPs such as gold and silver, or metal compounds such as metal oxide NPs (Menezes et al., 2019; Soleymaniha et al., 2019). Out of the metallic NPs, gold and silver NPs are commonly investigated for their potential use in OS treatment. Especially, gold NPs (AuNPs) have been investigated over the years as a potential tool in cancer treatment. This is due to their advantageous properties such as a high surface area to volume ratio, multi-functionalisation and high permeability and retention effect (Singh et al., 2018; Riley and Day, 2017)

A study conducted by Steckiewicz et al showed that the cytotoxicity of AuNPs against OS cells is shape-dependent (Steckiewicz et al., 2019). Moreover, Chakraborty et al, while exploring the potential theranostic applications of AuNPs in bone cancer, reported that AuNP-induced apoptotic activity in OS cells can also be size-dependent (Chakraborty et al., 2020). The proposed mechanism of AuNP-induced cytotoxicity in both cases involved the generation of reactive oxygen species (ROS) which causes mitochondria-dependent apoptosis by disrupting the mitochondrial membrane potential (Wang et al., 2020). Regarding metal oxide NPs, iron oxide NPs such as ferroferric oxide (Fe₃O₄) NPs have commonly been investigated in OS due to their known biocompatibility, their ability to convert magnetic energy into heat and their potential as drug delivery carriers (Jurek et al., 2017). Popescu et al, reported promising cytotoxicity of Gemcitabine conjugated Fe₃O₄ NPs against human OS cells (Popescu et al., 2017). However, agglomeration of NPs was reported in biological conditions, thus, further understanding and modifications are needed to overcome this problem when used in biomedical applications (Mondal et al., 2017). Finally, a study conducted by Susa et al, showed that dextran NPs loaded with doxorubicin improved multiple drug resistance in OS cell lines and increased drug-induced apoptosis, as opposed to doxorubicin alone (Susa et al., 2009).

Formyl-Peptide Receptor 3 (FPR3)

The formyl-peptide immune receptors are characterised to be a part of the classical G-protein coupled receptor subfamily and along with FPR3, two more FPRs have been classified in humans: FPR1-2 (Ye et al., 2009; Qi et al., 2021). FPR1 and 2 activation by chemotactic factors, initiates a series of downstream signalling pathways that subsequently lead to cellular events such as myeloid cell migration, mediator release, induction of gene transcription and increased phagocytosis (Cattaneo et al., 2013).

FPR1 and FPR2 have been reported to be differentially expressed across a range of tumour types (Prevete et al., 2015). Regarding FPR1, gene expression has been reported to be upregulated in gastric malignant tissue when compared to normal adjacent tissue and has been identified to be closely related to patient overall survival (Yang et al., 2011).

FPR3 receptor is known to be expressed on monocytes, macrophages, eosinophils and dendritic cells, although, the functionality of the receptor on these immune cells is unclear (Dorward et al., 2015; Nawaz et al., 2020). Likewise, very few scientific studies have been carried out with FPR3 as the gene of interest, thus, FPR3 when compared to its functionally similar receptor variants, is not well understood with regards to associated downstream signalling pathways and its role in immune cells of the TME (Qi et al., 2021).

When investigating FPR3 ligands, previous studies have identified and reported several. Two of the most annotated FPR3 ligands include F2L, which is an acetylated N-terminal fragment of human heme-binding protein (Migeotte et al., 2005) and the neuronal cytoprotective peptide humanin (Harada et al., 2004). Furthermore, it has been shown that FPR3 does not bind to and interact with FMLP chemoattractant ligands of the FPR1 and FPR2 receptor variants. From this result, it has been inferred that FPR3 may play a unique role in tumour progression when compared to the other FPR variants (Rabiet et al., 2011).

In addition to the described and well annotated endogenous ligands for FPR3, the synthetic immune-stimulating ligand WKYMVm has been developed and reported to be a FPR2/3 receptor-specific full agonist (S. D. Kim et al., 2013). The identified synthetic ligand portrays functional and chemical similarity to endogenous agonistic

ligands, such as F2L. Due to F2L being a competitive agonist for the FPR3 receptor and due to the chemical and functional ligand similarity between F2L and WKYMVm, the endogenous ligand competitively inhibits the binding of WKYMVm to FPR3 (Lee et al., 2007). Similarly, the synthetic immune receptor inhibitory ligand WRW4 has been developed and reported to be a FPR2/3 receptor-specific antagonist, thus, has the ability to inhibit FPR3 receptor activation and downstream signalling (Klaver et al., 2020).

Rationale

In silico analysis of gene expression patterns in primary human OS tissue biopsies, compared to healthy controls, identified the human immune-related receptor Formyl-Peptide Receptor 3 (FPR3) as a significantly upregulated gene in OS. Based on gene expression levels, the receptor was identified to be closely associated to the clinical trait. Henceforth, FPR3 was further investigated for its potential as a biomarker for targeted therapy in the immune microenvironment of OS tumours, with the aim of identifying therapeutic targeting methods including NP-based targeted DDS.

In previous studies, FPR3 has only been investigated as a potential therapeutic target within the immune microenvironment of breast cancer (Qi et al., 2021), thus, making FPR3 a potential novel therapeutic target in OS. Therefore, to put forward FPR3 as a therapeutic target in OS, levels of receptor expression in OS needed to be assessed, both in vivo and in vitro, in addition to the in-silico gene expression analysis conducted. Henceforth, we analysed the level of FPR3 protein expression within commercially acquired OS tumour tissue with immunohistochemistry (IHC). IHC was chosen as it is widely used in clinical and research labs for the detection of protein expression and localisation within tissues (Binch et al., 2020). In addition to the assessment of in vivo

FPR3 receptor expression in OS, further immunocytochemical staining for FPR3 was carried out on established human OS cell lines and normal primary human osteoblasts. Thereby, FPR3 expression levels in OS were both qualitatively and quantitatively analysed in vitro. Lastly, to further put forward FPR3 as a novel immune-based therapeutic target in the treatment of OS, a functional cell migration “scratch” assay was conducted. Through the cell migration assay, the therapeutic efficacy of targeting FPR3 with its respective antagonist and agonist peptide ligands can be determined. Therefore, determining the potential FPR3 targeting may have on malignant OS cell migration in vivo.

4.2 Methods

Immunohistochemistry of OS microarray

An IHC protocol for tissue biopsy sections and microarrays, described by Kerlake et al (Kerlake et al., 2021), was utilised to conduct immunohistochemical staining of commercially obtained human tissue sections or tissue microarrays. The paraffin-embedded normal human spleen tissue sections, along with Osteosarcoma, mixed sarcoma and normal adjacent bone tissue (NAT) microarrays were purchased from US Biomax Inc. (cat. no. HuFPT082, OS804d, T264a and BO244g, respectively). All of the tissue samples were collected under proper Health Insurance Portability and Accountability Act (HIPAA) approved protocols, which followed the appropriate and approved ethical standards of tissue donors being fully informed and providing their consent for biopsy acquisition. The Osteosarcoma microarray slide (OS804d) comprised of 80 biopsy tissue cores of mainly malignant Osteosarcoma tissue in duplicate, however, they also included biopsy tissue cores of normal adjacent bone tissue (Appendix B, table B1.1). Similarly, the mixed sarcoma tissue microarray slide (T264a) comprised of 24 biopsy tissue cores of bone and cartilage malignant tumour tissues, including chondrosarcoma, osteosarcoma and Ewing's sarcoma (Appendix B, table B1.2). The normal adjacent bone tissue microarray slides (BO244g) comprised of 24 biopsy cores of mainly normal (adjacent to Osteosarcoma) bone tissue, however, with the inclusion of limited malignant Osteosarcoma biopsy tissue cores (Appendix B, table B1.3). Human spleen tissue sections were stained for FPR3 to represent the negative and positive controls, respectively. This is due to the aberrant expression of FPR3 in splenic tissue, as presented by the Human Protein Atlas (Uhlén et al., 2015).

The paraffin-embedded tissue sections and microarrays were baked at 60°C for 2h prior to tissue de-paraffinisation, to aid in the prevention of tissue detachment during the subsequent antigen retrieval step. Thereafter, slides were deparaffinised and rehydrated by washing in the following steps of HistoClear and percentages of ethanol, in 50ml Coplin jars (Table 4.1).

Table 4.1: IHC: steps involved in tissue deparaffinisation and rehydration. Table describing the steps of paraffin embedded tissue deparaffinisation and rehydration, which takes place in 50ml coplin jars and the appropriate time for each procedure.

HistoClear	2 x 5 minutes
HistoClear: Ethanol (1:1)	3 minutes
100% Ethanol	3 minutes
95% Ethanol	3 minutes
70% Ethanol	3 minutes
50% Ethanol	3 minutes
Distilled water	1 minute

During the steps of tissue deparaffinisation and rehydration, the sodium citrate solution (10 mM Sodium citrate in dH₂O, 0.05% Tween-20, pH 6.0) was pre-warmed in the microwave for the subsequent step of tissue antigen retrieval. The sodium citrate solution was let to cool down to 60°C and the temperature of the solution was then maintained at 60°C, on a heat block while covering the jar with aluminium foil for heat retention. Once the tissue had been deparaffinised and rehydrated, tissue antigen retrieval was carried out by heating the slides in the sodium citrate solution (maintained at 60°C) for approximately 10 minutes. The step of antigen retrieval was conducted cautiously at the specific maintained sodium citrate solution temperature, due to the fragility of Osteosarcoma and normal bone tissues. Furthermore, during the process

of antigen retrieval, the tissue cores were constantly observed to prevent excessive tissue loss commonly observed during the process. After antigen retrieval had taken place, the slides were then left to cool briefly and then placed in water for 5 minutes. Thereafter, the slides were washed twice for 5 minutes each in 0.001% Tween-20 in phosphate buffered saline (PBST) (Thermo Fisher Scientific, Inc.). Subsequently, the slides were incubated in 3% H₂O₂ in a coplin jar, for 15 minutes, in order to block any endogenous hydrogen peroxide enzymes. After the blocking incubation, the slides were washed again with PBST 3 times for 5 minutes. Once washed, the slides were blocked with 5% bovine serum albumin (BSA) in phosphate buffered saline (PBS) by dispensing 200µl of the blocking buffer on top of each slide and incubating for 1h at room temperature, in a pre-prepared humidity chamber. This step of blocking with BSA was conducted to block any endogenous non-specific antibody binding sites within the tissue, that may react with the secondary antibody and produce false positive results. After blocking the slides with BSA, excess BSA was removed by dabbing on blue roll and the slides were then incubated with the anti-FPR3 Rabbit polyclonal Antibody (1:125) (Abcam, Cambridge, UK). Approximately, 200µl of the antibody diluted in 5% BSA was dispensed onto each slide and the slides were then left to incubate overnight at 4°C in a humidity chamber. In addition, sections of parafilm were added on top of the tissue to distribute the antibody and prevent the tissue from drying out.

The next day, the slides were retrieved from the incubation chamber, excess primary antibody was dabbed off and the slides were washed with PBST, 3 times for 5 minutes. Thereafter, similar to the primary antibody, the slides were incubated with the anti-rabbit secondary antibody (in 1% rabbit serum) (ZytoChem Plus HRP-DAB Kit, Zytomed Systems GmbH). Approximately, 200µl of the antibody was dispensed onto each slide and the slides were then left to incubate for 1h at room temperature in a

humidity chamber. Like with the primary antibody incubation, sections of parafilm were added on top of the tissue to distribute the antibody and prevent the tissue from drying out. After incubation with the secondary antibody, the slides were washed with PBST 3 times for 5 minutes to ensure the removal of any unbound secondary antibody. Thereafter, the slides were incubated with the streptavidin-horseradish peroxidase (HRP) conjugate (ZytoChem Plus HRP-DAB Kit, Zytomed Systems GmbH), which binds to the secondary antibody and enables the chromogen development of the tissue. Approximately, 200µl of the conjugate was dispensed onto each slide and the slides were then left to incubate for 45-min at room temperature in a humidity chamber. After incubation with the HRP-conjugate, the slides were washed with PBST 3 times for 5 minutes, to ensure the removal of excess streptavidin-HRP conjugate. During the washing steps, the 3,3'-Diaminobenzidine (DAB) chromogen (ZytoChem Plus HRP-DAB Kit, Zytomed Systems GmbH) used for developing the stained tissue was prepared (Table 4.2).

Table 4.2: IHC: components of the DAB chromogen solution for stained tissue development. Table describing the components and steps involved in the preparation of the DAB chromogen/HRP-substrate. In addition, the table describes the appropriate volumes of each component required to make 2.5ml of the substrate.

To 2.5ml of distilled water	
Buffer stock solution	2 drops
DAB stock solution	5 drops
Hydrogen peroxide solution	2 drops

Once the washes were complete, approximately, 200µl of the DAB chromogen solution was dispensed onto each slide and the slides were then left to incubate for 2-10 minutes at room temperature. The length of incubation depended on the length of time taken for the ideal chromogen development of the tissue. During the

development, all the tissue was developed until a distinctive brown colour change was observed on the slide. Furthermore, the positive control for FPR3 (human spleen tissue) was developed first and the time taken for ideal chromogen development/brown colour change was measured. The time taken for ideal development was then used on the osteosarcoma and normal bone tissue microarray slides, so as not to overexpose the biopsy tissue cores. After developing with the DAB chromogen, the slides were placed in distilled water, in a coplin jar, for 5 minutes to stop the reaction. Thereafter, the developed slides were counterstained with the tissue nuclear stain haematoxylin, for 15-30 seconds. The slides were then rinsed with distilled water in a coplin jar, to remove any excess counterstain. Subsequently, the stain was fixed onto the tissue by washing the slides in 0.1% sodium bicarbonate for 1 minute and rinsing the slides again with distilled water in a coplin jar. Once fixed, the slides were then dehydrated and cleared by washing in the following steps of Ethanol percentages and HistoClear (Table 4.3).

Table 4.3: IHC: steps involved in tissue dehydration and clearing. Table describing the steps of deparaffinised and immunohistochemically stained, tissue dehydration and clearing, which takes place in 50ml coplin jars and the appropriate time each tissue exposure is conducted for.

50% Ethanol	3 minutes
70% Ethanol	3 minutes
95% Ethanol	3 minutes
100% Ethanol	3 minutes
HistoClear: Ethanol (1:1)	3 minutes
HistoClear	3 minutes

Once the slides had been dehydrated and cleared, excess HistoClear was dabbed off and the biopsy tissues were then mounted with the use of DPX and an appropriate

coverslip for the slide. The slides were then left to dry overnight at 4°C. Coloured bright field images of stained tissue cores were acquired, and immunoreactivity was qualitatively analysed using a Cytation automated imaging microscope (Agilent technologies, Inc, Santa Clara, USA). Tissue immunoreactivity to FPR3 was quantified by two independent reviewers using a percentage score of positively stained tumour cells, with the reviewers being blinded of the tissue description and origin.

In vitro cell migration (scratch) assay

Due to the significant expression of FPR3 observed in OS tissues, both in vivo and in vitro, this study investigated the therapeutic potential of targeting FPR3 with its respective peptide ligands. For the determination of OS therapeutic potential in the context of FPR3 targeting, we investigated and quantified the effects of receptor ligand treatment with both agonist and antagonist on OS cell migration, in vitro.

Saos-2 or MG63 cells were seeded into a 12 well tissue culture microplate, at a concentration of 7.5×10^4 cells per well. OS cells were seeded in triplicate to represent each experimental condition (untreated, agonist treated, and antagonist treated), therefore, 9 wells in total were seeded per experiment. Thereafter, the cells were incubated at 37°C in humidified conditions at 5% CO₂ overnight, for the formation of a dense cell monolayer. After 24 h, the confluent cell monolayers in the wells were wounded (“scratched”) in a straight line across the well. All monolayer scratches were conducted with the use of a vertically held sterile p200 pipette tip, with the scratch creating a cell-free area within the monolayer. Once the monolayers were scratched, the growth medium in the wells was aspirated and the cells were washed twice with 1x PBS to remove detached cells. After the addition of fresh growth medium to each well and prior to starting the cell migratory assay, the appropriate scratched cell

monolayers were treated with either the FPR3 agnostic peptide ligand (WKYMVm) or antagonistic ligand (WRW4) (Abcam, Cambridge, UK), diluted in the growth medium. For each receptor peptide ligand, three different concentrations were assayed (10, 50 and 100 μ M). Immediately after cellular treatment with the respective peptide ligand, the plate was gently shaken for 30 seconds and placed inside the Cytation automated imaging microscope (Agilent technologies, Inc, Santa Clara, USA). The progression of cell migration and monolayer wound closure was monitored for 24h, with images of individual wells being taken in 30 minute intervals under phase contrast at 4x magnification.

Analysis of wound area and cell migration

Using the Cytation automated imaging microscope, cell monolayer wound closures were visualised. For the analysis of cell monolayer wound closures and quantification of cell migratory velocity (μ m/min), the Image J plugin wound healing size tool (<https://github.com/AlejandraArnedo/Wound-healing-size-tool/wiki#wound-healing-size-tool>) was used (Suarez-Arnedo et al., 2020).

The image J plugin traces the wound edge of a manually wounded cell monolayer image, using an automated process. Subsequently, the plugin measures and quantifies the entire width of the cell monolayer wound by calculating the width between the traced wound edges, in pixels. The plugin is able to measure the pixel width of a cell monolayer wound for individual phase contrast images or carry out batch processing of a sequence of images. The pixel units for the measured wound widths obtained from an individual captured image or a batch processed image sequence, were converted to micrometres using a graticule. Thereafter, the measured cell monolayer wound widths (in micrometres) were determined for the monolayer wound

images captured at the beginning of the cell migration assay and at the end of 24h. Using the wound width values, the velocity of cell migration was calculated for each experimental condition and therefore, peptide ligand concentration ($\mu\text{m}/\text{min}$). Data are presented as mean \pm SD, with five to six replicates for each peptide concentration being included in the analysis. To calculate the level of significance in the cell migratory velocity differences between peptide concentrations and conditions, an unpaired t-test was performed with significance being considered at $p < 0.05$.

Statistical analysis

During immunohistochemical analysis of purchased tissue microarrays, FPR3 staining intensity for tissue cores from an individual patient was considered as a single repeat. In some cases of malignancy stage and lesion site, there were less than two clinical patients, thus, preventing the calculation of average and standard deviation. Both the OS (OS804d) and NAT (BO244g) tissue microarrays were stained for FPR3 in duplicate, in two independent experiments, with each experiment including independent negative and positive controls. During immunofluorescent staining of OS cells and primary HOBs, each condition was carried out in duplicate along with triplicate independent experiments. Similarly, flow cytometric analysis of FPR3 stained OS cells was carried out in triplicate for the receptor-stained conditions and singularly for the unstained controls. Complete flow cytometry experiments were carried out as duplicate independent experiments. For the cell migration assay, peptide treated and control conditions for each concentration was carried out in duplicate or triplicate, with independent experiments carried out in duplicate for each concentration. All statistical analyses were performed using GraphPad prism9® software (GraphPad Software, Inc.). All statistical column graphs present the mean and error bars present standard deviation (SD). Statistical significance was calculated using unpaired T-tests with

Welch's correction, with significance set at P-value <0.05. Similarly, for the in vitro cell migration assay, statistical significance was calculated using multiple-unpaired T-tests and one-way ANOVA with Welch's correction. Thereby, determining the significance when comparing an independent dataset to more than one other independent dataset (as recommended by Prism based on the datasets being analysed).

4.3 Results

Expression of Formyl-peptide receptor 3 (FPR3) in OS

Previous studies have investigated OS tumour cells themselves, for the identification of relevant OS therapeutic targets (Gill and Gorlick, 2021). However, it is thought that surrounding tumour niches, such as the immune niche of the tumour microenvironment, might hold proteins of interest that can be put forward as novel therapeutic targets for the treatment of OS. This result was further supported by functional enrichment analysis of DEGs in OS, presented in chapter 3. Functional enrichment of DEGs demonstrated the upregulation of immunological processes in OS, and a significant immune involvement within the tumour microenvironment. Therefore, protein targets within the tumour immune niche, largely represented by surface immune receptors, should be investigated as potential novel OS therapeutic targets.

Henceforth, in chapter 3, through differential gene expression analysis and GO based gene list filtration, specific immune receptors were identified that are significantly upregulated in OS. These immune receptors were further investigated through WGCNA, and receptors closely associated with OS were identified and screened for their novelty in regard to OS therapeutic targets and potential therapeutic efficacy.

From the various gene filtration and OS therapeutic target screenings, FPR3 was identified to be an upregulated immune receptor of interest in OS.

FPR3 was identified within the top 10 immune receptors significantly upregulated in OS at the cut-offs of $|\log_2FC| > 1$ (adjusted $P < 0.01$). Furthermore, in chapter 3, FPR3 was categorised within the pink gene module when WGCNA was conducted on all the probed genes, thus, FPR3 was identified to be an immune receptor closely associated with the OS clinical trait. To put forward FPR3 as a therapeutic target in OS, levels of receptor expression in OS needed to be assessed, both in vivo and in vitro, in addition to in silico gene expression analysis.

To determine the significance of our data mining results, levels of FPR3 protein expression in OS tumour tissue were investigated by IHC staining of commercially acquired OS tumour tissue biopsies. The OS based tissue microarray contained 80 OS malignancy tissue cores in total. The cores represented 40 different clinical cases of OS, with each case having duplicate cores. Further immunohistochemical staining for FPR3 was conducted on a mixed sarcoma tissue microarray, containing 24 tissue cores of mixed Sarcoma origin. The tissue cores were of bone and cartilage malignant tumours and represented 6 patient clinical cases, with quadruple tissue cores from each patient. Lastly, IHC analysis was also conducted on a tissue microarray containing 22 NAT cores in total. The cores represented 11 different cases of normal bone tissue, with each case having duplicate cores. IHC analysis of the tissue microarrays, was used to subsequently measure the protein expression of FPR3 within OS tumours.

Human spleen tissue sections were stained for FPR3 and represented the negative and positive controls, as spleen tissues express FPR3 at different sites. This allowed

for the determination of potential non-specific/experimental artefact binding of the primary antibody, along with confirming the functionality of the antibody for IHC staining. The results obtained from these experiments showed that the anti-FPR3 antibody was valid for use in further IHC staining (Figure 4.1).

The results of IHC staining showed that FPR3 is aberrantly expressed across all different OS primary malignant tumours contained within the tissue array. Coloured bright field images captured of OS biopsy tissues stained for FPR3, show receptor expression specifically in malignant OS cells that form immature neoplastic bone (osteoid) and in bone lining cells (Figure 4.2a-c). (Figure 4.3) presents an alternate OS tissue biopsy core that was stained for FPR3 during IHC analysis. The tissue core presents histological characteristics of an early-stage OS tumour and when stained, showed strong FPR3 expression on tumour mesenchymal stromal cells in addition to receptor expression on malignant osteoblasts that form osteoid. Staining of NAT tissue cores, which are comprised of normal bone marrow and bone tissue regions, showed that only the bone marrow tissue regions of the cores strongly express the FPR3 receptor. This is due to the known expression of the immune receptor on the surface of some immune cells of hematopoietic lineage. Unlike the bone marrow tissue regions, no FPR3 expression was observed in normal bone tissues or normal bone cells involved in bone homeostasis and maintenance (Figure 4.2d).

The results of the OS tumour microarray showed that FPR3 is least expressed in OS tumours arising in the lower jaw, however, further staining of more OS tissue cores from this region is needed to confirm this finding (Figure 4.4a). Furthermore, FPR3 expression showed no obvious signs of malignant stage-specific variations. This was observed through staining of tumour tissue cores representing localised low and high-grade OS tumours, along with staining of tumour tissue cores from metastasised OS

tumours (Figure 4.4b). In the case of OS tumour stage IVB, a low level of FPR3 expression was observed, however, further staining of more OS tissue cores sampled from tumours at the described OS cancer stage is needed to confirm this result.

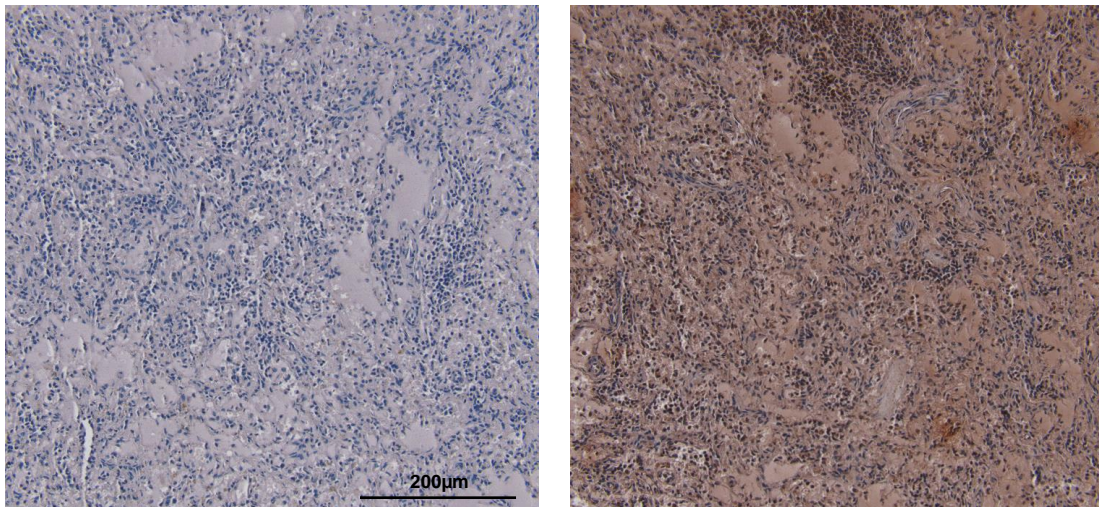


Figure 4.1: Staining of human spleen tissue for FPR3. Normal human spleen tissue sections, stained with anti-human FPR3 antibody (1:125). Negative control with splenic tissue exposed to secondary antibody and HRP conjugate only (left) and positive control, with splenic tissue stained with anti-human FPR3 antibody (right). The results confirm that the primary antibody is functional during IHC staining. Negative and positive controls, respectively, were included as appropriate controls during the two independent IHC experiments conducted. Representative images are shown at x20 magnification. Scale bar: 200µm pertains to both images.

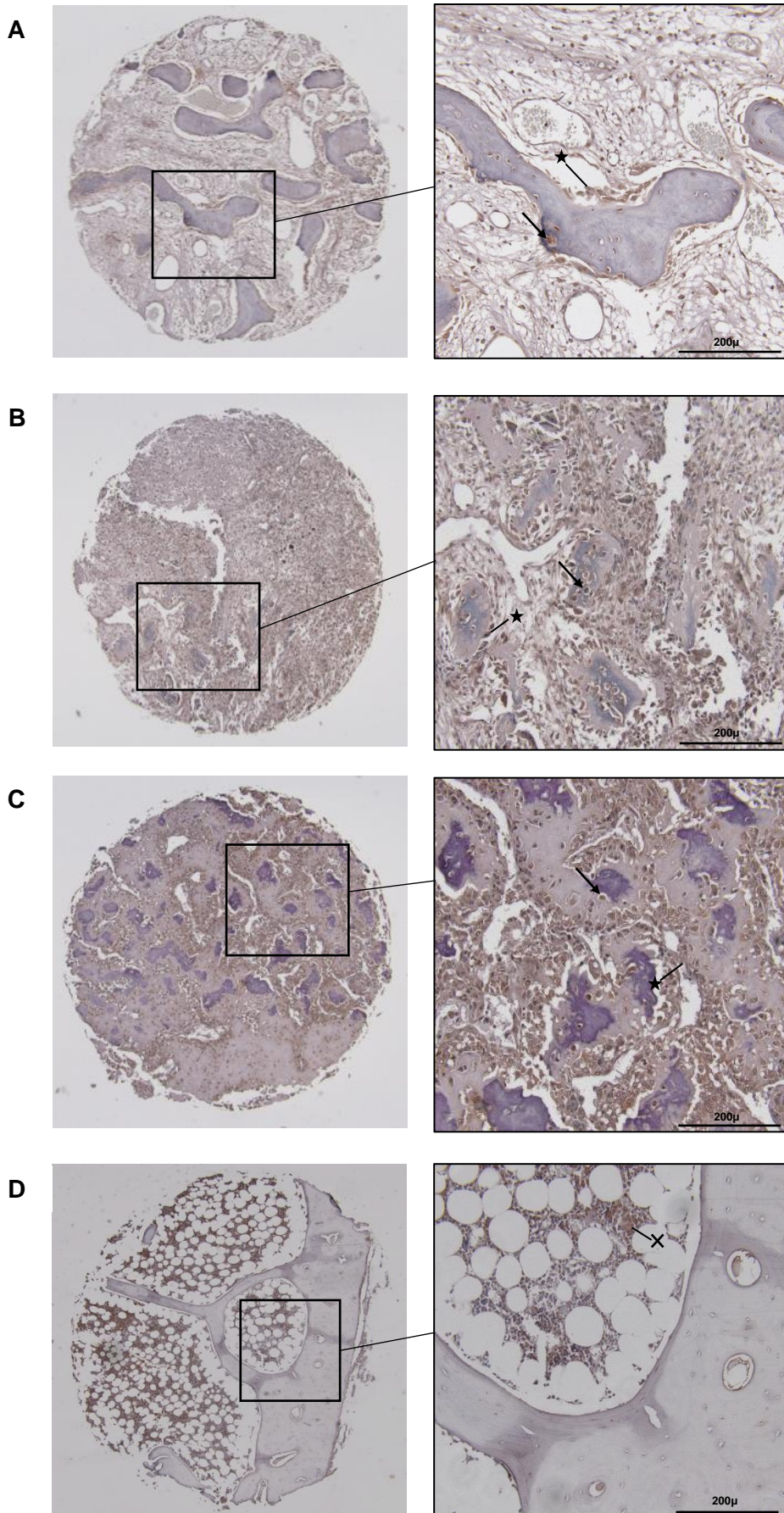


Figure 4.2: A commercially acquired OS tissue microarray, stained for FPR3. Osteosarcoma tissue microarray, including 80 duplicate Osteosarcoma tumour tissue cores (n=40), stained with anti-human FPR3 antibody (1:125). (A) Osteosarcoma of the femur stage IIB at x4 (left), with a greater magnification (x20) highlighted within the black box and presented on the (right). (B) Osteosarcoma of the femur stage IB at x4 (left), with a greater magnification (x20) highlighted within the black box and presented on the (right). (C) Osteosarcoma of the femur stage IA at x4 (left), with a greater magnification (x20) highlighted within the black box and presented on the (right). Malignant OS tumour cells that are positively stained for FPR3 (outlined by black arrows), are represented by an identifiable brown stain (a consequence of DAB chromogen tissue development) and shown to be forming immature neoplastic bone (osteoid). Likewise, FPR3 is also strongly expressed on bone lining cells (outlined by stars). (D) Normal, adjacent to OS, bone tissue of the human rib, at x4 (left) and x20 (right) magnification. (n= 11 for cases of normal human bone tissue, stained for FPR3). Immune cells of haematopoietic lineage, within bone marrow tissue of NAT cores, are shown to be positively stained for FPR3 (represented by an identifiable brown stain and outlined by a cross). FPR3 staining intensity of tissue cores from individual patients were considered as a single repeat. The NAT tissue microarray was stained for FPR3, during two separate independent experiments. Scale bar: 200µm pertains to all x20 magnification images.

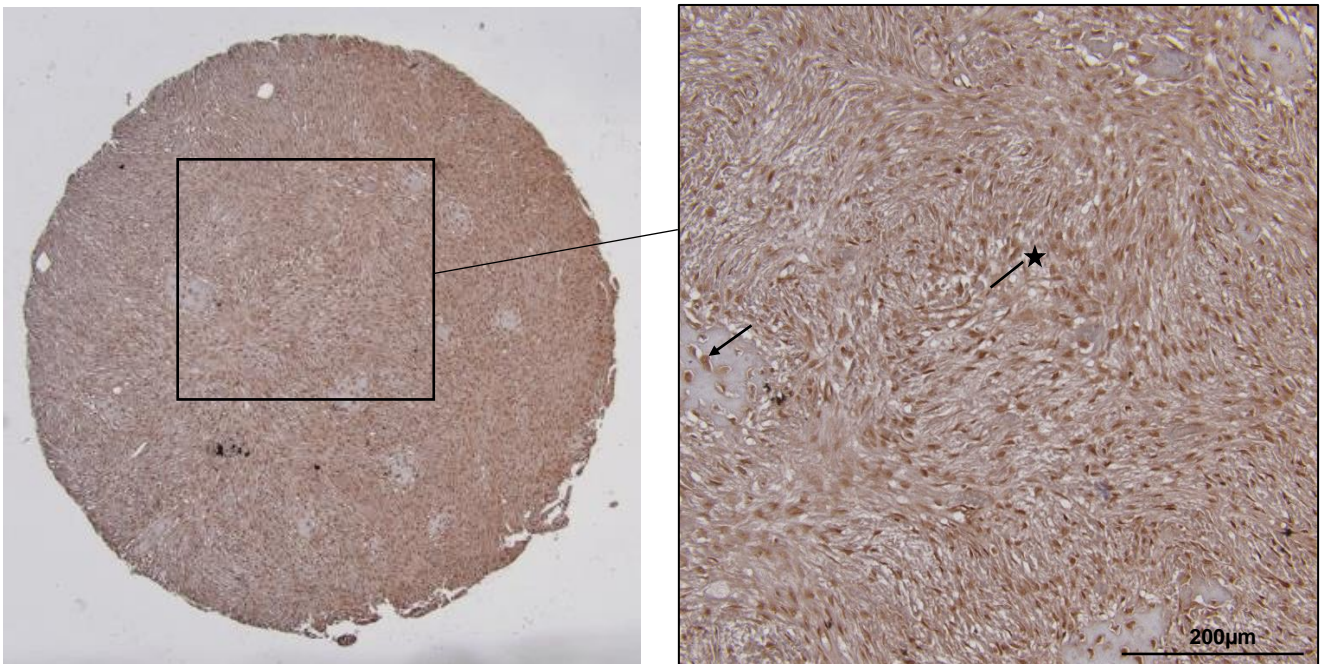


Figure 4.3: A commercially acquired OS tissue microarray, stained for FPR3. Osteosarcoma tissue microarray, including 80 duplicate Osteosarcoma tumour tissue cores ($n=40$), stained with anti-human FPR3 antibody (1:125). Osteosarcoma of the rib stage IA at $\times 4$ (left), with a greater magnification ($\times 20$) highlighted within the black box and presented on the (right). Malignant OS tumour cells that are positively stained for FPR3 (outlined by black arrows), are represented by an identifiable brown stain (a consequence of DAB chromogen tissue development) and shown to be forming immature neoplastic bone (osteoid). Likewise, FPR3 is also strongly expressed on tumour mesenchymal stromal cells (outlined by stars). Scale bar: $200\mu\text{m}$ pertains to the $\times 20$ magnification image.

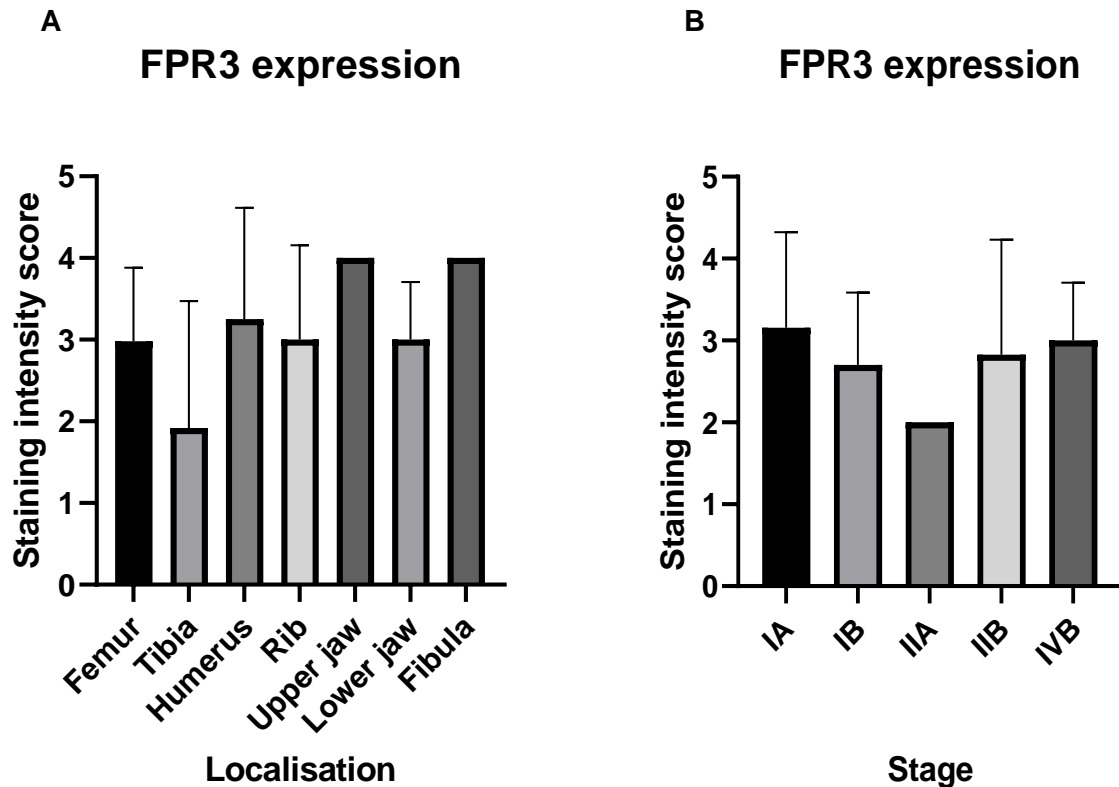


Figure 4.4: Staining intensity scorings for the OS tissue microarray. Osteosarcoma tissue microarray, including 80 duplicate OS tumour tissue cores, along with the addition of OS tissue cores included in the mixed Sarcoma tissue microarray, stained with anti-human FPR3 antibody (1:125). Standardised values for scoring staining intensity: 0, <10%; 1, 10–25%; 2, 26–50%; 3, 51–75%; and 4, >76% of cells stained. (A) Osteosarcoma cores stained for FPR3, based on specific primary malignant tumour localisation. (n= 25 for femur, n= 9 for tibia, n= 4 for humerus; n= 2 for rib; n= 1 for upper jaw, lower jaw, and fibula). (B) FPR3 staining of tissue cores from tumours of differing Osteosarcoma stages, revealing no significant difference between stages. (n= 8 for stages IA, n= 15 for IB, n= 1 for IIA, n= 20 for IIB, n= 1 for IVB). FPR3 staining intensity of tissue cores from individual patients were considered as a single repeat. The tissue microarray was stained for FPR3, during a single experiment.

The result from the immunohistochemical analysis conducted on the mixed sarcoma tissue microarray, showed that FPR3 was aberrantly expressed across most of the different Sarcoma tumour subtypes included in the tissue microarray (OS, Chondrosarcoma and Ewing's sarcoma). FPR3 was shown to be most expressed in biopsy tissue cores acquired from Ewing's Sarcoma tumours (Figure 4.5a), with staining intensity similar to that of the positive control. Comparatively, tissue cores acquired from Chondrosarcoma tumours portrayed little to no FPR3 tissue expression (Figure 4.5b), which was similar to that of the negative control. In addition, FPR3

expression within bone and cartilage tumour tissues contained in the mixed tissue microarray, portrayed no site-specific variations, with FPR3 being expressed widely in Sarcoma subtypes from differing regions (Figure 4.6b). Lastly, the results showed that FPR3 expression, like in the OS tissue microarray, portrayed no stage-specific variation specifically in regard to OS and Ewing's sarcoma cancer stages (Figure 4.6c).

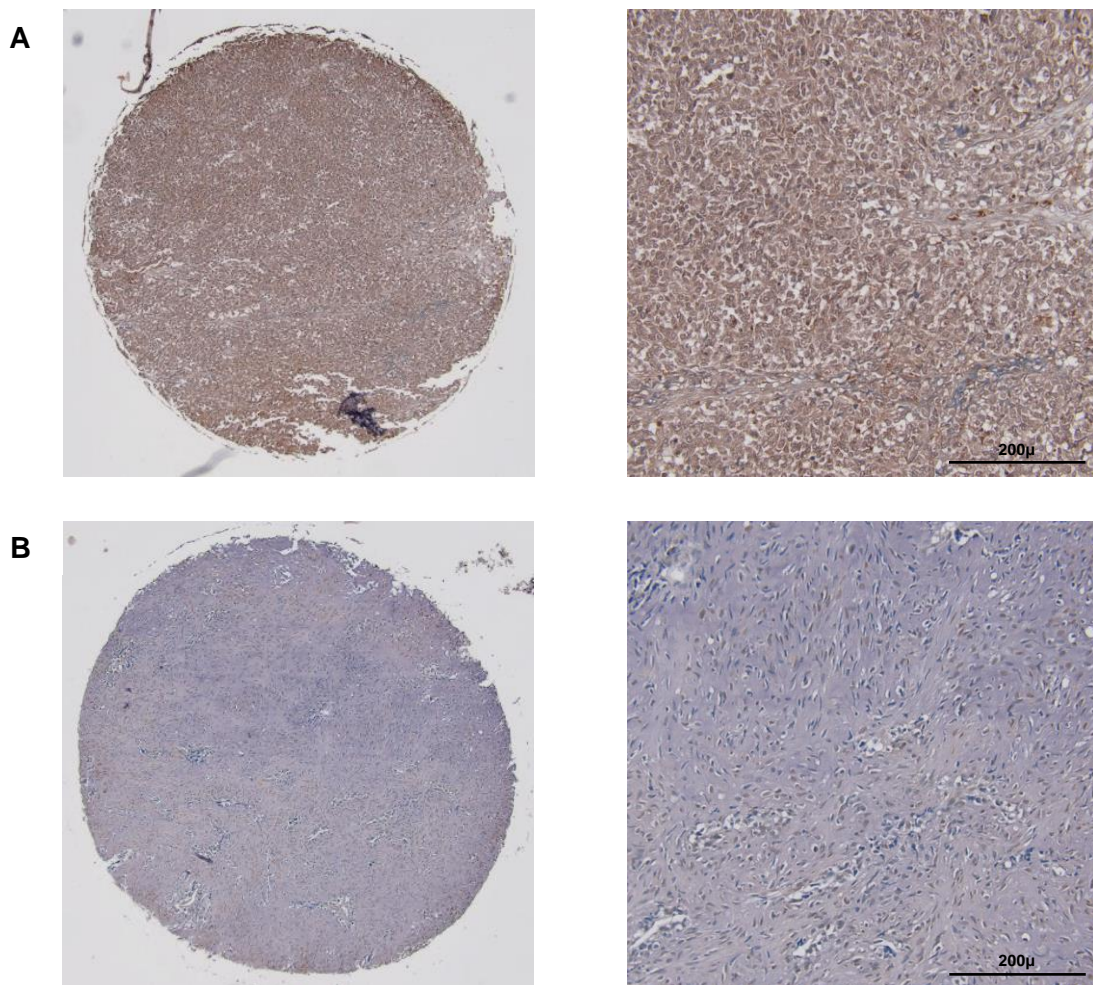


Figure 4.5: A commercially acquired mixed sarcoma tissue microarray, stained for FPR3. Mixed sarcoma tissue microarray, including 24 quadruple tissue cores of bone and cartilage malignant tumour tissues, representing $n=6$ clinical cases from 3 different Sarcoma subtypes, stained with anti-human FPR3 antibody (1:125). (A) Ewing's sarcoma of the left femur, stage IIB at $\times 4$ (left) and $\times 20$ (right) magnification. (B) Undifferentiated chondrosarcoma of pars sacralis, $\times 4$ (left) and $\times 20$ (right) magnification. FPR3 staining intensity of tissue cores from individual patients were considered as a single repeat. The tissue microarray was stained for FPR3, during a single experiment. Scale bar: $200\mu\text{m}$ pertains to both $\times 20$ magnification images.

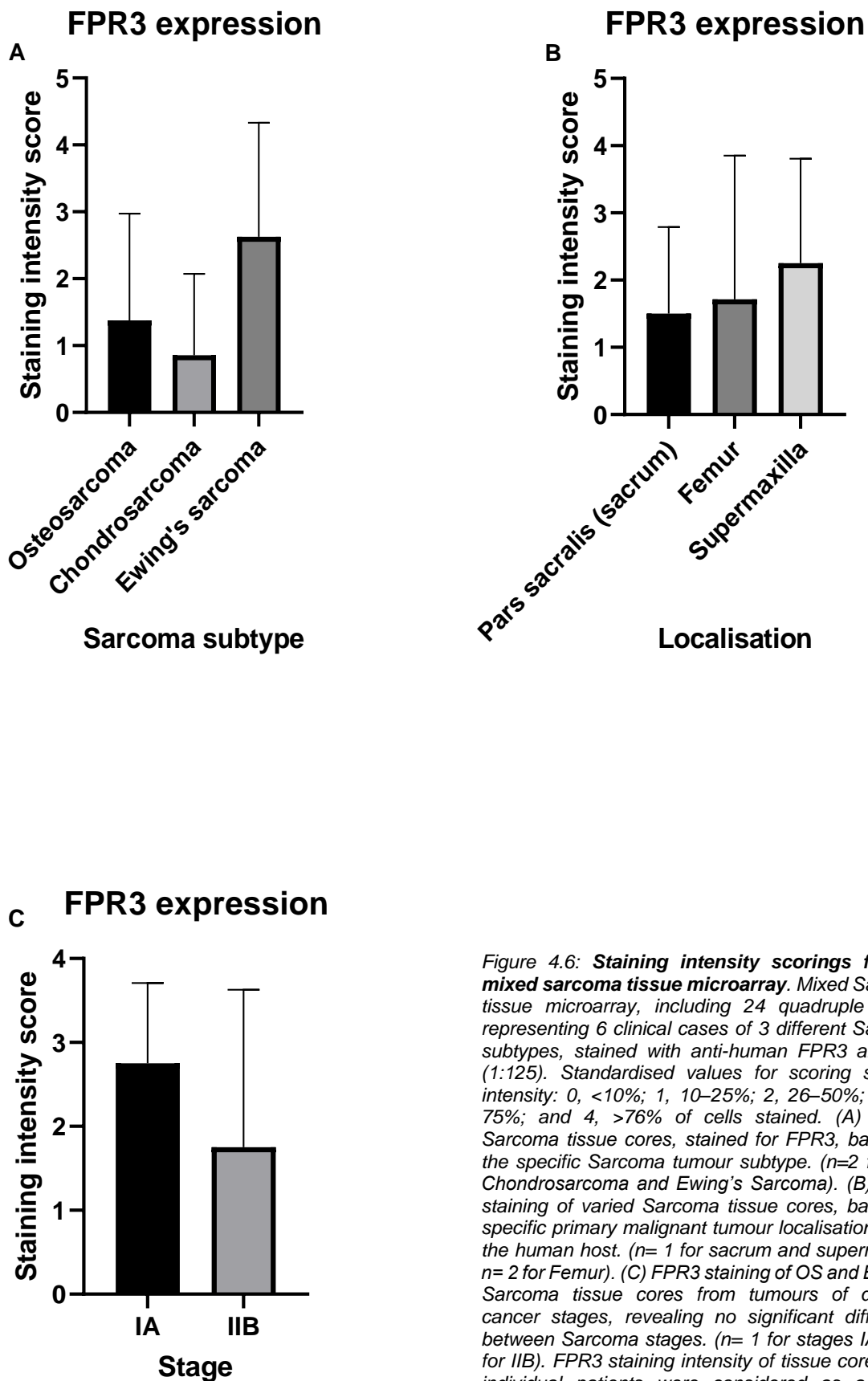


Figure 4.6: Staining intensity scorings for the mixed sarcoma tissue microarray. Mixed Sarcoma tissue microarray, including 24 quadruple cores, representing 6 clinical cases of 3 different Sarcoma subtypes, stained with anti-human FPR3 antibody (1:125). Standardised values for scoring staining intensity: 0, <10%; 1, 10–25%; 2, 26–50%; 3, 51–75%; and 4, >76% of cells stained. (A) Varied Sarcoma tissue cores, stained for FPR3, based on the specific Sarcoma tumour subtype. (n=2 for OS, Chondrosarcoma and Ewing's Sarcoma). (B) FPR3 staining of varied Sarcoma tissue cores, based on specific primary malignant tumour localisation within the human host. (n= 1 for sacrum and supermaxilla, n= 2 for Femur). (C) FPR3 staining of OS and Ewing's Sarcoma tissue cores from tumours of differing cancer stages, revealing no significant difference between Sarcoma stages. (n= 1 for stages IA, n= 3 for IIB). FPR3 staining intensity of tissue cores from individual patients were considered as a single repeat. The tissue microarray was stained for FPR3, during a single experiment.

Expression of Formyl-peptide receptor 3 (FPR3) in OS (in vitro)

The importance of the tumour niche within the OS tumour microenvironment has been previously discussed. Despite this, a lack of investigations into immune-based therapeutic targets as potential novel therapeutic modalities in the treatment of OS is of clear evidence. Through immunohistochemical staining of OS and mixed Sarcoma tumour tissue microarrays, FPR3 receptor expression was visualised and quantified within OS tumours. Further immunofluorescence staining for FPR3 was carried out on two established human OS cell lines derived from bone tissue of OS patients, and on normal primary human osteoblasts. Thereby, FPR3 surface receptor expression levels in OS were both qualitatively analysed and quantified.

Immunocytochemical staining for FPR3 was conducted on the MG63 human OS cell line, which portrays a fibroblast like morphology and had been derived from the primary osteosarcoma of a 14-year-old White male. Further immunostaining for FPR3 was conducted on the Saos-2 human OS cell line, that was derived from the primary osteosarcoma of a 11-year-old Caucasian female. Moreover, through immunostaining of primary healthy human osteoblasts for FPR3, we wanted to visualise and qualitatively analyse the level of FPR3 protein expression on normal healthy bone cells in vitro. Thereby, comparing FPR3 expression levels on OS cell lines to levels of expression on healthy human osteoblasts in vitro, and further validating the lack of FPR3 expression in normal NAT cores.

Figure 4.7 shows FPR3 expression levels on MG63 and Saos-2 human OS cell lines. Likewise, figures 4.8 and 4.9 present higher magnification fluorescence microscopy images that further show FPR3 expression on MG63 and Saos-2 human OS cell lines, respectively. In the case of the MG63 cells, immunofluorescent images captured under

FITC (green channel) showed that the receptor was expressed and localised largely on the cell surface. The plasma membrane was counterstained with concanavalin A (red), a lectin which binds to the sugar moieties of membrane proteins. The nuclei of the cells were stained with Hoechst 33342 (blue). The green channel, which represents FPR3 receptor specific staining, was observed to be merged with the plasma membrane specific red fluorescence (Figures 4.7 and 4.8). FPR3 receptor expression and localisation largely on MG63 OS cell surfaces, is further supported by the confocal microscopy image presented in figure 4.11. The confocal image confirms FPR3 receptor specific staining to be localised to the plasma membrane and thus, merged with the plasma membrane specific red fluorescence.

Similarly, when Saos-2 human OS cells were immunostained for FPR3, results showed that FPR3 was expressed and localised largely on the cell surface of these OS cancer cells. However, when compared to the level of FPR3 staining observed with the MG63 cells, the Saos-2 cells stained stronger for the receptor. With respect to the level of FPR3 expression observed with the Saos-2 cells, a greater percentage of cells were observed to be stained positive for the receptor and the receptor staining was observed to be of greater intensity. Similar to the receptor staining observed with MG63 OS cells, the receptor was again observed to be on the cell surface, which is emphasised by the merging of green and red fluorescent channels (Figures 4.7 and 4.9). Lastly, when normal human primary osteoblasts were immunostained for FPR3, the results were observed to be negative (Figures 4.7 and 4.10). FPR3 is thus, specifically expressed on OS tumours and tumour cells.

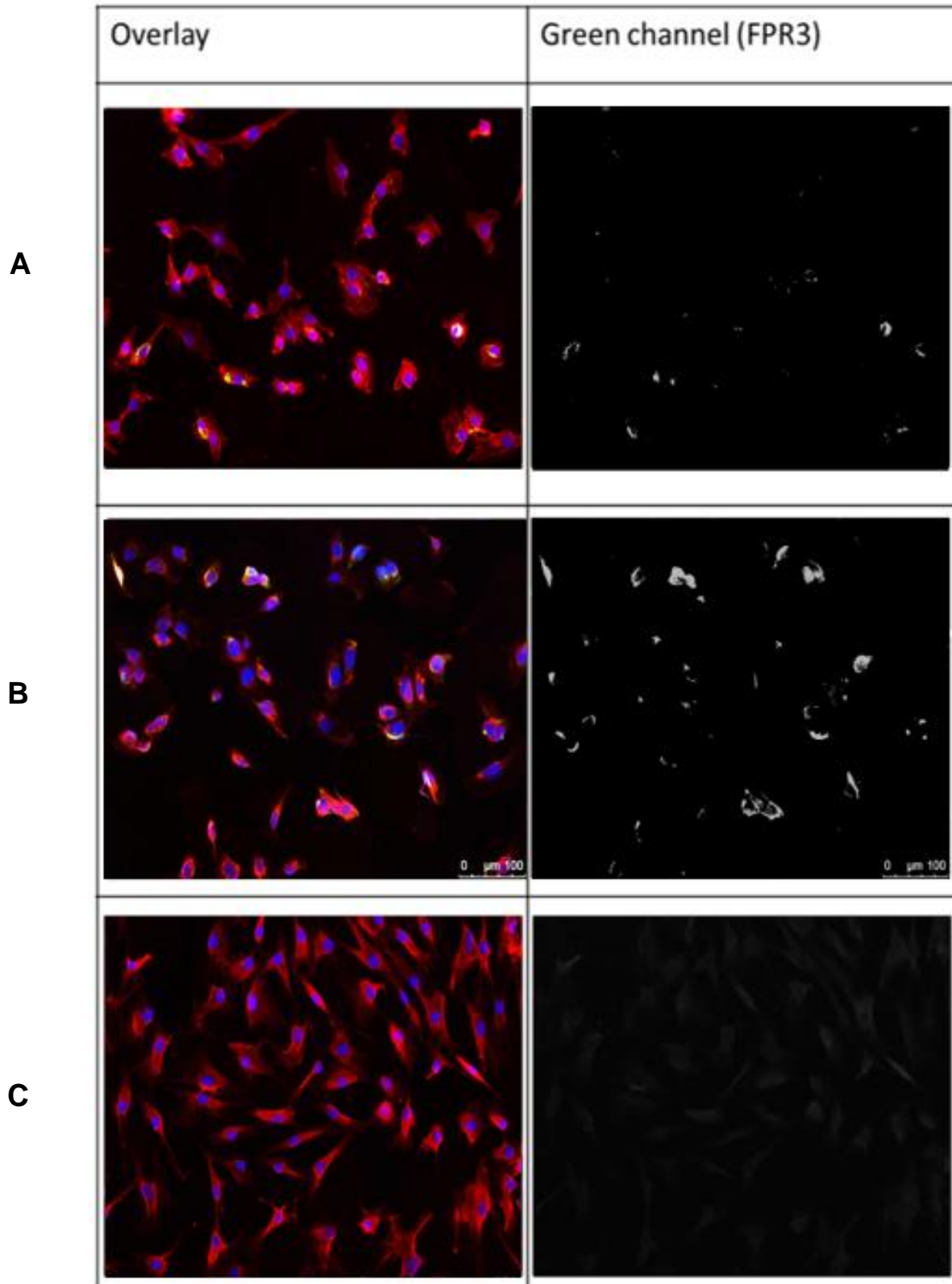


Figure 4.7: Staining of OS cells and primary HOBs for FPR3. Immunofluorescence imaging of malignant human OS cells (MG63 (A) and Saos-2 (B)) and normal primary human osteoblasts (HOBs) (C) stained with anti-human FPR3 antibody. The fluorescence microscopy images depict Hoechst 33342 nuclear staining of cells (blue), Concanavalin-A cellular plasma membrane staining (red) and FPR3 staining (green) but grayscale on the right. FPR3, Formyl peptide receptor 3. Immunofluorescent staining of MG63, Saos-2 and primary HOBs, respectively, were carried out as duplicate coverslips per condition and with independent experiments for each cell type carried out in triplicate. All fluorescent microscopy images are shown at x20 magnification. Scale bar: 100µm pertains to all.

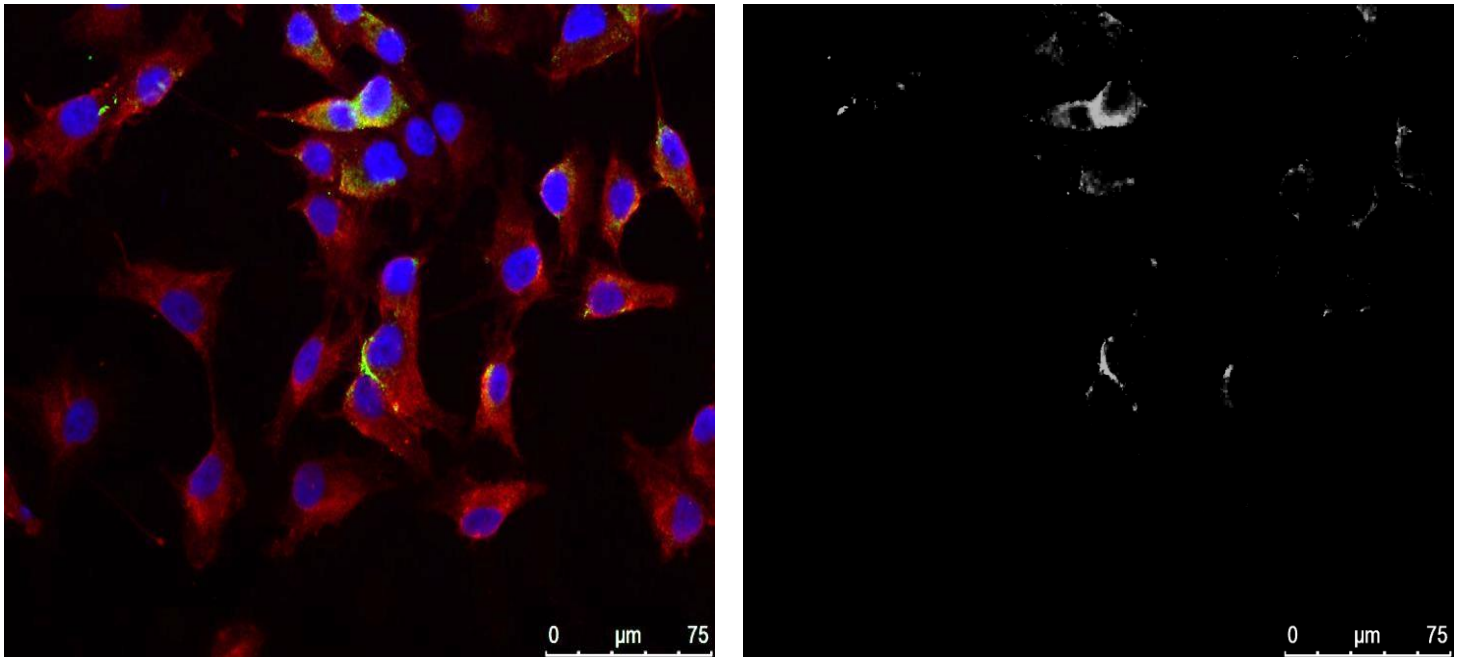


Figure 4.8: Staining of human OS cells for FPR3. Immunofluorescence imaging of malignant human OS cells (MG63), stained with an anti-human FPR3 antibody. The fluorescence microscopy images depict Hoechst 33342 nuclear staining of cells (blue), Concanavalin-A cellular plasma membrane staining (red) and FPR3 staining (green) but grayscale on the right. White arrows show positive cell surface staining for FPR3. FPR3, Formyl peptide receptor 3. Both fluorescent microscopy images are shown at x40 magnification. Scale bar: 75µm pertains to both images.

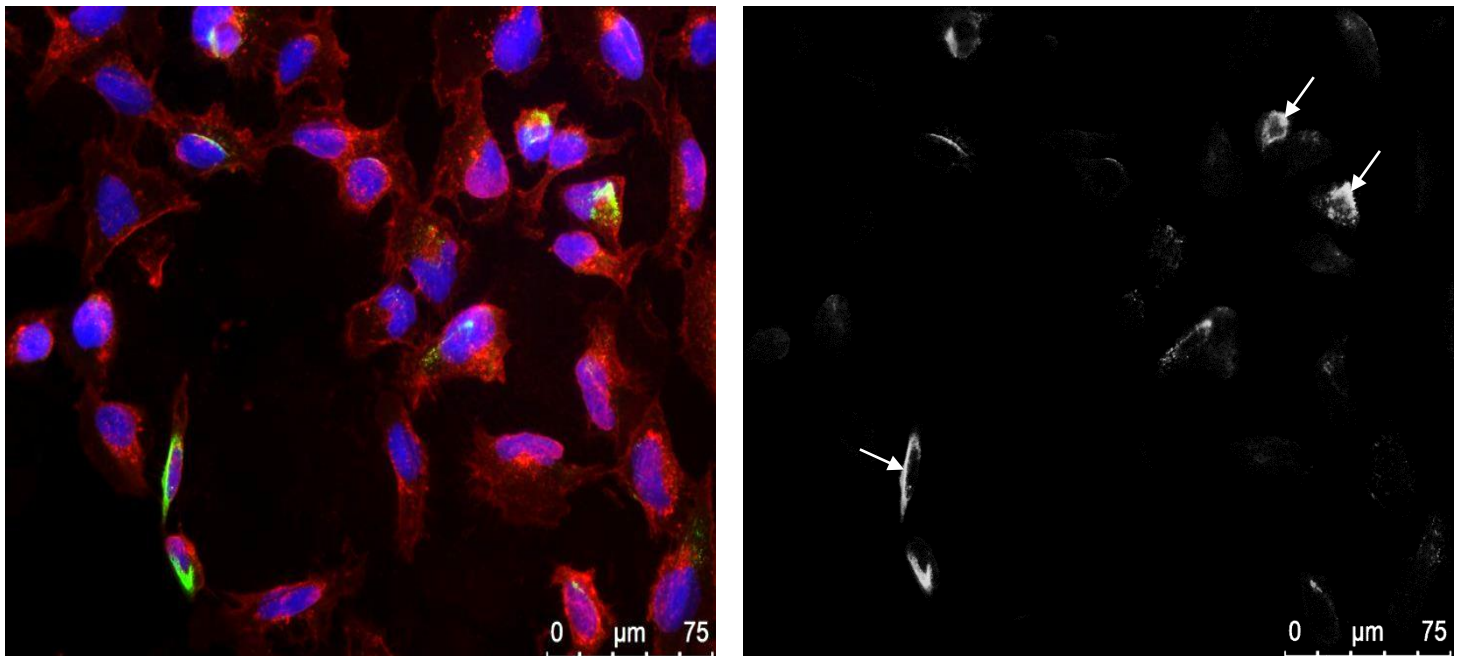


Figure 4.9: Staining of human OS cells for FPR3. Immunofluorescence imaging of malignant human OS cells (Saos-2), stained with an anti-human FPR3 antibody. The fluorescence microscopy images depict Hoechst 33342 nuclear staining of cells (blue), Concanavalin-A cellular plasma membrane staining (red) and FPR3 staining (green) but grayscale on the right. White arrows show positive cell surface staining for FPR3. FPR3, Formyl peptide receptor 3. Both fluorescent microscopy images are shown at x40 magnification. Scale bar: 75µm pertains to both images.

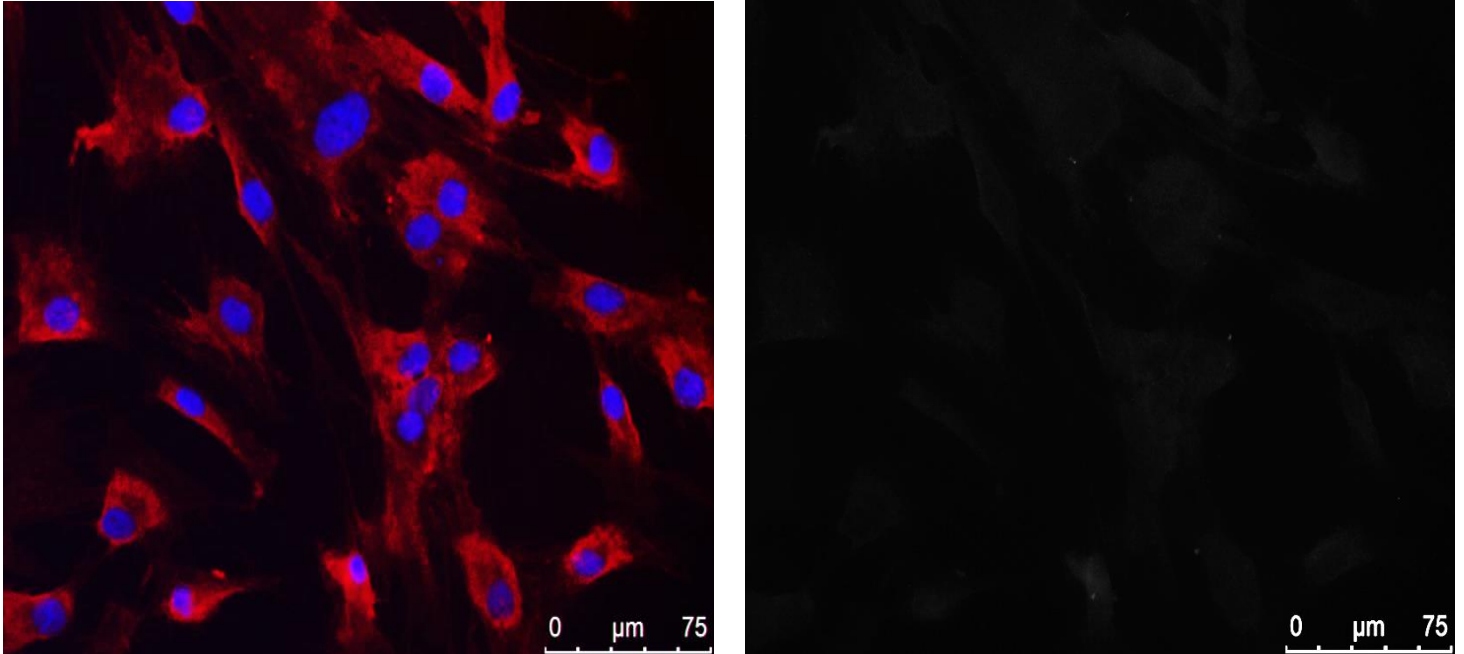


Figure 4.10: **Staining of normal human primary HOBs.** Immunofluorescence imaging of normal primary HOBs, stained with an anti-human FPR3 antibody. The fluorescence microscopy images depict Hoechst 33342 nuclear staining of cells (blue), Concanavalin-A cellular plasma membrane staining (red) and FPR3 staining (green) but grayscale on the right. FPR3, Formyl peptide receptor 3. Both fluorescent microscopy images are shown at x40 magnification. Scale bar: 75μm pertains to both images.

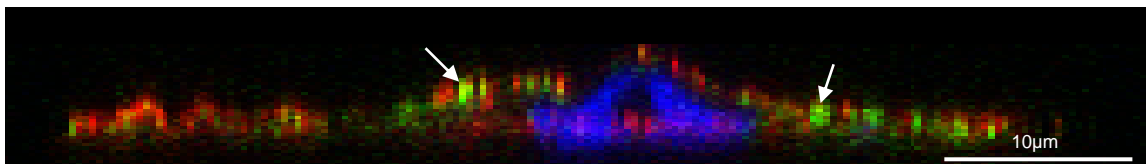
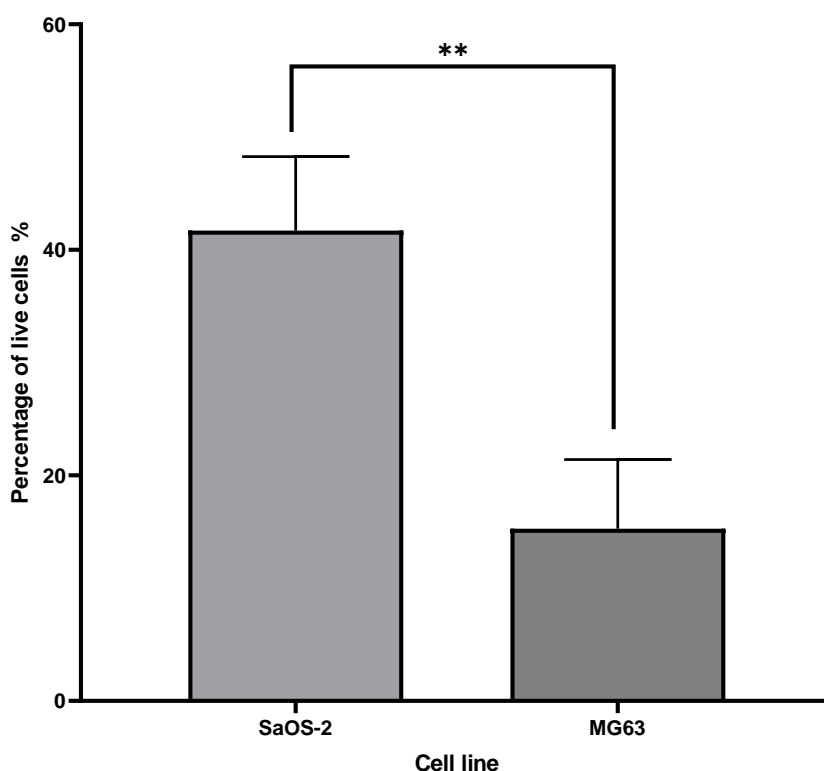


Figure 4.11: **Staining of human OS cells for FPR3.** Confocal cross-section (ZX) image of a malignant human OS cell (MG63), stained with an anti-human FPR3 antibody. The fluorescence microscopy images depict Hoechst 33342 nuclear staining of cells (blue), Concanavalin-A cellular plasma membrane staining (red) and FPR3 staining (green). FPR3 receptor specific staining is shown to be localised to the plasma membrane and thus, merged with the plasma membrane specific red fluorescence. White arrows show positive cell surface staining for FPR3. FPR3, Formyl peptide receptor 3. Confocal microscopy image is shown at x60 magnification. Scale bar: 10μm.

Flow cytometric analysis

Immunofluorescence staining gave qualitative results for FPR3 expression on the two OS cell lines (MG63 and Saos-2). To quantify the percentage of cells staining positive for FPR3, flow cytometric analysis was used. The results showed that the percentage of Saos-2 OS cells stained positive for FPR3, was more than two-fold greater than the percentage of MG63 cells positively stained for the receptor (Figure 4.12) (Average percentage of cells stained positive for FPR3: Saos-2 (41.71%), MG63 (15.27%); P value = 0.0035).

Expression of FPR3 in MG63 and SaOS-2 human OS cells (percentage of live cells stained positive for FPR3 (%))



*Figure 4.12: **Flow cytometric analysis of OS cells stained for FPR3.** Figure portraying the overall percentage (%) of live OS cells stained positive for the immune receptor of interest (FPR3), for both the OS cell types included in this study (MG63 and Saos-2). Flow cytometric analysis of the respective FPR3 stained OS cells, were carried out as triplicate repeats per condition. Similarly, flow cytometric analysis of the respective unstained control cells, was carried out as a singular repeat. Overall, OS cells were analysed through the use of flow cytometry, during two independent experiments. Asterisks represent a statistically significant difference when compared to the relevant unstained control, in an unpaired t-test (*: p-value <0.05; **: p-value <0.01; ***: p-value <0.001; ****: p-value <0.0001).*

In vitro cell migration (scratch) assay

Taken together, the bioinformatic and immunostaining results show that the immune receptor FPR3 is significantly upregulated in OS and closely associated to the diseased trait. To put forward FPR3 as a novel immune-based therapeutic target in the treatment of OS, a functional cell migration “scratch” assay was conducted. The aim of the assay was to determine the therapeutic efficacy of targeting FPR3 with agonist or antagonist peptide ligands. Therapeutic efficacy was measured, based on the impact of FPR3 receptor targeting on decreasing OS cell migration, in vitro. If FPR3 receptor targeting was found to be effective in decreasing cell migration, FPR3 could be considered as a potential novel OS therapeutic target.

In the cell migratory assay, we assessed the impact of FPR3 receptor targeting, using the agonistic peptide ligand (WKYMVm) and antagonist ligand (WRW4) on OS cell migration in vitro. The cell migration (scratch) assay was first conducted on the MG63 OS cells. Results from the assay, showed that the receptor agonistic ligand (WKYMVm) had no significant impact on the velocity of OS cell migration, at all of the assayed peptide ligand concentrations (10, 50 and 100 μ M), when compared to the untreated negative control (Figure 4.13) (Mean velocity of cell migration: 10 μ M = 0.00194, 50 μ M = 0.00269, 100 μ M = 0.00220, control = 0.00282 μ m/min). When MG63 OS cells were treated with the receptor peptide antagonist (WRW4), the results showed a contrasting effect on cell migration to that of the agonistic peptide ligand. The antagonist was observed to have a statistically significant negative impact on the velocity of OS cell migration, at all of the assayed peptide concentrations (Figure 4.13) (Mean velocity of cell migration: 10 μ M = 0.00180, 50 μ M = 0.00171, 100 μ M = 0.00176, control = 0.00282 μ m/min).

Thereafter, the cell migration (scratch) assay was conducted on the Saos-2 OS cells. The results showed that the receptor agonistic ligand (WKYMVm), had a significant cell migration stimulatory effect at the assayed concentration of 10 μ M, not observed at other concentrations (Figure 4.14). In contrast, at the 10 μ M assayed peptide ligand concentration, the receptor peptide antagonist (WRW4) had no significant impact on the velocity of OS cell migration (Mean velocity of cell migration: WKYMVm = 0.01521, WRW4 = 0.00439, control = 0.00475 μ m/min). Furthermore, at the 50 μ M assayed peptide ligand concentration, only the receptor antagonist WRW4 produced a significant reduction in OS cell migratory velocity. This decrease in OS cell migratory velocity was the largest and thus, the most significant decrease across all assayed peptide concentrations, when compared to the negative control (Figure 4.14) (Mean velocity of cell migration: WKYMVm = 0.00475, WRW4 = 0.00179, control = 0.00475 μ m/min). Lastly, at the 100 μ M assayed peptide ligand concentration, both receptor agonist and antagonist produced a significant reduction in OS cell migratory velocity. The reductions in migratory velocity were found to be of equal significance, when compared to the negative control, respectively (Figure 4.14) (Mean velocity of cell migration: WKYMVm = 0.00251, WRW4 = 0.00194, control = 0.00475 μ m/min). Statistical significance was calculated using multiple-unpaired T-tests and one-way ANOVA with Welch's correction. Original velocity of cell migration data (μ m/min), for both the MG63 and Saos-2 cells, are presented in Appendix B, tables 2.1-2.4. In the appendix, the standard deviations for each treatment condition and P-values acquired from the conducted multiple-unpaired T-tests and one-way ANOVA are also presented. Appendix B also contains cloud-based weblinks, which lead to ImageJ generated in vitro cell migration assay videos. The videos present in vitro cell migration of MG63 and Saos-2 human OS cells, once treated with FPR3 peptide ligands.

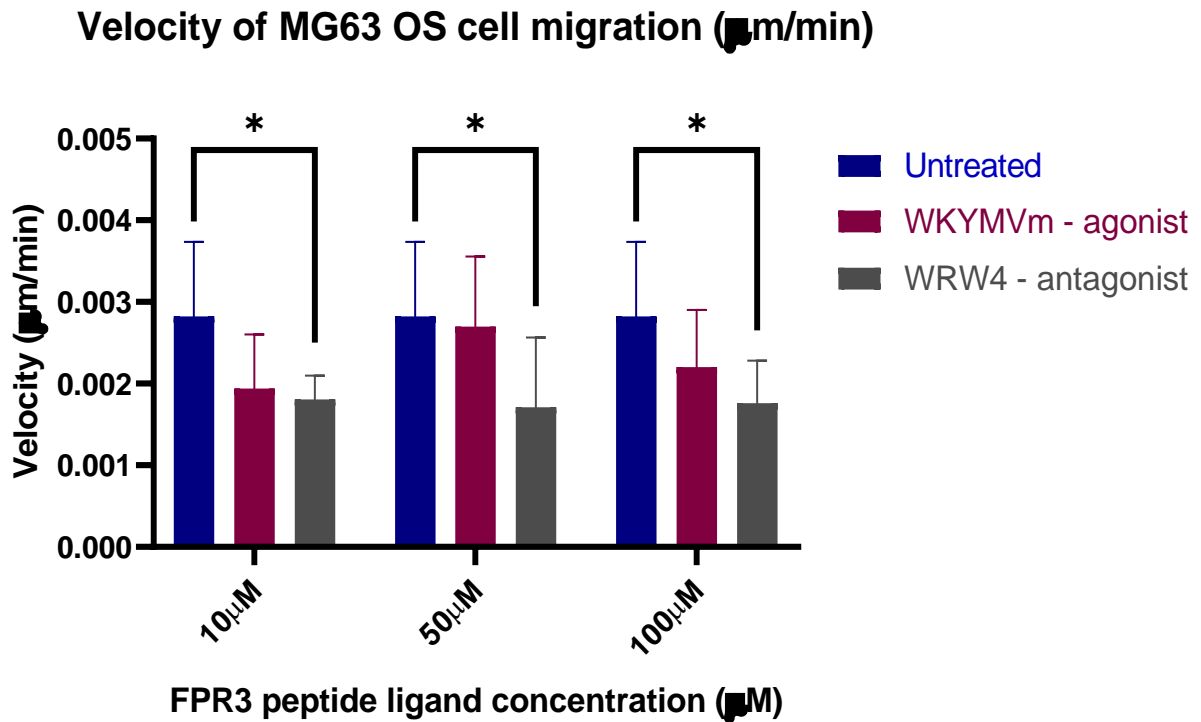


Figure 4.13: *In vitro* cell migration assay conducted on MG63 cells. Figure showing the migration velocity of MG63 OS cells, in response to treatment with FPR3 peptide ligands (WKYMVm agonist and WRW4 antagonist at concentrations of 10, 50 and 100 μM), measured over 24h after a scratch wound. Treatments and controls for each peptide concentration were carried out in duplicate or triplicate. Asterisks represent a statistically significant difference when compared to the relevant untreated control, in an unpaired *t*-test (*: *p*-value <0.05; **: *p*-value <0.01; ***: *p*-value <0.001; ****: *p*-value <0.0001).

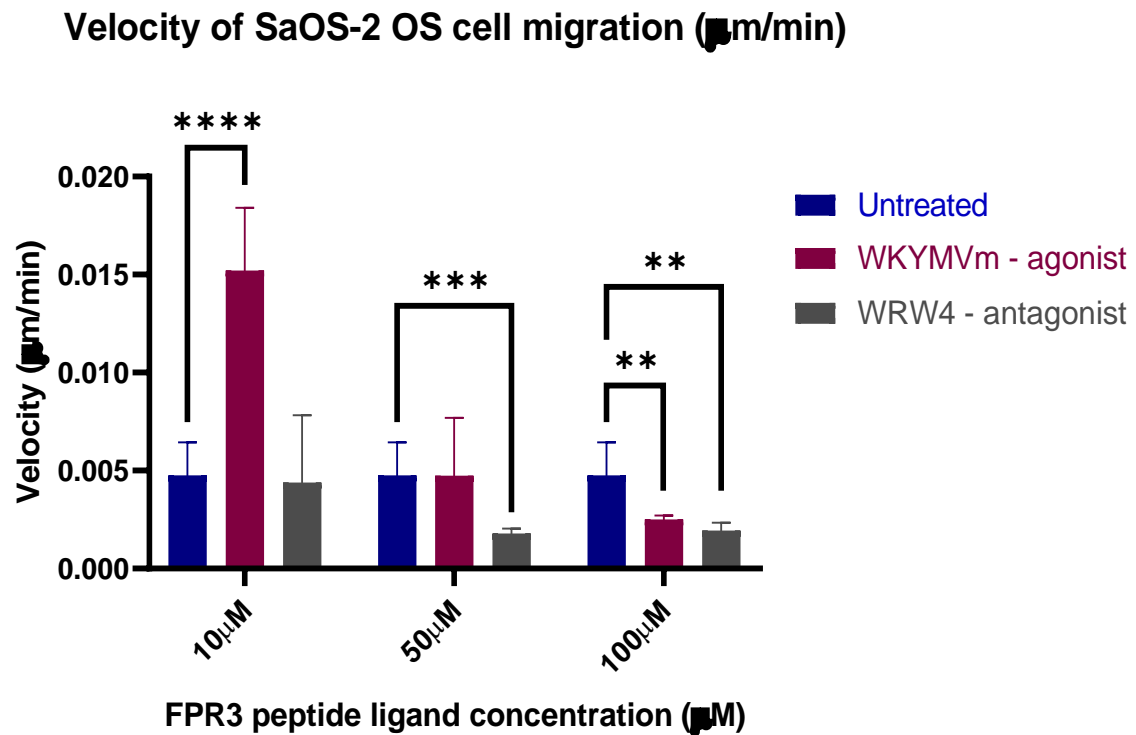


Figure 4.14: *In vitro* cell migration assay conducted on Saos-2 cells. Figure showing the migration velocity of Saos-2 OS cells, in response to treatment with FPR3 peptide ligands (WKYMVm agonist and WRW4 antagonist at concentrations of 10, 50 and 100 μM), measured over 24h after a scratch wound. Treatments and controls for each peptide concentration were carried out in duplicate or triplicate. Asterisks represent a statistically significant difference when compared to the relevant untreated control, in an unpaired t-test (*: p-value <0.05; **: p-value <0.01; ***: p-value <0.001; ****: p-value <0.0001).

4.4 Discussion

The aim of this study was to investigate the therapeutic targeting potential of the immune receptor FPR3, identified to be significantly differentially expressed in OS during in silico analysis presented in chapter 3. This was first done by assessing levels of FPR3 expression in OS, both in vitro and in vivo. Thereafter, the therapeutic efficacy of targeting FPR3 was investigated with an in vitro cell migration “scratch assay”. Whereby, human OS cell lines were treated with receptor specific peptide ligands and the impact of receptor ligand treatment on OS cell migration was quantified. Overall, the results show peptide ligand concentration dependent effects on OS cell migration, in vitro, particularly with the FPR3 antagonist WRW4. Moreover, FPR3 portrayed desirable prognostic effects in Sarcoma clinical cases (presented in chapter 3), which may be transferable to OS due to clinical similarities between these cancer types. In addition, FPR3 showed specific staining of malignant OS cells in OS tissue biopsies, with lack of receptor staining in normal bone tissue and on normal bone cells. Therefore, these results strongly suggest the potential use of FPR3 as a prognostic biomarker in OS, with low receptor expression possibly being associated with poor OS patient survival.

FPR3 belongs to the Formyl-peptide receptor (FPR) family, which is a classical GPCR subfamily with three family members in humans (FPR1-FPR3). Activation of FPR1 and FPR2 by chemotactic agonists leads to myeloid cell migration, increased phagocytosis, and gene transcription (Cattaneo et al., 2013). FPR2 has also been shown to promote the invasion and metastasis of gastric cancer cells, through the stimulation of two of its known endogenous ligands (Hou et al., 2017). Much less is known about FPR3, which is mainly expressed on eosinophils, monocytes,

macrophages, and dendritic cells (Dorward et al., 2015; Nawaz et al., 2020). However, FPR3 expression is also found on endothelial cells and in HUVEC, where it is involved in neovascularisation (Nawaz et al., 2020).

Through the use of *in vivo* and *in vitro* techniques, we aimed to further investigate and validate the OS related therapeutic targeting potential of FPR3, found *in silico*. For the receptor to be proposed as a viable tumour specific therapeutic target for the clinical treatment of OS, the receptor must present a significant upregulation and strong expression within OS tumours, when compared to normal tissue. As an ideal OS therapeutic target, the receptor's expression in adjacent normal (non-cancerous) bone tissue should be minimal or completely null.

Henceforth, to study FPR3 as an immune receptor of interest with OS therapeutic targeting potential, we conducted IHC staining on commercially obtained OS, mixed Sarcoma and NAT tissue microarrays. Thus, we analysed the expression of FPR3 in pre-treatment OS biopsies, differing Sarcoma tumours and (normal adjacent to malignancy) bone tissue, *in vivo*. FPR3 did not display OS tumour stage-specific changes in protein expression, with the receptor being similarly expressed across tissues acquired from localised OS tumours (low and high-grade) and metastasised OS tumours (stage IVB).

Staining of normal (healthy) adjacent bone tissue, showed that FPR3 was strongly expressed on immune cells of hematopoietic lineage, found within the bone marrow tissue of the NAT cores. However, FPR3 was not found to be expressed in normal bone tissue and on the surface of normal bone cells, which was confirmed *in vitro*, with a lack of FPR3 expression observed on normal primary HOBs. Therefore, we identified a clear shift in expression from immune cells in the bone marrow of healthy controls

to cells of osteoblastic lineage, including malignant OS tumour cells and bone lining cells.

Within the mixed Sarcoma tissue microarray, strong FPR3 receptor expression was particularly observed once again in OS tumours and additionally, in Ewing's sarcoma tumours, *in vivo*. In Ewing's sarcoma, a clear shift in expression from immune cells in the bone marrow of healthy controls to cells of osteoblastic lineage was observed. Taken together, these findings indicate that FPR3 expression is induced in the malignant tissue. In breast cancer, FPR3 expression has been associated with the immune microenvironment, and its expression was shown to be accompanied by the activation of typical cancer signalling pathways (Qi et al., 2021). However, when the prognostic effects of FPR3 expression was assessed in Sarcoma patient overall survival, the Kaplan-Meier survival plot showed that lower FPR3 expression was associated with poor overall survival (chapter 3, figure 3.24). This suggests that increased receptor expression is more associated with improved overall survival in Sarcoma patients and therefore, potentially in OS patients. This is in contrast to the prognostic effects of CXCR4 for example, whereby, high levels of CXCR4 expression have been reported to be associated with poor overall survival in OS patients (Y. J. Li et al., 2017). Thus, leading to an increase in investigations assessing the effects of CXCR4 receptor signalling downregulation in OS, with results showing promise in decreasing OS tumour cell growth and metastasis. One study investigated this effect with the use of siRNA technology and reports showed suppression of CXCR4 mediated osteosarcoma cell growth and lung metastases through direct CXCR4 downregulation (Zhu et al., 2018).

Results from the IHC staining of OS tumour and normal bone tissue cores, put forward FPR3 as a tumour specific therapeutic target for possible use in targeted OS therapies

and therefore, potentially improving overall OS treatment. This potential is suggested by the receptor's strong expression in primary OS tumour samples, along with the lack of expression in normal bone tissue. Similarly, the receptor CD74, which was also identified in our study to be a significantly upregulated immune receptor in OS, has also been investigated as a potential key regulator in OS tumorigenesis (Han et al., 2017). Han et al reported CD74 overexpression in 56% of all assayed OS patients and linked the receptor to having a role in OS resistance to cisplatin (Han et al., 2017).

Moreover, through in vitro immunostaining, we aimed to validate and potentially replicate the significant upregulation and strong expression of FPR3, observed in OS patients. Thus, we conducted immunofluorescent staining of two different human OS cell lines (MG63 and Saos-2). We first qualitatively determined the level of FPR3 protein expression in OS in vitro. Contrary to findings from transfected HEK cells and reports of FPR3 localisation to mostly small intracellular vesicles (Klaver et al., 2020; Rabiet et al., 2011), FPR3 staining was observed largely on the plasma membrane of OS cells, thus, indicating a differential role of naturally occurring FPR3 expression in OS. This is especially shown in the confocal cross-section (ZX) image obtained of an FPR3 stained MG63 OS cell (Figure 4.11).

The observed positive staining further validated the significant upregulation of FPR3 protein expression in OS, which we had identified in silico. However, the IF staining results showed that not all cells within the OS cell lines stained positive, with only a subset showing expression of the receptor, thus, indicating cell heterogeneity. Pautke et al conducted an in-depth characterisation of a range of OS cell lines, including MG63 and Saos-2, using different cellular characterisation techniques comparing OS cells to normal human osteoblasts. In the study, the group reported similar heterogeneity (Pautke et al., 2004). In the Pautke et al study, Saos-2 cells were found

to be more osteogenically differentiated than MG63 OS cells, because Saos-2 cells express specific osteoblastic markers, including osteocalcin (OC), bone sialoprotein (BSP), decorin and procollagen-I. Whereas in the MG63 cell line, only a small subpopulation was found to be positive for osteoblastic markers. Importantly, in animal models, Saos-2 cells are highly metastatic whereas MG63 are only mildly metastatic, therefore, further underlining a possible role for FPR3 in OS metastasis (Pautke et al., 2004). This is in line with the results gathered from IHC staining of commercial OS tissue core biopsies, whereby, a strong expression of the receptor was observed on malignant OS cells making up the tumour tissue. Quantification of FPR3 expression with flow cytometry showed that Saos-2 have a greater than two-fold higher expression than MG63 cells (Figure 4.12).

To investigate the impact of the differing levels of FPR3 expression on cell behaviour, a cell migratory “scratch” assay was conducted on both OS cell lines (Saos-2 and MG63), which were treated with the FPR3 receptor agonist (WKYMVm) and antagonist (WRW4) at varying peptide concentrations. In line with the percentage of positively stained Saos-2 cells being two-fold greater than the percentage of positively stained MG63 cells, the response to treatment with receptor agonists and antagonist was much more pronounced in Saos-2 cells compared to MG63 cells. In Saos-2 cells, the FPR3 receptor peptide agonist (WKYMVm) had a significant cell migration stimulatory effect at a concentration of 10 μ M, not observed at other concentrations and therefore, indicating receptor saturation. For MG63 cells, only the receptor antagonist (WRW4) induced a statistically significant reduction in cell migration velocity. However, excessive saturation of the receptor with increased agonistic peptide concentrations, portrays an inhibition of cell migratory stimulation and complete reversal in its effects at very high concentrations (100 μ M).

In relation to the therapeutic efficacy of FPR3 peptide ligands in OS malignancies, an extremely desirable reduction in the velocity of OS cell migration was observed in vitro. However, in the case of FPR3 receptor expression in vivo on OS tumours, the receptor was found to be expressed strongly and aberrantly across various OS tumours from differing primary lesion sites and tumour stages. Therefore, it can be inferred that in vivo treatment of OS tumours with FPR3 peptide ligands and particularly the receptor antagonist (WRW4), a greater therapeutic effect could be achieved to that seen in vitro. In a clinical setting, targeting FPR3 in OS with the use of WRW4 may cause inhibition of downstream signalling and may improve OS clinical management. FPR3 receptor inactivation can result in a depreciation of cell migration levels, in vivo, and therefore, decrease the chances of OS primary tumour metastasis. On the other hand, when survival analysis was conducted on Sarcoma patients in chapter 3, the prognostic effects of FPR3 was determined and results indicated a positive patient outcome when FPR3 expression is higher (chapter 3, figure 3.24). Therefore, due to clinical similarities between OS and Sarcoma, it can be inferred that low FPR3 expression is associated with poor OS patient outcome. FPR3 receptor activation may result in a depreciation of tumour cell migration, in vivo, and therefore, decrease the chances of OS tumour metastasis.

However, evidence of FPR3's importance in carcinogenesis has been previously described in a study investigating biomarkers for targeted therapy in breast cancer. The study reported that, through gene list enrichment analysis, FPR3 upregulation is positively correlated with the upregulation of many carcinogenic pathways. Therefore, highlighting the receptor's importance in cancer progression. FPR3 was identified as a hazard factor in the immune niche of breast cancers and thus, a prognostic

biomarker. Henceforth, FPR3 was proposed and investigated as an attractive therapeutic target in breast cancer (Qi et al., 2021).

Finally, significant improvement in OS patient survival has long been considered a challenge for both researchers and clinicians alike, with advancements in the field of OS disease therapeutics being of utmost importance (Gill and Gorlick, 2021). Since the marked improvement in OS patient survival, observed in the 1970s, patient overall outcomes have not portrayed further significant improvements (Longhi et al., 2006; Lamplot et al., 2013), with the overall prognosis of OS patients remaining poor and markedly unimproved in over 30 years (Kawai et al., 2017). To date, the most common cause of OS related death is tumour metastases to the lungs (Meazza and Scanagatta, 2016). FPR3 receptor specific antagonism using antagonistic peptide ligands like WRW4 showed a reduction in OS cell migration. This result could indicate that targeted blockade of FPR3 signalling with the use of anti-FPR3 monoclonal antibodies, could be considered as an alternate form of FPR3 targeted OS therapeutics. This alternate, monoclonal antibody blockade mediated mode of targeted OS therapy, was previously investigated in a study which proposed the gene SEMA4C as a novel therapeutic target for metastatic OS treatment. In the study, targeted blockade of SEMA4C downstream signalling using monoclonal antibodies, resulted in appreciably slowed tumour cell proliferation and migration, in vitro. Therefore, supporting the concept of SEMA4C targeting as a therapeutic option in OS (Smeester et al., 2020).

The data gathered in this study provides a rationale for FPR3 receptor antagonism or receptor blockade, as potential novel treatment options for patients with metastatic OS. The consolidation of FPR3 therapeutic targeting as a novel OS treatment option, could allow the expansion of the therapeutic portfolio currently available to OS patients

with metastatic disease. Results gathered from this study may also be applied to other cancer types, including Ewing's Sarcoma, in which high levels of FPR3 expression were observed.

In summary, our results show that FPR3 may have the potential in becoming a novel therapeutic target in the treatment of malignant OS. However, an alternate point of view is the prognostic effects that FPR3 has shown to have on the overall survival rate of Sarcoma patients. The Kaplan-Meier plot showed that lower FPR3 expression was significantly associated with poor overall survival in Sarcoma patients (chapter 3, figure 3.24). This strongly suggests that in the case of OS patients, higher expression of the receptor may improve overall patient survival rates. However, this is in contrast to the results gathered from the functional assays conducted in this study. The in vitro cell migration assay showed that treatment with the FPR3 receptor peptide agonist resulted in an increase in OS cell migration for the Saos-2 cells, with no significant effect on OS cell migration for the MG63 cells. On the other hand, receptor inhibition using an antagonistic peptide resulted in a decrease in OS cell migration in both of the OS cell types assayed. However, despite the observed significant decrease in OS cell migration, seen in vitro with the receptor agonist, the overall impact on OS cell migration and therefore, tumour metastasis in vivo, was not at a clinically desirable level.

The assayed receptor ligands are not known to be FPR3 specific, with interactions being reported to take place between the peptides and FPR1/2 (He and Ye, 2017). The lack of receptor specificity may have resulted in lower receptor ligand efficacy when bound to FPR3, thus, resulting in reduced efficacy. Therefore, for further studies, it is important to carry out screening assays to identify more therapeutically efficacious FPR3 receptor peptide ligands. By further using functional migration assay, it may be

possible to identify a more powerful receptor peptide ligand that can decrease OS migration to a more clinically desirable level. In addition, it can be of importance to also carry out genetic studies on the human OS cell lines (Saos-2 and MG63) utilised in this study. Whereby, RNAi knockdown of FPR3 can be used to confirm or more accurately show the effects of receptor antagonism, such as its true impact on OS cell migration.

However, FPR3 portrays a strong indication towards its use as a prognostic biomarker in OS, due to differential staining between malignant OS tumour tissue and NAT from healthy controls. Therefore, suggesting that the increased expression of FPR3 found in OS biopsies, is specifically induced by the malignancy. This, in conjunction with the survival data portraying the prognostic effects of FPR3 in Sarcoma patients, further emphasises a role for FPR3 as a novel prognostic biomarker in OS. Based on the survival analysis results, low expression of FPR3 in OS tumour biopsies would suggest a poor overall survival probability than that of high receptor expression.

5. *Galleria Mellonella Larvae: An Invertebrate Model System to Study Nanoparticle Toxicity*

Aims and hypotheses

The aim of this chapter was to use the larvae of the invertebrate model system *Galleria Mellonella*, to study the biological safety and systemic as well as immune toxicities of a range of inorganic NPs, in vivo. In particular, the biosafety of four inorganic NP variants including SPIONs, IONPs, CNTs and AuNPs was studied in normal controls, after immunosuppression and after a challenge of the larval innate immune system. We hypothesise that some of the inorganic NPs could potentially be used in NP-based drug delivery formulations.

5.1 Introduction

The uniqueness of GM larvae in understanding nanotoxicity

The GM larvae model organism has been developed as an important tool for the preliminary screening of novel drug compounds, such as antimicrobial and fungicidal agents. It is currently used as an *in vivo* model to rapidly and reliably evaluate the activity and toxicity of these compounds (Cutuli et al., 2019). Furthermore, the potential of GM larvae as a model system in toxicology/biosafety studies is further emphasised by the fact that GM larvae are well-established models of the mammalian innate immune system. Therefore, GM larvae are a useful tool to model the complex mammalian innate immune response against exogenous stimuli (Asai et al., 2019). An innate immune response may involve distinct changes to both the cellular and humoral components of the innate immune system, in addition to cellular ROS production (Marshall et al., 2018; Shekhova, 2020).

Due to the increasing use of NPs in industrial and biomedical applications, many concerns with regard to environmental health and their potential to induce DNA damage and cytotoxicity, have been raised over the years (Nurullahoğlu, Eskin and Kaya, 2015). The GM larvae, therefore, represent an attractive tool for the evaluation of nanoparticle biosafety. The GM larvae can provide both an *in vivo* platform for the determination of NP systemic toxicity and a platform for the assessment of nanoparticle immunotoxicity/immunomodulatory effects (Moya-Andérico et al., 2021; Tuncsoy and Mese, 2021). GM larvae have been used as model organisms for *in vivo* toxicity testing, to study the potential adverse effects of NPs released into the environment with respect to their impact on ecosystems and living organisms (Zorlu et al., 2018). However, the GM larvae are yet to be used as an *in vivo* model system

to study the biological safety of inorganic NPs delivered subcutaneously, thereby, determining their potential for use as drug delivery agents in NP-based drug delivery systems.

Currently, targeting and modulating the immune system with NPs is an extremely active area of research. Most novel immunosuppressive strategies involving NPs rely on them being drug delivery agents for small molecule immunosuppressive drugs (Ngobili and Daniele, 2016). However, direct interactions between NPs and the immune system have been long overlooked. It is understood that the immunological activity of NPs is dependent on their physicochemical properties and subsequent cellular internalisation by immune cells (Ngobili and Daniele, 2016). In relation, GM larvae can be a useful tool when evaluating the direct immunosuppressive potential of engineered NPs, along with their potential for complementing current immunosuppressive drugs. The relatively large larval size facilitates inoculation with precise doses of NPs via an injection and hemolymph collection for subsequent analysis (Vertyporokh and Wojda, 2020). Furthermore, unlike some other models, GM larvae can survive at 37°C, thus, allowing for nanotoxicity studies to take place at a standardised human body temperature (Junqueira, 2012; Champion et al., 2016).

Measuring Nanoparticle toxicity in GM larvae

Evidence has shown that the immune system is sensitive to a variety of biologically active agents, including NPs. This sensitivity is associated with the induction of an inflammatory response as well as the accumulation and activation of neutrophils and macrophages (Johnston et al., 2018). Aside from being drug carriers, NPs strongly interact with both the innate and adaptive immune systems, thus having various immunological effects (Engin and Hayes, 2018).

Immunotoxicity can be defined as the toxic effect of xenobiotics on the normal functioning of the immune system, through direct or indirect effects. Direct immunotoxicity results in immune suppression, therefore, leading to a lack of resistance against various pathogens, exogenous stimuli and cancers (Lankveld et al., 2010). NP immunotoxicity/immunomodulation has been demonstrated in multiple studies, with the most common underlying mechanism being cellular oxidative stress due to NP-induced cellular ROS production (Krishnaraj et al., 2016). Some NPs have also been linked with allergic sensitisation, which can increase the likelihood of diseases such as asthma (Di Gioacchino et al., 2011). Therefore, measuring NP interactions with the immune system and determining adverse toxicities they may have on immune components, may be useful methods for determining NP toxicity, in vivo. Gwokyalya and Altuntas reported that the toxic chemical Boric acid induces apoptosis and immunotoxicity in GM larvae, thus, potentiating the use of GM larvae in immunotoxicity studies (Gwokyalya and Altuntaş, 2019).

Furthermore, acute exposure to various NPs can increase the chances of critical illness as well as leading to an increase in systemic toxicities and thus, mortality (Chakraborty et al., 2016). Virulence and toxicity of certain microorganisms or biologically active agents, respectively, have previously been evaluated by quantifying the survival rate of GM larvae post-exposure (Hernandez et al., 2019). Thus, in vivo levels of NP systemic toxicity can be quantified through the determination of GM larval mortality. In relation, larval mortality can be easily quantified as it is characterised by the activation of the melanisation pathway, resulting in the deposition of melanin on the outer cuticle and presenting a black GM larval phenotype (Kay et al., 2019).

Lastly, another important mode of assessing NP toxicity, in vivo, is through the use of microscopy techniques. Fluorescent imaging techniques can be carried out on NP

treated GM larval hemocytes, post larval hemolymph extraction, to visualise and quantify NP immunotoxicity through the determination of hemocyte counts. Furthermore, visualisation of NP internalisation can be used as an indication of GM immune system activation and response against exogenous NP exposure (Villiers et al., 2010).

Present study

In this study, we used GM larvae as a potential high-throughput, economical and robust in vivo toxicity model for assessing nanotoxicity of specific NPs, both with and without treatment with the immunosuppressive drug Cyclophosphamide (Cyclo), for their potential use as drug delivery agents in nanomedicines. We utilised flow cytometry as an accurate and reliable method for the quantification of total circulating larval hemocytes. Furthermore, techniques such as immunocytochemistry, immunohistochemistry and confocal imaging were developed and employed to determine NP biodistribution and localisation in GM larvae.

5.2 Material and Methods

Materials

Acute and chronic in vivo NP toxicity of four different NPs was assessed in this study: superparamagnetic iron oxide NPs (SPIONs), iron oxide NPs (IONPs), carbon nanotubes (CNTs) and gold NPs (AuNPs). The starch coated (SC) SPIONs have no overall charge, an outer (red or green) fluorescent dye coat and are encapsulated in a polysaccharide matrix (starch) coat (Chemicell, Berlin, Germany). Similarly, anionic-SPIONs have an overall negative charge, an outer (green) fluorescent dye coat and no starch matrix coating (Chemicell, Berlin, Germany). All SPIONs have an overall particle size of 100nm and were prepared at a concentration of 300 mg/kg for larval

injections. Similarly, the IONPs are presented as a nanopowder that is not in suspension, with no surrounding surface complexed matrices or fluorescent coating, therefore, the IONPs are non-coated (NC) (Sigma-Aldrich, Poole, UK). Unlike the uniform size of the SPIONs, the NC-IONPs arrive as a nanopowder with an overall particle size in the range of 50-100nm, confirmed by SEM. The IONPs were prepared at a concentration of 300 mg/kg for larval injections, similar to that of the SPIONs. Likewise, three different CNTs were utilised: Oxidised, RAW (unmodified) and Carboxymethyl cellulose (CMC) coated single wall carbon nanotubes (Pondman et al., 2017). All of the CNTs have an approximate length of 600nm and were prepared at a concentration of 200 mg/kg for larval injections. Finally, AuNPs of varying sizes were utilised: 20nm, 40nm, 60nm, 80nm (BBI solution, Kent, United Kingdom) and 100nm (Sigma-Aldrich, Poole, UK). All were prepared at a concentration of 113 mg/kg for injections. Based on the average weight of a GM larva (200 mg), the larvae were injected on average with 0.06 mg (SPIONs and IONPs), 0.04 mg (CNTs) and 0.02 mg (AuNPs).

Sorting GM

Commercially available Galleria Mellonella larvae were acquired from LiveFood UK Ltd (Somerset, United Kingdom). The larvae first needed to be sorted to discard any damaged, already deceased, or pupated larvae. Secondly, to select the larvae for subsequent use in an experiment, the age of the larvae was assessed, and the larvae were checked for infections such as intestinal tract infections. After the larvae were assessed, the required number of young and non-infected larvae, which were identifiable as firm to the touch and not internally pigmented when slightly compressed, were chosen. After sorting, larvae were stored at 4°C until subsequent use.

GM larval NP inoculations

For the inoculation stage of the experiment, young and non-infected GM larvae were chosen. The larvae were separated into groups of ten, by placing them in pre-prepared petri-dishes containing circular cut-outs of Whatman type 1 filter paper. The following experimental conditions were tested: PBS control, PBS plus NPs, Cyclo and Cyclo plus NPs. Depending on the experiment 4 to 8 petri-dishes were prepared the day before the experiment, then closed and taped shut to prevent the larvae from escaping. The larvae were then placed in the fridge, where the colder temperatures would act as an anaesthetic, slowing down their movements and aiding in the prevention of pain that may be felt during injections.

Before injections could take place, the class two hood in which the injections were carried out, the 22s-gauge microlitre syringe (Hamilton, Reno, NV, USA) used for the injections and the lysogeny broth (LB) agar plates used to check for contaminations of the injected fluids, needed to be prepared. The class two hood was turned on and cleaned with 70% ethanol. Next, the syringe was sterilised within the hood. Syringe sterilisation involves taking up 70% ethanol into the syringe, then covering the syringe in tissue, placing it in the hood and then soaking it with 70% ethanol. While the syringe was being soaked, four conical tubes containing 70% ethanol, 70% industrial methylated spirit (IMS) and two tubes of PBS were prepared, for further syringe sterilisation. The tubes were then placed in the hood, in the order stated and the syringe was rinsed with the contents of each tube for its sterilisation. E.g., 70% ethanol is taken up by the syringe, then expelled onto discardable tissue, then this was repeated with 70% IMS and with PBS, to wash off any organic solvent residue. This process was repeated twice and then the tip of the needle was unblocked of any

residual matter using a thin metal wire. The syringe was then passed once more across the sterilisation tubes and was then ready for injections.

On day one of the experiment, appropriate groups of GM larvae were injected with PBS (PBS control and PBS plus NPs conditions). Similarly, appropriate groups of larvae were injected with the immunosuppressant Cyclo (Cyclo and the Cyclo plus NPs conditions). Similar to PBS, 10 µl of the immunosuppressant Cyclo was used (Acros organics, Fisher Scientific, Loughborough, UK), which had a prepared stock concentration of 11 mM and a prepared working concentration of 3.18 mg/ml (12mM), for larval injections. By taking the average weight of larvae as 200 mg, the larvae were injected on average with 0.636 mg of Cyclo, which equals 0.24M. Before larval injections began, 10 µl of 1x PBS (Fisher Scientific, Loughborough, UK) was taken up using the syringe and placed on one half of an LB agar plate, to check for possible contamination of PBS the following day. Thereafter, the first group of larvae to be injected with PBS was taken and 10µl of PBS was injected into the top right proleg, as seen in figure 5.1. Once the first group of ten larvae were injected with PBS, the time of completion was written on the petri-dish and the larvae were placed in an incubator at 37°C in the dark. Next, the syringe was sterilised with two passes across the sterilisation tubes, the needle was unblocked of any residue and afterwards, the syringe was passed across the tubes once more. The second group of ten larvae to be injected with PBS was then taken and each larva was injected in the same way. Once finished, the time of completion was marked on the petri-dish, and the larvae were placed in the incubator. Finally, 10µl of PBS was placed on the other half of the LB agar plate used before the injections, to check for any contamination that may have occurred during the injections. The plate was then placed in the incubator to be checked the following day. The syringe was then sterilised in the way stated, before

the first group of injections, and the procedure involving the LB agar plate and two sets of injections was repeated but with Cyclo as the sample. Larvae were then placed in an incubator at 37°C for 24h.



*Figure 5.1: **GM larval inoculations using a Hamilton syringe.** Image showing a NP or control agent inoculum being injected into the top right proleg, from the first pair of prolegs, starting from the top. All larval inoculations were carried out with the use of a Hamilton microlitre syringe.*

The following day the LB agar plates were checked for possible contamination and the groups of GM larvae were monitored for survival. The class two hood, the LB agar plates, a new PBS sample and new conical tubes for syringe sterilisation were all prepared again in the same way as stated above. The syringe was soaked in ethanol and sterilised by passing it across the tubes the same way as stated above, so it is

ready for the second set of injections involving PBS, to simulate a secondary injection for the control conditions and NPs for the NP conditions. The NPs were prepared by diluting the stock solution with PBS in a class two hood. The sample was then vortexed and placed in a bath sonicator for 1 hour, to separate NP clusters within the sample.

With the NPs in the sonicator, a group of larvae injected with PBS on the previous day was identified by the completion time written on their petri-dish. They were taken out from the incubator once 24h from initial injection had surpassed. Before larvae injections began, 10µl of PBS was taken up by the syringe and placed on one half of an LB agar plate, to check for possible contaminations the following day. Thereafter, for each larva, 10µl of PBS was injected into the proleg, opposite to the one injected during the first set of injections, hence, representing a secondary injection and creating the PBS control condition. The rule of injecting the proleg opposite to the one already injected was repeated for each larva. The time of completion for the secondary injections was then written on the petri-dish and the larvae were placed in the incubator. The syringe was sterilised and unblocked as mentioned above. Next, the NP sample was retrieved from the bath sonicator and another group of larvae that had been injected with PBS on the previous day was taken out of the incubator. Before larvae injections began, 10µl of the NP solution was taken up by the syringe and placed on one half of an LB agar plate, to check for possible contamination of the solution the following day. Then, each larva from the group was injected with 10µl of the NP solution, hence, creating the PBS plus NPs condition. The time of completion was noted, the larvae were placed in the incubator, the NPs solution was placed back in the bath sonicator, and the syringe was once again sterilised and unblocked as stated.

The process stated above was repeated to create the Cyclo control and the Cyclo plus NPs conditions, starting with the group of larvae injected first with Cyclo on the previous day. The larvae in this group were injected with Cyclo again to create the Cyclo control condition. Once finished, 10µl of PBS was placed on the other half of the LB agar plate used before the PBS control condition was created, to check for any contamination that may have occurred during the injections. Finally, the next group of larvae injected with Cyclo on the previous day were injected with the NPs to create the Cyclo plus NPs condition. Once completed 10µl of the NPs solution was placed on the other half of the LB agar plate used before the PBS plus NPs condition was created, to check for any contamination that may have occurred during the injections. Larvae were then incubated at 37°C and monitored over the course of 72h. The flow chart presented below, describes the larval injection and monitoring steps involved during each day of the NP toxicity assays (Figure 5.2).

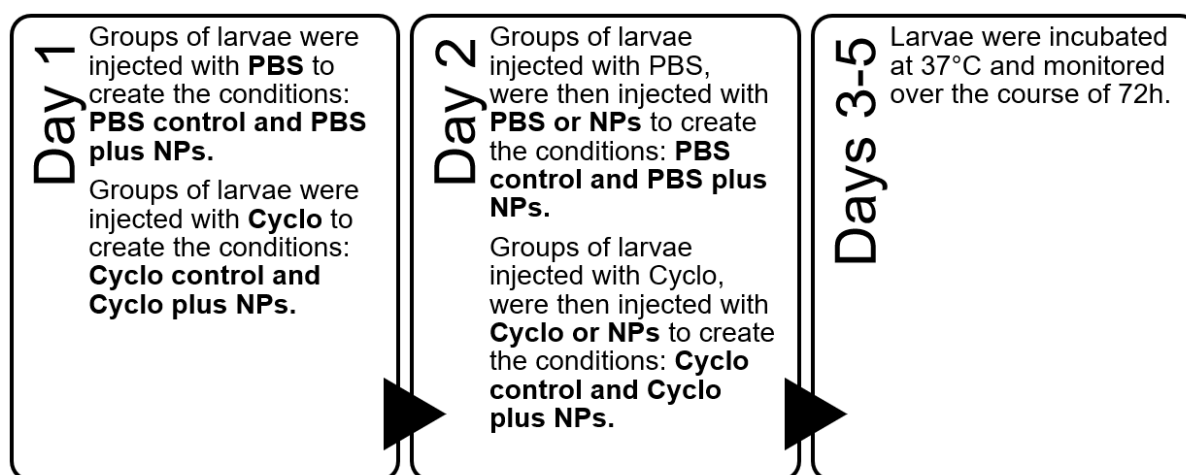


Figure 5.2: GM larval injections and monitoring during NP toxicity assays. A flow chart presenting the various GM larval injections and monitoring steps involved during each day of the NP toxicity assays. Day 1 involved GM larval injections with PBS to begin generating the PBS control and PBS+NP conditions. Similarly, larval groups were injected with Cyclo to generate the Cyclo control and Cyclo+NP conditions. Day 2 involved further larval injections with either PBS or NPs to thus, generate the PBS control and PBS+NP conditions. This was also carried out with the Cyclo treated larvae, with Cyclo or NP injections creating the Cyclo control and Cyclo+NP conditions. On days 3-5, the larvae from the different conditions were monitored over the course of 72h.

GM inoculations (NPs with PA14 bacterial strain)

In this study, we challenged the GM larval innate immune systems (IIS) in order to assess its impact on larval survival and hemocyte cell count over time. As a method of challenging the IIS, GM bacterial assays were carried out with inoculums of the highly virulent bacterial strain *Pseudomonas aeruginosa* (PA14) (Miyata et al., 2003). In addition, the bacterial assays were also utilised in conjunction with the immunosuppressant Cyclophosphamide and 60nm AuNPs, in order to assess the impact of the respective treatments on larval survival and hemocyte count once challenged with the bacterial strain. Like the GM and NP toxicity assay above, a required number of healthy GM larvae were chosen. The larvae were separated into groups of ten, by placing them in pre-prepared petri-dishes lined with circular cut-outs of Whatman filter, for the prevention of larval adherence to the plastic and larval hemolymph cross-contaminations. The following experimental conditions were used: PBS control, PBS plus NPs, PBS plus bacteria, Cyclo control, Cyclo plus NPs and Cyclo plus bacteria.

On day one of the experiment, respective groups of GM larvae were inoculated with 1x PBS to mimic a primary injection. Likewise, respective larval groups were also inoculated with the immunosuppressant Cyclo, prepared at a concentration of 3.18 mg/ml (12mM), to induce immunosuppression. Lastly, respective larval groups were also inoculated with 60nm AuNPs, at a concentration of 113 mg/kg. Before larvae injections began, 10µl of PBS was taken up using the syringe and placed on one half of an LB agar plate, to check for possible contamination of PBS the following day. Thereafter, the first group of larvae to be inoculated with PBS was taken and a 10µl inoculum of PBS was injected into each larva via the top right proleg (Figure 2). The location of the injection was replicated for each larva in the respective groups during

the first set of inoculations. Once each group of larvae was inoculated, the time of completion was written on the petri-dish and the larvae were placed in an incubator at 37°C without light. Next, the syringe was sterilised with two passes across the sterilisation tubes, the needle was unblocked of any residue and afterwards, the syringe was passed across the tubes once more. This process of syringe sterilisation was repeated after the inoculation of each larval group. The remaining groups of larvae to be inoculated with PBS were then taken and each larva was inoculated in the same way. Finally, 10µl of PBS was placed on the other half of the LB agar plate used before the inoculations, to check for any larval transmitted contamination that may have occurred during the injections. The plate was then placed in the incubator to be checked the following day. The procedure involving the LB agar plate and inoculations was then repeated for the Cyclo and 60nm AuNP experimental groups. AuNPs were prepared by diluting the stock solution with PBS in a class two hood. The sample was then vortexed and placed in a bath sonicator for 1 hour, to separate NP clusters within the sample. Thereafter, the NP sample was vortexed to disperse the now separated NPs, prior to inoculations.

The following day, LB agar plates were checked for possible contamination and the groups of GM larvae were monitored. The groups of larvae were then injected as described above. For bacterial inoculations, 10µl of the bacteria sample was taken up by the syringe and placed on one half of an LB agar plate, thereby, allowing for the bacterial load to be confirmed the following day. Thereafter, each larva was inoculated with 10µl of the bacterial sample to be assayed, via the top left larval proleg, that is directly opposite to the top right proleg injections shown in figure 5.1.

The process stated above was repeated to create the Cyclo control and the Cyclo plus bacteria conditions, along with the 60nm AuNP control and the 60nm AuNP plus

bacteria conditions. The larvae in these groups were injected with PBS to create the appropriate controls. Once finished, 10µl of PBS was placed on the other half of the LB agar plate used before the PBS control condition was created, to check for any larval transmitted contamination that may have occurred during the injections. Finally, the groups of larvae that had been injected with Cyclo or AuNPs on the previous day, were inoculated with bacteria to create the Cyclo plus bacteria and 60nm AuNP plus bacteria conditions. Once finished, 10µl of the bacterial sample was placed on the other half of the LB agar plate used before to check for any larval transmitted contamination that may have occurred during the injections. Larvae were then incubated at 37°C and monitored over the course of 72h.

Preparation of bacterial culture

To prepare the bacterial culture for subsequent GM inoculations, 5ml of LB medium (Sigma-Aldrich, Poole, UK) was inoculated with PA14 and the bacteria was left to grow overnight at 37°C with agitation. Thereafter, a pre-determined concentration of 33×10^7 CFU/ml or 33×10^9 CFU per larva was prepared of the PA14 bacterial culture through serial dilutions and thereafter, used to inject the respective GM larvae. Briefly, the stock bacterial culture was diluted 1:100 with autoclaved 1x PBS and an optical density (OD) reading was taken. The OD reading was then used to carry out a serial dilution of the stock culture and obtain the desired pre-determined concentration. The concentration of PA14 had been assayed in previous experiments involving GM larvae, with results showing a significant innate immune challenge, however, a lack of complete population systemic toxicity. Therefore, the concentration was used in the experiments, due to the induction of a significant innate immune challenge with a lack of complete population systemic toxicity allowing for further analyses.

Post-bacterial inoculations, the larvae were left in the incubator overnight and mortality was assessed each hour for a total of 3h while still in the incubator, to measure acute toxicity. The next day, larval mortality was assessed up to the point of 24h since bacterial inoculations and hemolymph extractions were carried out from each condition for further analysis. In addition, a parallel experiment was carried out with the same experimental conditions and methodologies as stated, with the intention of assessing survival past the point of 24h and up to the point of 72h.

Assessing the survival rate of GM

In all of the conducted in vivo toxicity assays, GM larval mortality was assessed on the first day straight after the first set of injections. Thereafter, larval mortality was assessed the following day, before and after the second set of injections with either NPs or the bacterial sample/strain to be assayed. Lastly, larval mortality was assessed the day after (24h post-secondary injections), which is the third and final day of the toxicity assay, up until the point of hemolymph extractions. In addition, parallel experiments were carried out with the same experimental conditions and methodologies as stated. This was done with the intention of assessing larval survival and thus, NP toxicity, past the point of 24h and up to the point of 72h. In all assays, larval mortality was determined as complete melanisation of the larval epicuticle and complete loss of motility (McCarthy et al., 2017), as seen in figure 5.3. Non-melanised larvae were assessed by gentle prodding using a blunt tool. If the larvae reacted to the prodding by showing movement, they were noted as alive, if they did not react, they were noted to be deceased. Mortality was initially assessed each hour for a total of 3h, to measure acute NP toxicity. Thereafter, larval mortality was assessed in hourly steps to accurately acquire changes in larval survival numbers at 24, 48 and 72h. All survival curves were plotted using Kaplan-Meier analysis and statistically significant

differences between survival curves were determined using the log-rank test (Prism 8.0, GraphPad Software, San Diego, CA, USA). NP toxicity experiments were carried out in triplicate for each tested NP variant, with the inclusion of controls and Cyclo treated conditions in each repeat.



Figure 5.3: Larval melanisation and assessment of survival. Image of deceased GM larvae versus healthy larvae. Notice the systemic black melanised phenotype of the deceased larvae, in response to an acquired infection or administered inoculum. Administered test inoculum agents, included the assayed inorganic NPs or bacterial sample/strain included in the NP+bacteria toxicity assay.

Hemolymph extractions

Hemolymph extractions took place 24h after the last set of injections, thus, making it the third day of the experiment. The GM larval hemolymph that was required for fluorescent imaging and flow cytometry in the following steps, was extracted from each larva with the use of a puncture-proof glove, a hypodermic needle and a pipette. The larva was folded in half along its dorsal side and held in one hand, with the puncture-proof glove. The hypodermic needle was used to create an opening along the exposed lateral side, allowing the hemolymph to escape quickly, due to the internal pressure caused by the folding. The escaped, near clear yellow hemolymph, was taken up with a pipette whilst making sure to avoid collecting the intestinal tract which was white in colour. Once the hemolymph was extracted, the larva was discarded by freezing at -20°C.

Histological analysis of larval cryosections

Histological analysis of GM larvae was carried out on cryosections obtained from larvae inoculated with different CNTs or fluorescent SPIONs, to determine the in vivo biodistribution of these NPs.

As a negative control, a group of larvae were injected with 10µl of PBS only. For the test conditions, groups of larvae were injected with 10µl of the respective nanoparticle suspension. For CNTs, Oxidised, RAW (unmodified) and CMC-coated nanotubes were injected at a final concentration of 200 mg/kg. Similarly, starch-coated, and anionic (charged) SPIONs were injected at a final concentration of 300 mg/kg. The inoculated larvae were then placed in an incubator at 37°C without light. During the incubation period, labelled 15ml falcon tubes were prepared for each larval test group, which were used in the subsequent fixation step.

Once 1h had passed since the initial inoculations, half the larvae from each test group were fixed inside the falcon tubes in order to avoid significant body bending and to preserve the molecules of interest. The remaining larvae were placed back in the incubator overnight. Fixation worked better when performed soon after larval injection. This may be due to an exposed injection wound that allows more efficient penetration of the small molecular size PFA. Hence, a 22-gauge needle alone was used to reopen the same initial injection point, prior to adding the larvae to the 2% PFA fixative. Once the groups of larvae were in the fixative, the falcon tubes were placed on a rotary tube mixer for approximately 60-90 minutes, to aid in the penetration of the fixative. Thereafter, the larvae were left to fix overnight at 4°C.

The following day, the fixed larvae were rinsed in PBS and then euthanised/frozen at -20°C for approximately 30 minutes in petri-dishes labelled with the experimental condition. The frozen larvae were then transferred to a Leica CM1860 Cryostat (Leica, Wetzlar, Germany), with a pre-set temperature of -27°C. Within the cryostat, some OCT embedding compound (Fisher Scientific, Loughborough, UK) was first added to appropriately labelled cryomoulds to form the base of the OCT block. Thereafter, the respective larvae were immediately placed in the cryomoulds with a dorsal side up orientation before the compound had time to harden. Next, the compound was given 5 minutes to partially harden and for the larva to fixate in the required orientation. Finally, more OCT compound was added to fill the mould and the OCT block was given approximately 30-40 minutes to fully solidify and turn white in colour.

The opaque OCT blocks were then mounted onto a 25mm cryostat chuck, with the addition of more OCT compound to aid in fixation. The blocks were then shaped by taking thick cryosections (e.g 100µm) until the larval tissue was reached. Thereafter, the OCT blocks were sectioned at 20µm and the resulting GM cryosections were

collected on snowcoat microscope slides (Leica, Wetzlar, Germany), maintained at room temperature. The sections were left to dry for approximately 30 minutes on a hotplate set to 60°C and then refrigerated overnight at 4°C. The 24h samples were treated as described above. Thereafter, all GM tissue cryosections were stained with haematoxylin and eosin (H&E) per the standard staining protocols (Table 5.1).

Table 5.1: H&E staining of larval cryosections. Table describing the standard haematoxylin and eosin (H&E) staining protocol carried out on the GM larval cryosections, for subsequent histological analysis.

Procedure	Time (seconds)
Tissue fixation (70% ethanol)	30
Wash the slide with tap water	
Haematoxylin stain (immersion)	30
Wash the slide with tap water	
Rinse the slide with tap water	
Eosin stain (immersion)	90
Dehydration of tissue	
Immersion in 95% ethanol	10
Immersion in 95% ethanol	10
Immersion in 100% ethanol	10
Immersion in 100% ethanol	10
Immersion in Xylene	30

The H&E stained sections were further counterstained with the cell nuclear dye Hoechst 33342. The slides were placed into an opaque horizontal staining box which was filled with Hoechst diluted 1:10,000 in 200ml of PBS. The sections were incubated at room temperature for 30 minutes and then washed with immersions in PBS, three times at 5 minutes for each wash, again in opaque staining boxes. The stained

cryosections were immediately mounted using DPX histology mounting medium (Sigma-Aldrich, Poole, UK) and analysed using a Cytation 5 automated imaging microscope (Agilent technologies, Inc, Santa Clara, USA). Low and higher magnification coloured bright field images were acquired using a x4 and x10 PL FL phase objective, respectively.

5.3 Results

NP toxicity (in vivo) with the use of GM larvae

GM larvae were injected with different inorganic NPs; SPIONs, IONPs, CNTs and AuNPs, in order to study NP systemic toxicity with or without the addition of the immunosuppressive drug Cyclophosphamide. SPIONs and IONPs were injected at a concentration of 300 mg/kg, CNTs at a concentration of 200 mg/kg and AuNPs at a concentration of 113 mg/kg, with GM larval survival being assessed across a 72h period. The NP concentrations stated above were chosen for these experiments, due to prior in vitro experiments and published literature (Ghosh et al., 2020; Aoki and Saito, 2020; Shukla et al., 2005) reporting a lack of significant cellular toxicity with no in vivo data to support. Survival data was used to generate Kaplan Meier survival plots, and these showed that the tested NPs exhibited varying levels of systemic toxicity, which was dependent on their size, composition and importantly on the immunological state of the larvae (Figures 5.4-5.6). The Kaplan Meier survival plot generated for larvae inoculated with metallic SPIONs or IONPs (Figure 5.4) showed that the starch coated (SC) SPIONs were the least toxic, with no significant larval death observed in the controls and after treatment with Cyclo. In contrast, the survival curves showed that the anionic-SPIONs only induced significant larval death in the controls, but not after immunosuppression with Cyclo. Lastly, unlike the SC-SPIONs and the anionic

charged SPIONs, the non-coated (NC)-IONPs were found to be the most toxic, with significant larval death being observed in both the controls and after immunosuppression with Cyclo.

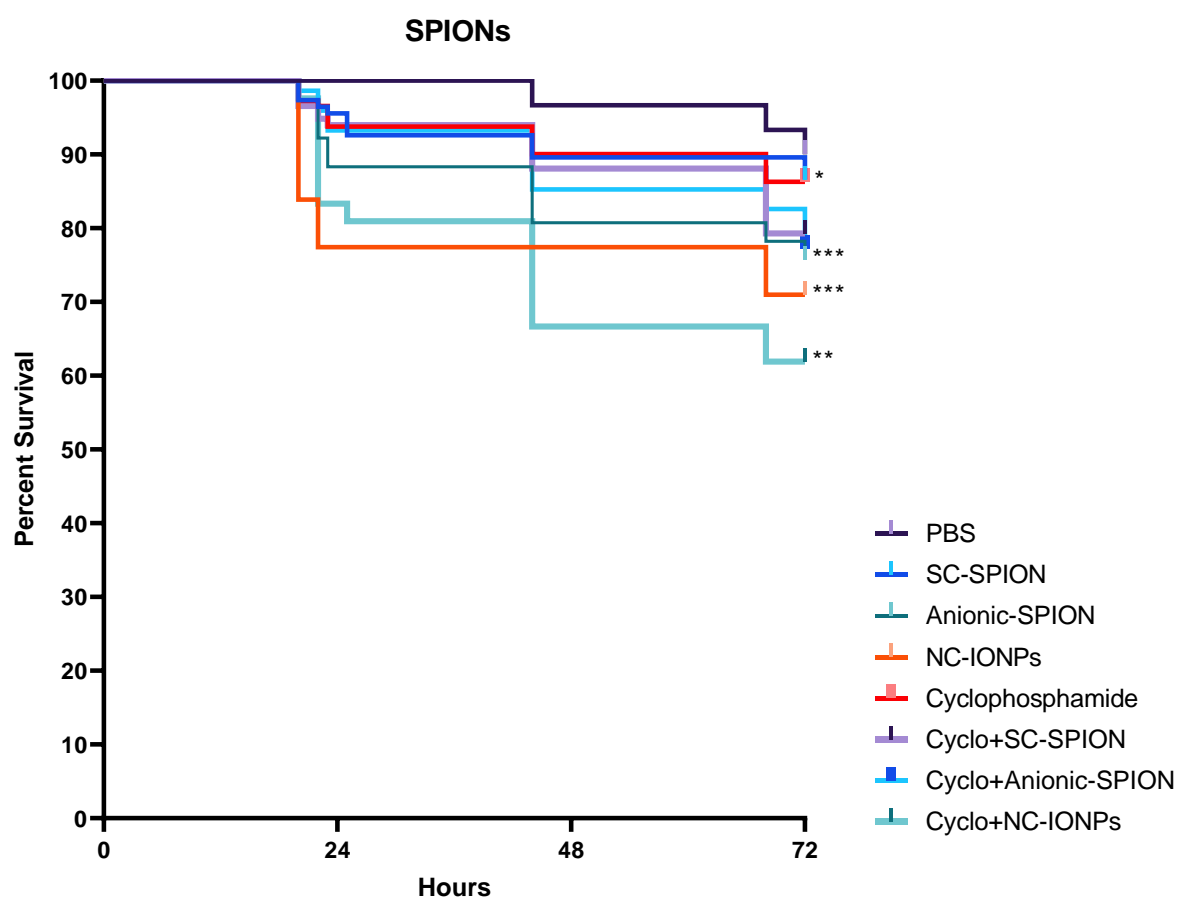


Figure 5.4: Larval survival analysis to determine in vivo toxicity of SPIONs and IONPs. Kaplan-Meier survival curve, presenting percentage survival of GM larvae after injection with SPIONs (starch-coated and anionic charged) and NC-IONPs. Larval survival after injecting with SPIONs or IONPs was assessed in the controls (PBS injected) and immunosuppressed (Cyclo treated state), up to the point of 72h post-NP injections. Asterisks represent a statistically significant difference in larval survival, when compared to the relevant control, in a Log-Rank (Mantel-Cox) test (*: p-value <0.05; **: p-value <0.01; ***: p-value <0.001; ****: p-value <0.0001). $n \geq 45$ per treatment condition with three independent NP toxicity experiments.

The Kaplan Meier survival plot generated for larvae inoculated with CNTs (Figure 5.5) shows that all CNT variants induce significant larval death, with the RAW (unmodified) CNTs being the most toxic in the control. However, no significant larval death was observed after immunosuppression with Cyclo. Similarly, both oxidised and CMC-coated CNTs induced significant larval death in the controls but no significant death after immunosuppression. Furthermore, oxidised CNTs are the least toxic of the CNTs.

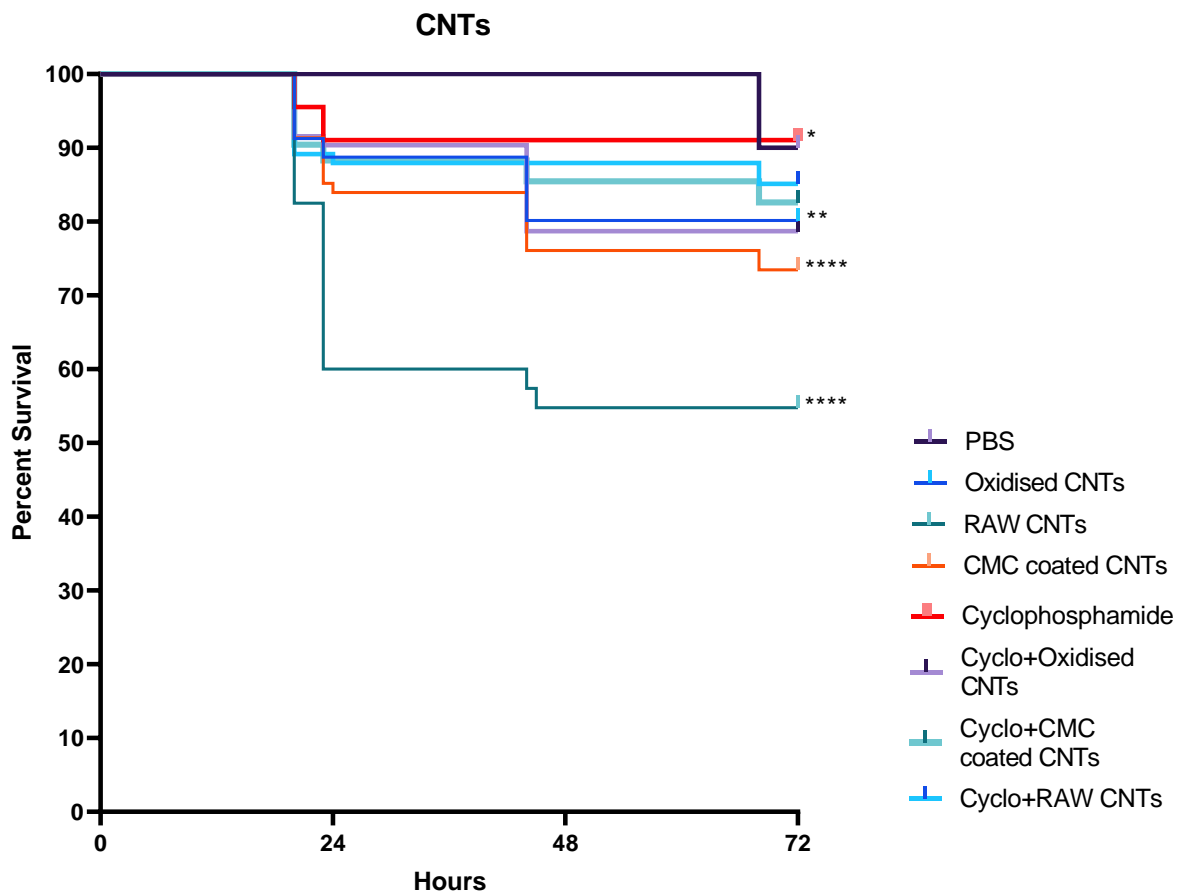


Figure 5.5: **Larval survival analysis to determine in vivo toxicity of CNTs.** Kaplan-Meier survival curve, presenting percentage survival of GM larvae after injection with differing CNTs (Oxidised, Raw (unmodified) and CMC-coated). Larval survival after injecting with CNTs was assessed in the controls (PBS injected) and immunosuppressed (Cyclo treated state), up to the point of 72h post-NP injections. Asterisks represent a statistically significant difference in larval survival, when compared to the relevant control, in a Log-Rank (Mantel-Cox) test (*: p-value <0.05; **: p-value <0.01; ***: p-value <0.001; ****: p-value <0.0001). n≥45 per treatment condition with three independent NP toxicity experiments.

The Kaplan Meier survival plot generated for larvae inoculated with AuNPs of different sizes (Figure 5.6) shows that all the AuNP size variants induced significant larval death in the controls, with exception of the 100nm size variant. Post-Cyclo treatment, significant systemic toxicity was only induced by the 20nm size variant. Overall, in all of the conducted NP toxicity assays, NP-induced systemic toxicity was mild despite statistical significance. Additionally, larval inoculation with PBS had no significant impact on larval survival, with most larval death observed later in the time series. However, the immunosuppressant Cyclo induced significant larval death.

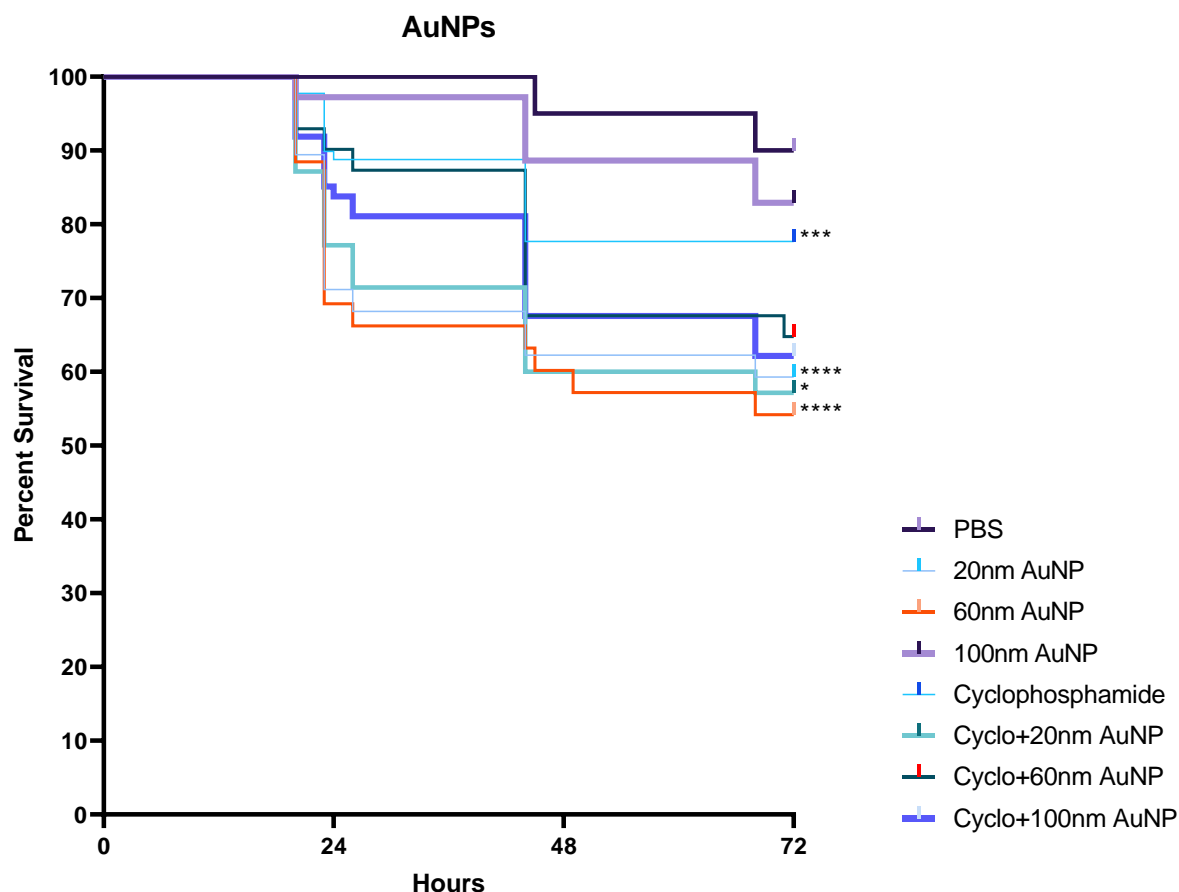


Figure 5.6: **Larval survival analysis to determine in vivo toxicity of AuNPs.** Kaplan-Meier survival curve, presenting percentage survival of GM larvae after injection with AuNPs of differing sizes (20, 60 and 100nm). Larval survival after injecting with AuNPs was assessed in the controls (PBS injected) and immunosuppressed (Cyclo treated state), up to the point of 72h post-NP injections. Asterisks represent a statistically significant difference in larval survival, when compared to the relevant control, in a Log-Rank (Mantel-Cox) test (*: p-value <0.05; **: p-value <0.01; ***: p-value <0.001; ****: p-value <0.0001). n≥45 per treatment condition with three independent NP toxicity experiments.

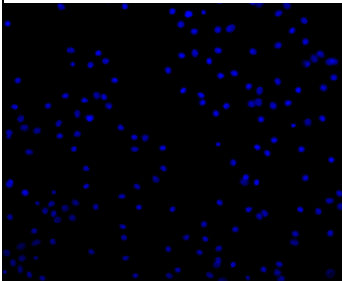
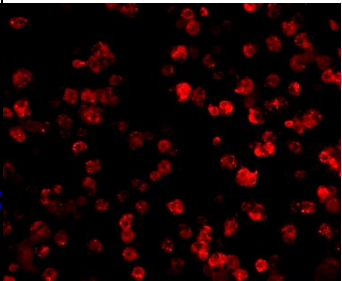

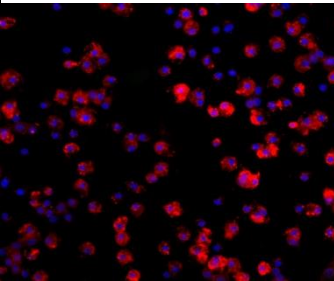
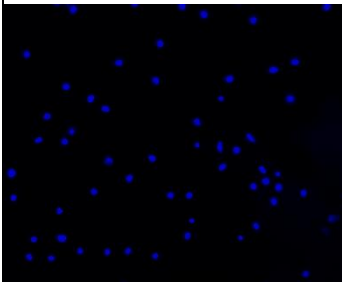
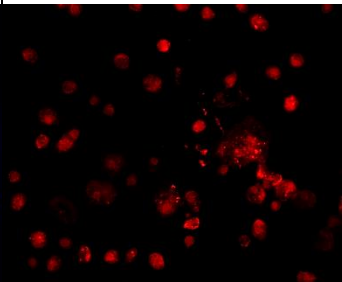
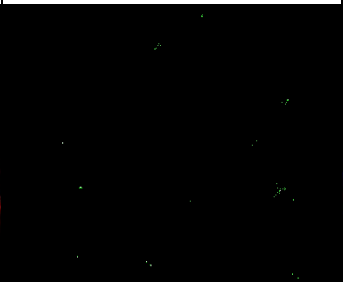
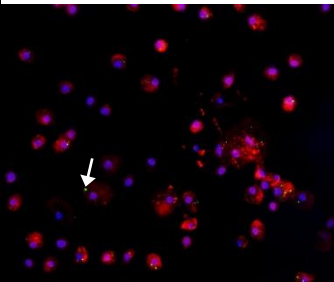
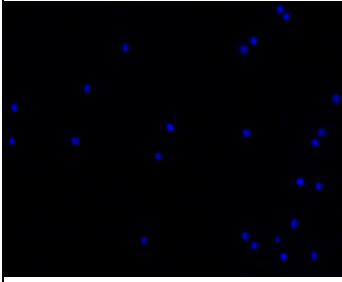
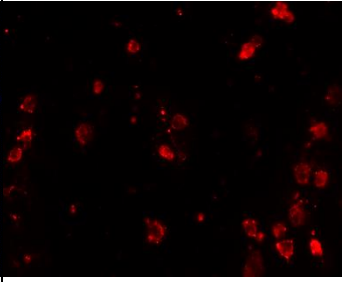
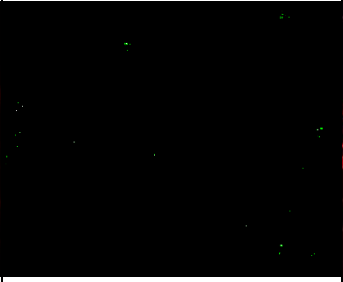
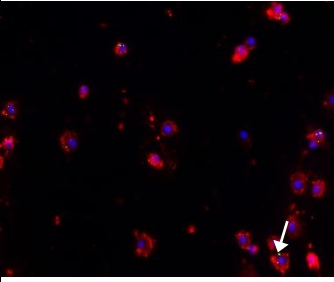
Overall, the gathered percentage larval survival data suggests that none of the tested NP variants had a considerable impact on systemic toxicity and therefore, larval survival. Tables detailing changes to percentage larval survival at varying time points during the complete 72h toxicity assay, for each of the tested NP variants, are shown in appendix C, tables C1-C3. Therefore, we further investigated to see if there was an effect at the tissue/cellular level within the larvae 24h post-NP inoculation. To do so, immunofluorescent imaging of isolated hemocytes, as well as flow cytometry analysis, were utilised to measure the impact of NP inoculation on circulating hemocyte concentration.

NP in vivo biodistribution

Fluorescent imaging techniques were carried out on NP treated GM larval hemocytes, post hemolymph extraction and isolation, for the qualitative analysis of potential NP-induced immunotoxicity and cellular NP internalisation. Furthermore, visualisation of NP internalisation can be used as an indication of GM IIS activation, which subsequently mounts an innate immune response against the NP exogenous stimulus.

In the context of immunology, NPs will often be recognised as foreign materials with the potential to activate various innate immune responses (Jones and Grainger, 2009; Engin and Hayes, 2018). To determine the effect of injected NPs on GM IIS activation, hemocytes were isolated 24h after treatment for visualisation of hemocyte-mediated NP internalisation. Fluorescent microscopy images portray NP aggregates within larval hemocytes, as outlined by the white arrows (Figures 5.7-5.9). Enlarged fluorescent microscopy images showing NP uptake by larval hemocytes are presented in appendix C, figures C1-C3. It can be noted that a single hemocyte was capable of internalising multiple NPs simultaneously, as depicted by the clusters of NPs within a

singular larval hemocyte particularly seen in figure 5.8. Furthermore, fluorescent microscopy images also showed changes to hemocyte density in the treated samples versus PBS control, suggesting NP-induced immunomodulation. Fluorescent microscopy experiments to determine NP in vivo biodistribution were done in triplicate, per assayed NP variant.

<u>Control</u>				
<u>Condition</u>	Nuclei	Plasma membrane	NPs	Overlay
PBS Control				
SC-SPION				
Anionic-SPION				
<u>Immunosuppressed</u>				

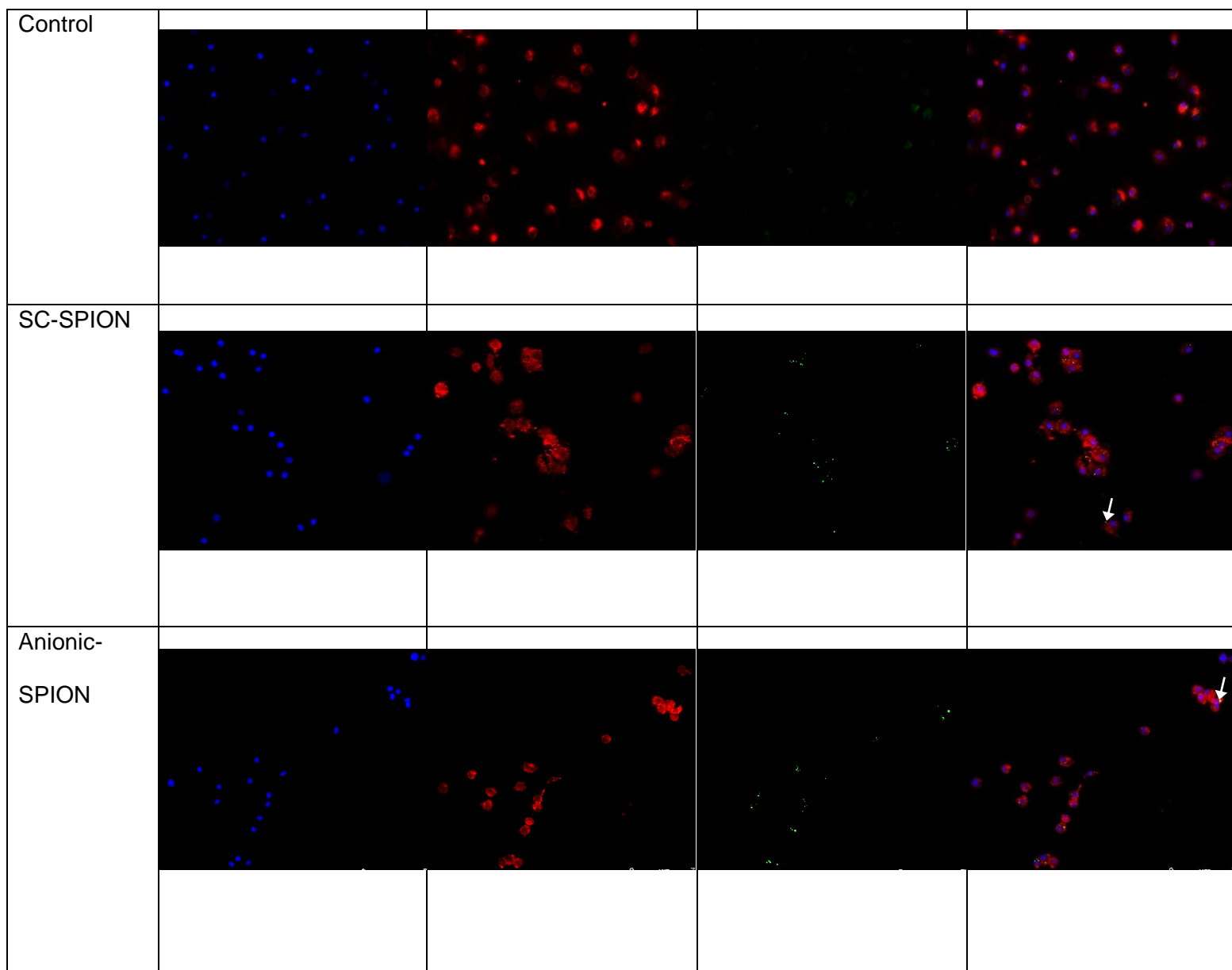
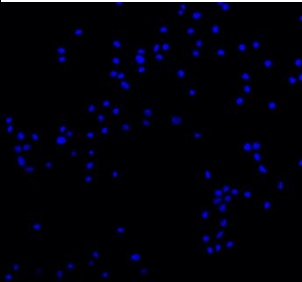
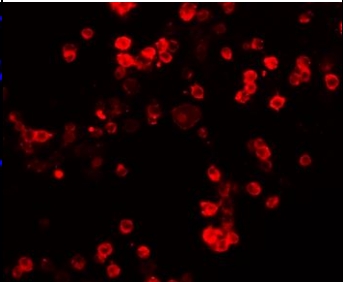
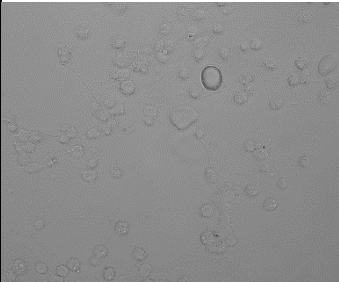
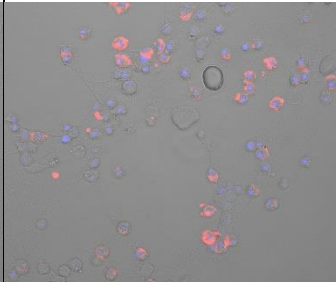
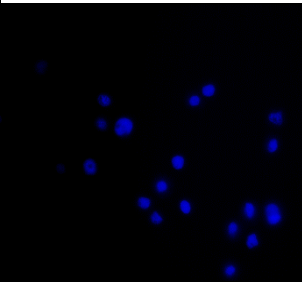
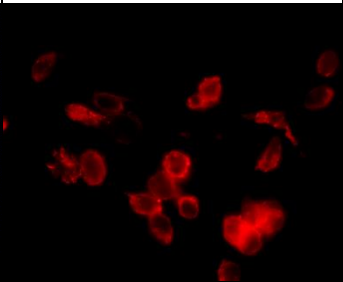
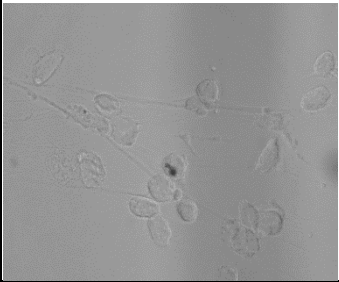
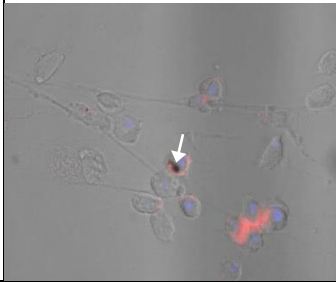
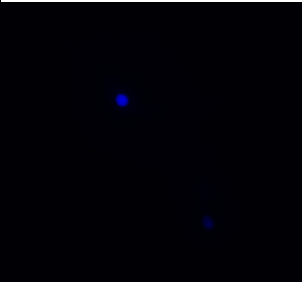
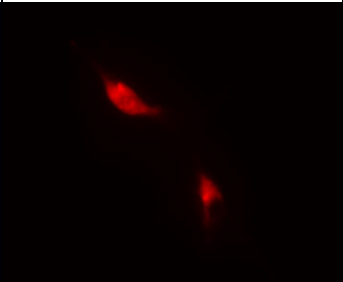
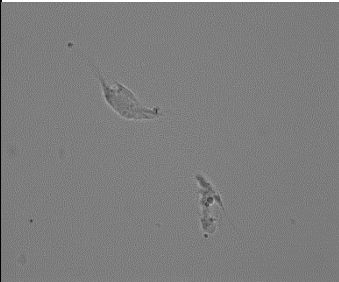
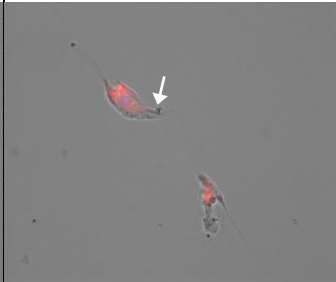
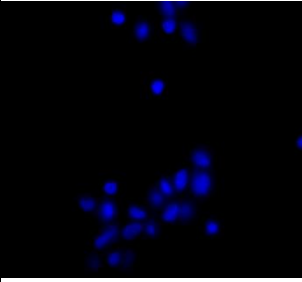
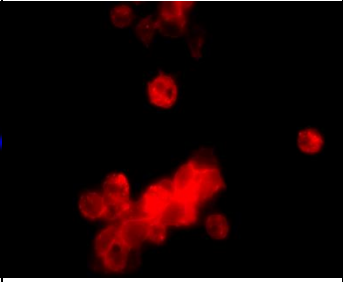
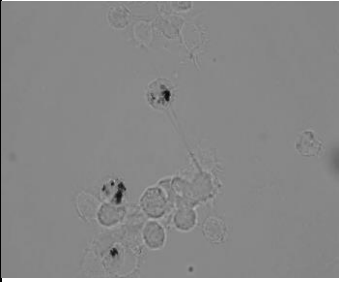
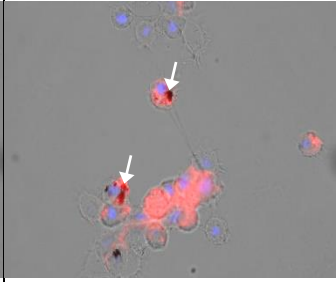


Figure 5.7: In vivo biodistribution of SPIONs in the control and immunosuppressed states. Figure showing x40 magnification fluorescent microscopy images of GM hemocytes, isolated from GM hemolymph, 24 h post-treatment with either PBS or the relevant SPION. Column one shows the blue channel, where HOECHST 33342 has stained dsDNA for the visualisation of cellular nuclei and thus, visualising cellular density. Column two shows the red channel, where the fluorescently labelled lectin stain (Alexa 546 labelled Wheat Germ Agglutinin (WGA)) has stained glycoproteins on the plasma membrane. Column three shows the green channel, which presents green fluorescent SPION aggregates outlined by white arrows in the overlay image. The final column shows an overlay image of all the channels, which can be used to visualise hemocyte NP internalisation. Larval hemocytes, from the respective conditions, were isolated after each of the three independent NP toxicity experiments and stained in duplicate.

<u>Control</u>				
<u>Condition</u>	Nuclei	Plasma membrane	NPs	Overlay
PBS Control				
Oxidised CNT (x100)				
RAW CNT (x100)				
CMC- coated CNT (x100)				
<u>Immunosuppressed</u>				

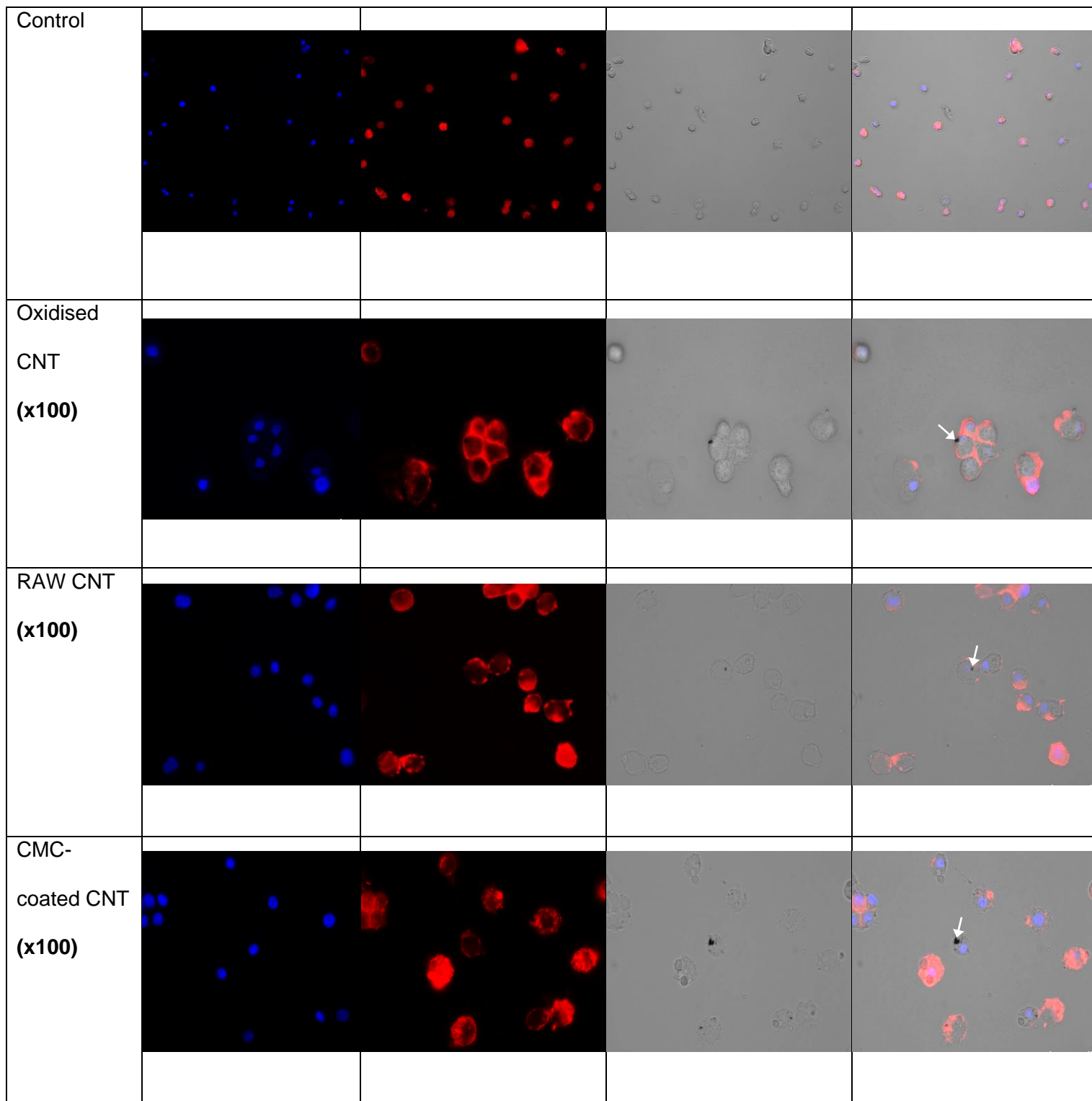
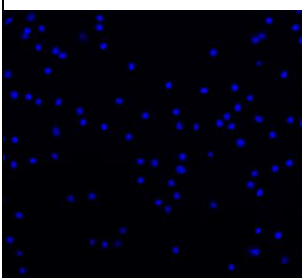
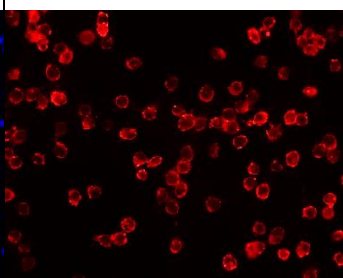
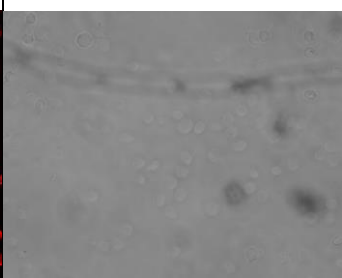
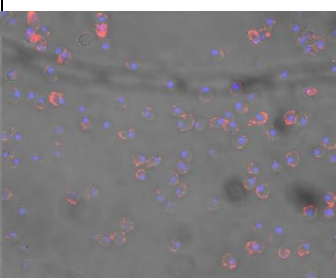
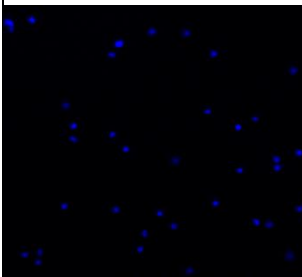
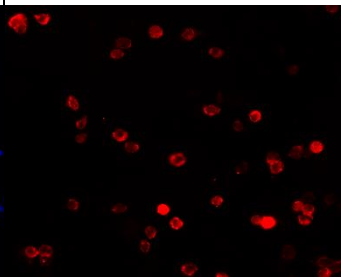
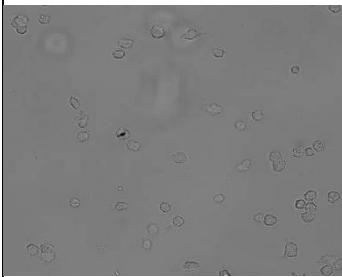
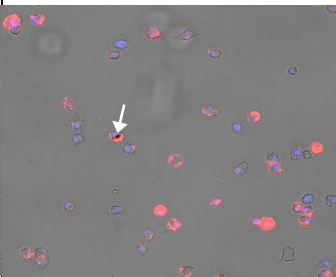
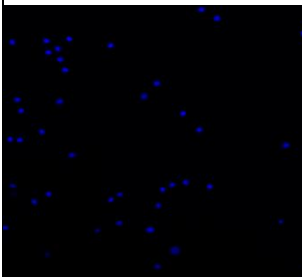
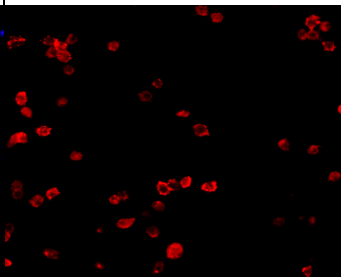
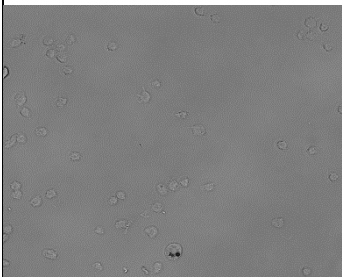
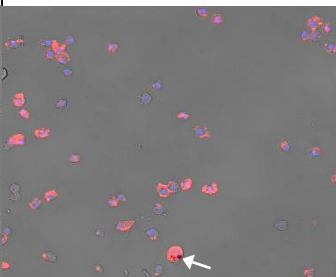
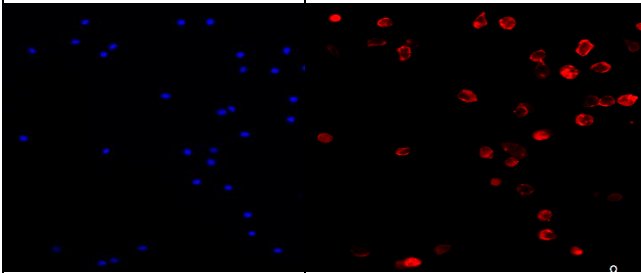
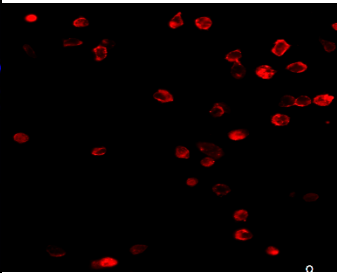
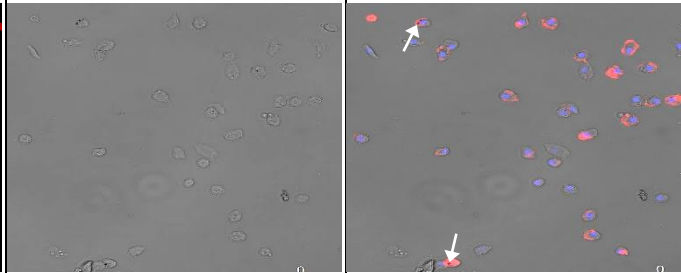
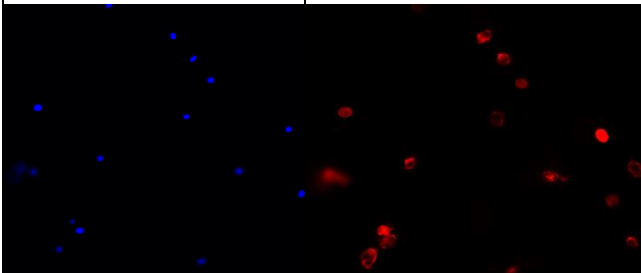
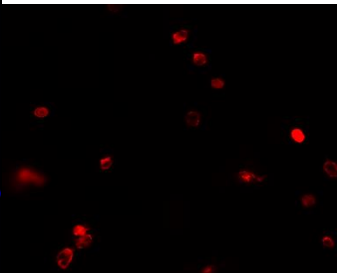
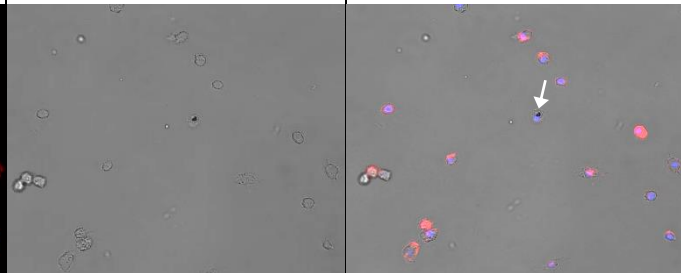
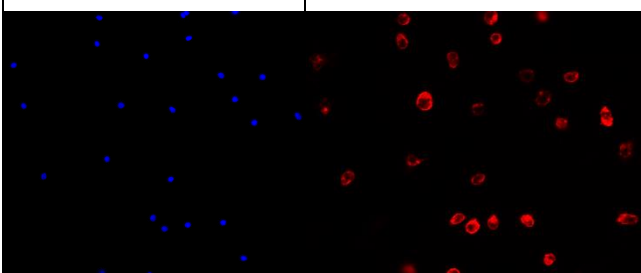
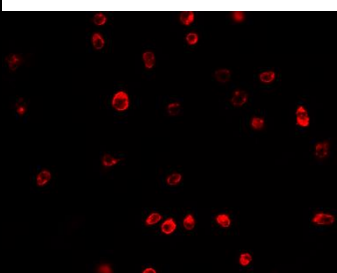
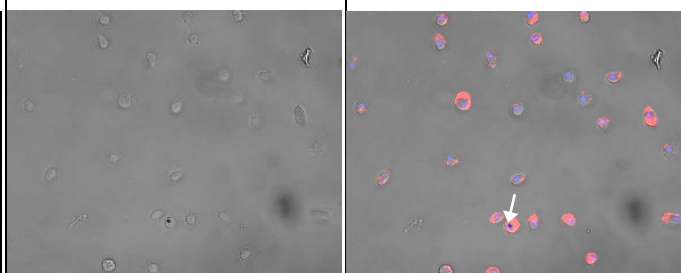
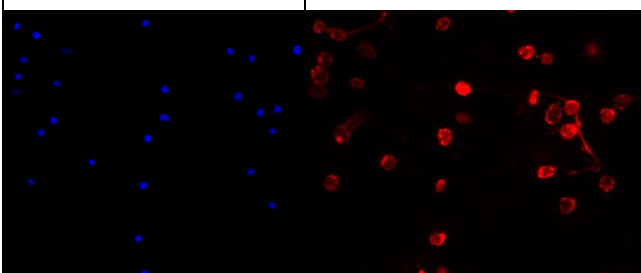
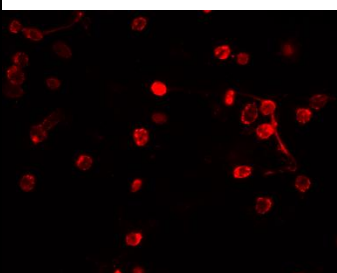
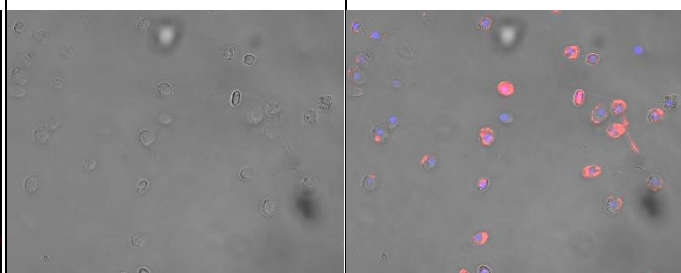
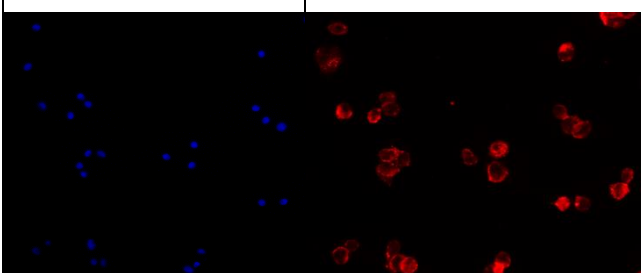
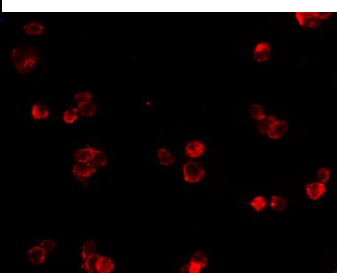
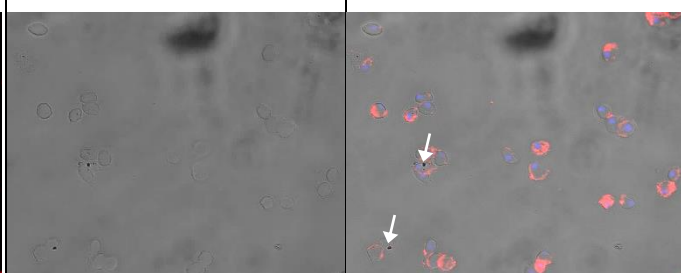


Figure 5.8: In vivo biodistribution of CNTs in the control and immunosuppressed states. Figure showing x40 and x100 magnification fluorescent microscopy images of GM hemocytes, 24h post-treatment with either PBS or the relevant CNT. Column one shows the blue channel, where HOECHST 33342 has stained dsDNA for the visualisation of cellular nuclei and thus, visualising cellular density. Column two shows the red channel, where the fluorescently labelled lectin stain (Alexa 546 labelled Wheat Germ Agglutinin (WGA)) has stained glycoproteins on the plasma membrane. Column three shows the bright field channel, which shows dark, non-fluorescent CNT aggregates outlined by white arrows in the overlay image. The final column shows an overlay image of all the channels, which can be used to visualise hemocyte NP internalisation. Larval hemocytes, from the respective conditions, were isolated after each of the three independent NP toxicity experiments and stained for in duplicate.

Control				
Condition	Nuclei	Plasma membrane	NPs	Overlay
PBS Control				
20nm AuNP				
40nm AuNP				

60nm AuNP			
80nm AuNP			
100nm AuNP			
<u>Immunosuppressed</u>			
Control			
20nm AuNP			

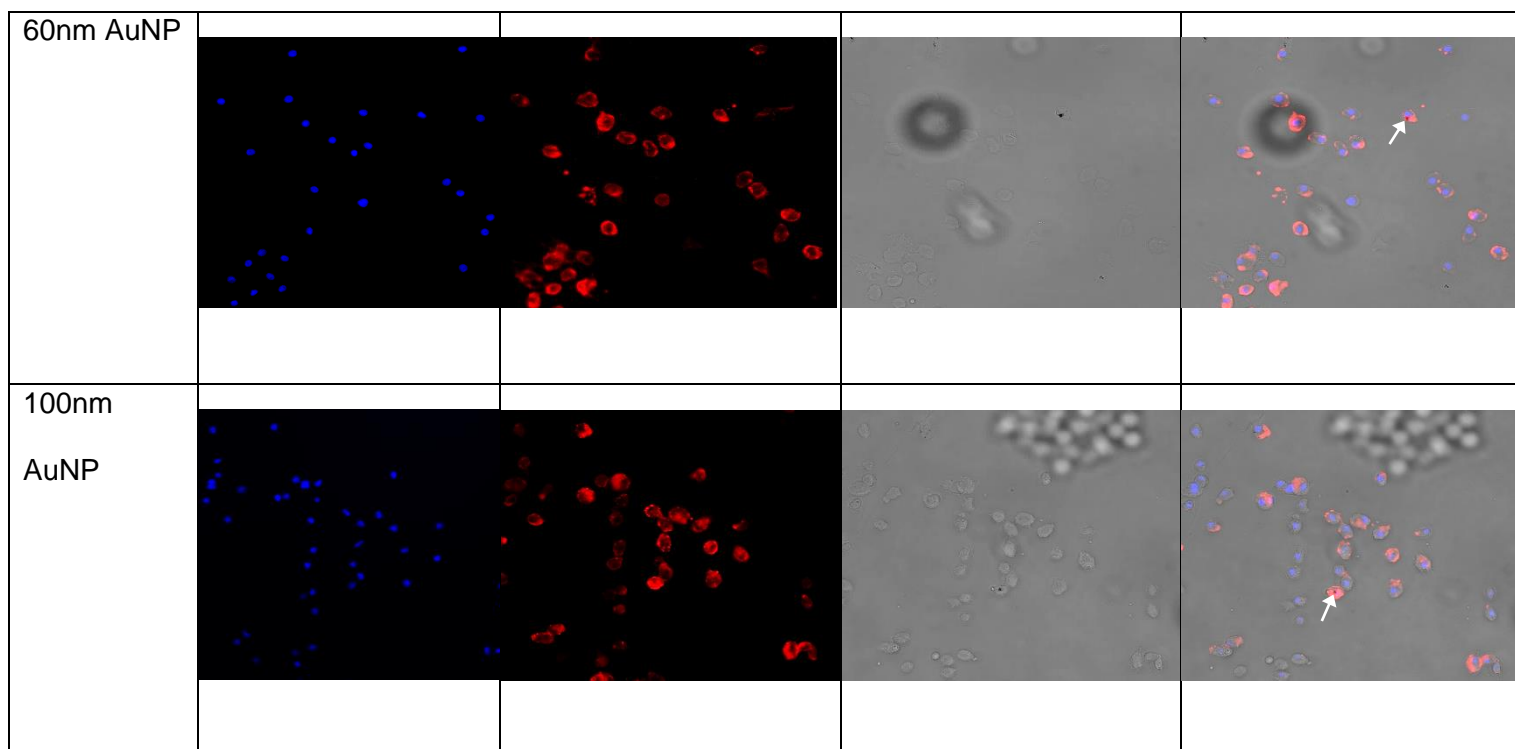
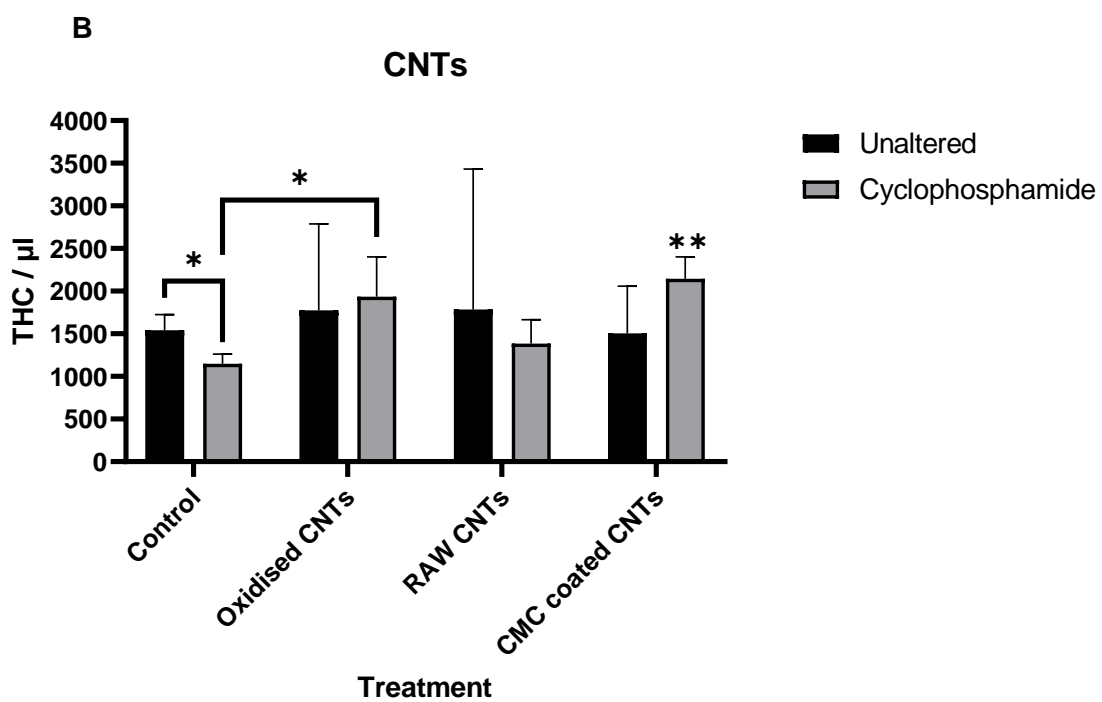
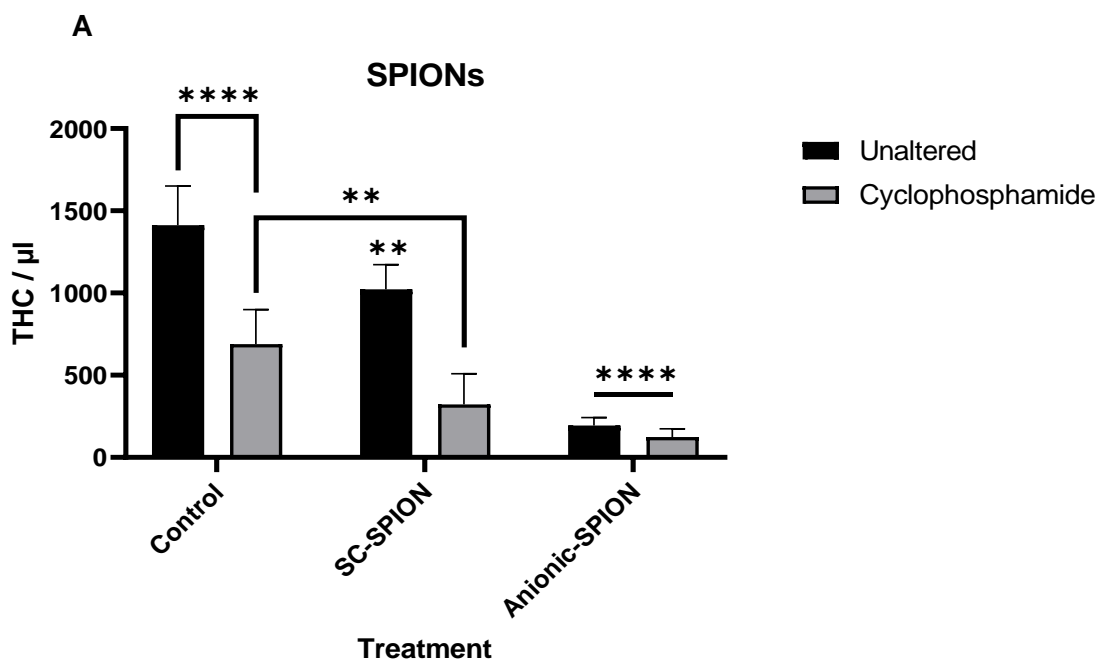


Figure 5.9: In vivo biodistribution of AuNPs in the control and immunosuppressed states. Figure showing x40 magnification fluorescent microscopy images of GM hemocytes 24 h post-treatment with either PBS or the relevant AuNP. Column one shows the blue channel, where HOECHST 33342 has stained dsDNA for the visualisation of cellular nuclei and thus, visualising cellular density. Column two shows the red channel, where the fluorescently labelled lectin stain (Alexa 546 labelled Wheat Germ Agglutinin (WGA)) has stained glycoproteins on the plasma membrane. Column three shows the bright field channel, which will present dark non-fluorescent AuNP aggregates outlined by white arrows in the overlay image. The final column shows an overlay image of all the channels, which can be used to visualise hemocyte NP internalisation. Larval hemocytes, from the respective conditions, were isolated after each of the three independent NP toxicity experiments and stained for in duplicate.

GM hemocyte quantification

Activation of the GM innate immune system can lead to changes in total hemocyte count (THC) (Browne et al., 2013). Therefore, changes in larval THC in response to NP exposure or due to NP-induced levels of immunotoxicity, were measured and quantified with flow cytometric analysis of isolated larval hemocytes 24h post-NP injection (Figure 5.10).

SC-SPIONs produced a statistically significant decrease in THC when compared to the PBS control group. This significant decrease in cell count was then exacerbated in the immunosuppressed state. Like SC-SPIONs, treatment with anionic-SPIONs also induced a decrease in THC, in both the control and immunosuppressed states. However, the decreases in hemocyte counts were of greater significance (Figure 5.10a). Unlike the SPIONs, none of the CNTs produced a significant change in THC. However, in the immunosuppressed state, oxidised and CMC-coated CNTs produced a statistically significant increase in THC (Figure 5.10b). Finally, all AuNP size variants produced significant decreases in larval THCs. These decreases were replicated by the 20, 60 and 100nm AuNPs, in the immunosuppressed state (Figure 5.10c). The 60nm AuNPs in the immunosuppressed state, were used as a representative for the 40 and 80nm AuNPs. This was due to their statistically insignificant differences in larval immunotoxic potential in the controls. For the 60nm AuNPs, the level of immunosuppression was similar to that obtained with the addition of Cyclo. Similar to fluorescent microscopy experiments described above, larval hemocyte quantification through flow cytometric analysis was done in triplicate for the respective larval test conditions in each of the independent NP toxicity assays.



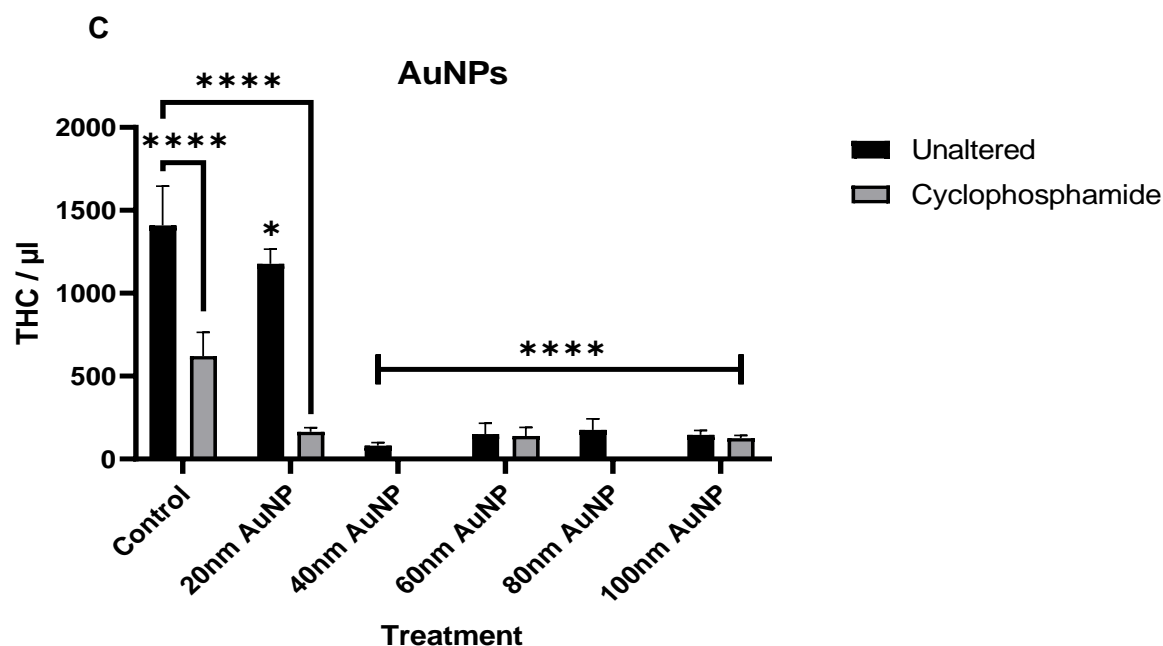


Figure 5.10: **Flow cytometric analysis of isolated larval hemocytes to determine THC.** Graphs presenting mean GM larval THC content per microlitre +/- SD for (a) SPIONs, (b) CNTs and (c) AuNPs, in both the control and immunosuppressed conditions. THC was measured via flow cytometry analysis 24h post-NP injections. Controls were injected with only PBS. Asterisks represent a statistically significant difference when compared to the relevant control, in an unpaired t-test (*: p-value <0.05; **: p-value <0.01; ***: p-value <0.001; ****: p-value <0.0001). Larval hemocytes were isolated after each of the three independent experiments and flow cytometric analysis was carried out on duplicate samples from each condition.

GM survival and hemocyte quantification post-bacterial (PA14) challenge

Flow cytometric analysis of isolated larval hemocytes was used to measure and quantify changes to larval THC post-NP treatment. Results showed that some of the assayed NPs significantly decreased larval THC, in both controls and after immunosuppression (Figure 5.10). Therefore, further investigations were carried out to determine the impact of an immune challenge (PA14) on GM larval survival and larval THC in the NP treated, immunosuppressed and control states.

When GM larvae were challenged with the virulent bacteria strain PA14, they produced an expected pathogen induced innate immune response, which is

represented by a significant increase in THC when compared to the control. However, in the immunosuppressed state, this response was significantly suppressed and the THC was the same as in the Cyclo only treated state. Similarly, pre-treatment with 60nm AuNPs (prepared concentration of 113 mg/kg) for 24h induced a highly significant suppression of THC increase, which was observed in response to PA14 in the control (PBS only treated) larvae. Moreover, this suppression of THC increase was of greater significance after AuNP treatment, when compared to Cyclo treatment. Lastly, Cyclo and 60nm AuNP treatment alone resulted in a statistically significant decrease in THC (Figure 5.11).

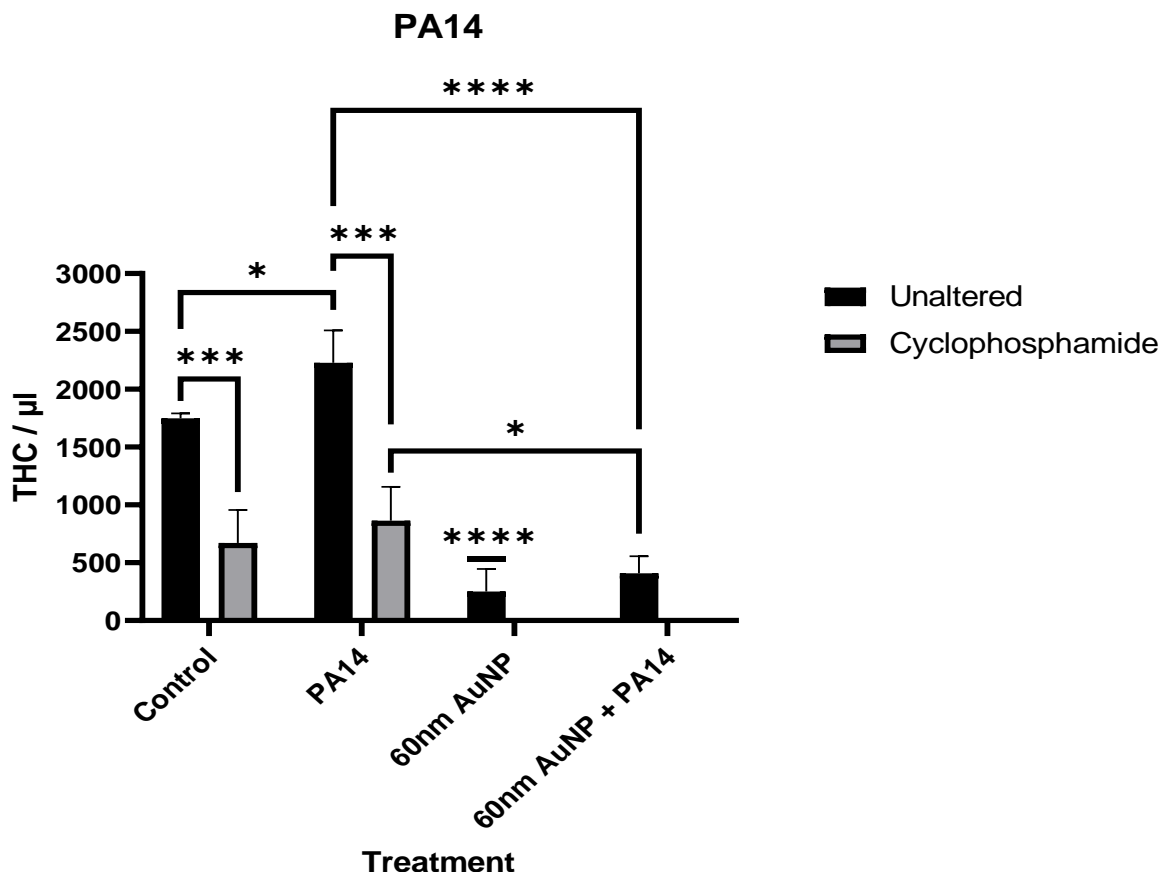


Figure 5.11: Flow cytometric analysis of isolated larval hemocytes to determine THC after immune challenge. Graph representing changes to GM larval THC, induced by Cyclo, PA14 and 60nm AuNP treatments either alone or in combination. THC was measured via flow cytometry analysis, 24h post-bacterial inoculations. As controls, THC of larvae injected with only PBS, Cyclo or 60nm AuNPs was measured. Mean THC from three independent experiments \pm SD are shown. Asterisks represent a statistically significant difference when compared to the relevant control, in an unpaired *t*-test (*: *p*-value <0.05; **: *p*-value <0.01; ***: *p*-value <0.001; ****: *p*-value <0.0001). Larval hemocytes, from the respective conditions, were isolated after each of the three independent NP toxicity experiments and flow cytometric analysis was carried out on duplicate samples from each condition.

When GM survival was assessed after pre-treatment with either Cyclo or AuNP and once challenged with the virulent bacterial strain (PA14), significant larval death 72h post-bacterial inoculation was observed (Figure 5.12). Larval death was more pronounced after immune challenge with PA14, when compared to larval treatment with Cyclo or AuNPs alone. The changes seen in larval survival after AuNP pre-treatment and once challenged with PA14, were of lesser significance when compared to Cyclo pre-treatment and of similar significance when compared to the controls. Like with the NP toxicity assays described above, inoculation with PBS had no impact on larval survival, while inoculation with Cyclo induced significant larval death.

Overall, larval immunosuppression translated into a significant increase in larval death, especially when challenged. Challenging the GM IIS with the PA14 bacterial strain induced significant larval death 72h post-bacterial inoculation. Pre-treatment with Cyclo decreased larval survival by ~40%, with a similar trend being observed after pre-treatment with 60nm AuNPs. Larval IIS challenge after AuNP treatment, decreased larval survival by ~25% (Figure 5.12). All in vivo toxicity experiments were carried out as three independent experiments.

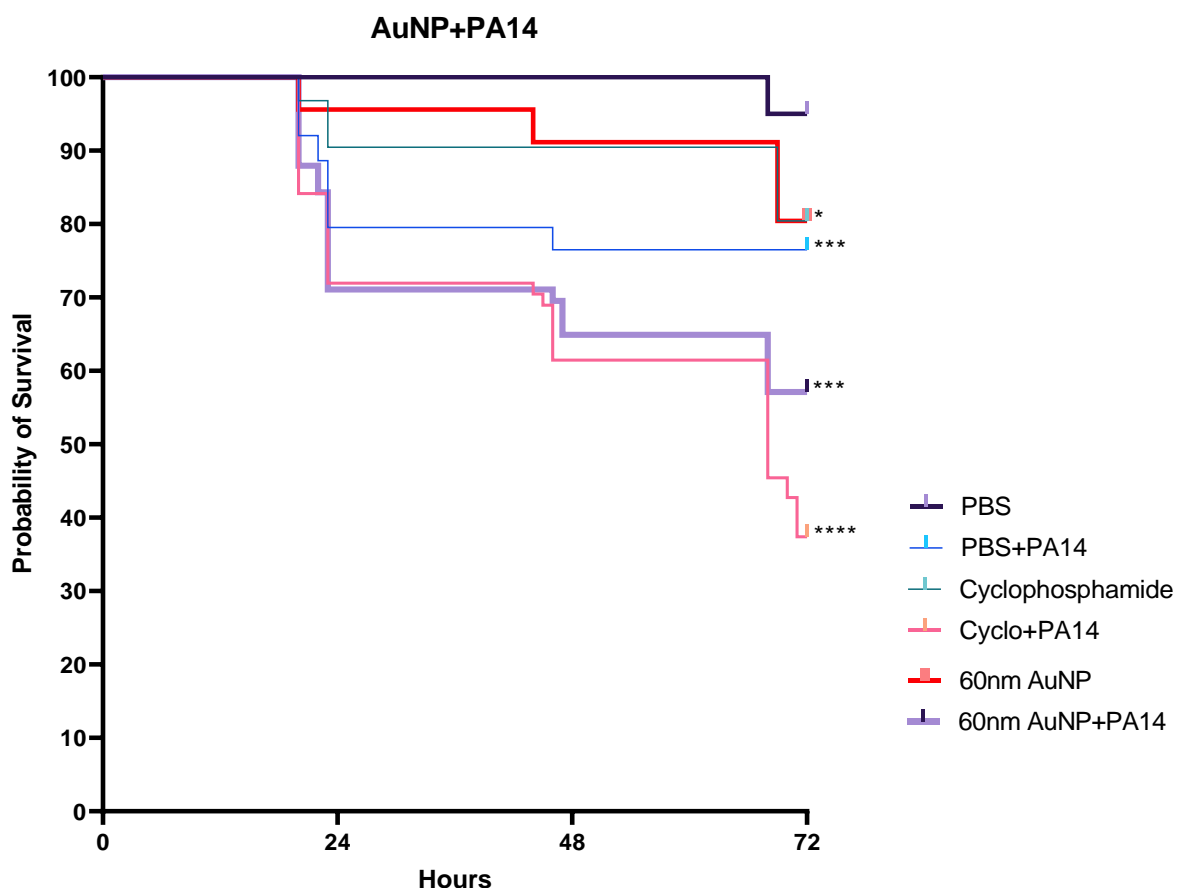


Figure 5.12: **Larval survival analysis to determine in vivo toxicity of AuNPs after immune challenge.** Kaplan-Meier survival curve, presenting percentage survival of GM larvae after inoculation with the bacterial strain PA14. Larval survival after injecting with PA14, was assessed in the control, immunosuppressed (Cyclophosphamide) and 60nm AuNP treated states, up to the point of 72h post-bacterial inoculations. Asterisks represent a statistically significant difference in larval survival, when compared to the relevant control, in a Log-Rank (Mantel-Cox) test (*: p-value <0.05; **: p-value <0.01; ***: p-value <0.001; ****: p-value <0.0001). n≥40 per condition with three independent in vivo toxicity experiments.

Histological analysis of larval cryosections

When levels of potential in vivo immunotoxicity were assessed for the CNT variants using flow cytometric analysis, no significant levels of CNT induced immunotoxicity were observed. However, through GM larval survival analysis, significant levels of CNT induced systemic toxicity were observed. Therefore, in order to investigate the causation behind observed CNT induced larval systemic toxicities, histological

analysis was conducted on GM larval cryosections to determine systemic biodistribution of injected CNTs in vivo.

Frozen tissue cryosections were obtained along the rostro-caudal (RC) axis of GM larvae, as depicted in (Figure 5.13). Thereafter, the sections were stained with a conventional H&E stain, for the localisation of CNTs within larval tissue. CNTs were easily distinguishable from the surrounding larval tissue due to their relative darkness under bright field. The NPs were observed to be mainly associated with larval hemocytes, the outer wall of the digestive tract, larval proleg muscle fascicles and the larval Malpighian tubules (insect counterparts to mammalian kidneys) (Figures 5.15-5.20). However, the lumen of the digestive tract appears to be clear of any CNT deposits. Furthermore, CNT association with larval hemocytes was mostly visualised with the aid of the nuclear counterstain Hoechst 33342. In contrast, larvae inoculated with PBS displayed a healthy anatomical phenotype with no noticeable changes in organ localisation and anatomical shape (Figure 5.14). This lack of change once inoculated with PBS is in agreement with other studies (Kristensen, 2003).

At 1h post-NP injections, RAW (unmodified) CNTs were found particularly in the medial regions of the larvae, mainly associated with the outer wall of the larval digestive tract (Figure 5.17). In contrast, oxidised and CMC-coated CNTs showed smaller, more dispersed and harder to define aggregates along the RC axis whilst being localised near a malpighian tubule (Figures 5.15 and 5.16). Furthermore, for all CNT aggregates at 1h post-injection, larval immune cells were found to be closely associated as indicated by the strong blue fluorescence surrounding them (Figures 5.15-5.17).

At 24h post-injection, oxidised CNTs were localised in small, hard to define aggregates, with persistent localisation in close proximity to the larval malpighian tubules (Figure 5.18). In contrast, CMC-coated CNTs were localised in larger, easily distinguishable aggregates within striate muscle fascicles of the larval prolegs (Figure 5.19). Similar to the oxidised CNTs, the RAW CNTs continued to be localised in large, easily distinguishable aggregates in close relation to the striate muscle fascicles (Figure 5.20). At 24h, larval immune cells were still found to be closely associated with the NPs (Figures 5.18-5.20).



Figure 5.13: **Rostro-caudal axis of a GM larva.** Image portraying the larva of the model organism *Galleria mellonella*, along the organism's rostro-caudal axis, following from left to right. The figure has been sectioned to represent (A) the larval tail, (B) the middle and (C) the larval head. Image from: (Insects as food Feed from Prod. to Consum., 2017).

PBS control:

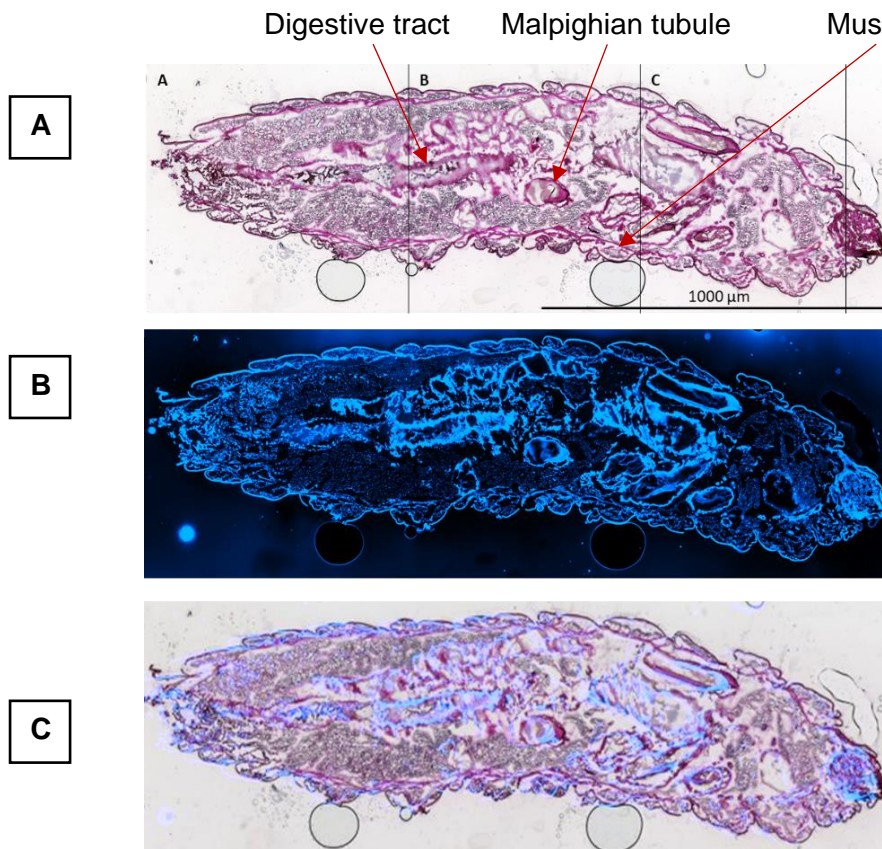


Figure 5.14: Histochemical analysis of larval cryosections: PBS control. Histological analysis of GM larvae, injected with PBS. (A-C) represent x4 magnification overview photomicrographs of the injected larva. (A), shows the coloured bright field (CBF) channel. (B), shows the blue channel (430nm) to observe HOECHST 33342 stained nuclei (dsDNA). (C), shows an overlay of the two channels. (D), is a figure showing respective sections of the larva (tail, middle and head), under x4 magnification. The table shows the CBF channel, the blue channel and finally the overlay channel. Scale bars: A = 1000 μ m pertains to all x4 magnification overview photomicrographs; D = 1000 μ m pertains to all x4 magnification images of the respective sections.

D	Location	Bright field	Dapi	Overlay
	A - tail			
	B - middle			
	C - head			

1h post-NP injections

Oxidised CNTs:

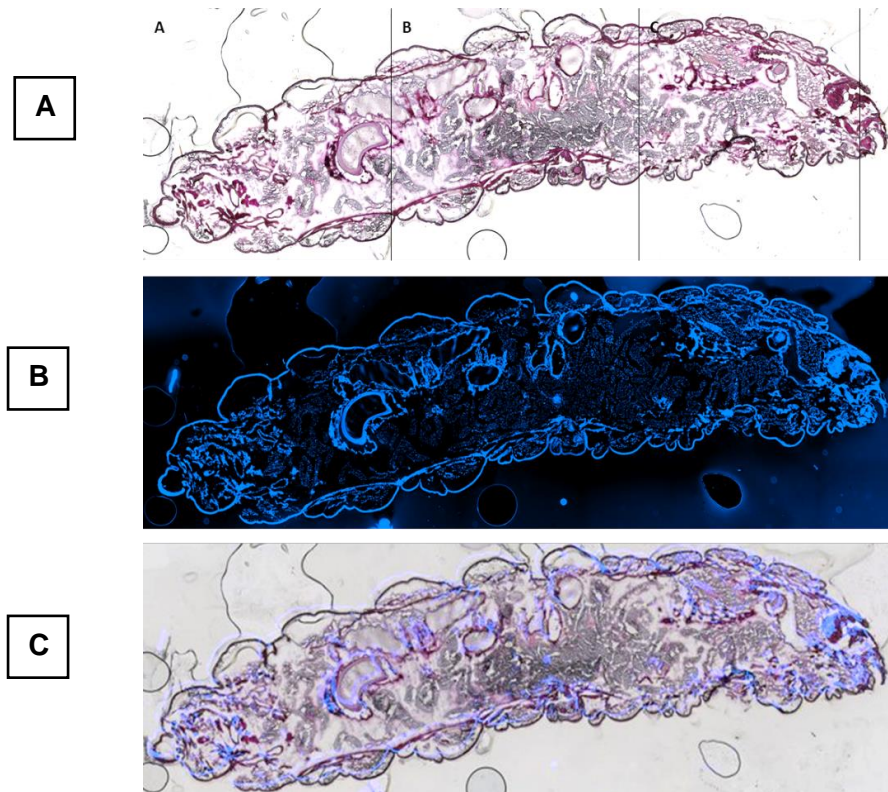


Figure 5.15: Histochemical analysis of larval cryosections: oxidised CNTs. Histological analysis of oxidised CNT biodistribution, 1h post-injection into GM larvae. (A-C) represent x4 magnification overview photomicrographs of the injected larva. (A), shows the coloured bright field (CBF) channel. (B), shows the blue channel (430nm) to observe HOECHST 33342 stained nuclei (dsDNA). (C), shows an overlay of the two channels. (D), is a figure showing respective sections of the larva (tail, middle and head), under x4 magnification. The table shows the CBF channel where the aggregated CNTs are identifiable by their relative darkness and are outlined by red arrows; the blue channel where the arrows outline CNT localisation and finally the overlay channel. Moreover, in the section(s) displaying CNTs, a x10 magnification photomicrograph further details nanoparticle localisation.

D	Location	Bright field	Dapi	Overlay
	A – tail			
	B – middle			
	C – head			

CMC-coated CNTs:

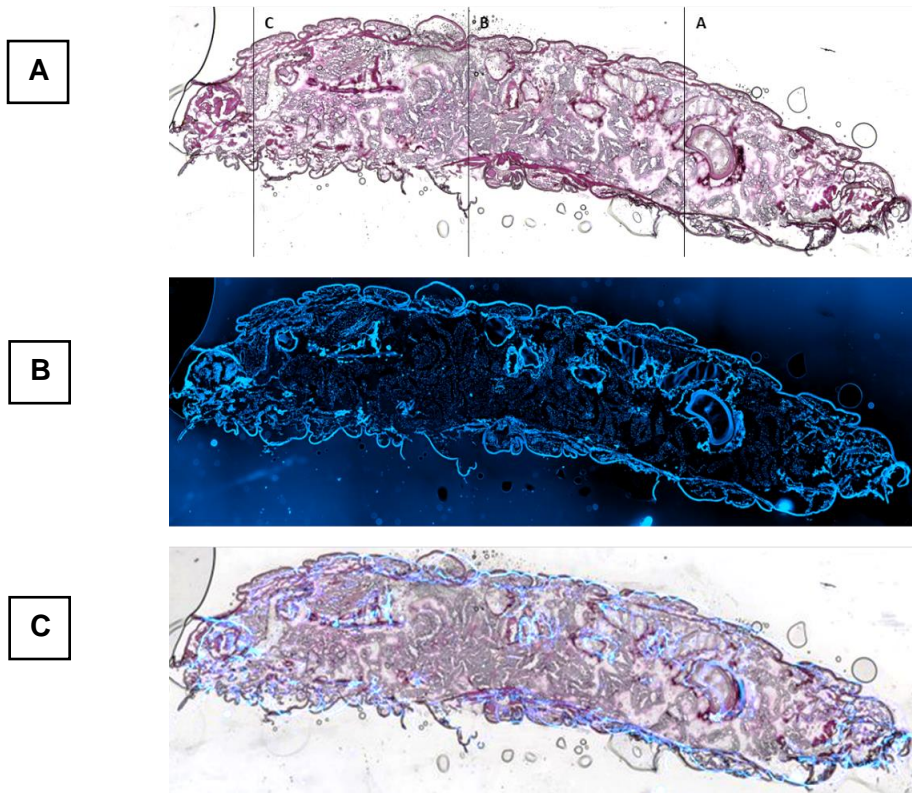


Figure 5.16: Histochemical analysis of larval cryosections: CMC-coated CNTs. Histological analysis of CMC-coated CNT biodistribution, in vivo, 1h post-injection into GM larvae. (A-C) represent x4 magnification overview photomicrographs of the injected larva. (A), shows the coloured bright field (CBF) channel. (B), shows the blue channel (430nm) to observe HOECHST 33342 stained nuclei (dsDNA). (C), shows an overlay of the two channels. (D), is a figure showing respective sections of the larva (tail, middle and head), under x4 magnification. The table shows the CBF channel where the aggregated CNTs are identifiable by their relative darkness and are outlined by red arrows; the blue channel where the arrows outline CNT localisation and finally the overlay channel. Moreover, in the section(s) displaying CNTs, a x10 magnification photomicrograph further details nanoparticle localisation.

D	Location	Bright field	Dapi	Overlay
	A – tail			
	B – middle			
	C – head			

RAW CNTs:

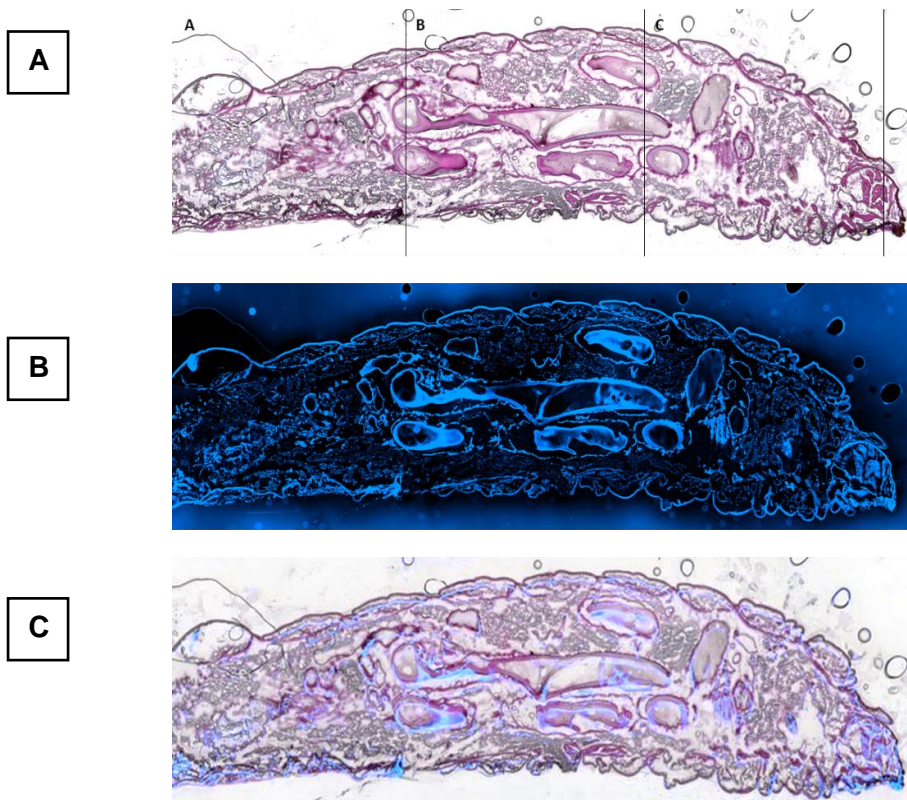


Figure 5.17: Histochemical analysis of larval cryosections: RAW CNTs. Histological analysis of RAW (unmodified) CNT biodistribution, in vivo, 1h post-injection into GM larvae. (A-C) represent x4 magnification overview photomicrographs of the injected larva. (A), shows the coloured bright field (CBF) channel. (B), shows the blue channel (430nm) to observe HOECHST 33342 stained nuclei (dsDNA). (C), shows an overlay of the two channels. (D), is a figure showing respective sections of the larva (tail, middle and head), under x4 magnification. The table shows the CBF channel where the aggregated CNTs are identifiable by their relative darkness and are outlined by red arrows; the blue channel where the arrows outline CNT localisation and finally the overlay channel. Moreover, in the section(s) displaying CNTs, a x10 magnification photomicrograph further details nanoparticle localisation.

D	Location	Bright field	Dapi	Overlay
A - tail				
B - middle				
C - head				

24h post-NP injections

Oxidised CNTs:

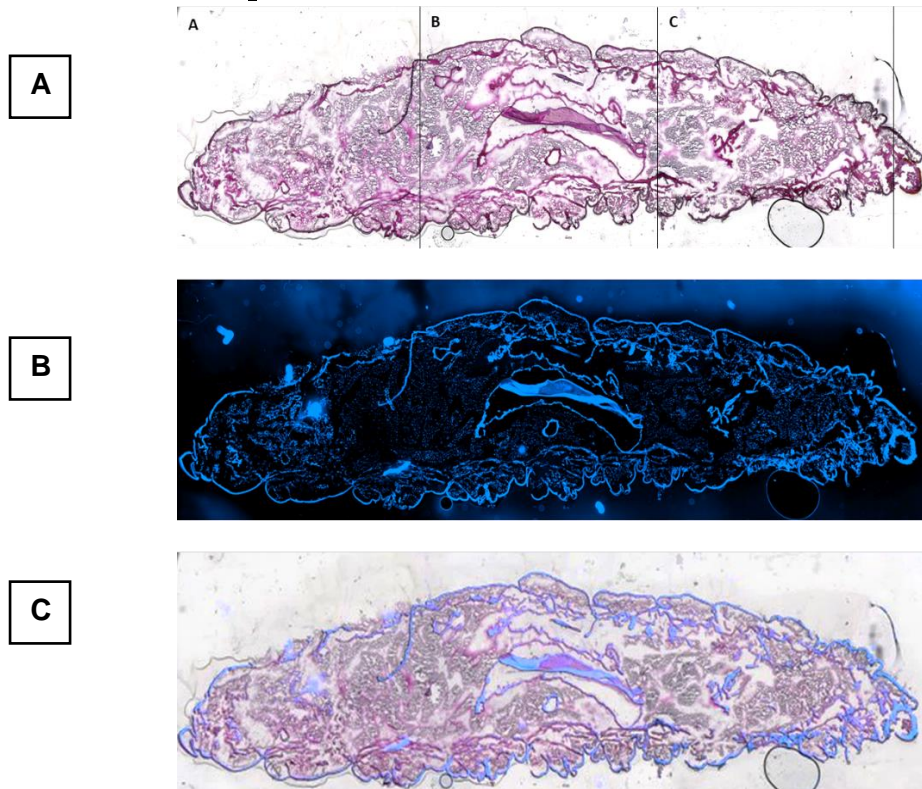


Figure 5.18: Histochemical analysis of larval cryosections: oxidised CNTs. Histological analysis of oxidised CNT biodistribution, in vivo, 24h post-injection into GM larvae. (A-C) represent x4 magnification overview photomicrographs of the injected larva. (A), shows the coloured bright field (CBF) channel. (B), shows the blue channel (430nm) to observe HOECHST 33342 stained nuclei (dsDNA). (C), shows an overlay of the two channels. (D), is a figure showing respective sections of the larva (tail, middle and head), under x4 magnification. The table shows the CBF channel where the aggregated CNTs are identifiable by their relative darkness and are outlined by red arrows; the blue channel where the arrows outline CNT localisation and finally the overlay channel. Moreover, in the section(s) displaying CNTs, a x10 magnification photomicrograph further details nanoparticle localisation.

D	Location	Bright field	Dapi	Overlay
	A – tail			
	B – middle			
	C – head			

CMC-coated CNTs:

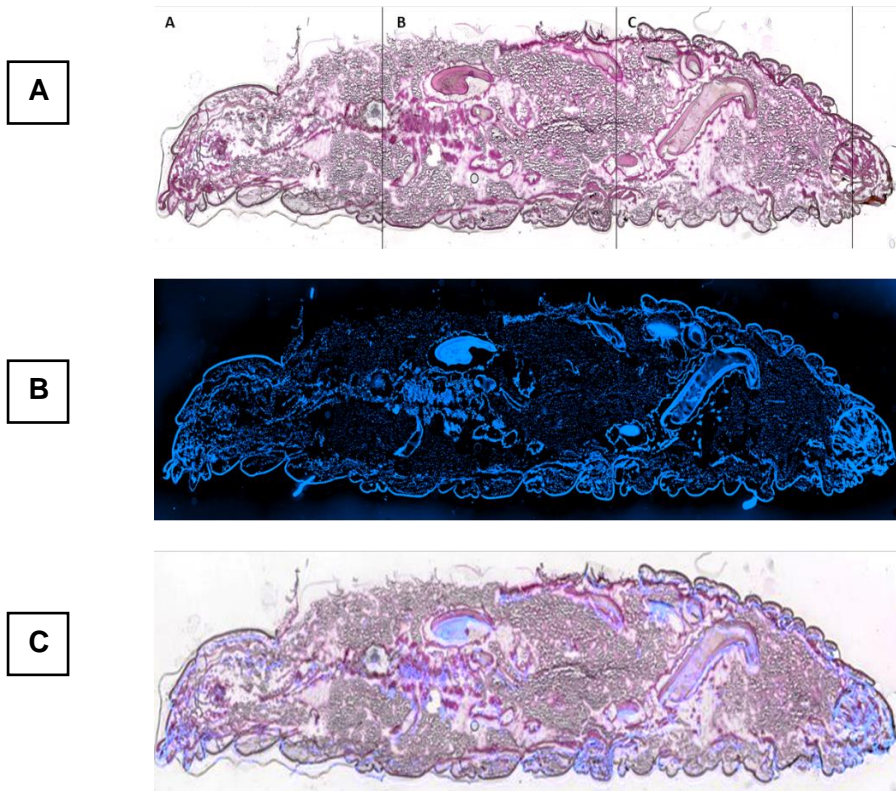
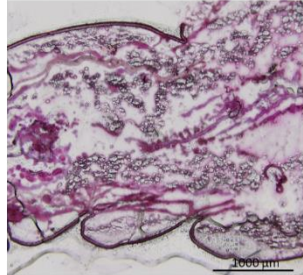
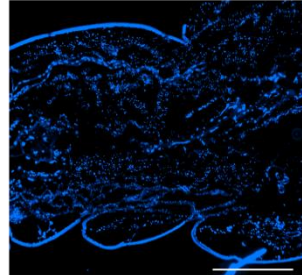
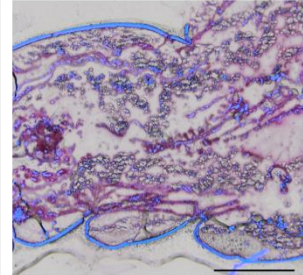
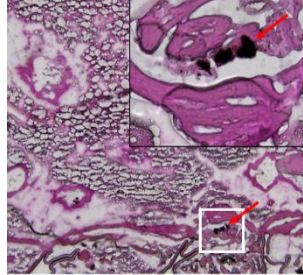
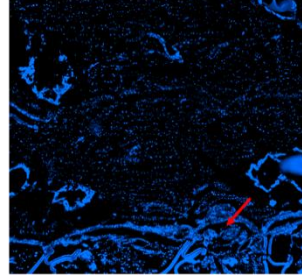
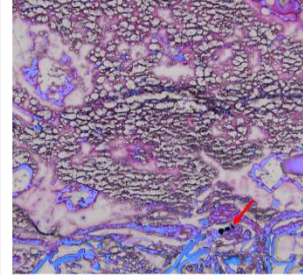
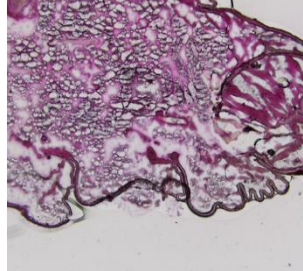
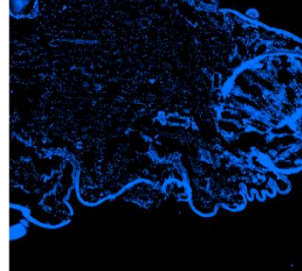
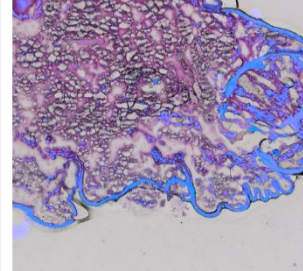


Figure 5.19: Histochemical analysis of larval cryosections: CMC-coated CNTs. Histological analysis of CMC-coated CNT biodistribution, in vivo, 24h post-injection into GM larvae. (A-C) represent x4 magnification overview photomicrographs of the injected larva. (A), shows the coloured bright field (CBF) channel. (B), shows the blue channel (430nm) to observe HOECHST 33342 stained nuclei (dsDNA). (C), shows an overlay of the two channels. (D), is a figure showing respective sections of the larva (tail, middle and head), under x4 magnification. The table shows the CBF channel where the aggregated CNTs are identifiable by their relative darkness and are outlined by red arrows; the blue channel where the arrows outline CNT localisation and finally the overlay channel. Moreover, in the section(s) displaying CNTs, a x10 magnification photomicrograph further details nanoparticle localisation.

D	Location	Bright field	Dapi	Overlay
A - tail				
B - middle				
C - head				

RAW CNTs:

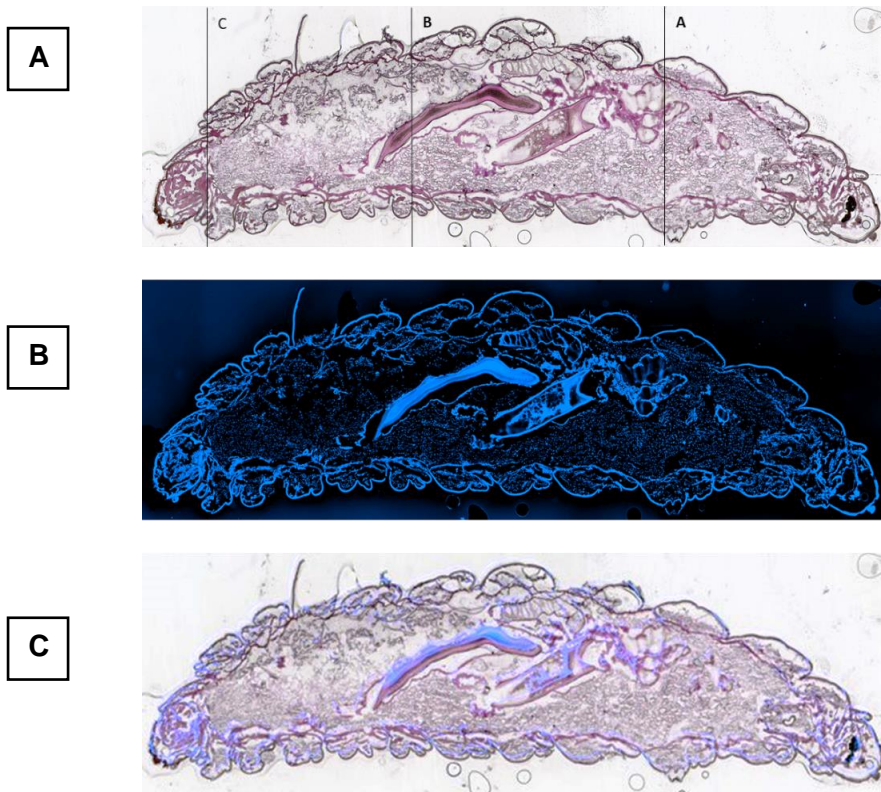


Figure 5.20: Histochemical analysis of larval cryosections: RAW CNTs. Histological analysis of RAW (unmodified) CNT biodistribution, in vivo, 24h post-injection into GM larvae. (A-C) represent x4 magnification overview photomicrographs of the injected larva. (A), shows the coloured bright field (CBF) channel. (B), shows the blue channel (430nm) to observe HOECHST 33342 stained nuclei (dsDNA). (C), shows an overlay of the two channels. (D), is a figure showing respective sections of the larva (tail, middle and head), under x4 magnification. The table shows the CBF channel where the aggregated CNTs are identifiable by their relative darkness and are outlined by red arrows; the blue channel where the arrows outline CNT localisation and finally the overlay channel. Moreover, in the section(s) displaying CNTs, a x10 magnification photomicrograph further details nanoparticle localisation.

D	Location	Bright field	Dapi	Overlay
	A – tail			
	B – middle			
	C – head			

Confocal microscopy of larval cryosections

In addition to the histological analysis that was conducted on cryosections of GM larvae injected with CNTs, we further conducted confocal microscopy of cryosections obtained from larvae injected with green fluorescently tagged anionic-SPIONs. Hence, NP systemic biodistribution along the Z-axis of the obtained 20µm cryosections was determined, as opposed to superficial NP tissue biodistribution determined through histological analysis. Thereby, any potential NP biodistribution and tissue accumulation can be determined, which could help understand the significant levels of systemic toxicity observed with the anionic-SPIONs injected GM larvae.

The frozen sections were obtained along the larval RC axis as described, and the sections were then stained with the nuclear stain Hoechst 33342 to visualise larval hemocytes and other cells within the organism. The injected anionic-SPIONs were easily distinguishable from the surrounding tissue when visualised under the FITC channel. The SPIONs presented a strong green fluorescence being emitted by their fluorescent outer-coating, hence, separating them from the background fluorescence emitted by surrounding tissue. Similar to the above described CNTs, the SPIONs were found to be mainly associated with the outer and/or inner walls of the digestive tract and with the muscle fascicles of the larval prolegs 24h post-injection (Figure 5.22). However, unlike the CNTs, the lumen of the larval digestive tract appears to contain deposits of SPIONs, with confocal imaging presenting NP deposits attached to the inner wall and within the lumen of the tract. In contrast, cryosections acquired from larvae inoculated with PBS displayed no signs of green fluorescent SPION deposits within superficial or deep larval anatomical tissue (Figure 5.23).

At 1h post-SPION injection, the SPIONs were found particularly in the medial to head regions of the larvae, hence, being localised near the inoculation site. The SPIONs were mainly localised near the outer wall of the larval digestive tract, within the lumen of the tract and near to striate muscle fascicles of the larval prolegs (Figure 5.21). In contrast, 24h post-NP injection, anionic-SPIONs were found particularly in the medial to caudal regions of the larvae, mainly associated with the outer and inner walls of the larval digestive tract. Furthermore, the NPs were again found within the lumen of the digestive tract and within the striate muscle fascicles of the larval prolegs (Figure 5.22).

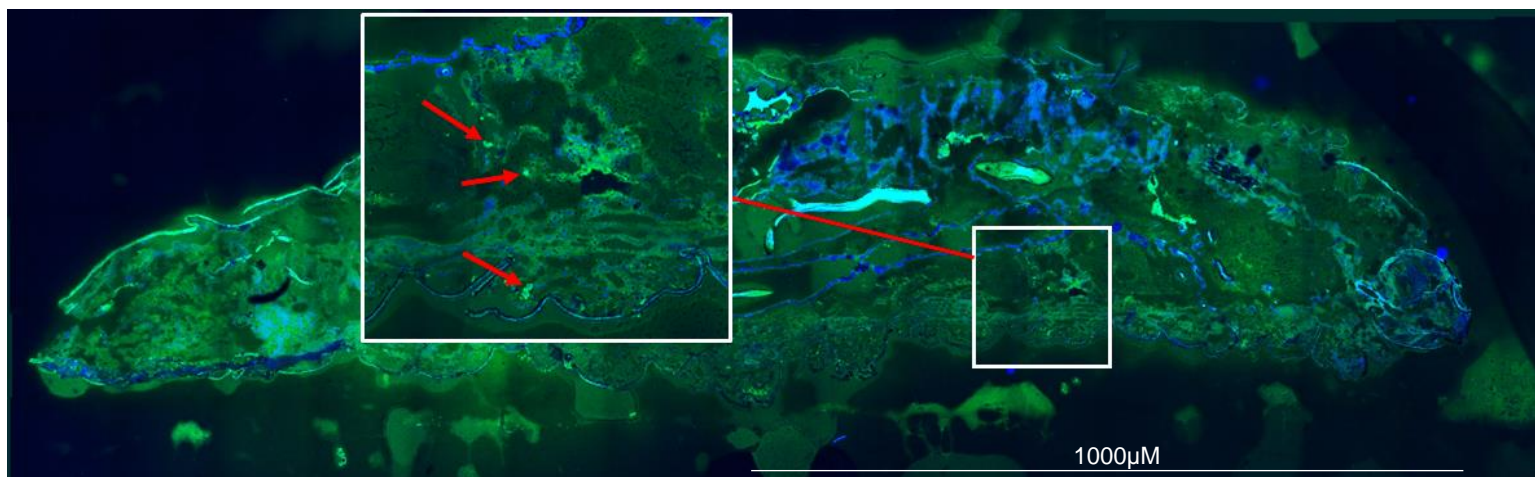


Figure 5.21: Confocal microscopy of larval cryosections (1h post-injection). Confocal microscopy analysis of the biodistribution of green fluorescent anionic-SPIONs, 1h post-injection into GM larvae. The figure represents a x10 magnification overlay image, generated by conducting a slide scan of the entire larval cryosection of the NP injected larva. In the overlay image displayed, the SPION aggregates are identifiable by their strong green fluorescence against the background fluorescence emitted by the surrounding larval tissue and are outlined by red arrows. Moreover, an enhanced x10 magnification image(s) of the larval region containing SPION aggregates, further details nanoparticle in vivo localisation. Scale bars: 1000 μm pertains to all overview photomicrographs of the larval cryosections.

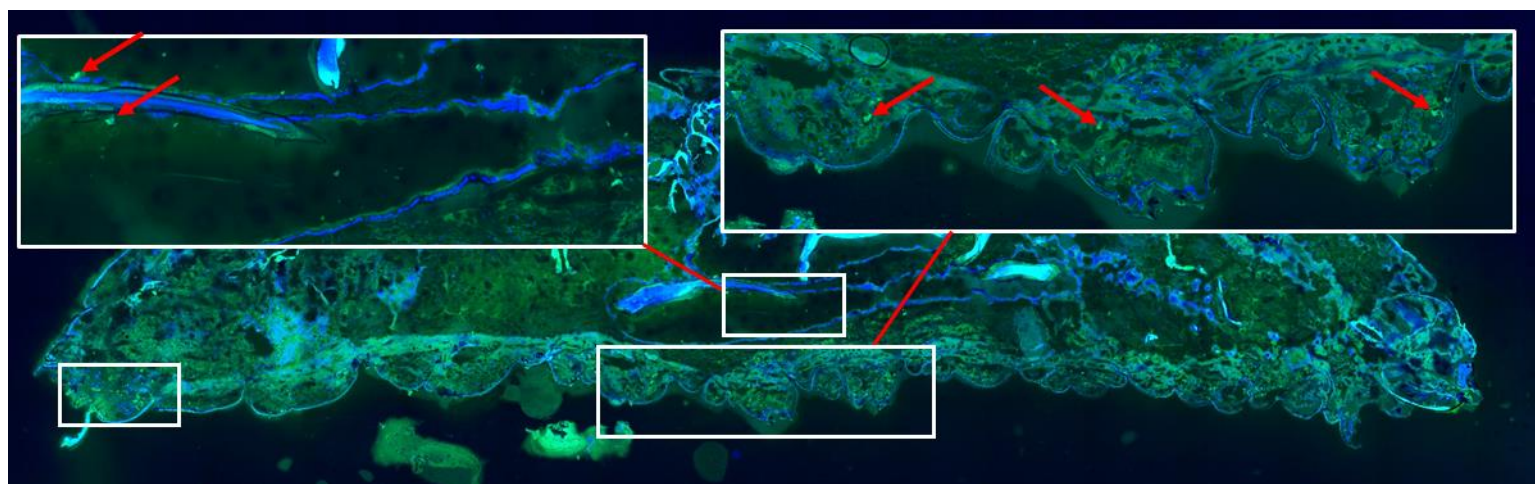


Figure 5.22: Confocal microscopy of larval cryosections (24h post-injection). Confocal microscopy analysis of the biodistribution of green fluorescent anionic-SPIONs, 24h post-injection into GM larvae. The figure represents a x10 magnification overlay image, generated by conducting a slide scan of the entire larval cryosection of the NP injected larva. In the overlay image displayed, the SPION aggregates are identifiable by their strong green fluorescence against the background fluorescence emitted by the surrounding larval tissue and are outlined by red arrows. Moreover, an enhanced x10 magnification image(s) of the larval region containing SPION aggregates, further details nanoparticle in vivo localisation.

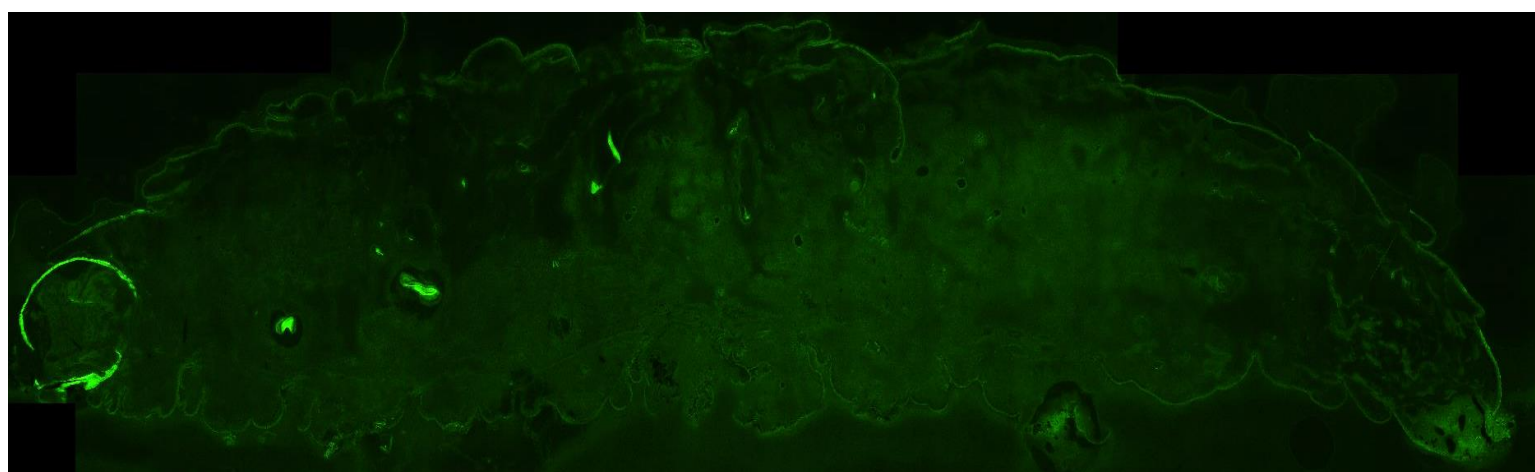


Figure 5.23: Confocal microscopy of larval cryosections (control). Confocal microscopy analysis of control GM larvae, injected with PBS. The figure represents a x10 magnification image, generated by conducting a slide scan of the entire larval cryosection of the PBS injected larva. In the image displayed, IONP aggregates are not identifiable due to a lack of strong green fluorescent aggregates against the green background fluorescence emitted by the surrounding larval tissue.

5.4 Discussion

Nanotechnology and in particular NPs, portray significant potential towards their use in differing, highly beneficial, industrial platforms. In relation to the growing popularity and rapid expansion of nanotechnology within these diverse industries, it is important to note the plethora of advantageous NP applications that have been realised. Recent advances in nanotechnology and in the use of NPs, have brought about new, innovative, and useful applications for NPs. These NP applications have been realised in valuable mega-industries, including food, textile, cosmetics and importantly, in the biomedical/medical industry (Sharma et al., 2021). Due to their nanoscale size and desirable physicochemical properties, it has been proven that NPs have strong potential to be used in various biomedical/medical applications. Examples of these clinically useful NP applications include drug delivery, protein and peptide delivery, clinical imaging, tissue engineering and cancer therapeutics (Nikalje, 2015). Unique physicochemical properties portrayed by NPs, including small size, the ability to encapsulate various drugs and alterable surface chemistries, allow for their use in disease therapeutics through improving drug bioavailability and efficacy (Patra et al., 2018; Nikalje, 2015).

Advances in the clinical applications of NPs have led to the generation of novel and unique NP-drug formulations, which are commonly composed of inorganic NPs. These NP-drug formulations, that can specifically target and deliver the drug cargo to the intended delivery site, has led to the generation of novel targeted therapeutic modalities. Namely, NP-based drug formulations/delivery systems are able to be put forward as novel therapeutic modalities for the treatment of cancers, including the primary bone malignancy Osteosarcoma (Prasad et al., 2021; Wang et al., 2020).

However, prior to using inorganic NPs in novel targeted therapeutic modalities, the biological safety and toxicity of NPs need to be determined. When NPs are introduced to a biological system, biological interactions take place, which can lead to inflammatory and allergic reactions (Liu et al., 2017). These reactions are due to the activation of immune components, including the complement system as the first line of defence, therefore, resulting in potential adverse side effects to NP exposure (Wibroe et al., 2017). Henceforth, this study was an investigation into the biological safety and toxicity of a range of inorganic NPs, prior to their potential utilisation in novel targeted drug delivery systems for diseases including OS.

Inorganic NP biological safety and systemic toxicity levels are commonly questioned by clinicians due to observed past toxicities (De Matteis, 2017). Therefore, there is a strong need for biologically accurate, high-throughput and efficient assays, that are able to determine potential NP toxicities prior to utilisation in clinical applications. Commonly, *in vitro* assays are used for the assessment and determination of NP biosafety and cellular toxicity. This is due to the fact that *in vitro* assays possess many advantages over *in vivo* assays, including low cost, simplicity, efficiency and lack of ethical restrictions (Savage et al., 2019). However, *in vivo* assays for the determination of NP biosafety and potential systemic toxicities, possess more significant advantages over *in vitro* assays. A major known advantage of using *in vivo* assays, over *in vitro* assays, include the ability to closely replicate and model the functional human systems, in either normal or diseased conditions (Committee on Methods of Producing Monoclonal Antibodies et al., 1999). However, unlike the use of *in vitro* assays for determining NP biological safety, *in vivo* assays utilising mammalian or vertebral models, are limited by their high costs and ethical constraints (Kumar et al., 2017). Hence, due to the described significant experimental limitations portrayed by certain

in vivo models, their use in early NP toxicity (phase I) assays long before potential clinical application is currently unjustifiable (Huang et al., 2021).

As a result, invertebrate organisms have been looked into as viable alternative in vivo models. Invertebrate models possess multiple desirable advantages over mammalian model organisms, including low cost, ease of use, efficiency and lack of ethical restraints (Prior et al., 2021). Therefore, these non-mammalian models provide a rapid and cost-effective alternative for an early stage screening (phase I), prior to use of more valuable mammalian models (Peterson et al., 2008). Thus, in this study, we conducted in vivo NP toxicity screenings using the alternate model organism, GM.

The aim of this study was to assess the biological safety and systemic toxicity of a range of differing inorganic NPs in vivo, using the GM larval model organism. In addition, we also aimed to determine the biodistribution of CNTs and anionic-SPIONs, in vivo, using histochemical analytical techniques not previously used on GM larvae.

Inorganic NP in vivo toxicities were assessed, and systemic toxicity levels determined over a period of 72h post-NP injections (Figures 5.4-5.6). Furthermore, NP-induced immunocytotoxicity was quantified through flow cytometric analysis of isolated larval hemocytes 24h post-NP injections (Figure 5.10). In the study, different inorganic NPs (SPIONs (starch-coated and anionic charged), IONPs, CNTs and AuNPs) were screened. Overall, the data strongly suggests that the assayed inorganic NPs portray varying levels of cellular and systemic toxicity, mediated by composition, size and other physicochemical properties. Furthermore, the data strongly suggests tissue bioaccumulation as the likely mechanism behind CNT induced systemic toxicity as opposed to NP-induced cellular ROS production.

The results of the conducted NP larval toxicity screenings showed that, when SPIONs were screened for their in vivo toxicity, the SC-SPIONs portrayed the least level of toxicity.

NP surface coatings play vital roles in the determination of NP toxicity; hence, surface coatings are able to modulate NP cellular uptake and biological responses to NP exposure, which impacts the safety and functional efficacy of nanomaterials (Zheng et al., 2017; Wilhelm et al., 2003). Studies have shown that appropriate stabilisers, such as surface coatings or modifications to SPION surface properties, are often employed to prevent particle aggregation, in vivo, and increase NP biocompatibility (Dung et al., 2009). Therefore, NP surface coatings are able to enhance NP performances when utilised in clinical applications, which is then reflected by enhancements in NP transportability/bioavailability and decreases in NP systemic toxicities (Auclair et al., 2019). This is reflected in the differences between the two SPION variants, where higher toxicity was observed with the anionic-SPIONs. This is further emphasised in a study conducted by Zheng et al, who assessed differences in NP-induced systemic toxicities, between SC-SPIONs and uncoated (bare) SPIONs using adult zebrafish. The study reported that NP starch coating played a vital role in determining NP characteristics and host biological responses to NPs. The starch coating on the NPs was able to mitigate toxic effects on Zebrafish tissues. Henceforth, it was concluded that toxicity of SPIONs is dependent on the presence of NP surface coatings and type of tissue exposed (Zheng et al., 2018).

Unlike the SC-SPIONs, the anionic (charged) SPIONs portrayed a significant level of in vivo NP systemic toxicity in the controls. In a study that assessed the biocompatibility of SPIONs possessing a negative or positive charged shell surface coating, in vitro, negatively charged (anionic) SPIONs were found to be more

biocompatible than positively charged (cationic) SPIONs (Mbeh et al., 2015). Furthermore, Zheng et al's study reported that SPIONs with a charged outer coating are more prone to attract and adhere to oppositely charged surface groups than SC-SPIONs. The starch coating suppresses any surface charge possessed by the SPION, thus, decreasing the levels of NP adherence to tissue surfaces through steric hindrance. Hence, charged SPIONs show increased particle aggregative characteristics and tissue bioaccumulation when compared to SC-SPIONs (Zheng et al., 2018).

To determine NP tissue accumulation as a plausible cause underlying the observed anionic-SPION induced in vivo NP toxicity in GM larvae, tissue cryosections of larvae injected with anionic-SPIONs were obtained, 1h and 24h post-injection. Confocal microscopy was utilised to penetrate the larval tissue cryosections along the Z-axis, thus, allowing for the investigation of SPION in vivo biodistribution, within superficial and deeper layers of tissue. The results showed that the anionic-SPIONs aggregated into NP clusters and accumulated within various larval tissue. Therefore, this data demonstrates increased NP tissue bioaccumulation, in vivo, as a possible reason for the observed significant anionic-SPION induced systemic toxicity.

Although the anionic-SPIONs were observed to produce a significant level of in vivo toxicity, in the controls, this systemic toxicity was not replicated in the immunosuppressed larvae. The larval innate immune system is the first line of defence against exposure to exogenous systemic challenges. Therefore, the larval innate immune cells (hemocytes) would have been the first point of cellular contact for the injected NPs (Stączek et al., 2020; Liu et al., 2017). Cyclo acts as an alkylating agent, preventing DNA replication and immune cell proliferation ('195. Mechanisms of Cyclophosphamide Enhancing Anti-Tumor Effects of Oncolytic Vesicular Stomatitis

Virus for Breast Cancer Treatment', 2010), therefore, resulting in a significant depletion in larval hemocytes. Hence, the lack of significant in vivo SPION toxicity, after Cyclo treatment, can be said to be due to the significant systemic toxicity generated by Cyclo alone. This induced decrease in larval innate immune cells would have resulted in a decrease in larval innate immune cell-NP interactions. Thus, the decrease in larval hemocytes may have resulted in a decrease in NP tissue bioaccumulations and larval hemocyte-NP aggregate formations within the organism, consequently, decreasing in vivo NP toxicity. This result is in opposition to the in vivo toxicity observed in the controls.

Unlike the SPIONs, the NC-IONPs portrayed a significant level of in vivo NP systemic toxicity, in both the control and immunosuppressed states. One of the reasons for the significant increase in NP systemic toxicity, when compared to SPIONs, could be due to the lack of a biocompatible NP surface coating. As described before, NP surface coatings are known to impact the safety and functional efficacy of nanomaterials. Previous studies have investigated the toxicity and biological safety of IONPs and it was reported that an albumin NP surface coating improves NP stability and biocompatibility (Abakumov et al., 2018). Therefore, NP surface coatings have the potential to reduce the cytotoxicity induced by the magnetite cores alone. Likewise, the same study reported a neutralisation of NP-induced cytotoxicity, through the incorporation of polyethylene glycol NP surface modifications (Abakumov et al., 2018). Henceforth, these results support the lack of a biocompatible coat as a likely causation behind the increased levels of in vivo NP systemic toxicity observed with the NC-IONPs. In contrast, when compared to the anionic (uncoated) SPIONs, the NC-IONPs may have produced increases in toxicity, in vivo, due to increases in NP aggregation and tissue bioaccumulation. The NC-IONPs assayed have a varying size range of 50-

100nm, which may have increased levels of tissue accumulation, thus, increasing in vivo systemic toxicity.

Unlike the SPIONs, the NC-IONPs portrayed a significant level of in vivo NP systemic toxicity, also in the immunosuppressed state. Therefore, despite potential Cyclo induced decreases in NP-innate immune cell interactions and NP cellular uptake, potential significant levels of tissue bioaccumulation may have remained, which could have acted as an additive to the systemic toxicity observed with Cyclo treatment alone.

All assayed CNT variants were observed to produce a significant level of toxicity. However, like the anionic-SPIONs, all CNT variants portrayed significant levels of in vivo NP toxicity, only in the controls. Due to the ever-expanding use of CNTs in differing industries and innovative applications, the toxicity of CNTs has always been a prime concern, despite their attractive features (Francis and Devasena, 2018). Hence, the observation of significant CNT systemic toxicity under normal conditions is of particular interest as it can be interpreted as a strong activation of the larval innate immune system. Consequently, resulting in adverse activation of inflammatory responses (Jafar et al., 2016). Furthermore, when compared to the in vivo toxicities of the other assayed metal-oxide NPs, such as SPIONs and IONPs, CNTs portrayed a greater level of in vivo toxicity. This was represented by a greater percentage of larval death over 72h post-NP injections (Figure 5.5). In relation, a study investigating the in vitro cytotoxicity of multiwalled CNTs reported that CNTs, like metal-oxide NPs, are able to enter cells and distribute within the cytoplasm. Cell membrane penetration and cellular entry can lead to physiological and functional alterations which are NP size dependent. Thereby, potentially resulting in cellular toxicity. However, when comparing CNTs to metal-oxide NPs, it was reported that CNTs show a greater level of toxicity, in vitro (Simon-Deckers et al., 2008). However, CNT induced cellular

toxicity, in vivo, was not supported by the results gathered in our study as the major mechanism underlying observed CNT induced systemic toxicity. When circulating larval THC was quantified through flow cytometric analysis, post-CNT treatment, none of the CNT variants were shown to induce significant in vivo immunotoxicity.

Similar to the SPIONs, none of the assayed CNTs were observed to induce significant levels of in vivo systemic toxicities in the immunosuppressed state. This lack of significant toxic effects compared to the Cyclo treated controls, can once again be said to be due to significant systemic toxicities generated by Cyclo injection alone. Moreover, similar to the anionic-SPION variant, all of the assayed CNTs, with the exception to the oxidised CNTs, induced a greater level of in vivo systemic toxicity in the controls, when compared to the Cyclo treated larvae. This phenomenon can be explained by a Cyclo induced reduction in hemocyte-NP interactions and consequently, NP tissue bioaccumulations and hemocyte-NP aggregate formation.

When AuNPs of varying sizes (20,60 and 100nm) were assayed for their in vivo toxicity, only the 20 and 60nm AuNPs were observed to produce a significant level of NP toxicity in the controls. The AuNP size-dependent differences in in vivo toxicity levels, emphasise the fact that NP toxicity is at times size-dependent. Due to in vivo tissue localisation of NPs having a profound effect on NP toxicity, the importance of AuNP size in determining organ distribution has previously been investigated. The results showed that smaller AuNPs of sizes 5-15nm demonstrated a wider range of organ distribution than that of larger AuNPs (50-100nm), which portrayed dominant tissue localisation toward the liver and spleen (De Jong et al., 2008; Sonavane et al., 2008; J. H. Kim et al., 2009; Chen et al., 2009; Cho et al., 2009; Semmler-Behnke et al., 2008). Therefore, it can be proposed that the smaller AuNPs of sizes 20 and 60nm, had a wider organ distribution within the injected GM larvae than that of the 100nm

AuNPs, which likely accumulated in larger organs or did not enter any vital organ. Hence, for the smaller sized AuNPs, the wider organ distribution may have resulted in increased NP tissue bioaccumulations, subsequently causing increased levels of toxicity.

Furthermore, a study assessed the in vivo toxicities of AuNPs with different sizes using a mouse model. The study reported that when mice were treated with 10nm, 50nm and 100nm AuNPs, in the presence or absence of a tested drug, only the 10nm and 50nm AuNPs caused kidney damage while the 100nm AuNPs did not cause any kidney tissue or systemic damage (Isoda et al., 2020). In addition to size-dependent variations in AuNP in vivo toxicity, it has further been shown that NP concentrations and route of administration can have profound effects on overall toxicity. In a study investigating the toxicity of naked AuNPs by different administration routes, it was reported that low concentrations of AuNPs had no obvious effect on organism health. However, high concentrations induced significant toxicological effects, resulting in reductions in body weight and red blood cells. Furthermore, it was reported that the route of administration plays a significant role in NP toxicity, with the AuNPs inducing significant toxicity through oral and intraperitoneal routes, with least toxicity observed through tail vein injections (Zhang et al., 2010). In the presented study, the larvae were all injected with AuNPs through the larval prolegs, therefore, variations in AuNP toxicity are likely explained by size-dependent NP toxicity rather than the route of administration.

In the immunosuppressed state, only the 20nm AuNP size variant was observed to induce significant levels of in vivo toxicity. With regards to the 60nm and 100nm AuNP size variants, the lack of significant toxic effects is most likely due to the significant in vivo systemic toxicity generated by Cyclo injection alone. The effect observed with the

20nm AuNPs, may be due to widespread organ distribution, when compared to the other size variants, therefore, resulting in significant levels of NP biodistribution and persistent tissue accumulation (Chen et al., 2013) even after immunosuppression. As described before, Cyclo treatment induces a significant decrease in larval hemocytes, therefore, resulting in significant decreases in hemocyte-NP aggregate formations and tissue bioaccumulation. Decreases in tissue bioaccumulation for the larger variants may thus, be the reason for the lack of significant in vivo NP toxicity in the immunosuppressed state.

From the NP toxicity assays conducted, significant levels of in vivo NP toxicities were observed, primarily in the case of the anionic-SPIONs, CNTs and AuNPs. Henceforth, with observable levels of NP-induced in vivo systemic toxicity, seen 24h post-NP injections, we decided to investigate NP interactions with the larval innate immune system. In order to investigate NP interactions with the innate immune system, we first investigated NP uptake and biodistribution within larval hemocytes. To do so, we isolated larval hemocytes of NP treated GM larvae through larval hemolymph extractions, and qualitatively analysed NP cellular uptake and biodistribution using fluorescent microscopy (Figures 5.7-5.9).

The images show that the GM larval hemocytes are able to internalise injected NPs in vivo. The mechanisms behind innate immune cell uptake of NPs, are likely endocytosis or continuous micropinocytosis, similar to the processes that are typically utilised by mammalian macrophages when internalising NPs in circulation (Canton, 2018). Figures 5.7-5.9 show that in the control and immunosuppressed states, the internalised NPs (SPIONs, CNTs and AuNPs) are localised in close proximity to the cellular membrane, within the cell cytoplasm and near to the cell nucleus. Studies have shown that the intracellular fate of NPs can have a profound effect on determining the

level of NP-induced cytotoxicity. One study reported that quantum dot NPs can easily enter cells and rapidly disperse throughout the cytoplasm and nucleus, thus, resulting in NP internalisation related cytotoxicity. This cytotoxicity was enhanced particularly when NPs entered the nucleus (Lovrić et al., 2005). Furthermore, a study investigated the effects of polystyrene nanoparticles on human alveolar epithelial cell viability. In the study, it was reported that the smaller NP variant was internalised more readily and efficiently into the cytoplasm of the epithelial cells, when compared to a larger NP size variant. The study further reported that the smaller NP size variant was more dispersed throughout the cell cytoplasm and portrayed a greater level of cellular toxicity at lower NP concentrations, when compared to the larger variant (Xu et al., 2019).

These results support the idea that NP intracellular fate and intracellular localisation play important roles in determining NP cellular toxicity, with abundant NP presence in the cell cytoplasm commonly translating to increased cytotoxicity. Overall, larval hemocyte mediated NP internalisation and subsequent NP fate/cellular localisation may have played a role in determining in vivo NP cytotoxicity and therefore, the observed levels of NP-induced systemic toxicity. In relation to further investigating NP interactions with the larval innate immune system, we looked to quantify NP immunotoxic/modulatory effects on larval hemocytes, in vivo. Through the quantifiable analysis of larval hemocytes obtained from NP treated GM larvae, we also aimed to determine the potential of NP immunotoxicity as a viable mechanism behind the observed in vivo NP systemic toxicity.

Macrophages are known to be a major component of the innate immune system and are characterised as cells that rapidly recognise and efficiently remove exogenous particles, including NPs (Sadauskas et al., 2007). Due to similarities between the

components of the GM larval and mammalian innate immune systems (Smith and Casadevall, 2021), larval THC was measured as an indicator of potential NP-induced immunotoxicity/immunosuppression. In GM larvae, larval hemocyte counts are commonly quantified with the use of a Neubauer haemocytometer (Titball and Senior, 2020) or with phase-contrast microscopy (Sezer and Ozalp, 2015). Flow cytometric analysis for larval hemocyte analysis and for the determination of hemocyte counts, however, has been utilised infrequently. Recently, flow cytometric analysis of larval hemocytes has been carried out to determine immunolocalisation of specific proteins (Wrońska and Boguś, 2020), to determine apoptosis of hemocytes in response to pathogens (Giannouli et al., 2014) and in a few cases, to detect changes in hemocyte density in response to cellular stimuli (Scorzoni et al., 2015). In this study, we utilised flow cytometry analysis as an accurate and reliable method for the quantification of larval THC. THC was quantified in all larval test groups, 24h post-NP inoculation, in both the control and immunosuppressed larvae (Figure 5.10).

Despite both SPION variants producing significant decreases in larval THC, the anionic variant produced a greater decrease. As described previously for the differences observed between anionic and SC-SPIONs with respect to systemic toxicities, NP surface coatings play a significant role in the determination of NP toxicity. It is understood that certain surface coatings/modifications of magnetite NPs, are capable of making them more biocompatible, efficacious and systematically safe, both in vitro and in vivo (Dung et al., 2009). Consequently, the differences in observed SPION induced immunocytotoxicity could be due to the lack of a starch coating on anionic-SPIONs. The toxicological differences observed between the variants, emphasise the importance of NP surface modifications when determining NP toxicity and, when considering their potential as drug delivery agents.

In a study that investigated the effects of NP surface coatings on cellular toxicity, it was reported that NP surface ligand composition has a stronger link to cellular ROS production, when compared to NP surface charge (Zheng et al., 2017). However, NP surface charge has more significance in deciding overall NP-induced cytotoxicity. Therefore, this study presents a reason towards the increased levels of NP immunotoxicity observed in vivo, with the anionic-SPIONs, when compared to the starch coated variant. The anionic surface charge, in addition to the lack of a biocompatible starch coating, may have played considerable roles in the observed SPION induced immunocytotoxicity differences between the two variants (Zheng et al., 2017). However, while a study that investigated the toxicity of cationic carbon NPs with varying surface charge densities showed that a positive NP surface charge is largely associated with NP toxicity, they also found that the positive surface charge does not translate into NP toxicity in a systematic way (Weiss et al., 2021). Hence, this led to the belief that the observed differences between anionic-SPION and SC-SPION immunotoxicities, were mainly caused by an alternate toxicity mechanism. NP-induced increases in intracellular ROS production and therefore, cellular oxidative stress, has been discussed in many nanomaterial studies as the major mechanism underlying nanotoxicity (M. Li et al., 2014). Therefore, differences in immunotoxicities between the two SPION variants can be explained by potential higher and sustained levels of ROS production in response to the anionic-SPIONs.

Like in the controls, both SPION variants induced significant decreases in larval THC in the immunosuppressed (Cyclo treated) larvae. As described above for the controls, SPION induced decreases in larval THC, observed also after Cyclo treatment, are likely to be explained by increased cellular ROS production and thus, cellular oxidative stress. The significant decreases in larval THC were of equal significances to that

observed in the control larvae. This result indicated relatively unaltered levels of NP-induced cellular ROS production, resulting in immunotoxicity, despite potential Cyclo mediated decreases in NP-immune cell interaction and uptake. Although significant levels of immunotoxicity were observed for both SPION variants in the immunosuppressed state, neither variant produced significant in vivo systemic toxicity when larvae were pre-treated with Cyclo (Figure 5.4).

Unlike the SPIONs, none of the assayed CNT variants produced a statistically significant decrease in larval THC, in both the controls and immunosuppressed states. In a study investigating the interactions between single-walled nanotubes and host macrophages, a lack of CNT mediated NP immunocytotoxicity was reported (Dumortier et al., 2006). A reason behind the lack of CNT induced immunotoxicity, could be due to the size of the assayed CNTs. The larger size of the CNTs may have prevented NP cellular uptake and therefore, induction of cellular oxidative stress via ROS production. In contrast, reports have shown that CNTs have the potential to preserve immune functionality, hence, explaining the lack of immunotoxicity (Dumortier et al., 2006). Furthermore, large variations in larval THC were observed post-CNT treatment. This was shown by large error bars and a statistically significant increase in larval THC, induced by both the oxidised and CMC coated CNT variants, in the immunosuppressed state. Although no significant levels of CNT induced immunocytotoxicity were observed, all CNT variants presented significant levels of systemic toxicity over 72h post-NP injections (Figure 5.5). Taken together with the lack of immunotoxicity, this points to an alternative mechanism mediating systemic toxicity, most likely to be significant levels of CNT tissue accumulation observed in the histological analysis of larval cryosections (Figures 5.15-5.20).

For the investigation of *in vivo* dissemination, accumulation, and invasion of exogenous matter within GM larvae, histological analysis has previously been conducted on whole body larval tissue sections. Histochemical analysis is commonly conducted on paraffin embedded whole body larval tissue sections to study infection progression (Djainal et al., 2020), host-pathogen interactions (Perdoni et al., 2014), and for the visualisation of pathogen invasiveness (Sheehan et al., 2018). In contrast, cryosectioning has not been used on GM larvae, with only Cryo-imaging having been previously employed to visualise stages of pathogen invasiveness within the larvae (Sheehan et al., 2018).

In this study, we utilised a unique and novel method of GM larval tissue histological analysis to determine CNT biodistribution and localisation *in vivo*. For larval tissue histochemical analysis, the larvae were cryosectioned and the sections were then histochemically stained. In the stained cryosections, the CNT aggregates are easily distinguishable and were found localised in close association to the larval digestive tract, striate muscle fascicles and Malpighian tubules, at 1h and 24h post-NP injections (Figures 5.15-5.20). Therefore, similar to the anionic-SPIONs, CNT *in vivo* tissue accumulation could be the reason for the observed significant systemic toxicity, in the controls. Evidence for significant levels of CNT tissue accumulations, was reported in a study which investigated the circulation and long-term fate of single-walled CNTs, *in vivo*. The study reported that in mice, significant levels of CNT accumulations were observed in the liver and spleen, potentially resulting in systemic toxicity (Liu et al., 2008).

All the assayed AuNP size variants produced a statistically significant decrease in larval THC, in both the control and immunosuppressed states. However, AuNP immunocytotoxicity was observed to have size-dependent variations, with the 20nm

AuNP size variant being the least toxic and a significant increase in immunotoxicity seen with the 40nm AuNPs. Evidence to support size-dependent toxicity of AuNPs, was reported in a study that investigated the toxicity of a range of AuNPs with varying sizes, using human embryonic stem cells. The study reported that the level of AuNP toxicity is dependent both on size and concentration (Senut et al., 2016). Furthermore, significant levels of AuNP-induced immunotoxicity have been observed in previous studies, including with human peripheral blood lymphocytes and murine splenic lymphocytes. In the study, the innate immune cells were significantly inhibited by AuNPs at a concentration of 200 mg/kg, with highly noticeable depletions in both innate immune cell types being observed (Devanabanda et al., 2016). In the GM assay, the 20nm AuNP size variant significantly depleted the larval THC in the immunosuppressed state, therefore, representing the largest decrease in THC seen with the AuNPs. The reason for the further decrease in innate immune cells, could be due to AuNP-induced immunotoxic effects acting as an additive to the induced immunosuppression with Cyclo treatment alone.

In the immunosuppressed state, the 60nm and 100nm AuNP size variants produced a statistically significant decrease in larval THC. The depletion of larval THC, was, however, not significantly greater than that of AuNP-induced immunotoxicities observed in the controls. Therefore, in the Cyclo mediated immunosuppression, the AuNPs were likely taken up by depleted levels of larval hemocytes, however, still resulting in AuNP-induced immunocytotoxicity. Therefore, further depleting larval hemocytes to a plateau which resulted in a lack of significant in vivo AuNP systemic toxicity (Figure 5.6).

To investigate if depletion of THC after AuNP treatment has a similar effect to that of Cyclo induced depletion, we investigated the impact of an innate immune challenge

on AuNP treated larvae. GM larvae were inoculated with a pre-determined inoculum of PA14. Thereafter, the impact of PA14 inoculation on THC and larval survival were assessed in the control, Cyclo treated and 60nm AuNP treated larvae. In the controls, the expected significant increase in larval THC was observed. This increase is likely to be an innate immune response against the introduction of the pathogenic PA14, which is a typical immune response against invading exogenous microbes (Thomaz et al., 2020). As expected, this PA14 induced increase in larval THC was not observed in the Cyclo treated larvae. Cyclo mediated immunosuppression of larval hemocytes likely resulted in the immunosuppression of the innate immune cellular component, thereby, preventing pathogen stimulated THC increases. Cyclo is known to induce immunosuppression through mitotic suppression of immune cells, however, Cyclo can also increase the number of myeloid-derived suppressor cells which modulate immune activity (Ahlmann and Hempel, 2016).

A similar effect of immunosuppression, despite the immunological challenge, was observed in the 60nm AuNP treated larvae. In a previous study investigating AuNP immune modulation, AuNPs were reported to directly induce an immunosuppressive response without measurable cytotoxicity (Fernández et al., 2015). Thus, similar to Cyclo treatment, the PA14 induced cellular innate immune response was not observed in the AuNP treated larvae. Similar to what was observed with the Cyclo treatment, AuNP-induced immunotoxicity/suppression was maintained after PA14 challenge and therefore, resulted in cellular innate immune response suppression. However, the suppression of PA14 induced hemocyte proliferation was more significant with the 60nm AuNP treatment, when compared to the Cyclo treated larvae.

Injection with PA14 induced significant larval death in all treated larval test groups, which demonstrates the pathogen's virulence and systemic pathogenesis. The

inoculum of PA14, like other bacterial inoculums, likely activated the cellular and humoral immune responses of GM larvae. Furthermore, while activating larval immune responses, the inoculum was likely proliferating and spreading throughout the organism, resulting in the formation of bacterial nodules and eventually larval death (Sheehan et al., 2019). When comparing the Cyclo and AuNP treated larvae, post pathogenic challenge, the rate of larval survival remained relatively similar near to the point of 72h post-PA14 inoculation. Thereafter, the larvae treated with Cyclo portrayed a greater level of systemic toxicity, when compared to the AuNP treated larvae. The increase in larval systemic toxicity, both after Cyclo and AuNP treatment, is most likely due to the suppression of the larval innate immune cellular component. Therefore, a protective immune response against the pathogen was likely prevented and thereby, resulted in increased larval mortality due to microbial pathogenesis. Furthermore, from the relatively close rate of larval survival observed between the AuNP and Cyclo treated larvae, it can be said that the AuNPs are a comparable immunosuppressive agent at the tested concentration.

The in vivo NP toxicity results gathered from this study, demonstrates the strong potential of GM larvae for use as model organisms in NP toxicity studies. The larvae are suitable models to study early infections and exogenous stimuli interactions not involving adaptive immune responses (Cools et al., 2019). This alternate invertebrate model allows for NP toxicity screenings to be carried out economically, efficiently and without the need for ethical approvals. Thus, the larvae prove to be suitable models for early-stage NP toxicity screenings, prior to potential biomedical and clinical applications, while overcoming the limitations portrayed by in vitro assays and murine models.

In addition to the advantages portrayed by GM larvae for use in NP toxicity screenings, the presented study puts emphasis on the use of qualitative and quantitative techniques not yet fully utilised with GM larvae. Firstly, the study presents the utility of flow cytometric analysis in combination with GM larvae. Larval hemolymph was shown to be extractable and once larval hemocytes were isolated, flow cytometric analysis was shown to be a useful tool in the assessment of THC changes induced by varying exogenous stimuli (Figure 5.10). Furthermore, this study presents a unique technique of tissue histological analysis, not known to be previously utilised in combination with GM larvae. Larval cryosectioning and subsequent tissue cryosection staining were for the first time utilised in the rapid and effective histological analysis of whole body larval cryosections. In the context of CNT in vivo NP toxicity, the histological analysis technique provided possible explanations for the observed significant levels of in vivo NP toxicity, despite lack of quantifiable immunotoxicity (Figures 5.15-5.20).

Overall, the results indicate that the NP variants are good starting points for the development of novel nanomedicines and drug delivery vehicles. With respect to the SC-SPIONs and the 100nm AuNPs, insignificant levels of NP systemic toxicity, determined through the lack of significant larval death, potentiates the NPs as biologically safe at the assayed concentrations. Moreover, it is evident that the SC-SPIONs and the AuNPs portray further advantageous properties, that may be of use in a clinical setting and is supported by the lack of systemic NP toxicity. In this study, the results gathered for the SPIONs demonstrate the direct immunosuppressive activity of metal oxide NPs on the cellular component of the innate immune system. Since the results show a significant reduction in larval hemocytes post-SPION treatment, it can be said that the NPs are most likely capable of suppressing the cellular component of the mammalian innate immune system as well. Similarly, the

results demonstrate the direct immunosuppressive activity of noble metal NPs (AuNPs), on the cellular component of the innate immune system. The NPs could act as standalone immunosuppressive agents or indirect complements to current immunosuppressive drugs, including Cyclo.

Metal oxide NPs have been shown to induce both immunosuppression and anti-inflammatory effects. SPIONs, have previously been reported to specifically reduce the humoral component of the innate immune system. In contrast, noble metal NPs such as the tested AuNPs, have been reported to interact with both the innate and adaptive immune systems. However, unlike the metal oxide NPs, only a few studies looked to uncover the underlying mechanisms behind noble metal NP-induced immunosuppressive effects (Ngobili and Daniele, 2016).

NP-induced direct innate immunosuppression can be desirable in the context of intended novel nanomedicines, or undesirable, when considered for biomedical applications such as imaging and drug delivery. NP-induced immunosuppression can lower the host's defences against pathogen infection and cancerous cell proliferation. This was emphasised by increased levels of larval systemic toxicity when the innate immune system was challenged with PA14 post-NP treatment. However, immunosuppression can be desirable to enhance therapeutic efficacy, improve the treatment of autoimmune diseases and enhance immune tolerance to prevent organ transplant rejection (Zolnik et al., 2010). In context, only a few studies investigated direct NP-induced immunosuppression and the related underlying mechanisms. Hence, excessive intracellular ROS production and thus, increased oxidative stress were investigated as the potential mechanisms behind the observed immunosuppression (chapter 6).

With exception to the SC-SPIONs and the 100nm AuNPs, the remaining NPs assayed should be used cautiously due to the increased levels of in vivo systemic toxicity and immunotoxicity. However, they may still have the potential to become novel therapeutics, if used at alternate concentrations and for specific patient requirements. Lastly, GM larvae can be utilised to link in vitro and in vivo murine assays, thus, providing more accurate predictions of nanoparticle toxicity at an early stage (Moya-Andérico et al., 2021).

Limitations

In this study, GM larvae were shown to be attractive in vivo model organisms for the assessment of NP toxicity. The larvae have previously been used to screen the toxicity of NPs, in the context of NPs released into the environment. However, despite the attractive toxicological screening characteristics portrayed by the GM larvae, the model organism is not a suitable replacement for mammalian models, which are the gold standards for in vivo toxicity assays. The GM larvae can only provide a rapid, ethically safe and cost-effective alternative at an early stage, prior to use of more rigorous toxicity screening using murine models and subsequently, clinical trials (Tsai et al., 2016).

The use of GM larvae as model organisms is still in its infancy, with the larvae not being as well established as some of the other invertebrate models, such as the nematode (*Caenorhabditis elegans*) or the fruit fly (*Drosophila melanogaster*) (Tsai et al., 2016). Currently, the full GM larval genome is yet to be sequenced, therefore, only a few mutant strains, gene microarrays and RNA interference libraries are available for use in translational and clinical research (Cutuli et al., 2019).

Champion et al, highlighted the lack of standardised scientific procedures as a significant issue, when using GM larvae as model organisms for toxicity assay (Champion et al., 2016). In most cases, GM larvae are used as infection models to study pathogen virulence and efficacy of antimicrobial agents. In these microbial infection studies, an infection is introduced as an intra hemocoelic injection of the inoculum through the last left larval pro-leg. However, post-larval infection, organism response to pathogenic infection is evaluated through varying unstandardised parameters, including larval mortality, melanisation, mobility and quantification of hemocytes. Despite methods of larval infection and exogenous stimuli introduction, and parameters for evaluating larval response to exogenous material remaining relatively similar between studies, numerous experimental variations remain. These include preparation method and quantity of sample injected, source and maintenance of larvae and levels of subjectivity when evaluating qualitative response parameters, such as morbidity or mortality. Due to these experimental variations when using GM larvae, the results gathered from these studies are not directly comparable (Cutuli et al., 2019).

The lack of standardisation when referring to the use of GM larvae as model organisms, is not limited to experimental procedures but also includes the larvae themselves. The GM larvae are available commercially, from angler's stores and a wide range of breeders/distributors who sell the larvae as pet food for reptiles and birds (Cutuli et al., 2019; Tsai et al., 2016). Comparatively, some companies provide lab-grade larvae that have been partially genotyped for extensive scientific use (Champion et al., 2016; Lange et al., 2018). However, there are phenotypical and genotypical differences between commercially purchased and lab-grade larvae. These differences, including larval genotype, breeding conditions or maintenance may have

a profound effect on larval response to exogenous stimuli, infection, and certain treatments. Furthermore, once received, the maintenance conditions such as diet and housing temperature may vary between research environments and may impact experimental results and thus, reproducibility. Overall, differences in larval supplier, maintenance and handling between research groups can lead to inconsistent results and lower reproducibility (Tsai et al., 2016). Thus, the use of lab-grade larvae that have been reared under lab conditions, although greater in cost than commercial larvae, provides greater levels of standardisation. The use of standardised larvae, offers greater levels of consistency within experiments and increased reproductivity when referenced and shared amongst research groups (Cutuli et al., 2019).

In the presented study, the GM larvae utilised were purchased from a commercial organisation, that provides the larvae as bait. Henceforth, the larvae arrive as a mixed cohort of live and dead larvae, with live larvae portraying varying sizes and physiological conditions. Thus, unlike lab-grade larvae, the utilised larvae lack standardisation between experimental cohorts. Therefore, at times, resulting in a lack of consistency between in vivo assays and may result in decreased experimental reproducibility. The lack of standardisation was also reflected by irregular occurrences of contaminations within experimental cohorts, resulting in inconsistent larval death. Lastly, due to the lack of standardisation presented by commercial GM larvae, significant variations in larval size and weight could have had a profound impact on the physiological response to NP exposure and thus, in vivo toxicity,

Future prospects

In this study, GM larvae were shown to have enormous potential as in vivo models for assessing nanomaterial toxicity. This study has portrayed multiple research

techniques, that are not known to have previously been used in combination with GM larvae. The research techniques, when used in combination with GM larvae, provide novel ways to better understand NP in vivo biodistribution and mechanisms behind in vivo NP toxicity. The results gathered, put forward tissue bioaccumulation, immunocytotoxicity and increases in cellular ROS production as major mechanisms behind in vivo NP toxicity, for the assayed synthetic NPs. However, the development of further molecular biology techniques and larval transgenic lines can further put forward GM larvae for nanomaterial toxicity studies. Advances in GM microarrays, full genome sequencing and genomic resources can make the larvae a multipurpose system for toxicogenomic studies of nanomaterials in the near future (Piatek et al., 2021). Moreover, a better understanding of GM protein and gene expression profiles can potentially uncover the truth behind ongoing nanomaterial toxicity debates, through the measurement of changes in gene expression post-NP exposure. Although GM larvae are currently being used as high throughput screening systems in environmental based nanomaterial toxicity studies, there is still potential for their use in early-stage nanomaterial toxicity clinical assays.

**6. Reactive Oxygen Species (ROS)
Production: A Major Mechanism
Underlying Nanoparticle Toxicity**

Aims and hypotheses

The aim of this chapter was to determine if NP-induced cellular ROS production was the major mechanism underlying NP-induced cellular toxicity, observed in vivo with the GM larvae. We hypothesise that excessive NP-induced cellular ROS production is indeed the mechanism, underlying NP-induced systemic and cellular toxicities.

6.1 Introduction

Evidence for NP-induced intracellular ROS production and subsequent oxidative stress has been observed both in vitro and in vivo. In most NP biomedical applications, including drug delivery, the induction of excessive intracellular ROS production is thought to be an adverse side-effect of NP exposure and is known to result in NP toxicity (Horie and Tabei, 2021). However, in a study investigating the antitumor and antimicrobial effects of ZnO NPs, in vitro, the NPs were reported to exhibit advantageous antitumor and antimicrobial activity which was based on their ability to generate ROS intracellularly. Excessive ROS production was reported to result in the activation of apoptotic signalling pathways in mammalian cells (Popescu et al., 2020). Similarly, NP-induced ROS production and oxidative stress have also been reported in vivo, in a study that investigated silver NP-induced ROS production within the nematode (*Caenorhabditis elegans*). The study reported that the silver NPs induced ROS-related effects in multiple tissues, resulting in biological molecule and cellular structure damage and potentially, oxidative stress (S. Kim et al., 2009; Roh et al., 2009; Lüersen et al., 2013; Ribeiro et al., 2015). Moreover, cell membrane damage as a result of NP cellular interaction and uptake in vitro has also been investigated and reported. In a study that investigated cell membrane damage by copper containing NPs, it was reported that certain copper NPs, based on their physicochemical properties, induced high levels of membrane damage (Karlsson et al., 2013). Thus, most NPs are known to cause toxicity through ROS production and subsequent oxidative stress (Fu et al., 2014). Excess ROS production has been reported to result in further toxicity related events, including protein oxidative carbonylation, lipid peroxidation and DNA/RNA damage (Yu et al., 2020; Fu et al., 2014).

Previous study

In the previous study (chapter 5), we assessed the biological safety/toxicity of synthetic nanoparticles, in vivo, using the GM larval model organism. In the study, detectable levels of NP-induced systemic and immunotoxicities were observed. By conducting GM larval survival analysis, we found that anionic-SPIONs, NC-IONPs, all three CNT variants and the 20nm and 60nm AuNP size variants portrayed significant levels of systemic toxicity. Furthermore, through flow cytometric analysis of isolated larval hemocytes, post-NP treatment, significant levels of immunocytotoxicity in response to SPION and AuNP treatment in the controls was observed. However, when the immunotoxicity potential of the assayed CNT variants was assessed, no significant levels of CNT induced immunotoxicity were observed. However, cryosectioning of the larvae showed CNT accumulation in larvae tissues, which we propose induces systemic toxicities as opposed to NP-induced immunotoxicity.

Present study

Assayed SPIONs and AuNPs portrayed significant levels of NP-induced immunotoxicity and in some variant cases, significant systemic toxicity too. It is understood that the most vital mechanism responsible for nanotoxicity is the induction of ROS production. Therefore, we hypothesised that NP-induced increases in ROS production and subsequent oxidative stress, were the likely major mechanism behind NP-induced systemic and immunotoxicity observed in the GM larvae. To investigate this hypothesis, ROS production was measured both in vitro and in vivo.

6.2 Methods

Cellular ROS production (in vivo)

The use of in vitro assays to qualitatively measure and quantify the level of cellular ROS production and thus, oxidative stress, induced by NP cellular exposure and uptake, has many limitations. The main limitation is the inability of the in vitro system to replicate crucial physiological conditions that are taking place in vivo. Thus, in order to effectively evaluate the potential of specific NPs in inducing cellular ROS production and oxidative stress as mechanisms of NP cellular toxicity, it is of importance to carry out in vivo ROS assays. Therefore, in this study, we utilise the GM larvae model organism to evaluate the level of cellular ROS production and oxidative stress, induced by systemic exposure to inorganic NPs, in vivo. It is important to note that, the GM larval model organism has not previously been used to evaluate levels of NP-induced cellular ROS production and oxidative stress, in vivo.

In order to measure and quantify NP-induced cellular ROS production and evaluate levels of NP-induced oxidative stress in vivo, groups of GM larvae were injected with a range of inorganic NPs that were also screened for their potential systemic toxicities. The injected larvae were then incubated for 24h at 37°C. Thereafter, 250µl of larval hemolymph was extracted from the GM larval groups and placed into 1.5ml Eppendorf tubes that were kept on ice. Prior to larval hemolymph extractions, 25µl of acid citrate dextrose (ACD) solution (Sigma-Aldrich, Poole, UK), which in this study was used as a hemolymph anticoagulant, was placed into respective Eppendorf tubes. The anticoagulant solution was used at its stock concentration and made up 10% of the final hemolymph volume, post-extraction. After extraction, the hemolymph was maintained on ice and then centrifuged at 2,800 rpm for 5 minutes at 4°C, thereby,

pelleting the hemocytes and creating a plasma supernatant for each sample. The samples were then maintained on ice and the supernatants (larval plasma) were aliquoted into Eppendorf tubes, snap frozen using liquid nitrogen and then stored at -80°C.

In order to measure and quantify NP-induced cellular ROS production in vivo, the levels of a metabolic by-product named 4-Hydroxynonenal (4-HNE) was measured and quantified in NP treated larval plasma samples. 4-HNE is known to be a metabolic by-product of cell membrane lipid peroxidation and is constantly produced by cells as a result of cellular ROS production and oxidative stress. Therefore, by quantifying the concentration of 4-HNE in plasma samples of GM larvae injected with NPs, we indirectly quantified NP-induced cellular ROS production and levels of oxidative stress in vivo. The levels of 4-HNE in larval plasma acquired from groups of treated larvae, were detected and concentration quantified using a 4-HNE ELISA kit (cat. no. E-EL-0128; all from Elabscience Biotechnology, Co., Ltd.), following the manufactures instructions. Plasma samples acquired from larvae injected with PBS were used as a negative control and plasma from larvae injected with Hydrogen Peroxide was used as positive control samples.

Aliquoted larval plasma was thawed and brought to room temperature prior to conducting the enzyme-linked immunosorbent assay (ELISA). Furthermore, the 4-HNE ELISA kit was also taken out of 4°C and brought to room temperature before use. Firstly, the required wash buffer was prepared by diluting the 25x concentrated wash buffer to a 1x working solution. Thereafter, the protein reference standard included in the kit was diluted to the recommended concentrations, by using the reference standard and sample diluent included and carrying out a serial dilution. Next, the 100x biotinylated detection antibody stock was diluted to its 1x working solution,

to then be used in the assay. Prior to conducting the ELISA, the thawed larval plasma samples were diluted using the sample diluent included in the kit, with a dilution factor of 1:5. This step was carried out after prior assay optimisation, in order for the optical density values at the end of the assay to fall within the range of the standard curve. 50µl of diluted reference standard and diluted larval plasma sample were added to wells of a 96 well microtiter plate. Immediately afterwards, 50µl of the detection antibody was added to each well. The standards and samples were then incubated in the presence of the detection antibody for 45 mins at 37°C. During the incubation, the 100x concentrated HRP conjugate stock was diluted to a 1x working solution. Post-incubation, all wells were decanted and washed 3 times using 350µl of the 1x wash buffer. Once washed, 100µl of the HRP conjugate working solution was immediately added to each well and the samples were incubated for 30 mins at 37°C. Once incubated, all wells were decanted and washed 5 times using the 1x wash buffer. Immediately after, 90µl of the included substrate reagent was added to each well and the samples were incubated for approximately 15 minutes at 37°C, in the dark. During the reaction, colour development was monitored, and the reaction time was adjusted. Finally, the enzymatic reaction was stopped by adding 50µl of the stop solution to each well, in the same order as when the substrate was added. The optical density (OD) value of each well was read immediately after with a Bio-Rad microplate reader (Bio-Rad, London, UK) set to an emission wavelength of 450nm. Using the standard curve generated from the OD values measured for the reference standard dilutions, the concentrations of 4-HNE for the respective larval plasma samples acquired from the differing GM treatment conditions were expressed as ng/ml.

6.3 Results

In vitro measurement of cellular ROS production

Live cell imaging

An increase in intracellular ROS production and overall cellular oxidative stress, has been described to be a major immunological response invoked against systemic exposure to inorganic NPs. Therefore, it is also said to be a major causative factor behind observed NP-mediated immunotoxicities, *in vivo* (Mohammadpour and Ghandehari, 2022).

Therefore, through the use of a cellular ROS assay, we wanted to confirm if excessive cellular ROS production and hence, cellular oxidative stress, was the causative mechanism behind NP-induced immunotoxicity in the GM larvae. NP-induced immunotoxicity was observed specifically in the SPION and AuNP injected GM larvae, when THC was analysed by flow cytometric analysis. Therefore, we used a commercially available live cell, *in vitro*, ROS assay, in order to assess the levels of cellular ROS production and thus, cellular oxidative stress, that is induced in response to NP exposure and cellular uptake. Due to difficulties culturing GM hemocytes, RAW264.7 mouse macrophages were used for live cell fluorescent imaging to qualitatively assess levels of NP-induced cellular ROS production. RAW264.7 cells are macrophage-like and commonly used to model mouse macrophages, which play a role in the cellular component of the mouse innate immune system. As such, they are similar to larval hemocytes. Due to the immunological similarities between the two cell types, mouse macrophages can act as alternatives to larval hemocytes. NP-induced cellular ROS production was assessed using the inorganic NPs (SC-SPIONs,

NC-IONPs and 100nm AuNPs), at 3h and 24h post-treatment timepoints and at concentrations of 10 ug/ml, 10 ug/ml and 1.6 ug/ml, respectively.

In the case of the untreated controls, fluorescence microscopy showed the unstimulated levels of intracellular ROS production, as depicted by the green fluorescence emitted from a low number of cells 24h and 48h post-seeding (Figures 6.1 and 6.2). Relative levels of cellular ROS production are expected from macrophage cells, due to their known functionality of being ROS producing and releasing innate immune cells (Baek et al., 2020). However, the overall level of unstimulated cellular ROS production, 24h post-seeding, was observed to be relatively low. Figure 6.1 shows a low number of untreated and thus, unstimulated cells, emitting a green fluorescence in response to cellular ROS production. Thereafter, 48h post-seeding of the cells, the untreated cells produced a noticeable increase in the levels of unstimulated cellular ROS production when compared to the 24h samples (Figure 6.2).

Regarding the positive control, treatment with TBHP induced a significant increase in cellular ROS production 3h post cellular treatment. Figure 6.3 shows the significant increase in overall cellular ROS production when compared to the respective negative (untreated) control. An increase in cellular ROS production is depicted by the increase in the number of cells emitting green fluorescence, when compared to the negative control.

Firstly, treatment of RAW264.7 cells with the SC-SPIONs, induced a noticeable increase in overall cellular ROS production, 3h post treatment, when compared to the untreated control. Figure 6.4 shows that the SC-SPIONs induced a noticeable increase in overall cellular ROS production, which is represented by a slight but visible

increase in the number of cells emitting green fluorescence, when compared to the control. However, cellular treatment with SC-SPIONs for 24 h, produced a dissimilar result to that observed at 3h post-cellular treatment. Figure 6.5 shows that after 24h of treatment with the SC-SPIONs, there is a significant increase in cellular ROS production. This is represented by a distinct increase in the total number of cells emitting green fluorescence, when compared to the relevant negative control (48h post-cell seeding).

Secondly, treatment with the NC-IONPs, induced a noticeable and significant increase in overall cellular ROS production, 3h post treatment, when compared to the untreated control. Figure 6.6 shows the NC-IONP-induced significant increase in overall cellular ROS production, which is represented by a significant increase in the total number of cells emitting green fluorescence, when compared to the negative control. Furthermore, the increase in the number of cells emitting green fluorescence, can be said to be comparable to that of the positive control, 3h post-cellular treatment. Similar to the SC-SPIONs, cellular treatment with NC-IONPs for 24h produced a dissimilar result to that observed at 3h post-cellular treatment. When the cells were treated for 24h with the IONPs, a visible but low change in overall cellular ROS production was observed, when compared to the negative control (Figure 6.7). Furthermore, the total number of cells emitting a green fluorescence is significantly lower than in the SC-SPION and AuNP treated samples, 24h post-cellular treatment with NPs.

Lastly, similar to that of the SC-SPION treatment, treatment with 100nm AuNPs also induced a noticeable increase in overall cellular ROS production, 3h post treatment, when compared to the untreated control. Figure 6.8 shows the AuNP-induced noticeable but overall low increase in cellular ROS production, which is represented by a slight but visible increase in the number of cells emitting green fluorescence,

when compared to the control. However, this increase is much lower than in the positive control, 3h post treatment. Similar to the SC-SPIONs, treatment with AuNPs for 24h induced a visible and significant increase in overall cellular ROS production, when compared to the negative control. Figure 6.9 shows a significant increase in the total number of cells emitting green fluorescence, when compared to the relevant negative control.

Untreated RAW264.7 cells

24h post-seeding of cells

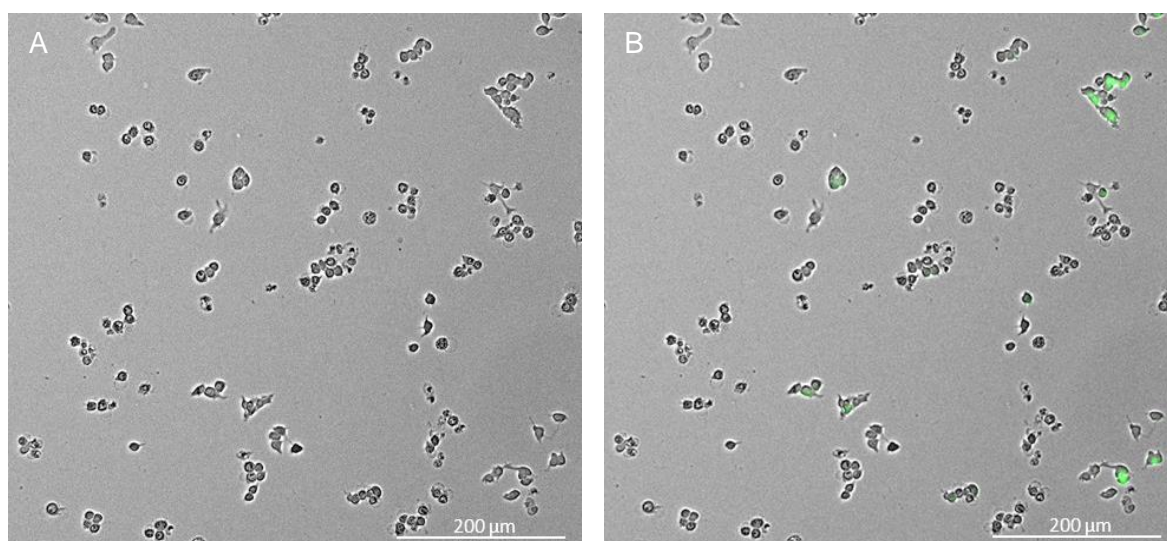


Figure 6.1: Live cell imaging of untreated macrophages stained for cellular ROS. Figure showing x20 magnification fluorescent microscopy images of untreated RAW264.7 cells, 24h post-seeding. (A), shows the bright field channel. (B) shows an overlay image of the bright field and green (GFP) channel, where ROS producing DCF stained cells are fluorescing green. Live cell imaging was carried out on triplicate wells for each treatment and respective timepoint. Independent experiments were repeated twice.

48h post-seeding of cells

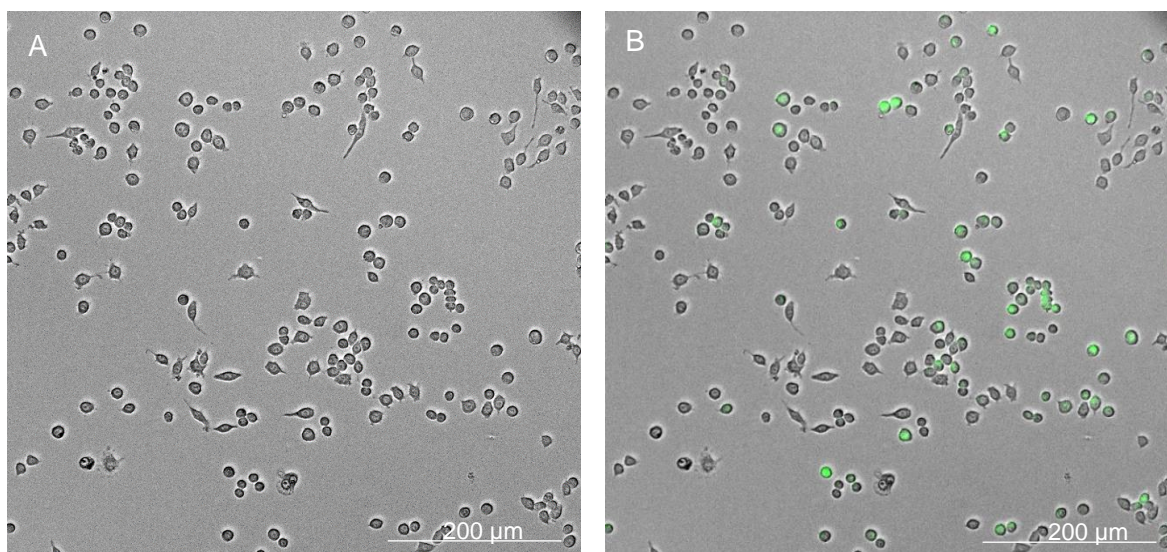


Figure 6.2: Live cell imaging of untreated macrophages stained for cellular ROS. Figure showing x20 magnification fluorescent microscopy images of untreated RAW264.7 cells, 48h post-seeding. (A), shows the bright field channel. (B) shows an overlay image of the bright field and green (GFP) channel, where ROS producing DCF stained cells are fluorescing green. Live cell imaging was carried out on triplicate wells for each treatment and respective timepoint. Independent experiments were repeated twice.

RAW264.7 cells treated with TBHP (positive control)

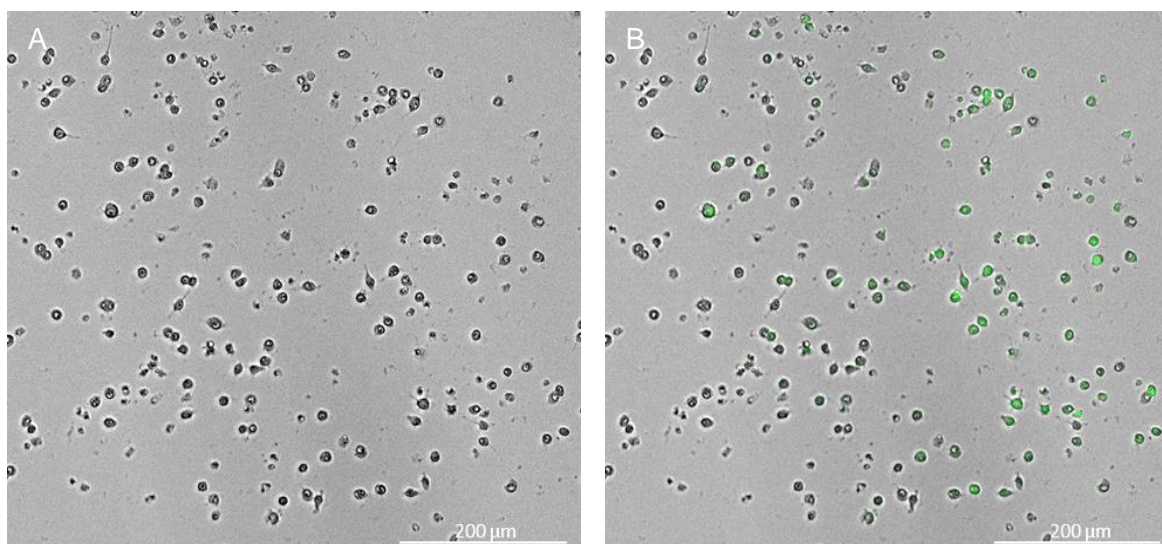


Figure 6.3: Live cell imaging of TBHP treated macrophages stained for cellular ROS. Figure showing x20 magnification fluorescent microscopy images of TBHP treated RAW264.7 cells, 3h post-treatment (positive control). (A), shows the bright field channel. (B) shows an overlay image of the bright field and green (GFP) channel, where ROS producing DCF stained cells are fluorescing green. Live cell imaging was carried out on triplicate wells for each treatment and respective timepoint. Independent experiments were repeated twice.

RAW264.7 cells treated with SC-SPIONs

3h post-NP treatment

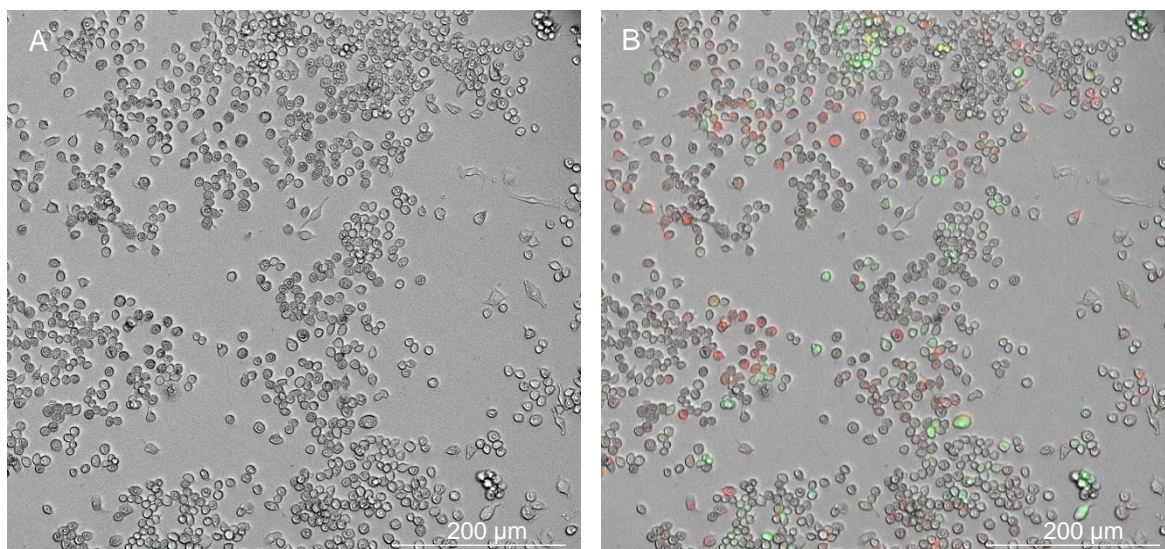


Figure 6.4: Live cell imaging of SC-SPION treated macrophages stained for cellular ROS. Figure showing x20 magnification fluorescent microscopy images of RAW264.7 cells, treated with red fluorescent SC-SPIONs for 3h. (A), shows the bright field channel. (B) shows an overlay image of the bright field and green (GFP) channel, where ROS producing DCF stained cells are fluorescing green. Live cell imaging was carried out on triplicate wells for each treatment and respective timepoint. Independent experiments were repeated twice.

24h post-NP treatment

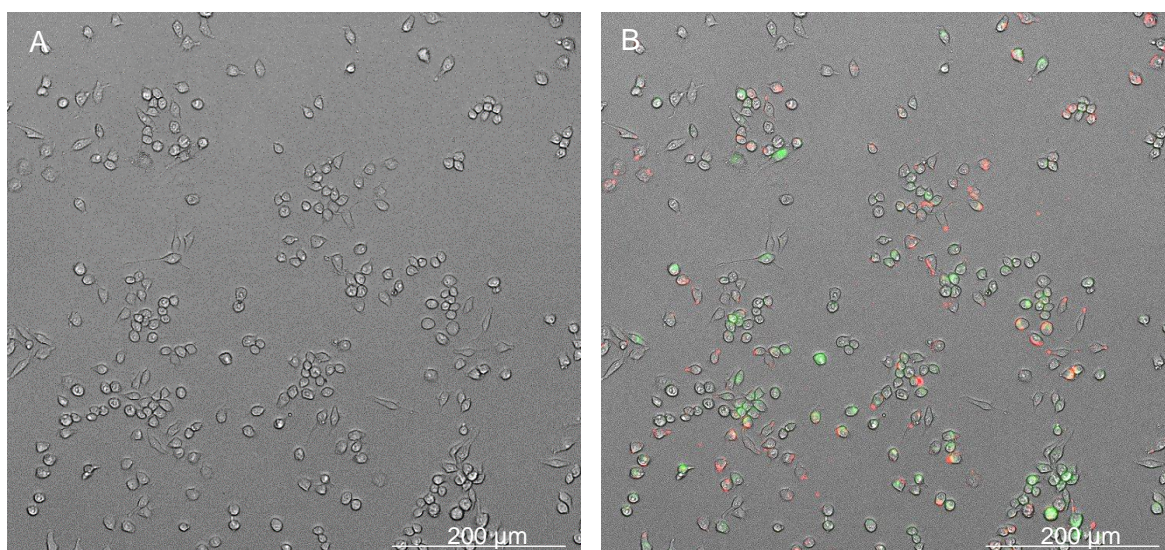


Figure 6.5: Live cell imaging of SC-SPION treated macrophages stained for cellular ROS. Figure showing x20 magnification fluorescent microscopy images of RAW264.7 cells, treated with red fluorescent SC-SPIONs for 24h. (A), shows the bright field channel. (B) shows an overlay image of the bright field and green (GFP) channel, where ROS producing DCF stained cells are fluorescing green. Live cell imaging was carried out on triplicate wells for each treatment and respective timepoint. Independent experiments were repeated twice.

RAW264.7 cells treated with NC-IONPs

3h post-NP treatment

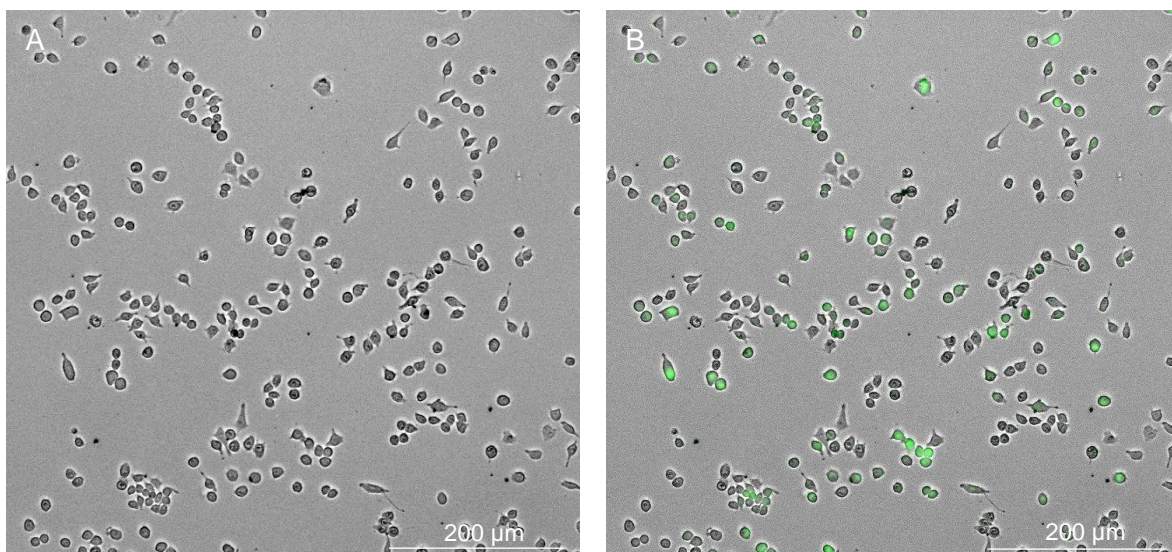


Figure 6.6: Live cell imaging of NC-IONP treated macrophages stained for cellular ROS. Figure showing x20 magnification fluorescent microscopy images of RAW264.7 cells, treated with NC-IONPs for 3h. (A), shows the bright field channel. (B) shows an overlay image of the bright field and green (GFP) channel, where ROS producing DCF stained cells are fluorescing green. Live cell imaging was carried out on triplicate wells for each treatment and respective timepoint. Independent experiments were repeated twice.

24h post-NP treatment

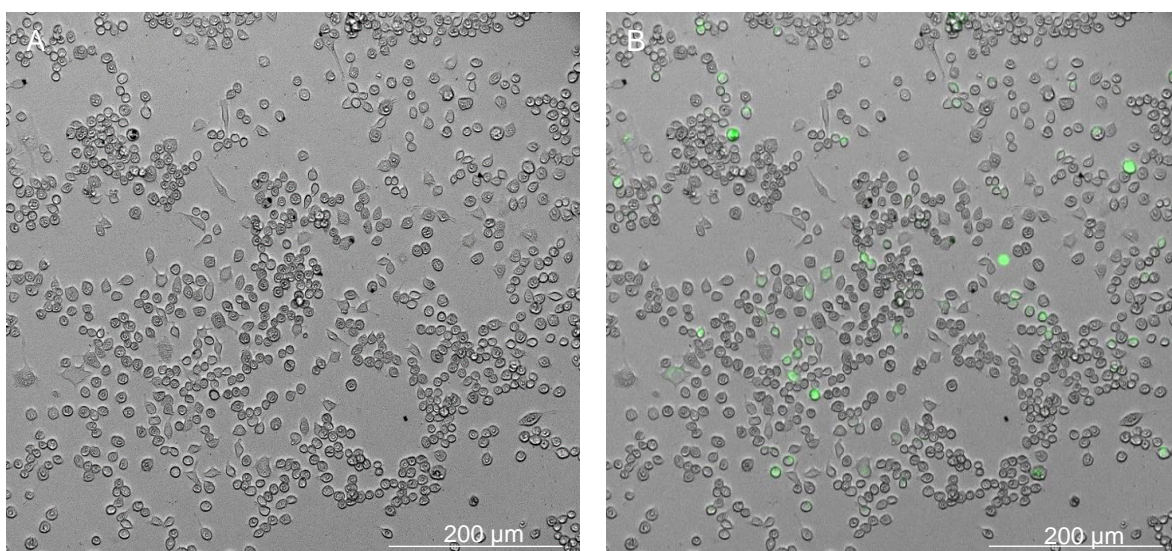


Figure 6.7: Live cell imaging of NC-IONP treated macrophages stained for cellular ROS. Figure showing x20 magnification fluorescent microscopy images of RAW264.7 cells, treated with NC-IONPs for 24h. (A), shows the bright field channel. (B) shows an overlay image of the bright field and green (GFP) channel, where ROS producing DCF stained cells are fluorescing green. Live cell imaging was carried out on triplicate wells for each treatment and respective timepoint. Independent experiments were repeated twice.

RAW264.7 cells treated with 100nm AuNPs

3h post-NP treatment

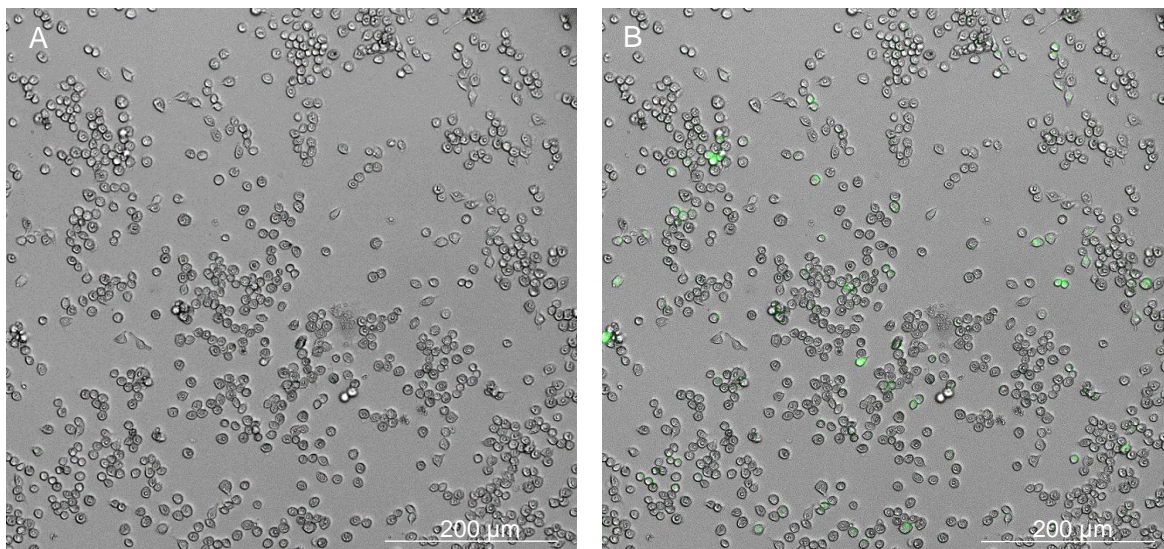


Figure 6.8: Live cell imaging of AuNP treated macrophages stained for cellular ROS. Figure showing x20 magnification fluorescent microscopy images of RAW264.7 cells, treated with 100nm AuNPs for 3h. (A), shows the bright field channel. (B) shows an overlay image of the bright field and green (GFP) channel, where ROS producing DCF stained cells are fluorescing green. Live cell imaging was carried out on triplicate wells for each treatment and respective timepoint. Independent experiments were repeated twice.

24h post-NP treatment

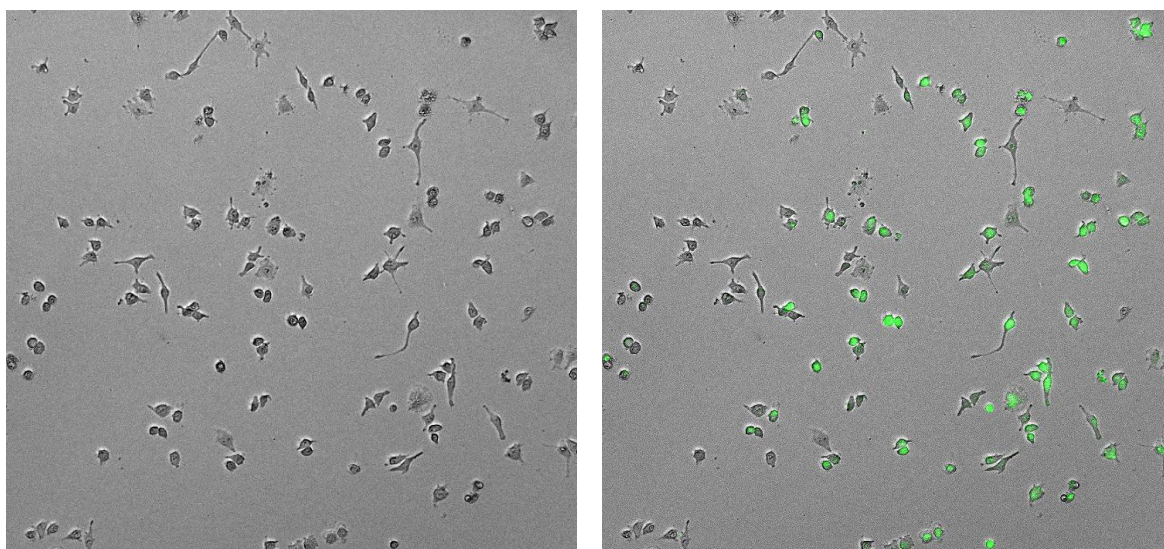


Figure 6.9: Live cell imaging of AuNP treated macrophages stained for cellular ROS. Figure showing x20 magnification fluorescent microscopy images of RAW264.7 cells, treated with 100nm AuNPs for 24h. (A), shows the bright field channel. (B) shows an overlay image of the bright field and green (GFP) channel, where ROS producing DCF stained cells are fluorescing green. Live cell imaging was carried out on triplicate wells for each treatment and respective timepoint. Independent experiments were repeated twice.

Flow cytometric analysis

The described ROS assay conducted with live cell imaging only allowed for the qualitative analysis of intracellular ROS production within RAW264.7, post-treatment with the tested NPs. Therefore, flow cytometry analysis was conducted on the RAW264.7 cells, for the detection and quantification of intracellular ROS production within the cells, 3h and 24h post-treatment with the tested NPs.

Figure 6.10 shows the untreated (negative) control, 24h post-seeding of the RAW cells, where a very low percentage of cells within the live cell population was quantified to be actively producing ROS. The cells were deemed to be actively producing intracellular ROS when they were detected to be positively stained by the green fluorescent probe DCF. The fluorescent probe is only generated in the presence of cellular ROS and fluoresces green when excited under the FITC channel, during flow cytometry analysis. 48h post-seeding of the cells, the untreated control cells portrayed a quantifiable increase in unstimulated intracellular ROS production, as seen in figure 6.11. The increase in overall unstimulated cellular ROS production was depicted by an increase in the percentage of live cells that were stained positive for DCF.

In the positive control, treatment with the cellular ROS and thus, oxidative stress inducing agent TBHP, produced the expected result of a statistically significant increase in overall intracellular ROS production, as seen in figures 6.10 and 6.11. This statistically significant increase in cellular ROS production, was presented by a greater than 2-fold increase in the percentage of cells that were stained positive for DCF, when compared to the untreated control.

Treatment with anionic-SPIONs produced a statistically significant increase in intracellular ROS production, 3h post-treatment, when compared to the respective

negative control (Figure 6.10). When the cells were treated with the SPIONs for 24h, the significant increase in intracellular ROS production observed at 3h post-treatment was maintained (Figure 6.11). However, the increase in the percentage of positively stained cells was to a lesser degree than 3h post-NP treatment.

SC-SPION treatment for 3h produced a statistically insignificant increase in intracellular ROS production, when compared to the control (Figure 6.10). On the other hand, figure 6.11 shows that treatment with the starch-coated NPs, for 24h, produced a statistically significant increase in intracellular ROS production compared to the negative control.

NC-IONP treatment for 3h produced a statistically significant increase in intracellular ROS production, when compared to the control. Furthermore, this increase in overall cellular ROS production was found to be the most significant amongst all the screened NP variants at the same treatment timepoint (Mean % cells positive for DCF, 3h post-NP treatment; untreated: 16.69, positive control: 46.08, anionic-SPION: 42.75, SC-SPION: 24.70, NC-IONPs: 40.46, AuNPs: 30.23). Like the anionic-SPIONs, figure 6.11 shows that treatment with NC-IONPs for 24h, also presented a significant increase in intracellular ROS production. Therefore, the increase in cellular ROS production, induced by IONP treatment, was maintained across the time course of the treatment.

Lastly, when cells were treated with 100nm AuNPs for 3h, figure 6.10 shows a statistically significant increase in intracellular ROS production, when compared to the control. However, this increase in intracellular ROS production was considerably less than that observed by the NC-IONPs and anionic-SPIONs, 3h post-NP cellular treatment. However, like these two NP variants, figure 6.11 shows that treatment with AuNPs for 24h also presented a significant increase in intracellular ROS production.

Therefore, the initial increase in cellular ROS production, induced by AuNP treatment, was maintained across the time course of the treatment. Furthermore, the 100nm AuNP-induced increase in intracellular ROS production, 24h post-treatment, was the most significant amongst all the screened NP variants at the same timepoint (Mean % cells positive for DCF, 24h post-NP treatment; untreated: 37.74, positive control: 84.61, anionic-SPION: 46.17, SC-SPION: 54.23, NC-IONPs: 55.40, AuNPs: 74.62). Cells were treated with 100nm SPIONs (anionic (charged) and starch coated NPs), prepared at a final concentration of 10 ug/ml, along with the NC-IONPs. Similarly, cells were treated with 100nm AuNPs, prepared at a concentration of 1.6 ug/ml, all diluted in the RPMI culture medium. The control reagent tert-butyl hydroperoxide (TBHP) (Abcam, UK) was prepared at a concentration of 55 μ M by diluting in the RPMI culture medium.

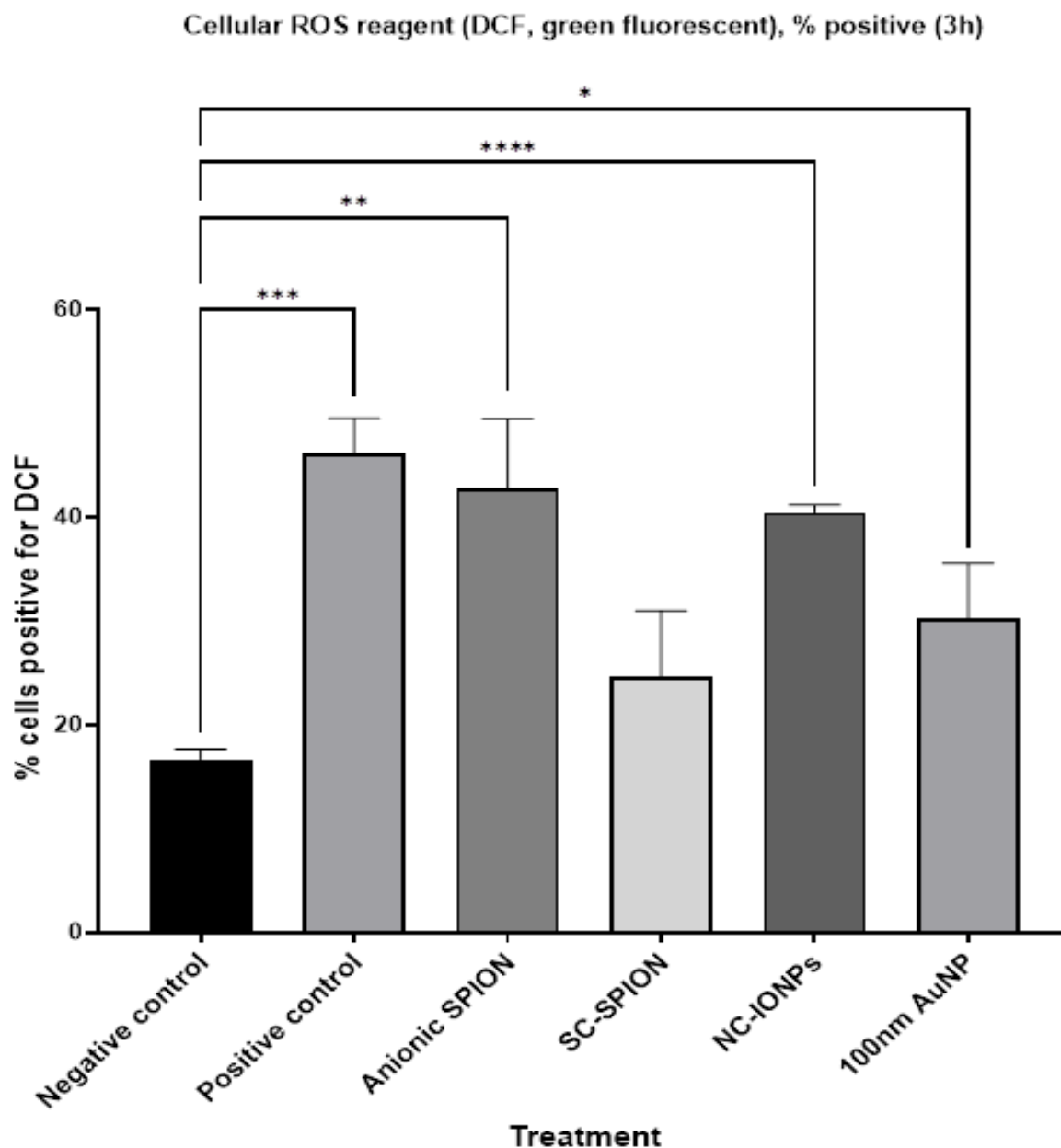


Figure 6.10: Flow cytometric analysis of untreated and treated macrophages, stained for cellular ROS. 3h. Graph representing the percentage of RAW264.7 cells stained positive for the cellular ROS detecting probe DCF, 3h post-treatment with either SPIONs (starch coated and anionic), NC-IONPs or 100nm AuNPs. As controls for analysis, untreated and unstained cells were measured, along with green fluorescent anionic SPION treated (unstained) cells. As experimental negative and positive controls, percentage of cells positive for DCF was measured in untreated and TBHP treated cells, respectively. Asterisks represent a statistically significant difference when compared to the relevant control, in an unpaired t-test (*: p-value <0.05; **: p-value <0.01; ***: p-value <0.001; ****: p-value <0.0001). Flow cytometric analysis was carried out on triplicate samples for each treatment condition, during two independent assays.

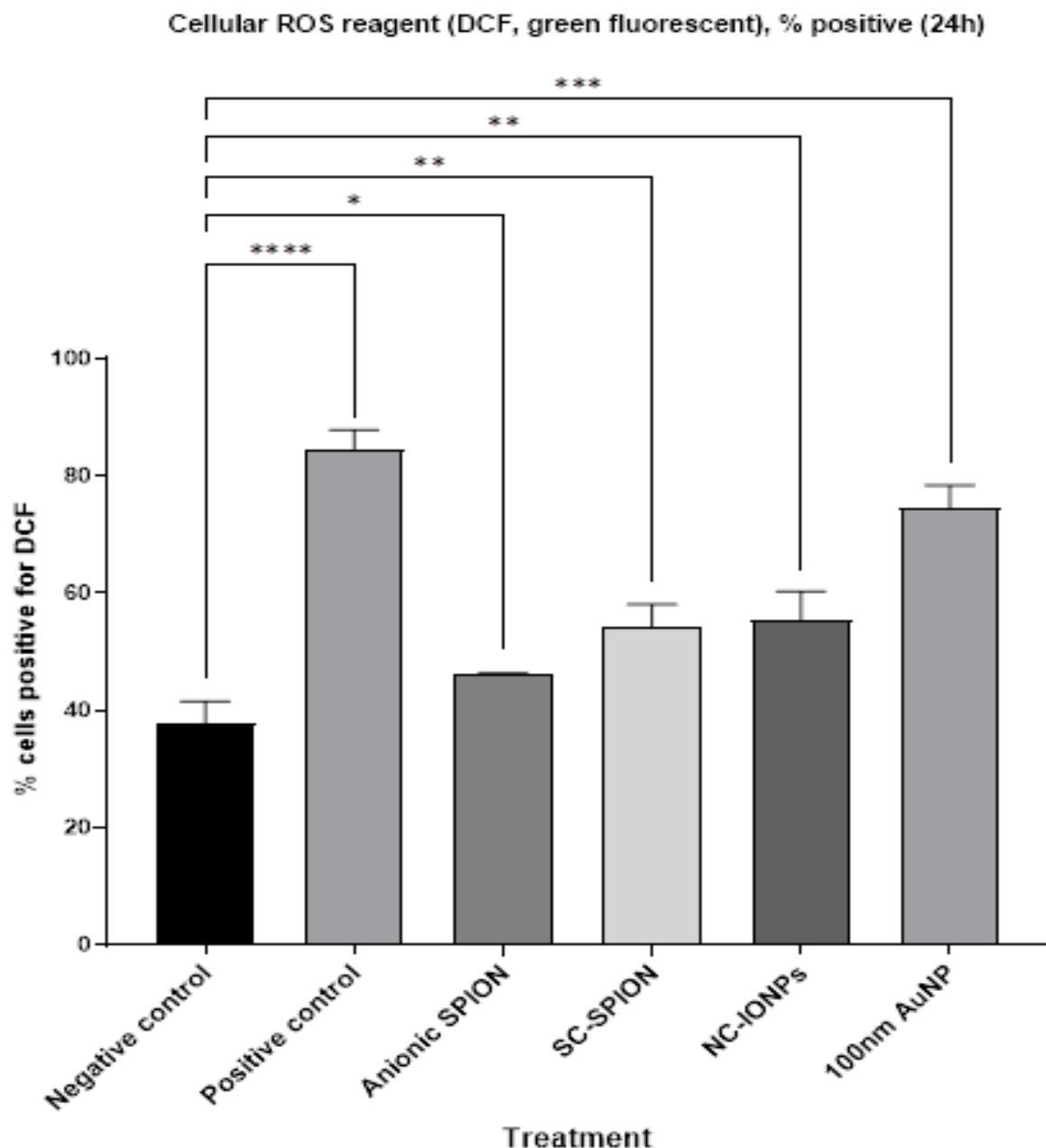


Figure 6.11: Flow cytometric analysis of untreated and treated macrophages, stained for cellular ROS. 24h. Graph representing the percentage of RAW264.7 cells stained positive for the cellular ROS detecting probe DCF, 24h post-treatment with either SPIONs (starch coated and anionic), NC-IONPs or 100nm AuNPs. As controls for analysis, untreated and unstained cells were measured, along with green fluorescent anionic SPION treated (unstained) cells. As experimental negative and positive controls, percentage of cells positive for DCF was measured in untreated and TBHP treated cells, respectively. Asterisks represent a statistically significant difference when compared to the relevant control, in an unpaired t-test (*: p-value <0.05; **: p-value <0.01; ***: p-value <0.001; ****: p-value <0.0001). Flow cytometric analysis was carried out on triplicate samples for each treatment condition, during two independent assays.

In vivo measurement of ROS production

The results gathered from the in vitro ROS assay, proved to be valuable when trying to determine the major cellular mechanism underlying NP-induced immunotoxicity observed in vivo. However, in vitro assays are limited by their inability to fully replicate host systemic physiologies and complex native conditions. Therefore, for the evaluation of NP-induced cellular ROS production and thus, cellular oxidative stress in vivo, we conducted a 4-HNE ELISA using isolated larval plasma samples. These plasma samples were extracted from GM larvae injected with a range of inorganic NPs. It has previously been shown that cellular ROS production and subsequent oxidative stress, are major mechanisms behind NP related cellular toxicity in vivo. 4-HNE is a metabolic by-product of lipid peroxidation, which is induced by cellular ROS production and oxidative stress. As a result, the utilised ELISA is able to indirectly measure cellular ROS production and levels of oxidative stress in vivo thus, giving an indication as to the level of oxidative stress induced in the GM larvae by NP treatment.

The first 4HNE ELISA was conducted using a set of larval plasma samples that were acquired from NP injected or control treated GM larvae, that were visually of an older age, slower and overall, in less prime condition (Repeat 1). The results from this ELISA showed an expected increase in larval plasma 4HNE concentration, when plasma samples acquired from the hydrogen peroxide treated positive controls were measured. Treatment with oxidative stress inducing Hydrogen peroxide should cause an increase in cellular ROS production in vivo and thus, an increase in plasma 4-HNE concentration. Likewise, with the NP injected GM larvae, Figure 6.12 shows a significant increase in plasma 4HNE concentration for all larvae injected with anionic-SPIONS, NC-IONPs or 100nm AuNPs. In contrast, plasma samples acquired from larvae injected with starch-coated SPIONS, RAW (unmodified) CNTs or CMC-coated

CNTs, portrayed no significant increase in plasma 4HNE concentration when compared to the negative control.

The described 4HNE ELISA experiment was then repeated with a new set of larval plasma samples that had been acquired from a different GM larval population, also injected with the same range of inorganic NPs at the same concentrations. However, unlike the GM larvae used for injections and plasma acquisition during the first 4HNE ELISA, the larvae in this population were visually of a younger age, more active, responsive, healthier looking and overall, in more prime condition (Repeat 2). Unlike in the first 4HNE ELISA experiment, Figure 6.12 shows no significant changes in plasma 4HNE concentration, when plasma samples extracted from larvae injected with any of the NPs were measured and compared to the negative control. A statically significant increase in larval plasma 4HNE concentration was only observed, expectedly, in the positive control. For each repeat of the ELISA, larval plasma samples extracted from the respective larval test groups were assayed in duplicate.

Larval plasma (4HNE concentration), ng/ml (Repeats 1 and 2)

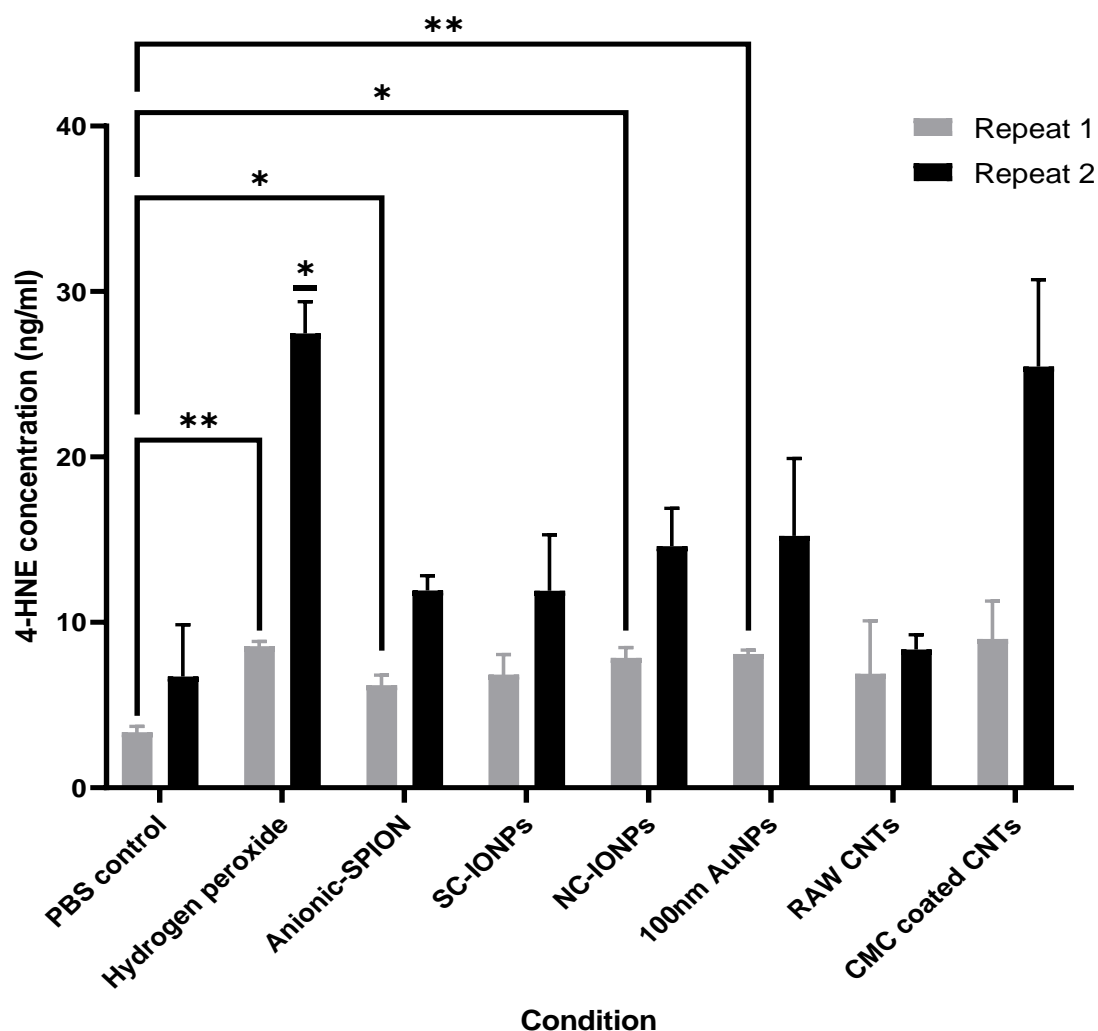


Figure 6.12: **4HNE-ELISA measuring cellular ROS, in vivo.** Graph presenting larval plasma 4-HNE metabolite concentrations (ng/ml), in samples acquired from differing GM NP treatment groups. 4-HNE concentrations were measured in plasma samples acquired from groups of larvae, 24h post-larval injections with either SPIONs (starch coated and anionic), NC-IONPs, 100nm AuNPs, RAW CNTs or CMC-coated CNTs. The figure presents mean concentrations of two independent experiments, in which larvae portrayed differences in physiological state. Asterisks represent a statistically significant difference when compared to the relevant control, in an unpaired t-test (*: p-value <0.05; **: p-value <0.01; ***: p-value <0.001; ****: p-value <0.0001). Larval plasma samples from the respective larval test conditions, were assayed in duplicate during each ELISA repeat.

6.4 Discussion

As is presented in results chapter 5, certain assayed NPs, namely the SPIONs and all assayed AuNP size variants, portrayed significant levels of NP-induced immunotoxicity in vivo. This result was obtained through flow cytometric analysis of larval hemocytes, post-NP treatment, where changes in larval THC due to NP-induced toxicity were quantified (chapter 5, figure 5.10). The major mechanism for NP-induced cytotoxicity/immunocytotoxicity is likely to be increases in ROS production and therefore, oxidative stress. This hypothesis has led to numerous studies investigating NP-induced ROS increases, with most NPs now being known to cause toxicity through ROS production and subsequent oxidative stress (Fu et al., 2014). Therefore, the aim of this supplementary study was to determine NP-induced cellular ROS in GM larvae. Hence, in vitro and in vivo cellular ROS assays were conducted for the qualitative and quantitative analysis of NP potential in increasing ROS production. Overall, the results strongly suggest that in the case of the metallic NPs (SPIONs and AuNPs), NP-induced cellular ROS production and cellular oxidative stress was the likely mechanism for NP-induced immunotoxicity, observed in vivo.

As shown in (chapter 5, figure 5.10a), both SPION variants produced a statistically significant decrease in larval THC, in both the control and immunosuppressed states. Previously, several in vitro studies have investigated the toxicity of differing NP variants (Fu et al., 2014; Habas et al., 2021). In a study that investigated IONP accumulation in rat alveolar macrophages and RAW264.7 cells, microarray analysis showed widespread reprogramming of genes mainly involved in oxidative stress and systemic inflammation (Shah and Dobrovolskaia, 2018). Furthermore, in a study investigating IONP-induced oxidative stress and genotoxicity in mammalian cell lines,

it was reported that the IONPs induced cellular oxidative stress in a dose-dependent manner. NP-induced oxidative stress was evident by the measurement of depleted glutathione and lipid peroxidation levels, indicative of increased cellular ROS production. The study concluded that IONPs have the potential to induce significant levels of toxicity in mammalian cells, *in vitro*, which was likely mediated through cellular ROS production and oxidative stress (Ahamed et al., 2013).

Therefore, we conducted an *in vitro* ROS assay to assess the potential of intracellular ROS production for the different tested NPs. The *in vitro* ROS assay used live cells to measure cellular ROS production in response to exogenous NP stimuli. Only live cells actively produce cellular ROS when stimulated by foreign bodies, thus, cellular ROS production can be directly measured (Auten and Davis, 2009). The described *in vitro* ROS assay was conducted on cultured live RAW264.7 mouse macrophage cells, due to their immunological similarity to larval hemocytes as innate immune cells. The results from the ROS assay, confirm the potential of cellular ROS production and oxidative stress, as the likely mechanism behind the observed *in vivo* SPION immunotoxicity, over 24h.

However, despite the usability and efficiency of *in vitro* assays, they are unable to fully replicate the complexity of an *in vivo* system or provide meaningful data surrounding the true physiological responses to an exogenous stimulus (X. D. Zhang et al., 2011). Henceforth, a 4HNE-lipid peroxidation ELISA, not known to have previously been attempted with GM larval biological samples, was conducted using NP treated larval plasma samples. Thereby, allowing us to measure levels of NP-induced ROS production *in vivo*. The increased levels of cellular ROS production portrayed by the anionic-SPIONs, in comparison to the SC-SPIONs, were replicated in the GM larvae as shown in the *in vivo* ROS assay. The *in vivo* assay portrayed a similar result to that

obtained in the *in vitro* assay, with figure 6.12 showing that in an overall non-prime physiological state, only the anionic-SPIONs induced a significant increase in cellular ROS production, 24h post-treatment. Furthermore, the differences in SPION induced immunotoxicities, between the variants, may also explain the significant differences in NP *in vivo* systemic toxicities. Lastly, figure 6.12 shows that in non-prime GM larvae, the anionic-SPIONs, NC-IONPs and the 100nm AuNPs induced a significant increase in cellular ROS production, *in vivo*, which was not observed after CNT treatment. The difference in cellular ROS production capabilities between the NP variants could explain why there was NP-induced immunotoxicity observed *in vivo* with the SPIONs, IONPs and the AuNPs, but not with the CNTs.

However, despite significant increases in NP systemic toxicity, the NC-IONPs did not induce significant differences in ROS production when compared to SPIONs. Therefore, systemic toxicity induced by the NC-IONPs most likely resulted not only from increases in ROS but possibly also from tissue bioaccumulation. Evidence for IONP tissue bioaccumulation was reported in a study that investigated the adverse effects of IONPs on neural tissue and the mechanisms behind NP tissue damage. The study reported that iron accumulation can result in protein aggregations, *in vivo*, which then results in an adverse positive feedback loop. The generation of a positive feedback loop is said to be toxic to cells. Henceforth, released free iron ions from exposed IONPs, *in vivo*, may result in iron accumulation within host tissues and therefore, activate a cellularly toxic feedback loop (Yarjanli et al., 2017). Thus, this potential IONP aggregation, in addition to IONP-induced ROS production, may explain the observed increase in IONP *in vivo* toxicity, when compared to the SPIONs.

On the other hand, significant levels of NP systemic toxicity were observed when CNTs were assessed, *in vivo*. However, figure 6.12 shows that when the RAW

(unmodified) and CMC-coated CNT variants were assayed for their ROS inducing capabilities in vivo, they did not induce a significant change in ROS production. It is known that not all NPs induce excessive cellular ROS production and oxidative stress. NP-induced cellular ROS production is said to be dependent on NP physicochemical properties, such as the crystalline phase, adsorption ability, and solubility. Furthermore, metallic NPs are the NP variants that are most known to be associated with NP-induced cellular ROS production, as opposed to non-metallic variants such as CNTs. This is due to the fact that NP cellular uptake and intracellular free metal ion release, are determining factors in NP mediated intracellular ROS production (Horie and Tabei, 2021). Therefore, as mentioned in chapter 5, CNT aggregations and tissue bioaccumulation are most likely major mechanisms underlying the observed in vivo toxicity, as opposed to increases in ROS production.

The two AuNP size variants (20nm and 60nm), portrayed significant levels of systemic toxicity, in vivo. Here, the likely mechanism is thought to be cellular ROS production and oxidative stress. The results gathered from the in vitro assay, using the 100nm AuNPs as an NP representative, support the idea that increases in cellular ROS production was the likely cause behind the observed AuNP mediated immunotoxicity. Evidence for AuNP-induced significant ROS production and subsequent oxidative stress, has previously been reported in a study that investigated AuNP distribution, bioaccumulation and toxicity through in vitro and in vivo studies. Similar to the results obtained in our study, the previous study reported a significant increase in ROS production, 16h post-treatment with AuNPs, in vitro (Lopez-Chaves et al., 2018).

This study puts forward the use of a 4-HNE lipid peroxidation ELISA, as a useful technique to measure ROS production in GM larvae. In the presented study, a 4HNE lipid peroxidation ELISA was conducted on NP treated GM larval plasma samples, for

the rapid and quantifiable detection of NP-induced ROS production in vivo. Although the described ELISA has been utilised before in combination with various biological samples, this was the first time that it was used with GM larval biological samples.

As mentioned in chapter 5, with exception of the SC-SPIONs and 100nm AuNPs, the remaining NPs assayed should be used cautiously due to detectable levels of systemic and immunotoxicity. However, when investigating the levels of NP-induced ROS production, both in vitro and in vivo, the results showed that only the 100nm AuNPs produced significant levels of ROS. Therefore, in the context of biological safety, despite the lack of significant systemic toxicity portrayed by the AuNPs, the NPs show a strong potential towards a significant increase in ROS production, hence, oxidative stress. The lack of significant increase in ROS production, portrayed by the SC-SPIONs, promotes them to be more biologically safe when compared to the AuNPs.

Some limitations were present in this NP-induced cellular ROS study, which need to be taken into consideration when concluding the true mechanism underlying NP toxicity for the assayed range of inorganic NPs. As already mentioned, in vitro cellular ROS assays are unable to fully replicate the complexity of an in vivo system (X. D. Zhang et al., 2011). Therefore, to overcome this limitation, a 4HNE-lipid peroxidation ELISA was conducted with the use of NP treated larval plasma samples, to indirectly measure NP-induced cellular ROS production, in vivo. However, the results from the in vivo cellular ROS assay, show that the physiological condition and overall health of the host organism plays a significant role in their physiological response to exogenous stimuli. In future, for the replicability of NP-induced cellular ROS production results, in vivo, more standardised GM larval organisms should be used with similar overall physiological conditions. In addition, further mechanisms of NP toxicity, such as membrane and mitochondrial damage, should be investigated in future studies.

7. Intracellular Trafficking and Cellular Fate of Superparamagnetic Iron Oxide Nanoparticles in Mouse Macrophages

Aims and hypotheses

NP cellular fate is known to be an important determining factor in NP-induced cytotoxicity (Chu et al., 2014). Therefore, predetermining NP cellular fate post-cellular uptake is of importance, when predicting potential levels of NP-induced cytotoxicity prior to their use in therapeutic formulations. The aim of this chapter was to present preliminary data on the intracellular fate of SPIONs in mouse macrophages. Thereafter, through future work, we aim to determine if NP endosomal escape plays a role in SPION induced immunotoxicity.

7.1 Introduction

NPs, due to their unique physicochemical properties, can be used to encapsulate and transport therapeutic compounds to desired target cell populations or whole tissues. Highly dependent on their physicochemical properties including size, shape, aspect ratio, surface charge, hydrophobicity, elasticity, stiffness, corona formation, and surface functionalisation, NPs are able to cross biological barriers, such as cell membranes, and enter target cells to carry out their intended functions (Varma et al., 2021; Foroozandeh and Aziz, 2018). However, the clinical translation of the described advantageous NP biomedical applications is known to be challenging (Rosenblum et al., 2018).

Despite NPs portraying the ability to carry out targeted drug delivery and improve therapeutic efficacies, one of the major challenges of NP clinical translation is the efficient localisation of NP drug carriers within specific cell populations and subcellular targets in the body (Björnmalm et al., 2017). Therefore, there is a critical need to further understand NP interactions with biological systems, thus, allowing for the control of *in vivo* NP transport and cellular/tissue uptake, hence, potentially improving the clinical efficacy of NP formulations (von Roemeling et al., 2017; Donahue et al., 2019). On the other hand, despite their desirable therapeutic purposes, NPs can induce negative effects on intended and non-intended targets, therefore, causing adverse systemic effects (Sharma et al., 2012). It is thus, important to better understand NP interactions with biological systems to then predict NP-induced toxicities. Elucidating NP-biological interactions may allow for future predictions of NP cellular uptake pathways and their intracellular fate, which are fundamental aspects of determining the end effect of NP exposure.

Overall, to achieve a desirable level of therapeutic efficacy, the safe entry of NP drug delivery carriers into the intended target cells is of great importance. However, factors such as NP intracellular fate and localisation are important for the determination of potential subsequent cytotoxic effects (Foroozandeh and Aziz, 2018).

Despite large bodies of research being devoted to the field of NP endocytosis (Sahay et al., 2010), only limited understandings have been obtained on the cellular fate of NPs after cell entry (Chu et al., 2014). It is known that NPs, right after being taken up through endocytosis, are localised within endosomes (Chithrani and Chan, 2007). These vesicles then evolve into lysosomes or autophagosomes at a later stage (Fader and Colombo, 2009). This process results in a drop in pH and supply of proteolytic enzymes (Figure 7.1). Internalised NPs can escape the endo-lysosomal system and their effect largely depends on their ability to undergo endosomal escape, which in turn, also impacts their cellular fate. Whether or not the NPs undergo endosomal escape and spread throughout the cytoplasm, prior to endosomal maturation and lysosomal degradation or exocytosis, is critical in determining their intended therapeutic efficacy (Chu et al., 2014).

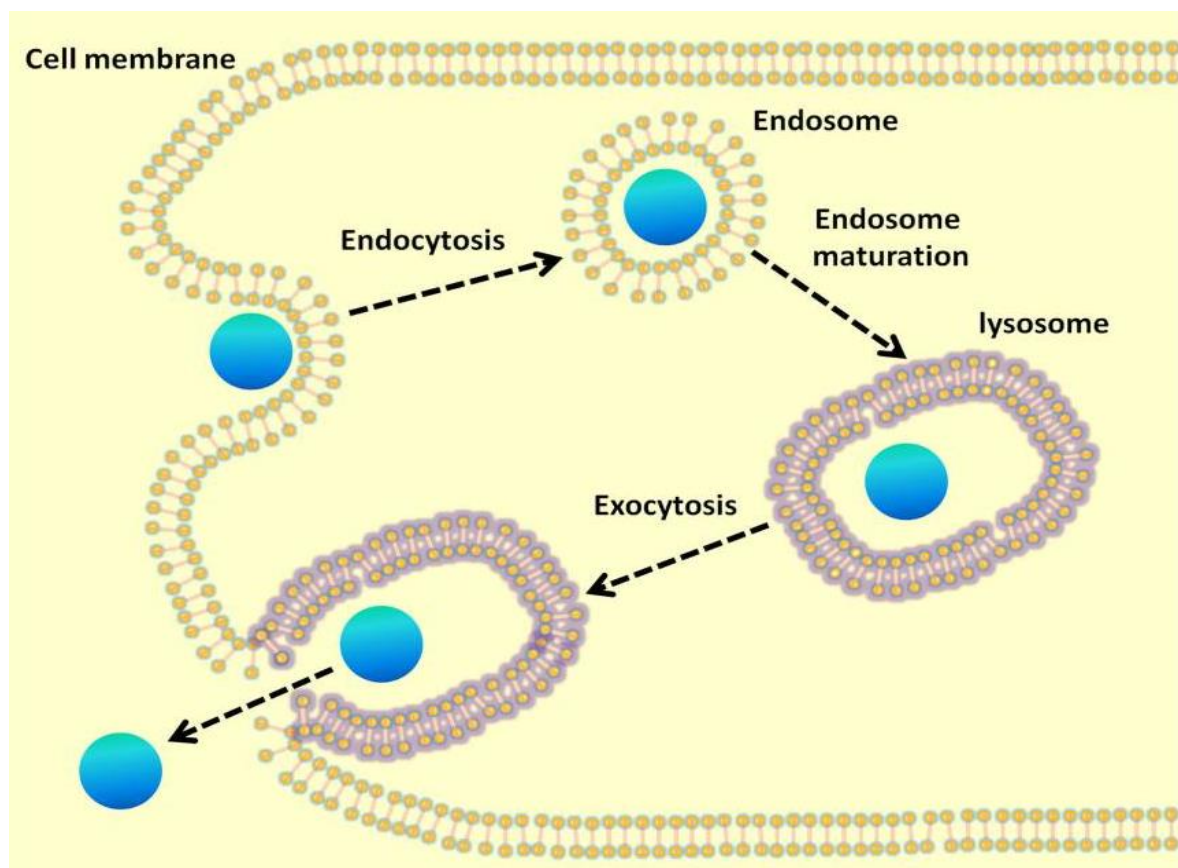
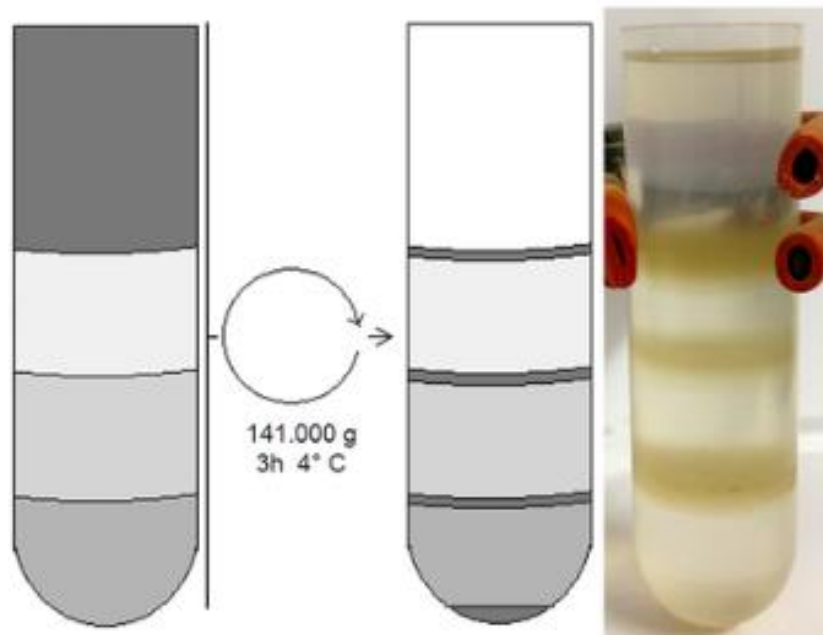


Figure 7.1: Cellular uptake of NPs and intracellular translocation/cellular fate. Figure representing the cellular uptake of NPs through the process of endocytosis. Thereafter, the NPs are shown to be localised within membrane bound vesicles/endosomes, which subsequently mature into lysosomes or autophagosomes. Therefore, significantly altering NP intracellular translocation and cellular fate. Image from: (Chu et al., 2014).

Commonly, visual representations including optical and electron-based microscopy techniques are utilised for the study of NP intracellular trafficking pathways and for the estimation of NP intracellular fate, post internalisation. However, microscopy techniques do not provide a high enough resolution and thus, an accurate representation of intracellular NP localisation and cellular fate. Therefore, alternate in vitro techniques such as the subcellular fractionation of cultured cells and subsequent organelle purification, post NP treatment, allow for a greater resolution and determination of intracellular compartments potentially containing NPs (Reifarth et al., 2018).

During subcellular fraction and organelle purification of cultured cells, intact cultured cells or whole tissue are mechanically or chemically homogenised into their major compositions. Thereafter, differential centrifugation can be utilised in order to crudely separate subcellular compartments/organelles based on their properties of mass, size and density (De Araújo and Huber, 2007). Using this technique, cellular nuclei can be pelleted and separated away from a heterogeneous sample of cellular organelles, with the pellet having the potential to be separated further into heavy and light mitochondrial fractions, along with the cytosol. Using the supernatant, the technique of equilibrium density centrifugation, which utilises further centrifugation steps and a density gradient made up of a non-ionic medium such as Iodixanol, can be carried out to further separate the subcellular organelles based on organelle density. Therefore, this step of subcellular fractionation allows for the enhanced isolation and purification of organelles that may contain internalised NPs and thus, could be used to determine the cellular fate of the NPs (Figure 7.2). Purified organelles can be analysed through different validation techniques, such as Western blot analysis and/or next generation protein sequencing. Alternate techniques for the isolation of cellular organelles include detergent-based extraction and free-flow electrophoresis. (German and Howe, 2009).



*Figure 7.2: **Subcellular fractionation using a discontinuous density gradient.** Figure representing the subcellular fractionation of cellular organelles, utilising a Sucrose based discontinuous density gradient. Once subcellular fractionation was carried out, utilising high-speed ultracentrifugation, the cellular organelles were fractionated into distinctive bands based on organelle density (right). Image from: (De Castro Moreira Dos Santos et al., 2015).*

Density gradient based subcellular organelle separations frequently utilise non-ionic mediums, such as Percoll, Ficoll, or Iodixanol (OptiPrep), to separate organelles based on their densities (Morand and Kent, 1986; Li and Donowitz, 2008). However, excessive homogenisation of cultured cells or tissues results in the formation of plasma membrane microsomes that tend to contaminate these organelle fractions (Morand and Kent, 1986). Furthermore, this technique of separation is limited by significant reagent costs and time for the acquisition of enriched organelle fractions (Morand and Kent, 1986; Li and Donowitz, 2008). Therefore, to mitigate the limitations of organelle fraction contaminations, time, reagent cost and cellular waste, a subcellular fractionation method entirely based on Balch homogenisation and differential centrifugations could be utilised (German and Howe, 2009).

In the presented study, RAW264.7 mouse macrophage cells were used as a homologue of human macrophages to study the intracellular trafficking pathways and thereby, the intracellular fate of superparamagnetic iron-oxide NPs (SPIONs), post cellular uptake. The study was carried out with the aim of determining if NP intracellular fate was a potential mechanism, underlying SPION induced cellular toxicity observed in chapter 5. RAW264.7 cells were incubated for 2h in the presence of SPIONs, for cellular uptake of the NPs to take place. Thereafter, the intact cells were opened using a mechanical homogenisation method (Balch homogeniser) to obtain a heterogenous cellular homogenate composed of major cellular organelles. Subsequently, differential centrifugation was conducted on the cell homogenate to pellet cellular debris and nuclei. Thereafter, the organelle enriched post-nuclear supernatant (PNS) was loaded on a discontinuous equilibrium density gradient, prepared using different percentages of Iodixanol. Lastly, validation techniques including fluorescent microscopy and Western blot analysis were conducted on the enriched cellular organelle fractions, thereby determining organelle purity and identifying cellular organelles associated with internalised NPs. Therefore, the intracellular fate of SPIONs post-cellular internalisation can be determined through the identification of specific organelles associated with NPs.

However, due to issues with enriched organelle fraction purity and resolution, along with cellular organelles of interest being heavily enriched in the nuclear pellet, post-differential centrifugation, a cellular vesicle isolation technique based entirely on Balch homogenisation and differential centrifugations was utilised (German and Howe, 2009). Using this technique, endosome-enriched vesicular fractions of interest were obtained. Briefly, RAW264.7 mouse macrophage cells were cultured using aseptic techniques and intact cells were opened using Balch homogenisation to achieve a

heterogenous cellular homogenate composed of major cellular organelles. Lastly, using various short-term differential centrifugations and a step of ultracentrifugation, endosome-enriched vesicular fractions were obtained for further validation analysis.

7.2 Methods

Preparation of homogenisation medium and Optiprep density fractions

Homogenisation medium

The cell homogenisation medium contained 0.25M sucrose, 1mM of Ethylenediaminetetraacetic acid (EDTA), 20mM HEPES-NaOH (pH to 7.4), and a universal protease inhibitor (complete Mini EDTA free protease cocktail) (Roche, UK) which was added fresh prior to use. The buffer was stored at 4 °C.

Optiprep fractions

The non-ionic density gradient medium Optiprep, composed of 60% (w/v) Iodixanol dissolved in water (Sigma-Aldrich, Poole, UK), was diluted using a HES buffer to first make a 50% working solution of Optiprep. The Optiprep diluent HES buffer contained 0.25M sucrose, 2mM EDTA and 40mM HEPES-NaOH (pH to 7.4). The buffer was stored at 4 °C. Thereafter, the 50% working solution of Optiprep was further diluted using the HES buffer to make the varying density gradient fractions, composed of different Optiprep percentages.

Preparation of RAW264.7 mouse macrophage cells and nanoparticles

A macrophage cell line was utilised in this study, due to the clinical significance of macrophages being innate immune cells and thus, the first point of NP contact with the immune system post NP exposure or administration. RAW264.7 mouse

macrophage cells were used as a homologue of human macrophages, as they do not require further differentiation and display a mature macrophage phenotype.

On the day of the experiments, starch-coated fluorescently labelled SPIONs (Chemicell, Berlin, Germany) were suspended by sonication in a waterbath sonicator for 1h. Next, the NPs were washed and dispersed in 1x PBS solution using a probe sonicator (MSE Soniprep 150 Sonicator, amplitude = 26) for 1 minute. Suspended SPIONs were added to the RAW264.7 cells in starvation media at a final concentration of 10 µg/ml. A magnet was slowly moved across the underside of the flask repeatedly, in order to pull the NPs to the bottom of the flask. The magnet was used to shorten the time taken by the NPs to naturally reach the bottom of the flask and make contact with the cells. Cells were incubated at 37°C in humidified conditions at 5% CO₂ for 2 hours.

Cellular homogenisation and inhibition of proteolytic degradation

After treatment, cells were immediately placed on ice, serum free media was aspirated, and the cells were washed twice with room temperature PBS and once with ice-cold PBS. Thereafter, the macrophage cells were scraped off the tissue culture flask with a cell scraper, resuspended in 0.5ml of PBS and transferred to 1.5ml microfuge tubes kept on ice for an overall cell count to be established. Using a haemocytometer, the number of macrophage cells was counted and a cell count of approximately 8.6×10^6 cells per ml was established. Thereafter, cells in suspension were pelleted following centrifugations and pellets were gently resuspended in 0.5ml of ice-cold homogenisation medium containing 1x universal protease inhibitor, thus, preventing the proteolytic degradation of exposed cellular contents (full composition described above and in chapter 2.1). Meanwhile, a Balch homogeniser was prepared

on ice with a 7µm gap tungsten-carbide ball bearing and two 2ml syringes. The cells were gently passed five times in each direction (10 passes total) through the Balch homogeniser, using constant manual pressure. Following cell homogenisation, samples were returned to fresh 2ml microfuge tubes kept on ice.

Differential centrifugation

Following cellular homogenisation, a series of low-speed differential centrifugation steps were performed for the elimination of cellular debris, cellular nuclei, and the heavy mitochondrial cellular fraction. Cell homogenates were centrifuged at 4 °C for 10 minutes at 3000g, in order to pellet cellular debris and nuclei. The PNS was transferred to a fresh 1.5ml microfuge tube. Thereafter, the PNS samples were centrifuged once again at 4 °C for 10 minutes at 20,000g to pellet the heavy mitochondrial fraction. Supernatants were transferred to fresh 1.5ml microfuge tubes and kept on ice.

Preparation of an Iodixanol based discontinuous density gradient

Supernatants acquired post-differential centrifugations were loaded onto Iodixanol based discontinuous density gradients. Gradients were prepared by carefully layering 670µl of Optiprep gradient fractions, composed of differing Optiprep medium percentages made from the 50% Optiprep working solution, in 4ml ultracentrifuge tubes (Fisher Scientific, Loughborough, UK). Gradients were created by layering the heaviest density gradient fraction composed of 27% Optiprep first, which was followed by 22.5% Optiprep. Subsequently, the 19% Optiprep gradient fraction was created using the 50% Optiprep working solution, the respective cellular organelle enriched samples and further 1x protease inhibitor for the prevention of proteolytic degradation of cellular components. The cellular organelle enriched samples were loaded onto the

discontinuous gradients, by carefully layering the 19% Optiprep gradient fraction containing the organelles on top of the 22.5% Optiprep fraction. Thereafter, the remaining gradient fractions of the discontinuous gradients, composed of 16, 12 and 8% Optiprep solution were layered on top.

Fractionation of subcellular organelles using equilibrium density centrifugation

Completed gradients were balanced using the ultracentrifuge buckets, placed in a Beckman SW-60Ti rotor, and spun in a Beckman Optima XE 100 K ultracentrifuge (Beckman Coulter, Buckinghamshire, UK) at 4 °C for 19hrs at 100,000g. Thereafter, the density gradients were retrieved and the bands representing fractions of enriched cellular organelles, separated based on density, identified. Fractions were collected from the top, the lightest fraction at the top (fraction 1) to the heaviest at the bottom, as 0.5ml gradient fractions.

Western blotting

Sample preparation

Western blot analysis was carried out on the collected density gradient fractions. The experiments were conducted primarily for the identification of cellular organelles enriched within each fraction. Thus, the protein content of the density gradient fractions was analysed by SDS-PAGE and Western blotting, which involved gradient fractions being immunostained for specific organelle markers. Collected gradient fractions were prepared for gel electrophoresis, by adding 1x Sodium dodecyl sulphate (SDS) sample buffer (full composition in chapter 2.1) to aliquots of each fraction. Prior to loading on the SDS gel, samples were boiled using a heat block set at 100°C for 5 minutes and centrifuged at 4 °C for 3min at 13,000 rpm using a microcentrifuge. Therefore, insoluble proteins and sample debris were pelleted.

SDS-PAGE and Western blotting

The supernatants were loaded onto a 12% SDS polyacrylamide gel (gel compositions in chapter 2.1), along with 5 μ l of a 'colour plus' protein marker (New England BioLabs). The gel was run for 1h at 25mA constant current, using a mini-PROTEAN electrophoresis tank (BioRad). Proteins separated along the polyacrylamide gel were then transferred onto a 0.22 μ m pore-size nitrocellulose membrane. The membrane 'sandwich' used for protein transfer onto the membrane, was prepared as illustrated in the figure below (Figure 7.3). The transfer was then run for 1h at 100 V constant voltage at 4 °C to prevent overheating.



Figure 7.3: **Order of assembly for the protein transfer 'sandwich'**. Once the SDS polyacrylamide gel containing protein samples was run, the protein transfer 'sandwich' to transfer the proteins onto a nitrocellulose membrane was prepared as shown above. The sponges, filter papers and nitrocellulose membrane were pre-soaked in 1X transfer buffer prior to assembly. Image from: abcam.

Thereafter, the membrane was stained with 5% ponceau-S in acetic acid (Sigma Life Sciences) in a petri dish for 3 minutes, to visualise the amount of protein in each of the loaded samples and for the detection of protein bands on the membrane. Once the protein bands were visualised, the membrane was destained using PBS containing 0.1% Tween 20 (PBST) (two 5-minute washes) and blocked with 5% milk in PBST for 1 h at room temperature, whilst rocking on an orbital shaker. Once blocked, the nitrocellulose membrane was washed twice with PBST (5 minutes each). Primary antibodies were diluted in either 5% milk in PBST or 5% BSA in PBST, thus, membranes were probed with the appropriate antibody overnight at 4 °C, whilst rocking on an orbital shaker. The following day, the primary antibody was removed, and the membrane was washed at room temperature with PBST (two 5 minute washes). Thereafter, the membrane was probed with an appropriate goat horseradish peroxidase (HRP)-conjugated secondary antibody, diluted 1:3000 in 5% milk in PBST, for 1h at room temperature whilst rocking. Following incubation with the secondary antibody, the membrane was washed with PBST (twice for 5 minutes and once for 10 minutes) and kept in PBST. Enhanced chemiluminescent (ECL) substrate solutions were prepared (solution compositions in chapter 2.1) and incubated with the nitrocellulose membrane for one minute at room temperature. Immediately after, the membrane was developed by exposing it onto a film in a dark room.

Fluorescence microscopy

To determine which collected density gradient fractions were enriched with fluorescent SPIONs, fluorescence microscopy was carried out on each of the fractions from the respective gradients. Aliquots from each of the gradient fractions were placed on individual microscope slides and a coverglass was placed on top. Fluorescent

microscopy images of the gradient fractions were obtained using a Leica DM400 fluorescent microscope (Leica, Wetzlar, Germany) using LAS software.

Subcellular fractionation based on differential centrifugations

To mitigate the limitations portrayed by density gradient based cellular fractionation, such as organelle fraction contaminations, time, reagent cost and cellular waste, a subcellular fractionation method entirely based on Balch homogenisation and differential centrifugations, put forward by German et al, was investigated (German and Howe, 2009).

Buffers

MES buffer containing 150mM NaCl and 25mM 2-(N-morpholino) ethanesulfonic acid sodium salt (Sigma-Aldrich, Poole, UK), pH to 6.5, dissolved in ddH₂O. A universal protease inhibitor (complete Mini EDTA free protease cocktail) (Roche, UK) was added fresh prior to use. The buffer was stored at 4°C.

Cellular homogenisation and inhibition of proteolytic degradation

Similar to the method of cellular homogenisation described above, cultured RAW264.7 cells were placed on ice, cell culture media was aspirated, and the cells were washed twice with ice-cold PBS. Thereafter, the macrophage cells were scraped, resuspended in 1ml of MES buffer and transferred to 1.5ml microfuge tubes kept on ice for an overall cell count to be established. Using a haemocytometer, the cell number was established at approximately 1×10^7 cells per ml. A Balch homogeniser with a 7µm gap was then assembled with 2ml syringes, on ice. Prior to the homogenisation of cells, 1ml of MES buffer was passed through the homogeniser to equilibrate the chamber. The macrophage cells were then gently passed six times in each direction (12 passes total) through the Balch homogeniser using constant manual pressure. Following

homogenisation, cell homogenates were returned to fresh 1.5ml microfuge tubes and kept on ice.

Subcellular fractionation

Cellular homogenates were then centrifuged at 4 °C for 10 minutes at 1000g, to pellet cellular debris and nuclei. The supernatant (S1) was retrieved and placed in a new 1.5ml microfuge tube, on ice. The nuclear pellet (P1) was resuspended in 1ml of MES buffer, for subsequent washing. Both S1 and P1 samples were spun down again at 4 °C for 10 minutes at 1000g, for the removal of contaminants. Thereafter, cleared S1 was transferred to a new 1.5ml microfuge tube, whilst the washed nuclear pellet P1 was resuspended in 50µl of 1x SDS sample buffer for subsequent Western blot analysis. Next, S1 was spun at 4 °C for 10 minutes at 16,000g, to obtain the 16,000g large cellular vesicle pellet and supernatant (S2). The supernatant S2 was transferred to a new 1.5ml microfuge tube, whilst the large vesicle pellet was resuspended in 200µl of MES buffer for subsequent washing. The S2 supernatant and large vesicle pellet were then spun at 4 °C for 10 minutes at 16,000g again to remove contaminants. The washed large cellular vesicle pellet was resuspended in 50µl of 1x SDS sample buffer for subsequent Western blot analysis. The cleared S2 sample was then transferred to a 14.29 × 88.9 mm polyallomer ultracentrifuge tube (Fisher Scientific, Loughborough, UK), balanced using the ultracentrifuge buckets, placed in a Beckman SW-40Ti rotor and spun in a Beckman Optima XE 100 K ultracentrifuge (Beckman Coulter, Buckinghamshire, UK) at 4 °C for 60 minutes at 115,000g. Once spun, the supernatant from the sample was removed and the 115,000g small cellular vesicle pellet was isolated. The vesicle pellet was then resuspended in 50µl of 1x SDS sample buffer for subsequent Western blot analysis. For Western blot analysis of

obtained subcellular vesicular fractions in SDS sample buffer, the same method described above was utilised.

7.3 Results

Subcellular fractionation based on equilibrium density centrifugation

Fluorescent microscopy

This study aimed to investigate and determine the intracellular trafficking pathways followed by SPIONs and their eventual intracellular fate, in RAW264.7 mouse macrophage cells which were used as homologues of human macrophages. NP cellular fate, post-cellular uptake, is said to play a contributing factor in NP toxicity (Adjei et al., 2014). Therefore, results gathered regarding the intracellular fate of SPIONs in innate immune cells, which are the host's first line of defence, can provide an indication towards the potential of NP fate as a mechanism underlying SPION induced cellular toxicity observed in vivo (chapter 5). Subcellular fractionation was used to separate cellular organelles based on their physiological characteristics and thereafter, determine which of these contained SPIONs. To carry out subcellular fractionation, the macrophages were first homogenised, whereby the cell membrane was ruptured through mechanical stress and a release of cellular contents was induced (Figure 7.4). The resulting cellular homogenate was enriched in cellular organelles. To separate these organelles, a discontinuous Iodixanol based density gradient was first utilised. The density gradient fractions, containing cellular organelles separated based on density, were visualised using fluorescent microscopy to first determine which fractions contained fluorescent SPIONs. Results showed that SPIONs were positively identifiable within density gradient fractions (6-10) only, as shown in figures 7.5 and 7.6. Therefore, the NPs were shown to be closely associated

with cellular organelle compartments that moved upwards and downwards along the gradient, thus, the NPs were shown to be associated with organelles of differing densities.

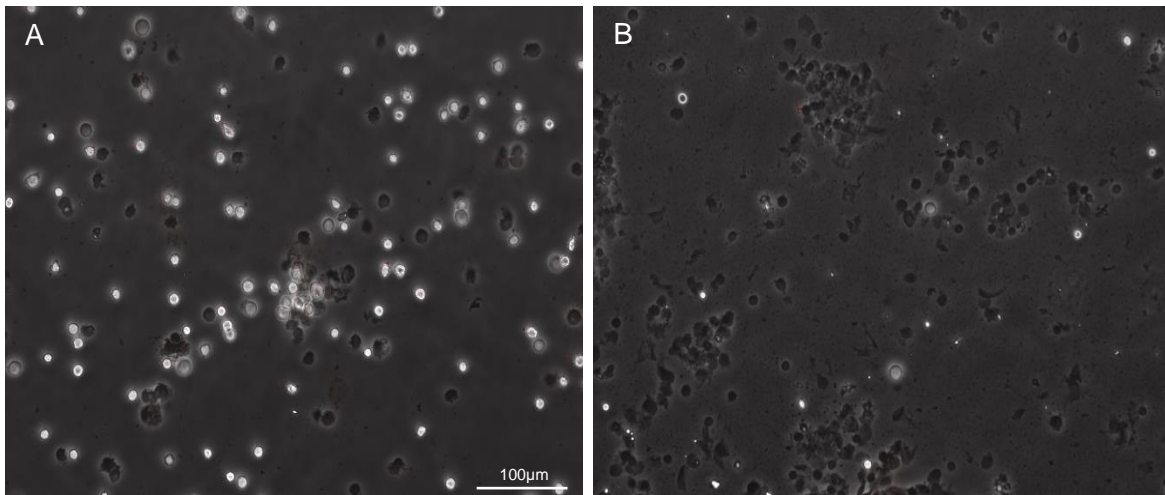


Figure 7.4: Cellular homogenisation using a Balch homogeniser. Prior to the subcellular fractionation of SPION treated mouse macrophages, to determine NP intracellular trafficking pathways and NP cellular fate, macrophages were first homogenised using a Balch homogeniser. Representative images of SPION treated mouse macrophage cells, prior to cellular homogenisation through mechanical stress (A) and after homogenisation, portraying the release of cellular content (B). Representative images are shown at x20 magnification. Scale bar: 100µm pertains to both images.

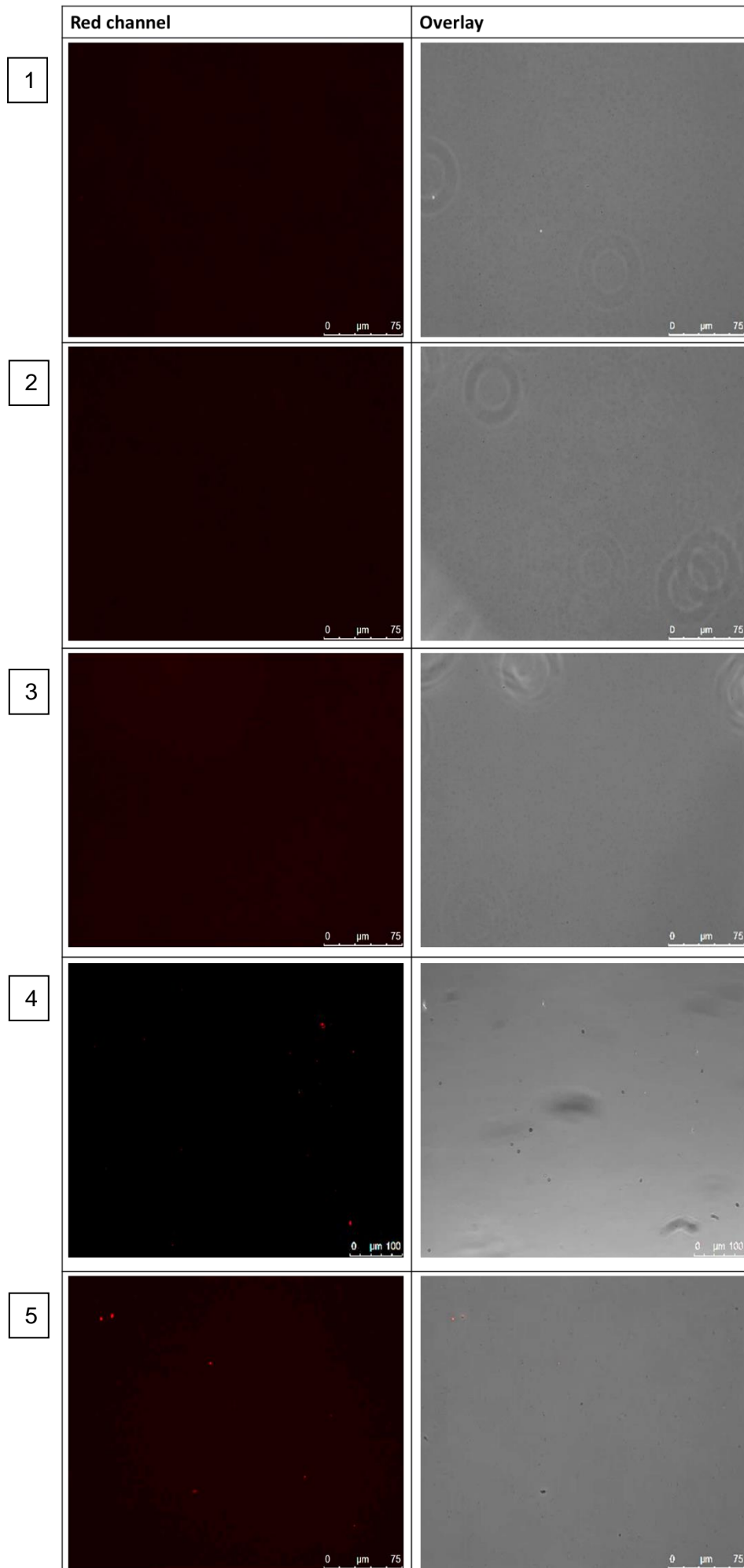


Figure 7.5: Fluorescent microscopy of density gradient cellular fractions. Images portraying representative fluorescent microscopy images of density gradient fractions, collected from the Iodixanol based density gradient used to separate SPION treated mouse macrophages, into subcellular fractions. The figure portrays representative images of density gradient fractions 1-5. Some representative images are shown at x20, while others at x40. Scale bars are indicated as 75 and 100 μ m where appropriate.

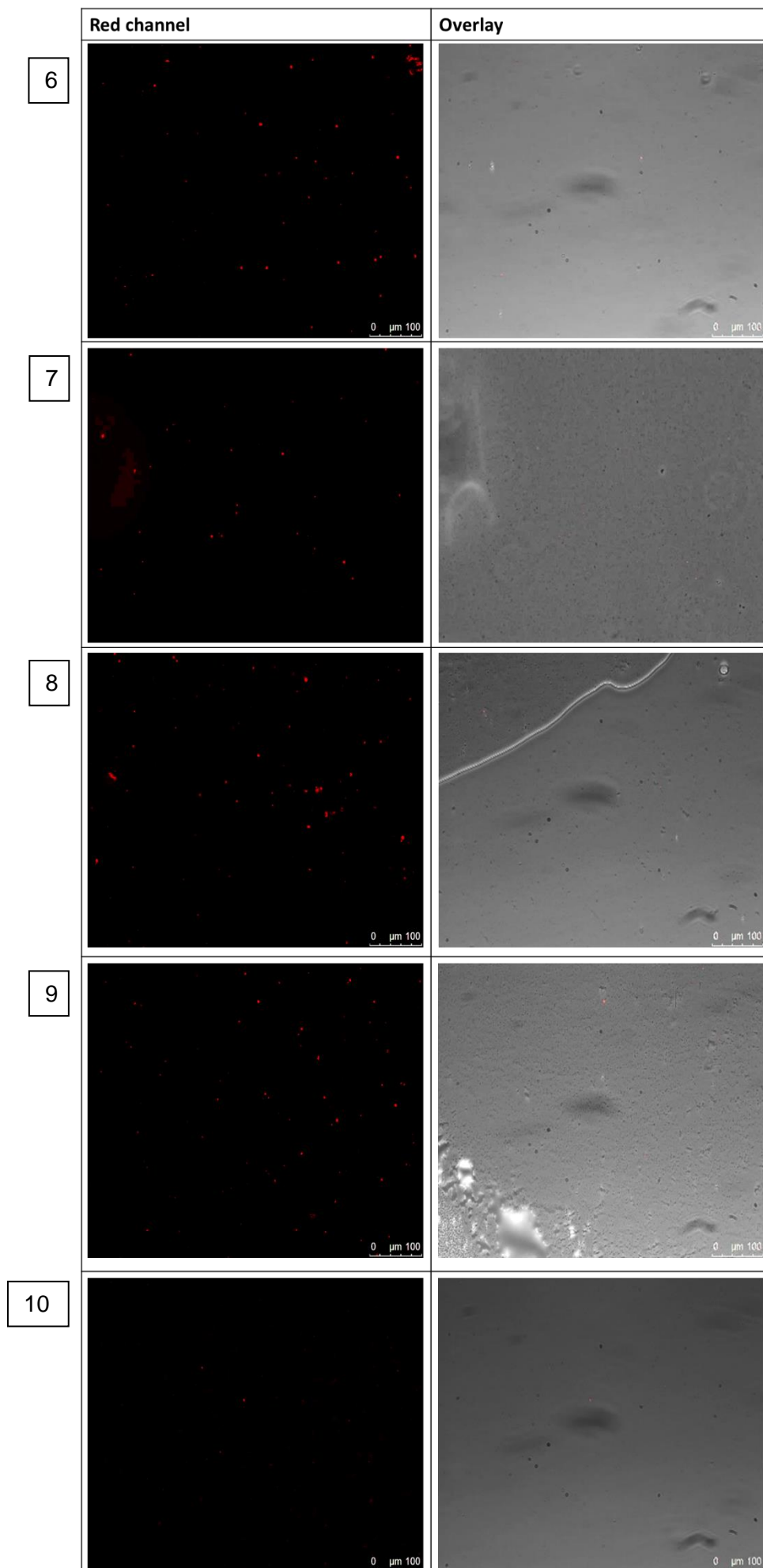


Figure 7.6: Fluorescent microscopy of density gradient cellular fractions. Figure portraying representative fluorescent microscopy images of density gradient fractions, collected from the Iodixanol based density gradient used to separate SPION treated mouse macrophages, into subcellular fractions. The figure shows representative images of density gradient fractions 6-10. Some representative images are shown at x20, while others at x40. Scale bars are indicated as 75 and 100 μ m where appropriate.

Western blot analysis

Fluorescent microscopy analysis was used to identify which of the respective density gradient fractions were positively associated with red fluorescent SPIONs, through the visualisation of SPION presence within the collected fraction. Western blot analysis was carried out to identify the separated cellular organelles, enriched within the respective density gradient fractions. Thereby, also determining the resolutive ability of the density gradient subcellular fractionation.

After resolving the gradient fractions with SDS-PAGE, Western blot analysis on the collected gradient fractions showed that when stained for LAMP1, gradient fractions 4-10 were stained positive (Figure 7.7). Therefore, cellular lysosomes were shown to be enriched across multiple density gradient fractions. Similarly, the gradient fractions were stained for Rab9, Rab27, GM130 and ERP72. Gradient fractions (6 and 7) were shown to be stained positive for Rab9 and fractions (5-10) were stained positive for Rab27. However, the level of Rab27 enrichment in fraction 5 was minimal. Unlike the results observed for LAMP1 and Rab27, portraying widespread protein enrichment across a range of gradient fractions, only gradient fractions (7-10) were stained positive for GM130, with fractions (6-10) stained positive for ERP72 (Figure 7.7).

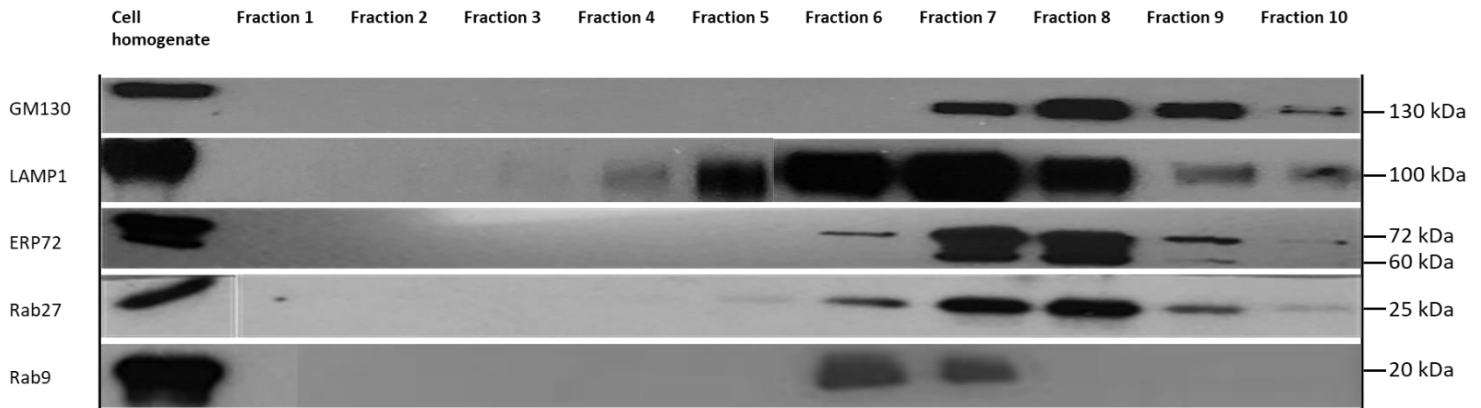


Figure 7.7: Western blot showing organelle enrichment across density gradient fractions. Western blot analysis conducted on density gradient cellular fractions, collected from the non-serum coated SPION treated cellular fractionation gradient. Density gradient fractions were stained for the lysosomal organelle maker (LAMP1), along with organelle markers Rab9, Rab27, GM130 and ERP72, which are characterised organelle markers for cellular endosomes, secretory exosomes, Golgi apparatus and endoplasmic reticulum, respectively. The figure shows a “streaking” pattern of organelle marker detection across the gradient, thus, depicting a low resolution of organelle separation and fraction contaminations with multiple cellular organelles.

Subcellular fractionation based on differential centrifugations

Western blot analysis

As described, to mitigate the limitations portrayed by density gradient based cellular fractionation and thus, subcellular component separation, a cellular fractionation method entirely based on Balch homogenisation and differential centrifugations (German and Howe, 2009) was investigated for potential further work. The method had previously been utilised to acquire endosome-enriched vesicular fractions, thus, making it a technique of interest due to the knowledge that NPs can be found in different organelles of the endocytic pathway. Therefore, the described methodology was investigated using untreated RAW264.7 mouse macrophage cells, for the potential reproducible acquisition of endosome-enriched vesicular fractions, in particular, small and large cell vesicular fractions. The isolated vesicular fractions were validated through western blot analysis. Thereby, identifying the enriched cellular organelles within the respective fractions and the purity of the vesicular fractions, based on the diversity of organelle composition.

The results of the Western blot analysis showed that both the isolated large and small vesicular fractions were enriched with cellular lysosomes, as represented by a positive band for LAMP1. However, the results showed that the large vesicular fraction was more enriched with cellular lysosomes when compared to the small vesicle fraction. This was represented by a stronger positive band for LAMP1, seen with the large vesicular fraction, when compared to the band observed for the small vesicular fraction (Figure 7.8). The same obtained vesicular fractions were stained for the endosomal organelle marker Rab9, during Western blot analysis. The results of the analysis showed that the small vesicular fraction portrayed the strongest stain for Rab9, with stains of lower strength seen in the large vesicular fraction. Therefore, the small vesicular fraction was observed to be more enriched with endosomes, when compared to the large vesicular fraction (Figure 7.8).

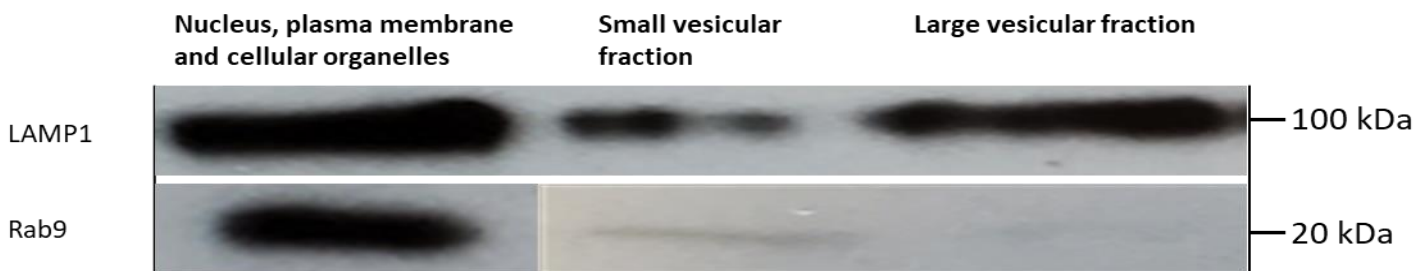


Figure 7.8: Western blot showing protein enrichment across two distinct vesicular fractions. Western blot analysis conducted on two distinct cellular vesicular fractions, which include small and large vesicular fractions. Vesicular fractions were obtained from untreated mouse macrophage cells, that were homogenised using Balch homogenisation and fractionated using steps of differential centrifugations. Cellular fractions were stained for the lysosomal organelle maker (LAMP1) and the endosomal organelle marker (Rab9). The figure shows lysosomal enrichment mainly in the large vesicular fraction, with lower enrichment in the smaller vesicular fraction, thus, depicting a low resolution of cellular lysosomal separation with contamination of the small vesicular fraction. The figure also shows endosomal enrichment mainly in the small vesicular fraction, with very little enrichment in the large vesicular fraction. Thus, depicting a greater resolution for endosomes, with minor contamination of the large vesicular fraction.

7.4 Discussion

Due to previously described unique physicochemical properties portrayed by both inorganic and organic NPs, they are increasingly growing in popularity within a diverse range of research fields and thus, have been placed at the forefront of cutting-edge research (Kamaly et al., 2012; Mout et al., 2012; Elsabahy and Wooley, 2012; Dreaden et al., 2012). Within the fields of biomedicine and biotechnology, NP technology and specific NPs have been utilised for various biological applications (Shi et al., 2017; Serpooshan et al., 2013), including drug and gene delivery (Pantarotto et al., 2003), pathogen bio detection (Edelstein et al., 2000), tissue engineering (De la Isla et al., 2003; Ma et al., 2003) and as agents to aid in bioimaging techniques (Rogach and Ogris, 2010).

However, prior to their potential use in clinical and biomedical applications, it is of vital importance to determine the biological safety of NPs, *in vivo*. In relation to NP biosafety, it has previously been shown that NP-induced cellular toxicity plays a major role in the overall biological safety of NPs. Cellular toxicity of NPs, in some cases, is said to be determined by the mechanism of NP cellular uptake and specific endocytic pathway utilised by NPs, in addition to their subsequent intracellular fate. Hence, in the investigation of NP biological safety prior to potential biomedical applications, determining NP intracellular trafficking pathways and eventual cellular fate is said to be crucial (Foroozandeh and Aziz, 2018). Thereby, allowing for predictions to be made on the potential deleterious toxicities that may arise based on the final NP intracellular destiny (Albanese et al., 2012). In this study, the intracellular fate of SPIONs after short-term incubation was investigated in RAW264.7 cells, thereby, determining if NP cellular fate was a potential mechanism underlying SPION induced cellular toxicity

observed in vivo (chapter 5). In particular, we wanted to determine if SPION endosomal escape into the cytoplasm, which is known to have profound effects on NP-induced cytotoxicity, plays a significant role in SPION cytotoxicity observed in vivo. Western blot analysis was conducted on the collected density gradient fractions, to first determine the cellular organelle compartments separated along the gradient and thus, enriched within the gradient fractions. The results from the analysis showed that lysosomes were enriched in a wide range of gradient fractions, 4-10, when fractions were stained for the lysosomal marker LAMP1. The lysosomal enriched fractions were the same fractions that contained a good amount of fluorescent SPIONs. Therefore, this data provides evidence towards SPION association with cellular lysosomes and the possibility of lysosomal induced NP degradation, as a likely NP cellular fate.

Unless iron oxide NP (IONP) endosomal escape takes place, which depends on the physicochemical properties of both the cell type and the internalised IONPs, the IONP containing endosomes are known to be directed to the lysosomal compartment. Within lysosomes, iron ions are liberated from the IONPs due to the reducing and acidic environment of these degradative organelles (Lévy et al., 2010). IONP and lysosomal interactions were further reported in a study that investigated IONP-induced cellular autophagy. In the study, iron-based NP cellular uptake was reported to result in lysosomal mediated NP degradation and excessive iron release intracellularly. Therefore, potentially leading to the excessive production of intracellular ROS through the catalytic breakdown of free iron ions by Fenton reactions and eventually, resulting in cellular ferroptosis (Wen et al., 2021). Therefore, these studies confirm previous knowledge on the associations between SPIONs and cellular lysosomes, with lysosomal degradation being highlighted as a likely NP cellular fate. However, as described previously, NP endosomal escape, lack of association with the cellular

lysosome compartment and therefore, lack of NP degradation by lysosomal enzymes aids in the promotion of NP biological and therapeutic functionalities (Smith et al., 2019).

A good number of fluorescent SPIONs were observed to be present in gradient fraction 6, through fluorescent microscopy. Therefore, confirming a potential lack of association between SPIONs and Golgi body, hence, reducing the likelihood of SPION associations with the Golgi body as a potential SPION cellular fate. Besides LAMP1, fraction 6 also contained Rab9 positive organelles indicating that this fraction is not pure but contains several endocytic organelles.

From the preliminary data gathered, SPIONs were shown to be present in good numbers within lysosome enriched gradient fractions. Therefore, it was inferred that SPION endosomal escape was unlikely to take place once uptaken, thereby, making it an unlikely toxicity mechanism underlying SPION induced cytotoxicity observed in vivo (chapter 5). However, as previously described, SPION endosomal escape and reductions in lysosomal internalisation and degradation would consequently promote the intended biological and therapeutic NP applications. Furthermore, the data gathered showed low associations between SPIONs and Golgi bodies, therefore, reducing SPION induced destructive effects on these cellular organelles. In addition, lack of association would also reduce the induction of cell toxicity responses including cell autophagy (Ma et al., 2019).

Despite the preliminary results gathered regarding SPION intracellular trafficking pathways and cellular fate, the use of an Iodixanol based discontinuous density gradient for cellular fractionation in this study, presented a lack of desirable cellular compartmental separation of high resolution. This lack of highly resolved cellular

fraction was observed during Western blot analysis of collected density gradient fractions.

Western blot analysis showed that gradient fractions 4 and 5 were homogenous fractions, potentially enriched in lysosomes, due to the fractions staining positive for LAMP1 only, with minimal protein enrichment of Rab27 seen in fraction 5. Fraction 6 was a heterogenous gradient fraction enriched in differing cellular organelles, thus, staining positive for all organelle makers, with the exception of GM130, the Golgi marker. Lastly, gradient fractions 7-10 is where the organelle enriched cellular homogenate gradient was loaded. These gradient fractions contained a heterogenous mix of cellular organelles, with the exception of Rab9 in fractions 8-10 (Figure 7.7).

Henceforth, a differing method of cellular fractionation was required to mitigate the limitations portrayed by density gradient based cellular fractionation and to overcome the undesirable result of impure organelle enriched density gradient fractions. Thus, a technique of cellular fractionation that allowed for the acquisition of endosome-enriched vesicular fractions with desirable levels of resolution and vesicular fraction purity was investigated, as proposed by German et al (German and Howe, 2009). Western blot analysis was conducted on the two acquired distinct vesicular fractions, which were described to be the large and small vesicular fractions. Results of the analysis showed that the large vesicular fraction, when stained for the cellular lysosomal maker LAMP1, was the fraction most enriched in cellular lysosomes when compared to the small vesicular fraction. Similarly, when the fractions were stained for the endosomal marker Rab9, results showed that the small vesicular fraction was the most enriched in endosomes when compared to the large vesicular fraction.

From the results gathered, the technique that is entirely based on Balch homogenisation and differential centrifugations for cellular fractionation, portrays identifiable advantages over density gradient mediated organelle separations. Comparatively, the method overcomes the limitations of reagent cost and time, portrayed by density gradient cellular fractionation techniques. However, in the context of organelle separation resolution and acquired cellular fraction purity, the acquired distinct vesicular fractions portray desirable cell vesicular separations with good resolution, and low levels of organelle fraction contaminations. This is portrayed by the lack of large vesicular fraction contamination by smaller vesicles and with only some level of small vesicular fraction contamination by larger vesicles, such as cellular lysosomes.

Future work

For the advancement of this study and for the improvement of current knowledge behind intracellular trafficking pathways of SPIONs post-cellular uptake, the ultimate SPION cellular fate and the impact of human serum coatings on SPION cellular fate, we look to optimise the described subcellular fractionation methods described in this study. Firstly, we plan to optimise the method of Optiprep (Iodixanol) based density gradient cellular fractionation, to separate the cellular organelles of SPION treated mouse macrophages with high resolution and low levels of organelle contaminations. Next, we plan to utilise different continuous and discontinuous gradients, which are composed of alternate density mediums including Sucrose, Percoll and Ficoll. Thereby, further optimising the method of density gradient mediated subcellular fractionation of cellular organelles. Lastly, we plan to carry out further density gradient mediated subcellular fractionation experiments with pre-isolated subcellular organelles, such as the heavy and light mitochondrial fractions, obtained through

differential centrifugations. Thereby, determining NP cellular fate with relevance to cellular organelles isolated within these subcellular fractions.

Furthermore, we plan to further utilise and investigate the method of cellular fractionation and distinct cellular vesicle fraction acquisition through Balch homogenisation and differential centrifugations. Thereby, determining which method allows for greater resolution in cellular organelle separation and the lowest levels of fractional contaminations. In addition, when determining the intracellular fate of IONPs and SPIONs, we will look to utilise their magnetic physicochemical properties to isolate subcellular organelles closely associated with the NPs through magnetic separation. Lastly, through future protein sequencing of collected enriched cellular fractions, we aim to properly determine the resolution of the cellular fractionation and the purity of the acquired fractions, thus, clearly defining intracellular trafficking pathways and SPION cellular fate.

8. General Discussion

Osteosarcoma (OS) is the most common non-haematological primary malignant tumour of the bone (Bielack et al., 2009; Luetke et al., 2014; Picci, 2007; Nagarajan et al., 2011; Mirabello et al., 2009b). It accounts for 20-40% of all identified bone cancers (Ho et al., 2017; Whelan et al., 2012) and commonly affects children, adolescents and young adults (Grimer, 2005; Akiyama et al., 2008; Bielack et al., 2009; Brown et al., 2017; Mirabello et al., 2009b; Armakolas et al., 2016; Nagarajan et al., 2011; Wang et al., 2020). Due to obstacles faced in regard to the improvement and implementation of effective OS treatment modalities, the overall improvement of OS patient survival has long proved to be a challenge. Therefore, advancements in OS disease treatment are a significant requirement (Gill and Gorlick, 2021).

Henceforth, research into understanding the mechanisms underlying OS tumorigenesis and progression, along with the discovery of novel OS therapeutic targets is of great importance. A greater understanding of the underlying disease mechanisms, may improve the clinical management of the disease and uncover rational and novel OS therapeutic targets (Yang et al., 2014). Furthermore, the identification of novel therapeutic targets and disease biomarkers for OS may aid in overcoming treatment limitations such as chemotherapeutic resistance and tumour metastasis (Xi et al., 2019; Z. Liu et al., 2022).

Previous studies have investigated OS tumour cells for the identification of relevant OS therapeutic targets (Gill and Gorlick, 2021). However, this approach is limited as it has become clear that the surrounding OS tumour niches play important roles in the manifestation and progression of the disease, thus, making it an important target for the identification of novel OS therapies. Due to the close proximity of OS tumours to the hematologic niche, immune cells are often found closely associated with the tumour, thus, when immune cells infiltrate the tumour, they generate the tumour

immune niche. The OS tumour cells dictate immune infiltration and differentiation to establish a favourable immune niche, which supports tumour growth, drug resistance and the occurrence of metastases (Heymann and Heymann, 2017). It is thought that the immune niche of the tumour microenvironment might hold proteins of interest, that can be put forward as novel therapeutic targets for the treatment of OS (Heymann and Heymann, 2017). Therefore, protein targets within the tumour immune niche, largely represented by surface immune receptors, should be investigated.

In this thesis, we conducted *in silico* bioinformatical analysis of an OS gene microarray dataset for the identification of genes that are differentially expressed in OS pre-chemotherapeutic tissues, when compared to bone-marrow mesenchymal stem cell controls (chapter 3, figure 3.4). The OS gene microarray dataset used in this thesis (chapter 3, table 3.1) provided several advantages with respect to the clinical applicability of genetic data deciphered. Importantly, for the OS biopsies, the dataset provided gene expression data obtained from biopsy tissues representing a patient group portraying desirable diversity with respect to age and sex. Furthermore, the study included samples that represent heterogenous OS tumour tissue and consequently, allows for the wider application of the gathered data.

We propose that these identified DEGs may improve our current understanding surrounding the mechanisms underlying OS tumorigenesis and progression, along with unveiling novel therapeutic targets for the treatment of OS.

Functional gene enrichment analysis conducted on our identified significantly DEGs in OS, show that the total DEGs are associated with biological processes including immune response, regulation of immune system processes, cell activation, leukocyte activation and immune effector processes. The results strongly suggest that the

immune system plays a significant role in OS tumorigenesis and progression. Therefore, we investigated upregulated immune receptors in OS, in particular, for the potential identification of novel therapeutic target(s) located within the OS tumour immune niche. From the in-silico analysis conducted, the immune receptor FPR3 was identified to be significantly upregulated in OS and therefore, a promising novel therapeutic target. FPR3 expression in OS, both in vivo and in vitro was assessed against appropriate control tissue and an in vitro cell migration assay was used to study the response of OS cell lines to treatment with receptor-specific peptide ligands (chapter 4).

Previous studies have investigated the therapeutic efficacy of targeting various immune related receptors and administering immunomodulating peptide ligands, in the treatment of OS (Khanna, 2008). A study investigated the therapeutic efficacy of targeting the chemokine immune receptor CXCR4 in the treatment of OS. Previous results have shown that high expression of CXCR4 is related to poor prognosis in many cancers, including OS. Furthermore, CXCL12, the peptide ligand for CXCR4, is expressed highly in sites to which OS tumours primarily metastasise to. Therefore, it was argued that disruption of CXCR4/CXCL12 complexes may lead to a decrease in OS tumour metastasis. The study, thus, investigated the therapeutic efficacy of targeting CXCR4 and its peptide ligand complex, with a small peptide receptor antagonist (CTCE-9908). The study showed that inhibition of the CXCR4/CXCL12 pathway decreased OS tumour metastasis in murine tumour models (Kim et al., 2008).

In our study, the immune receptor FPR3 was identified to be significantly upregulated in OS primary tissue (chapter 3, table 3.4). FPR3 has previously only been investigated as a potential immune related therapeutic target in relation to breast cancer. In the study, FPR3 was first identified as a novel disease biomarker for breast

cancer and thereafter, investigated for its potential as a therapeutic target within the breast cancer tumour immune microenvironment. The study discussed the results, which showed that FPR3 gene upregulation is positively correlated with the activation of multiple biological pathways involved in carcinogenesis. Furthermore, it concluded that FPR3 shows strong potential in becoming a key immune-related biomarker, with increased expression related to poor prognosis in breast cancer patients. Therefore, FPR3 was proposed as a promising therapeutic target for breast cancer immunotherapy (Qi et al., 2021). Overall, FPR3 has not been previously investigated as a potential therapeutic target in relation to Osteosarcoma, therefore, emphasising its novelty towards the diseased trait of interest.

Due to the novelty of FPR3 as a potential disease biomarker and therapeutic target in OS treatment and patient prognosis, we investigated the receptor's expression across different OS tumour samples. The results from our investigation show that FPR3 was aberrantly expressed across multiple malignant OS tumour tissues, which differed based on localisation, stage and phenotypic differences. FPR3 expression was also validated in vitro through immunofluorescent microscopy and flow cytometric analysis of human OS cell lines. We further show that targeting FPR3 with its peptide antagonist could be an attractive therapeutic effect in OS treatment. Overall, the results strongly suggest the possibility of FPR3 being utilised as a novel therapeutic target for the treatment of metastatic OS.

A previous study investigated the therapeutic targeting potential of the protein angiopoietin-like 4 (ANGPTL4) in the treatment of OS. The protein plays a role in driving the progression and metastasis of many solid tumours, in addition, ANGPTL4 is also known to enhance osteoclast activity in bone which is a significant requirement for OS tumour growth. Therefore, similar to our study, for the potentiation of the protein

as a therapeutic target that could potentially reduce OS tumour progression, reduce bone destruction and prevent OS metastasis, the study first investigated the expression of ANGPTL4 in human OS tissue and cell lines. Similar to FPR3 in our study, ANGPTL4 was reported to show aberrant expression in OS primary tissues (Zhang et al., 2018).

In addition, previous studies have identified novel therapeutic targets in OS, by assessing their therapeutic efficacy on OS cell migration when targeted using appropriate peptide ligands/agents. An example is a study that investigated the effects of histone deacetylase inhibition, using the drug PXD-101, on human OS cell migration. The results of the investigation showed that treatment of human OS cells with PXD-101, significantly decreased the rate of wound closure in an in vitro cell migration assay (Rossi et al., 2023). These results were similar to that observed in our study. From the described study, it is evident that in vitro cell migration assays are reliable methods when determining the therapeutic efficacy of novel therapeutic targets, in the treatment of OS.

Thus far, in our study, we utilised immunofluorescence and immunohistochemical staining techniques for the evaluation of FPR3 expression in OS tissues, in vivo and in vitro. Furthermore, we utilised an in vitro cell migration assay for the determination of receptor targeting therapeutic efficacy in OS progression and metastasis. However, further techniques would need to be carried out to put forward FPR3 as a novel therapeutic target for the treatment of metastatic OS. Similar to our study's investigations into FPR3, a previous study investigated the role of semaphorin 4C (SEMA4C) in osteosarcoma growth, progression, and metastasis. Similar to our study, the expression and localisation of SEMA4C were evaluated in primary OS patient tissues. However, the study further investigated the tumorigenic functions of SEMA4C

in OS with the use of genetic studies and other experimental techniques. The genetic studies involved the generation of gene overexpression and knockdown in human OS cell lines, which were combined with assays including cell proliferation, colony formation, migration and wound healing for the determination of the gene's tumorigenic functions (Smeester et al., 2020). Therefore, our study is limited by the lack of further genetic studies that can be carried out to determine the tumorigenic functions of FPR3 in OS, thus, consolidating the therapeutic targeting potential of FPR3 to a greater extent. For example, RNAi knockdown of FPR3 can be used to confirm or more accurately show the effects of receptor antagonism on OS cell migration or tumour progression.

The close association of FPR3 with malignant bone cells may be exploited as a target for novel OS therapeutic modalities, such as NP-based targeted drug delivery systems. Utilising functionalised NP formulations for receptor targeted drug delivery, could improve the bioavailability and therefore, the therapeutic efficacy of FPR3 targeted OS therapy. However, despite the advantages portrayed by NPs when considering their use as drug delivery agents, there is still concern regarding cellular and systemic toxicity for the majority of inorganic NP based drug delivery systems (DDS) (De Matteis, 2017). Therefore, prior to designing and administering NP-based DDS, for the treatment of diseases such as OS, it is important to investigate and determine the biological safety of NPs. Thereafter, strategies to decrease NP toxicity can be developed prior to their potential use in disease therapeutics.

NPs administered for their therapeutic functionalities, alone or as NP-based DDS formulations, will inevitably interact with the cellular component of the innate and for longer circulating NPs also the adaptive immune system as well as surrounding tissues (Dobrovolskaia et al., 2016). Therefore, understanding NP systemic

biodistribution, in vivo, and NP interactions with innate immune cells such as macrophages, are important aspects when determining NP toxicity. Therefore, in this thesis, we present the strong potential of the *Galleria Mellonella* (GM) larval model organism in studying the cellular toxicity of NPs on the innate immune system, in vivo. Furthermore, the model organism can also be used to determine the biodistribution of administered NPs and their potential impact on systemic toxicity. Thereafter, NP-induced cellular ROS production and cellular oxidative stress, was found to be the likely mechanisms underlying observed NP induced immunotoxicity. Finally, we began to investigate NP intracellular trafficking pathways and cellular fate in macrophages, through subcellular fractionation techniques.

FPR3 could thus be specifically targeted within OS tumours, with the use of novel therapeutic modalities, such as NP-based DDS. These DDS are capable of carrying out receptor specific and efficient delivery of receptor peptide ligands, thus, potentially inducing therapeutic effects (Cevaal et al., 2021). However, as mentioned, prior to the use of NP-based DDS for targeted therapy of diseases including OS, the biological safety and systemic toxicity of the NPs needs to first be determined. Therefore, in our study, we investigated the GM larvae as a model organism to assess the level of systemic toxicity induced by a range of inorganic NPs, and their toxicity on the cellular component of the innate immune system. The results show that NP physicochemical properties, such as size, composition and surface chemistry, play profound roles in determining the overall biosafety of NPs. With regards to the SPIONs, the inclusion of a biocompatible coating may improve the biological safety of the formulation for therapeutic administration.

In regard to the assayed CNTs, none of the CNT variants produced significant immunotoxicity despite levels of systemic toxicity. Therefore, the results strongly

suggest that a non-cellular mediated mechanism contributes to the observed systemic toxicity in GM larvae. Previous studies have reported CNT bioaccumulation, in vivo, following successful CNT uptake, translocation and retention within the host organism (Jackson et al., 2013). One study investigated the biodistribution and tissue accumulation of CNTs within the common fruit fly (*Drosophila melanogaster*) model organism. When a low dose of CNTs was ingested by the model organism, small fractions of CNTs were reported to have translocated into the larval hemolymph, the brain and to a lesser extent, surrounding tissue. Therefore, the majority of the CNTs were excreted (Leeuw et al., 2007). However, at higher doses, larval ingestion was reported to have led to systemic CNT uptake and tissue integration/accumulation (Liu et al., 2009). Hence, based on these results, tissue bioaccumulation of CNTs was thought to be a likely mechanism for CNT induced systemic toxicity and lack of immunotoxicity. To further investigate reports of CNT bioaccumulation, we conducted immunohistochemical analysis on cryosections obtained from CNT injected GM larvae. The results show highly noticeable regions of CNT bioaccumulation within the anatomical regions, with amounts of NP bioaccumulation differing depending on the CNT variant and length of NP exposure. Overall, when considering CNTs and CNT-based DDS for targeted therapy of diseases such as OS, it is important to consider dosage mediated CNT retention and accumulation, which may result in varying levels of systemic toxicity. Furthermore, no significant differences in systemic toxicity and tissue bioaccumulation were observed between the CNT variants, therefore, CNT physicochemical properties had little effect.

Lastly, in regard to the assayed AuNPs of differing sizes, our results strongly support the current knowledge that the toxicity of AuNPs, in vivo and in vitro, is greatly influenced by particle size. Previous studies have investigated the in vivo tissue

biodistribution and systemic fate of AuNPs, reporting that both factors are strongly influenced by particle size (Jia et al., 2017). A study investigated the tissue distribution of AuNPs of varying sizes, in rats, reporting that the smallest NPs show the most widespread organ distribution (De Jong et al., 2008). Hence, the existing literature may explain the differing results observed for the 20nm AuNPs in our study, which show highly significant systemic toxicity but the least amounts of immunotoxicity amongst all assayed AuNP variants. It can be proposed that the 20nm AuNPs had greater levels of organ distribution and tissue bioaccumulation, when compared to the other variants, therefore, resulting in significant systemic toxicity despite low levels of immunotoxicity. Overall, when considering AuNPs and AuNP-based DDS for targeted disease therapeutics, it is evident that the size of the AuNPs and NP dosage need to be considered when designing appropriate formulations. The results are clear in showing that the chosen AuNP size, may have a role in determining the biocompatibility and safety of the designed NP therapeutic formulation. This is based on their role in determining NP retention and tissue accumulation, alongside cellular uptake mediated cytotoxicity.

We also investigated the effect of an innate immune challenge (PA14) on larval THC and survival, to assess the immunomodulatory effects of AuNPs when compared to the known immunosuppressive function of Cyclo. Overall, our results show that the AuNPs can be useful as immunomodulators, similar to Cyclo. A previous study investigated the immunomodulatory effects of AuNPs on innate immune cells, including Natural killer cells and macrophages. The study aimed to determine the pro-inflammatory cytokine inhibitory properties of AuNPs, and reported that the AuNPs show immunosuppressive effects by lowering levels of pro-inflammatory cytokines (Elbagory et al., 2019). Therefore, the current literature supports the concept of AuNP-

induced innate immune suppression, similar to that of the known immunosuppressant Cyclophosphamide. Overall, the results from our study, show that the AuNPs portray significant potential to be used within the clinical setting as immunosuppressive agents, in functionalised NP formulations, as opposed to Cyclo. Furthermore, depending on particle size, AuNPs are shown to portray a lack of systemic toxicity whereas Cyclo portrayed a significant level of systemic toxicity.

Despite the lack of *in vivo* systemic toxicity shown by the SC-SPIONs and the 100nm AuNPs, the NPs portrayed significant levels of immunotoxicity, which has previously been reported to be due to increased cellular ROS production and oxidative stress (Fu et al., 2014). Therefore, to investigate the potential of cellular ROS production and oxidative stress as the likely mechanisms underlying NP induced immunotoxicity, we first carried out an *in vitro* cellular ROS assay. The results strongly suggest that cellular ROS production and oxidative stress were the likely mechanisms underlying observed NP-induced immunotoxicity.

Thereafter, to measure NP-induced cellular oxidative stress *in vivo*, we carried out a 4-HNE lipid peroxidation ELISA with NP treated GM larval plasma samples. Importantly, the results show that the overall physiological condition of the host plays a crucial role in the activation of the innate immune system and its ability to generate ROS, in response to NP exposure. The lack of NP-induced cellular ROS production, in younger larvae, can be explained by a study that reports a decline in larval hemocyte innate immune functionality with age (Horn et al., 2014). Therefore, it can be said that the GM larval hemocytes in older larvae portray lower levels of immune functionality. This is an important observation pointing to the usefulness of the GM model, as similar declines in immune system responses are also observed in humans with increasing age. However, the data gathered emphasises the need for standardised model

organisms, to allow for data reproducibility between experiments and research groups. In relation to CNT induced cellular ROS production, in vivo, the results show that neither of the assayed CNT variants induced significant cellular ROS production, in either of the larval physiological states. The two assayed CNT variants were identified to be the most systematically toxic variants when their toxicity was assayed using GM larvae. However, the lack of induced cellular ROS production is in line with the lack of CNT induced immunotoxicity, and further emphasises the likelihood of tissue bioaccumulation as the major mechanism behind observed CNT systemic toxicity.

As part of the NP cellular toxicity studies, we also began to investigate the potential cellular toxicities portrayed by SPIONs, through the determination of their intracellular trafficking pathways and cellular fate. To do so, we looked to investigate the intracellular trafficking and fate of SPIONs within mouse macrophages (RAW264.7) post-uptake. Overall, the preliminary results show that SPIONs were localised within subcellular fractions that were positively stained for LAMP1, a lysosome marker. SPIONs being localised within lysosomes and therefore, exposed to lysosomal degradation has been previously reported. Therefore, by capitalising on the magnetic physicochemical property of SPIONs, a study reports the use of SPIONs for the rapid isolation of lysosomes from tissue culture cells (Rofe and Pryor, 2016).

For further investigations into the intracellular trafficking pathways and the cellular fate of SPIONs, we aim to carry out future work to first improve the resolution of density gradient based subcellular fraction and also, further investigate cellular fractionation through Balch homogenisation and differential centrifugations. Thereafter, we hope to utilise data gathered from future protein sequencing of enriched cellular fractions, to accurately determine SPION intracellular trafficking pathways and cellular fate. We hypothesise that, in relation to NP-induced cellular toxicity, the intracellular trafficking

pathway uptaken by the NPs and their cellular fate play roles in determining their cellular ROS producing potential. Therefore, possibly further potentiating cellular fate as a mechanism underlying nanotoxicity.

In conclusion, we believe that the results and data generated within the presented thesis will have first, contributed greatly towards the study and understanding of OS pathogenesis, novel OS therapeutic targets and tumour specific therapeutic strategies. Specifically, we believe the findings provide a good foundation to further determine mechanisms underlying tumorigenesis and progression of OS and unveil further novel therapeutic targets in OS. In addition, the findings in regard to FPR3 as a potential OS therapeutic target, may contribute towards the improvement of OS treatment and patient overall survival.

In relation to NP-based therapeutic targeting of FPR3 in OS, we believe the results presented also contribute to current understandings of NP toxicity, for a range of inorganic NPs, at the cellular and systemic levels. We especially put forward the *Galleria Mellonella* larval model organism as a valid, reliable, and high-throughput tool that portrays several advantages over mammalian models for determining the toxicity of exogenous substances, such as NPs. We show that GM larvae can be used to investigate and quantify cellular responses to exogenous stimuli, *in vivo*. Through this, AuNP-induced immunosuppression was observed *in vivo* and put forward the use of GM larvae in determining further immunomodulatory agents. We also showed the novel use of GM larvae, when measuring cellular ROS production *in vivo* through the incorporation of an 4HNE ELISA. The results also provide a foundation for further investigations to be conducted towards a better understanding of the toxic effects of the screened NPs. Therefore, fully establishing their biosafety prior to their use in drug-delivery formulations, for targeted therapy of diseases such as OS.

9. References

- Abakumov, M. A. et al. (2018) Toxicity of iron oxide nanoparticles: Size and coating effects. *Journal of Biochemical and Molecular Toxicology*. [Online] 32 (12), e22225.
- Abarrategi, A. et al. (2016) Osteosarcoma: Cells-of-Origin, Cancer stem cells, and targeted therapies. *Stem Cells International* 2016, ID 3631764, 13 pages.
- Van Acker, H. H. et al. (2018) Interleukin-15-cultured dendritic cells enhance anti-tumor gamma delta T cell functions through IL-15 secretion. *Frontiers in Immunology*. [Online] 9,658.
- Adepu, S. & Ramakrishna, S. (2021) Controlled drug delivery systems: Current status and future directions. *Molecules* 26 (19), 5905.
- Adjei, I. M. et al. (2014) Nanoparticles: Cellular uptake and cytotoxicity. *Advances in Experimental Medicine and Biology*. [Online] 811, 73-91.
- Ahamed, M. et al. (2013) Iron Oxide Nanoparticle-induced Oxidative Stress and Genotoxicity in Human Skin Epithelial and Lung Epithelial Cell Lines. *Current Pharmaceutical Design*. [Online] 19 (37), 6681–6690.
- Ahlmann, M. & Hempel, G. (2016) The effect of cyclophosphamide on the immune system: implications for clinical cancer therapy. *Cancer Chemotherapy and Pharmacology* 78 (4), 661–671.
- Ahmed, N. et al. (2015) Human epidermal growth factor receptor 2 (HER2) - Specific chimeric antigen receptor - Modified T cells for the immunotherapy of HER2-positive sarcoma. *Journal of Clinical Oncology*. [Online] 33 (15), 1688–1696.
- Ahmed, N. et al. (2009) Immunotherapy for osteosarcoma: Genetic modification of T cells overcomes low levels of tumor antigen expression. *Molecular Therapy*. [Online] 17 (10), 1779–1787.
- Ahmet, D. S. et al. (2020) Application of small molecule FPR1 antagonists in the

- treatment of cancers. *Scientific Reports*. [Online] 10 (1), 17249.
- Akiyama, T. et al. (2008) Novel therapeutic strategy for osteosarcoma targeting osteoclast differentiation, bone-resorbing activity, and apoptosis pathway. *Molecular Cancer Therapeutics* 7 (11), 3461–3469.
- Akter, M. et al. (2018) A systematic review on silver nanoparticles-induced cytotoxicity: Physicochemical properties and perspectives. *Journal of Advanced Research* 9, 1–16.
- Alavi, M. & Hamidi, M. (2019) Passive and active targeting in cancer therapy by liposomes and lipid nanoparticles. *Drug Metabolism and Personalized Therapy* 34 (1), 20180032.
- Albanese, A. et al. (2012) The effect of nanoparticle size, shape, and surface chemistry on biological systems. *Annual Review of Biomedical Engineering* 14(1), 1-16.
- Alfranca, A. et al. (2015) Bone microenvironment signals in osteosarcoma development. *Cellular and Molecular Life Sciences* 21(19), 6985.
- Ali, E. S. et al. (2021) Targeting cancer cells with nanotherapeutics and nanodiagnostics: Current status and future perspectives. *Seminars in Cancer Biology* 69, 52–68.
- Alkilany, A. M. & Murphy, C. J. (2010) Toxicity and cellular uptake of gold nanoparticles: What we have learned so far? *Journal of Nanoparticle Research*. [Online] 12 (7), 2313–2333.
- Almeida Furquim De Camargo, B. et al. (2020) New Silver(I) Coordination Compound Loaded into Polymeric Nanoparticles as a Strategy to Improve in Vitro Anti-*Helicobacter pylori* Activity. *Molecular Pharmaceutics*. [Online] 17 (7), 2287–2298.

- An, Y. et al. (2021) Identification of key genes in osteosarcoma - before and after CDK7 treatment. *Medicine (United States)*. [Online] 100 (39), E27304.
- Andrian, T. et al. (2021) Nanoscopy for endosomal escape quantification. *Nanoscale Advances* 3 (1), 10–23.
- Andronescu, E. et al. (2016) Nanomaterials for Medical Applications: Benefits and Risks. *Journal of Nanomaterials* ID 8284319, 2 pages.
- Hongxun W, et al. (2010) 195. Mechanisms of Cyclophosphamide Enhancing Anti-Tumor Effects of Oncolytic Vesicular Stomatitis Virus for Breast Cancer Treatment. [Online] 18, S74–S75.
- Anon (2017) *Insects as food and feed: from production to consumption*. [Online].
- Aoki, K. & Saito, N. (2020) Biocompatibility and carcinogenicity of carbon nanotubes as biomaterials. *Nanomaterials* 10 (2), 264.
- De Araújo, M. E. G. & Huber, L. A. (2007) Subcellular fractionation. *Methods in Molecular Biology* [Online] 357, 73–85.
- Arias, L. S. et al. (2018) Iron oxide nanoparticles for biomedical applications: A perspective on synthesis, drugs, antimicrobial activity, and toxicity. *Antibiotics* 7 (2), 46.
- Armakolas, N. et al. (2016) The role of the IGF-1 Ec in myoskeletal system and osteosarcoma pathophysiology. *Critical Reviews in Oncology/Hematology* 108, 137–145.
- Asai, M. et al. (2019) *Galleria mellonella*: An Infection Model for Screening Compounds Against the Mycobacterium tuberculosis Complex. *Frontiers in Microbiology*. [Online] 10, 2630.
- Asano, T. & Kleinerman, E. S. (1993) Liposome-encapsulated MTP-PE: A novel biologic agent for cancer therapy. *Journal of Immunotherapy*. [Online] 14 (4), 286–

292.

- AshaRani, P. V. et al. (2009) Cytotoxicity and genotoxicity of silver nanoparticles in human cells. *ACS Nano*. [Online] 3 (2), 279–290.
- AshaRani, P. V. et al. (2012) Differential regulation of intracellular factors mediating cell cycle, DNA repair and inflammation following exposure to silver nanoparticles in human cells. *Genome Integrity*. [Online] 3 (1), 2.
- Assa, F. et al. (2017) Chitosan magnetic nanoparticles for drug delivery systems. *Critical Reviews in Biotechnology* 37(4), 492-509.
- Atkin-Smith, G. K. et al. (2015) A novel mechanism of generating extracellular vesicles during apoptosis via a beads-on-a-string membrane structure. *Nature Communications*. [Online] 6,7439.
- Attia, M. F. et al. (2019) An overview of active and passive targeting strategies to improve the nanocarriers efficiency to tumour sites. *Journal of Pharmacy and Pharmacology* 71 (8), 1185–1198.
- Auclair, J. et al. (2019) The Influence of Surface Coatings of Silver Nanoparticles on the Bioavailability and Toxicity to *Elliptio complanata* Mussels. *Journal of Nanomaterials*. [Online] 226, 108623.
- Auten, R. L. & Davis, J. M. (2009) Oxygen toxicity and reactive oxygen species: The devil is in the details. *Pediatric Research* 66 (2), 121–127.
- de Azevedo, J. W. V. et al. (2020) Biology and pathogenesis of human osteosarcoma (Review). *Oncology Letters* 19 (2), 1099–1116.
- Baek, S. H. et al. (2020) Anti-inflammatory activity and ROS regulation effect of sinapaldehyde in LPS-stimulated RAW 264.7 macrophages. *Molecules*. [Online] 25 (18), 4089.
- Baghban, R. et al. (2020) Tumor microenvironment complexity and therapeutic

- implications at a glance. *Cell Communication and Signaling* 18 (1), 59.
- Bala Tannan, N. et al. (2021) Tumor-targeted nanoparticles improve the therapeutic index of BCL2 and MCL1 dual inhibition. *Blood*. [Online] 137 (15), 2057–2069.
- Balkwill, F. & Mantovani, A. (2001) Inflammation and cancer: Back to Virchow? *Lancet* 357 (9255), 539–545.
- Bantz, C. et al. (2014) The surface properties of nanoparticles determine the agglomeration state and the size of the particles under physiological conditions. *Beilstein Journal of Nanotechnology*. [Online] 5 (1), 1774–1786.
- Barile, F. A. (2013) *Principles of Toxicology Testing*. [Online].
- Barré-Sinoussi, F. & Montagutelli, X. (2015) Animal models are essential to biological research: Issues and perspectives. *Future Science OA* 1 (4), FSO63.
- Barrett, T. et al. (2013) NCBI GEO: Archive for functional genomics data sets - Update. *Nucleic Acids Research*. [Online] 41, D991-D995.
- Bateman, A. et al. (2021) UniProt: the universal protein knowledgebase in 2021. *Nucleic Acids Research*. [Online] 49 (D1), D480–D489.
- Baudino, T. (2015) Targeted Cancer Therapy: The Next Generation of Cancer Treatment. *Current Drug Discovery Technologies*. [Online] 12 (1), 3–20.
- Baxevanis, C. N. et al. (1994) Tumor specific cytolysis by tumor infiltrating lymphocytes in breast cancer. *Cancer*. [Online] 74 (4), 1275–1282.
- Behzadi, S. et al. (2017) Cellular uptake of nanoparticles: Journey inside the cell. *Chemical Society Reviews* 46 (14), 4218–4244.
- Berghuis, D. et al. (2012) The CXCR4-CXCL12 axis in Ewing sarcoma: promotion of tumor growth rather than metastatic disease. *Clinical Sarcoma Research*. [Online] 2 (1), 24.
- Bi, Q. et al. (2021) Predicted CD4+ T cell infiltration levels could indicate better overall

- survival in sarcoma patients. *Journal of International Medical Research*. [Online] 49 (1), 300060520981539.
- Bielack, S. et al. (2009) Osteosarcoma: ESMO clinical recommendations for diagnosis, treatment and follow-up. *Annals of Oncology*. [Online] 20 (SUPPL. 4), 137-9.
- Bielack, S. S. et al. (2002) Prognostic factors in high-grade osteosarcoma of the extremities or trunk: An analysis of 1,702 patients treated on neoadjuvant cooperative osteosarcoma study group protocols. *Journal of Clinical Oncology*. [Online] 20 (3), 776–790.
- Binch, A. et al. (2020) Immunohistochemical analysis of protein expression in formalin fixed paraffin embedded human intervertebral disc tissues. *JOR Spine*. [Online] 3 (3), e1098.
- Bingle, L. et al. (2002) The role of tumour-associated macrophages in tumour progression: Implications for new anticancer therapies. *Journal of Pathology* 196 (3), 254–265.
- Björnmalm, M. et al. (2017) Bridging Bio-Nano Science and Cancer Nanomedicine. *ACS Nano* 11 (10), 9594–9613.
- Boisselier, E. & Astruc, D. (2009) Gold nanoparticles in nanomedicine: preparations, imaging, diagnostics, therapies and toxicity. *Chemical Society Reviews*. [Online] 38 (6), 1759–1782.
- Bonilla, F. A. & Oettgen, H. C. (2010) Adaptive immunity. *Journal of Allergy and Clinical Immunology*. [Online] 125 (2 SUPPL. 2), S33-S40.
- Bonneville, M. & Scotet, E. (2006) Human V γ 9V δ 2 T cells: promising new leads for immunotherapy of infections and tumors. *Current Opinion in Immunology* 18 (5), 539–546.

- Bono, H. (2020) All of gene expression (AOE): An integrated index for public gene expression databases. *PLoS ONE*. [Online] 15 (1), e0227076.
- Boraschi, D. et al. (2017) Nanoparticles and innate immunity: new perspectives on host defence. *Seminars in Immunology* 34, 33–51.
- Böttcher, J. P. et al. (2018) NK Cells Stimulate Recruitment of cDC1 into the Tumor Microenvironment Promoting Cancer Immune Control. *Cell*. [Online] 172 (5), 1022-1037.e14.
- Bouvier, C. et al. (2016) Prognostic value of the Hippo pathway transcriptional coactivators YAP/TAZ and β 1-integrin in conventional osteosarcoma. *Oncotarget*. [Online] 7 (40), 64702–64710.
- Bouwmeester, H. et al. (2014) State of the safety assessment and current use of nanomaterials in food and food production. *Trends in Food Science and Technology*. [Online] 40 (2), 200–210.
- Boye, K. et al. (2021) Pembrolizumab in advanced osteosarcoma: results of a single-arm, open-label, phase 2 trial. *Cancer Immunology, Immunotherapy*. [Online] 70 (9), 2617–2624.
- Brassart-Pasco, S. et al. (2020) Tumor Microenvironment: Extracellular Matrix Alterations Influence Tumor Progression. *Frontiers in Oncology* 10, 397.
- Brinkkemper, M. & Slieden, K. (2019) Nanoparticle vaccines for inducing HIV-1 neutralizing antibodies. *Vaccines* 7 (3), 76.
- Brosjö, O. et al. (1985) Influence of Human α -Interferon on Four Human Osteosarcoma Xenografts in Nude Mice. *Cancer Research* 45, 455598–5602.
- Brown, H. K. et al. (2017) Cancer stem cells in osteosarcoma. *Cancer Letters* 386, 189–195.
- Browne, N. et al. (2013) An analysis of the structural and functional similarities of insect

- hemocytes and mammalian phagocytes. *Virulence* 4 (7), 597–603.
- Buchman, J. T. et al. (2019) Understanding Nanoparticle Toxicity Mechanisms to Inform Redesign Strategies to Reduce Environmental Impact. *Accounts of Chemical Research*. [Online] 52 (6), 1632–1642.
- Bukowski, R. M. et al. (2002) Treating cancer with PEG intron: Pharmacokinetic profile and dosing guidelines for an improved interferon-alpha-2b formulation. *Cancer*. [Online] 95 (2), 389–396.
- Bulbake, U. et al. (2017) Liposomal formulations in clinical use: An updated review. *Pharmaceutics* 9 (2), 12.
- Bumgarner, R. (2013) Overview of dna microarrays: Types, applications, and their future. *Current Protocols in Molecular Biology*. [Online] (SUPPL.101), 22.1 .
- Calvert, G. T. et al. (2012) At-risk populations for osteosarcoma: The syndromes and beyond. *Sarcoma* 2012, 152382.
- Camacho-Vanegas, O. et al. (2013) Shaking the family tree: Identification of novel and biologically active alternatively spliced isoforms across the KLF family of transcription factors. *FASEB Journal*. [Online] 27 (2), 432–436.
- Canton, J. (2018) Macropinocytosis: New insights into its underappreciated role in innate immune cell surveillance. *Frontiers in Immunology* 9, 2286.
- Cardelli, J. (2001) Phagocytosis and macropinocytosis in Dictyostelium: Phosphoinositide-based processes, biochemically distinct. *Traffic* 2 (5), 311–320.
- Carlson, C. et al. (2008) Unique cellular interaction of silver nanoparticles: Size-dependent generation of reactive oxygen species. *Journal of Physical Chemistry B*. [Online] 112 (43), 13608–13619.
- Carlson, M. (2022) Genome wide annotation for Rhesus. *R package version 3.2.3. Bioconductor*. [online]. Available from:

- <https://bioconductor.org/packages/release/data/annotation/html/org.Mmu.eg.db.html>.
- Cascini, C. & Chiodoni, C. (2021) The immune landscape of osteosarcoma: Implications for prognosis and treatment response. *Cells*. [Online] 10 (7), 1668.
- Cattaneo, F. et al. (2013) Distinct signaling cascades elicited by different formyl peptide receptor 2 (FPR2) agonists. *International Journal of Molecular Sciences* 14 (4), 7193–7230.
- Cavallaro, U. & Christofori, G. (2001) Cell adhesion in tumor invasion and metastasis: Loss of the glue is not enough. *Biochimica et Biophysica Acta - Reviews on Cancer* 1552 (1), 39–45.
- Cevaal, P. M. et al. (2021) In Vivo T Cell-Targeting Nanoparticle Drug Delivery Systems: Considerations for Rational Design. *ACS Nano* 15 (3), 3736–3753.
- Chakraborty, A. et al. (2020) Size-dependent apoptotic activity of gold nanoparticles on osteosarcoma cells correlated with SERS signal. *Journal of Photochemistry and Photobiology B: Biology*. [Online] 203, 111778.
- Chakraborty, C. et al. (2016) Zebrafish: A complete animal model to enumerate the nanoparticle toxicity. *Journal of Nanobiotechnology*. [Online] 14 (1), 65.
- Chakravarty, D. et al. (2017) OncoKB: A Precision Oncology Knowledge Base. *JCO Precision Oncology*. [Online] (1), 1–16.
- Champion, O. L. et al. (2016) *Galleria mellonella* as a model host for microbiological and toxin research. *Virulence* 7 (7), 840–845.
- Chaplin, D. D. (2010) Overview of the immune response. *Journal of Allergy and Clinical Immunology*. [Online] 125(2), S3–23.
- Chatterjee, S. et al. (2014) ‘The intricate role of CXCR4 in cancer’, in *Advances in Cancer Research*. [Online] 124, 31–82.

- Chee, C. F. et al. (2018) 'Superparamagnetic iron oxide nanoparticles for drug delivery', in *Applications of Nanocomposite Materials in Drug Delivery*. [Online]. 37, 861–903.
- Chen, C. et al. (2021) Immunotherapy for osteosarcoma: Fundamental mechanism, rationale, and recent breakthroughs. *Cancer Letters* 500, 1–10.
- Chen, F. et al. (2014) Theranostic nanoparticles. *Journal of Nuclear Medicine*. [Online] 55 (12), 1919–1922.
- Chen, H. et al. (2013) In Vivo Study of Spherical Gold Nanoparticles: Inflammatory Effects and Distribution in Mice. *PLoS ONE*. [Online] 8 (2), e58208.
- Chen, K. et al. (2017) Regulation of inflammation by members of the formyl-peptide receptor family. *Journal of Autoimmunity* 85, 64–77.
- Chen, Y. C. et al. (2018) Defective formyl peptide receptor 2/3 and annexin A1 expressions associated with M2a polarization of blood immune cells in patients with chronic obstructive pulmonary disease. *Journal of Translational Medicine*. [Online] 16 (1), 69.
- Chen, Y. S. et al. (2009) Assessment of the in vivo toxicity of gold nanoparticles. *Nanoscale Research Letters*. [Online] 4 (8), 858–864.
- Cheng, F. Y. et al. (2010) Multifunctional polymeric nanoparticles for combined chemotherapeutic and near-infrared photothermal cancer therapy in vitro and in vivo. *Chemical Communications*. [Online] 46 (18), 3167–3169.
- Chithrani, B. D. & Chan, W. C. W. (2007) Elucidating the mechanism of cellular uptake and removal of protein-coated gold nanoparticles of different sizes and shapes. *Nano Letters*. [Online] 7(6), 1542-1550.
- Cho, W. S. et al. (2009) Comparison of gene expression profiles in mice liver following intravenous injection of 4 and 100 nm-sized PEG-coated gold nanoparticles.

- Toxicology Letters*. [Online] 191 (1), 96–102.
- Choi, Y. H. et al. (2015) Injectable PLGA microspheres encapsulating WKYMVM peptide for neovascularization. *Acta Biomaterialia*. [Online] 25, 76-85.
- Chou, A. J. et al. (2008) Therapy for osteosarcoma: Where do we go from here? *Pediatric Drugs* 10 (5), 315–327.
- Chou, L. Y. T. et al. (2011) Strategies for the intracellular delivery of nanoparticles. *Chemical Society Reviews*. [Online] 40 (1), 233–245.
- Chu, Z. et al. (2011) Cellular uptake, evolution, and excretion of silica nanoparticles in human cells. *Nanoscale*. [Online] 3 (8), 3291–3299.
- Chu, Z. et al. (2014) Unambiguous observation of shape effects on cellular fate of nanoparticles. *Scientific Reports*. [Online] 28 (4), 4495.
- Clermont, G. et al. (2009) Bridging the gap between systems biology and medicine. *Genome Medicine* 1 (9), 88.
- Cohen, A. W. et al. (2004) Role of caveolae and caveolins in health and disease. *Physiological Reviews* 84 (4), 1341–1379.
- Cole, A. J. et al. (2011) Cancer theranostics: The rise of targeted magnetic nanoparticles. *Trends in Biotechnology* 29 (7), 323–332.
- Committee on Methods of Producing Monoclonal Antibodies et al. (1999) 'Summary of Advantages and Disadvantages of In Vitro and In Vivo Methods - Monoclonal Antibody Product', in *Monoclonal Antibody Production*. 0–3.
- Conery, A. L. et al. (2014) High-throughput screening for novel anti-infectives using a *C. elegans* pathogenesis model. *Current protocols in chemical biology*. [Online] 6 (1), 25–37.
- Cools, F. et al. (2019) Optimization and characterization of a *Galleria mellonella* larval infection model for virulence studies and the evaluation of therapeutics against

- Streptococcus pneumoniae. *Frontiers in Microbiology*. [Online] 10, 311.
- Cornwall, S. M. J. et al. (2016) Human mesothelioma induces defects in dendritic cell numbers and antigen-processing function which predict survival outcomes. *Oncolmmunology*. [Online] 5 (2), e1082028.
- Corre, I. et al. (2020) The Osteosarcoma Microenvironment: A Complex But Targetable Ecosystem. *Cells* 9 (4), 976.
- Cutuli, M. A. et al. (2019) Galleria mellonella as a consolidated in vivo model hosts: New developments in antibacterial strategies and novel drug testing. *Virulence* 10(1), 527-541.
- Cypriyana P J, J. et al. (2021) Overview on toxicity of nanoparticles, it's mechanism, models used in toxicity studies and disposal methods – A review. *Biocatalysis and Agricultural Biotechnology* 36, 102117.
- Dayem, A. A. et al. (2017) The role of reactive oxygen species (ROS) in the biological activities of metallic nanoparticles. *International Journal of Molecular Sciences* 18 (1), 120.
- Degors, I. M. S. et al. (2019) Carriers break barriers in drug delivery: endocytosis and endosomal escape of gene delivery vectors. *Accounts of Chemical Research*. [Online] 52 (7), 1750–1760.
- Delorme-Axford, E. et al. (2015) The yeast *Saccharomyces cerevisiae*: An overview of methods to study autophagy progression. *Methods*. [Online] 75, 3-12.
- Deng, Y. et al. (2020) Application of the Nano-Drug Delivery System in Treatment of Cardiovascular Diseases. *Frontiers in Bioengineering and Biotechnology* 7, 489.
- Desbois, A. P. & Coote, P. J. (2012) 'Utility of greater wax moth larva (*Galleria mellonella*) for evaluating the toxicity and efficacy of new antimicrobial agents', in *Advances in Applied Microbiology*. [Online] 78, 25-53.

- Devanabanda, M. et al. (2016) Immunotoxic effects of gold and silver nanoparticles: Inhibition of mitogen-induced proliferative responses and viability of human and murine lymphocytes in vitro. *Journal of Immunotoxicology*. [Online] 13 (6), 897–902.
- Diaz-Montero, C. M. et al. (2014) Myeloid-derived suppressor cells in cancer: Therapeutic, predictive, and prognostic implications. *Seminars in Oncology*. [Online] 41 (2), 174–184.
- Din, F. U. et al. (2017) Effective use of nanocarriers as drug delivery systems for the treatment of selected tumors. *International Journal of Nanomedicine* 12, 7291–7309.
- Djainal, W. A. S. et al. (2020) Larva of greater wax moth *Galleria mellonella* is a suitable alternative host for the fish pathogen *Francisella noatunensis* subsp. *orientalis*. *BMC Microbiology*. [Online] 20 (1), 8.
- Dobrovolskaia, M. A. et al. (2016) Current understanding of interactions between nanoparticles and the immune system. *Toxicology and Applied Pharmacology*. [Online] 299, 78–89.
- Doherty, G. J. & McMahon, H. T. (2009) Mechanisms of endocytosis. *Annual Review of Biochemistry* 78, 857–902.
- Donahue, N. D. et al. (2019) Concepts of nanoparticle cellular uptake, intracellular trafficking, and kinetics in nanomedicine. *Advanced Drug Delivery Reviews* 143, 68–96.
- Donegan, W. L. (1997) Tumor-related prognostic factors for breast cancer. *CA: A Cancer Journal for Clinicians*. [Online] 47 (1), 28–51.
- Donovan, M. J. et al. (2018) Development and validation of a novel automated Gleason grade and molecular profile that define a highly predictive prostate

- cancer progression algorithm-based test. *Prostate Cancer and Prostatic Diseases*. [Online] 21 (4), 594–603.
- Dorward, D. A. et al. (2015) The role of formylated peptides and formyl peptide receptor 1 in governing neutrophil function during acute inflammation. *American Journal of Pathology* 185 (5), 1172–1184.
- Dreaden, E. C. et al. (2012) The golden age: Gold nanoparticles for biomedicine. *Chemical Society Reviews*. [Online] 41 (7), 2740–2779.
- Dumortier, H. et al. (2006) Functionalized carbon nanotubes are non-cytotoxic and preserve the functionality of primary immune cells. *Nano Letters*. [Online] 6 (7), 1522–1528.
- Dung, T. T. et al. (2009) Structural and magnetic properties of starch-coated magnetite nanoparticles. *Journal of Experimental Nanoscience*. [Online] 4 (3), 259–267.
- Durfee, R. A. et al. (2016a) Review of Osteosarcoma and Current Management. *Rheumatology and Therapy*. [Online] 3 (2), 221–243.
- Durfee, R. A. et al. (2016b) Review of Osteosarcoma and Current Management. *Rheumatology and Therapy* 3 (2), 221–243.
- Edelstein, R. L. et al. (2000) The BARC biosensor applied to the detection of biological warfare agents. *Biosensors and Bioelectronics*. [Online] 14 (10–11), 805–813.
- Elbagory, A. M. et al. (2019) The in vitro immunomodulatory effects of gold nanoparticles synthesized from hypoxis hemerocallidea aqueous extract and hypoxoside on macrophage and natural killer cells. *International Journal of Nanomedicine*. [Online] 14, 9007–9018.
- Elder, D. E. et al. (1983) Immunoperoxidase localization of lymphocyte subsets in the host response to melanoma and nevi. *Cancer Research*. 43 (6), 2749–2753.
- Elsabahy, M. & Wooley, K. L. (2012) Design of polymeric nanoparticles for biomedical

- delivery applications. *Chemical Society Reviews*. [Online] 41 (7), 2545–2561.
- Emerich, D. F. & Thanos, C. G. (2006) The pinpoint promise of nanoparticle-based drug delivery and molecular diagnosis. *Biomolecular Engineering* 23 (4), 171–184.
- Endo-Munoz, L. et al. (2012) The role of osteoclasts and tumour-associated macrophages in osteosarcoma metastasis. *Biochimica et Biophysica Acta - Reviews on Cancer* 1826 (2), 434–442.
- Engin, A. B. et al. (2017) Mechanistic understanding of nanoparticles' interactions with extracellular matrix: The cell and immune system. *Particle and Fibre Toxicology* 14 (1), 22.
- Engin, A. B. & Hayes, A. W. (2018) The impact of immunotoxicity in evaluation of the nanomaterials safety. *Toxicology Research and Application*. [Online] 2, 1–9.
- Eskin, A. et al. (2019) Determination of the acute toxic effects of zinc oxide nanoparticles (ZnO NPs) in total hemocytes counts of *Galleria mellonella* (Lepidoptera: Pyralidae) with two different methods. *Ecotoxicology*. [Online] 28 (7), 801–808.
- Fader, C. M. & Colombo, M. I. (2009) Autophagy and multivesicular bodies: Two closely related partners. *Cell Death and Differentiation* 16 (1), 70–78.
- Fang, C. & Zhang, M. (2010) Nanoparticle-based theragnostics: Integrating diagnostic and therapeutic potentials in nanomedicine. *Journal of Controlled Release* 146 (1), 2–5.
- Fang, F. et al. (2020) Different Strategies for Organic Nanoparticle Preparation in Biomedicine. *ACS Materials Letters*. [Online] 2 (5), 531–549.
- Farc, O. & Cristea, V. (2020) An overview of the tumor microenvironment, from cells to complex networks (Review). *Experimental and Therapeutic Medicine*. [Online]

21 (1), 96.

Farr, L. et al. (2020) Role of MIF Cytokine/CD74 Receptor Pathway in Protecting Against Injury and Promoting Repair. *Frontiers in Immunology* 11, 1273.

Ferguson, W. S. & Goorin, A. M. (2001) Current treatment of osteosarcoma. *Cancer Investigation*. [Online] 19 (3), 292–315.

Fernández, T. D. et al. (2015) Intracellular accumulation and immunological properties of fluorescent gold nanoclusters in human dendritic cells. *Biomaterials*. [Online] 43 (1), 1–12.

Ferrari, S. et al. (2012) Neoadjuvant chemotherapy with methotrexate, cisplatin, and doxorubicin with or without ifosfamide in nonmetastatic osteosarcoma of the extremity: An Italian Sarcoma Group Trial ISG/OS-1. *Journal of Clinical Oncology*. [Online] 30 (17), 2112–2118.

Fidler, I. J. et al. (1981) Eradication of spontaneous metastases and activation of alveolar macrophages by intravenous injection of liposomes containing muramyl dipeptide. *Proceedings of the National Academy of Sciences of the United States of America*. [Online] 78 (3 I), 1680–1684.

Fiore, F. et al. (2007) Enhanced ability of dendritic cells to stimulate innate and adaptive immunity on short-term incubation with zoledronic acid. *Blood*. [Online] 110 (3), 921–927.

Foriel, S. et al. (2015) Mitochondrial diseases: *Drosophila melanogaster* as a model to evaluate potential therapeutics. *International Journal of Biochemistry and Cell Biology* 63, 60–65.

Foroozandeh, P. & Aziz, A. A. (2018) Insight into Cellular Uptake and Intracellular Trafficking of Nanoparticles. *Nanoscale Research Letters* 13 (1), 339.

Franceschini, N. et al. (2019) Bone: Conventional osteosarcoma. *Atlas of Genetics*

- and Cytogenetics in Oncology and Haematology*. [Online] 23 (8), 236–241.
- Francia, V. et al. (2019) Corona Composition Can Affect the Mechanisms Cells Use to Internalize Nanoparticles. *ACS Nano*. [Online] 13 (10), 11107–11121.
- Francis, A. P. & Devasena, T. (2018) Toxicity of carbon nanotubes: A review. *Toxicology and Industrial Health* 34 (3), 200–210.
- Freitas, R. A. (2013) ‘Welcome to the Future of Medicine’, in *The Transhumanist Reader: Classical and Contemporary Essays on the Science, Technology, and Philosophy of the Human Future*. [Online]. pp. 67–72.
- Frisch, J. et al. (2019) STIM-Orai channels and reactive oxygen species in the tumor microenvironment. *Cancers* 11 (4), 457.
- Fu, P. P. et al. (2014) Mechanisms of nanotoxicity: Generation of reactive oxygen species. *Journal of Food and Drug Analysis* 22 (1), 64–75.
- Gaetke, L. M. & Chow, C. K. (2003) Copper toxicity, oxidative stress, and antioxidant nutrients. *Toxicology* 189 (1–2), 147–163.
- Gajewski, T. F. et al. (2013) Innate and adaptive immune cells in the tumor microenvironment. *Nature Immunology* 14 (10), 1014–1022.
- Gambardella, C. et al. (2014) Toxicity and transfer of metal oxide nanoparticles from microalgae to sea urchin larvae. *Chemistry and Ecology*. [Online] 30 (4), 308–316.
- Garg, A. D. et al. (2017) Trial watch: Dendritic cell-based anticancer immunotherapy. *OncolImmunology*. [Online] 6 (7), e1328341.
- Garnis, C. et al. (2004) Genetic alteration and gene expression modulation during cancer progression. *Molecular Cancer* 3, 9.
- Gatoo, M. A. et al. (2014) Physicochemical properties of nanomaterials: Implication in associated toxic manifestations. *BioMed Research International* 2014, 498420.

- Gavas, S. et al. (2021) Nanoparticles for Cancer Therapy: Current Progress and Challenges. *Nanoscale Research Letters* 16 (1), 173.
- German, C. L. & Howe, C. L. (2009) Preparation of biologically active subcellular fractions using the Balch homogenizer. *Analytical Biochemistry*. [Online] 394 (1), 117–124.
- Ghaffari, M. et al. (2020) 'Drug delivery nanosystems for musculoskeletal regeneration', in *Nanoengineering in Musculoskeletal Regeneration*. [Online] 3, 77–103.
- Ghosh, S. et al. (2020) Genotoxicity and biocompatibility of superparamagnetic iron oxide nanoparticles: Influence of surface modification on biodistribution, retention, DNA damage and oxidative stress. *Food and Chemical Toxicology*. [Online] 136, 110989.
- Giannouli, M. et al. (2014) Use of larvae of the wax moth *Galleria mellonella* as an in vivo model to study the virulence of *Helicobacter pylori*. *BMC Microbiology*. [Online] 14 (1), 228.
- Gil-Yarom, N. et al. (2017) CD74 is a novel transcription regulator. *Proceedings of the National Academy of Sciences of the United States of America*. [Online] 114 (3), 562–567.
- Gill, J. & Gorlick, R. (2021) Advancing therapy for osteosarcoma. *Nature Reviews Clinical Oncology* 18 (10), 609–624.
- Di Gioacchino, M. et al. (2011) Immunotoxicity of nanoparticles. *International journal of immunopathology and pharmacology* 24 (1 Suppl), 65S-71S.
- Gleichman, N. (2020) Endocytosis and Exocytosis: Differences and Similarities | Technology Networks. *Technology Networks* [online]. Available from: <https://www.technologynetworks.com/immunology/articles/endocytosis-and->

exocytosis-differences-and-similarities-334059.

- Gojova, A. et al. (2007) Induction of inflammation in vascular endothelial cells by metal oxide nanoparticles: Effect of particle composition. *Environmental Health Perspectives*. [Online] 115 (3), 403–409.
- Gomez-Brouchet, A. et al. (2017) CD163-positive tumor-associated macrophages and CD8-positive cytotoxic lymphocytes are powerful diagnostic markers for the therapeutic stratification of osteosarcoma patients: An immunohistochemical analysis of the biopsies from the French OS2006 phase 3 trial. *OncotImmunology*. [Online] 6 (9), e1331193.
- Gonzalez-Moragas, L. et al. (2015) *C. elegans* as a tool for in vivo nanoparticle assessment. *Advances in Colloid and Interface Science* 219, 10–26.
- Gouirand, V. et al. (2018) Influence of the tumor microenvironment on cancer cells metabolic reprogramming. *Frontiers in Oncology* 8, 117.
- Gresham, D. et al. (2008) Comparing whole genomes using DNA microarrays. *Nature Reviews Genetics* 9 (4), 291–302.
- Griffith, M. et al. (2017) CIViC is a community knowledgebase for expert crowdsourcing the clinical interpretation of variants in cancer. *Nature Genetics* 49 (2), 170–174.
- Grimer, R. J. (2005) Surgical options for children with osteosarcoma. *Lancet Oncology* 6 (2), 85–92.
- Gu, W. et al. (2013) Nanotechnology in the targeted drug delivery for bone diseases and bone regeneration. *International Journal of Nanomedicine* 8, 2305–2317.
- Gu, Y. et al. (2021) Role of CXCR4 as a Prognostic Biomarker Associated With the Tumor Immune Microenvironment in Gastric Cancer. *Frontiers in Cell and Developmental Biology*. [Online] 9, 654504.

- Gupta, R. & Xie, H. (2018) Nanoparticles in daily life: Applications, toxicity and regulations. *Journal of Environmental Pathology, Toxicology and Oncology*. [Online] 37 (3), 209–230.
- Gwokyalya, R. & Altuntaş, H. (2019) Boric acid-induced immunotoxicity and genotoxicity in model insect *Galleria mellonella* L. (Lepidoptera: Pyralidae). *Archives of Insect Biochemistry and Physiology*. [Online] 101 (4), e21588.
- Den Haan, J. M. M. et al. (2000) CD8⁺ but not CD8⁻ dendritic cells cross-prime cytotoxic T cells in vivo. *Journal of Experimental Medicine*. [Online] 192 (12), 1685-96.
- Habas, K. et al. (2021) Toxicity mechanisms of nanoparticles in the male reproductive system. *Drug Metabolism Reviews* 53 (4), 604–617.
- Han, I. et al. (2017) Role of CD74 and Its Relationship with Macrophage Migration Inhibitory Factor in Osteosarcoma Tumorigenesis. *Journal of the Korean Orthopaedic Association*. [Online] 52 (2), 192.
- Han, R. et al. (2016) ‘De Novo Deep Transcriptome Analysis of Medicinal Plants for Gene Discovery in Biosynthesis of Plant Natural Products’, in *Methods in Enzymology*. [Online] 576, 19–45.
- Hanahan, D. & Coussens, L. M. (2012) Accessories to the Crime: Functions of Cells Recruited to the Tumor Microenvironment. *Cancer Cell* 21 (3), 309–322.
- Hanahan, D. and Weinberg, Robert A. (2011). Hallmarks of cancer: the next Generation. *Cell*, 144(5), pp.646–674.
- Hansen, C. G. & Nichols, B. J. (2009) Molecular mechanisms of clathrin-independent endocytosis. *Journal of Cell Science*. [Online] 122 (11), 1713–1721.
- Haque, E. & Ward, A. C. (2018) Zebrafish as a model to evaluate nanoparticle toxicity. *Nanomaterials* 8 (7), 561.

- Harada, M. et al. (2004) N-Formylated humanin activates both formyl peptide receptor-like 1 and 2. *Biochemical and Biophysical Research Communications*. [Online] 324 (1), 255–261.
- Harris, M. A. et al. (2004) The Gene Oncology (GO) database and informatics resource. *Nucleic Acids Research*. [Online] 32, D258-61.
- Harush-Frenkel, O. et al. (2007) Targeting of nanoparticles to the clathrin-mediated endocytic pathway. *Biochemical and Biophysical Research Communications*. [Online] 353 (1), 26–32.
- Hashiguchi, M. H. et al. (2021) A case of lung adenocarcinoma with a novel CD74-ROS1 fusion variant identified by comprehensive genomic profiling that responded to crizotinib and entrectinib. *Thoracic Cancer*. [Online] 12 (18), 2504–2507.
- Hattori, H. & Yamamoto, K. (2012) Lymph node metastasis of osteosarcoma. *Journal of Clinical Oncology*. [Online] 30 (33), e345-9.
- He, H. et al. (2013) Carbon nanotubes: Applications in pharmacy and medicine. *BioMed Research International*. [Online] 2013, 578290.
- He, H. Q. & Ye, R. D. (2017) The formyl peptide receptors: Diversity of ligands and mechanism for recognition. *Molecules* 22 (3), 455.
- He, K. & Tang, M. (2018) Safety of novel liposomal drugs for cancer treatment: Advances and prospects. *Chemico-Biological Interactions* 295, 13–19.
- He, W. et al. (2016) In vitro uptake of silver nanoparticles and their toxicity in human mesenchymal stem cells derived from bone marrow. *Journal of Nanoscience and Nanotechnology*. [Online] 16 (1), 219–228.
- He, Y. T. et al. (2016) In vitro generation of cytotoxic T lymphocyte response using dendritic cell immunotherapy in osteosarcoma. *Oncology Letters*. [Online] 12 (2),

1101–1106.

- Heiligtag, F. J. & Niederberger, M. (2013) The fascinating world of nanoparticle research. *Materials Today* 16 (7–8), 262–271.
- Heller, R. A. et al. (1997) Discovery and analysis of inflammatory disease-related genes using cDNA microarrays. *Proceedings of the National Academy of Sciences of the United States of America*. [Online] 94 (6), 2150–2155.
- Hernandez, R. J. et al. (2019) Using the wax moth larva *Galleria mellonella* infection model to detect emerging bacterial pathogens. *PeerJ*. [Online] 2019 (1), 6, e6150.
- Herranz, F. et al. (2011) The application of nanoparticles in gene therapy and magnetic resonance imaging. *Microscopy Research and Technique* 74 (7), 577–591.
- Heymann, M.-F. & Heymann, D. (2017) ‘Immune Environment and Osteosarcoma’, in *Osteosarcoma - Biology, Behavior and Mechanisms*. [Online] 105-120.
- Heymann, M. F. et al. (2019) The contribution of immune infiltrates and the local microenvironment in the pathogenesis of osteosarcoma. *Cellular Immunology*. [Online] 343, 103711.
- Hillaireau, H. & Couvreur, P. (2009) Nanocarriers’ entry into the cell: Relevance to drug delivery. *Cellular and Molecular Life Sciences* 66 (17), 2873–2896.
- Hirota, K. & Ter, H. (2012) ‘Endocytosis of Particle Formulations by Macrophages and Its Application to Clinical Treatment’, in *Molecular Regulation of Endocytosis*. [Online].
- Ho, X. D. et al. (2017) Whole transcriptome analysis identifies differentially regulated networks between osteosarcoma and normal bone samples. *Experimental Biology and Medicine*. [Online] 242 (18), 1802–1811.
- Horie, M. & Tabei, Y. (2021) Role of oxidative stress in nanoparticles toxicity. *Free Radical Research* 55 (4), 331–342.

- Horn, L. et al. (2014) Phagocytic ability declines with age in adult *Drosophila* hemocytes. *Aging Cell*. [Online] 13 (4), 719–728.
- Hou, X. L. et al. (2017) FPR2 promotes invasion and metastasis of gastric cancer cells and predicts the prognosis of patients. *Scientific Reports*. [Online] 7 (1), .
- Hsu, C.-H. et al. (2007) The Zebrafish Model: Use in Studying Cellular Mechanisms for a Spectrum of Clinical Disease Entities. *Current Neurovascular Research*. [Online] 4 (2), 111–120.
- Huang, H. J. et al. (2021) Current strategies in assessment of nanotoxicity: Alternatives to in vivo animal testing. *International Journal of Molecular Sciences* 22 (8), 4216.
- Huang, J. et al. (2012) HMGB1 promotes drug resistance in osteosarcoma. *Cancer Research*. [Online] 72 (1), 230–238.
- Huang, J. et al. (2018) The multidisciplinary treatment of osteosarcoma of the proximal tibia: A retrospective study. *BMC Musculoskeletal Disorders*. [Online] 19 (1), 315.
- Hughes, M. S. et al. (2005) Transfer of a TCR gene derived from a patient with a marked antitumor response conveys highly active T-cell effector functions. *Human Gene Therapy*. [Online] 16 (4), 457–472.
- Iguchi, Y. et al. (2015) Tumor-specific delivery of BSH-3R for boron neutron capture therapy and positron emission tomography imaging in a mouse brain tumor model. *Biomaterials*. [Online] 56, 10–17.
- Isakoff, M. S. et al. (2015) Osteosarcoma: Current treatment and a collaborative pathway to success. *Journal of Clinical Oncology* 33 (27), 3029–3035.
- Isoda, K. et al. (2020) Toxicity of Gold Nanoparticles in Mice due to Nanoparticle/Drug Interaction Induces Acute Kidney Damage. *Nanoscale Research Letters*. [Online] 15 (1), 141.

- Jackson, P. et al. (2013) Bioaccumulation and ecotoxicity of carbon nanotubes. *Chemistry Central Journal*. [Online] 7 (1), 154.
- Jafar, A. et al. (2016) Carbon nanotube toxicity: The smallest biggest debate in medical care. *Cogent Medicine*. [Online] 3 (1), 1217970.
- Jahanban-Esfahlan, R. et al. (2018) Combination of nanotechnology with vascular targeting agents for effective cancer therapy. *Journal of Cellular Physiology* 233 (4), 2982–2992.
- Jahanban-Esfahlan, R., Seidi, K., Monhemi, H., et al. (2017) RGD delivery of truncated coagulase to tumor vasculature affords local thrombotic activity to induce infarction of tumors in mice. *Scientific Reports*. [Online] 7 (1), 8126.
- Jahanban-Esfahlan, R., Seidi, K. & Zarghami, N. (2017) Tumor vascular infarction: prospects and challenges. *International Journal of Hematology* 105 (3), 244–256.
- Jamal-Hanjani, M. et al. (2015) Translational implications of tumor heterogeneity. *Clinical Cancer Research* 21 (6), 1258–1266.
- Jander, G. et al. (2000) Positive correlation between virulence of *Pseudomonas aeruginosa* mutants in mice and insects. *Journal of Bacteriology*. [Online] 182 (13), 3843–3845.
- Janeway CA Jr Walport M, et al., T. P. (2001) Principles of innate and adaptive immunity - Immunobiology - NCBI Bookshelf. *New York: Garland Science*. 1–9. [online]. Available from: <https://www.ncbi.nlm.nih.gov/books/NBK27090/>.
- Janib, S. M. et al. (2010) Imaging and drug delivery using theranostic nanoparticles. *Advanced Drug Delivery Reviews* 62 (11), 1052–1063.
- Jia, Y. P. et al. (2017) The in vitro and in vivo toxicity of gold nanoparticles. *Chinese Chemical Letters*. [Online] 28 (4), 691–702.
- Jo, V. Y. & Fletcher, C. D. M. (2014) WHO classification of soft tissue tumours: An

- update based on the 2013 (4th) edition. *Pathology*. [Online] 46 (2), 95–104.
- Johnston, H. J. et al. (2018) Adoption of in vitro systems and zebrafish embryos as alternative models for reducing rodent use in assessments of immunological and oxidative stress responses to nanomaterials. *Critical Reviews in Toxicology* 48 (3), 252–271.
- Johnston, H. J. et al. (2010) Evaluating the uptake and intracellular fate of polystyrene nanoparticles by primary and hepatocyte cell lines in vitro. *Toxicology and Applied Pharmacology*. [Online] 242 (1), 66–78.
- Jones, C. F. & Grainger, D. W. (2009) In vitro assessments of nanomaterial toxicity. *Advanced Drug Delivery Reviews* 61 (6), 438–456.
- De Jong, W. H. et al. (2008) Particle size-dependent organ distribution of gold nanoparticles after intravenous administration. *Biomaterials*. [Online] 29 (12), 1912–1919.
- De Jong, W. H. & Borm, P. J. A. (2008) Drug delivery and nanoparticles: Applications and hazards. *International Journal of Nanomedicine* 3 (2), 133–149.
- Jovic, M. et al. (2010) The early endosome: A busy sorting station for proteins at the crossroads. *Histology and Histopathology* 25 (1), 99–112.
- Junqueira, J. C. (2012) *Galleria mellonella* as a model host for human pathogens: Recent studies and new perspectives. *Virulence*. [Online] 3 (6), 474–476.
- Jurek, P. M. et al. (2017) Anti-FGFR1 aptamer-tagged superparamagnetic conjugates for anticancer hyperthermia therapy. *International Journal of Nanomedicine*. [Online] 12, 2941–2950.
- Kager, L. et al. (2003) Primary metastatic osteosarcoma: Presentation and outcome of patients treated on neoadjuvant Cooperative Osteosarcoma Study Group protocols. *Journal of Clinical Oncology*. [Online] 21 (10), 2011–2018.

- Kamaly, N. et al. (2012) Targeted polymeric therapeutic nanoparticles: Design, development and clinical translation. *Chemical Society Reviews*. [Online] 41 (7), 2971–3010.
- Kansara, M. et al. (2014) Translational biology of osteosarcoma. *Nature Reviews Cancer* 14 (11), 722–735.
- Karaman, D. Ş. et al. (2017) 'Current Approaches for Exploration of Nanoparticles as Antibacterial Agents', in *Antibacterial Agents*. [Online].
- Karlsson, H. L. et al. (2013) Cell membrane damage and protein interaction induced by copper containing nanoparticles-Importance of the metal release process. *Toxicology*. [Online] 313 (1), 59–69.
- Kavanagh, K. & Sheehan, G. (2018) The use of galleria mellonella larvae to identify novel antimicrobial agents against fungal species of medical interest. *Journal of Fungi* 4 (3), 113.
- Kawai, A. et al. (2017) Systemic Therapy for Soft Tissue Sarcoma: Proposals for the Optimal Use of Pazopanib, Trabectedin, and Eribulin. *Advances in Therapy* 34 (7), 1556–1571.
- Kawano, M. et al. (2010) Cryoimmunologic antitumor effects enhanced by dendritic cells in osteosarcoma. *Clinical Orthopaedics and Related Research*. [Online] 468 (5), 1373–1383.
- Kawano, M. et al. (2013) Enhancement of antitumor immunity by combining anti-cytotoxic T lymphocyte antigen-4 antibodies and cryotreated tumor lysate-pulsed dendritic cells in murine osteosarcoma. *Oncology Reports*. [Online] 29 (3), 1001–1006.
- Kay, S. et al. (2019) Galleria mellonella infection model identifies both high and low lethality of clostridium perfringens toxigenic strains and their response to

- antimicrobials. *Frontiers in Microbiology*. [Online] 10, 1281.
- Kenny, M. C. et al. (2018) How temperature influences the viscosity of hornworm hemolymph. *Journal of Experimental Biology*. [Online] 221 (21), jeb186338.
- Kerr, M. C. & Teasdale, R. D. (2009) Defining macropinocytosis. *Traffic* 10 (4), 364–371.
- Kerslake, R. et al. (2021) A pancancer overview of FBN1, asprosin and its cognate receptor OR4M1 with detailed expression profiling in ovarian cancer. *Oncology Letters*. [Online] 22 (3), 650.
- Khalil, N. M. et al. (2011) Potential of polymeric nanoparticles in AIDS treatment and prevention. *Expert Opinion on Drug Delivery* 8 (1), 95–112.
- Khan, Ibrahim et al. (2019) Nanoparticles: Properties, applications and toxicities. *Arabian Journal of Chemistry* 12 (7), 908–931.
- Khanbabaie, R. & Jahanshahi, M. (2012) Revolutionary Impact of Nanodrug Delivery on Neuroscience. *Current Neuropharmacology*. [Online] 10 (4), 370–392.
- Khanna, C. (2008) Novel targets with potential therapeutic applications in osteosarcoma. *Current Oncology Reports* 10 (4), 350–358.
- Khau, T. et al. (2011) Annexin-1 signals mitogen-stimulated breast tumor cell proliferation by activation of the formyl peptide receptors (FPRs) 1 and 2. *FASEB Journal*. [Online] 25 (2), 483–496.
- Kievit, F. M. et al. (2012) Targeting of primary breast cancers and metastases in a transgenic mouse model using rationally designed multifunctional SPIONs. *ACS Nano*. [Online] 6 (3), 2591–2601.
- Kievit, F. M. & Zhang, M. (2011a) Cancer nanotheranostics: Improving imaging and therapy by targeted delivery across biological barriers. *Advanced Materials* 23 (36), H217-47.

- Kievit, F. M. & Zhang, M. (2011b) Surface engineering of iron oxide nanoparticles for targeted cancer therapy. *Accounts of Chemical Research*. [Online] 44 (10), 853–862.
- Kim, J. H. et al. (2009) Intravenously administered gold nanoparticles pass through the blood-retinal barrier depending on the particle size, and induce no retinal toxicity. *Nanotechnology*. [Online] 20 (50), 505101.
- Kim, S.-H. et al. (2017) Cutting Edge: LL-37–Mediated Formyl Peptide Receptor-2 Signaling in Follicular Dendritic Cells Contributes to B Cell Activation in Peyer's Patch Germinal Centers. *The Journal of Immunology*. [Online] 198 (2), 629–633.
- Kim, S. et al. (2009) Oxidative stress-dependent toxicity of silver nanoparticles in human hepatoma cells. *Toxicology in Vitro*. [Online] 23 (6), 1076–1084.
- Kim, S. D. et al. (2013) The immune-stimulating peptide WKYMVm has therapeutic effects against ulcerative colitis. *Experimental and Molecular Medicine*. [Online] 45 (9), e40.
- Kim, S. Y. et al. (2008) Inhibition of the CXCR4/CXCL12 chemokine pathway reduces the development of murine pulmonary metastases. *Clinical and Experimental Metastasis*. [Online] 25 (3), 201–211.
- Kim, T. H. et al. (2013) Nanotheranostics for personalized medicine. *Expert Review of Molecular Diagnostics* 13 (3), 257–269.
- Kirchhausen, T. (2000) Clathrin. *Annual Review of Biochemistry* 69, 699-727.
- Kiss, A. L. & Botos, E. (2009) Endocytosis via caveolae: Alternative pathway with distinct cellular compartments to avoid lysosomal degradation? *Journal of Cellular and Molecular Medicine*. [Online] 13 (7), 1228–1237.
- Klaver, D. et al. (2020) Peptides from allergenic lipocalins bind to formyl peptide receptor 3 in human dendritic cells to mediate TH2 immunity. *Journal of Allergy*

- and Clinical Immunology*. [Online] 145 (2), 654–665.
- Kleinerman, E. S. et al. (1991) Influence of chemotherapy administration on monocyte activation by liposomal muramyl tripeptide phosphatidylethanolamine in children with osteosarcoma. *Journal of Clinical Oncology*. [Online] 9 (2), 259–267.
- Kleinerman, E. S. et al. (1992) Phase II study of liposomal muramyl tripeptide in osteosarcoma: The cytokine cascade and monocyte activation following administration. *Journal of Clinical Oncology*. [Online] 10 (8), 1310–1316.
- Kohane, D. S. (2007) Microparticles and nanoparticles for drug delivery. *Biotechnology and Bioengineering* 96 (2), 203–209.
- Kolluru, L. P. et al. (2013) Formulation development of albumin based theragnostic nanoparticles as a potential delivery system for tumor targeting. *Journal of Drug Targeting*. [Online] 21 (1), 77–86.
- Kong, F. Y. et al. (2017) Unique roles of gold nanoparticles in drug delivery, targeting and imaging applications. *Molecules* 22 (9), 1445.
- Kononenko, V. et al. (2015) Nanoparticle interaction with the immune system. *Arhiv za Higijenu Rada i Toksikologiju*. [Online] 66 (2), 97–108.
- Korkor, M. T. et al. (2011) Microarray analysis of differential gene expression profile in peripheral blood cells of patients with human essential hypertension. *International journal of medical sciences*. [Online] 8 (2), 168–179.
- Koury, J. et al. (2018) Immunotherapies: Exploiting the immune system for cancer treatment. *Journal of Immunology Research* 2018, 9585614.
- Kresse, S. H. et al. (2009) LSAMP, a novel candidate tumor suppressor gene in human osteosarcomas, identified by array comparative genomic hybridization. *Genes Chromosomes and Cancer*. [Online] 48 (8), 679–693.
- Krishnaraj, C. et al. (2016) In Vivo toxicological assessment of biologically synthesized

- silver nanoparticles in adult Zebrafish (*Danio rerio*). *Journal of Hazardous Materials*. [Online] 301, 480–491.
- Kristensen, N. (2003) Lepidoptera, Moths and Butterflies: Morphology, Physiology, and Development: Teilband (Vol. 2). de Gruyter. *The insects of Australia* 99 (5), 988–989
- Kruzelock, R. P. et al. (1997) Localization of a novel tumor suppressor locus on human chromosome 3q important in osteosarcoma tumorigenesis. *Cancer Research*. 57 (1), 106–109.
- Kuijjer, M. L. et al. (2013) IR/IGF1R signaling as potential target for treatment of high-grade osteosarcoma. *BMC Cancer*. [Online] 13, 245.
- Kumar, V. et al. (2017) In vitro and in vivo toxicity assessment of nanoparticles. *International Nano Letters*. [Online] 7 (4), 243–256.
- Kumari, A. et al. (2010) Biodegradable polymeric nanoparticles based drug delivery systems. *Colloids and Surfaces B: Biointerfaces* 75 (1), 1–18.
- Kumari, P. et al. (2016) Nanocarriers for cancer-targeted drug delivery. *Journal of Drug Targeting* 24 (3), 179–191.
- Kumari, S. et al. (2010) Endocytosis unplugged: Multiple ways to enter the cell. *Cell Research* 20 (3), 256–275.
- Kundu, Z. S. (2014) ‘Classification, imaging, biopsy and staging of osteosarcoma’, in *Indian Journal of Orthopaedics*. [Online]. 2014 48, 238–246.
- Kus-liśkiewicz, M. et al. (2021) Biocompatibility and cytotoxicity of gold nanoparticles: Recent advances in methodologies and regulations. *International Journal of Molecular Sciences* 22 (20), 10952.
- De la Isla, A. et al. (2003) Nanohybrid scratch resistant coatings for teeth and bone viscoelasticity manifested in tribology. *Materials Research Innovations*. [Online] 7

- (2), 110–114.
- Labani-Motlagh, A. et al. (2020) The Tumor Microenvironment: A Milieu Hindering and Obstructing Antitumor Immune Responses. *Frontiers in Immunology* 11, 940.
- Lage, K. et al. (2008) A large-scale analysis of tissue-specific pathology and gene expression of human disease genes and complexes. *Proceedings of the National Academy of Sciences of the United States of America*. [Online] 105 (52), 20870–20875.
- Lai, S. K. et al. (2007) Privileged delivery of polymer nanoparticles to the perinuclear region of live cells via a non-clathrin, non-degradative pathway. *Biomaterials*. [Online] 28 (18), 2876–2884.
- Lamplot, J. et al. (2013) The Current and Future Therapies for Human Osteosarcoma. *Current Cancer Therapy Reviews*. [Online] 9 (1), 55–77.
- Lange, A. et al. (2018) Genome sequence of *Galleria mellonella* (greater wax moth). *Genome Announcements*. [Online] 6 (2), e01220-17.
- Langfelder, P. & Horvath, S. (2008) WGCNA: An R package for weighted correlation network analysis. *BMC Bioinformatics*. [Online] 9, 559.
- Lankveld, D. P. et al. (2010) In vitro testing for direct immunotoxicity: state of the art. *Methods in molecular biology (Clifton, N.J.)*. [Online] 598, 401–423.
- Laoui, D. et al. (2014) Functional relationship between tumor-associated macrophages and macrophage colony-stimulating factor as contributors to cancer progression. *Frontiers in Immunology* 5, 489.
- Laverdiere, C. et al. (2005) Messenger RNA expression levels of CXCR4 correlate with metastatic behavior and outcome in patients with osteosarcoma. *Clinical Cancer Research*. [Online] 11 (7), 2561–2567.
- Lee, A. R. et al. (2018) A genome-wide screening of target genes against silver

- nanoparticles in fission yeast. *Toxicological Sciences*. [Online] 161 (1), 171–185.
- Lee, H. Y. et al. (2007) F2L, a peptide derived from heme-binding protein, inhibits formyl peptide receptor-mediated signaling. *Biochemical and Biophysical Research Communications*. [Online] 359 (4), 985–990.
- Lee Ventola, C. (2012) The nanomedicine revolution: Part 1: Emerging Concepts. *P and T*. 37 (9), 512-525.
- Lee, Y. H. et al. (2014) Cytotoxicity, oxidative stress, apoptosis and the autophagic effects of silver nanoparticles in mouse embryonic fibroblasts. *Biomaterials*. [Online] 35 (16), 4706–4715.
- Leeuw, T. K. et al. (2007) Single-walled carbon nanotubes in the intact organism: Near-IR imaging and biocompatibility studies in drosophila. *Nano Letters*. [Online]
- Lévy, M. et al. (2010) Degradability of superparamagnetic nanoparticles in a model of intracellular environment: Follow-up of magnetic, structural and chemical properties. *Nanotechnology*. [Online] 21 (39), 395103.
- Lewis, C. E. & Pollard, J. W. (2006) Distinct role of macrophages in different tumor microenvironments. *Cancer Research* 66 (2), 605–612.
- Li, B. et al. (2016) Comprehensive analyses of tumor immunity: Implications for cancer immunotherapy. *Genome Biology*. [Online] 17 (1), 174.
- Li, B. et al. (2014) Induction of a specific CD8+ T-cell response to cancer/testis antigens by demethylating pre-treatment against osteosarcoma. *Oncotarget*. [Online] 5 (21), 10791–10802.
- Li, C. J. et al. (2016) Advances in Bone-targeted Drug Delivery Systems for Neoadjuvant Chemotherapy for Osteosarcoma. *Orthopaedic Surgery* 8 (2), 105–110.
- Li, G. et al. (2013) Prognostic value of CXCR4 expression in patients with clear cell

- renal cell carcinoma. *Histology and Histopathology*. 28 (9), 1217–1222.
- Li, J. et al. (2011) DOSim: An R package for similarity between diseases based on Disease Ontology. *BMC Bioinformatics*. [Online] 12, 266.
- Li, L. et al. (2016) New development in studies of formyl-peptide receptors: critical roles in host defense. *Journal of Leukocyte Biology*. [Online] 99 (3), 425–435.
- Li, L. et al. (2013) Toxicity of superparamagnetic iron oxide nanoparticles: Research strategies and implications for nanomedicine. *Chinese Physics B*. [Online] 22 (12), 127503.
- Li, M. et al. (2020) Key genes with prognostic values in suppression of osteosarcoma metastasis using comprehensive analysis. *BMC Cancer*. [Online] 20 (1), 65.
- Li, M. et al. (2014) Mechanistic characterization of titanium dioxide nanoparticle-induced toxicity using electron spin resonance. *Journal of Food and Drug Analysis* 22 (1), 76–85.
- Li, T. et al. (2017) TIMER: A web server for comprehensive analysis of tumor-infiltrating immune cells. *Cancer Research*. [Online] 77 (21), e108–e110.
- Li, T. et al. (2020) TIMER2.0 for analysis of tumor-infiltrating immune cells. *Nucleic Acids Research*. [Online] 48 (W1), W509–W514.
- Li, X. & Donowitz, M. (2008) Fractionation of subcellular membrane vesicles of epithelial and nonepithelial cells by optiPrep™ density gradient ultracentrifugation. *Methods in Molecular Biology*. [Online] 440, 97–110.
- Li, Y. J. et al. (2017) Clinicopathological and prognostic significance of chemokine receptor CXCR4 in patients with bone and soft tissue sarcoma: a meta-analysis. *Clinical and Experimental Medicine*. [Online] 17 (1), 59–69.
- Li, Z. (2013) Potential of human $\gamma\delta$ T cells for immunotherapy of osteosarcoma. *Molecular Biology Reports* 40 (1), 427–437.

- Liao, Y. et al. (2019) WebGestalt 2019: gene set analysis toolkit with revamped UIs and APIs. *Nucleic Acids Research*. [Online] 47 (W1), W199–W205.
- Lila, A. S. A. & Ishida, T. (2017) Liposomal delivery systems: Design optimization and current applications. *Biological and Pharmaceutical Bulletin* 40 (1), 1–10.
- Lim, J. P. & Gleeson, P. A. (2011) Macropinocytosis: An endocytic pathway for internalising large gulps. *Immunology and Cell Biology* 89 (8), 836–843.
- Liu, C. F. et al. (2014) The prognostic value of CXCR4 in ovarian cancer: A meta-analysis. *PLoS ONE*. [Online] 9 (3), e92629.
- Liu, J. et al. (2022) The interaction between nanoparticles and immune system: application in the treatment of inflammatory diseases. *Journal of Nanobiotechnology* 20(1), 127.
- Liu, J. J. et al. (2013) Telangiectatic osteosarcoma: A review of literature. *OncoTargets and Therapy* 6, 593–602.
- Liu, L. et al. (2018) Impact of Morphology on Iron Oxide Nanoparticles-Induced Inflammasome Activation in Macrophages. *ACS Applied Materials and Interfaces*. [Online] 10 (48), 41197–41206.
- Liu, W. et al. (2021) Exploration of Immune-Related Gene Expression in Osteosarcoma and Association with Outcomes. *JAMA Network Open*. [Online] 4 (8), e2119132.
- Liu, X. et al. (2009) Differential toxicity of carbon nanomaterials in *Drosophila*: Larval dietary uptake is benign, but adult exposure causes locomotor impairment and mortality. *Environmental Science and Technology*. [Online] 43 (16), 6357–6363.
- Liu, Y. et al. (2017) Effects of engineered nanoparticles on the innate immune system. *Seminars in Immunology* 34, 25–32.
- Liu, Y. et al. (2019) Multi-omic measurements of heterogeneity in HeLa cells across

- laboratories. *Nature Biotechnology*. [Online] 37 (3), 314–322.
- Liu, Z. et al. (2008) Circulation and long-term fate of functionalized, biocompatible single-walled carbon nanotubes in mice probed by Raman spectroscopy. *Proceedings of the National Academy of Sciences of the United States of America*. [Online] 105 (5), 1410–1415.
- Liu, Z. et al. (2022) Identification of a seven-gene prognostic signature using the gene expression profile of osteosarcoma. *Annals of Translational Medicine*. [Online] 10 (2), 53–53. [online]. Available from: <https://atm.amegroups.com/article/view/88148>.
- Lockhart, D. J. et al. (1996) Expression monitoring by hybridization to high-density oligonucleotide arrays. *Nature Biotechnology*. [Online] 14 (13), 1675–1680.
- Longhi, A. et al. (2006) Primary bone osteosarcoma in the pediatric age: State of the art. *Cancer Treatment Reviews* 32 (6), 423–436.
- Lopez-Chaves, C. et al. (2018) Gold nanoparticles: Distribution, bioaccumulation and toxicity. In vitro and in vivo studies. *Nanomedicine: Nanotechnology, Biology, and Medicine*. [Online] 14 (1), 1–12.
- Lovrić, J. et al. (2005) Differences in subcellular distribution and toxicity of green and red emitting CdTe quantum dots. *Journal of Molecular Medicine*. [Online] 83 (5), 377–385.
- Lu, Y. et al. (2022) Novel Immunotherapies for Osteosarcoma. *Frontiers in Oncology* 12, 830546.
- Lüersen, K. et al. (2013) The Glutathione Reductase GSR-1 Determines Stress Tolerance and Longevity in *Caenorhabditis elegans*. *PLoS ONE*. [Online] 8 (4), e60731.
- Luetke, A. et al. (2014) Osteosarcoma treatment - Where do we stand? A state of the

- art review. *Cancer Treatment Reviews* 40 (4), 523–532.
- Luke, J. J. et al. (2022) Pembrolizumab versus placebo as adjuvant therapy in completely resected stage IIB or IIC melanoma (KEYNOTE-716): a randomised, double-blind, phase 3 trial. *The Lancet*. [Online] [400_\(10352\)](#), 559.
- Luksch, R. et al. (2003) Immunomodulation in a treatment program including pre- and post-operative interleukin-2 and chemotherapy for childhood osteosarcoma. *Tumori*. [Online] 89 (3), 263–268.
- Lundquist, C. et al. (2014) Characterization of Free and Porous Silicon-Encapsulated Superparamagnetic Iron Oxide Nanoparticles as Platforms for the Development of Theranostic Vaccines. *Medical Sciences*. [Online] 2 (1), 51–69.
- Luo, Y. H. et al. (2015) Metal-Based Nanoparticles and the Immune System: Activation, Inflammation, and Potential Applications. *BioMed Research International* 2015, 143720.
- Ma, J. et al. (2003) Biomimetic processing of nanocrystallite bioactive apatite coating on titanium. *Nanotechnology*. [Online] 14 (6), 619–623.
- Ma, J. et al. (2020) Identification of novel prognosis-related genes in the endometrial cancer immune microenvironment. *Aging*. [Online] 12 (21), 22152–22173.
- Ma, X. et al. (2019) Evaluation of Turning-Sized Gold Nanoparticles on Cellular Adhesion by Golgi Disruption in Vitro and in Vivo. *Nano Letters*. [Online] 19 (12), 8476–8487.
- Macewen, E. G. et al. (1989) Therapy for osteosarcoma in dogs with intravenous injection of liposome-encapsulated muramyl tripeptide. *Journal of the National Cancer Institute*. [Online] 81 (12), 935–938.
- Macro, L. et al. (2012) Dynamics of clathrin-mediated endocytosis and its requirement for organelle biogenesis in Dictyostelium. *Journal of Cell Science*. [Online] 125

- (23), 5721–5732.
- Makaraci, P. & Kim, K. (2018) trans-Golgi network-bound cargo traffic. *European Journal of Cell Biology* 97 (3), 137–149.
- Mali, S. (2013) Delivery systems for gene therapy. *Indian Journal of Human Genetics* 19 (1), 3–8.
- Mamelak, A. N. & Jacoby, D. B. (2007) Targeted delivery of antitumoral therapy to glioma and other malignancies with synthetic chlorotoxin (TM-601). *Expert Opinion on Drug Delivery*. [Online] 4 (2), 175–186.
- Mamo, T. et al. (2010) Emerging nanotechnology approaches for HIV/AIDS treatment and prevention. *Nanomedicine* 5 (2), 269–285.
- Man, Y. G. et al. (2013) Tumor-infiltrating immune cells promoting tumor invasion and metastasis: Existing theories. *Journal of Cancer* 4 (1), 84–95.
- Mangematin, V. & Walsh, S. (2012) The future of nanotechnologies. *Technovation*. [Online] 32 (3–4), 157–160.
- Mantovani, A. et al. (2004) The chemokine system in diverse forms of macrophage activation and polarization. *Trends in Immunology* 25 (12), 677–686.
- Manuel, M. et al. (2012) Lymphopenia combined with low TCR diversity (divpenia) predicts poor overall survival in metastatic breast cancer patients. *OncolImmunology*. [Online] 1 (4), 432–440.
- Marina, N. M. et al. (2016) Comparison of MAPIE versus MAP in patients with a poor response to preoperative chemotherapy for newly diagnosed high-grade osteosarcoma (EURAMOS-1): an open-label, international, randomised controlled trial. *The Lancet Oncology*. [Online] 17 (10), 1396–1408.
- Markiewicz, K. et al. (2012) [Evaluation of selected parameters of cellular immunity in children with osteosarcoma at diagnosis]. *Medycyna wieku rozwojowego*. 16 (3),

212–221.

Marshall, J. S. et al. (2018) An introduction to immunology and immunopathology.

Allergy, Asthma and Clinical Immunology 14 (2), 49.

Martin, J. W. et al. (2012) The genetics of osteosarcoma. *Sarcoma* 2012, 627254.

Martin, S. A. et al. (2010) Genomic instability and the selection of treatments for cancer. *Journal of Pathology* 220 (2), 281–289.

Masood, S. (2016) Neoadjuvant chemotherapy in breast cancers. *Women's Health* 12 (5), 480–491.

Mathur, S. & Dinakarbandian, D. (2012) Finding disease similarity based on implicit semantic similarity. *Journal of Biomedical Informatics*. [Online] 45 (2), 363–371.

De Matteis, V. (2017) Exposure to inorganic nanoparticles: Routes of entry, immune response, biodistribution and in vitro/In vivo toxicity evaluation. *Toxics* 5 (4), 29.

Mayor, S. & Pagano, R. E. (2007) Pathways of clathrin-independent endocytosis. *Nature Reviews Molecular Cell Biology* 8 (8), 603–612.

Mbeh, D. A. et al. (2015) Human alveolar epithelial cell responses to core-shell superparamagnetic iron oxide nanoparticles (spions). *Langmuir*. [Online] 31 (13), 3829–3839.

McCarthy, R. R. et al. (2017) 'Contribution of cyclic di-GMP in the control of type III and type VI secretion in *Pseudomonas aeruginosa*', in *Methods in Molecular Biology*. [Online] 1657, 213–224.

McMaster, J. H. et al. (1975) The host immune response in human osteosarcoma. *Clinical Orthopaedics and Related Research*. [Online] 111, 76–82.

Meazza, C. & Scanagatta, P. (2016) Metastatic osteosarcoma: a challenging multidisciplinary treatment. *Expert Review of Anticancer Therapy* 16 (5), 543–556.

- Mei, M. G. et al. (2022) Response-adapted anti-PD-1–based salvage therapy for Hodgkin lymphoma with nivolumab alone or in combination with ICE. *Blood*. [Online] 139 (25), 3605-3616.
- Menezes, P. dos P. et al. (2019) Advances of nanosystems containing cyclodextrins and their applications in pharmaceuticals. *International Journal of Pharmaceutics* 559, 312–328.
- Meng, L. et al. (2013) Short multiwall carbon nanotubes promote neuronal differentiation of PC12 cells via Up-regulation of the neurotrophin signaling pathway. *Small*. [Online] 9 (9–10), 1786–1798.
- Metsalu, T. & Vilo, J. (2015) ClustVis: A web tool for visualizing clustering of multivariate data using Principal Component Analysis and heatmap. *Nucleic Acids Research*. [Online] 43 (W1), W566–W570.
- Meyers, P. A. et al. (2008) Osteosarcoma: The addition of muramyl tripeptide to chemotherapy improves overall survival - A report from the children's oncology group. *Journal of Clinical Oncology*. [Online] 26 (4), 633–638.
- Meyers, P. A. & Chou, A. J. (2014) Muramyl tripeptide-phosphatidyl ethanolamine encapsulated in liposomes (L-MTP-PE) in the treatment of osteosarcoma. *Advances in Experimental Medicine and Biology*. [Online] 804, 307–321.
- Mialou, V. et al. (2005) Metastatic osteosarcoma at diagnosis: Prognostic factors and long-term outcome - The French pediatric experience. *Cancer* 104(5), 1100-9.
- Migeotte, I. et al. (2005) Identification and characterization of an endogenous chemotactic ligand specific for FPRL2. *Journal of Experimental Medicine*. [Online] 201 (1), 83–93.
- Mihm, M. C. et al. (1996) Tumor infiltrating lymphocytes in lymph node melanoma metastases: A histopathologic prognostic indicator and an expression of local

- immune response. *Laboratory Investigation*. 74 (1), 43–47.
- Mikulak, E. et al. (2018) *Galleria mellonella* L. as model organism used in biomedical and other studies. *Przegląd epidemiologiczny* 72 (1), 57–73.
- Mirabello, L. et al. (2011) Height at diagnosis and birth-weight as risk factors for osteosarcoma. *Cancer Causes and Control*. [Online] 22 (6), 899–908.
- Mirabello, L. et al. (2009a) International osteosarcoma incidence patterns in children and adolescents, middle ages and elderly persons. *International Journal of Cancer*. [Online] 125 (1), 229–234.
- Mirabello, L. et al. (2009b) Osteosarcoma incidence and survival rates from 1973 to 2004: Data from the surveillance, epidemiology, and end results program. *Cancer*. [Online] 115 (7), 1531–1543.
- Misaghi, A. et al. (2018) Osteosarcoma: A comprehensive review. *Sicot-J*. [Online] 4.
- Mitchell, M. J. et al. (2021) Engineering precision nanoparticles for drug delivery. *Nature Reviews Drug Discovery* 20 (2), 101–124.
- Miwa, S. et al. (2019) Current and Emerging Targets in Immunotherapy for Osteosarcoma. *Journal of Oncology* 2019, 7035045.
- Miwa, S. et al. (2017) Current status of immunotherapy for sarcomas. *Immunotherapy*. [Online] 9 (16), 1331–1338.
- Miyata, S. et al. (2003) Use of the *Galleria mellonella* caterpillar as a model host to study the role of the type III secretion system in *Pseudomonas aeruginosa* pathogenesis. *Infection and Immunity*. [Online] 71 (5), 2404–2413.
- Mogensen, T. H. (2009) Pathogen recognition and inflammatory signaling in innate immune defenses. *Clinical Microbiology Reviews* 22 (2), 240–273.
- Mohammadpour, R. & Ghandehari, H. (2022) Mechanisms of immune response to inorganic nanoparticles and their degradation products. *Advanced Drug Delivery*

Reviews 180.

- Mondal, S. et al. (2017) Hydroxyapatite coated iron oxide nanoparticles: A promising nanomaterial for magnetic hyperthermia cancer treatment. *Nanomaterials*. [Online] 7 (12), 426.
- Montazerolghaem, M. et al. (2015) Zebrafish: A possible tool to evaluate bioactive ions. *Acta Biomaterialia*. [Online] 19, 10–14.
- Moore, A. et al. (2000) Tumoral distribution of long-circulating dextran-coated iron oxide nanoparticles in a rodent model. *Radiology*. [Online] 214 (2), 568–574.
- Moore, D. D. & Luu, H. H. (2014) Osteosarcoma. *Cancer Treatment and Research*. [Online] 162, 65–92.
- Morand, J. N. & Kent, C. (1986) A one-step technique for the subcellular fractionation of total cell homogenates. *Analytical Biochemistry*. [Online] 159 (1), 157–162.
- Morgan, R. A. et al. (2003) High Efficiency TCR Gene Transfer into Primary Human Lymphocytes Affords Avid Recognition of Melanoma Tumor Antigen Glycoprotein 100 and Does Not Alter the Recognition of Autologous Melanoma Antigens. *The Journal of Immunology*. [Online] 171 (6), 3287–3295.
- Morrow, J. J. & Khanna, C. (2015) Osteosarcoma genetics and epigenetics: Emerging biology and candidate therapies. *Critical Reviews in Oncogenesis*. [Online] 20 (3–4), 173–197.
- Mosquera, J. et al. (2018) Cellular Uptake of Nanoparticles versus Small Molecules: A Matter of Size. *Accounts of Chemical Research*. [Online] 51 (9), 2305–2313.
- Mout, R. et al. (2012) Surface functionalization of nanoparticles for nanomedicine. *Chemical Society Reviews*. [Online] 41 (7), 2539–2544.
- Moya-Andérico, L. et al. (2021) Utility of *Galleria mellonella* larvae for evaluating nanoparticle toxicology. *Chemosphere*. [Online] 266, 129235.

- Mudshinge, S. R. et al. (2011) Nanoparticles: Emerging carriers for drug delivery. *Saudi Pharmaceutical Journal* 19 (3), 129–141.
- Mukherjee, S. G. et al. (2012) Comparative in vitro cytotoxicity study of silver nanoparticle on two mammalian cell lines. *Toxicology in Vitro*. [Online] 26 (2), 238–251.
- Murgai, M. et al. (2015) Physiological, tumor, and metastatic niches: Opportunities and challenges for targeting the tumor microenvironment. *Critical Reviews in Oncogenesis*. [Online] 20 (3–4), 301–314.
- Musselman, J. R. B. et al. (2012) Case-parent analysis of variation in pubertal hormone genes and pediatric osteosarcoma: A children's oncology group (COG) study. *International Journal of Molecular Epidemiology and Genetics*. 3 (4), 286–293.
- Nagarajan, R. et al. (2011) Twenty years of follow-up of survivors of childhood osteosarcoma. *Cancer*. [Online] 117 (3), 625–634.
- Nagasaka, M. & Ou, S. H. I. (2022) NRG1 and NRG2 fusion positive solid tumor malignancies: a paradigm of ligand-fusion oncogenesis. *Trends in Cancer* 8 (3), 242–258.
- Nagy, Á. et al. (2021) Pancancer survival analysis of cancer hallmark genes. *Scientific Reports*. [Online] 11 (1), 6047.
- Naqvi, S. et al. (2010) Concentration-dependent toxicity of iron oxide nanoparticles mediated by increased oxidative stress. *International Journal of Nanomedicine* 5 (1), 983–989.
- Natarajan, S. et al. (2019) Multifunctional magnetic iron oxide nanoparticles: diverse synthetic approaches, surface modifications, cytotoxicity towards biomedical and industrial applications. *BMC Materials*. [Online] 1 (1).

- Nawaz, M. I. et al. (2020) d-Peptide analogues of Boc-Phe-Leu-Phe-Leu-Phe-COOH induce neovascularization via endothelial N-formyl peptide receptor 3. *Angiogenesis*. [Online] 23 (3), 357–369.
- Nel, A. et al. (2006) Toxic potential of materials at the nanolevel. *Science* 311 (5761), 622–627.
- Neophytou, C. M. et al. (2021) The role of tumor microenvironment in cancer metastasis: Molecular mechanisms and therapeutic opportunities. *Cancers* 13 (9), 2053.
- Neuberger, T. et al. (2005) ‘Superparamagnetic nanoparticles for biomedical applications: Possibilities and limitations of a new drug delivery system’, in *Journal of Magnetism and Magnetic Materials*. [Online] 293 (1), 483–496.
- Ngobili, T. A. & Daniele, M. A. (2016) Nanoparticles and direct immunosuppression. *Experimental Biology and Medicine* 241 (10), 1064–1073.
- Nie, Z. & Peng, H. (2018) Osteosarcoma in patients below 25 years of age: An observational study of incidence, metastasis, treatment and outcomes. *Oncology Letters*. [Online] 16 (5), 6502–6514.
- Nikalje, A. P. (2015) Nanotechnology and its Applications in Medicine. *Medicinal Chemistry*. [Online] 5 (2), 081-089.
- Nishikawa, H. & Sakaguchi, S. (2014) Regulatory T cells in cancer immunotherapy. *Current Opinion in Immunology* 27 (1), 1–7.
- Noy, R. & Pollard, J. W. (2014) Tumor-Associated Macrophages: From Mechanisms to Therapy. *Immunity* 41 (1), 49–61.
- Oh, N. & Park, J. H. (2014) Endocytosis and exocytosis of nanoparticles in mammalian cells. *International Journal of Nanomedicine* 9 (1), 51–63.
- Ong, C. et al. (2015) *Drosophila melanogaster* as a model organism to study

- nanotoxicity. *Nanotoxicology* 9 (3), 396–403.
- Ordóñez-Morán, P. & Huelsken, J. (2014) Complex metastatic niches: Already a target for therapy? *Current Opinion in Cell Biology* 31 (1), 29–38.
- Otoukesh, B. et al. (2018) Novel molecular insights and new therapeutic strategies in osteosarcoma. *Cancer Cell International*. [Online] 18 (1).
- Ottaviani, G. & Jaffe, N. (2009) ‘The epidemiology of osteosarcoma’, in *Cancer Treatment and Research*. [Online]. 2009 pp. 3–13.
- Pagès, F. et al. (2010) Immune infiltration in human tumors: A prognostic factor that should not be ignored. *Oncogene* 29 (8) p.1093–1102.
- Pahl, J. H. et al. (2014) Macrophages inhibit human osteosarcoma cell growth after activation with the bacterial cell wall derivative liposomal muramyl tripeptide in combination with interferon- γ . *Journal of Experimental and Clinical Cancer Research*. [Online] 33 (1), 27.
- Paillard, A. et al. (2010) The importance of endo-lysosomal escape with lipid nanocapsules for drug subcellular bioavailability. *Biomaterials*. [Online] 31 (29), 7542–7554.
- Pantarotto, D. et al. (2003) Immunization with peptide-functionalized carbon nanotubes enhances virus-specific neutralizing antibody responses. *Chemistry and Biology*. [Online] 10 (10), 961–966.
- Paoloni, M. et al. (2009) Canine tumor cross-species genomics uncovers targets linked to osteosarcoma progression. *BMC genomics*. [Online] 10:625.
- Papatestas, A. E. et al. (1976) The prognostic significance of peripheral lymphocyte counts in patients with breast carcinoma. *Cancer*. [Online] 37 (1), 164–168.
- Parkin, J. & Cohen, B. (2001) An overview of the immune system. *Lancet* 357 (9270) p.1777–1789.

- Parton, R. G. & Del Pozo, M. A. (2013) Caveolae as plasma membrane sensors, protectors and organizers. *Nature Reviews Molecular Cell Biology*. [Online] 14 (2), 98–112.
- Parton, R. G. & Simons, K. (2007) The multiple faces of caveolae. *Nature Reviews Molecular Cell Biology* 8 (3) p.185–194.
- Passos, J. S. et al. (2020) Development, skin targeting and antifungal efficacy of topical lipid nanoparticles containing itraconazole. *European Journal of Pharmaceutical Sciences*. [Online] 149:105296.
- Patlolla, A. K. et al. (2015) Silver nanoparticle-induced oxidative stress-dependent toxicity in Sprague-Dawley rats. *Molecular and Cellular Biochemistry*. [Online] 399 (1–2), 257–268.
- Patra, J. K. et al. (2018) Nano based drug delivery systems: Recent developments and future prospects. *Journal of Nanobiotechnology*. [Online] 16 (1), 71.
- Pautke, C. et al. (2004) Characterization of osteosarcoma cell lines MG-63, Saos-2 and U-2 OS in comparison to human osteoblasts. *Anticancer Research*. 24 (6), 3743–3748.
- Pei, D. & Buyanova, M. (2019) Overcoming Endosomal Entrapment in Drug Delivery. *Bioconjugate Chemistry* 30 (2) p.273–283.
- Peng, H. et al. (2016) The Tumour Response to Induction Chemotherapy has Prognostic Value for Long-Term Survival Outcomes after Intensity-Modulated Radiation Therapy in Nasopharyngeal Carcinoma. *Scientific Reports*. [Online] 6, 24835.
- Perdoni, F. et al. (2014) A histological procedure to study fungal infection in the wax moth *Galleria mellonella*. *European Journal of Histochemistry*. [Online] 58 (3), 258–262.

- Pereira-Silva, M. et al. (2020) Nanomedicine in osteosarcoma therapy: Micelleplexes for delivery of nucleic acids and drugs toward osteosarcoma-targeted therapies. *European Journal of Pharmaceutics and Biopharmaceutics*. [Online] 148, 88-106.
- Peterson, R. T. et al. (2008) Use of non-mammalian alternative models for neurotoxicological study. *NeuroToxicology*. [Online] 29 (3), 546–555.
- Petros, R. A. & Desimone, J. M. (2010) Strategies in the design of nanoparticles for therapeutic applications. *Nature Reviews Drug Discovery*. 9 (8) p.615–627.
- Piatek, M. et al. (2021) *Galleria mellonella*: The versatile host for drug discovery, in vivo toxicity testing and characterising host-pathogen interactions. *Antibiotics*. 10 (12).
- Picci, P. (2007) Osteosarcoma (Osteogenic sarcoma). *Orphanet Journal of Rare Diseases* 2, (6).
- Pilarsky, C. et al. (2004) Identification and validation of commonly overexpressed genes in solid tumors by comparison of microarray data. *Neoplasia*. [Online] 6 (6), 744–750.
- Pirooznia, M. et al. (2007) GeneVenn - A web application for comparing gene lists using Venn diagrams. *Bioinformatics*. [Online] 1 (10), 420–422.
- Plaks, V. et al. (2015) The cancer stem cell niche: How essential is the niche in regulating stemness of tumor cells? *Cell Stem Cell* 16 (3) p.225–238.
- Poljsak, B. et al. (2013) Achieving the balance between ROS and antioxidants: When to use the synthetic antioxidants. *Oxidative Medicine and Cellular Longevity*. 2013:956792.
- Pondman, K. M. et al. (2017) Pulmonary surfactant protein SP-D opsonises carbon nanotubes and augments their phagocytosis and subsequent pro-inflammatory immune response. *Nanoscale*. [Online] 9 (3), 1097–1109.

- Popescu, R. C. et al. (2017) Fabrication and cytotoxicity of gemcitabine-functionalized magnetite nanoparticles. *Molecules*. [Online] 22 (7), 1080.
- Popescu, T. et al. (2020) Influence of surfactant-tailored Mn-doped ZnO nanoparticles on ROS production and DNA damage induced in murine fibroblast cells. *Scientific Reports*. [Online] 10 (1), 18062.
- Popova, N. V. et al. (2013) Clathrin-mediated endocytosis and adaptor proteins. *Acta Naturae* 5 (18) p.62–73.
- Prasad, S. R. et al. (2021) Nanocarrier-based drug delivery systems for bone cancer therapy: A review. *Biomedical Materials (Bristol)*. [Online] 16 (4).
- Prevete, N. et al. (2015) The formyl peptide receptor 1 exerts a tumor suppressor function in human gastric cancer by inhibiting angiogenesis. *Oncogene*. [Online] 34 (29), 3826–3838.
- Price, P. M. et al. (2018) Magnetic drug delivery: Where the field is going. *Frontiers in Chemistry*. [Online] 6, 619.
- Pridgen, E. M. et al. (2015) Polymeric nanoparticle drug delivery technologies for oral delivery applications. *Expert Opinion on Drug Delivery*. 12 (9) p.1459–1473.
- Prior, H. et al. (2021) Justification for species selection for pharmaceutical toxicity studies. *Toxicology Research*. [Online] 9 (6), 758–770.
- Pruneri, G. et al. (2018) Tumor infiltrating lymphocytes in early breast cancer. *Breast*. [Online] 37207–214.
- Qi, J. et al. (2021) Identification of FPR3 as a Unique Biomarker for Targeted Therapy in the Immune Microenvironment of Breast Cancer. *Frontiers in Pharmacology*. [Online] 11, 593247.
- Qin, M. et al. (2020) Proteomic analysis of intracellular protein corona of nanoparticles elucidates nano-trafficking network and nano-bio interactions. *Theranostics*.

- [Online] 10 (3), 1213–1229.
- Qiu, Y. et al. (2010) Surface chemistry and aspect ratio mediated cellular uptake of Au nanorods. *Biomaterials*. [Online] 31 (30), 7606–7619.
- Quatromoni, J. G. & Eruslanov, E. (2012) Tumor-associated macrophages: Function, phenotype, and link to prognosis in human lung cancer. *American Journal of Translational Research*. [Online] 4 (4), 376-389.
- Rabiet, M. J. et al. (2011) N-formyl peptide receptor 3 (FPR3) departs from the homologous FPR2/ALX receptor with regard to the major processes governing chemoattractant receptor regulation, expression at the cell surface, and phosphorylation. *Journal of Biological Chemistry*. [Online] 286 (30), 26718–26731.
- Rajoria, S. et al. (2019) Glycine-Poly-L-Lactic Acid Copolymeric Nanoparticles for the Efficient Delivery of Bortezomib. *Pharmaceutical Research*. [Online] 36 (11), 160.
- Ramarao, N. et al. (2012) The insect *Galleria mellonella* as a powerful infection model to investigate bacterial pathogenesis. *Journal of visualized experiments : JoVE*. [Online] (70), e4392.
- Ray, P. C. et al. (2009) Toxicity and environmental risks of nanomaterials: Challenges and future needs. *Journal of Environmental Science and Health - Part C Environmental Carcinogenesis and Ecotoxicology Reviews* 27 (1) p.1–35.
- Reifarth, M. et al. (2018) Uptake and Intracellular Fate of Engineered Nanoparticles in Mammalian Cells: Capabilities and Limitations of Transmission Electron Microscopy—Polymer-Based Nanoparticles. *Advanced Materials*. 30 (9).
- Reiner, A. et al. (2003) Identifying differentially expressed genes using false discovery rate controlling procedures. *Bioinformatics*. [Online] 19 (3), 368–375.
- Ribeiro, M. J. et al. (2015) Oxidative stress mechanisms caused by Ag nanoparticles

- (NM300K) are different from those of AgNO₃: Effects in the soil invertebrate *Enchytraeus Crypticus*. *International Journal of Environmental Research and Public Health*. [Online] 12 (8), 9589–9602.
- Riccio, E. K. et al. (2015) Molecular and immunological tools for the evaluation of the cellular immune response in the neotropical monkey *Saimiri sciureus*, a non-human primate model for malaria research. *Malaria Journal*. [Online] 14 (1), 1–17.
- Rickel, K. et al. (2017) Molecular genetics of osteosarcoma. *Bone*. [Online] 10269–79.
- des Rieux, A. et al. (2006) Nanoparticles as potential oral delivery systems of proteins and vaccines: A mechanistic approach. *Journal of Controlled Release* 116 (1) p.1–27.
- Riley, M. K. & Vermerris, W. (2017) Recent advances in nanomaterials for gene delivery—A review. *Nanomaterials*. 7 (5), 94.
- Riley, R. S. & Day, E. S. (2017) Gold nanoparticle-mediated photothermal therapy: applications and opportunities for multimodal cancer treatment. *Wiley Interdisciplinary Reviews: Nanomedicine and Nanobiotechnology* 9 (4): 10.1002/wnan.1449.
- Rivolta, I. et al. (2011) Cellular uptake of coumarin-6 as a model drug loaded in solid lipid nanoparticles. *Journal of Physiology and Pharmacology*. 62 (1), 45–53.
- Rizvi, S. A. A. & Saleh, A. M. (2018) Applications of nanoparticle systems in drug delivery technology. *Saudi Pharmaceutical Journal* 26 (1) p.64–70.
- Rizzo, L. Y. et al. (2013) Recent progress in nanomedicine: Therapeutic, diagnostic and theranostic applications. *Current Opinion in Biotechnology* 24 (6) p.1159–1166.
- Robbins, P. F. et al. (2015) A pilot trial using lymphocytes genetically engineered with

- an NY-ESO-1-reactive T-cell receptor: Long-term follow-up and correlates with response. *Clinical Cancer Research*. [Online] 21(5), 1019-27.
- Robbins, P. F. et al. (2011) Tumor regression in patients with metastatic synovial cell sarcoma and melanoma using genetically engineered lymphocytes reactive with NY-ESO-1. *Journal of Clinical Oncology*. [Online] 29 (7), 917–924.
- Rodrigues, J. et al. (2022) Osteosarcoma tumor microenvironment: the key for the successful development of biologically relevant 3D in vitro models. *In vitro models*. [Online] 1 (1), 5–27.
- von Roemeling, C. et al. (2017) Breaking Down the Barriers to Precision Cancer Nanomedicine. *Trends in Biotechnology* 35 (2) p.159–171.
- Rofe, A. P. & Pryor, P. R. (2016) Purification of lysosomes using supraparamagnetic iron oxide nanoparticles (SPIONs). *Cold Spring Harbor Protocols*. [Online] 2016 (4), 338–342.
- Rogach, A. L. & Ogris, M. (2010) Near-infrared-emitting semiconductor quantum dots for tumor imaging and targeting. *Current Opinion in Molecular Therapeutics* 12 (3) p.331–339.
- Roh, J. Y. et al. (2009) Ecotoxicity of silver nanoparticles on the soil nematode *Caenorhabditis elegans* using functional ecotoxicogenomics. *Environmental Science and Technology*. [Online] 43 (10), 3933-40.
- Rosenberg, S. A. (2001) Progress in human tumour immunology and immunotherapy. *Nature* 411 (6835) p.380–384.
- Rosenblum, D. et al. (2018) Progress and challenges towards targeted delivery of cancer therapeutics. *Nature Communications* 9 (1), 1410.
- Rosenthal, N. & Brown, S. (2007) The mouse ascending: Perspectives for human-disease models. *Nature Cell Biology*. [Online] 9 (9), 993–999.

- Rudge, S. et al. (2001) Adsorption and desorption of chemotherapeutic drugs from a magnetically targeted carrier (MTC). *Journal of Controlled Release*. [Online] 74 (1–3), 335–340.
- Rytlewski, J. et al. (2021) Turning ‘Cold’ tumors ‘Hot’: immunotherapies in sarcoma. *Annals of Translational Medicine*. [Online] 9 (12), 1039–1039.
- Sadauskas, E. et al. (2007) Kupffer cells are central in the removal of nanoparticles from the organism. *Particle and Fibre Toxicology*. [Online] 4, 10.
- Sadikovic, B. et al. (2009) Identification of interactive networks of gene expression associated with osteosarcoma oncogenesis by integrated molecular profiling. *Human Molecular Genetics*. [Online] 18 (11), 1962–1975.
- Saha, R. N. et al. (2010) Nanoparticulate drug delivery systems for cancer chemotherapy. *Molecular Membrane Biology* 27 (7) p.215–231.
- Sahay, G. et al. (2010) Endocytosis of nanomedicines. *Journal of Controlled Release* 145 (3) p.182–195.
- Saheki, Y. & De Camilli, P. (2012) Synaptic vesicle endocytosis. *Cold Spring Harbor Perspectives in Biology*. [Online] 4 (9), a005645.
- Saini, R. et al. (2010) Nanotechnology: The future medicine. *Journal of Cutaneous and Aesthetic Surgery*. [Online] 3 (1), 32.
- Sakamoto, A. & Iwamoto, Y. (2008) Current Status and Perspectives Regarding the Treatment of Osteosarcoma: Chemotherapy. *Reviews on Recent Clinical Trials*. [Online] 3 (3), 228–231.
- Sakhtianchi, R. et al. (2013) Exocytosis of nanoparticles from cells: Role in cellular retention and toxicity. *Advances in Colloid and Interface Science* 201–202 p.18–29.
- SALAH, S. et al. (2014) Osteosarcoma with metastasis at initial diagnosis: Current

- outcomes and prognostic factors in the context of a comprehensive cancer center. *Molecular and Clinical Oncology*. [Online] 2 (5), 811–816.
- Samadian, H. et al. (2016) Folate-conjugated gold nanoparticle as a new nanoplatform for targeted cancer therapy. *Journal of Cancer Research and Clinical Oncology* 142 (11) p.2217–2229.
- Samardziski, M. et al. (2009) Parosteal osteosarcoma. *Bratislava Medical Journal*. [Online] 110 (4), 240–244.
- Sandvig, K. et al. (2008) Clathrin-independent endocytosis: From nonexisting to an extreme degree of complexity. *Histochemistry and Cell Biology* 129 (3) p.267–276.
- Sarkans, U. et al. (2021) From ArrayExpress to BioStudies. *Nucleic Acids Research*. [Online] 49(D1):D1502-D1506.
- Sarkar, M. et al. (2006) Flow-cytometric analysis of reactive oxygen species in peripheral blood mononuclear cells of patients with thyroid dysfunction. *Cytometry Part B - Clinical Cytometry*. [Online] 70 (1), 20–23.
- Savage, D. T. et al. (2019) 'In vitro methods for assessing nanoparticle toxicity', in *Methods in Molecular Biology*. [Online]. pp. 1–29.
- Savvidou, O. D. et al. (2016) Applied nanotechnology and nanoscience in orthopedic oncology. *Orthopedics*. [Online] 39 (5), 280–286.
- Schroit, A. J. & Fidler, I. J. (1982) Effects of Liposome Structure and Lipid Composition on the Activation of the Tumoricidal Properties of Macrophages by Liposomes Containing Muramyl Dipeptide. *Cancer Research*. 42 (1), 161–167.
- Schultz, K. T. & Grieder, F. (1987) Structure and Function of the Immune System. *Toxicologic Pathology*. [Online] 15 (3), 262–264.
- Schwinger, W. et al. (2005) Feasibility of high-dose interleukin-2 in heavily pretreated

- pediatric cancer patients. *Annals of Oncology*. [Online] 16 (7), 1199–1206.
- Scorzoni, L. et al. (2015) Comparison of virulence between *Paracoccidioides brasiliensis* and *Paracoccidioides lutzii* using *Galleria mellonella* as a host model. *Virulence*. [Online] 6 (8), 766–776.
- Ségaly, A. I. et al. (2015) Interleukin-34 promotes tumor progression and metastatic process in osteosarcoma through induction of angiogenesis and macrophage recruitment. *International Journal of Cancer*. [Online] 137 (1), 73–85.
- Semmler-Behnke, M. et al. (2008) Biodistribution of 1.4- and 18-nm gold particles in rats. *Small*. [Online] 4 (12), 2108–2111.
- Sena, L. A. & Chandel, N. S. (2012) Physiological roles of mitochondrial reactive oxygen species. *Molecular Cell*. 48 (2) p.158–167.
- Senut, M. C. et al. (2016) Size-Dependent Toxicity of Gold Nanoparticles on Human Embryonic Stem Cells and Their Neural Derivatives. *Small*. [Online] 12 (5), 631–646.
- Serpooshan, V. et al. (2013) Hydraulic permeability of multilayered collagen gel scaffolds under plastic compression-induced unidirectional fluid flow. *Acta Biomaterialia*. [Online] 9 (1), 4673-4680.
- Sezer, B. & Ozalp, P. (2015) Effects of pyriproxyfen on hemocyte count and morphology of *Galleria mellonella*. *Fresenius Environmental Bulletin*. 24 (2A), 621–625.
- Shadel, G. S. & Horvath, T. L. (2015) Mitochondrial ROS Signaling in Organismal Homeostasis. *Cell* 163 (3) p.560–569.
- Shah, A. & Dobrovolskaia, M. A. (2018) Immunological effects of iron oxide nanoparticles and iron-based complex drug formulations: Therapeutic benefits, toxicity, mechanistic insights, and translational considerations. *Nanomedicine*:

- Nanotechnology, Biology, and Medicine 14 (3) p.977–990.
- Shang, L. et al. (2014) Engineered nanoparticles interacting with cells: Size matters. *Journal of Nanobiotechnology*. 12 (5).
- Sharma, A. et al. (2012) Toxicological considerations when creating nanoparticle-based drugs and drug delivery systems. *Expert Opinion on Drug Metabolism and Toxicology* 8 (1) p.47–69.
- Sharma, P. K. et al. (2021) 'Nanotechnology and its application: a review', in *Nanotechnology in Cancer Management*. [Online]. pp. 1–33.
- Sheehan, G. et al. (2018) Characterisation of the cellular and proteomic response of *Galleria mellonella* larvae to the development of invasive aspergillosis. *BMC Microbiology*. [Online] 18 (1), 63.
- Sheehan, G. et al. (2019) Utilization of *Galleria mellonella* larvae to characterize the development of *Staphylococcus aureus* infection. *Microbiology (United Kingdom)*. [Online] 165(8):863-875.
- Shekhova, E. (2020) Mitochondrial reactive oxygen species as major effectors of antimicrobial immunity. *PLoS Pathogens*. [Online] 16(5): e1008470.
- Sheng, G. et al. (2021) Osteosarcoma and Metastasis. *Frontiers in Oncology* 11.
- Sherman, B. T. et al. (2022) DAVID: a web server for functional enrichment analysis and functional annotation of gene lists (2021 update). *Nucleic Acids Research*. [Online] 50 (W1), W216–W221. [online]. Available from: <https://doi.org/10.1093/nar/gkac194>.
- Shi, J. et al. (2017) Cancer nanomedicine: Progress, challenges and opportunities. *Nature Reviews Cancer* 17 (1) p.20–37.
- Shrivastava, R. et al. (2016) Oxidative stress following exposure to silver and gold nanoparticles in mice. *Toxicology and Industrial Health*. [Online] 32 (8), 1391–

1404.

- Shukla, R. et al. (2005) Biocompatibility of gold nanoparticles and their endocytotic fate inside the cellular compartment: A microscopic overview. *Langmuir* 21 (23) p.10644–10654.
- Siddiqui, A. S. et al. (2006) Sequence biases in large scale gene expression profiling data. *Nucleic Acids Research*. [Online] 34(12):e83.
- Siegel, R. L. et al. (2021) Cancer Statistics, 2021. *CA: A Cancer Journal for Clinicians*. [Online] 71 (1), 7–33.
- Simon-Deckers, A. et al. (2008) In vitro investigation of oxide nanoparticle and carbon nanotube toxicity and intracellular accumulation in A549 human pneumocytes. *Toxicology*. [Online] 253 (1–3), 137–146.
- Simpson, E. & Brown, H. L. (2018) Understanding osteosarcomas. *Journal of the American Academy of Physician Assistants*. [Online] 31 (8), 15–19.
- Singh, P. et al. (2018) Gold nanoparticles in diagnostics and therapeutics for human cancer. *International Journal of Molecular Sciences* 19 (7), 1979.
- Skubitz, K. M. (2003) 'Phase II trial of pegylated-liposomal doxorubicin (Doxil™) in sarcoma', in *Cancer Investigation*. [Online]. 2003 pp. 167–176.
- Smeester, B. A. et al. (2020) SEMA4C is a novel target to limit osteosarcoma growth, progression, and metastasis. *Oncogene*. [Online] 39 (5), 1049–1062.
- Smith, D. F. Q. & Casadevall, A. (2021) Fungal immunity and pathogenesis in mammals versus the invertebrate model organism *Galleria mellonella*. *Pathogens and Disease* 79(3):ftab013.
- Smith, S. A. et al. (2019) The Endosomal Escape of Nanoparticles: Toward More Efficient Cellular Delivery. *Bioconjugate Chemistry* 30 (2) p.263–272.
- Snyder, P. W. (2017) 'Diseases of Immunity', in *Pathologic Basis of Veterinary*

- Disease Expert Consult*. [Online]. pp. 242-285.e5.
- Soares, S. et al. (2018) Nanomedicine: Principles, properties, and regulatory issues. *Frontiers in Chemistry* 6 (AUG). 6: 360.
- Sohaebuddin, S. K. et al. (2010) Nanomaterial cytotoxicity is composition, size, and cell type dependent. *Particle and Fibre Toxicology*. [Online] 7, 22.
- Soleymaniha, M. et al. (2019) Promoting Role of MXene Nanosheets in Biomedical Sciences: Therapeutic and Biosensing Innovations. *Advanced Healthcare Materials*. 8 (1), 1801137.
- Sonavane, G. et al. (2008) Biodistribution of colloidal gold nanoparticles after intravenous administration: Effect of particle size. *Colloids and Surfaces B: Biointerfaces*. [Online] 66 (2), 274–280.
- Song, M. F. et al. (2012) Metal nanoparticle-induced micronuclei and oxidative DNA damage in mice. *Journal of Clinical Biochemistry and Nutrition*. [Online] 50 (3), 211–216.
- Spadari, C. de C. et al. (2019) Alginate nanoparticles as non-toxic delivery system for miltefosine in the treatment of candidiasis and cryptococcosis. *International Journal of Nanomedicine*. [Online] 145187–5199.
- Spits, H. et al. (2013) Innate lymphoid cells—a proposal for uniform nomenclature. *Nature Reviews Immunology*. [Online] 13 (2), 145–149.
- Stączek, S. et al. (2020) Activation of cellular immune response in insect model host *Galleria mellonella* by fungal α -1,3-glucan. *Pathogens and Disease*. [Online] 78(9):ftaa062.
- Steckiewicz, K. P. et al. (2019) Impact of gold nanoparticles shape on their cytotoxicity against human osteoblast and osteosarcoma in in vitro model. Evaluation of the safety of use and anti-cancer potential. *Journal of Materials Science: Materials in*

- Medicine*. [Online] 30(2):22.
- Stempel, H. et al. (2016) Strain-specific loss of Formyl peptide receptor 3 in the murine vomeronasal and immune systems. *Journal of Biological Chemistry*. [Online] 291 (18), 9762–9775.
- Strander, H. & Einhorn, S. (1977) Effect of human leukocyte interferon on the growth of human osteosarcoma cells in tissue culture. *International Journal of Cancer*. [Online] 19 (4), 468–473.
- Su, H. et al. (2017) The biological function and significance of CD74 in immune diseases. *Inflammation Research*. 66 (3) p.209–216.
- Su, L. et al. (2005) Differential expression of CXCR4 is associated with the metastatic potential of human non-small cell lung cancer cells. *Clinical Cancer Research*. [Online] 11 (23), 8273–8280.
- Suarez-Arnedo, A. et al. (2020) An image J plugin for the high throughput image analysis of in vitro scratch wound healing assays. *PLoS ONE*. [Online] 15(7):e0232565.
- Sun, J. et al. (2019) Identification of key genes in osteosarcoma by meta-analysis of gene expression microarray. *Molecular Medicine Reports*. [Online] 20 (4), 3075–3084.
- Sun, L. et al. (2015) Gene expression profiling analysis of osteosarcoma cell lines. *Molecular Medicine Reports*. [Online] 12 (3), 4266–4272.
- Suryawanshi, A. & Manicassamy, S. (2015) Tumors induce immune tolerance through activation of β -catenin/TCF4 signaling in dendritic cells: A novel therapeutic target for cancer immunotherapy. *Oncotarget*. [Online] 4(12): e1052932.
- Susa, M. et al. (2009) Doxorubicin loaded polymeric nanoparticulate delivery system to overcome drug resistance in osteosarcoma. *BMC Cancer*. [Online] 16, 9:399.

- Swann, J. B. & Smyth, M. J. (2007) Immune surveillance of tumors. *Journal of Clinical Investigation*. [Online] 117(5):1137-46
- Szklarczyk, D. et al. (2021) The STRING database in 2021: Customizable protein-protein networks, and functional characterization of user-uploaded gene/measurement sets. *Nucleic Acids Research*. [Online] 49 (D1), D605–D612.
- Taciak, B. et al. (2018) Evaluation of phenotypic and functional stability of RAW 264.7 cell line through serial passages. *PLoS ONE*. [Online] 13(6):e0198943.
- Tang, Z. et al. (2017) GEPIA: A web server for cancer and normal gene expression profiling and interactive analyses. *Nucleic Acids Research*. [Online] 45 (W1), W98–W102.
- Tarca, A. L. et al. (2006) Analysis of microarray experiments of gene expression profiling. *American Journal of Obstetrics and Gynecology*. [Online] 195 (2), 373–388.
- Tarek, N. & Lee, D. A. (2014) Natural killer cells for osteosarcoma. *Advances in Experimental Medicine and Biology*. [Online] 804:341-53.
- Tarhini, A. A. & Kirkwood, J. M. (2012) How much of a good thing? What duration for interferon Alfa-2b adjuvant therapy? *Journal of Clinical Oncology*. 30 (31) p.3773–3776.
- Tas, F. & Erturk, K. (2017) Tumor Infiltrating Lymphocytes (TILs) May be Only an Independent Predictor of Nodal Involvement but not for Recurrence and Survival in Cutaneous Melanoma Patients. *Cancer Investigation*. [Online] 35 (8), 501–505.
- Tawbi, H. A. et al. (2017) Pembrolizumab in advanced soft-tissue sarcoma and bone sarcoma (SARC028): a multicentre, two-cohort, single-arm, open-label, phase 2 trial. *The Lancet Oncology*. [Online] 18 (11), 1493–1501.
- Thanh, N. T. K. & Green, L. A. W. (2010) Functionalisation of nanoparticles for

- biomedical applications. *Nano Today* 5 (3) p.213–230.
- Thayanithy, V. et al. (2012) Perturbation of 14q32 miRNAs-cMYC gene network in osteosarcoma. *Bone*. [Online] 50 (1), 171–181.
- Théoleyre, S. et al. (2005) Phenotypic and functional analysis of lymphocytes infiltrating osteolytic tumors: Use as a possible therapeutic approach of osteosarcoma. *BMC Cancer*. [Online] 5:123.
- Thomas, O. S. & Weber, W. (2019) Overcoming Physiological Barriers to Nanoparticle Delivery—Are We There Yet? *Frontiers in Bioengineering and Biotechnology*. 7: 415.
- Thomas, R. J. et al. (2013) *Galleria mellonella* as a model system to test the pharmacokinetics and efficacy of antibiotics against *Burkholderia pseudomallei*. *International Journal of Antimicrobial Agents*. [Online] 41 (4), 330–336.
- Thomaz, L. et al. (2020) In vivo Activity of Silver Nanoparticles Against *Pseudomonas aeruginosa* Infection in *Galleria mellonella*. *Frontiers in Microbiology*. [Online] 11.
- Thul, P. J. et al. (2017) A subcellular map of the human proteome. *Science*. [Online] 356 (6340).
- Tinkle, S. et al. (2014) Nanomedicines: Addressing the scientific and regulatory gap. *Annals of the New York Academy of Sciences*. [Online] 1313 (1), 35–56.
- Titball, R. W. & Senior, N. J. (2020) Isolation and primary culture of *Galleria mellonella* hemocytes for infection studies. *F1000Research*. [Online] 9:1392.
- Tiwari, G. et al. (2012) Drug delivery systems: An updated review. *International Journal of Pharmaceutical Investigation*. [Online] 2 (1), 2.
- Tomankova, K. et al. (2015) Cytotoxicity, cell uptake and microscopic analysis of titanium dioxide and silver nanoparticles in vitro. *Food and Chemical Toxicology*. [Online] 82:106–115.

- Traub, L. M. & Bonifacino, J. S. (2013) Cargo recognition in clathrin-mediated endocytosis. *Cold Spring Harbor Perspectives in Biology*. [Online] 5 (11).
- Trevijano-Contador, N. & Zaragoza, O. (2019) Immune response of *Galleria mellonella* against human fungal pathogens. *Journal of Fungi*. 5 (1).
- Tsai, C. J. Y. et al. (2016) *Galleria mellonella* infection models for the study of bacterial diseases and for antimicrobial drug testing. *Virulence* 7 (3) p.214–229.
- Tsukahara, T. et al. (2006) Prognostic significance of HLA class I expression in osteosarcoma defined by anti-pan HLA class I monoclonal antibody, EMR8-5. *Cancer Science*. [Online] 97 (12), 1374–1380.
- Tsuzuki, T. (2009) Commercial scale production of inorganic nanoparticles. *International Journal of Nanotechnology*. [Online] 6 (5–6), 567–578.
- Tuncsoy, B. & Mese, Y. (2021) Influence of titanium dioxide nanoparticles on bioaccumulation, antioxidant defense and immune system of *Galleria mellonella* L. *Environmental Science and Pollution Research*. [Online] 28 (28), 38007–38015.
- Tuncsoy, B. S. & Ozalp, P. (2017) Effects of copper oxide nanoparticles on hemocytes of *Galleria mellonella*. *Toxicology Letters*. [Online] 280S187.
- Tynga, I. M. & Abrahamse, H. (2018) Nano-mediated photodynamic therapy for cancer: Enhancement of cancer specificity and therapeutic effects. *Nanomaterials* 8 (11).
- Uhlén, M. et al. (2015) Tissue-based map of the human proteome. *Science*. [Online] 347 (6220).
- Vaishnavi, A. et al. (2013) Oncogenic and drug-sensitive NTRK1 rearrangements in lung cancer. *Nature Medicine*. [Online] 19 (11), 1469–1472.
- Valdiglesias, V. et al. (2016) Are iron oxide nanoparticles safe? Current knowledge

- and future perspectives. *Journal of Trace Elements in Medicine and Biology* 38 p.53–63.
- Varma, S. et al. (2021) Cellular Uptake Pathways of Nanoparticles: Process of Endocytosis and Factors Affecting their Fate. *Current Pharmaceutical Biotechnology*. [Online] 23 (5), 679–706.
- Veisheh, O. et al. (2011) Cancer Cell Invasion: Treatment and Monitoring Opportunities in Nanomedicine. *Advanced Drug Delivery Reviews* 63 (8) p.582–596.
- Veisheh, O. et al. (2009) Inhibition of tumor-cell invasion with chlorotoxin-bound superparamagnetic nanoparticles. *Small*. [Online] 5 (2), 256–264.
- Vera-González, N. et al. (2020) Anidulafungin liposome nanoparticles exhibit antifungal activity against planktonic and biofilm *Candida albicans*. *Journal of Biomedical Materials Research - Part A*. [Online] 108 (11), 2263–2276.
- Vertyporokh, L. & Wojda, I. (2020) Immune response of *Galleria mellonella* after injection with non-lethal and lethal dosages of *Candida albicans*. *Journal of Invertebrate Pathology*. [Online] 170.
- Villiers, C. L. et al. (2010) Analysis of the toxicity of gold nano particles on the immune system: Effect on dendritic cell functions. *Journal of Nanoparticle Research*. [Online] 12 (1), 55–60.
- Wadhwa, N. (2014) 'Osteosarcoma: Diagnostic dilemmas in histopathology and prognostic factors', in *Indian Journal of Orthopaedics*. [Online]. 2014 pp. 247–254.
- Wahajuddin & Arora, S. (2012) Superparamagnetic iron oxide nanoparticles: Magnetic nanoplatforms as drug carriers. *International Journal of Nanomedicine* 7 p.3445–3471.
- Wang, L. et al. (2017) The antimicrobial activity of nanoparticles: Present situation and prospects for the future. *International Journal of Nanomedicine* 12 p.1227–1249.

- Wang, S. Y. et al. (2020) Recent advances of drug delivery nanocarriers in osteosarcoma treatment. *Journal of Cancer* 11 (1) p.69–82.
- Wang, X. et al. (2012) Pluronic F108 coating decreases the lung fibrosis potential of multiwall carbon nanotubes by reducing lysosomal injury. *Nano Letters*. [Online] 12 (6), 3050–3061.
- Wang, Xinwen et al. (2021) Classification of Osteosarcoma Based on Immunogenomic Profiling. *Frontiers in Cell and Developmental Biology*. [Online] 9: 696878.
- Wang, Z. Q. et al. (2017) CD74 and intratumoral immune response in breast cancer. *Oncotarget*. [Online] 8 (8), 12664–12674.
- Wang, Zenan et al. (2019) Innate immune cells: A potential and promising cell population for treating osteosarcoma. *Frontiers in Immunology*. 10: 1114.
- Weiss, M. et al. (2021) Density of surface charge is a more predictive factor of the toxicity of cationic carbon nanoparticles than zeta potential. *Journal of Nanobiotechnology*. [Online] 19 (1).
- Wen, J. et al. (2021) Ultrasmall iron oxide nanoparticles induced ferroptosis via Beclin1/ATG5-dependent autophagy pathway. *Nano Convergence*. [Online] 8 (1).
- Wessel, K. M. & Kaplan, R. N. (2022) Targeting tumor microenvironment and metastasis in children with solid tumors. *Current Opinion in Pediatrics* 34 (1) p.53–60.
- Westra, A. et al. (1998) Late peritoneal metastasis in a patient with osteosarcoma. *Annals of Oncology*. [Online] 9 (8), 907-911.
- Whelan, J. et al. (2012) Incidence and survival of malignant bone sarcomas in England 1979-2007. *International Journal of Cancer*. [Online] 131 (4).
- Whelan, J. et al. (2010) The role of interferons in the treatment of osteosarcoma. *Pediatric Blood and Cancer* 54 (3) p.350–354.

- Whirl-Carrillo, M. et al. (2021) An Evidence-Based Framework for Evaluating Pharmacogenomics Knowledge for Personalized Medicine. *Clinical Pharmacology and Therapeutics*. [Online] 110 (3), 563–572.
- Whiteside, T. L. (2008) The tumor microenvironment and its role in promoting tumor growth. *Oncogene* 27 (45) p.5904–5912.
- Wibroe, P. P. et al. (2017) Bypassing adverse injection reactions to nanoparticles through shape modification and attachment to erythrocytes. *Nature Nanotechnology*. [Online] 12 (6), 589–594.
- Wilczewska, A. Z. et al. (2012) Nanoparticles as drug delivery systems. *Pharmacological Reports* 64 (5) p.1020–1037.
- Wilhelm, C. et al. (2003) Intracellular uptake of anionic superparamagnetic nanoparticles as a function of their surface coating. *Biomaterials*. [Online] 24 (6), 1001–1011.
- Wilson-Sanders, S. E. (2011) Invertebrate models for biomedical research, testing, and education. *ILAR Journal* 52 (2) p.126–152.
- Winkler, J. et al. (2020) Concepts of extracellular matrix remodelling in tumour progression and metastasis. *Nature Communications* 11 (1).
- Wolfbeis, O. S. (2015) An overview of nanoparticles commonly used in fluorescent bioimaging. *Chemical Society Reviews* 44 (14) p.4743–4768.
- Wolfram, J. et al. (2015) Safety of Nanoparticles in Medicine. *Current Drug Targets*. [Online] 16 (14), 1671–1681.
- Wongkajornsilp, A. et al. (2005) Effective osteosarcoma cytolysis using cytokine-induced killer cells pre-inoculated with tumor RNA-pulsed dendritic cells. *Journal of Orthopaedic Research*. [Online] 23 (6), 1460–1466.
- Woo, S. R. et al. (2015) Innate immune recognition of cancer. *Annual Review of*

- Immunology*. [Online] 33445–474.
- Wrońska, A. K. & Boguś, M. I. (2020) Heat shock proteins (HSP 90, 70, 60, and 27) in *Galleria mellonella* (Lepidoptera) hemolymph are affected by infection with *Conidiobolus coronatus* (Entomophthorales). *PLoS ONE*. [Online] 15 (2).
- Wu, L. et al. (2016) Organic Phase Syntheses of Magnetic Nanoparticles and Their Applications. *Chemical Reviews* 116 (18) p.10473–10512.
- Wu, Y. N. et al. (2011) The selective growth inhibition of oral cancer by iron core-gold shell nanoparticles through mitochondria-mediated autophagy. *Biomaterials*. [Online] 32 (20), 4565-73.
- Xi, Y. et al. (2019) Differential expression and bioinformatics analysis of circRNA in osteosarcoma. *Bioscience Reports*. [Online] 39 (5).
- Xu, M. et al. (2019) Internalization and toxicity: A preliminary study of effects of nanoplastic particles on human lung epithelial cell. *Science of the Total Environment*. [Online] 694:133794.
- Xu, S. et al. (2021) CD74 Correlated With Malignancies and Immune Microenvironment in Gliomas. *Frontiers in Molecular Biosciences*. [Online] 8: 706949.
- Yahiro, K. & Matsumoto, Y. (2021) Immunotherapy for osteosarcoma. *Human Vaccines and Immunotherapeutics*. [Online] 17 (5), 1294–1295.
- Yameen, B. et al. (2014) Insight into nanoparticle cellular uptake and intracellular targeting. *Journal of Controlled Release*. 190 p.485–499.
- Yan, L. et al. (2020) Nanoparticle-Based Drug Delivery System: A Patient-Friendly Chemotherapy for Oncology. *Dose-Response*. 18(3): 1559325820936161.
- Yan, Y. et al. (2013) Differential roles of the protein corona in the cellular uptake of nanoporous polymer particles by monocyte and macrophage cell lines. *ACS*

- Nano*. [Online] 7 (12), 10960–10970.
- Yang, B. et al. (2021) Identification of prognostic biomarkers associated with metastasis and immune infiltration in osteosarcoma. *Oncology Letters*. [Online] 21 (3).
- Yang, S. et al. (2020) Comprehensive analysis of prognostic immune-related genes in the tumor microenvironment of cutaneous melanoma. *Journal of Cellular Physiology*. [Online] 235 (2), 1025–1035.
- Yang, Y. et al. (2011) Annexin 1 released by necrotic human glioblastoma cells stimulates tumor cell growth through the formyl peptide receptor 1. *American Journal of Pathology*. [Online] 179 (3), 1504–1512.
- Yang, Z. et al. (2014) Meta-analysis of differentially expressed genes in osteosarcoma based on gene expression data. *BMC Medical Genetics*. [Online] 15 (1).
- Yao, Y. et al. (2020) Nanoparticle-Based Drug Delivery in Cancer Therapy and Its Role in Overcoming Drug Resistance. *Frontiers in Molecular Biosciences*. 7:193.
- Yarjanli, Z. et al. (2017) Iron oxide nanoparticles may damage to the neural tissue through iron accumulation, oxidative stress, and protein aggregation. *BMC Neuroscience*. 18 (1).
- Ye, R. D. et al. (2009) International union of basic and clinical pharmacology. LXXIII. Nomenclature for the formyl peptide receptor (FPR) family. *Pharmacological Reviews*. 61 (2) p.119–161.
- Yen, C. C. et al. (2009) Identification of chromosomal aberrations associated with disease progression and a novel 3q13.31 deletion involving LSAMP gene in osteosarcoma. *International Journal of Oncology*. [Online] 35 (4), 775–788.
- Yoo, J.-W. et al. (2010) Factors that Control the Circulation Time of Nanoparticles in Blood: Challenges, Solutions and Future Prospects. *Current Pharmaceutical*

- Design*. [Online] 16 (21), 2298–2307.
- Yoo, J. et al. (2019) Active targeting strategies using biological ligands for nanoparticle drug delivery systems. *Cancers*. [Online] 11 (5).
- Yoo, S. M. et al. (2009) Applications of DNA microarray in disease diagnostics. *Journal of Microbiology and Biotechnology*. 19(7):635-46.
- Yu, F. X. et al. (2015) Bone marrow mesenchymal stem cells promote osteosarcoma cell proliferation and invasion. *World Journal of Surgical Oncology*. [Online] 13 (1).
- Yu, G. et al. (2015) DOSE: An R/Bioconductor package for disease ontology semantic and enrichment analysis. *Bioinformatics*. [Online] 31 (4), 608–609.
- Yu, Y. (2018) Resolving Endosome Rotation in Intracellular Trafficking. *Biophysical Journal*. [Online] 114 (3), 630a.
- Yu, Z. et al. (2020) Reactive Oxygen Species-Related Nanoparticle Toxicity in the Biomedical Field. *Nanoscale Research Letters*. 15 (1).
- Yuan, X. et al. (2019) Cellular Toxicity and Immunological Effects of Carbon-based Nanomaterials. *Particle and Fibre Toxicology*. 16 (1).
- Zavaleta, C. et al. (2018) Theranostic Nanoparticles for Tracking and Monitoring Disease State. *SLAS Technology*. [Online] 23 (3), 281–293.
- Zeglis, B. M. et al. (2015) Optimization of a pretargeted strategy for the PET imaging of colorectal carcinoma via the modulation of radioligand pharmacokinetics. *Molecular Pharmaceutics*. [Online] 12 (10), 3575–3587.
- Zeineddine, R. & Yerbury, J. J. (2015) The role of macropinocytosis in the propagation of protein aggregation associated with neurodegenerative diseases. *Frontiers in Physiology*. 6: 277.
- Zhang, D. et al. (2020) AllEnricher: A comprehensive gene set function enrichment

- tool for both model and non-model species. *BMC Bioinformatics*. [Online] 21 (1).
- Zhang, Q. wen et al. (2012) Prognostic Significance of Tumor-Associated Macrophages in Solid Tumor: A Meta-Analysis of the Literature. *PLoS ONE*. [Online] 7 (12).
- Zhang, S. & Cao, J. (2009) A close examination of double filtering with fold change and t test in microarray analysis. *BMC Bioinformatics*. [Online] 10, 402.
- Zhang, T. et al. (2018) Angiopoietin-like 4 promotes osteosarcoma cell proliferation and migration and stimulates osteoclastogenesis. *BMC Cancer*. [Online] 18 (1).
- Zhang, W. et al. (2011) The application of carbon nanotubes in target drug delivery systems for cancer therapies. *Nanoscale Research Letters*. 6 p.1–22.
- Zhang, X. D. et al. (2011) Size-dependent in vivo toxicity of PEG-coated gold nanoparticles. *International journal of nanomedicine*. [Online] 62071–2081.
- Zhang, X. D. et al. (2010) Toxicologic effects of gold nanoparticles in vivo by different administration routes. *International Journal of Nanomedicine*. [Online] 5 (1), 771–781.
- Zhang, Y. et al. (2019) The roles of circular RNAs in osteosarcoma. *Medical Science Monitor*. [Online] 256378–6382.
- Zhang, Z. et al. (2022) Immune checkpoint inhibitors in osteosarcoma: A hopeful and challenging future. *Frontiers in Pharmacology*. 13: 1031527.
- Zhao, F. et al. (2011) Cellular uptake, intracellular trafficking, and cytotoxicity of nanomaterials. *Small*. [Online] 7 (10), 1322–1337.
- Zhao, Hongli et al. (2015) CXCR4 over-expression and survival in cancer: A system review and meta-analysis. *Oncotarget*. [Online] 6 (7), 5022–5040.
- Zhao, S. J. et al. (2018) SPARCL1 suppresses osteosarcoma metastasis and recruits macrophages by activation of canonical WNT/ β -catenin signaling through

- stabilization of the WNT-receptor complex. *Oncogene*. [Online] 37(8):1049-1061.
- Zhao, X. et al. (2021) Osteosarcoma: a review of current and future therapeutic approaches. *BioMedical Engineering*. Online 20 (1).
- Zheng, H. et al. (2017) Effect of nanoparticle surface coating on cell toxicity and mitochondria uptake. *Journal of Biomedical Nanotechnology*. [Online] 13 (2), 155–166.
- Zheng, M. et al. (2018) Effects of starch-coating of magnetite nanoparticles on cellular uptake, toxicity and gene expression profiles in adult zebrafish. *Science of the Total Environment*. [Online] 622–623930–941.
- Zhou, W. et al. (2014) Advances in targeted therapy for osteosarcoma. *Discovery Medicine*. 17 (96), 301–307.
- Zhu, T. et al. (2022) Immune Microenvironment in Osteosarcoma: Components, Therapeutic Strategies and Clinical Applications. *Frontiers in Immunology*. 13:907550.
- Zhu, Y. et al. (2018) CXCR4-mediated osteosarcoma growth and pulmonary metastasis is suppressed by MicroRNA-613. *Cancer Science*. [Online] 109 (8), 2412–2422.
- Zitvogel, L. et al. (2006) Cancer despite immunosurveillance: Immunoselection and immunosubversion. *Nature Reviews Immunology* 6 (10) p.715–727.
- Zolnik, B. S. et al. (2010) Minireview: Nanoparticles and the immune system. *Endocrinology* 151 (2) p.458–465.
- Zorlu, T. et al. (2018) Influence of dietary titanium dioxide nanoparticles on the biology and antioxidant system of model insect, *Galleria mellonella* (L.) (Lepidoptera: Pyralidae). *Journal of the Entomological Research Society*. 20 (3), 89–103.

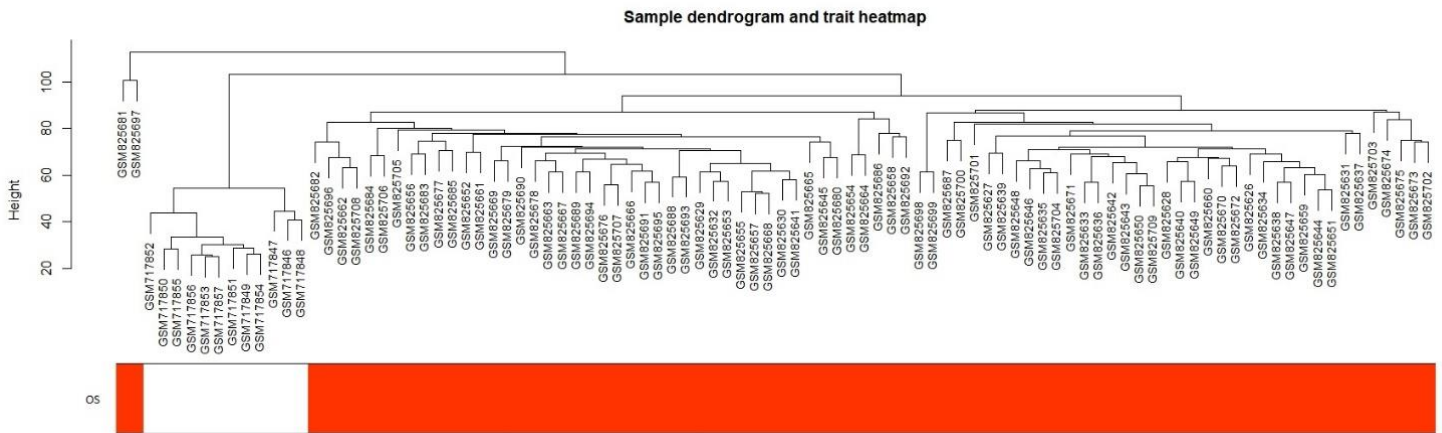


Figure A2: **WGCNA: matching external clinal traits to microarray samples.** Figure portraying the generated clustered dendrogram for the microarray samples that have been inputted into WGCNA and which have been matched to the inputted OS external clinical trait data. The figure, thus, allows for the classification of OS and control samples, with the colour white representing BM-MSD samples and orange representing OS samples.

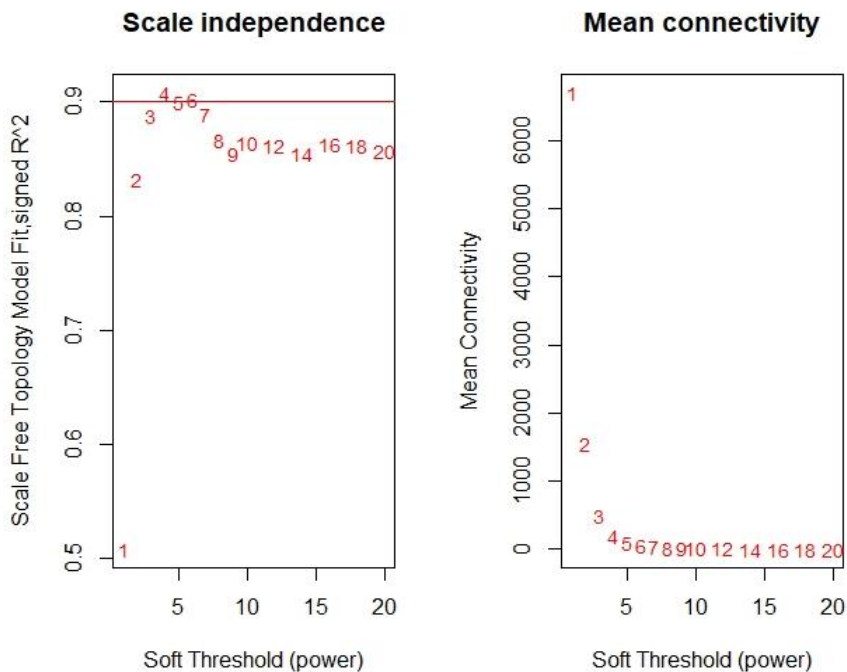


Figure A3: **WGCNA: determining soft-thresholding power for analysis.** Analysis of network topology for various soft-thresholding powers. The left panel shows the scale-free fit index (y-axis) as a function of the soft-thresholding power (x-axis). The right panel displays the mean connectivity (degree, y-axis) as a function of the soft-thresholding power (x-axis). The generated panels were used to pick the appropriate soft-thresholding power for further analysis.

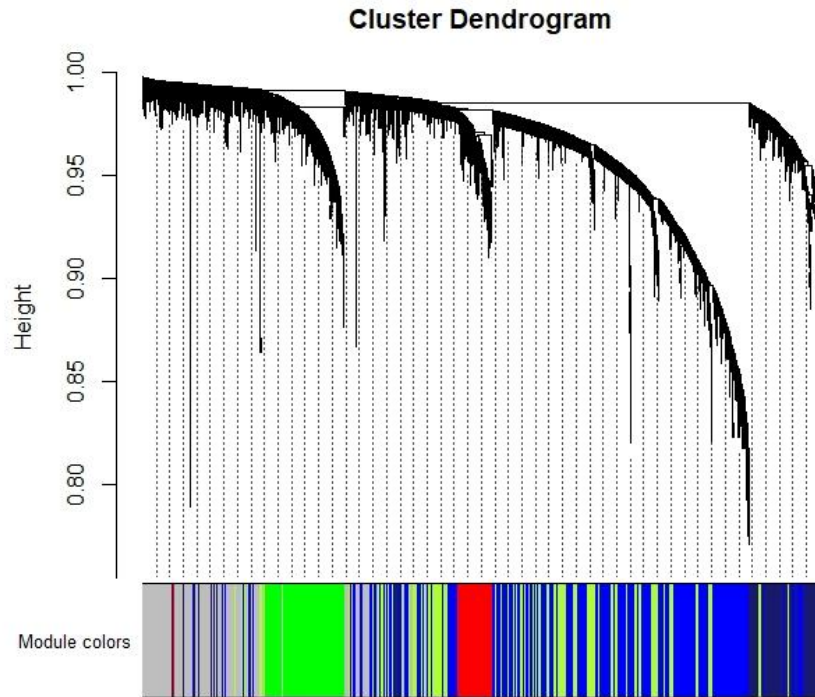


Figure A4: **WGCNA: clustering of functionally similar genes into gene modules.** Figure portraying the statistical clustering dendrogram of genes, with gene dissimilarity based on topological overlap, together with the randomly assigned gene module colours.

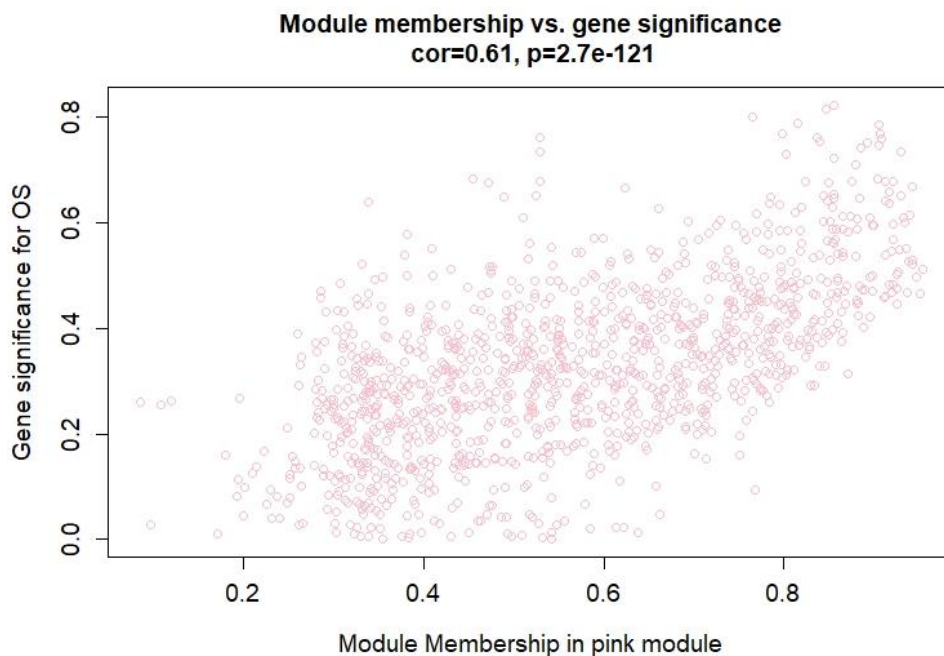
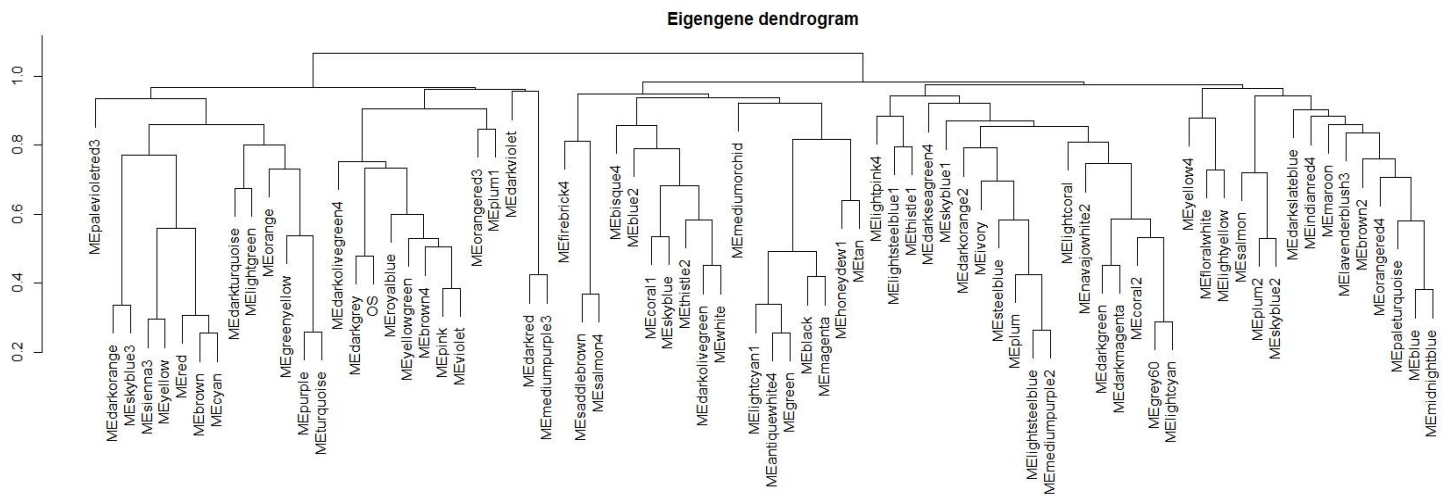
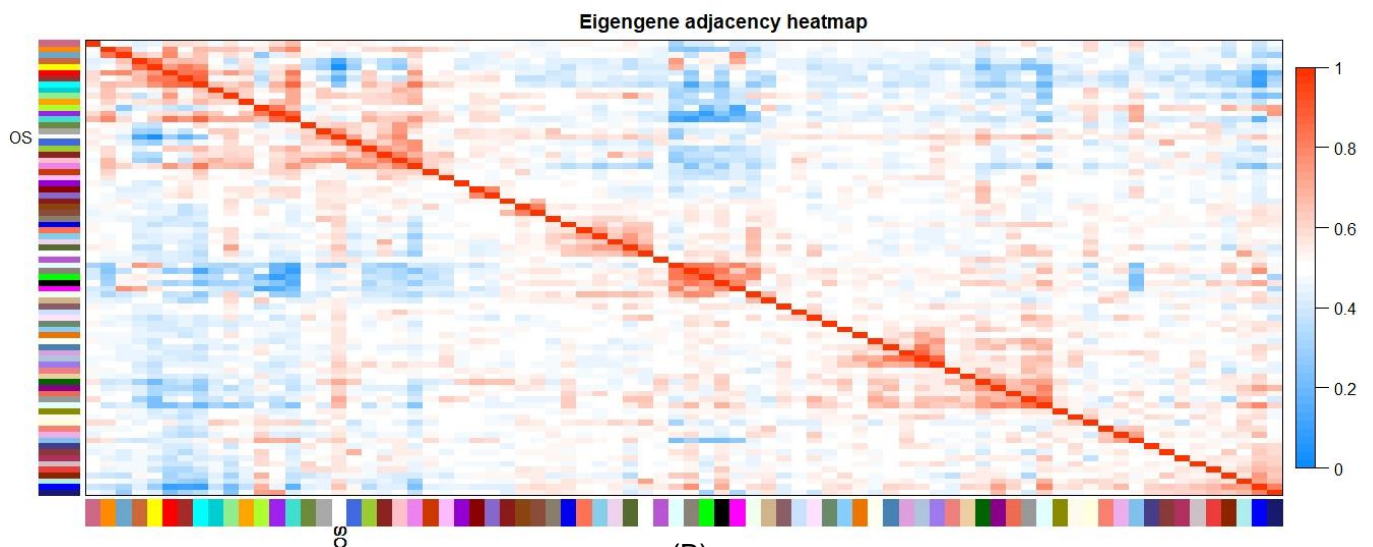


Figure A5: **WGCNA: Gene significance to OS Vs module membership.** Figure displaying a scatterplot of Gene Significance (GS) for OS vs. Module Membership (MM), for individual genes within the pink module. There is a highly significant correlation between the gene's significance (GS) to OS and the importance of the gene with the pink module, (MM) ($P<0.05$).



(A)



(B)

Figure A6: WGCNA: gene module clustering and inter-modular associations. Figure, allowing for the visualisation of the eigengene network representing the relationships among the gene modules and OS clinical trait. Panel (A) shows a hierarchical statistical clustering dendrogram of the gene modules and the clinical trait. The heatmap in panel (B) shows the gene module adjacency and adjacency to the clinical trait.

❖ Appendix B: Formyl-Peptide Receptor 3 (FPR3) as A Novel Immune-Based Therapeutic Target in Osteosarcoma.

Table B1.1: Name, OS804d; Description, Osteosarcoma tissue array, including TNM and clinical stage, 40 cases/80 cores. Table presenting appropriate clinical information for the OS tumour biopsy cores included in the OS tissue array (OS804d), which were stained for FPR3 in this study. The table provides OS patient clinical information, including age and sex. In addition, tumour biopsy clinical and histological information are also presented, which include site of biopsy, diagnosis, TNM, stage and type of tissue.

Position	Age, years	Sex	Organ/anatomic site	Pathology diagnosis	TNM	Stage	Type
A1	13	F	Bone	Osteosarcoma of femur	T2N0M0 G2	IB	Malignant
A2	13	F	Bone	Osteosarcoma of femur	T2N0M0 G2	IB	Malignant
A3	12	M	Bone	Osteosarcoma of femur	T2N0M0 G3	IIB	Malignant
A4	12	M	Bone	Osteosarcoma of femur	T2N0M0 G3	IIB	Malignant
A5	23	F	Bone	Osteosarcoma of femur	T2N0M0 G3	IIB	Malignant
A6	23	F	Bone	Osteosarcoma of femur	T2N0M0 G3	IIB	Malignant
A7	21	M	Bone	Osteosarcoma of femur	T2N0M0 G2	IB	Malignant
A8	21	M	Bone	Osteosarcoma of femur	T2N0M0 G2	IB	Malignant
A9	42	M	Bone	Osteosarcoma of femur	T2N0M0 G4	IIB	Malignant
A10	42	M	Bone	Osteosarcoma of femur	T2N0M0 G4	IIB	Malignant
B1	16	F	Bone	Osteosarcoma of femur	T2N0M0 G3	IIB	Malignant
B2	16	F	Bone	Osteosarcoma of femur	T2N0M0 G3	IIB	Malignant
B3	15	F	Bone	Osteosarcoma of femur	T2N0M0 G2	IB	Malignant
B4	15	F	Bone	Osteosarcoma of femur	T2N0M0 G2	IB	Malignant
B5	35	M	Bone	Osteosarcoma of femur	T2N0M0 G2	IB	Malignant
B6	35	M	Bone	Osteosarcoma of femur	T2N0M0 G2	IB	Malignant
B7	64	M	Bone	Osteosarcoma of femur	T2N0M0 G2	IB	Malignant
B8	64	M	Bone	Osteosarcoma of femur	T2N0M0 G2	IB	Malignant
B9	29	M	Bone	Osteosarcoma of femur	T1N0M0 G2	IA	Malignant
B10	29	M	Bone	Osteosarcoma of femur	T1N0M0 G2	IA	Malignant
C1	30	M	Bone	Osteosarcoma of femur	T2N0M0 G2	IB	Malignant
C2	30	M	Bone	Osteosarcoma of femur	T2N0M0 G2	IB	Malignant
C3	51	M	Bone	Osteosarcoma of femur	T2N0M0 G2	IB	Malignant
C4	51	M	Bone	Osteosarcoma of femur	T2N0M0 G2	IB	Malignant
C5	11	M	Bone	Osteosarcoma of femur	T1N0M0 G2	IA	Malignant
C6	11	M	Bone	Osteosarcoma of femur	T1N0M0 G2	IA	Malignant
C7	47	F	Bone	Osteosarcoma of femur	T2N0M0 G2	IB	Malignant
C8	47	F	Bone	Osteosarcoma of femur	T2N0M0 G2	IB	Malignant
C9	47	M	Bone	Osteosarcoma of femur	T2N0M0 G3	IIB	Malignant
C10	47	M	Bone	Osteosarcoma of femur	T2N0M0 G3	IIB	Malignant
D1	16	F	Bone	Osteosarcoma of femur	T2N0M0 G2	IB	Malignant
D2	16	F	Bone	Osteosarcoma of femur	T2N0M0 G2	IB	Malignant
D3	12	F	Bone	Osteosarcoma of femur	T2N0M0 G3	IIB	Malignant
D4	12	F	Bone	Osteosarcoma of femur	T2N0M0 G3	IIB	Malignant
D5	16	M	Bone	Osteosarcoma of femur	T2N0M0 G2	IB	Malignant
D6	16	M	Bone	Osteosarcoma of femur	T2N0M0 G2	IB	Malignant
D7	16	M	Bone	Osteosarcoma of femur	T2N0M0 G3	IIB	Malignant
D8	16	M	Bone	Osteosarcoma of femur	T2N0M0 G3	IIB	Malignant
D9	37	F	Bone	Osteosarcoma of femur	T1N0M0 G2	IA	Malignant
D10	37	F	Bone	Osteosarcoma of femur	T1N0M0 G2	IA	Malignant
E1	14	M	Bone	Osteosarcoma of femur	T2N0M0 G3	IIB	Malignant
E2	14	M	Bone	Osteosarcoma of femur	T2N0M0 G3	IIB	Malignant
E3	14	F	Bone	Osteosarcoma of femur	T2N0M0 G3	IIB	Malignant
E4	14	F	Bone	Osteosarcoma of femur	T2N0M0 G3	IIB	Malignant
E5	32	F	Bone	Osteosarcoma of femur	T2N0M0 G3	IIB	Malignant
E6	32	F	Bone	Osteosarcoma of femur	T2N0M0 G3	IIB	Malignant
E7	46	M	Bone	Osteosarcoma of femur	T2N0M0 G2	IB	Malignant
E8	46	M	Bone	Osteosarcoma of femur	T2N0M0 G2	IB	Malignant
E9	16	M	Bone	Osteosarcoma of femur	T2N0M0 G3	IIB	Malignant
E10	16	M	Bone	Osteosarcoma of femur	T2N0M0 G3	IIB	Malignant
F1	17	M	Bone	Osteosarcoma of tibia	T2N0M0 G2	IB	Malignant
F2	17	M	Bone	Osteosarcoma of tibia	T2N0M0 G2	IB	Malignant
F3	17	M	Bone	Osteosarcoma of tibia	T2N0M0 G2	IB	Malignant
F4	17	M	Bone	Osteosarcoma of tibia	T2N0M0 G2	IB	Malignant
F5	14	F	Bone	Osteosarcoma of tibia	T2N0M0 G3	IIB	Malignant
F6	14	F	Bone	Osteosarcoma of tibia	T2N0M0 G3	IIB	Malignant
F7	38	M	Bone	Osteosarcoma of tibia	T2N0M0 G3	IIB	Malignant
F8	38	M	Bone	Osteosarcoma of tibia	T2N0M0 G3	IIB	Malignant
F9	20	F	Bone	Osteosarcoma of tibia	T2N0M0 G3	IIB	Malignant
F10	20	F	Bone	Osteosarcoma of tibia	T2N0M0 G3	IIB	Malignant
G1	60	M	Bone	Osteosarcoma of tibia	T2N0M0 G3	IIB	Malignant
G2	60	M	Bone	Osteosarcoma of tibia	T2N0M0 G3	IIB	Malignant
G3	31	M	Bone	Osteosarcoma of humerus	T2N0M0 G3	IIB	Malignant
G4	31	M	Bone	Osteosarcoma of humerus	T2N0M0 G3	IIB	Malignant
G5	18	M	Bone	Osteosarcoma of humerus	T2N0M0 G2	IB	Malignant
G6	18	M	Bone	Osteosarcoma of humerus	T2N0M0 G2	IB	Malignant
G7	32	F	Bone	Osteosarcoma of humerus	T2N0M0 G2	IB	Malignant
G8	32	F	Bone	Osteosarcoma of humerus	T2N0M0 G2	IB	Malignant
G9	41	F	Bone	Osteosarcoma of humerus	T1N0M0 G2	IA	Malignant
G10	41	F	Bone	Osteosarcoma of humerus	T1N0M0 G2	IA	Malignant
H1	30	M	Bone	Osteosarcoma of rib	T1N0M0 G2	IA	Malignant
H2	30	M	Bone	Osteosarcoma of rib	T1N0M0 G2	IA	Malignant
H3	32	M	Bone	Osteosarcoma of rib	T1N0M0 G3	IIA	Malignant
H4	32	M	Bone	Osteosarcoma of rib	T1N0M0 G3	IIA	Malignant
H5	33	M	Bone	Osteosarcoma of upper jaw	T1N0M0 G2	IA	Malignant
H6	33	M	Bone	Osteosarcoma of upper jaw	T1N0M0 G2	IA	Malignant
H7	15	M	Bone	Osteosarcoma of lower jaw	T2N1M0 G2	IVB	Malignant
H8	15	M	Bone	Osteosarcoma of lower jaw	T2N1M0 G2	IVB	Malignant
H9	51	M	Bone	Osteosarcoma of fibula	T2N0M0 G3	IIB	Malignant
H10	51	M	Bone	Osteosarcoma of fibula	T2N0M0 G3	IIB	Malignant

Table B1.2: Name, T264a; Description, bone and cartilage malignant tumour (chondrosarcoma, osteosarcoma, Ewing's sarcoma) tissue array, including TNM and clinical stage, 6 cases/24 cores. Table presenting appropriate clinical information for the Sarcoma tumour biopsy cores included in the mixed Sarcoma tissue array (T264a), which were stained for FPR3 in this study. The table provides patient clinical information, including age and sex. In addition, tumour biopsy clinical and histological information are also presented, which include site of biopsy, diagnosis, TNM, stage and type of tissue.

Position	Age, years	Sex	Organ/anatomic site	Pathology diagnosis	TNM	Stage	Type
A1	47	M	Bone	Undifferentiated chondrosarcoma of pars sacralis	-	-	Malignant
A2	42	F	Bone	Chondrosarcoma of femur	-	-	Malignant
A3	10	M	Bone	Osteosarcoma of left tibia	T2N0M0 G2	IIB	Malignant
A4	47	M	Bone	Undifferentiated chondrosarcoma of pars sacralis	-	-	Malignant
A5	42	F	Bone	Chondrosarcoma of femur	-	-	Malignant
A6	10	M	Bone	Osteosarcoma of left tibia	T2N0M0 G2	IIB	Malignant
B1	21	F	Bone	Osteosarcoma	T1N0M0 G2	IA	Malignant
B2	14	M	Bone	Ewing's sarcoma of left femur	T2N0M0 G4	IIB	Malignant
B3	18	F	Bone	Ewing's sarcoma right supermaxilla	T2N0M0 G4	IIB	Malignant
B4	21	F	Bone	Osteosarcoma	T1N0M0 G2	IA	Malignant
B5	14	M	Bone	Ewing's sarcoma of left femur	T2N0M0 G4	IIB	Malignant
B6	18	F	Bone	Ewing's sarcoma right supermaxilla	T2N0M0 G4	IIB	Malignant
C1	47	M	Bone	Undifferentiated chondrosarcoma of pars sacralis	-	-	Malignant
C2	42	F	Bone	Chondrosarcoma of femur	-	-	Malignant
C3	10	M	Bone	Osteosarcoma of left tibia	T2N0M0 G2	IIB	Malignant
C4	47	M	Bone	Undifferentiated chondrosarcoma of pars sacralis (sparse)	-	-	Malignant
C5	42	F	Bone	Chondrosarcoma of femur	-	-	Malignant
C6	10	M	Bone	Osteosarcoma of left tibia	T2N0M0 G2	IIB	Malignant
D1	21	F	Bone	Osteosarcoma	T1N0M0 G2	IA	Malignant
D2	14	M	Bone	Ewing's sarcoma of left femur	T2N0M0 G4	IIB	Malignant
D3	18	F	Bone	Ewing's sarcoma right supermaxilla	T2N0M0 G4	IIB	Malignant
D4	21	F	Bone	Osteosarcoma	T1N0M0 G2	IA	Malignant
D5	14	M	Bone	Ewing's sarcoma of left femur	T2N0M0 G4	IIB	Malignant
D6	18	F	Bone	Ewing's sarcoma right supermaxilla	T2N0M0 G4	IIB	Malignant

Table B1.3: Name, BO244g; Description, Normal bone tissue array with osteosarcoma tissue, including TNM and clinical stage, 12 cases/24 cores. Table presenting appropriate clinical information for the normal bone and OS biopsy cores included in the normal bone tissue array (BO244g), which were stained for FPR3 in this study. The table provides patient clinical information, including age and sex. In addition, tissue biopsy clinical and histological information are also presented where appropriate, which include site of biopsy, diagnosis, TNM, stage and type of tissue.

Position	Age, years	Sex	Organ/anatomic site	Pathology diagnosis	TNM	Stage	Type
A1	58	M	Bone/Rib	Bone and bone marrow tissue	-	-	NAT
A2	58	M	Bone/Rib	Bone and bone marrow tissue	-	-	NAT
A3	57	M	Bone/Rib	Bone and bone marrow tissue	-	-	NAT
A4	57	M	Bone/Rib	Bone and bone marrow tissue	-	-	NAT
A5	56	M	Bone/Rib	Bone and bone marrow tissue	-	-	NAT
A6	56	M	Bone/Rib	Bone and bone marrow tissue	-	-	NAT
A7	56	M	Bone/Rib	Bone and bone marrow tissue	-	-	NAT
A8	56	M	Bone/Rib	Bone and bone marrow tissue	-	-	NAT
B1	62	M	Bone/Rib	Bone and bone marrow tissue	-	-	NAT
B2	62	M	Bone/Rib	Bone and bone marrow tissue	-	-	NAT
B3	70	M	Bone/Rib	Bone and bone marrow tissue	-	-	NAT
B4	70	M	Bone/Rib	Bone and bone marrow tissue	-	-	NAT
B5	75	M	Bone/Rib	Bone and bone marrow tissue	-	-	NAT
B6	75	M	Bone/Rib	Bone and bone marrow tissue	-	-	NAT
B7	67	M	Bone/Rib	Bone and bone marrow tissue	-	-	NAT
B8	67	M	Bone/Rib	Bone tissue	-	-	NAT
C1	58	M	Bone/Rib	Bone and bone marrow tissue	-	-	NAT
C2	58	M	Bone/Rib	Bone and bone marrow tissue	-	-	NAT
C3	41	M	Bone/Rib	Bone and bone marrow tissue	-	-	NAT
C4	41	M	Bone/Rib	Bone tissue	-	-	NAT
C5	66	F	Bone/Rib	Bone and bone marrow tissue	-	-	NAT
C6	66	F	Bone/Rib	Bone and bone marrow tissue	-	-	NAT
C7	19	M	Bone/Left tibia	Osteosarcoma of left tibia	T2N0M0 G3	IIB	Malignant
C8	19	M	Bone/Left tibia	Osteosarcoma of left tibia	T2N0M0 G3	IIB	Malignant

Table B2.1: Original velocity of MG63 cell migration with WKYMVm peptide treatment ($\mu\text{m}/\text{min}$). Table presenting the original velocity of MG63 cell migration data, once treated with the FPR3 receptor peptide agonist WKYMVm at differing concentrations. Also presented, are the standard deviations for each treatment condition and P-values acquired from the conducted multiple-unpaired T-tests and one-way ANOVA.

Velocity of MG63 cell migration with WKYMVm treatment ($\mu\text{m}/\text{min}$)			
Untreated	10 μM	50 μM	100 μM
0.002236	0.002463	0.003282	0.002513
0.002028	0.002053	0.003659	0.002257
0.00194	0.002569	0.003444	0.00317
0.005242	0.000711	0.002204	0.001675
0.00242	0.001876	0.001849	0.001401
0.001995	0.001972	0.001754	
0.003611			
0.004244			
0.003281			
0.003488			
0.002819			
0.002485			
0.002262			
0.002985			
0.002626			
0.001865			
0.002454			

	Untreated	10 μM	50 μM	100 μM
Standard deviation (SD)	0.000884	0.000605	0.000783	0.000625
P-value (unpaired T-test)		0.042329	0.774763	0.178685

Table B2.2: Original velocity of MG63 cell migration with WRW4 peptide treatment ($\mu\text{m}/\text{min}$). Table presenting the original velocity of MG63 cell migration data, once treated with the FPR3 receptor peptide antagonist WRW4 at differing concentrations. Also presented, are the standard deviations for each treatment condition and P-values acquired from the conducted multiple-unpaired T-tests and one-way ANOVA.

Velocity of MG63 cell migration with WRW4 treatment ($\mu\text{m}/\text{min}$)			
Untreated	10 μM	50 μM	100 μM
0.002236	0.002238	0.002064	0.002232
0.002028	0.002027	0.002913	0.001988
0.00194	0.001645	0.002143	0.002099
0.005242	0.001413	0.001119	0.000964
0.00242	0.001814	0.001536	0.001518
0.001995	0.0017	0.00049	
0.003611			
0.004244			
0.003281			
0.003488			
0.002819			
0.002485			
0.002262			
0.002985			
0.002626			
0.001865			
0.002454			

	Untreated	10 μM	50 μM	100 μM
Standard deviation (SD)	0.000884	0.000267	0.000778	0.000465
P-value (unpaired T-test)		0.015063	0.016441	0.022999

P-values from one-way ANOVA: 10 μM : 0.0062, 50 μM : 0.0670, 100 μM : 0.0296.

Table B2.3: Original velocity of Saos-2 cell migration with WKYMVm peptide treatment ($\mu\text{m}/\text{min}$). Table presenting the original velocity of Saos-2 cell migration data, once treated with the FPR3 receptor peptide agonist WKYMVm at differing concentrations. Also presented, are the standard deviations for each treatment condition and P-values acquired from the conducted multiple-unpaired T-tests and one-way ANOVA.

Velocity of Saos-2 cell migration with WKYMVm treatment ($\mu\text{m}/\text{min}$)			
Untreated	10 μM	50 μM	100 μM
0.003208	0.010074	0.003077	0.002821
0.003426	0.014776	0.002588	0.002464
0.004122	0.018113	0.002923	0.002379
0.00358	0.01545	0.008762	0.002336
0.003162	0.017641	0.008308	0.002554
0.003432		0.002841	
0.003316			
0.003366			
0.002965			
0.006997			
0.006351			
0.006841			
0.005362			
0.005747			
0.007322			
0.006958			

	Untreated	10 μM	50 μM	100 μM
Standard deviation (SD)	0.001623	0.002862	0.002684	0.000172
P-value (unpaired T-test)		<0.000001	0.992149	0.008373

Table B2.4: Original velocity of Saos-2 cell migration with WRW4 peptide treatment ($\mu\text{m}/\text{min}$). Table presenting the original velocity of Saos-2 cell migration data, once treated with the FPR3 receptor peptide antagonist WRW4 at differing concentrations. Also presented, are the standard deviations for each treatment condition and P-values acquired from the conducted multiple-unpaired T-tests and one-way ANOVA.

Velocity of Saos-2 cell migration with WRW4 treatment ($\mu\text{m}/\text{min}$)			
Untreated	10 μM	50 μM	100 μM
0.003208	0.002414	0.00184	0.002542
0.003426	0.00255	0.001661	0.001851
0.004122	0.002737	0.002118	0.001932
0.00358	0.003865	0.001384	0.001949
0.003162	0.010432	0.001831	0.001419
0.003432		0.001947	
0.003316			
0.003366			
0.002965			
0.006997			
0.006351			
0.006841			
0.005362			
0.005747			
0.007322			
0.006958			

	Untreated	10 μM	50 μM	100 μM
Standard deviation (SD)	0.001623	0.00306	0.00023	0.000358
P-value (unpaired T-test)		0.748873	0.000395	0.001631

P-values from one-way ANOVA: 10 μM : 0.0015, 50 μM : 0.0001, 100 μM : 0.0003.

Cloud-based weblinks to in vitro cell migration assay videos: In vitro migration of MG63 and Saos-2 human OS cells, once treated with FPR3 receptor peptide ligands (agonist and antagonist) at differing concentrations.

- In vitro cell migration of MG63 cells:

Scratch assay videos - MG63

- In vitro cell migration of Saos-2 cells:

Scratch assay videos - Saos-2

❖ Appendix C: Galleria Mellonella Larvae: An Invertebrate Model System to Study Nanoparticle Toxicity.

Table C1: GM larval percentage survival changes caused by SPIONs during 72h post-NP injections. Table providing a detailed description of SPION induced changes to GM larval percentage survival, at varying timepoints, along the complete 72h NP toxicity assay. Changes to percentage larval survival was tallied, calculated and presented by the GraphPad software.

Hours	PBS Percentage	SC-SPION Percentage	Anionic- SPION Percentage	Cyclophosphamide Percentage	Cyclo+SC-SPION Percentage	Cyclo+Anionic-SPION Percentage
24	100	95.74	91.22	96	94.73	94.33
44						88.44
72	90	88.90	86.42	96	94.73	76.65

Table C2: GM larval percentage survival changes caused by CNTs during 72h post-NP injections. Table providing a detailed description of CNT induced changes to GM larval percentage survival, at varying timepoints, along the complete 72h NP toxicity assay. Changes to percentage larval survival was tallied, calculated and presented by the GraphPad software.

Hours	PBS Percentage	Oxidised CNTs Percentage	RAW CNTs Percentage	CMC coated CNTs Percentage	Cyclo Percentage	Cyclo+Oxidised CNTs Percentage	Cyclo+RAW CNTs Percentage	Cyclo+CMC coated CNTs Percentage
0	100	100	100	100	100	100	100	100
20		91.93	88.52	91.93	98.27	92.18	87.09	91.89
23		88.70	60.65	83.87	93.10	90.62		90.54
24	100	88.70	60.65	82.25	93.10	90.62	87.09	90.54
44		70.96		65.80		77.67		84.50
68	90						79.83	78.46
72	90	70.96	60.65	65.80	93.10	77.67	79.83	78.46

Table C3: GM larval percentage survival changes caused by AuNPs during 72h post-NP injections. Table providing a detailed description of AuNP-induced changes to GM larval percentage survival, at varying timepoints, along the complete 72h NP toxicity assay. Changes to percentage larval survival was calculated and presented by the GraphPad software.

Hours	PBS	20nm AuNP	40nm AuNP	60nm AuNP	80nm AuNP	100nm AuNP	Cyclo	Cyclo+20nm AuNP	Cyclo+60nm AuNP	Cyclo+100nm AuNP
	Percentage	Percentage	Percentage	Percentage	Percentage	Percentage	Percentage	Percentage	Percentage	Percentage
0	100	100	100	100	100	100	100	100	100	100
20		93.10		91.95		98.18	98.73	92.30	94.23	94.54
23		71.26	77.77	68.96	86.66		91.13	78.84	90.38	85.45
24	100	71.26	77.77	68.96	86.66	98.18	91.13	78.84	90.38	83.63
26				62.69				67.58	84.35	78.06
44		59.38		56.42		81.81	81.01	45.05	42.17	50.18
45	90			50.15						
49				43.88						
68	80	53.44		37.61		70.90		39.42		39.03
71					100				36.15	
72	80	53.44		37.61		70.90	81.01	39.42	36.15	39.03

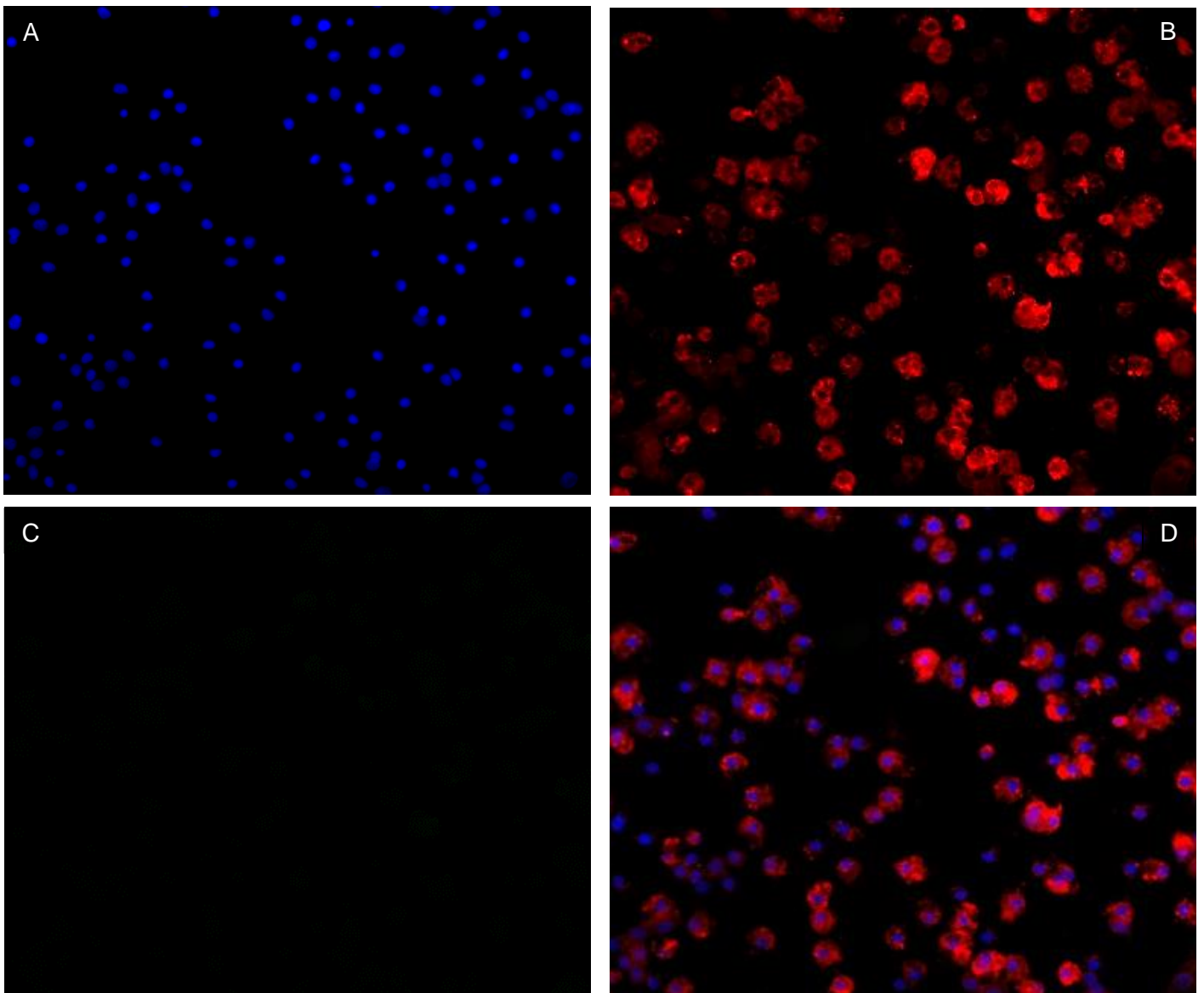
Enlarged fluorescent microscopy images: SPION assay

Figure C1.1: Figure showing x40 magnification fluorescent microscopy images of larval hemocytes, extracted from GM larvae of the PBS control condition (SPION assay). (A), shows the blue channel, with HOECHST 33342 stained dsDNA identifying the nuclei. (B), shows the red channel, where the fluorescent lectin WGA (labelled with Alexa 546) stained the glycoproteins on the plasma membrane. (C), shows the green channel, which will show green fluorescent NPs, if present. (D), shows an overlay image of all the channels.

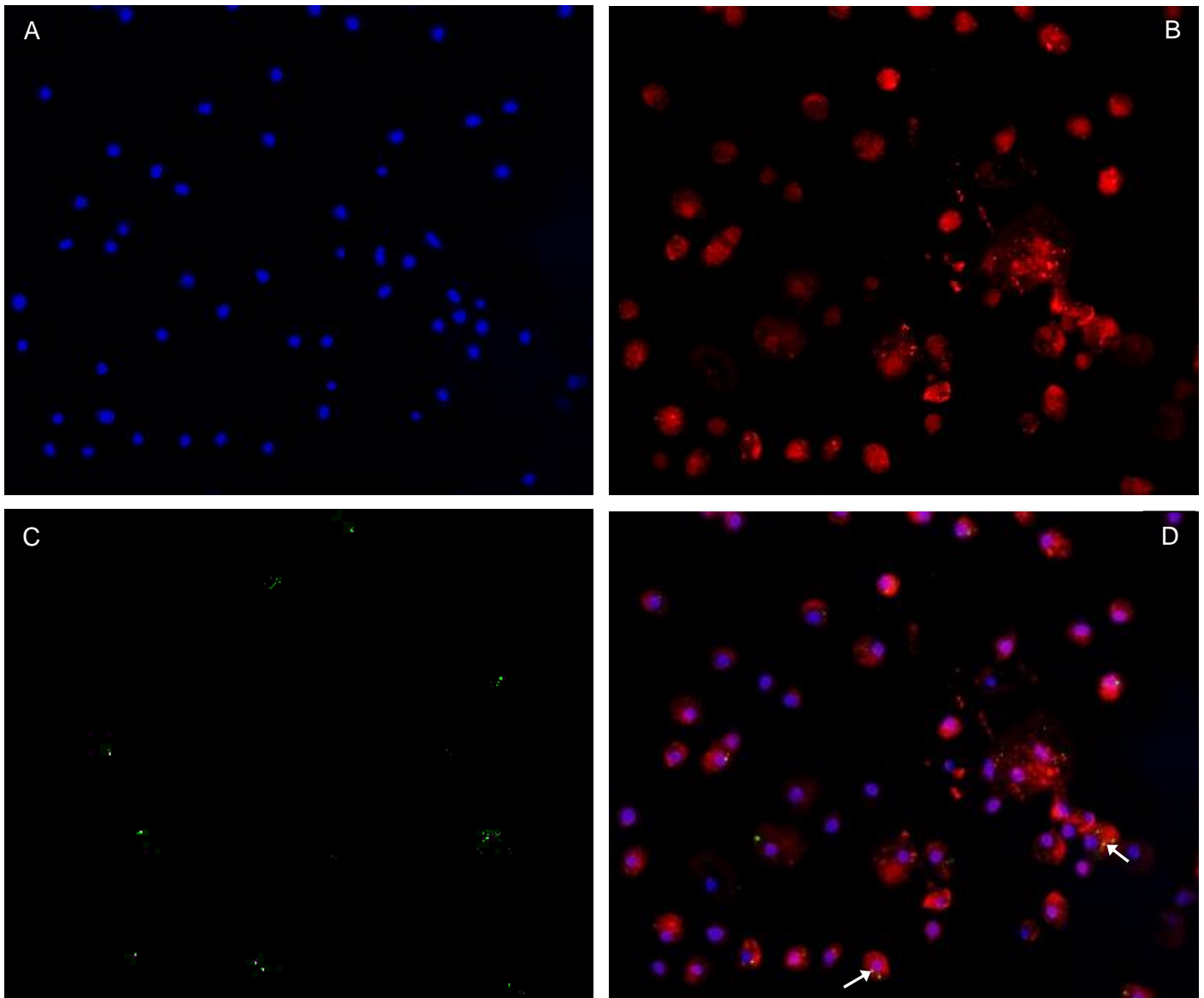


Figure C1.2: Figure showing x40 magnification fluorescent images of hemocytes, extracted from GM larvae of the SC-SPION condition. (A), shows the blue channel, with HOECHST 33342 stained dsDNA identifying the nuclei. (B), shows the red channel, where the fluorescent lectin WGA (labelled with Alexa 546) stained the glycoproteins on the plasma membrane. (C), shows the green channel, where green fluorescent SC-SPIONs that have been taken up by larval hemocytes are shown. (D), shows an overlay image of all the channels and NP uptake by hemocytes are outlined by white arrows.

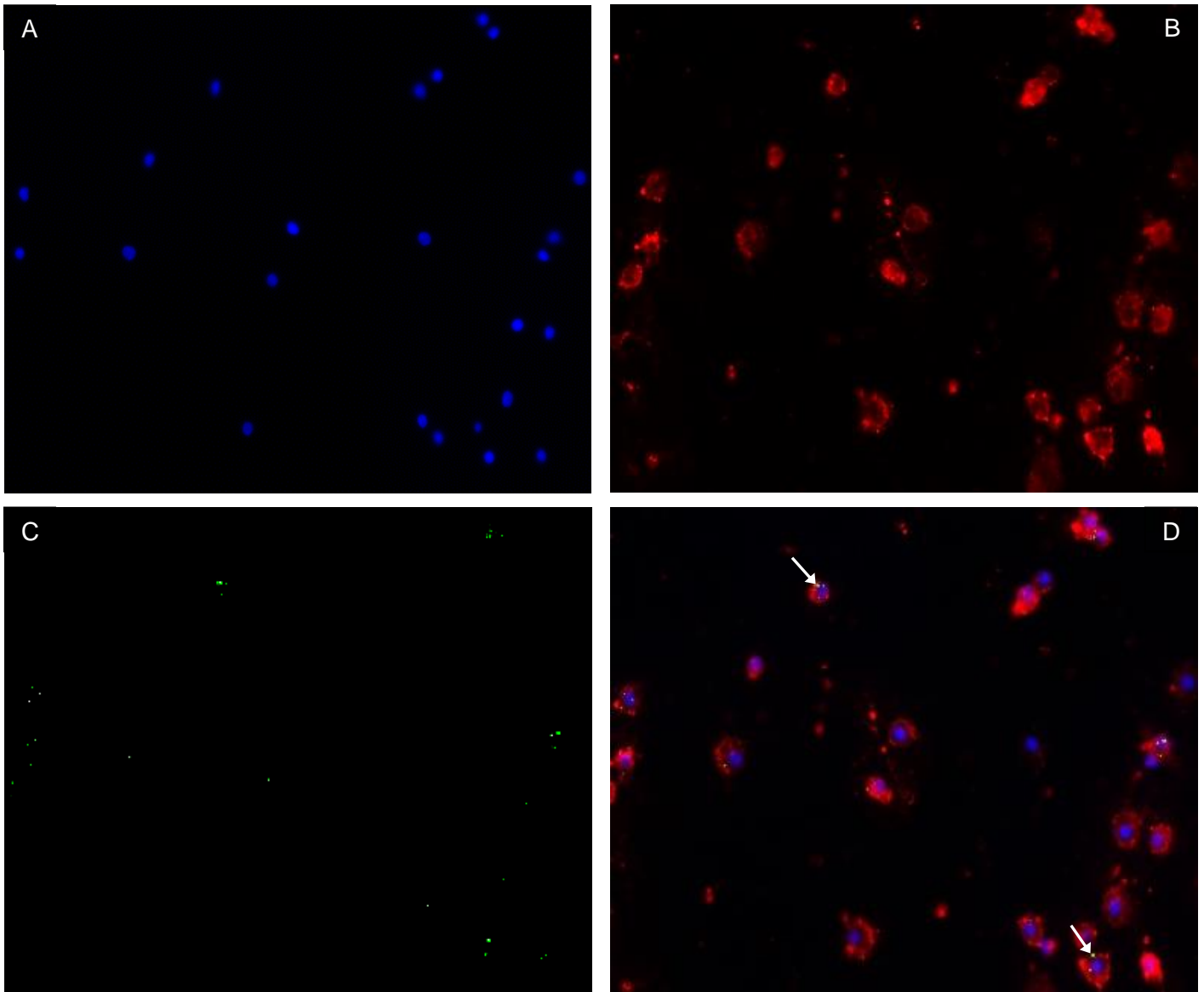


Figure C1.3: Figure showing x40 magnification fluorescent images of hemocytes, extracted from GM larvae of the anionic-SPION condition. (A), shows the blue channel, with HOECHST 33342 stained dsDNA identifying the nuclei. (B), shows the red channel, where the fluorescent lectin WGA (labelled with Alexa 546) stained the glycoproteins on the plasma membrane. (C), shows the green channel, where green fluorescent anionic-SPIONs that have been taken up by larval hemocytes are shown. (D), shows an overlay image of all the channels and NP uptake by hemocytes are outlined by white arrows.

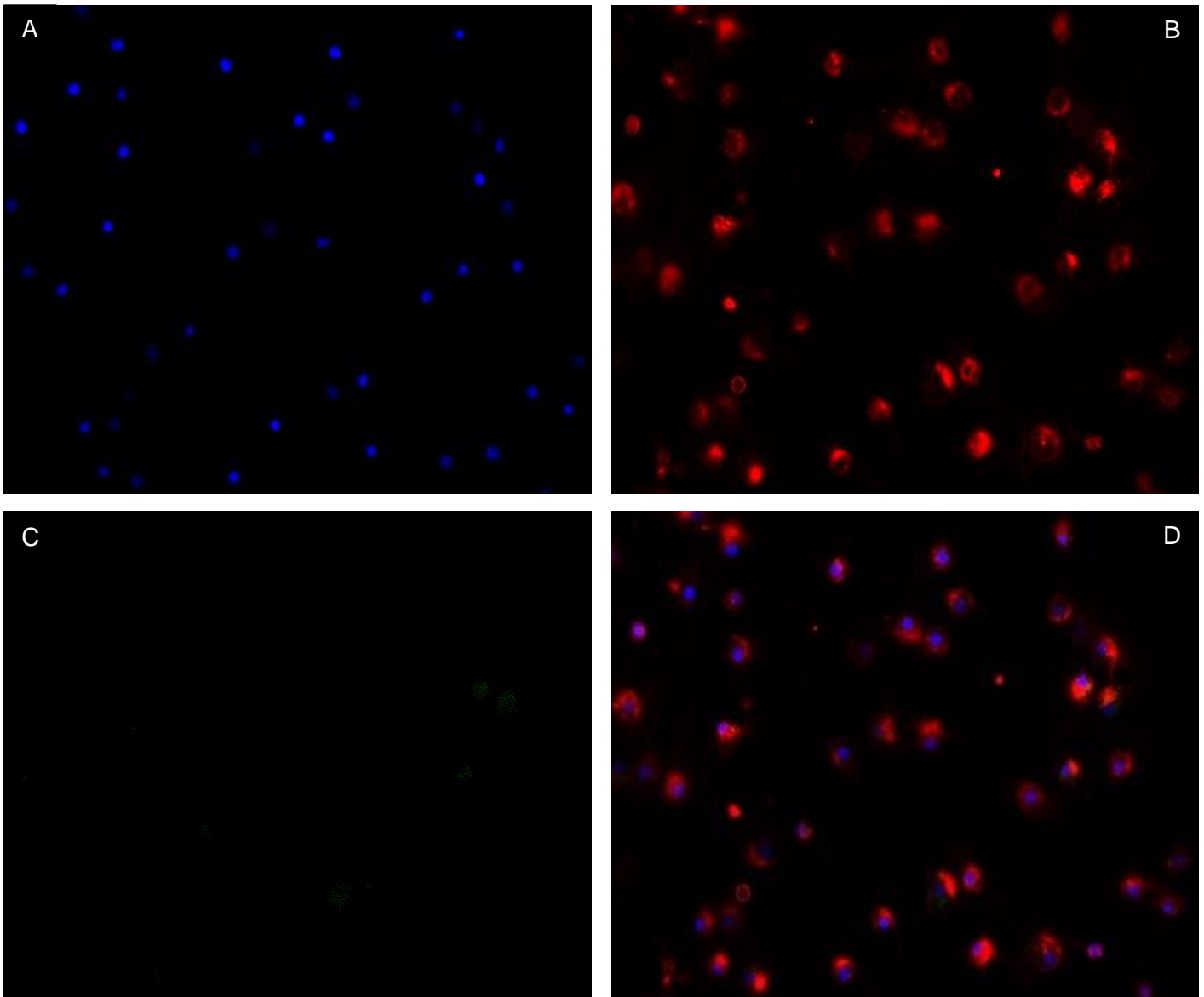


Figure C1.4: Figure showing x40 magnification fluorescent images of hemocytes, extracted from GM larvae of the Cyclophosphamide control condition (SPION assay). (A), shows the blue channel, with HOECHST 33342 stained dsDNA identifying the nuclei. (B), shows the red channel, where the fluorescent lectin WGA (labelled with Alexa 546) stained the glycoproteins on the plasma membrane. (C), shows the green channel, which will show the green fluorescent NPs, if present. (D), shows an overlay image of all the channels.

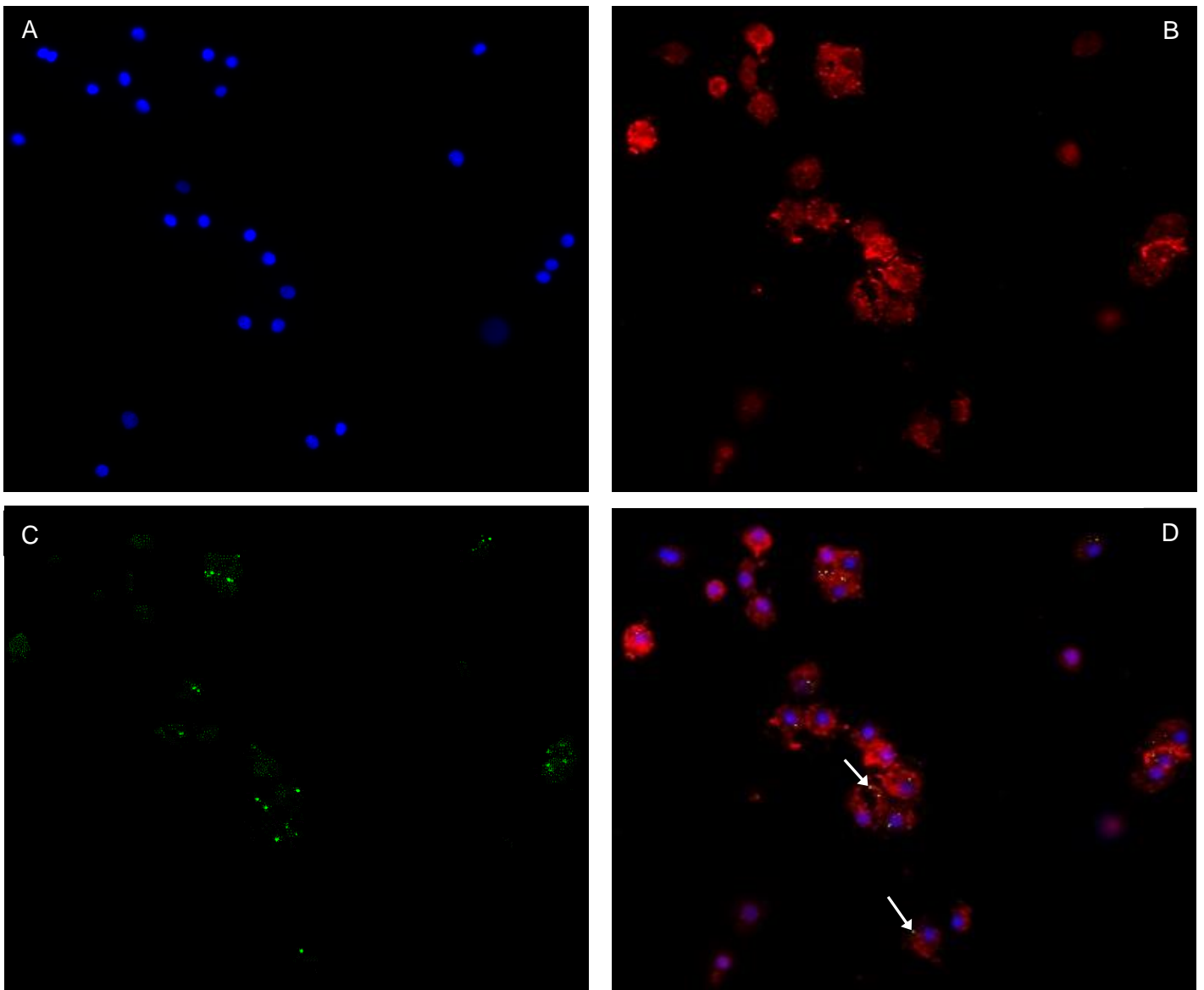


Figure C1.5: Figure showing x40 magnification fluorescent images of hemocytes, extracted from GM larvae of the Cyclophosphamide + SC-SPION condition. (A), shows the blue channel, with HOECHST 33342 stained dsDNA identifying the nuclei. (B), shows the red channel, where the fluorescent lectin WGA (labelled with Alexa 546) stained the glycoproteins on the plasma membrane. (C), shows the green channel, where green fluorescent SC-SPIONs that have been taken up by larval hemocytes are shown. (D), shows an overlay image of all the channels and NP uptake by hemocytes are outlined by white arrows.

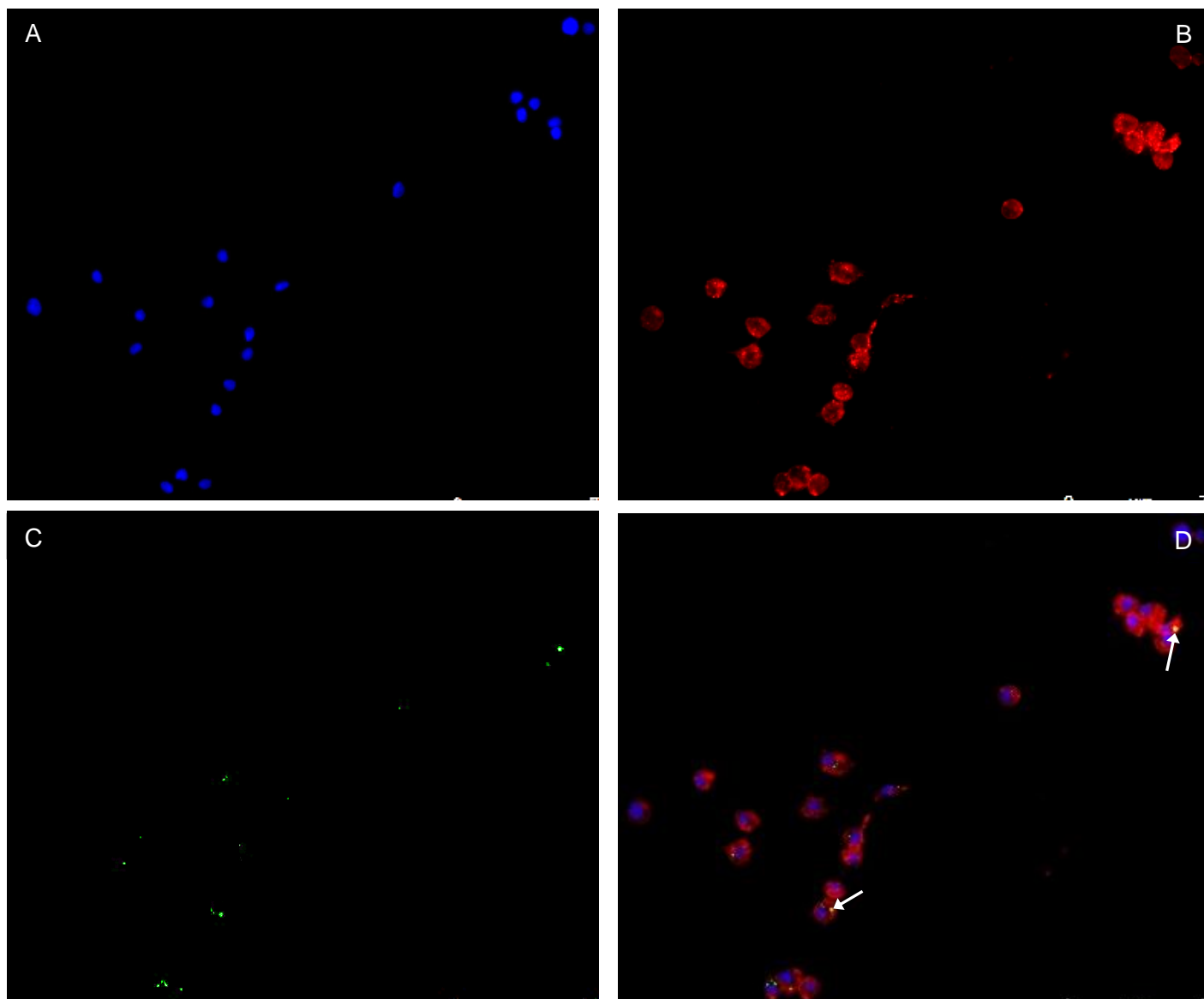


Figure C1.6: Figure showing x40 magnification fluorescent images of hemocytes, extracted from GM larvae of the Cyclophosphamide + anionic-SPION condition. (A), shows the blue channel, with HOECHST 33342 stained dsDNA identifying the nuclei. (B), shows the red channel, where the fluorescent lectin WGA (labelled with Alexa 546) stained the glycoproteins on the plasma membrane. (C), shows the green channel, where green fluorescent anionic-SPIONs that have been taken up by larval hemocytes are shown. (D), shows an overlay image of all the channels and NP uptake by hemocytes are outlined by white arrows.

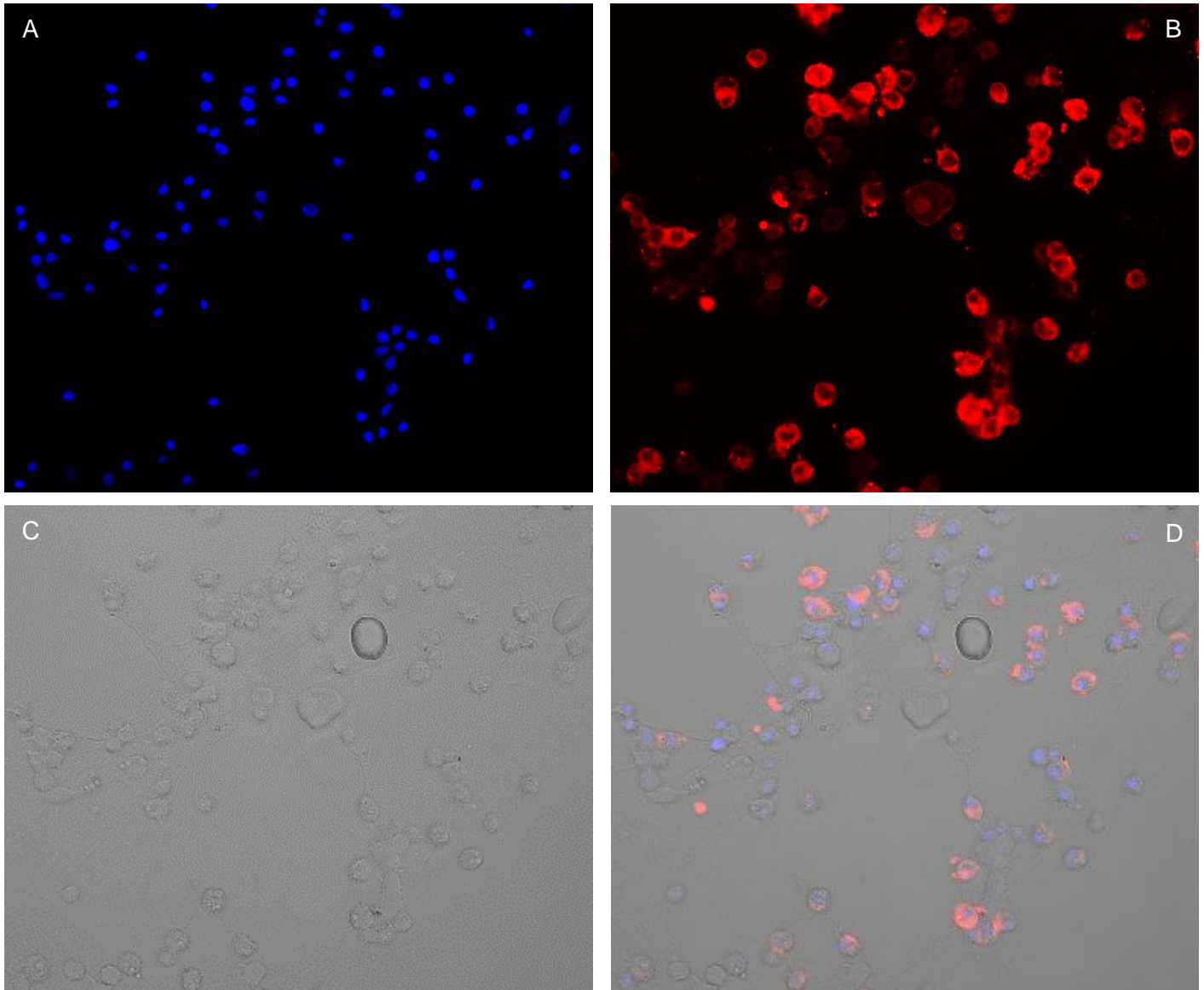
Enlarged fluorescent microscopy images: CNT assay

Figure C2.1: Figure showing x40 magnification fluorescent images of hemocytes, extracted from GM larvae of the PBS control condition (CNT assay). (A), shows the blue channel, with HOECHST 33342 stained dsDNA identifying the nuclei. (B), shows the red channel, where the fluorescent lectin WGA (labelled with Alexa 546) stained the glycoproteins on the plasma membrane. (C), shows the bright field channel, which will show the dark non-fluorescent CNTs, if present. (D), shows an overlay image of all the channels.

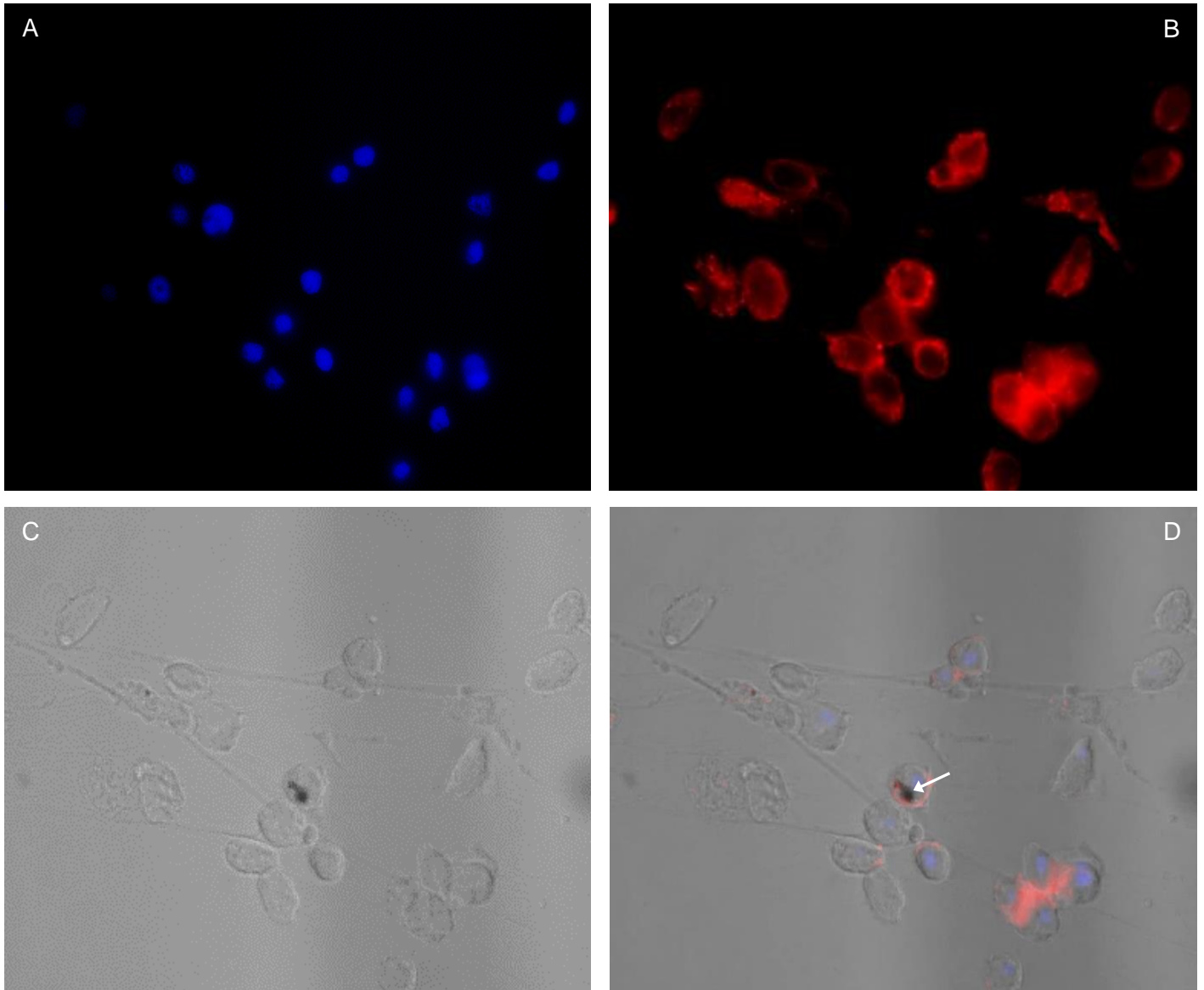


Figure C2.2: Figure showing x100 magnification fluorescent images of hemocytes, extracted from GM larvae of the Oxidised CNT condition. (A), shows the blue channel, with HOECHST 33342 stained dsDNA identifying the nuclei. (B), shows the red channel, where the fluorescent lectin WGA (labelled with Alexa 546) stained the glycoproteins on the plasma membrane. (C), shows the bright field channel, where Oxidised CNTs that have been taken up by larval hemocytes are shown. (D), shows an overlay image of all the channels and NP uptake by hemocytes are outlined by white arrows.

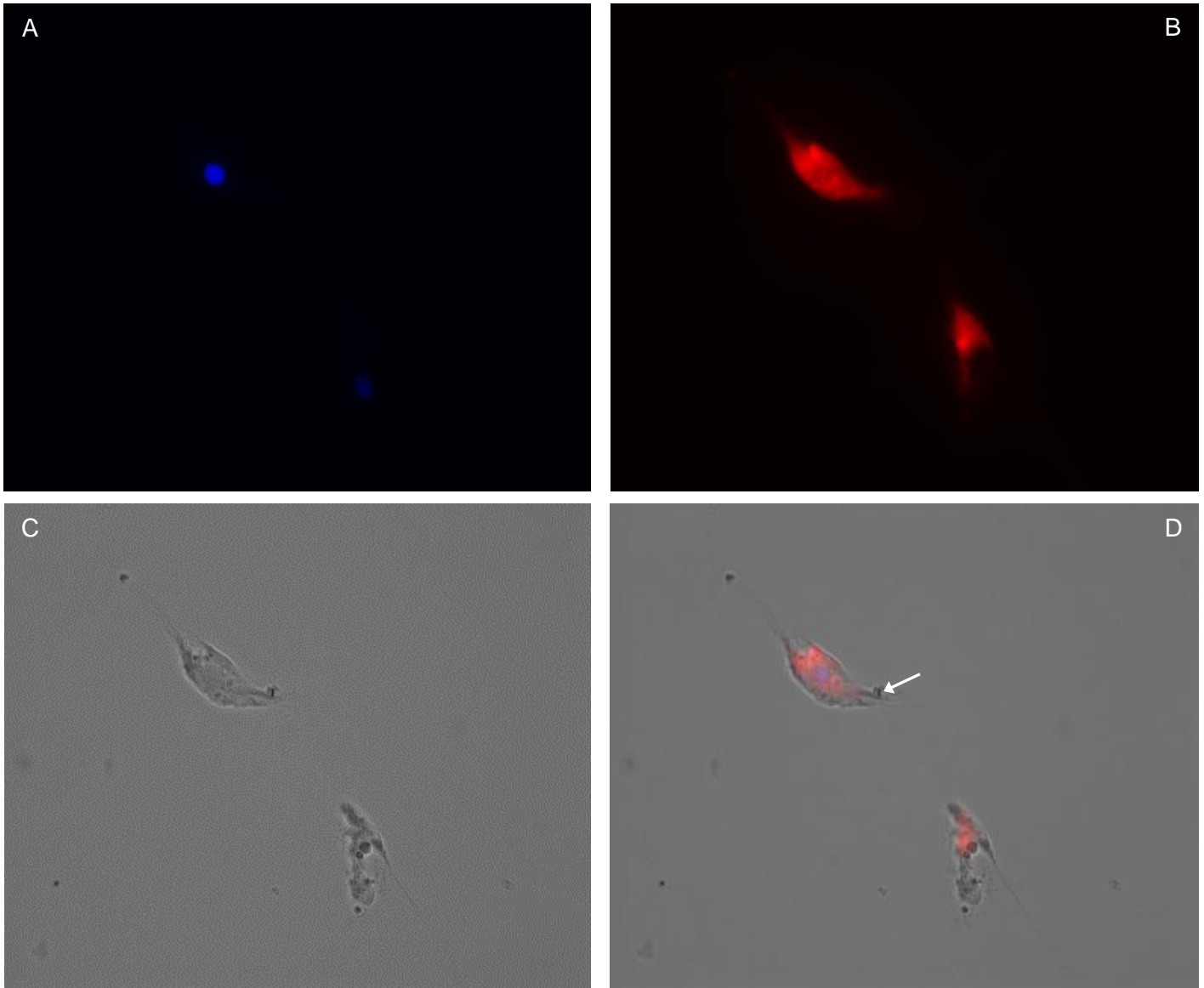


Figure C2.3: Figure showing x100 magnification fluorescent images of hemocytes, extracted from GM larvae of the RAW CNT condition. (A), shows the blue channel, with HOECHST 33342 stained dsDNA identifying the nuclei. (B), shows the red channel, where the fluorescent lectin WGA (labelled with Alexa 546) stained the glycoproteins on the plasma membrane. (C), shows the bright field channel, where RAW CNTs that have been taken up by larval hemocytes are shown. (D), shows an overlay image of all the channels and NP uptake by hemocytes are outlined by white arrows.

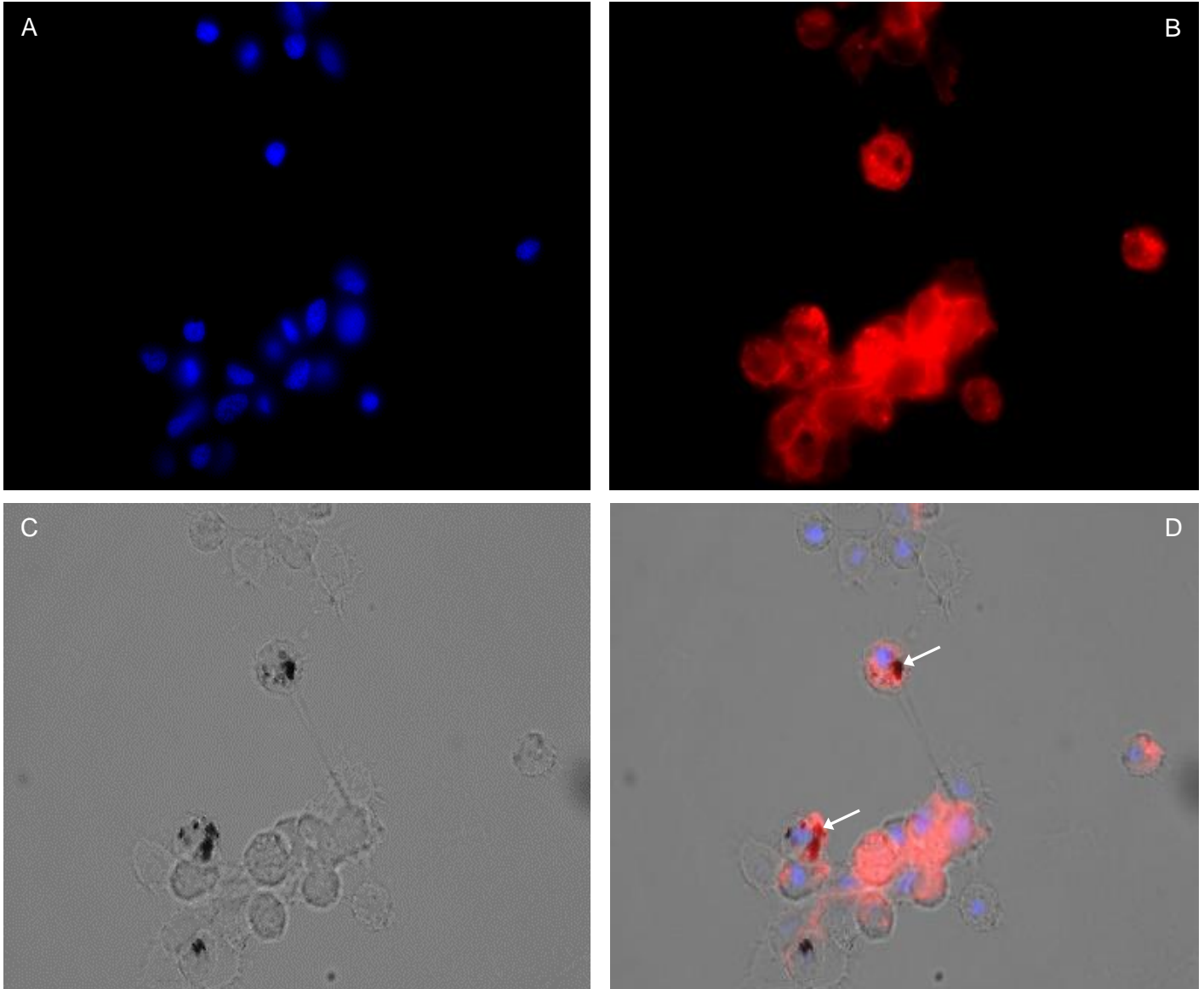


Figure C2.4: Figure showing x100 magnification fluorescent images of hemocytes, extracted from GM larvae of the CMC-coated CNT condition. (A), shows the blue channel, with HOECHST 33342 stained dsDNA identifying the nuclei. (B), shows the red channel, where the fluorescent lectin WGA (labelled with Alexa 546) stained the glycoproteins on the plasma membrane. (C), shows the bright field channel, where CMC-coated CNTs that have been taken up by larval hemocytes are shown. (D), shows an overlay image of all the channels and NP uptake by hemocytes are outlined by white arrows.

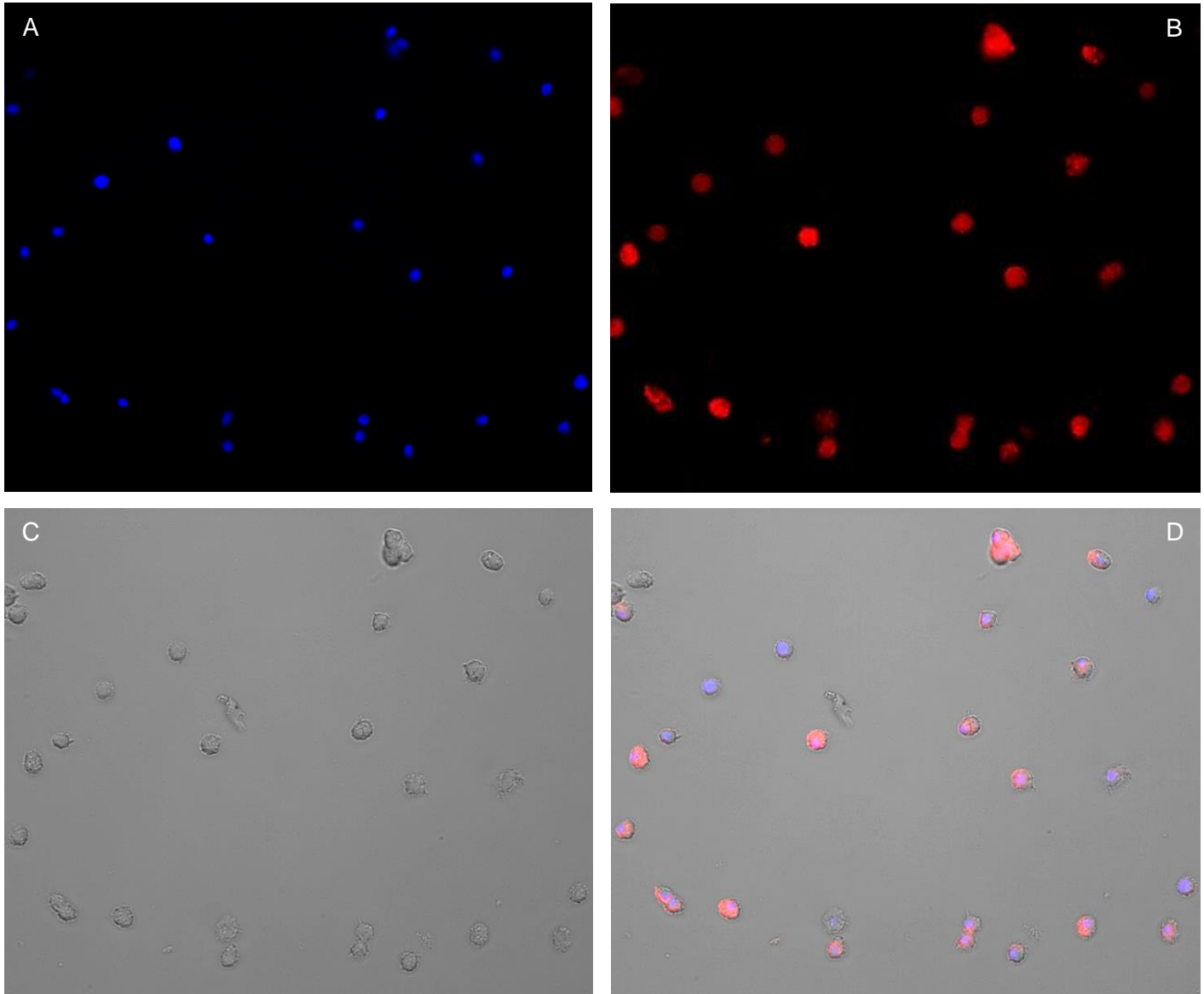


Figure C2.5: Figure showing x40 magnification fluorescent images of hemocytes, extracted from GM larvae of the Cyclophosphamide control condition (CNT assay). (A), shows the blue channel, with HOECHST 33342 stained dsDNA identifying the nuclei. (B), shows the red channel, where the fluorescent lectin WGA (labelled with Alexa 546) stained the glycoproteins on the plasma membrane. (C), shows the bright field channel, which will show the dark non-fluorescent CNTs, if present. (D), shows an overlay image of all the channels.

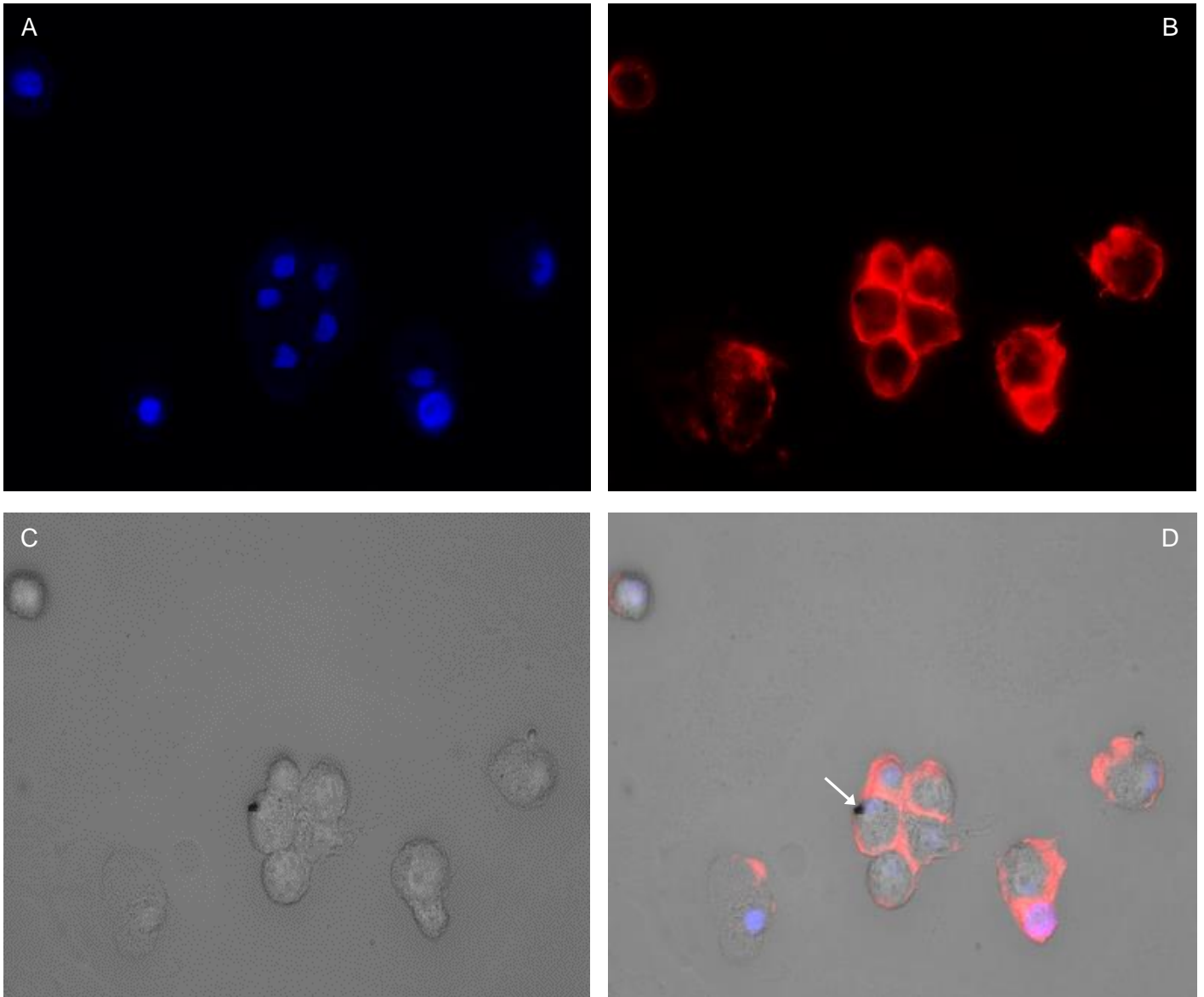


Figure C2.6: Figure showing x100 magnification fluorescent images of hemocytes, extracted from GM larvae of the Cyclophosphamide + Oxidised CNT. (A), shows the blue channel, with HOECHST 33342 stained dsDNA identifying the nuclei. (B), shows the red channel, where the fluorescent lectin WGA (labelled with Alexa 546) stained the glycoproteins on the plasma membrane. (C), shows the bright field channel, where Oxidised CNTs that have been taken up by larval hemocytes are shown. (D), shows an overlay image of all the channels and NP uptake by hemocytes are outlined by white arrows.

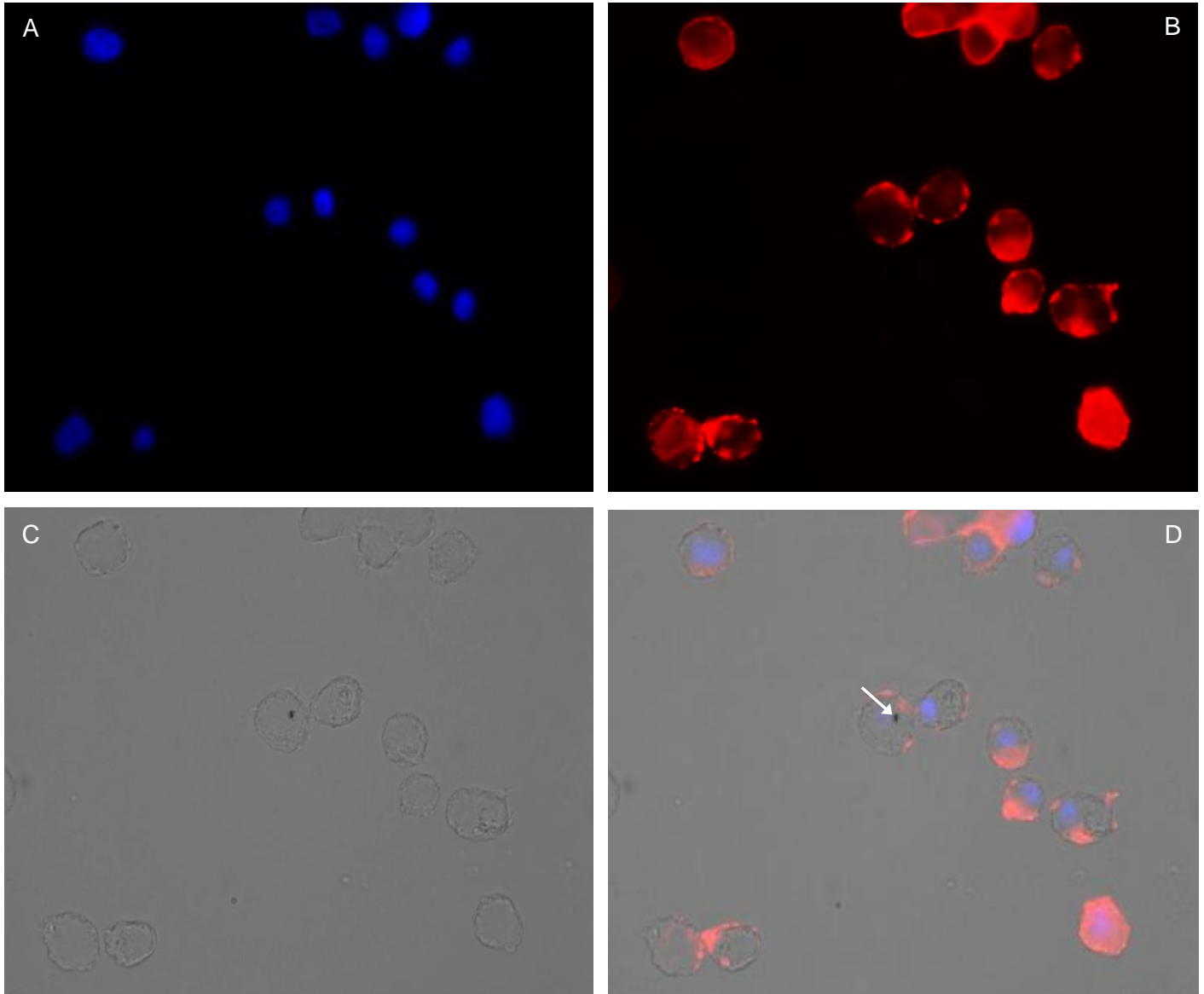


Figure C2.7: Figure showing x100 magnification fluorescent images of hemocytes, extracted from GM larvae of the Cyclophosphamide + RAW CNT. (A), shows the blue channel, with HOECHST 33342 stained dsDNA identifying the nuclei. (B), shows the red channel, where the fluorescent lectin WGA (labelled with Alexa 546) stained the glycoproteins on the plasma membrane. (C), shows the bright field channel, where RAW CNTs that have been taken up by larval hemocytes are shown. (D), shows an overlay image of all the channels and NP uptake by hemocytes are outlined by white arrows.

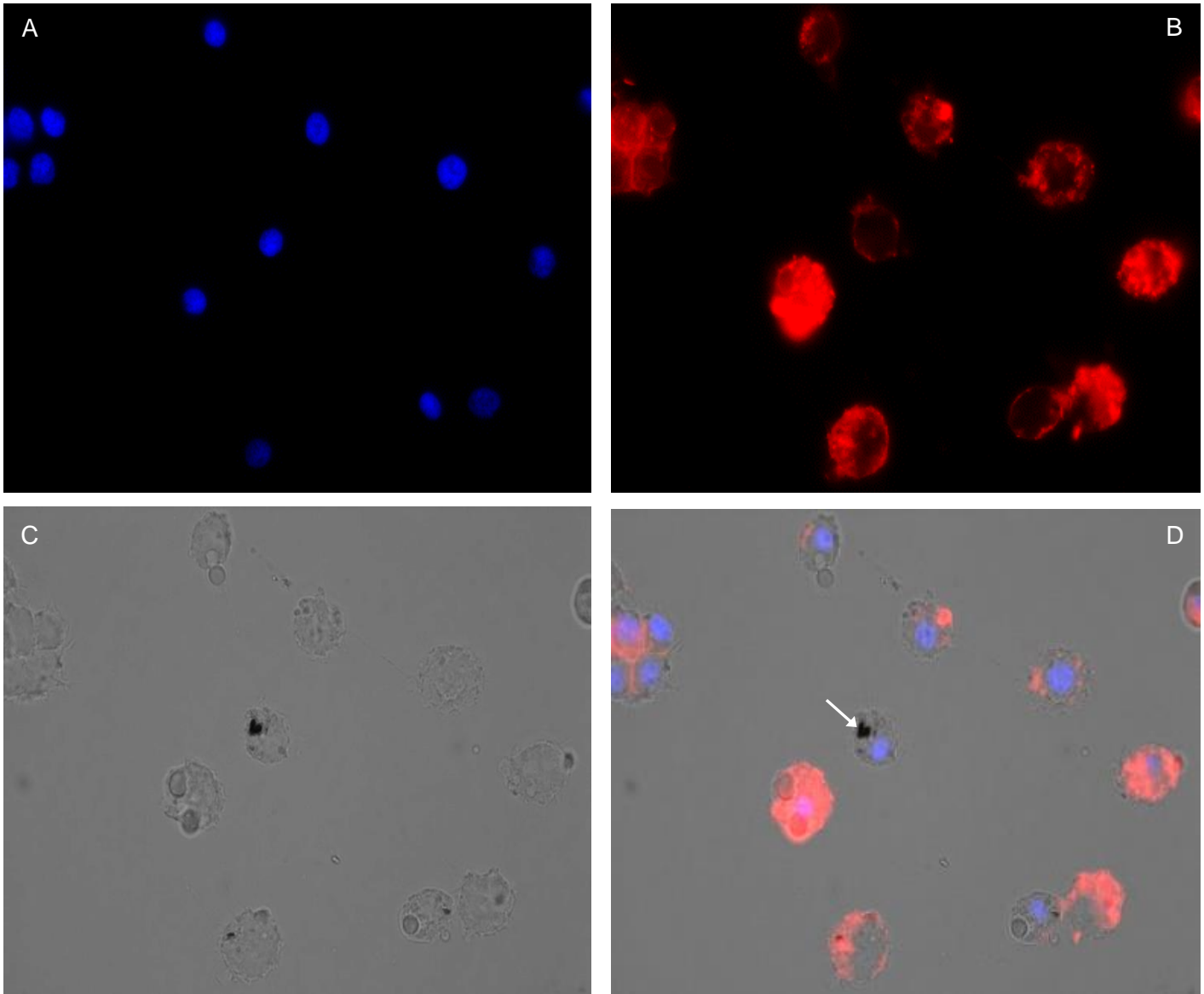


Figure C2.8: Figure showing x100 magnification fluorescent images of hemocytes, extracted from GM larvae of the Cyclophosphamide + CMC-coated CNT. (A), shows the blue channel, with HOECHST 33342 stained dsDNA identifying the nuclei. (B), shows the red channel, where the fluorescent lectin WGA (labelled with Alexa 546) stained the glycoproteins on the plasma membrane. (C), shows the bright field channel, where CMC-coated CNTs that have been taken up by larval hemocytes are shown. (D), shows an overlay image of all the channels and NP uptake by hemocytes are outlined by white arrows.

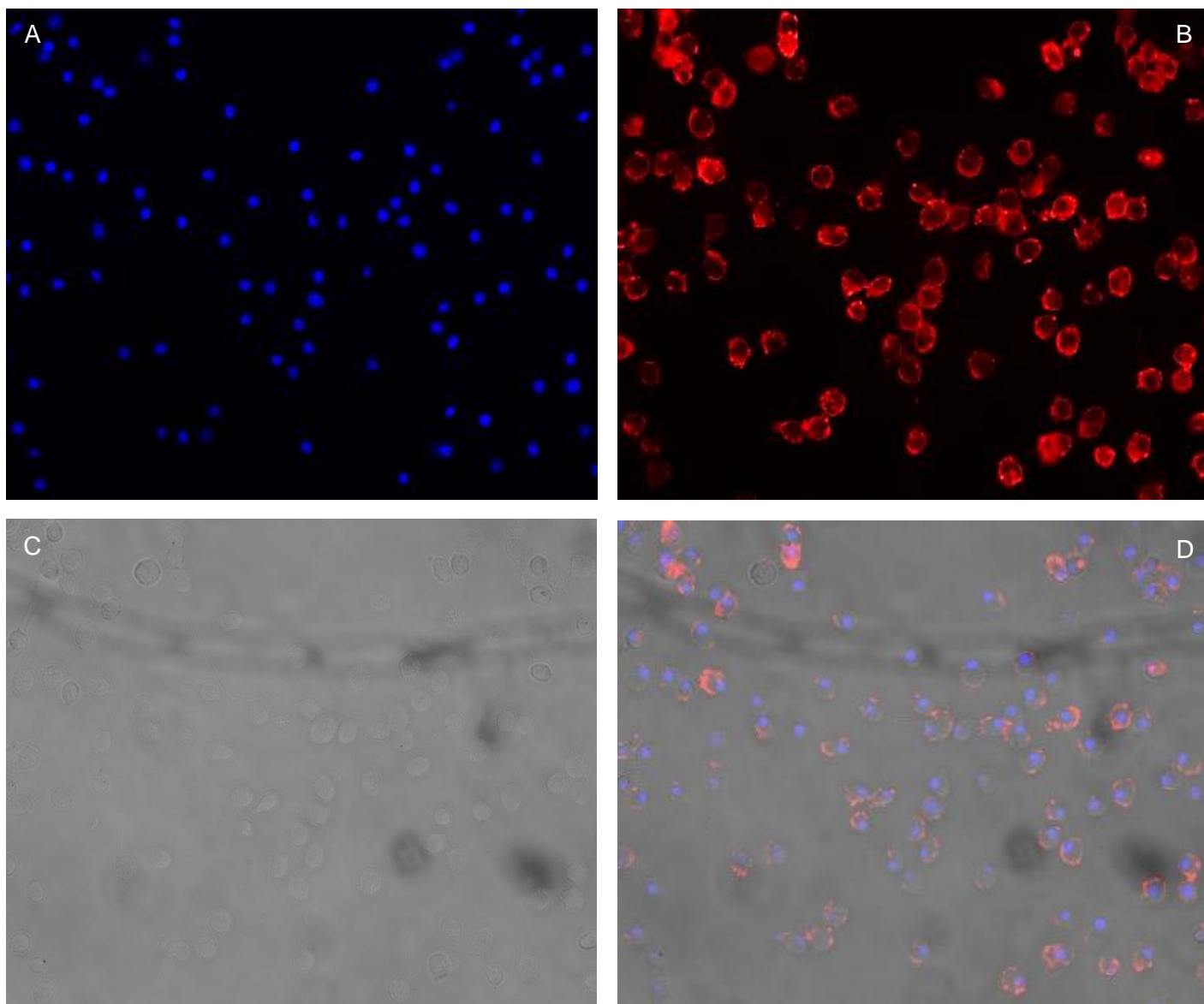
Enlarged fluorescent microscopy images: AuNP assay

Figure C3.1: Figure showing x40 magnification fluorescent images of hemocytes, extracted from GM larvae of the PBS control condition (AuNP assay). (A), shows the blue channel, with HOECHST 33342 stained dsDNA identifying the nuclei. (B), shows the red channel, where the fluorescent lectin WGA (labelled with Alexa 546) stained the glycoproteins on the plasma membrane. (C), shows the bright field channel, which will show the dark non-fluorescent AuNPs, if present. (D), shows an overlay image of all the channels.

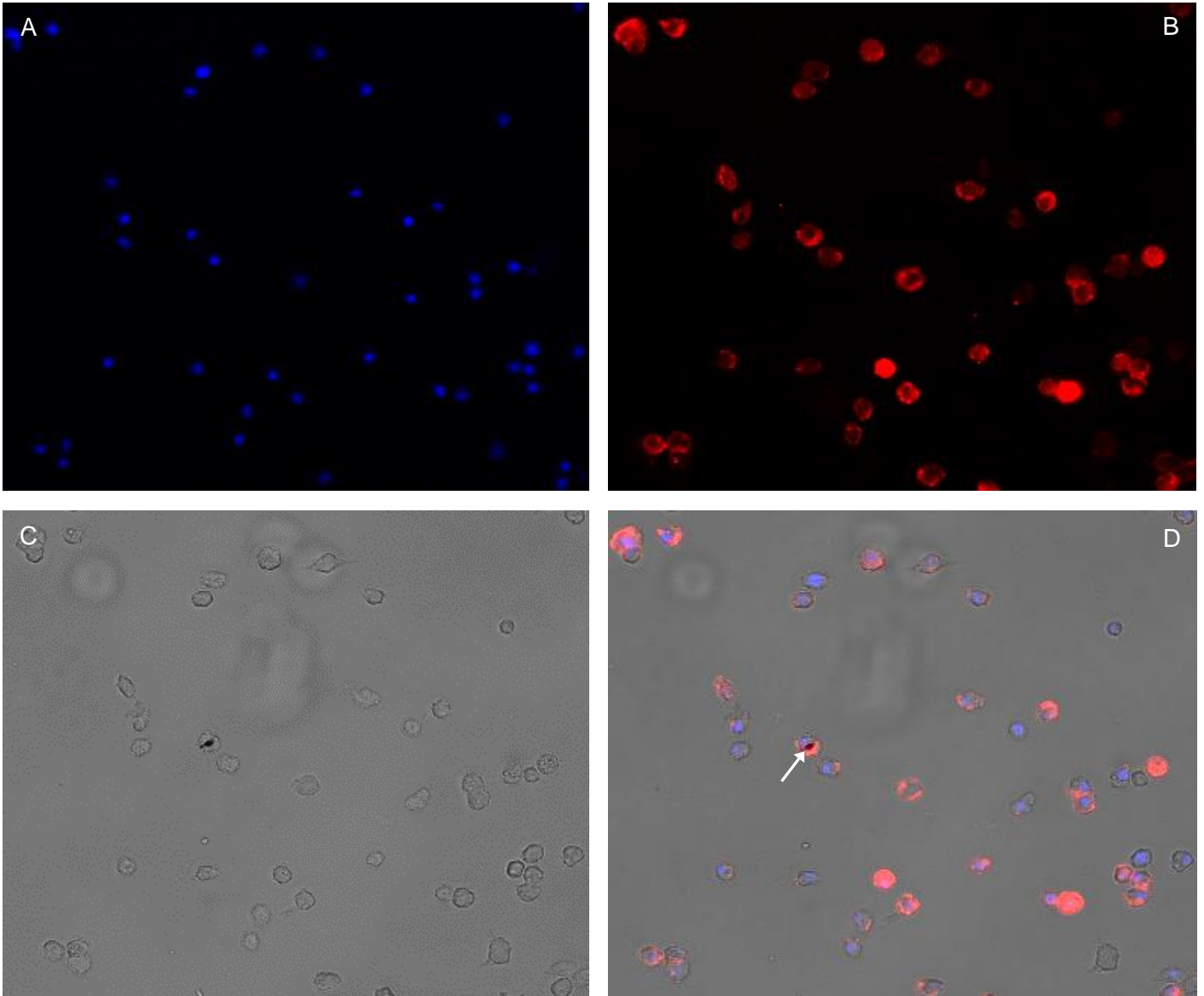


Figure C3.2: Figure showing x40 magnification fluorescent images of hemocytes, extracted from GM larvae of the 20nm AuNP condition. (A), shows the blue channel, with HOECHST 33342 stained dsDNA identifying the nuclei. (B), shows the red channel, where the fluorescent lectin WGA (labelled with Alexa 546) stained the glycoproteins on the plasma membrane. (C), shows the bright field channel, where 20nm AuNPs that have been taken up by larval hemocytes are shown. (D), shows an overlay image of all the channels and NP uptake by hemocytes are outlined by white arrows.

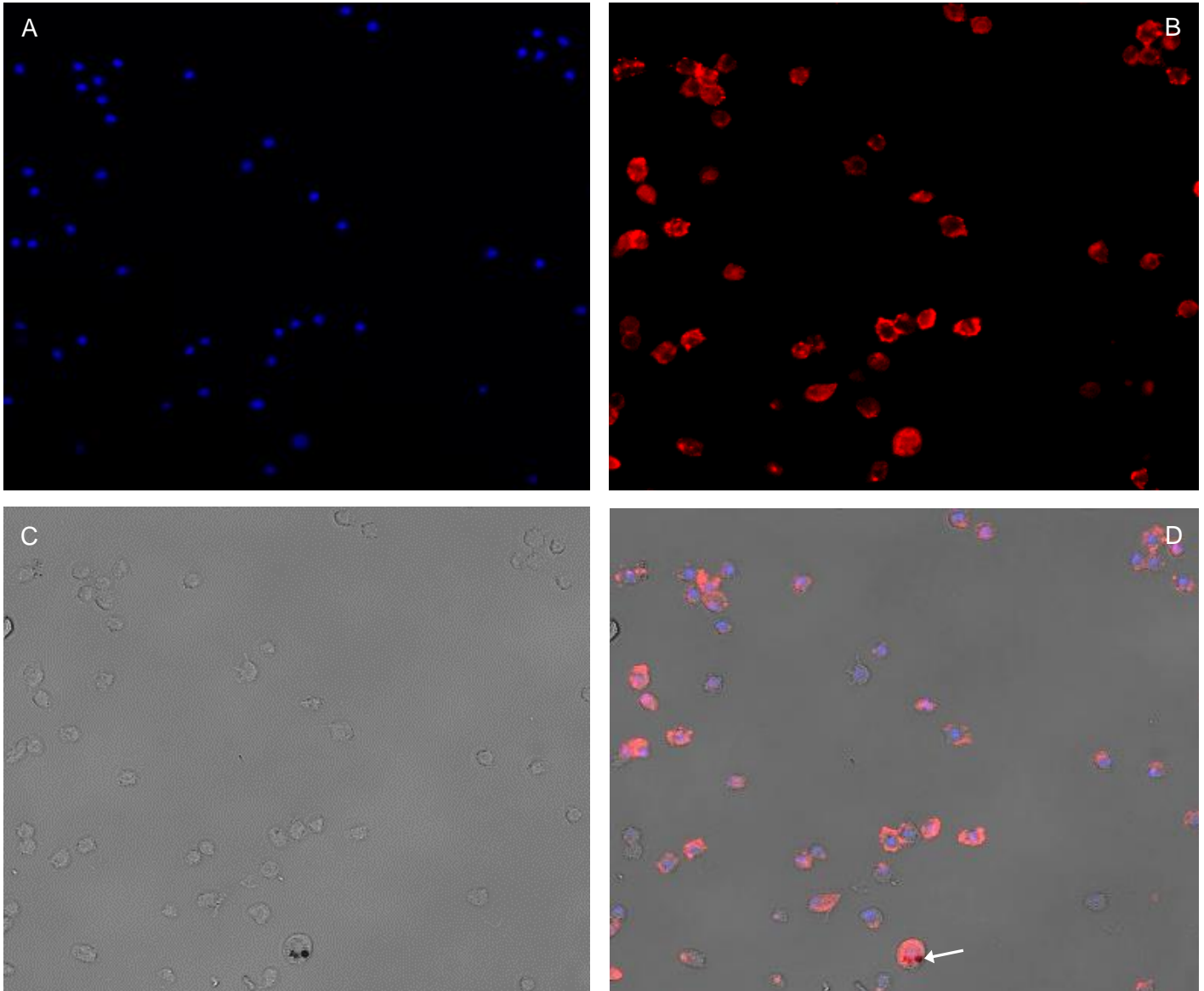


Figure C3.3: Figure showing x40 magnification fluorescent images of hemocytes, extracted from GM larvae of the 40nm AuNP condition. (A), shows the blue channel, with HOECHST 33342 stained dsDNA identifying the nuclei. (B), shows the red channel, where the fluorescent lectin WGA (labelled with Alexa 546) stained the glycoproteins on the plasma membrane. (C), shows the bright field channel, where 40nm AuNPs that have been taken up by larval hemocytes are shown. (D), shows an overlay image of all the channels and NP uptake by hemocytes are outlined by white arrows.

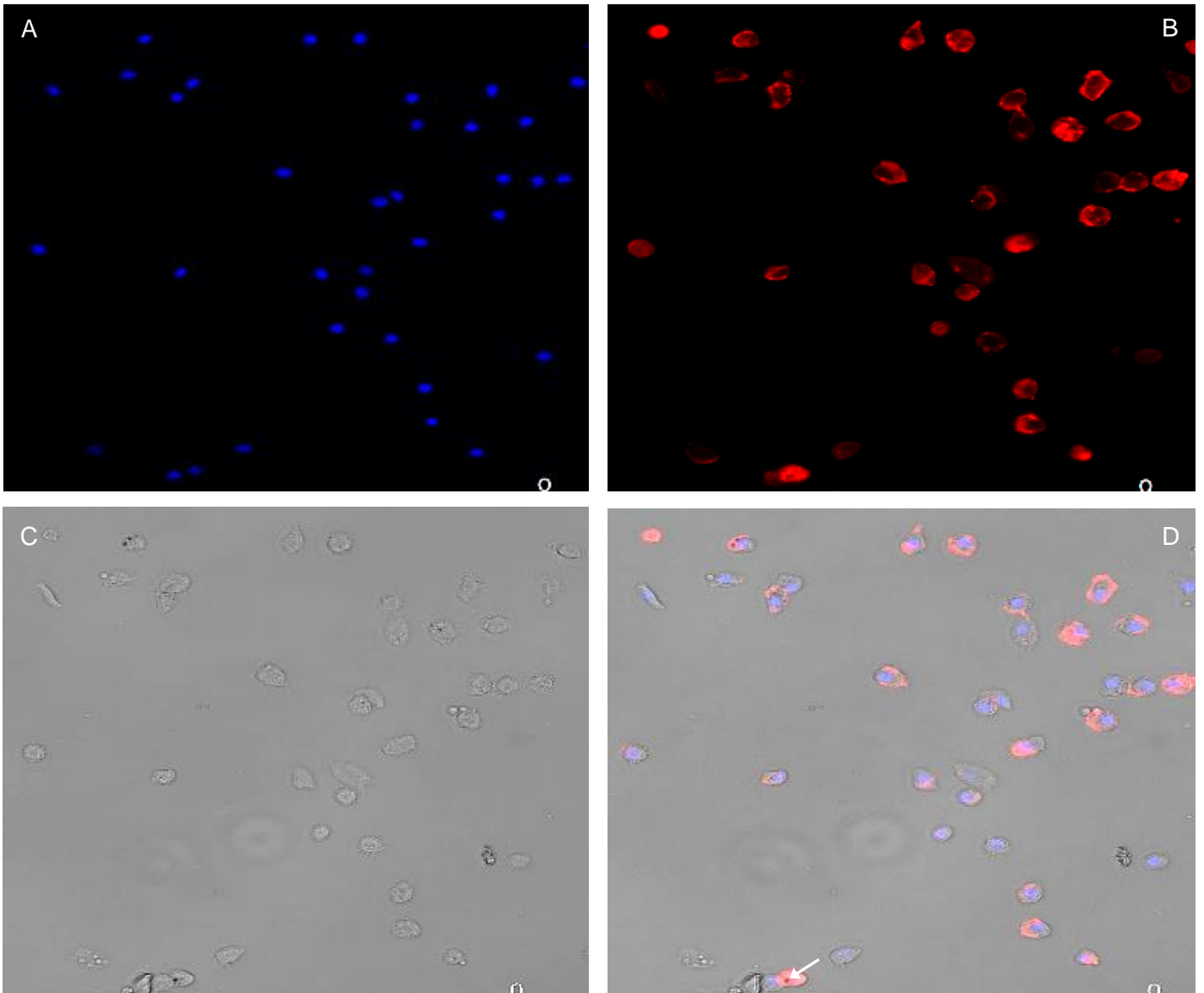


Figure C3.4: Figure showing x40 magnification fluorescent images of hemocytes, extracted from GM larvae of the 60nm AuNP condition. (A), shows the blue channel, with HOECHST 33342 stained dsDNA identifying the nuclei. (B), shows the red channel, where the fluorescent lectin WGA (labelled with Alexa 546) stained the glycoproteins on the plasma membrane. (C), shows the bright field channel, where 60nm AuNPs that have been taken up by larval hemocytes are shown. (D), shows an overlay image of all the channels and NP uptake by hemocytes are outlined by white arrows.

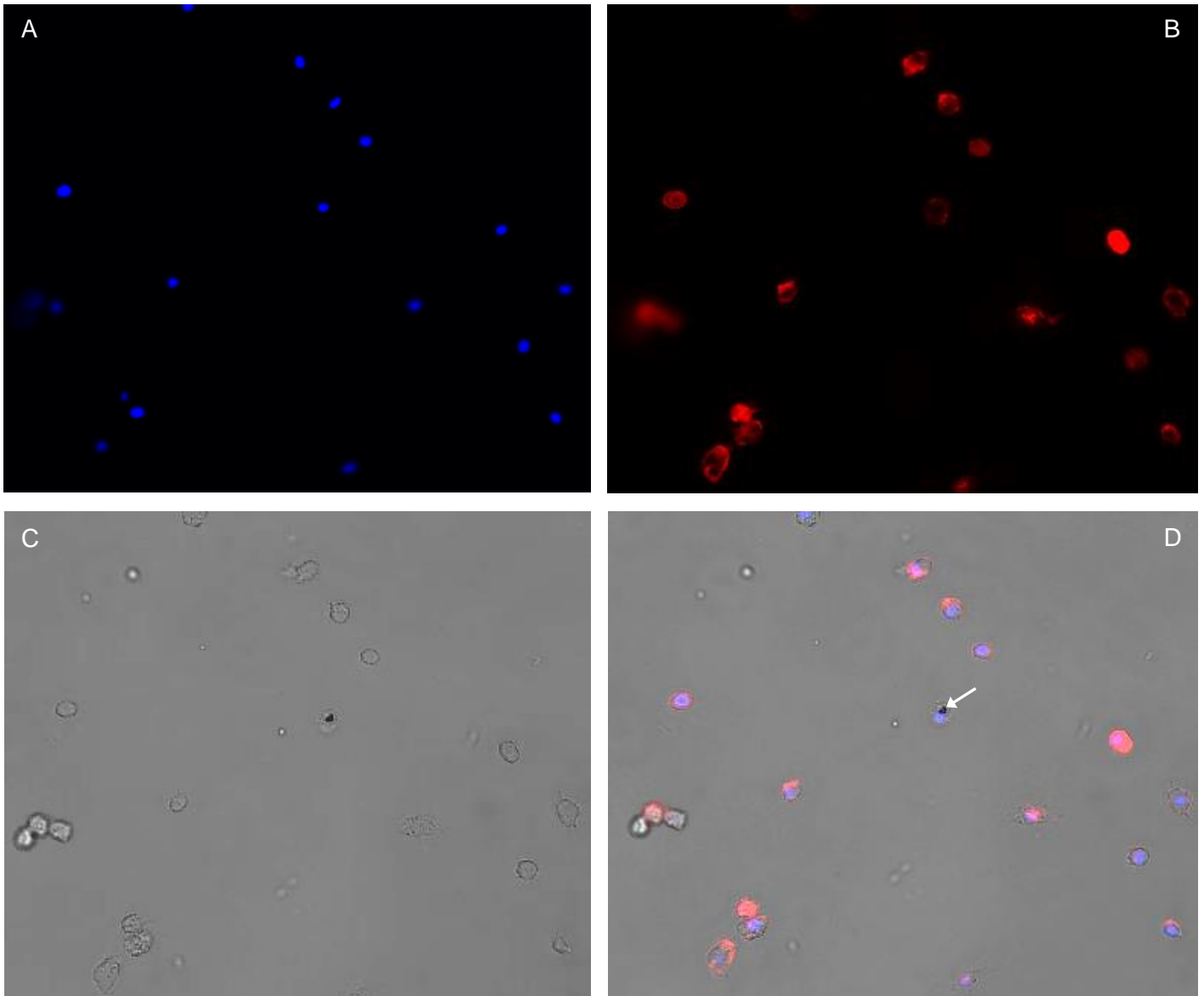


Figure C3.5: Figure showing x40 magnification fluorescent images of hemocytes, extracted from GM larvae of the 80nm AuNP condition. (A), shows the blue channel, with HOECHST 33342 stained dsDNA identifying the nuclei. (B), shows the red channel, where the fluorescent lectin WGA (labelled with Alexa 546) stained the glycoproteins on the plasma membrane. (C), shows the bright field channel, where 80nm AuNPs that have been taken up by larval hemocytes are shown. (D), shows an overlay image of all the channels and NP uptake by hemocytes are outlined by white arrows.

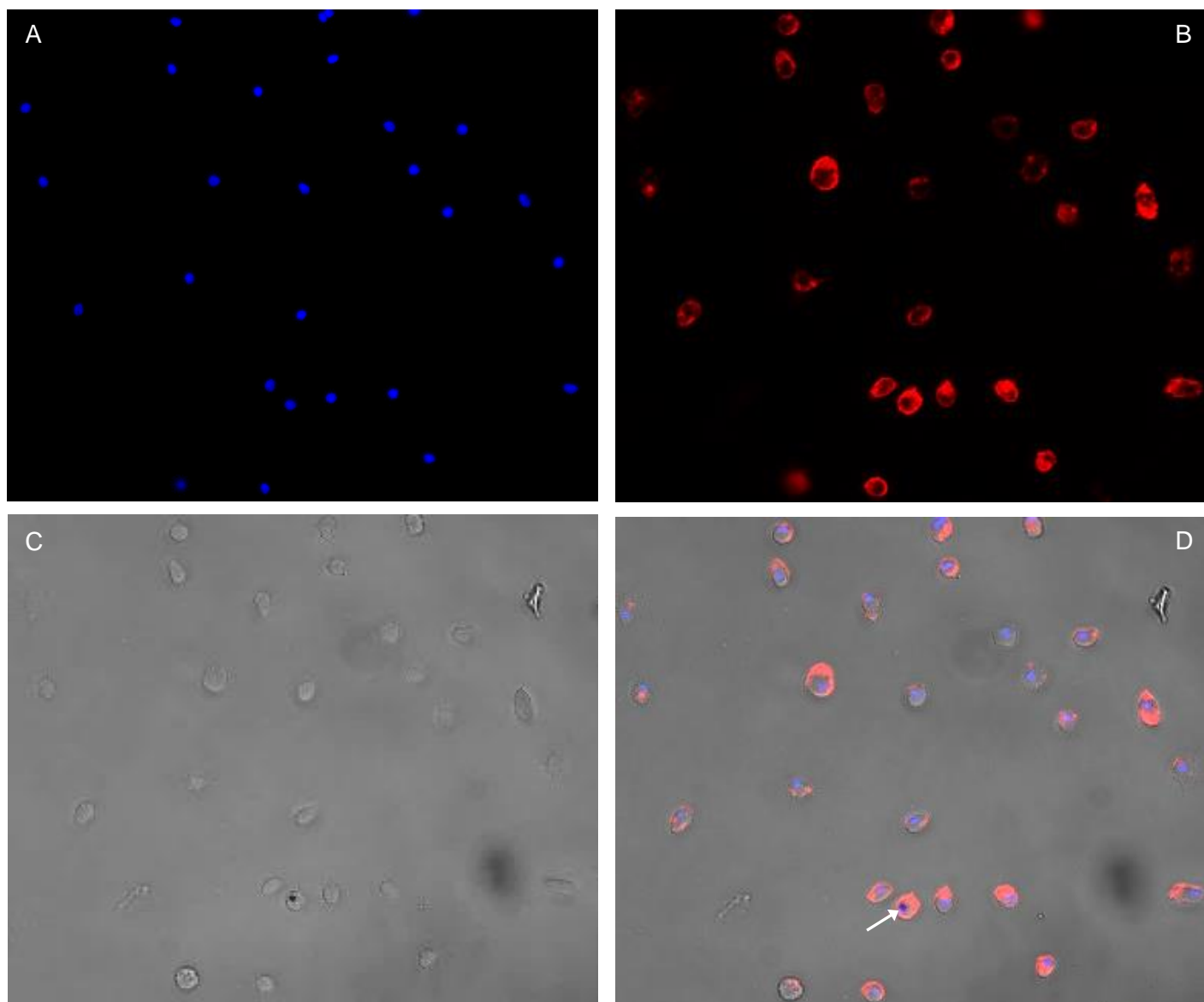


Figure C3.6: Figure showing x40 magnification fluorescent images of hemocytes, extracted from GM larvae of the 100nm AuNP condition. (A), shows the blue channel, with HOECHST 33342 stained dsDNA identifying the nuclei. (B), shows the red channel, where the fluorescent lectin WGA (labelled with Alexa 546) stained the glycoproteins on the plasma membrane. (C), shows the bright field channel, where 100nm AuNPs that have been taken up by larval hemocytes are shown. (D), shows an overlay image of all the channels and NP uptake by hemocytes are outlined by white arrows.

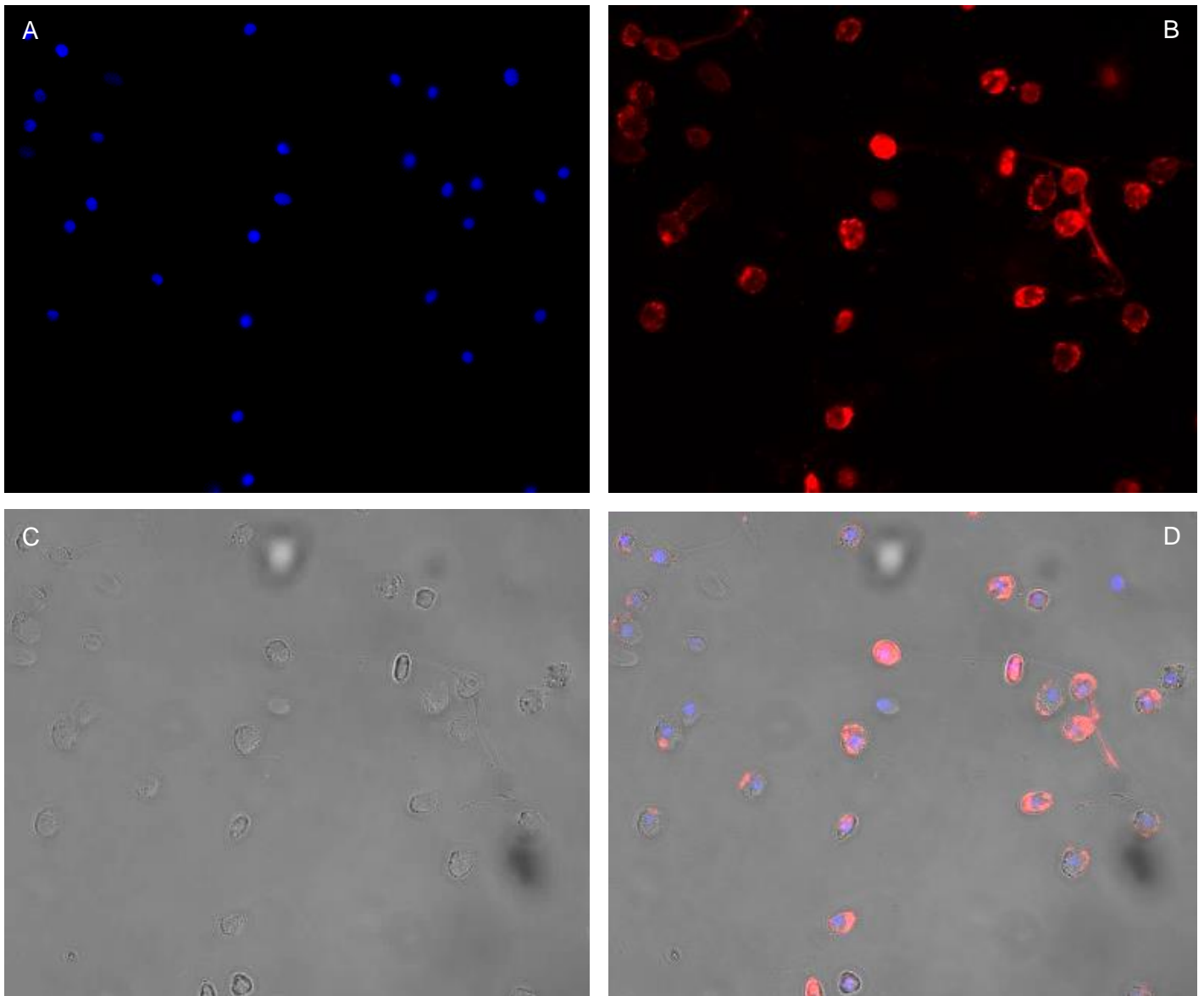


Figure C3.7: Figure showing x40 magnification fluorescent images of hemocytes, extracted from GM larvae of the Cyclophosphamide control condition (AuNP assay). (A), shows the blue channel, with HOECHST 33342 stained dsDNA identifying the nuclei. (B), shows the red channel, where the fluorescent lectin WGA (labelled with Alexa 546) stained the glycoproteins on the plasma membrane. (C), shows the bright field channel, which will show the dark non-fluorescent AuNPs, if present. (D), shows an overlay image of all the channels.

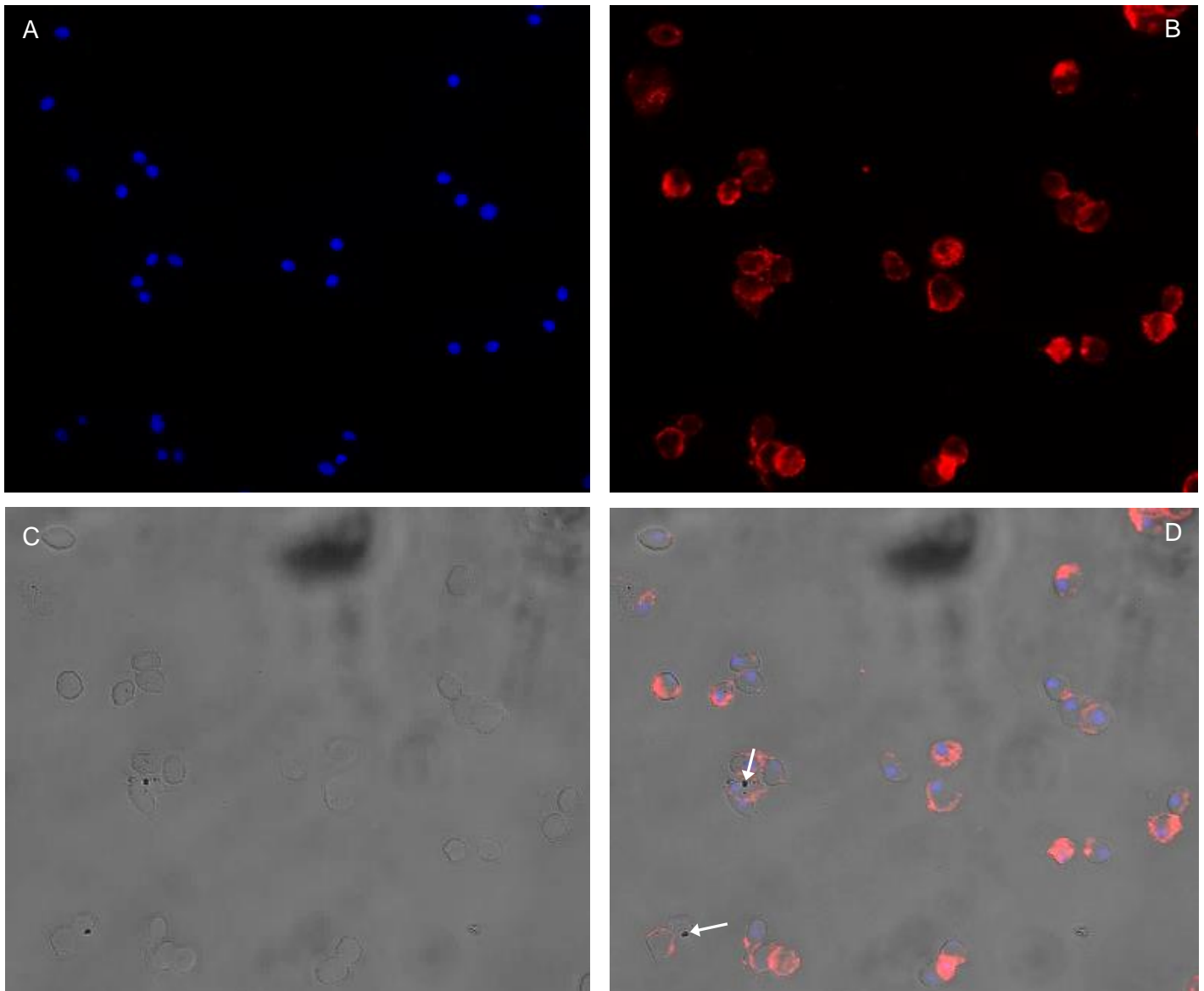


Figure C3.8: Figure showing x40 magnification fluorescent images of hemocytes, extracted from GM larvae of the Cyclophosphamide + 20nm AuNP condition. (A), shows the blue channel, with HOECHST 33342 stained dsDNA identifying the nuclei. (B), shows the red channel, where the fluorescent lectin WGA (labelled with Alexa 546) stained the glycoproteins on the plasma membrane. (C), shows the bright field channel, where 20nm AuNPs that have been taken up by larval hemocytes are shown. (D), shows an overlay image of all the channels and NP uptake by hemocytes are outlined by white arrows.

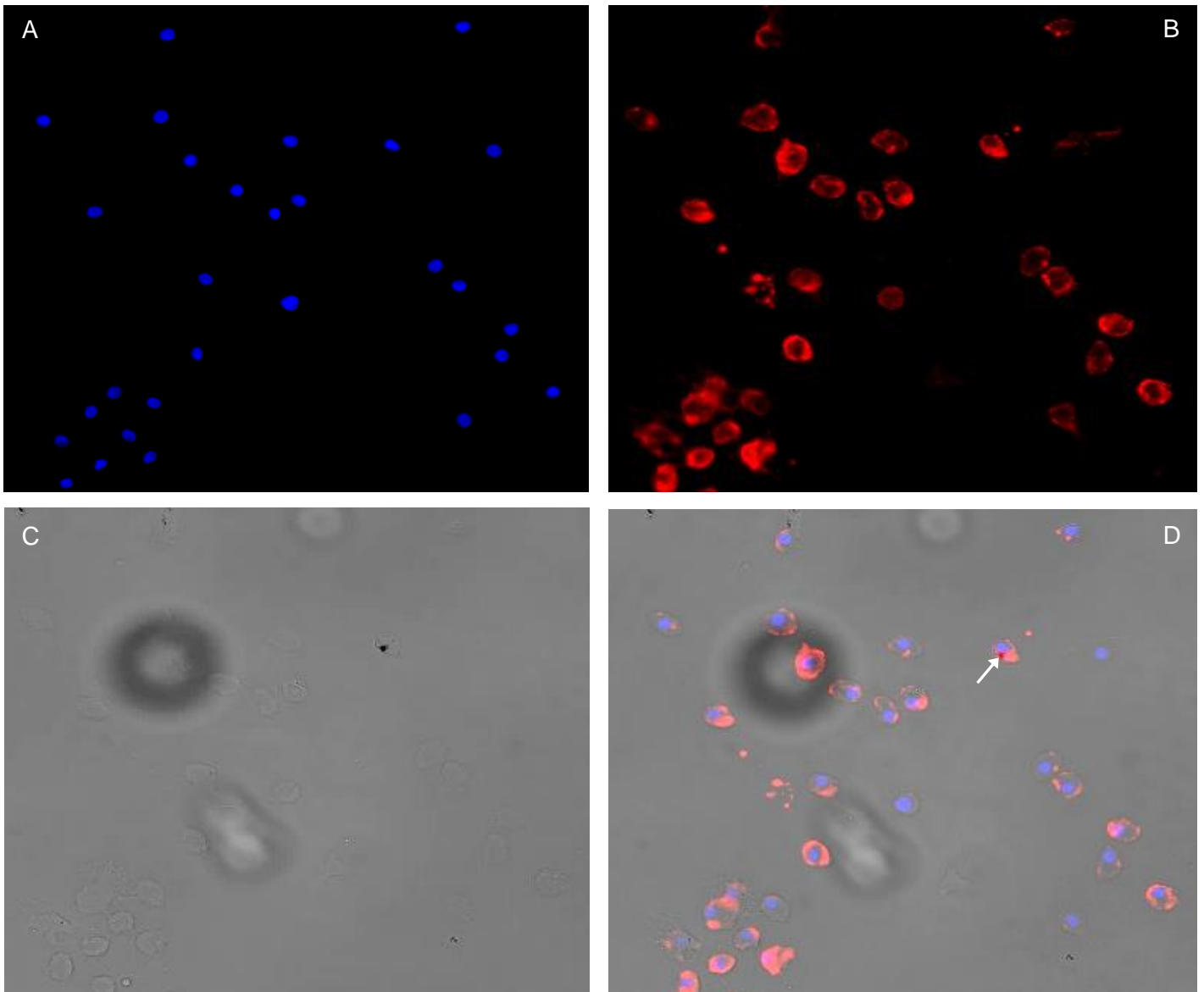


Figure C3.9: Figure showing x40 magnification fluorescent images of hemocytes, extracted from GM larvae of the Cyclophosphamide + 60nm AuNP condition. (A), shows the blue channel, with HOECHST 33342 stained dsDNA identifying the nuclei. (B), shows the red channel, where the fluorescent lectin WGA (labelled with Alexa 546) stained the glycoproteins on the plasma membrane. (C), shows the bright field channel, where 60nm AuNPs that have been taken up by larval hemocytes are shown. (D), shows an overlay image of all the channels and NP uptake by hemocytes are outlined by white arrows.

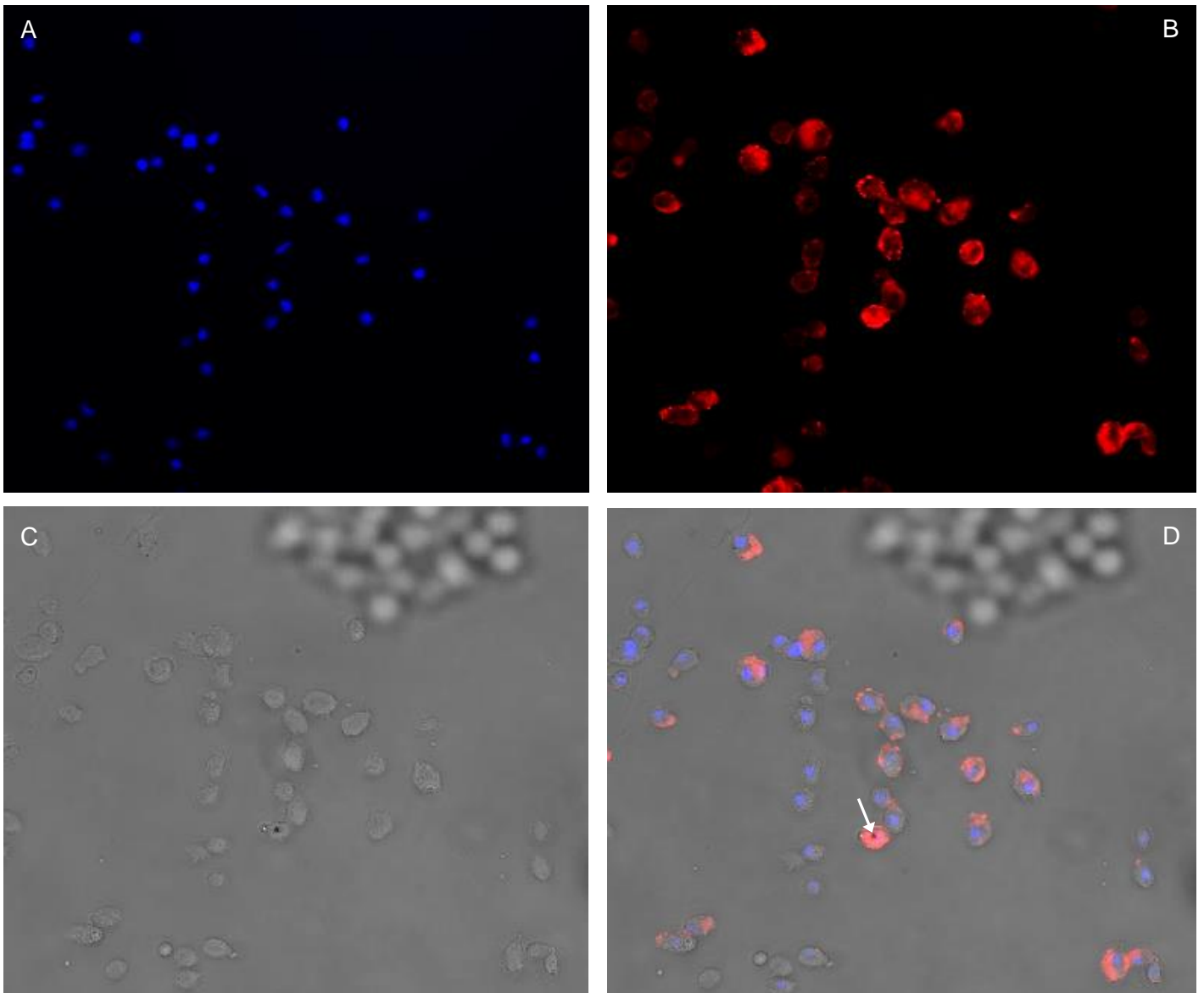


Figure C3.10: Figure showing x40 magnification fluorescent images of hemocytes, extracted from GM larvae of the Cyclophosphamide + 100nm AuNP condition. (A), shows the blue channel, with HOECHST 33342 stained dsDNA identifying the nuclei. (B), shows the red channel, where the fluorescent lectin WGA (labelled with Alexa 546) stained the glycoproteins on the plasma membrane. (C), shows the bright field channel, where 100nm AuNPs that have been taken up by larval hemocytes are shown. (D), shows an overlay image of all the channels and NP uptake by hemocytes are outlined by white arrows.